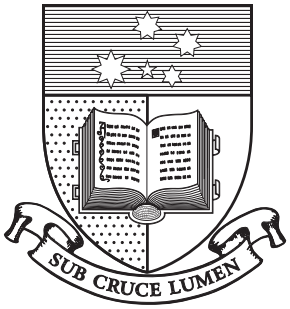

UNREINFORCED MASONRY WALLS SUBJECTED TO OUT-OF-PLANE SEISMIC ACTIONS

JAROSLAV VACULIK

A thesis submitted to

The University of Adelaide
School of Civil, Environmental & Mining Engineering

in fulfilment of the requirements for the degree of
Doctor of Philosophy

April, 2012.

Part III

APPENDICES

Appendix A

MATERIAL TESTING

Abstract

This appendix reports the methods and detailed results of material tests performed as part of the experimental studies in Chapters 2 and 3.

A.1 INTRODUCTION

As part of the quasistatic and dynamic experimental tests reported in Chapters 2 and 3, complimentary tests on small-sized masonry specimens were conducted in order to quantify values of key material properties. The main engineering parameters of interest were:

- Flexural tensile strength of the masonry, f_{mt} (Section A.2).
- Lateral modulus of rupture of the brick units, f_{ut} (Section A.3).
- Unconfined compressive strength of the masonry, f_{mc} (Section A.4).
- Young's modulus of elasticity of the brick units (E_u), mortar joints (E_j), and overall masonry (E_m) (Section A.4).
- Coefficient of friction along the masonry bond, μ_m (Section A.5).

The material tests reported herein were conducted on masonry specimens constructed with two different types of units: (i) perforated full-sized brick units (Figure 2.1) with dimensions $230 \times 110 \times 76$ mm and 10 mm mortar joints, as used

Table A.1: Types of material properties determined by experimental testing.

Material property	Full-sized perforated units (Quasistatic test study)	Half-sized solid units (Dynamic test study)
f_{mt}	Yes	Yes
f_{ut}	Yes	No
f_{mc}	Yes	Yes
E_m, E_u, E_j	Yes	Yes
μ_m	No	Yes

in the quasistatic test study; and (ii) solid half-sized brick units with dimensions $110 \times 50 \times 39$ mm and 5 mm mortar joints, as used in the dynamic test study. Table A.1 summarises the properties determined for the respective types of brickwork. Mean values of the material properties are presented in Sections 2.3.1 and 3.2.1. The purpose of this appendix is to report these results, including the test methods, in greater detail.

A.2 FLEXURAL TENSILE STRENGTH

A.2.1 Test Method

The flexural tensile strength of the masonry, f_{mt}, was determined using the bond wrench method as prescribed by AS 3700. The test arrangement (Figure A.1) consisted of a clamp and vice system used to secure the test specimen, and the bond wrench fastened to the top unit in the specimen. The test was performed by manually applying a downward force on the wrench handle using one's hands, thus subjecting the joint to a bending moment in addition to a small compressive axial load. The load was slowly increased until failure of the bond. A calibrated strain gauge on the horizontal arm of the wrench conveyed the load applied to the handle to the data acquisition system. For each joint tested, the load to cause failure was recorded and used to calculate the corresponding f_{mt} based on the procedure outlined in Section A.2.2.

The bond wrench used for the full-sized brick specimens (Figure A.1) was an AS 3700 compliant wrench which had already been used in previous experimental studies [*Doherty*, 2000; *Willis*, 2004]. The wrench used for the half-sized brick specimens was designed according to AS 3700 specifically for this test study. Its specifications are shown by Figure A.2.

In both the quasistatic and dynamic test studies, a total of 12 joints were tested for every batch of mortar used in constructing the main test walls. Two types of test specimens were used: five-unit masonry prisms (Figure A.3a), and (ii) masonry

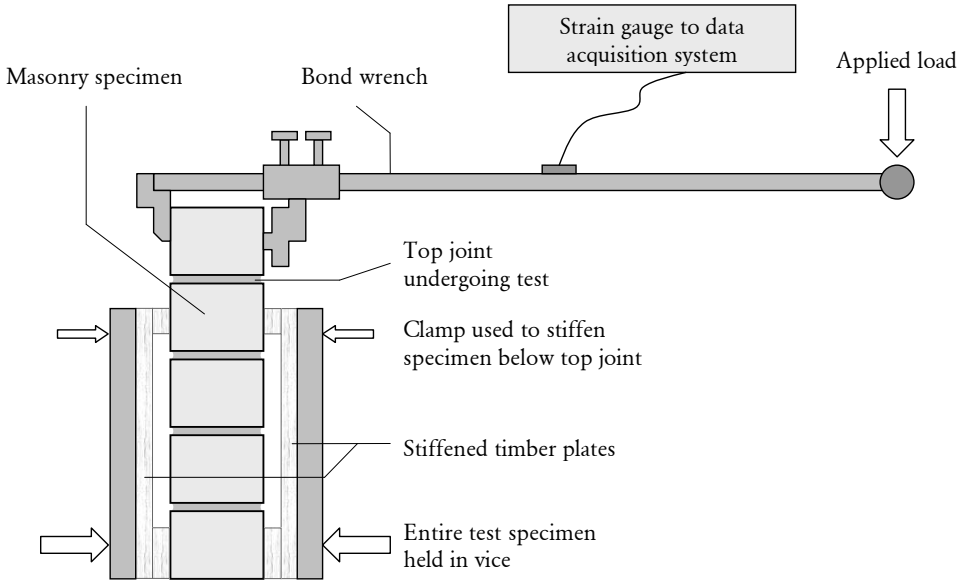

Figure A.1: Bond wrench test arrangement, shown for the five-brick prism specimens constructed using full-sized brick units.

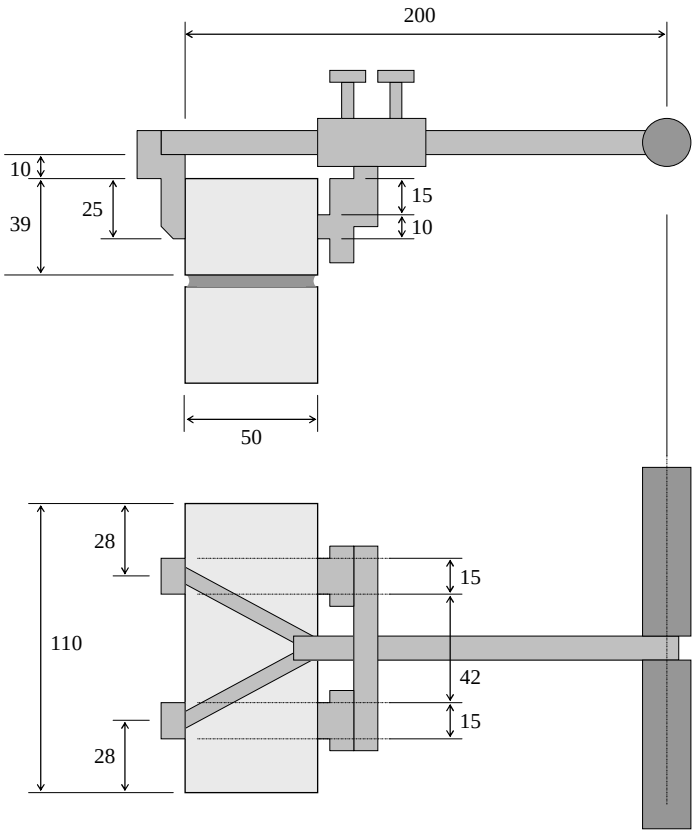

Figure A.2: Bond wrench designed specifically for the half-sized brick units used in the dynamic test study. Dimensions are in millimetres.

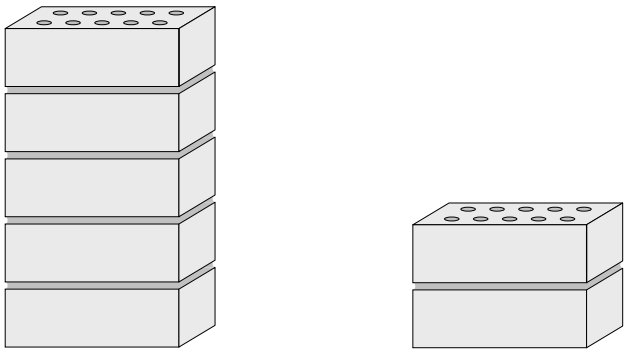

(a) Five-brick prism **(b)** Couplet

Figure A.3: Types of masonry specimens used for bond wrench tests.

couplets (Figure A.3b). The purpose of the prisms was to reduce the wastage of brick units, since a prism would yield four tests from five bricks, as opposed to a couplet yielding only a single test from two bricks. In both types of specimens, the mortar joint was made to a thickness equal to that used in the construction of the main panels, which was 10 mm for the full-sized units in the quasistatic test study and 5 mm for the half-sized units in the dynamic test study.

The prism specimens were used initially, including for mortar batches from walls S1–S6. During tests on prisms, steel-stiffened timber plates were clamped onto the brick units below the top joint, in order to isolate the top joint and protect the joints below by providing additional flexural stiffness (Figure A.1). It was found, however, that this arrangement was not always successful in preventing premature failure of one the other joints, and as a consequence, there were numerous joints for which no data was recorded. Therefore, after testing the prism specimens from walls S1–S6, this arrangement was abolished, and only couplets were used for the remaining walls S7–S8 and D1–D5.

A.2.2 Calculation of f_{mt}

Calculation of f_{mt} assumes that at the point of failure, the section along the bonded interface exhibits a linear stress profile and that failure occurs due to the stress in the extreme tensile fibre exceeding the tensile strength. By accounting for the induced stresses due to the combined applied moment and axial load, the tensile bond strength is calculated as

$$f_{mt} = \frac{M}{Z} - \frac{N}{A}, \tag{A.1}$$

where M is the applied moment at failure, N is the applied axial load at failure, Z is the elastic section modulus of the bedded area, and A is the bedded area.

A.2.3 Results for Perforated Full-Sized Brick Specimens

Typical examples of the observed bond failure for the perforated brick unit specimens are shown by Figure A.4. Failure occurred predominantly by separation of the bond interface between the brick unit and mortar. In some specimens, the failed surface was confined to one brick unit with the entirety of the mortar remaining adhered to the second unit, whilst in others, the failure surface cut across from one unit to the other. Furthermore, since the mortar had a tendency to key into the perforations in the brick units; in order for the joint to fail, this mortar had to either break or pull out of the holes. Typically, a combination of both of these modes was

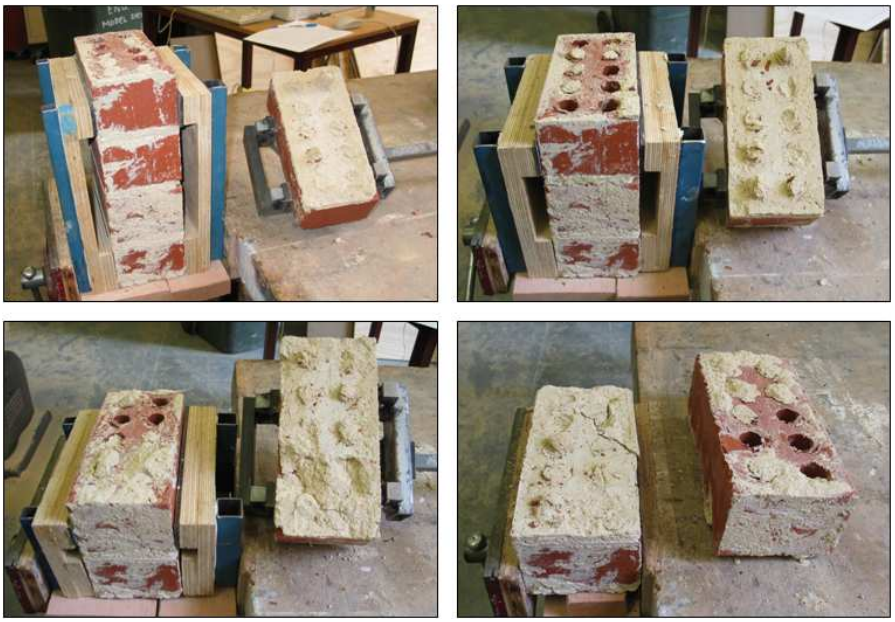

Figure A.4: Typical bond failure of the full-sized perforated brick specimens during bond wrench test.

observed, as shown by the examples in Figure A.4. The interlock effects between the brick units and mortar are generally expected to have a beneficial effect on f_{mt}.

The values of f_{mt} determined from the bond wrench tests are provided in Table A.2, with three different approaches used to group the data. For each approach, the table provides the number of data points n, mean value of f_{mt}, and the coefficient of variation (CoV). Figure A.5 also shows the measured f_{mt} data points graphically for each wall.

The methods of data grouping used in Table A.2 are as follows.

1. The first approach (columns 1–5) is based on individual bond data grouped by batches. Each set consists of approximately 12 data points depending on the number of joints successfully tested from each batch.[1]

2. The second approach (columns 5–8) is based on individual bond data grouped by walls. The number of data points corresponds to the number of joints tested from each wall, which ranged between 59 and 83. Further statistical tests are conducted on the pooled data sets in Section 5.3.1, including probability distribution fitting.

3. The third approach (columns 9–11) is based on batch mean values grouped by walls. Hence, in this approach, each constituent batch is given the same

[1]Batches 4.6 and 6.1 have additional data points, because extra test specimens were constructed by mistake.

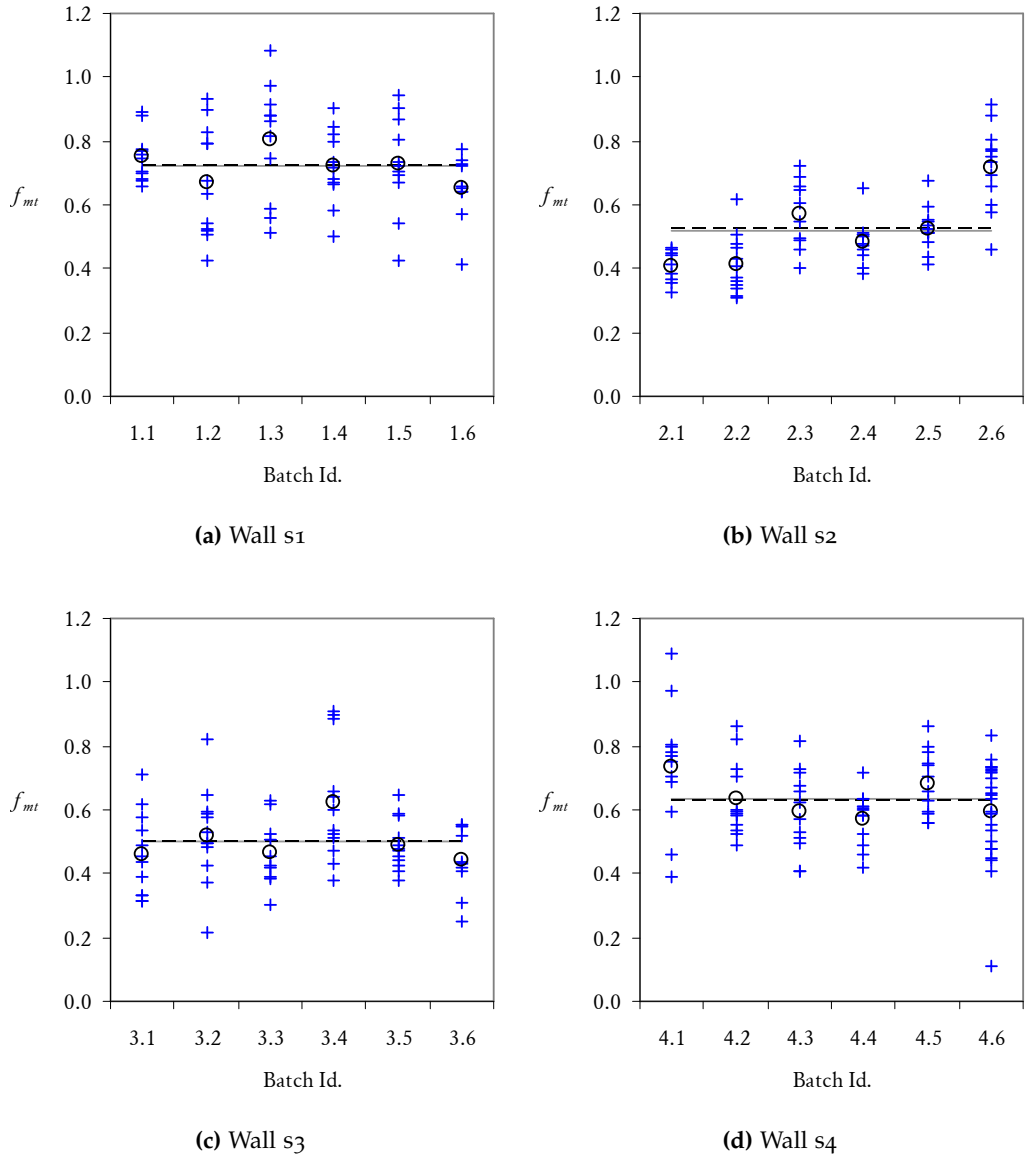

(a) Wall s1 **(b)** Wall s2

(c) Wall s3 **(d)** Wall s4

Figure A.5: Measured f_{mt} data (in MPa) for perforated full-sized unit specimens used in the quasistatic test study. Results are shown for the individual mortar batches used in the construction of each wall. Blue crosses (+) show individual joint data; black circles (○) show mean values for each batch; solid gray line (——) shows the average f_{mt} for the wall, calculated as the mean of the batch averages; and dashed black line (----) shows the average f_{mt} for the wall, calculated as the mean of the individual bond data.

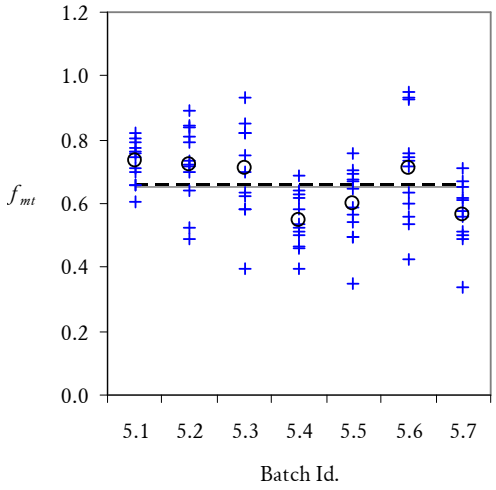

(e) Wall s5

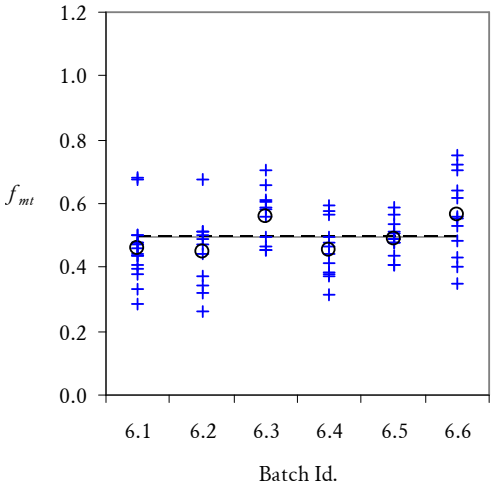

(f) Wall s6

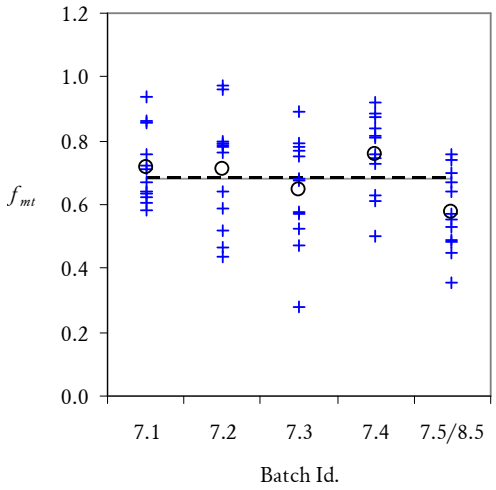

(g) Wall s7

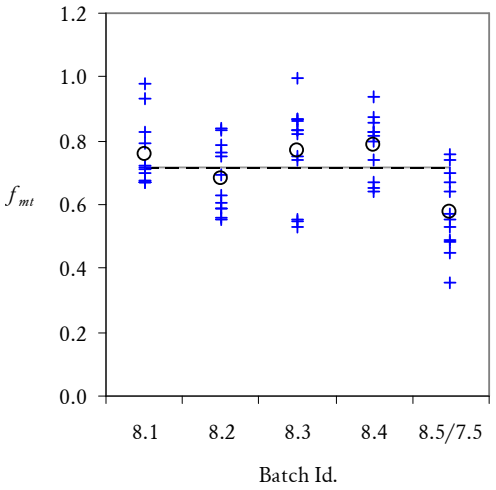

(h) Wall s8

Figure A.5: (cont'd).

Table A.2: Results of bond wrench tests on full-sized perforated brick units used in the quasistatic test study.

Batch	Sample consisting of bond data within batch				Wall	Sample consisting of pooled bond data			Sample consisting of batch averages		
	n	mean f_{mt} [MPa]	CoV	t-test P-value		n	mean f_{mt} [MPa]	CoV	n	mean f_{mt} [MPa]	CoV
1.1	11	0.749	0.10	0.53	s1	66	0.721	0.20	6	0.721	0.07
1.2	12	0.672	0.25	0.29							
1.3	11	0.802	0.23	0.10							
1.4	11	0.720	0.16	0.98							
1.5	11	0.728	0.21	0.88							
1.6	10	0.654	0.16	0.16							
2.1	9	0.407	0.12	0.02	s2	66	0.524	0.27	6	0.520	0.22
2.2	12	0.413	0.22	0.01							
2.3	10	0.571	0.19	0.31							
2.4	11	0.483	0.14	0.35							
2.5	12	0.526	0.13	0.95							
2.6	12	0.718	0.18	0.00							
3.1	12	0.459	0.29	0.33	s3	68	0.502	0.28	6	0.499	0.13
3.2	12	0.520	0.29	0.69							
3.3	10	0.465	0.22	0.43							
3.4	12	0.621	0.30	0.01							
3.5	12	0.489	0.16	0.76							
3.6	10	0.443	0.24	0.20							
4.1	12	0.733	0.26	0.03	s4	81	0.636	0.21	6	0.639	0.09
4.2	12	0.632	0.19	0.95							
4.3	12	0.595	0.22	0.44							
4.4	12	0.572	0.15	0.19							
4.5	12	0.684	0.15	0.21							
4.6	22	0.616	0.20	0.31							
5.1	12	0.732	0.09	0.07	s5	83	0.656	0.21	7	0.655	0.12
5.2	12	0.725	0.17	0.11							
5.3	12	0.709	0.21	0.23							
5.4	12	0.546	0.16	0.01							
5.5	12	0.598	0.19	0.17							
5.6	12	0.710	0.24	0.23							
5.7	11	0.567	0.19	0.04							
6.1	16	0.460	0.22	0.25	s6	74	0.494	0.22	6	0.496	0.11
6.2	11	0.446	0.26	0.17							
6.3	11	0.562	0.15	0.05							
6.4	12	0.457	0.19	0.25							
6.5	12	0.492	0.11	0.93							
6.6	12	0.562	0.23	0.05							
7.1	12	0.718	0.16	0.45	s7	60	0.682	0.23	5	0.682	0.10
7.2	12	0.709	0.25	0.59							
7.3	12	0.647	0.26	0.48							
7.4	12	0.760	0.17	0.11							
7.5/8.5	12	0.578	0.22	0.03							
8.1	12	0.756	0.14	0.31	s8	59	0.713	0.19	5	0.714	0.12
8.2	12	0.683	0.16	0.49							
8.3	12	0.767	0.20	0.23							
8.4	11	0.786	0.12	0.10							
8.5/7.5	12	0.578	0.22	0.00							

weighting toward the mean f_{mt} value for the wall, regardless of the number of joints tested. The number of data points corresponds to the number of batches used in a particular wall, which ranged between 5 and 7. The mean values of f_{mt} for each wall determined using this method are reported in Chapter 2 (Table 2.3) and are further used in the analytical studies reported in Section 4.5. It is worth noting that the difference between the mean values of f_{mt} calculated using this method and the second approach is minor (less than 1%).

Student's t-test (two-sample with assumed equal variance) was performed to assess whether the data for individual batches of mortar (first data grouping approach) could be considered to have the same underlying distribution as the data when it was pooled for the parent wall (second data grouping approach). The calculated P-values are listed in the 5th column of Table A.2. These represent the probability that the batch data follows the same distribution as the pooled data. By adopting a fairly conservative P-value of 0.25 as the limit of statistical significance, the results indicate that the difference between the distribution of the batch data and the pooled wall data is statistically significant (P-value < 0.25) in approximately 50% of the batches. This suggests that the bond data for the individual batches should not be pooled together into a single data set for the overall wall, because the mean values of the batches are statistically different. However, it can likewise be argued that since inter-batch variability would naturally occur in practice, and calculation of the strength of a wall tends to be based on a single value of f_{mt}, pooling of the individual batch data sets in order to calculate a mean value of f_{mt} to use for analysis, is also valid.

On the basis of the mean-of-batch-average approach, the mean bond strength for the different walls ranges between 0.496 and 0.721 MPa. The CoV in the different walls ranges between 0.19 and 0.28 based on the pooled bond data. These values are considered to be typical of the 1:2:9 (cement, lime, sand) mortar mix used.

A.2.4 Results for Solid Half-Sized Brick Specimens

Bond failure of solid half-sized brick couplet specimens consistently occurred such that the failure plane cut between the mortar and one unit in the couplet, leaving the mortar adhered entirely to the second unit. This observation is in contrast to the type of failure observed for the perforated unit specimens (Figure A.4), where, due to the interlock between the mortar and the brick unit, the failure surface had a tendency to cut through the mortar itself. Because of the lack of interlock between the solid units and the adjoining mortar, the bond strength is expected to be lower

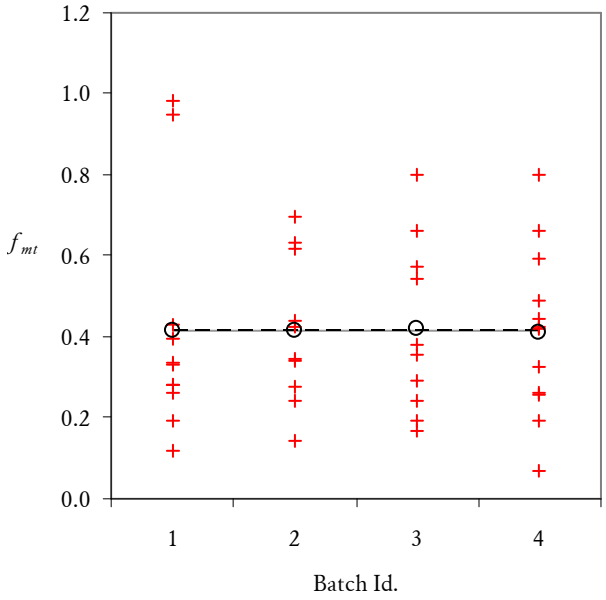

Figure A.6: Measured f_{mt} data in (in MPa) for solid half-sized unit specimens used in the dynamic test study. Data is shown for the 4 batches of mortar which were used to construct all of the five walls. Red crosses (+) show individual joint data; black circles (○) show mean values for each batch; solid gray line (——) shows the average f_{mt} for the wall, calculated as the mean of the batch averages; and dashed black line (----) shows the average f_{mt} for the wall, calculated as the mean of the individual bond data.

Table A.3: Results of bond wrench tests on the half-sized solid brick units used from the dynamic test study.

Batch	Sample consisting of bond data within batch				Sample consisting of pooled bond data			Sample consisting of batch averages		
	n	mean f_{mt} [MPa]	CoV	t-test P-value	n	mean f_{mt} [MPa]	CoV	n	mean f_{mt} [MPa]	CoV
1	11	0.414	0.69	0.99	43	0.415	0.53	4	0.416	0.01
2	10	0.416	0.44	0.99						
3	10	0.421	0.51	0.94						
4	12	0.411	0.51	0.95						

than for the perforated units. Indeed, the results show this to be the case.

Figure A.6 graphs the data for the four batches of mortar tested. The associated results are provided in Table A.3 for each of the three methods of data grouping discussed in Section A.2.3. The mean values of f_{mt} for the four batches all range between 0.411 and 0.421 MPa. The t-test was used to assess whether the four batches can be considered to all originate from the same batch. The resulting P-values of the t-test are provided in the 5th column of Table A.3. That the P-values for all four batches are greater than 0.9 suggests that they can be treated as originating from the same batch. Pooling the data from the individual batches

together gives a single data set consisting of 43 data points, with a mean f_{mt} of 0.415 MPa and a CoV of 0.53. Therefore, not only is the bond strength of these units lower than for the perforated units (Section A.2.3), but it also has higher variability.

A.3 LATERAL MODULUS OF RUPTURE

A.3.1 Test Method

The lateral modulus of rupture of the brick units, f_{ut}, was determined using a four point bending test as illustrated by Figure A.7. A single test specimen consisted of three units glue bonded together end-to-end to form a beam. With the specimen resting on simple supports at either end, two point loads of equal magnitude were applied onto the central unit, generating a region of constant bending moment and zero shear force along the central unit. The applied load was increased until failure. A total of 12 beam specimens were tested using the perforated brick units from the quasistatic test study.

A.3.2 Calculation of f_{ut}

Based on the assumptions that the section exhibits a linear elastic profile at the instance of failure and that failure occurs when the tensile stress in the extreme fibre reaches the tensile capacity, the lateral modulus of rupture is calculated as

$$f_{ut} = \frac{M}{Z}, \tag{A.2}$$

where Z is the elastic section modulus of the beam (equal to $h_u t_u^2/6$), and M is the applied moment at failure. Using statics, M is calculated from the applied point load P at failure (Figure A.7) as

$$M = \frac{P\,L_x}{2}, \tag{A.3}$$

where is L_x is the horizontal distance between the support and loading point on the beam (150 mm in these tests).

A.3.3 Results for Perforated Full-Sized Bricks

In each of the 12 beam specimens, failure occurred somewhere within the maximum moment region in the central unit, such that the failure plane cut across the perforations in the brick unit. An example of typical failure is shown in Figure A.7.

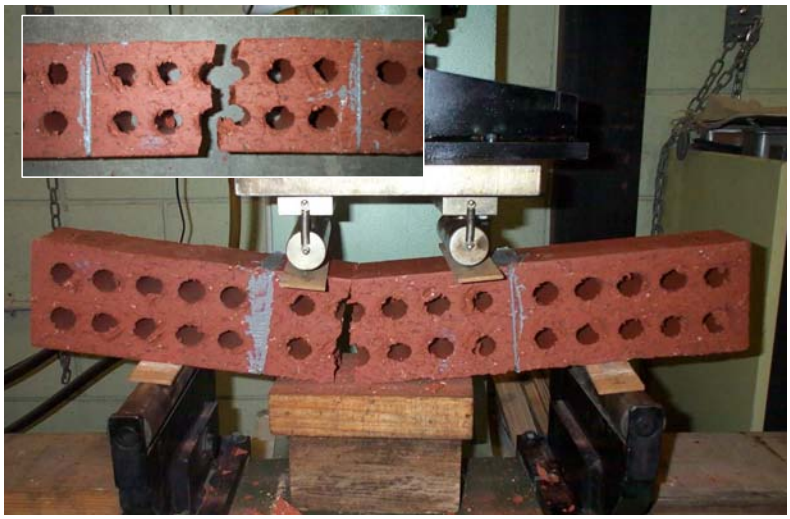

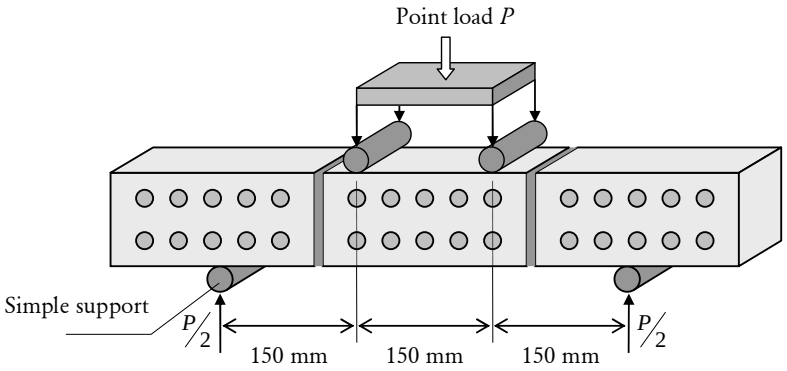

Figure A.7: Four point bending test used to determine the lateral modulus of rupture, including typical failure of the specimens.

The measured f_{ut} data for the 12 specimens (Figure A.8) has a mean value of 3.55 MPa and a CoV of 0.27.

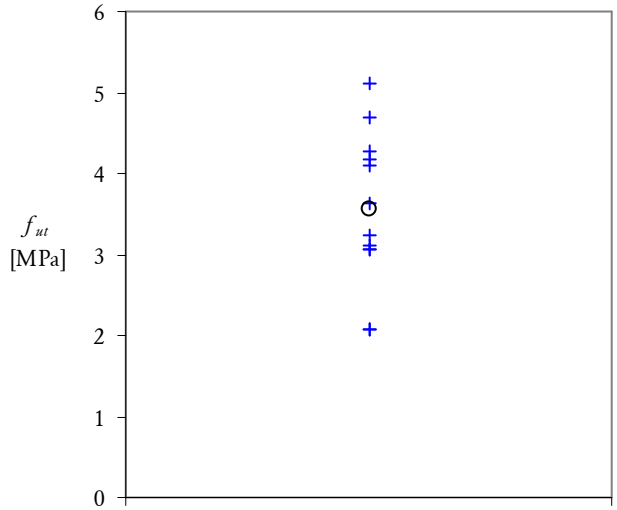

Figure A.8: Measured f_{ut} data (in MPa) for the perforated full-sized bricks units. Blue crosses (+) show individual data points; black circle (○) indicates the mean value.

A.4 COMPRESSION TESTS

Compression tests were performed to determine several properties, including the compressive strength of the masonry (f_{mc}); and the Young's modulus of elasticity of the brick units (E_u), mortar joints (E_j), and overall masonry (E_m).

A.4.1 Test Method

The test arrangements used for the full-sized and half-sized brick specimens were slightly different; hence, they will be discussed separately.

Arrangement Used on Full-Sized Brick Specimens

For the full-sized brickwork from the quasistatic tests, the specimens were identical to the 5-brick prisms used in the bond wrench tests (Figure A.3a). A single specimen was built and tested for each batch of mortar. The compression test arrangement is illustrated in Figure A.9. For the purpose of quantifying the Young's modulus of elasticity, deflections were measured using Demec gauges at two locations along the specimen: an 8-inch gauge, used to measure deformations across a combination of bricks and mortar joints on one side of the specimen (spanning across two mortar joints); and a 2-inch gauge, positioned on the opposite side of the prism and used directly to measure the deformation along on the central brick. Note that since the Demec points for the 8-inch gauge could not be positioned precisely at the centre

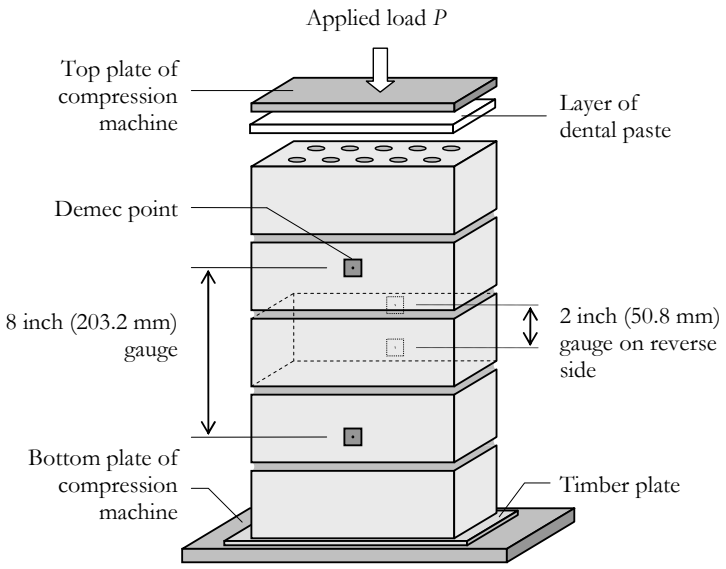

Figure A.9: Compression test arrangement used for full-sized brick specimens.

points of the bricks, the gauge did not span a representative proportion of bricks and mortar joints; however, this was corrected in the subsequent calculation of the Young's moduli using the procedure outlined in Section A.4.3.

The specimens were tested using a mechanical compression rig capable of imposing loads up to 1000 kN. A thin timber plate was placed between the test specimen and the bottom plate of the compression machine. Prior to the application of a load, a moderate quantity of dental paste was spread between the top loading face of the specimen and the top plate of the compression machine, which was left to harden to ensure a uniform distribution of the compressive load. Before taking any deformation measurements, the specimen was subjected to a compressive load of 150 kN (approximately 40% of the ultimate compressive strength) and unloaded back to zero load in order to allow it to settle. The test was performed by applying a compressive load to the specimen at increments of 25 kN up to a maximum load of 150 kN. At each level of compression, the deformations were measured across the 2-inch and 8-inch gauges. The load was then dropped back to zero and the process repeated three times for each test prism. The specimen was then subjected to an increasing compressive load until failure.

Arrangement Used on Half-Sized Brick Specimens

Due to complications with the results obtained from the original compression test arrangement used on the full-sized brick specimens, which are discussed in greater detail in Section A.4.4, a revised arrangement was implemented for tests on the

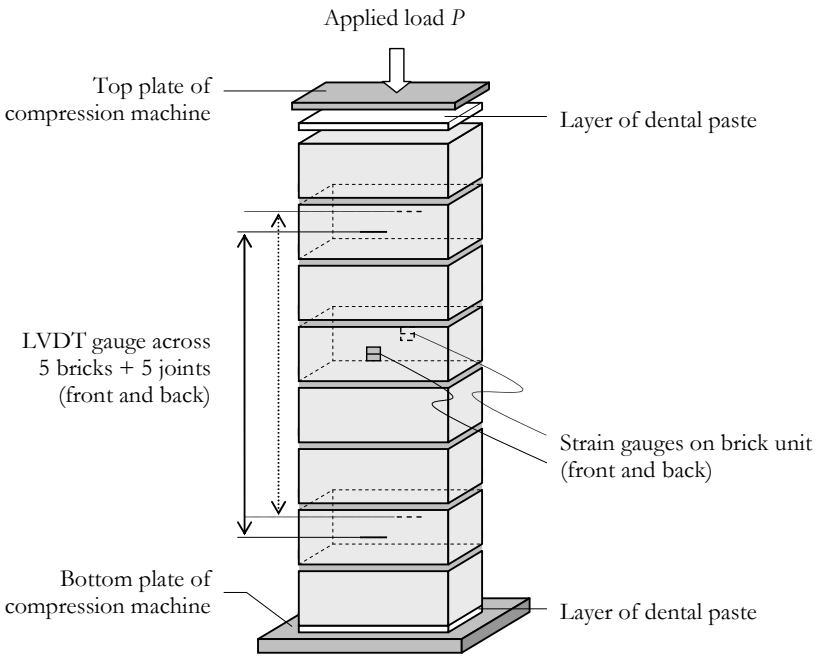

Figure A.10: Compression test arrangement used for half-sized brick specimens.

half-sized brick specimens used in the dynamic test study. The revised arrangement is shown by Figure A.10. Its main improvements over the original setup (Figure A.9) were as follows.

- Deformation along the masonry gauge (bricks + mortar joints) was measured using a linear variable differential transformer (LVDT) displacement transducer and deformation along the brick as measured using a strain gauge. In addition to this instrumentation being far more accurate than the Demec gauges used in the original setup, because the data was recorded automatically by a data acquisition system it meant that tests could be performed much quicker. A further advantage of using LVDTs was that the length of masonry over which deformation was measured was designed to span precisely between the centres of the (second and seventh) bricks, in contrast to the predefined distance of the 8-inch Demec gauge used in the original tests.

- Deformation measurements were made on both sides of the specimen using separate LVDTs and strain gauges. Subsequent averaging of the deformation measurements on the two opposite sides was performed to remove any effects of undesired bending within the specimen. It is believed that bending may have significantly affected the results obtained using the original test setup, as discussed in Section A.4.4.

- As the half-sized brick specimens comprised eight-brick prisms, the gauge measuring deformation spanned across five bricks and five mortar joints. This is in contrast to the original setup, where the gauge spanned across only two bricks and two joints.

Another minor aspect of the revised test arrangement was that dental paste was applied above and below the specimen and the compression machine in order to facilitate a uniform distribution of the applied pressure.

The test was conducted by slowly applying a compressive force to the specimen up to 35 kN (approximately 25% of the failure load), during which data was recorded by a data acquisition system. The load was slowly released and reapplied for a total of four repetitions. Of these, only the last three were used in calculating the Young's moduli. Finally the specimen was subjected to an increasing load until failure.

A.4.2 Calculation of f_{mc}

The unconfined compressive strength of the masonry, f_{mc}, was determined in accordance with AS 3700 as

$$f_{mc} = k_a \left(\frac{F_{sp}}{A_d} \right), \tag{A.4}$$

where k_a is a factor obtained from the code, F_{sp} is the applied compressive force at failure, and A_d is the bedded area of the specimen. The factor k_a is dependent on the height/thickness aspect ratio of the specimen and accounts for the effects of horizontal confinement of the specimen due to platen restraint. Based on the code, k_a was taken as 0.911 for the full-sized 5-brick prisms and 1.0 for the half-sized eight-brick prisms.

A.4.3 Calculation of E_u, E_j and E_m

The steps to calculate the Young's modulus for the brick units (E_u), mortar joints (E_j), and the masonry consisting of bricks and mortar joints (E_m), are outlined as follows:

1. The recorded data was converted from its original format to stress versus strain (σ-ε).

2. For both gauges within a specimen, a linear regression was fitted to the σ-ε data during each push to determine the respective Young's moduli. The

Young's modulus for each gauge was then taken as the average of the three pushes. For the i^{th} specimen, let us denote the value measured across the brick gauge as $(E_u)_i$, and the value measured across the masonry gauge as $(E_{mg})_i$.

From the resulting data, the mean value of the Young's modulus for the brick units, $\widehat{E_u}$, was calculated as the average value of $(E_u)_i$ for the tested specimens:

$$\widehat{E_u} = \frac{1}{n}\sum_{i=1}^{n}(E_u)_i. \tag{A.5}$$

Similarly, this data set was used to calculate other statistical properties for E_u, including the CoV.

Calculation of the mean Young's modulus of the masonry, $\widehat{E_m}$, however, was not as straightforward as simply averaging the measured $(E_{mg})_i$ for all specimens, for two reasons: Firstly, the stiffness of the brick $(E_u)_i$ measured in the i^{th} specimen may have varied significantly from the mean value $\widehat{E_u}$ due to the random variability in E_u, which will influence the stiffness $(E_{mg})_i$ recorded across the masonry gauge. Secondly, in the case of the full-sized brick specimens, the Demec gauge measuring the deformation across the masonry was not able to span between the centres of the bricks;[2] therefore, the relative proportions of brick and mortar captured by the masonry gauge were not representative of the true relative proportions of these constituents within the masonry.

To correct for these effects, a back-calculation process was firstly used to calculate the Young's modulus of the mortar joints, $(E_j)_i$, for the i^{th} specimen (according to Step 3). Then, a forward-calculation process was used to determine the Young's modulus of the masonry, $(E_m)_i$, corresponding to the i^{th} specimen (as per Step 4).

It can be shown that for a member composed of multiple elements a, b, c, ... joined in series, the relationship between the overall member's apparent Young's modulus E_{tot} and the Young's moduli E_a, E_b, E_c, ... of the components is

$$\frac{1}{E_{\text{tot}}} = \frac{r_a}{E_a} + \frac{r_b}{E_b} + \frac{r_c}{E_c} + \ldots, \tag{A.6}$$

where r_a, r_b, r_c, ... are the respective proportions of each component element within the overall member. These must all add up to unity, such that

$$1 = r_a + r_b + r_c + \ldots. \tag{A.7}$$

[2] This was not an issue for the half-sized brickwork due to the different test arrangement used.

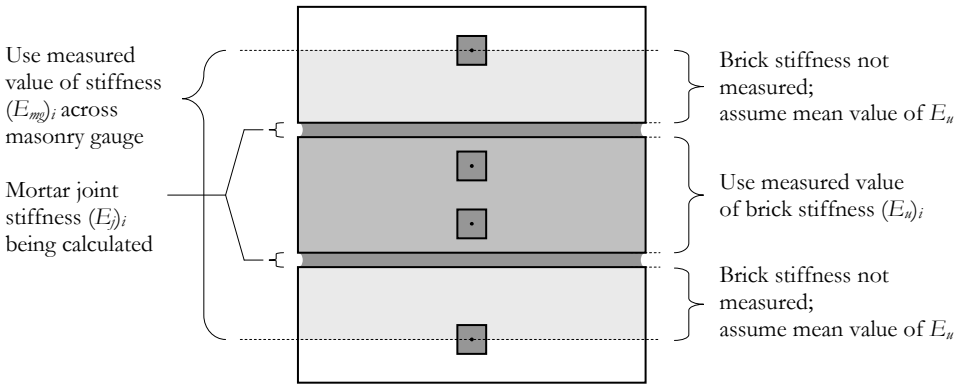

Figure A.11: Information used in back-calculation of the Young's modulus of the mortar joints $(E_j)_i$ for the i^{th} specimen. Shown for the full-size brick specimen test arrangement.

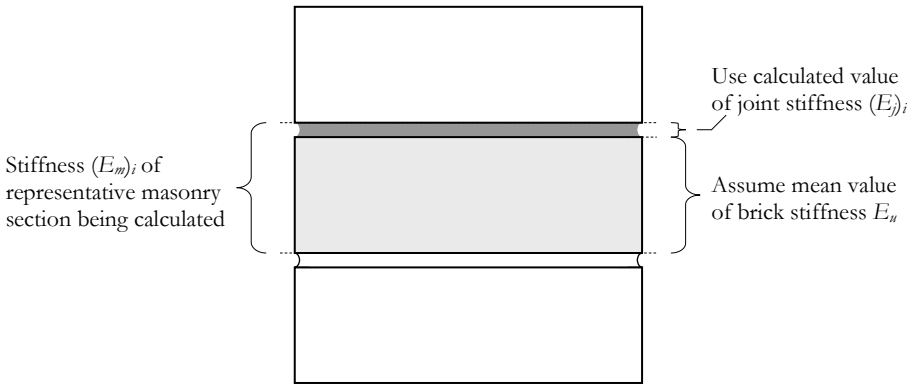

Figure A.12: Information used in forward-calculation of the representative Young's modulus of the masonry, $(E_m)_i$, for the i^{th} specimen.

Equations (A.6) and (A.7) form the basis for remaining steps in the calculation procedure, outlined as follows:

3. The Young's modulus of the mortar joints $(E_j)_i$ in each specimen was then back-calculated. Figure A.11 shows the information assumed during this process. The calculation assumed that the brick along which deformation was measured had the measured value of stiffness $(E_u)_i$, and that the remaining bricks had the mean value $\widehat{E_u}$. Substituting these into the general relationship, Eq. (A.6), and rearranging in terms of $(E_j)_i$ gives

$$(E_j)_i = r_j \left(\frac{1}{(E_{mg})_i} - \frac{r_{u\ \text{known}}}{(E_u)_i} - \frac{r_{u\ \text{unknown}}}{\widehat{E_u}} \right)^{-1}, \tag{A.8}$$

where r_j, $r_{u\ \text{known}}$ and $r_{u\ \text{unknown}}$ are the relative span proportions of the mortar joints, the brick along which deformation was measured, and the bricks for

which deformation was not measured, respectively, within the sample. These must add up to unity:

$$r_j + r_{u\,\text{known}} + r_{u\,\text{unknown}} = 1. \tag{A.9}$$

4. Finally, a forward-calculation was used to determine a representative Young's modulus of the masonry, $(E_m)_i$, for each specimen. Figure A.12 shows the information used in this calculation. It was assumed that for each specimen, all bricks had the mean Young's modulus $\widehat{E_u}$ and that the mortar joints had the Young's modulus $(E_j)_i$ for the i^{th} specimen, as calculated using Step 3. Substituting these into Eq. (A.6) and rearranging in terms of $(E_m)_i$ gives

$$(E_m)_i = \left(\frac{r_u}{\widehat{E_u}} + \frac{r_j}{(E_j)_i} \right)^{-1}, \tag{A.10}$$

where r_u and r_j are the relative proportions of brick and mortar within the masonry, whose sum is unity:

$$r_j + r_u = 1. \tag{A.11}$$

These are calculated as

$$r_u = \frac{h_u}{h_u + t_j}, \qquad \text{and} \qquad r_j = \frac{t_j}{h_u + t_j}, \tag{A.12}$$

where h_u is the height of the brick and t_j is the thickness of the mortar joint. For example, for the full-sized masonry with brick height $h_u = 76\,\text{mm}$ and joint thickness $t_j = 10\,\text{mm}$, we get $r_j = 10/(76+10) = 0.12$ and $r_u = 76/(76+10) = 0.88$.

Once the Young's moduli of the masonry, $(E_m)_i$, and mortar joints, $(E_m)_i$, were calculated for each specimen using Steps 3 and 4, the mean values and CoVs were determined for both E_m and E_j.

A.4.4 Results for Perforated Full-Sized Brick Specimens

Horizontal tensile splitting was the most commonly observed mode of compressive failure, as shown by Figure A.13a. In most instances of splitting failure, the onset of the failure was preceded by a gradual decline in the load resisted by the specimen following the peak load capacity. Less commonly observed was an 'explosive' mode of failure, whereby the specimen failed almost immediately after attaining its ultimate load capacity. This type of failure was typically accompanied by a loud

(a) Splitting failure **(b)** Explosive failure

Figure A.13: Typical compressive failure of perforated full-sized brick specimens.

'explosion' sound from the specimen, due to the sudden release of energy. The remains after such failure are shown by Figure A.13b.

The results for the various properties including E_u, E_j, E_m and f_{mc} are presented in Table A.4 for each batch (specimen), with the mean values for each wall presented in Table A.5. The data points for each individual test are also displayed graphically by Figure A.14.

Student's t-test was used to compare the data for each wall to a global pooled data set, in order to establish whether there was a statistically significant difference between the data for the different walls. The resulting P-values from the t-tests are provided in Table A.5. By adopting a typical statistical significance limit value of 0.25, approximately three out of eight P-values fall below this value for each of the parameters investigated. This indicates that there is a significant difference between the batches from the different walls.

A peculiar result of the t-test is that there appears to be a significant difference between the measured Young's modulus of the bricks (E_u) for specimens originating from the different walls. This should not be the case, since E_u is independent of the mortar surrounding the brick units, and furthermore, all brick units originated from the same batch at manufacture.

A second peculiarity can be seen by comparing the mean values of E_u and E_j in Figures A.14a and A.14b, which show a general trend whereby when one of these values is high, the other is low, and vice versa. This is likely to be due to internal

Table A.4: Material properties determined from compression tests on perforated brick units, with the results organised according to each batch.

Batch	E_u [MPa]	E_j [MPa]	E_m [MPa]	f_{mc} [MPa]
1.1	37,400	448	3,620	15.9
1.2	32,600	447	3,610	17.1
1.3	45,300	307	2,530	17.1
1.4	32,700	417	3,390	16.1
1.5	41,600	333	2,730	18.7
1.6	51,900	399	3,250	21.1
2.1	100,000	187	1,570	10.8
2.2	45,300	272	2,250	12.6
2.3	62,900	248	2,060	11.7
2.4	54,000	233	1,940	12.1
2.5	57,000	259	2,150	15.7
2.6	47,000	429	3,470	18.4
3.1	45,100	335	2,740	17.4
3.1(r)	38,900	445	3,590	12.3
3.2	42,300	307	2,530	16.1
3.3	49,200	351	2,880	14.6
3.4	41,300	662	5,200	18.0
3.5	73,400	267	2,210	12.3
3.6	52,400	249	2,070	15.3
4.1	24,800	969	7,310	17.8
4.2	34,400	776	6,000	15.4
4.3	51,900	469	3,780	20.3
4.4	33,600	466	3,760	14.1
4.5	38,200	620	4,890	16.1
4.6	38,100	1,090	8,120	15.2
4.6(r)	38,500	661	5,190	18.3
5.1	58,100	377	3,070	18.0
5.2	40,800	595	4,710	17.9
5.3	112,000	212	1,770	17.5
5.4	79,300	857	6,560	17.5
5.5	42,700	583	4,620	17.4
5.6	43,600	504	4,040	17.2
5.7	53,200	388	3,160	16.2
6.1	51,300	360	2,950	15.8
6.2	41,900	365	2,990	16.8
6.3	51,400	434	3,520	13.0
6.4	54,300	230	1,920	15.3
6.5	47,900	341	2,800	15.2
6.6	69,300	275	2,280	18.8
7.1	51,700	526	4,210	15.8
7.2	71,900	369	3,020	13.5
7.3	42,700	769	5,950	16.5
7.4	89,900	528	4,220	15.2
7.5/8.5	53,500	402	3,260	14.6
8.1	41,800	331	2,720	16.7
8.2	95,900	338	2,770	15.7
8.3	72,700	370	3,020	17.3
8.4	52,800	433	3,510	16.2
8.5/7.5	53,500	402	3,260	14.6
Mean	52,700	442	3,540	16.0
CoV	0.35	0.44	0.41	0.14

NOTES:
· Extra specimens were mistakenly built for batches 3.1 and 4.6.
· The calculated mean and CoV values do not double count batch 7.5/8.5, which was shared between walls s7 and s8.

Table A.5: Material properties determined from compression tests on perforated brick units, with the results organised according to each wall. The mean and CoV values are calculated from the individual mortar batches used in each wall. Results are also provided for a *t*-test examining whether there is a statistically significant difference between the batches in a particular wall and a pooled batch data set. The P-value represents the probability that the two data sets have the same distribution.

Wall	E_u			E_j			E_m			f_{mc}		
	Mean [MPa]	CoV	*t*-test P-value	Mean [MPa]	CoV	*t*-test P-value	Mean [MPa]	CoV	*t*-test P-value	Mean [MPa]	CoV	*t*-test P-value
s1	40,300	0.19	0.110	392	0.15	0.538	3,190	0.14	0.560	17.6	0.11	0.088
s2	61,100	0.33	0.303	271	0.30	0.041	2,240	0.29	0.035	13.6	0.21	0.016
s3	49,000	0.24	0.607	374	0.38	0.378	3,030	0.36	0.377	15.1	0.15	0.328
s4	37,100	0.22	0.032	722	0.33	0.001	5,580	0.30	0.001	16.8	0.13	0.405
s5	61,400	0.42	0.273	502	0.41	0.459	3,990	0.38	0.446	17.4	0.03	0.105
s6	52,700	0.17	0.999	335	0.22	0.192	2,740	0.21	0.189	15.8	0.12	0.828
s7	62,000	0.31	0.291	519	0.30	0.407	4,130	0.28	0.381	15.1	0.07	0.375
s8	63,300	0.34	0.230	375	0.11	0.451	3,060	0.11	0.464	16.1	0.06	0.918
Mean	53,300			436			3,490			15.9		
CoV	0.19			0.32			0.30			0.08		

NOTES:
· Extra specimens were mistakenly built for batches 3.1 and 4.6. Their results are also included in the statistical analyses.
· The calculated mean and CoV values, as well as the pooled sample in the *t*-test, do not double count batch 7.5/8.5, which was shared between walls s7 and s8.

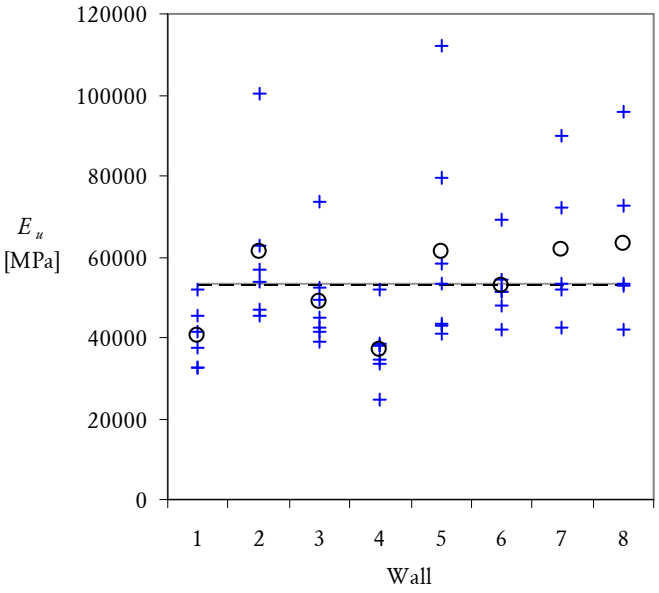

(a) Young's modulus of elasticity of the brick units, E_u.

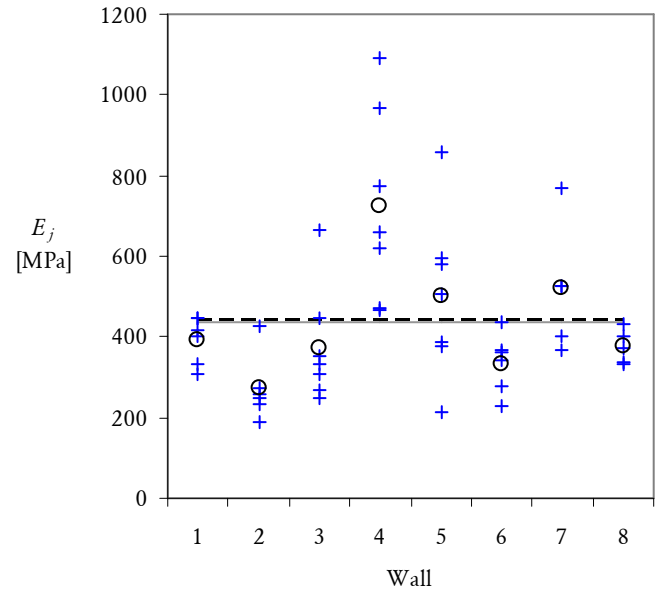

(b) Young's modulus of elasticity of the mortar joints, E_j.

Figure A.14: Material property data determined from compression tests on full-sized perforated unit specimens. Blue crosses (+) indicate data points for the different batches; black circles (○) show the mean values for each wall; solid gray line (——) shows the average value for all walls calculated as the mean of the wall averages; and dashed black line (----) shows the average value for all walls calculated as the mean of the individual batch data.

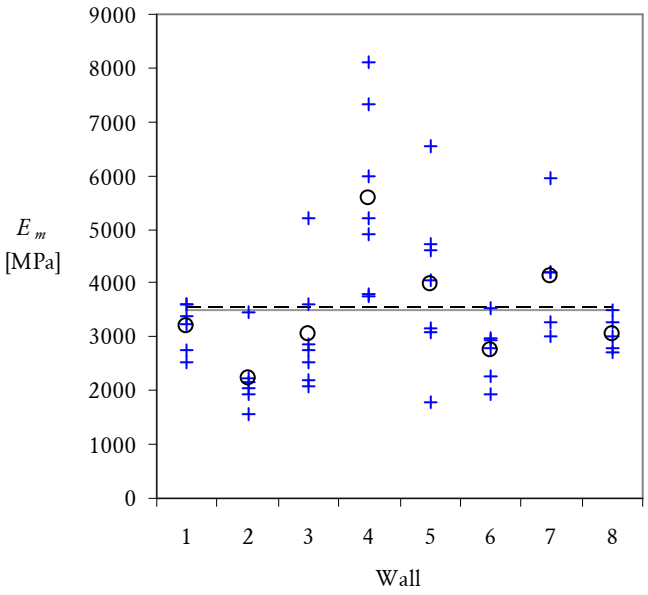

(c) Young's modulus of elasticity of the masonry, E_m.

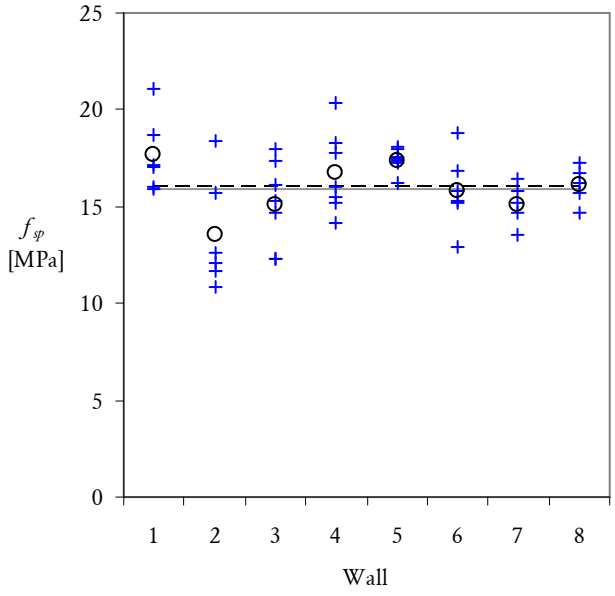

(d) Unconfined compressive strength of the masonry, f_{mc}.

Figure A.14: (cont'd).

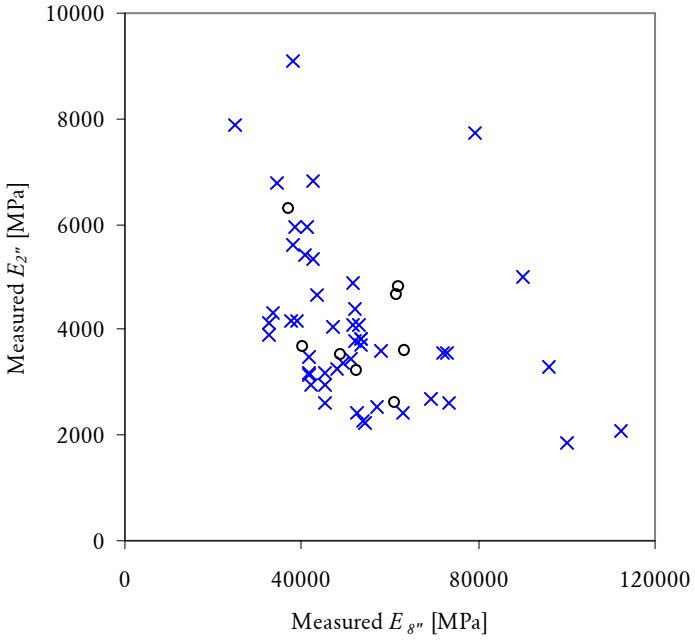

Figure A.15: Relationship between the measured Young's moduli for the 8 inch and 2 inch gauges, located on opposite sides of the specimen. Blue crosses (×) indicate data for individual batches; black circles (○) show the average values for each wall.

bending within the specimens combined with a design flaw in the test arrangement, in that deformations across the 2-inch masonry gauge and the 8-inch brick unit gauge were measured on opposite sides of the specimen (Figure A.9). If the top and bottom surfaces of the specimen are not parallel, then the specimen can undergo bending due to eccentric application of the axial force. On the basis of the results, it is likely that such effects occurred, even though care was taken in the design of the test arrangement to ensure that the pressure exerted onto the specimens was evenly distributed. This conclusion is further supported by Figure A.15, which plots the value of the Young's modulus measured across the 2-inch brick gauge versus the value measured across the 8-inch gauge (for the masonry). Whilst the data points are highly scattered, there appears to be an inverse relationship between the two moduli.

A simple improvement to the test arrangement would be to position both types of gauges on each side of the specimen, as this would enable any influence of bending to be eliminated by averaging the deformations measured along the two sides. This modification was implemented in the test arrangement subsequently used for the small-sized brick specimens (Figure A.10).

Because of the aforementioned faults in the test arrangement, it is suggested that the E_j and E_m results provided in Table A.5 should be treated with caution, as there

Figure A.16: Typical compressive failure of solid half-sized brick specimens.

appears to be significant variation in the values from wall to wall. As an attempt to minimise the error, it is recommended that the overall average results should be used, as given at the bottom of Table A.4. On this basis, the brickwork had the mean material properties: $E_u = 52{,}700$ MPa, $E_j = 442$ MPa, $E_m = 3{,}540$ MPa, and $f_{mc} = 16.0$ MPa.

A.4.5 Results for Solid Half-Sized Brick Specimens

All four specimens underwent splitting failure as shown by Figure A.16. The onset of failure was 'gentle' and could be anticipated due to a reduction in the resisted load.

The stress–strain curves for the masonry and brick components of the four specimens are shown by Figure A.17. It is seen that the curves are consistent for each of the four specimens. An exception is the specimen from batch 3, which had one of its mortar joints broken during transportation and is shown to have a much softer response than the other three. As a result, this specimen was omitted from the calculation of the Young's modulus of the masonry, E_m.

Results for each specimen are given in Table A.6. The mean material properties of the brickwork include: $E_u = 32{,}100$ MPa, $E_j = 1{,}410$ MPa, $E_m = 9{,}180$ MPa, and $f_{mc} = 25.9$ MPa.

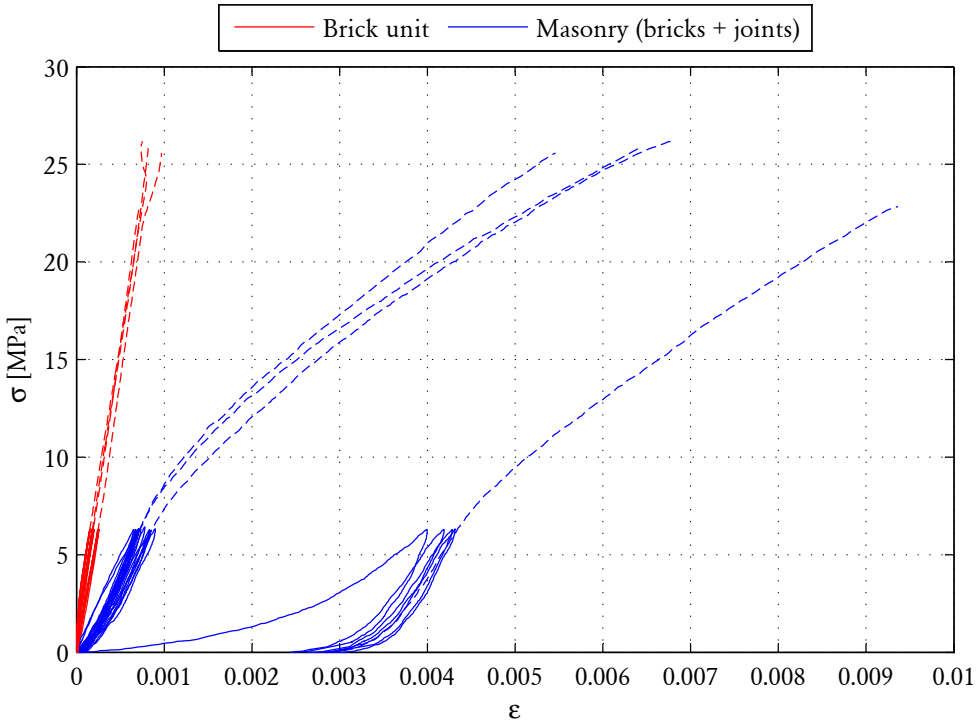

Figure A.17: Compressive stress versus strain for half-sized brick specimens. All four tests conducted are superimposed. The solid lines show tests used to calculate the Young's moduli and dashed line shows the push to failure. The rightmost curve represents the response of specimen 3 which was broken prior to testing and was omitted from the calculation of the mean Young's modulus of the masonry. Curves are only shown up to ultimate load, as the deformation measurements became inaccurate beyond this point.

Table A.6: Results of compression tests on the half-sized solid brick units used in the dynamic test study.

Batch	E_m [MPa]	E_u [MPa]	E_j [MPa]	f_{mc} [MPa]
1	7,720	37,900	1,110	26.2
2	9,360	33,600	1,430	26.1
3	–	31,100	–	22.9
4	10,500	25,700	1,670	28.6
Mean	9,180	32,100	1,410	25.9
CoV	0.15	0.16	0.20	0.09

A.5 COEFFICIENT OF FRICTION

A.5.1 Test Method

The test apparatus used to determine the coefficient of friction, μ_m, along the broken joint interface is shown by Figure A.18. The specimens used in these tests were put together from the broken couplets used in the bond wrench tests (described in Section A.2.1). Each specimen consisted of three bricks, each with its originally adhered mortar, stacked on top of each other. A vertical load was applied to the top brick using either a 20, 40, 60 or 80 kg weight. These weights were chosen in order to generate similar levels of vertical stress to those used in the main test walls in the shaketable test study. The test was conducted by applying a horizontal load to the central brick using a hand operated hydraulic ram, while the top and bottom units were restrained from moving horizontally. The load exerted by the ram onto the central brick, together with the displacement of the central brick, were conveyed to a data acquisition system. The test was stopped once the central brick displaced by approximately 16 mm. A total of eight sets of specimens were tested at each level of axial compression.

A.5.2 Calculation of μ_m

The forces applied to the specimen are shown by Figure A.18. Since the specimen is subjected to the fixed vertical force F_v, at the point of slip, the horizontal forces across the two joints must be $\mu_1 F_v$ and $\mu_2 F_v$, where μ_1 and μ_2 are their respective friction coefficients. Therefore, from horizontal force equilibrium, the average friction coefficient for the two joints is

$$\mu_m = \frac{\mu_1 + \mu_2}{2} = \frac{F_h}{2F_v}, \tag{A.13}$$

where F_h is the applied horizontal load.

A.5.3 Results for Solid Half-Sized Brick Specimens

Figure A.19 shows the typical measured response in terms of the friction coefficient μ_m [calculated from the resisted horizontal force F_h using Eq. (A.13)] versus the horizontal displacement of the central brick, Δ. The graphs demonstrate the response to be highly ductile and approximately elastoplastic in shape. The friction coefficient for each specimen was calculated as the average value or μ_m over the displacement range of 2 to 15 mm.

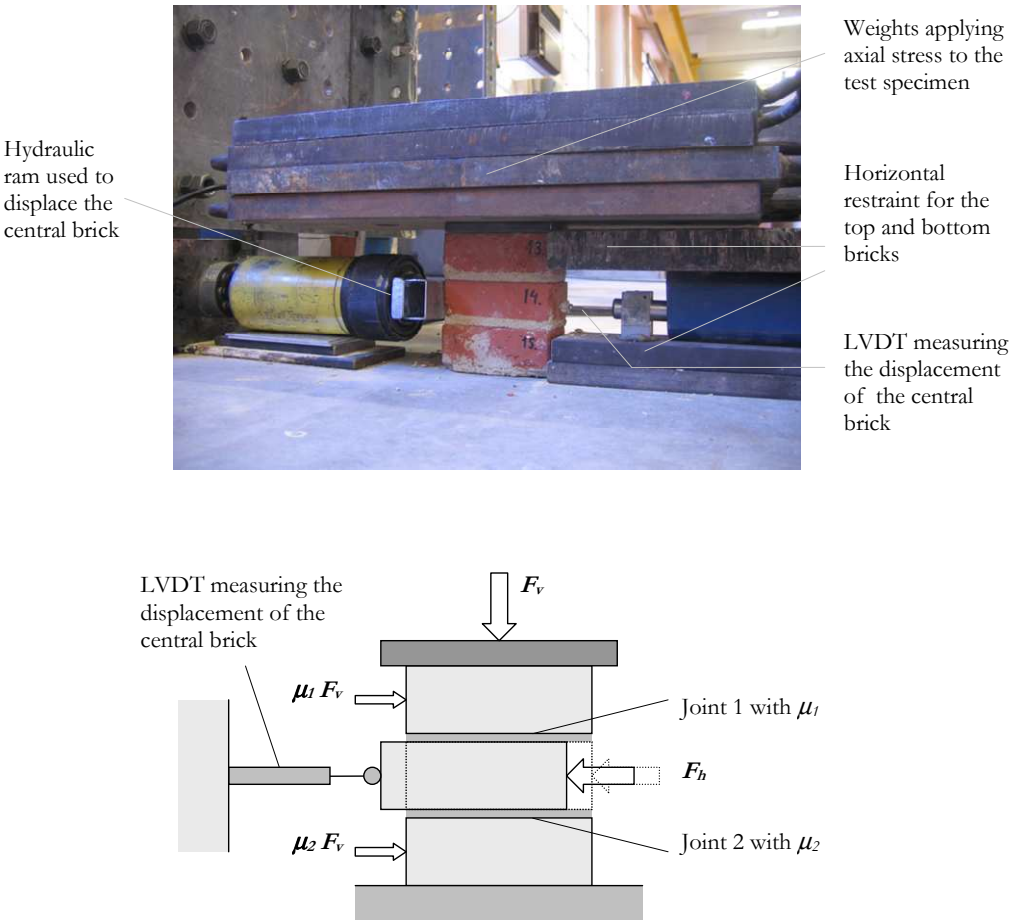

Figure A.18: Friction test arrangement (top) and forces applied to the test specimen at the instance of slip (bottom).

Table A.7: Coefficient of friction μ_m at different levels of axial stress σ_v, for half-sized solid brick specimens.

σ_v [MPa]	n	mean μ_m	CoV	t-test P-value
0.037	8	0.582	0.13	0.80
0.073	8	0.583	0.08	0.77
0.108	8	0.569	0.12	0.78
0.144	8	0.570	0.08	0.79
Pooled	32	0.576	0.10	

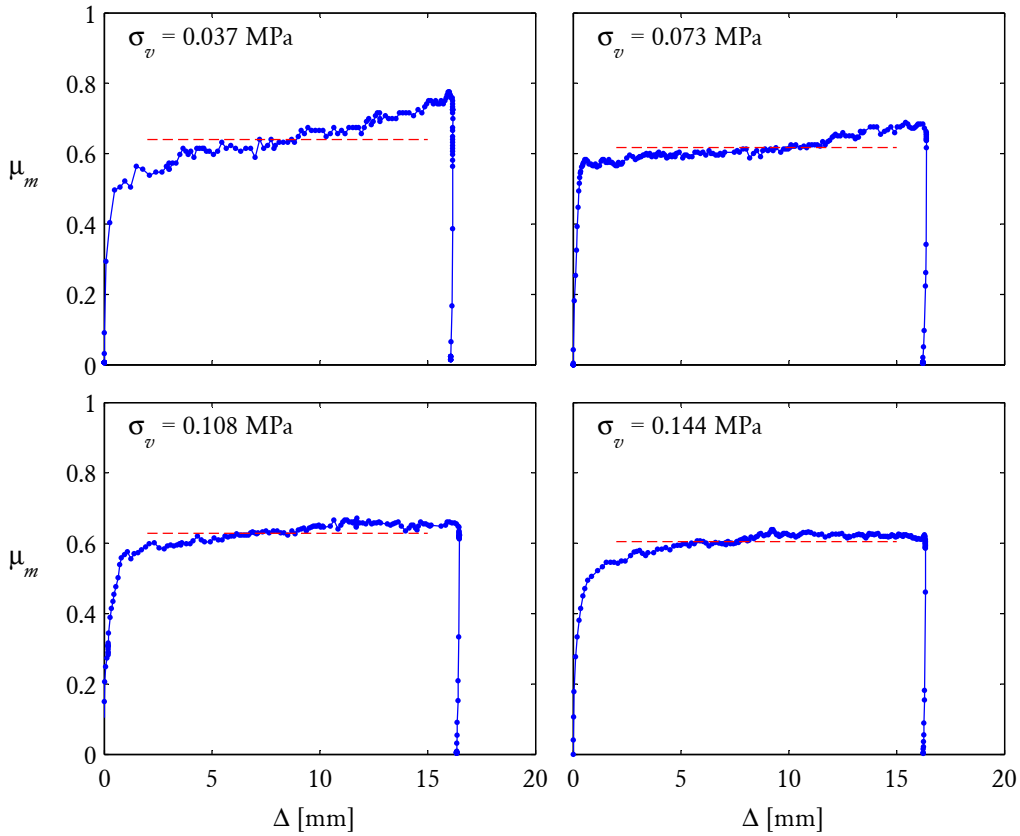

Figure A.19: Typical response of frictional resistance (as μ_m) at varied displacement Δ. These results correspond to a single specimen under different levels axial stress σ_v. Dashed red line (----) shows the mean value calculated over the displacement range 2–15 mm.

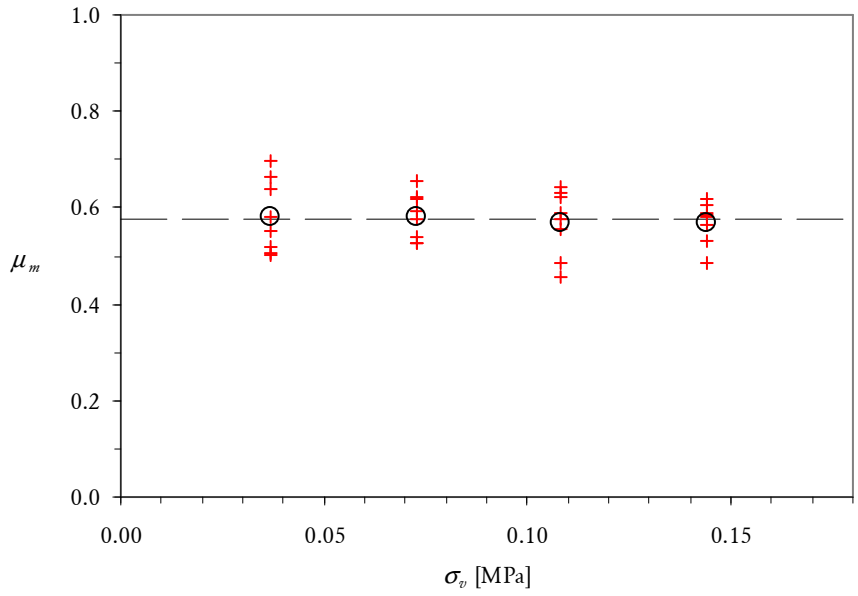

Figure A.20: Measured friction coefficient data for solid half-sized brick units at different levels of axial stress. Red crosses (+) indicate individual data points; black circles (○) show the mean values at each level of axial stress; and dashed black line (----) shows the overall mean value.

The measured μ_m data is plotted in Figure A.20 at different levels of the axial stress σ_v. The associated mean values and CoVs are summarised in Table A.7. Whilst the coefficient of friction is typically assumed to be independent of the acting normal stress, a Student's t-test was conducted to assess whether there was a significant difference between the measured values of μ_m at different levels of σ_v in these specimens. The large P-values produced by the t-test indicate that indeed, σ_v had negligible influence on μ_m and that all data may be assumed to come from the same distribution. Pooling the entire data set gives a mean μ_m value of 0.576.

Appendix B

QUASISTATIC CYCLIC TESTING

Abstract

This appendix contains additional detail related to Chapter 2.

B.1 MISCELLANEOUS TECHNICAL DETAILS

This section contains miscellaneous technical information regarding the test arrangement.

Figure B.1 shows the plan view of the arrangement used to impose vertical precompression onto the test walls, consisting of a series of weights suspended from horizontal bars cantilevered over the wall. An elevation view of this arrangement is also shown in Figure 2.7.

The layout of the airbags used for each of the three different wall geometries is shown in Figure B.2. The airbags were mounted on a stiffened backing board positioned between the test wall and the reaction frame (refer to Figures 2.8a and 2.8b). These airbag layouts were arranged to provide the best possible coverage with the airbags available.

Figure B.3 shows the positions of the load cells which were used to measure the horizontal load transferred between the airbag backing board and the reaction frame (refer to Figures 2.8a and 2.8b). The criteria used for positioning the load cells was to produce similar reaction forces in each cell, whilst minimising the expected deformation of the airbag backing frame to promote uniform airbag coverage over the face of the wall. The number of load cells used (either four or six) was selected based on preliminary predictions of the walls' load capacities.

Figure B.4 shows the displacement transducer layout used during the initial push on each wall (i.e. the ultimate strength test). This layout monitored displacements at 15 different locations (14 in walls containing an opening) including the main wall face and wall boundaries. The displacement transducers comprised a series of linear variable differential transformers (LVDTs) accurate to ± 0.01 mm and string potentiometers accurate to ± 0.1 mm.

During the cyclic test phase, displacement transducers were only used at key positions along the wall due to the impracticalities with measuring the deformations when airbags were present on both sides of the wall. These locations, corresponding to the position where the maximum displacement was measured during the initial push, are shown by Figure B.5 for each wall. The displacements were monitored using the string potentiometers accurate to ± 0.1 mm, which were connected to the wall and encased in protective tubing to prevent contact between the airbags and the string (refer to Figure 2.8b). In walls s3–s8, the central displacements were measured on both sides of the wall as a redundancy measure. In walls s7 and s8, the main displacement was measured at the central point of the opening, using an aluminium bar spanning horizontally across the window.

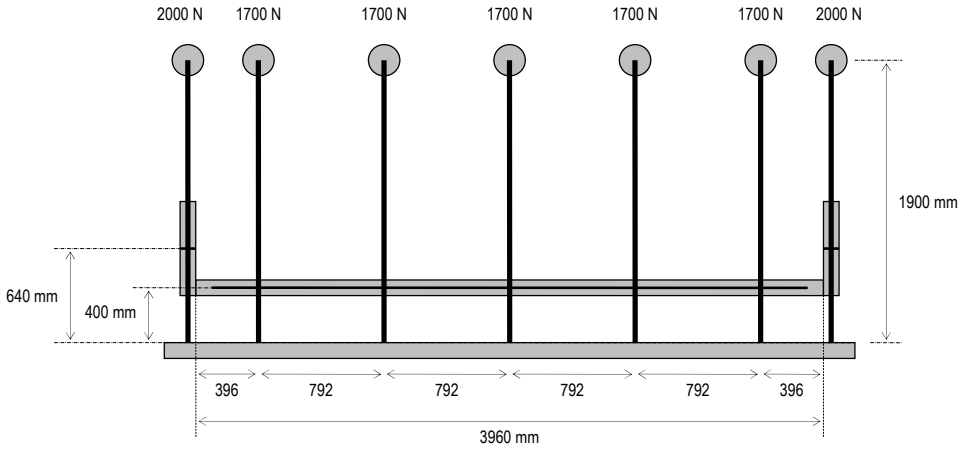

(a) Walls s1 and s3 ($\sigma_{vo} = 0.10$ MPa)

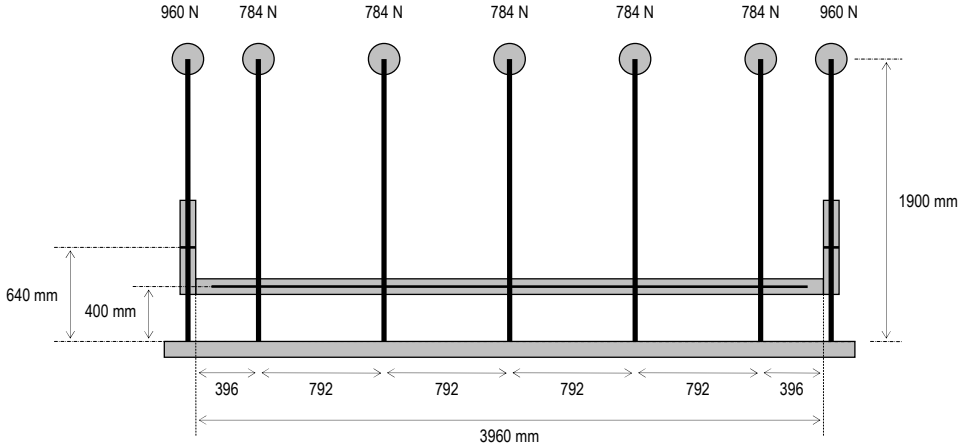

(b) Wall s4 ($\sigma_{vo} = 0.05$ MPa)

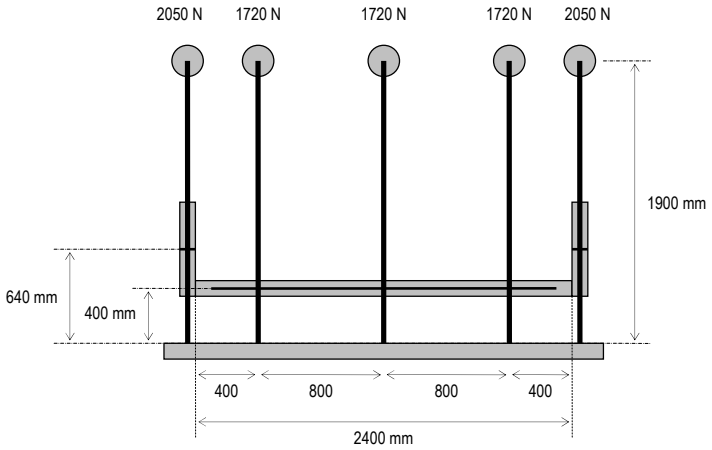

(c) Wall s7 ($\sigma_{vo} = 0.10$ MPa)

Figure B.1: Plan view of the vertical precompression loading arrangement.

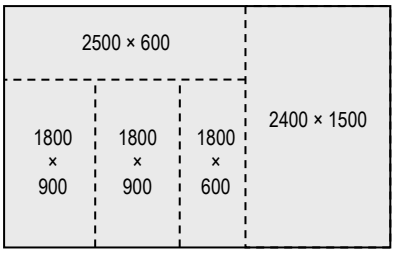

(a) 4000 × 2500 mm solid walls.

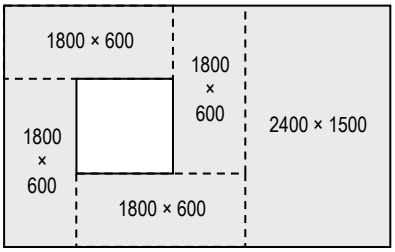

(b) 4000 × 2500 mm walls with openings.

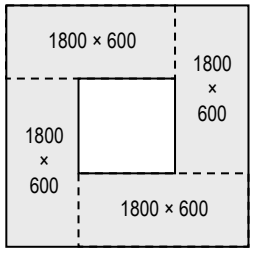

(c) 2500 × 2500 mm walls with openings.

Figure B.2: Airbag layouts, designed to provide maximum possible coverage along the face of each wall. Dimensions shown in millimetres.

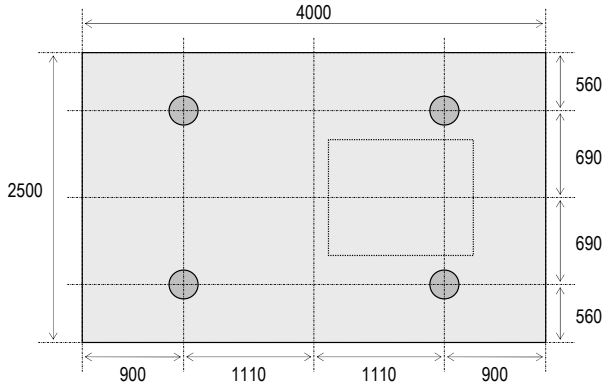

(a) Walls s1–s6.

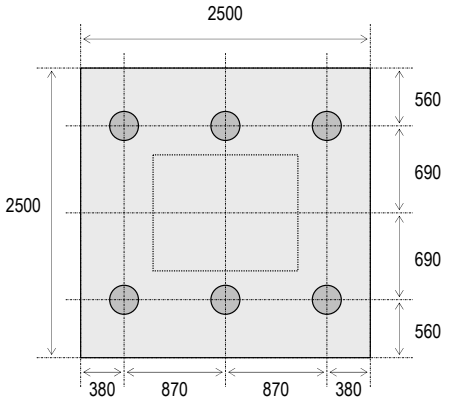

(b) Wall s7 (ultimate strength test only).

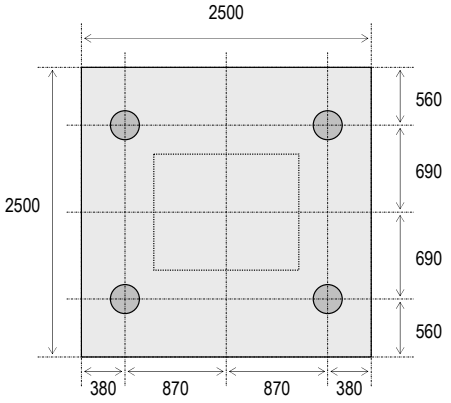

(c) Remaining wall s7 and s8 tests.

Figure B.3: Load cell positioning along the airbag backing frame. Dimensions shown in millimetres.

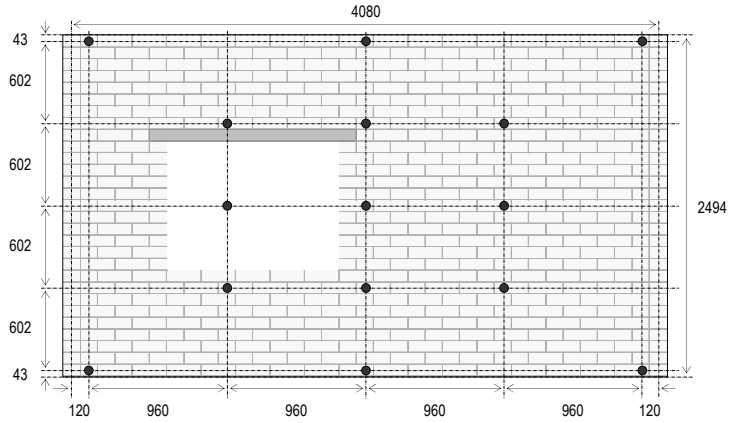

(a) Walls s1–s6. (Opening is illustrated despite being absent from walls s1 and s2.)

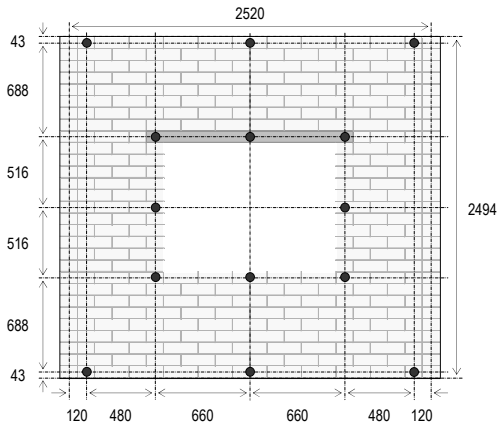

(b) Walls s7 and s8

Figure B.4: Displacement transducer layout during ultimate load capacity tests. Dimensions shown in millimetres.

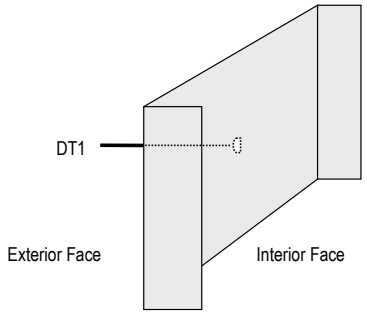

(a) Walls s1–s3

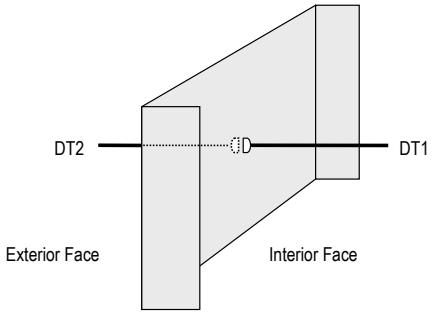

(b) Walls s4–s5

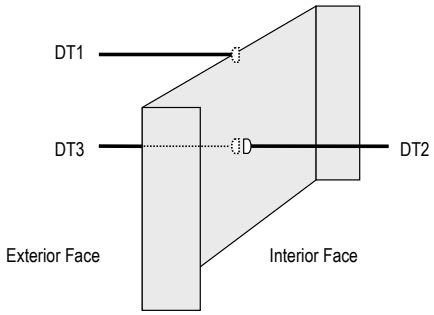

(c) Wall s6

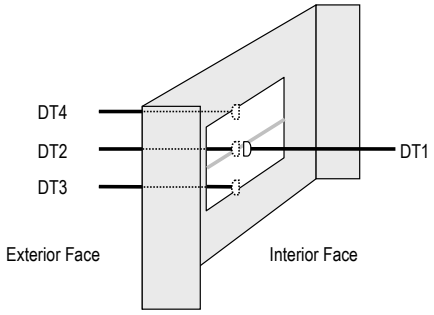

(d) Walls s7–s8

Figure B.5: Displacement transducer positioning during cyclic tests. Note that the openings are not shown for walls s3–s6

B.2 ANALYSIS OF RESPONSE DURING INITIAL PUSH

Figures B.6–B.13 demonstrate the load-displacement response for each wall during the initial push. The location of the displacement measurement is shown by Figures 2.11–2.13 for the respective walls. Shown on each graph are the key parameters derived from the respective tests, which are also summarised in Table 2.6 and include the following:

ULTIMATE STRENGTH The wall's ultimate strength F_{ult} was taken as the maximum load resisted during the test, based on the force recorded by the load cells. Inspection of the response in the subsequent cyclic tests shows that the maximum load resisted occurred during the initial push for each wall, as intended.

INITIAL UNCRACKED STIFFNESS The initial uncracked stiffness of the wall, K_{ini}, was taken as the slope of the F/Δ loading branch up to 40% of the ultimate load capacity. The value of the slope was calculated by first condensing the number of data points within this region (due to the different rates of loading at the start of each test), and subsequently fitting a linear regression to the condensed data.

PERCENTAGE OF RECOVERED DISPLACEMENT The proportion of displacement recovered upon unloading was calculated as

$$\text{displacement recovery ratio} = \frac{\Delta_{max} - \Delta_{final}}{\Delta_{max}},$$

where Δ_{max} was the maximum displacement imposed on the wall and Δ_{final} was the final displacement upon unloading. Since the maximum displacement to which the walls were subjected is somewhat arbitrary, these values are intended to be only indicative of the walls' self-centring characteristics.

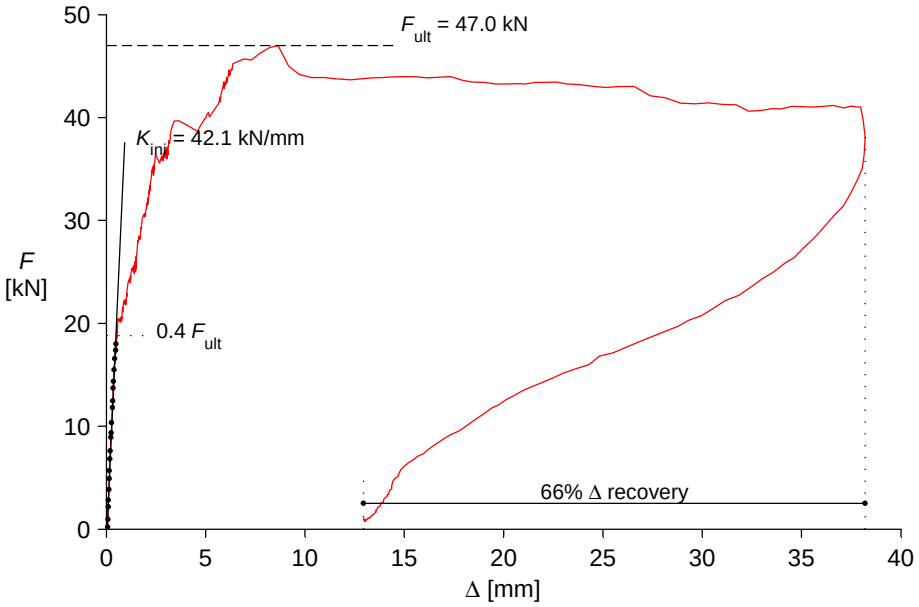

Figure B.6: F-Δ response of wall s1 during the initial push.

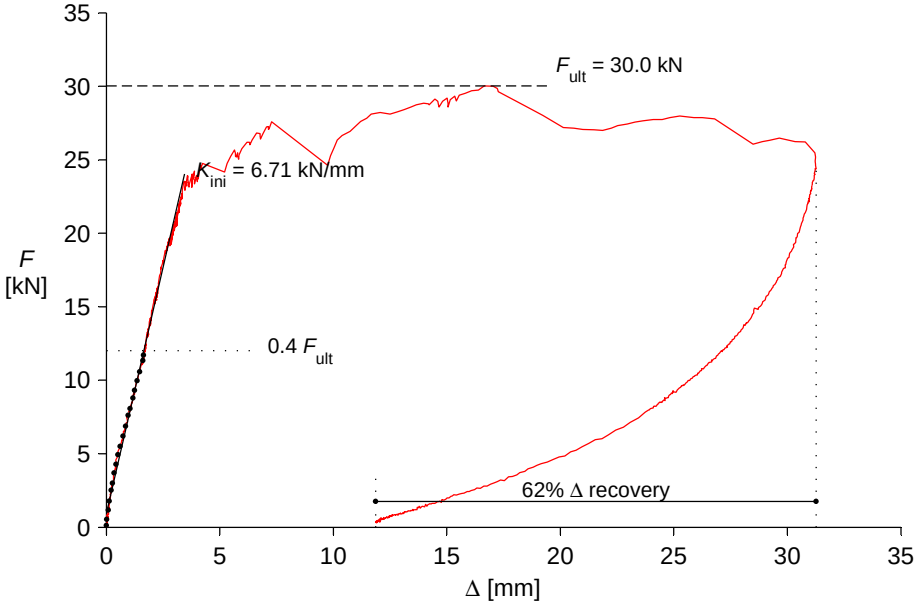

Figure B.7: F-Δ response of wall s2 during the initial push.

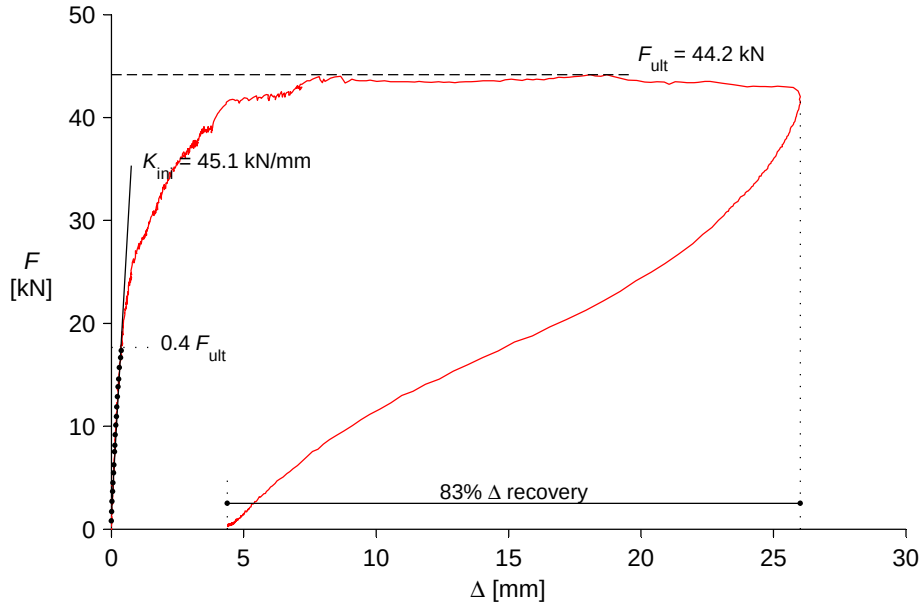

Figure B.8: F-Δ response of wall s3 during the initial push.

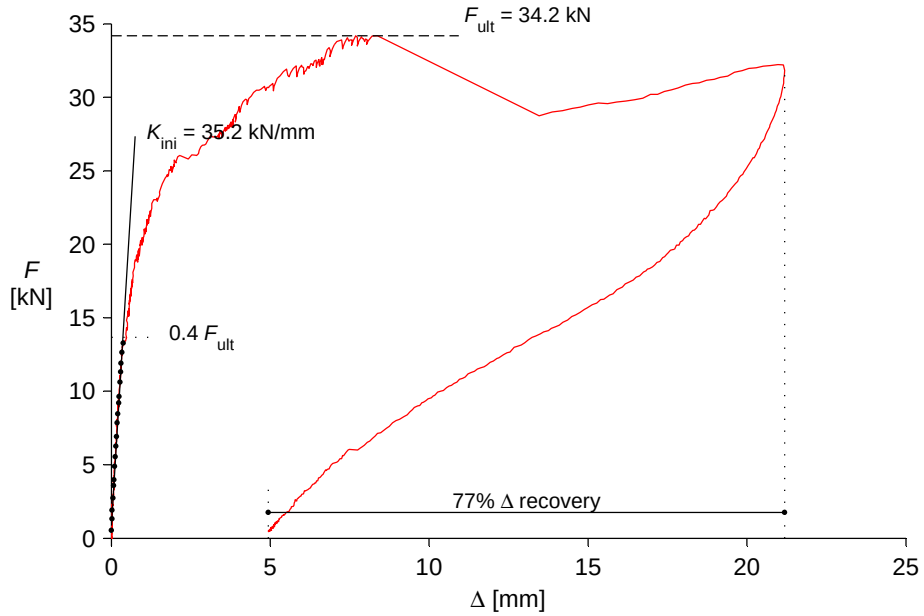

Figure B.9: F-Δ response of wall s4 during the initial push.

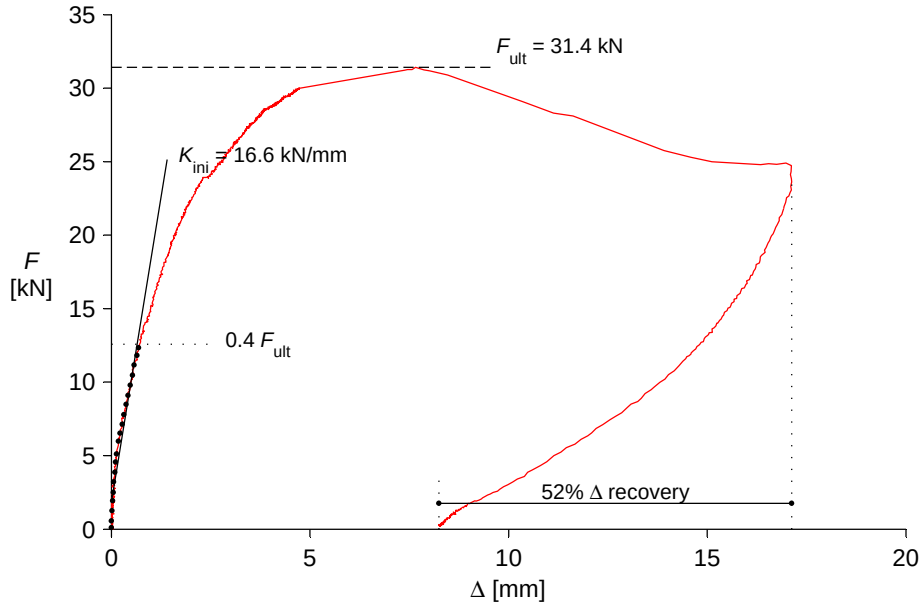

Figure B.10: F-Δ response of wall s5 during the initial push.

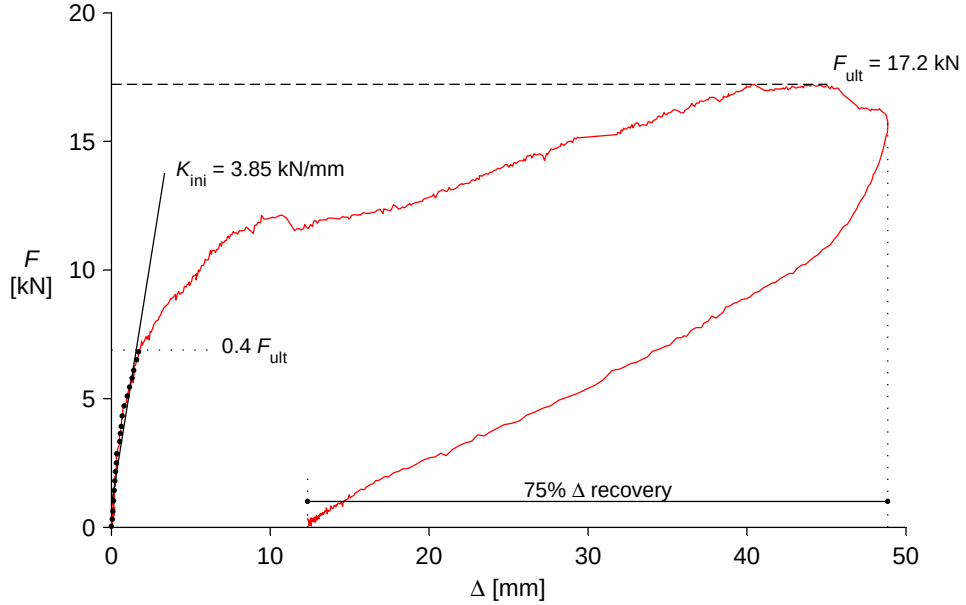

Figure B.11: F-Δ response of wall s6 during the initial push.

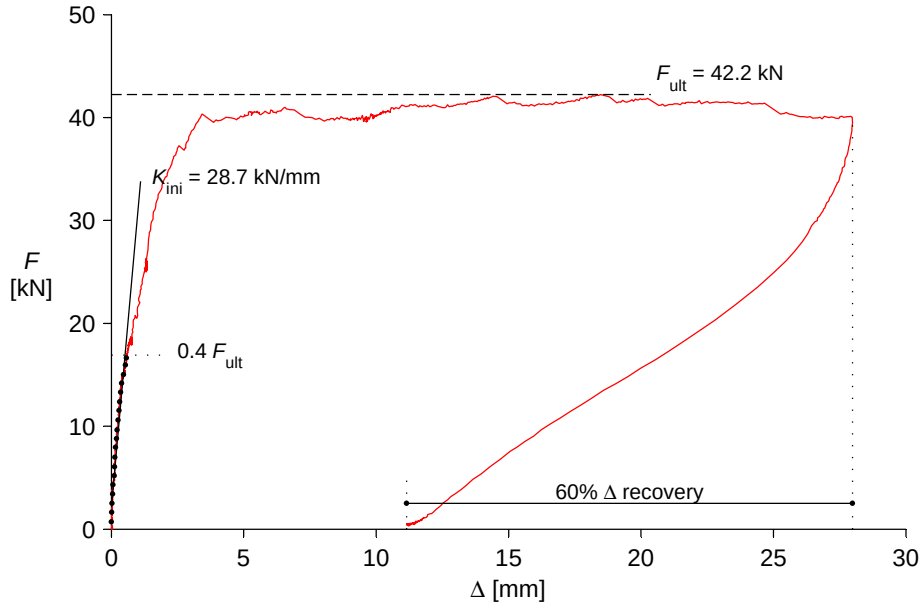

Figure B.12: F-Δ response of wall s7 during the initial push.

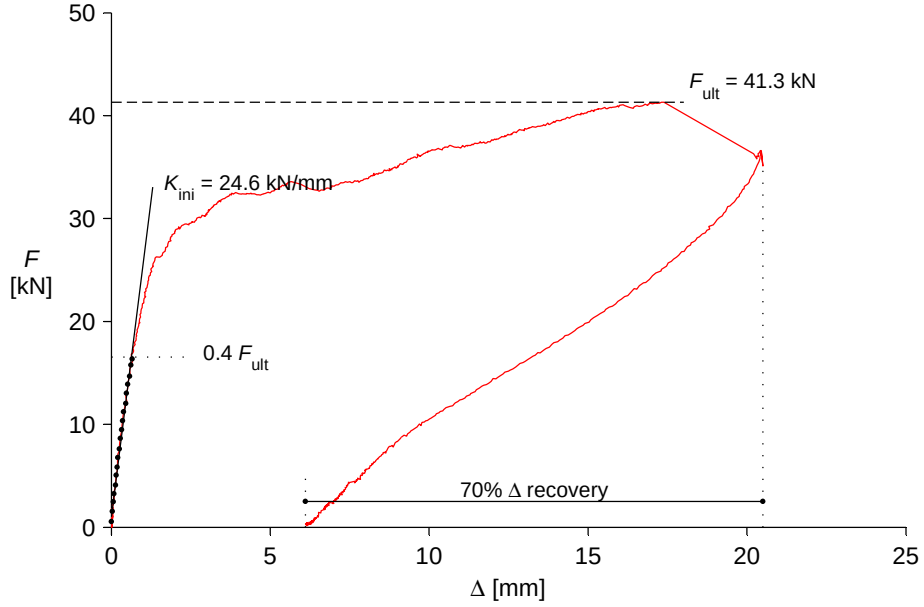

Figure B.13: F-Δ response of wall s8 during the initial push.

B.3 ANALYSIS OF CYCLIC RESPONSE

B.3.1 Properties from Individual Cycles

For each half-cycle run performed during the course of testing, several properties were determined from the measured F-Δ response. These include: peak displacement, cyclic displacement and force amplitudes, effective secant stiffness, equivalent viscous damping, and envelope point coordinates. The results of these properties are summarised in Tables B.1–B.8, including for each test run during the cyclic test phase, as well as the initial push to ultimate strength which can be considered as the first half-cycle of the wall's overall response. The results are also graphed throughout Figures B.16–B.23. The methods used to determine each of these properties will now be described.

PEAK DISPLACEMENT The peak displacement Δ_{peak} was taken as the largest imposed displacement during the cycle.

DISPLACEMENT CYCLE AMPLITUDE The method used to determine the displacement amplitude Δ_{amp} was dependent on whether the half-cycle under consideration was in the reverse direction or reload direction (Figure B.14). For reverse direction cycles, Δ_{amp} was taken directly as the peak imposed displacement (Figure B.14a). For reload direction cycles, Δ_{amp} was taken as the difference between the peak imposed displacement and the initial displacement at the beginning of the cycle (Figure B.14b).

FORCE CYCLE AMPLITUDE The force amplitude F_{amp} was taken as the peak force resisted by the wall during the half-cycle.

EFFECTIVE STIFFNESS The effective secant stiffness of a half-cycle was calculated as

$$K = \frac{F_{amp}}{\Delta_{amp}}.$$

EQUIVALENT VISCOUS DAMPING The equivalent viscous damping based on hysteresis, ξ_{hyst}, was calculated using the area-based method according to the equation

$$\xi_{hyst} = \frac{1}{\pi} \frac{U_{1/2cyc}}{F_{amp}\,\Delta_{amp}},$$

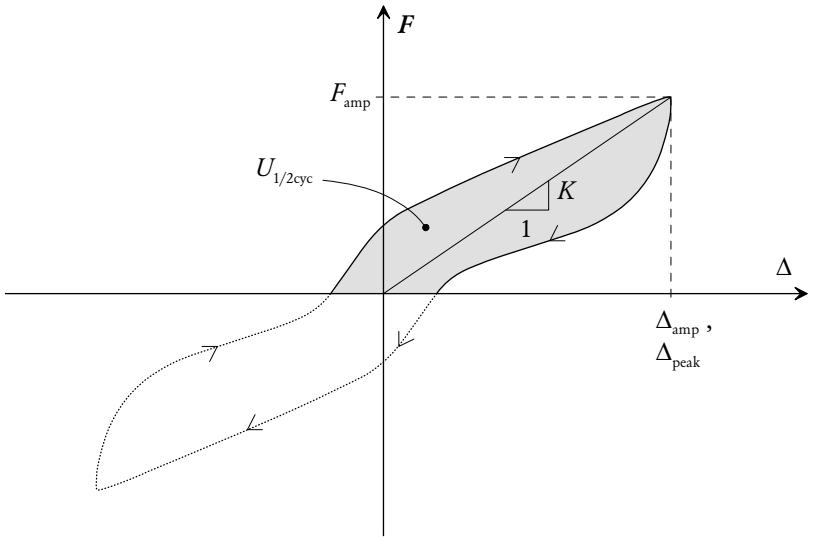

(a) Reverse direction half-cycle.

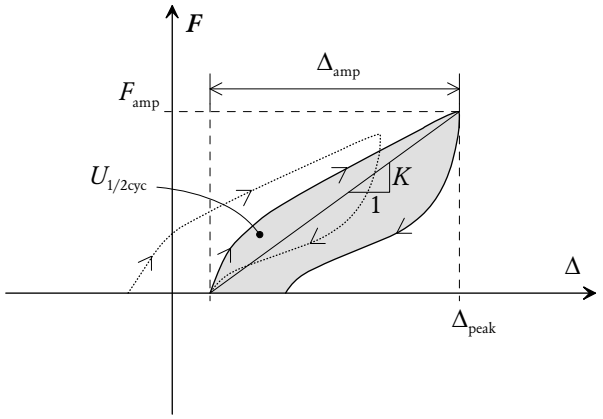

(b) Reload direction half-cycle.

Figure B.14: Properties determined from individual half-cycles in cyclic testing. Shown assuming loading in the positive direction.

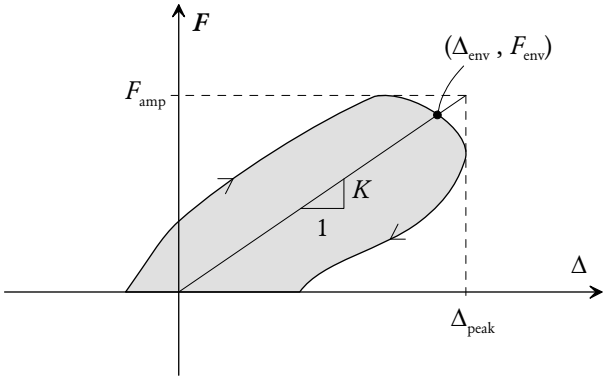

Figure B.15: Envelope point coordinates for half-cycle.

where $U_{1/2cyc}$ is the energy dissipated during the half-cycle (as shown in Figure B.14). In general terms, the energy dissipated during hysteresis is given by the integral

$$U = \int F \, d\Delta.$$

To obtain $U_{1/2cyc}$, this integral was evaluated from the measured F and Δ data vectors using the summation

$$U_{1/2cyc} = \sum_{k=1}^{n-1} 0.5 \left(F_k + F_{k+1}\right) \left(\Delta_{k+1} - \Delta_k\right),$$

where k is the data point index and n in the number of data points recorded during the test run.

ENVELOPE POINT COORDINATES For each half-cycle run, the coordinates F_{env} and Δ_{env} at a representative envelope point were determined for the purpose of subsequently using these points to define the overall envelope curve for each wall (refer to Figures B.16–B.23). In most half-cycle runs, the point of peak force generally coincided with the point of peak displacement. However, in certain half-cycles, these points did not coincide due to a reduction in strength with increasing displacement, as shown in Figure B.15. Therefore, as shown by the figure, the envelope point was taken as the intersection of the measured F-Δ curve with the line defined by the effective secant stiffness of the half-cycle (i.e. line joining the origin and the point Δ_{peak} and F_{amp}).

B.3.2 Properties for Each Wall

After quantifying the various properties based on each half-cycle run (as outlined in Section B.3.1), several properties indicative of the overall response of each wall were determined by collectively considering all individual test runs. These include: the ultimate strength, the displacement range encompassing 80% of the ultimate strength, the residual strength and effective stiffness at $\delta = 0.5$, and the equivalent viscous damping in the range $0.25 \leq \delta \leq 0.75$. The resulting values of these properties are summarised in Table 2.7 and also plotted throughout Figures B.16–B.23. Note that each of the properties were determined separately in the positive and negative directions, as denoted by superscripts $+$ and $-$. The methods used to determine them will now be described.

ULTIMATE STRENGTH Ultimate load capacities were determined in each direction, as denoted by F^+_{ult} and F^-_{ult} in Table 2.7. In each of the eight walls tested,

the highest strength was measured during the initial push in the positive loading direction as intended, and this value was adopted as the overall ultimate strength of the wall (F_{ult}).

DISPLACEMENT RANGE ENCOMPASSING 80% OF F_{ULT} As an indicative measure of the wall's ability to maintain its load resistance with increasing deformation, the displacement range encompassing the zone where the wall's strength exceeded 80% of the ultimate strength, was quantified. Values of this range were determined in both directions, by using the respective value of F^{+}_{ult} or F^{-}_{ult} as the reference strength. The results are shown graphically in Figures B.16–B.23 (right, top graph) and summarised in Table 2.7, as $\Delta^{+}_{0.8Fu}$ and $\Delta^{-}_{0.8Fu}$.

RESIDUAL STRENGTH AND EFFECTIVE STIFFNESS AT $\delta = 0.5$ As an alternative measure of the wall's ability to maintain its strength at large displacement, its strength and stiffness were quantified at $\delta = 0.5$ (displacement equal to half the wall's thickness, i.e. 55 mm). These properties were determined as follows: Firstly, the effective secant stiffness K for each half-cycle was plotted against the cycle's displacement amplitude Δ_{amp}, as shown in Figures B.16–B.23 (right, middle graph). Next, a second order exponential regression was fitted to the K–Δ_{amp} data in each direction. For consistency, only data points within $0.25 \leq \delta \leq 0.75$ were used in the data fitting process. Based on the trendlines (indicated in the respective graphs), values of the secant stiffness at $\delta = \pm 0.5$ were determined, as denoted by K^{+}_{ht} and K^{-}_{ht} in Table 2.7. The corresponding values of the force resistance at $\delta = \pm 0.5$ were calculated using the relationship $F_{ht} = (0.5t_u)K_{ht}$, and are denoted by F^{+}_{ht} and F^{-}_{ht} in Table 2.7.

EQUIVALENT VISCOUS DAMPING AT $0.25 \leq \delta \leq 0.75$ Average values of ξ_{hyst} were determined for cycles whose displacement amplitude was within the range $0.25 \leq \delta \leq 0.75$. The results are shown graphically in Figures B.16–B.23 (right, bottom graph), and are summarised in Table 2.7 in both the positive and negative directions as denoted by ξ^{+}_{hyst} and ξ^{-}_{hyst}.

B.3.3 Results

Tables B.1–B.8 provide the results of properties that were described in Section B.3.1 for each half-cycle performed, including the initial push on the wall and the subsequent cyclic tests. The 1st column gives the test index, and the 2nd column states whether the test was the initial push to ultimate strength ('ult') or a cyclic

test ('cyc'). The 3rd column gives the target displacement rounded to the nearest 10 mm (except for the initial ultimate strength test, which is rounded to the nearest mm). The 4th column states the number of repetitions performed at the particular target displacement by taking into account the previous cyclic loading history but ignoring the initial ultimate strength test. The numeral 'i' means that it was the first excursion at the given target displacement, whilst higher numerals denote the repetition number; for example, 'ii' means that the test was the second excursion at the given target displacement. The 5th column denotes whether the half-cycle was in the same or opposite direction to the previous half-cycle. Half-cycles in the same direction are denoted as 'reload', whilst half-cycles in the opposite direction are denoted as 'reverse'. The remaining columns in each table provide results for the properties discussed in Section B.3.1 and include: peak displacement Δ_{peak}; displacement amplitude Δ_{amp}; force amplitude F_{amp}; effective stiffness K; equivalent viscous damping ratio ξ_{hyst}; and the envelope point coordinates Δ_{env} and F_{env}.

Figures B.16–B.23 provide several different graphs for each wall tested. On the left-hand side of each figure (from top to bottom) are plots of the peak displacement Δ_{peak} versus test index; force amplitude F_{amp} versus test index; effective stiffness K versus test index; and equivalent viscous damping ratio ξ_{hyst} versus test index. On the right-hand side (from top to bottom) are plots of the force F versus displacement Δ; effective stiffness K versus displacement amplitude Δ_{amp}; and equivalent viscous damping ratio ξ_{hyst} versus displacement amplitude Δ_{amp}. Values of key results for each wall, as described in Section B.3.2, are also annotated.

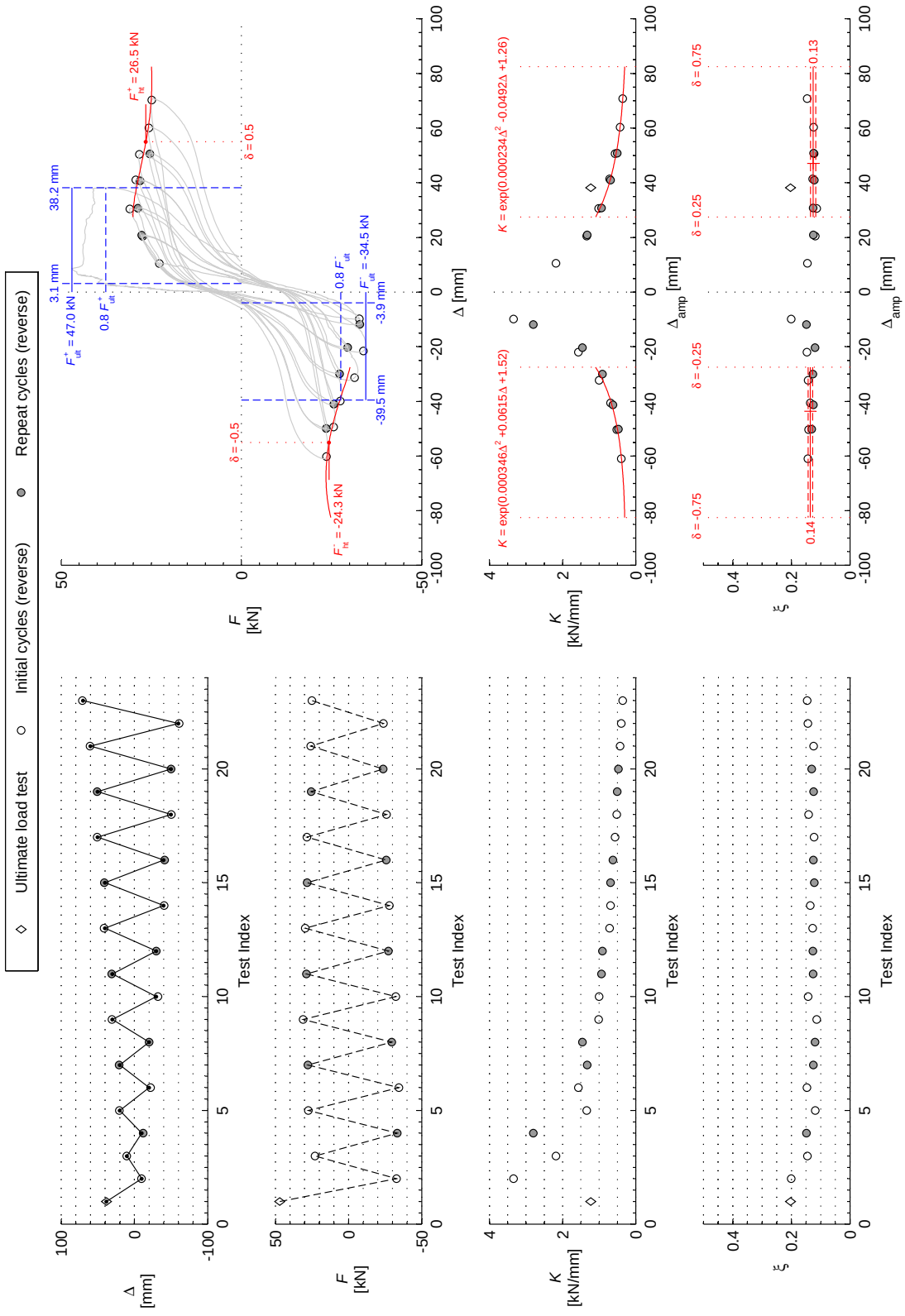

Figure B.16: Cycle analysis results for wall S1.

Table B.1: Results of individual cycles for wall s1.

Test Index	Test Type	Target Δ [mm]	Cycle Type		Measured Cycle Properties					Envelope Point	
			Rep. no	Dir.	Δ_{peak} [mm]	Δ_{amp} [mm]	F_{amp} [kN]	K [kN/mm]	ξ	Δ_{env} [mm]	F_{env} [kN]
1	ult	+38			38.2	*	47.0	1.230	0.20	33.1	40.7
2	cyc	−10	i	reverse	−9.8	*	−32.8	3.340	0.20	−9.8	−32.7
3	cyc	+10	i	reverse	10.5	*	22.9	2.176	0.15	10.4	22.7
4	cyc	−10	ii	reverse	−11.9	*	−33.3	2.799	0.15	−11.7	−32.8
5	cyc	+20	i	reverse	20.5	*	27.5	1.340	0.12	20.4	27.3
6	cyc	−20	i	reverse	−22.0	*	−34.5	1.568	0.15	−21.6	−33.8
7	cyc	+20	ii	reverse	20.9	*	27.8	1.328	0.12	20.8	27.6
8	cyc	−20	ii	reverse	−20.3	*	−29.6	1.457	0.12	−20.2	−29.5
9	cyc	+30	i	reverse	30.6	*	31.0	1.015	0.11	30.5	30.9
10	cyc	−30	i	reverse	−32.2	*	−32.3	1.002	0.14	−31.3	−31.4
11	cyc	+30	ii	reverse	30.8	*	28.8	0.933	0.13	30.7	28.7
12	cyc	−30	ii	reverse	−30.0	*	−27.3	0.910	0.13	−29.9	−27.2
13	cyc	+40	i	reverse	41.4	*	29.5	0.713	0.13	41.1	29.3
14	cyc	−40	i	reverse	−40.5	*	−27.9	0.688	0.14	−39.9	−27.4
15	cyc	+40	ii	reverse	41.0	*	28.2	0.689	0.12	40.8	28.1
16	cyc	−40	ii	reverse	−41.3	*	−25.8	0.625	0.13	−41.0	−25.6
17	cyc	+50	i	reverse	50.7	*	28.5	0.562	0.12	50.4	28.3
18	cyc	−50	i	reverse	−50.3	*	−26.0	0.517	0.14	−49.4	−25.5
19	cyc	+50	ii	reverse	50.9	*	25.5	0.502	0.12	50.6	25.4
20	cyc	−50	ii	reverse	−50.2	*	−23.7	0.472	0.13	−49.9	−23.5
21	cyc	+60	i	reverse	60.4	*	25.8	0.427	0.12	60.1	25.6
22	cyc	−60	i	reverse	−61.0	*	−23.9	0.392	0.14	−60.2	−23.6
23	cyc	+70	i	reverse	70.8	*	25.0	0.354	0.15	70.3	24.9

(*) indicates that Δ_{amp} is same as Δ_{peak}, which is the case for reverse cycles.

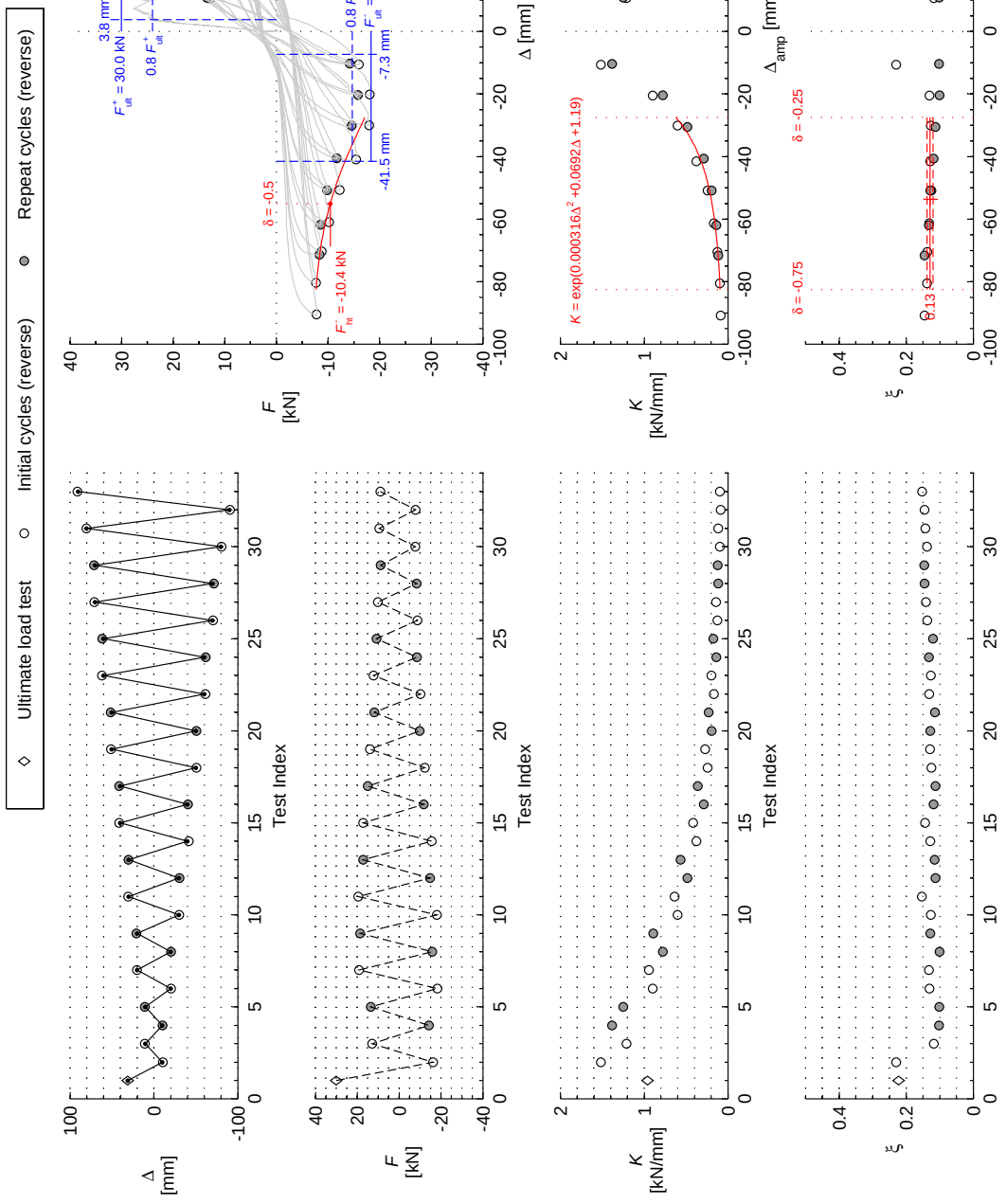

Figure B.17: Cycle analysis results for wall s2.

Table B.2: Results of individual cycles for wall s2.

Test Index	Test Type	Target Δ [mm]	Cycle Type		Measured Cycle Properties					Envelope Point	
			Rep. no	Dir.	Δ_{peak} [mm]	Δ_{amp} [mm]	F_{amp} [kN]	K [kN/mm]	ξ	Δ_{env} [mm]	F_{env} [kN]
1	ult	+31			31.3	*	30.0	0.961	0.22	27.8	26.7
2	cyc	−10	i	reverse	−10.7	*	−16.2	1.515	0.23	−10.6	−16.0
3	cyc	+10	i	reverse	10.6	*	12.9	1.211	0.12	10.6	12.8
4	cyc	−10	ii	reverse	−10.3	*	−14.3	1.384	0.10	−10.3	−14.2
5	cyc	+10	ii	reverse	10.8	*	13.5	1.249	0.10	10.8	13.4
6	cyc	−20	i	reverse	−20.5	*	−18.4	0.897	0.13	−20.2	−18.1
7	cyc	+20	i	reverse	20.2	*	19.1	0.943	0.13	20.1	19.0
8	cyc	−20	ii	reverse	−20.4	*	−15.8	0.777	0.10	−20.3	−15.8
9	cyc	+20	ii	reverse	20.8	*	18.5	0.890	0.13	20.5	18.2
10	cyc	−30	i	reverse	−30.1	*	−18.0	0.600	0.13	−30.0	−18.0
11	cyc	+30	i	reverse	30.6	*	19.4	0.636	0.15	30.4	19.3
12	cyc	−30	ii	reverse	−30.5	*	−14.8	0.485	0.11	−30.1	−14.6
13	cyc	+30	ii	reverse	30.3	*	17.1	0.565	0.11	30.2	17.0
14	cyc	−40	i	reverse	−41.5	*	−15.6	0.377	0.13	−40.9	−15.4
15	cyc	+40	i	reverse	41.3	*	17.1	0.414	0.14	40.9	16.9
16	cyc	−40	ii	reverse	−40.7	*	−11.7	0.288	0.12	−40.6	−11.7
17	cyc	+40	ii	reverse	41.4	*	14.9	0.361	0.11	41.3	14.9
18	cyc	−50	i	reverse	−50.9	*	−12.3	0.242	0.12	−50.7	−12.3
19	cyc	+50	i	reverse	51.1	*	13.9	0.272	0.13	50.8	13.8
20	cyc	−50	ii	reverse	−50.9	*	−9.9	0.194	0.13	−50.7	−9.8
21	cyc	+50	ii	reverse	51.5	*	11.7	0.228	0.11	51.3	11.7
22	cyc	−60	i	reverse	−61.3	*	−10.3	0.168	0.13	−61.0	−10.2
23	cyc	+60	i	reverse	61.9	*	12.1	0.196	0.13	61.6	12.1
24	cyc	−60	ii	reverse	−61.9	*	−8.6	0.139	0.13	−61.7	−8.6
25	cyc	+60	ii	reverse	61.4	*	10.8	0.176	0.12	61.2	10.7
26	cyc	−70	i	reverse	−70.5	*	−8.8	0.125	0.14	−70.3	−8.8
27	cyc	+70	i	reverse	70.8	*	10.1	0.142	0.14	70.5	10.0
28	cyc	−70	ii	reverse	−71.6	*	−8.4	0.117	0.14	−71.3	−8.3
29	cyc	+70	ii	reverse	71.3	*	8.8	0.123	0.15	71.2	8.7
30	cyc	−80	i	reverse	−80.5	*	−7.7	0.096	0.14	−80.4	−7.7
31	cyc	+80	i	reverse	80.3	*	9.4	0.117	0.14	80.1	9.4
32	cyc	−90	i	reverse	−90.8	*	−7.8	0.086	0.15	−90.4	−7.8
33	cyc	+90	i	reverse	91.2	*	8.9	0.097	0.15	90.9	8.8

(*) indicates that Δ_{amp} is same as Δ_{peak}, which is the case for reverse cycles.

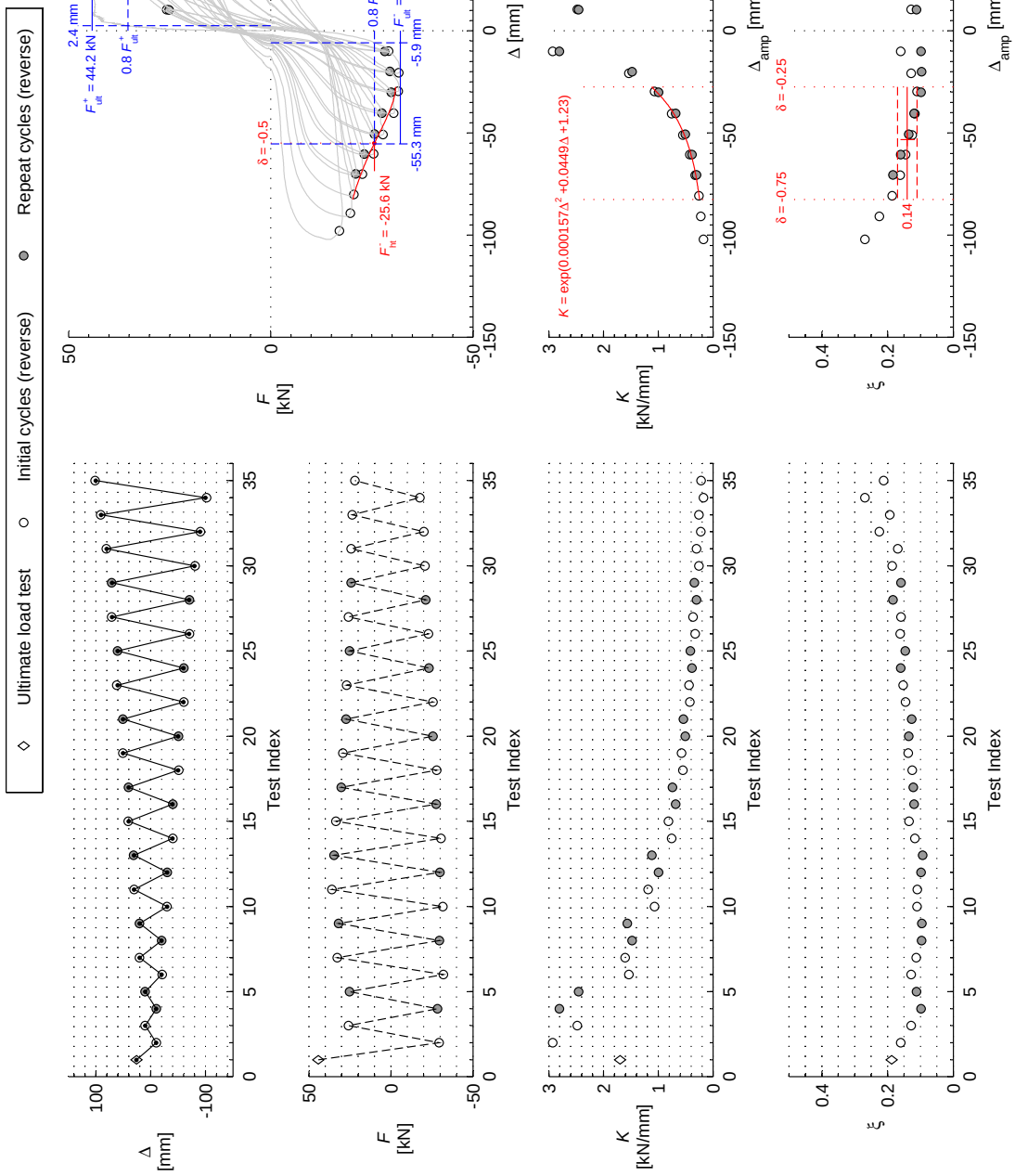

Figure B.18: Cycle analysis results for wall s3.

Table B.3: Results of individual cycles for wall s3.

Test Index	Test Type	Target Δ [mm]	Cycle Type		Measured Cycle Properties					Envelope Point	
			Rep. no	Dir.	Δ_{peak} [mm]	Δ_{amp} [mm]	F_{amp} [kN]	K [kN/mm]	ξ	Δ_{env} [mm]	F_{env} [kN]
1	ult	+26			26.0	*	44.2	1.698	0.19	25.3	43.0
2	cyc	−10	i	reverse	−10.0	*	−29.4	2.929	0.16	−10.0	−29.1
3	cyc	+10	i	reverse	10.4	*	25.8	2.478	0.13	10.4	25.7
4	cyc	−10	ii	reverse	−10.1	*	−28.3	2.809	0.10	−10.0	−28.2
5	cyc	+10	ii	reverse	10.3	*	25.2	2.453	0.11	10.2	25.1
6	cyc	−20	i	reverse	−20.8	*	−32.0	1.537	0.13	−20.6	−31.7
7	cyc	+20	i	reverse	20.4	*	32.7	1.605	0.11	20.3	32.6
8	cyc	−20	ii	reverse	−20.0	*	−29.6	1.479	0.10	−19.9	−29.5
9	cyc	+20	ii	reverse	20.3	*	31.8	1.568	0.10	20.2	31.7
10	cyc	−30	i	reverse	−29.7	*	−31.7	1.068	0.11	−29.6	−31.6
11	cyc	+30	i	reverse	30.2	*	35.9	1.187	0.11	30.0	35.7
12	cyc	−30	ii	reverse	−30.1	*	−29.9	0.992	0.10	−30.0	−29.8
13	cyc	+30	ii	reverse	31.0	*	34.6	1.116	0.09	30.9	34.5
14	cyc	−40	i	reverse	−40.6	*	−30.6	0.754	0.12	−40.3	−30.4
15	cyc	+40	i	reverse	41.0	*	33.4	0.815	0.13	40.7	33.1
16	cyc	−40	ii	reverse	−40.5	*	−27.6	0.682	0.12	−40.3	−27.5
17	cyc	+40	ii	reverse	40.7	*	30.2	0.741	0.12	40.5	30.0
18	cyc	−50	i	reverse	−51.0	*	−28.0	0.548	0.13	−50.7	−27.8
19	cyc	+50	i	reverse	50.9	*	29.3	0.576	0.14	50.6	29.1
20	cyc	−50	ii	reverse	−50.6	*	−25.7	0.507	0.14	−50.5	−25.6
21	cyc	+50	ii	reverse	50.6	*	27.4	0.540	0.13	50.4	27.2
22	cyc	−60	i	reverse	−60.6	*	−25.7	0.423	0.15	−60.1	−25.5
23	cyc	+60	i	reverse	61.8	*	27.0	0.436	0.15	61.2	26.7
24	cyc	−60	ii	reverse	−60.6	*	−23.2	0.383	0.16	−60.4	−23.1
25	cyc	+60	ii	reverse	60.7	*	25.2	0.415	0.15	60.5	25.1
26	cyc	−70	i	reverse	−70.6	*	−22.8	0.323	0.16	−70.1	−22.7
27	cyc	+70	i	reverse	71.2	*	25.9	0.364	0.16	70.7	25.7
28	cyc	−70	ii	reverse	−70.5	*	−21.2	0.300	0.18	−70.0	−21.0
29	cyc	+70	ii	reverse	71.1	*	24.2	0.340	0.16	70.9	24.1
30	cyc	−80	i	reverse	−80.7	*	−20.7	0.256	0.19	−80.1	−20.5
31	cyc	+80	i	reverse	81.2	*	24.2	0.299	0.17	80.7	24.1
32	cyc	−90	i	reverse	−90.8	*	−20.1	0.221	0.22	−89.2	−19.7
33	cyc	+90	i	reverse	91.1	*	23.5	0.258	0.19	90.4	23.3
34	cyc	−100	i	reverse	−102.1	*	−17.7	0.173	0.27	−97.9	−17.0
35	cyc	+100	i	reverse	101.4	*	21.9	0.216	0.21	100.3	21.7

(*) indicates that Δ_{amp} is same as Δ_{peak}, which is the case for reverse cycles.

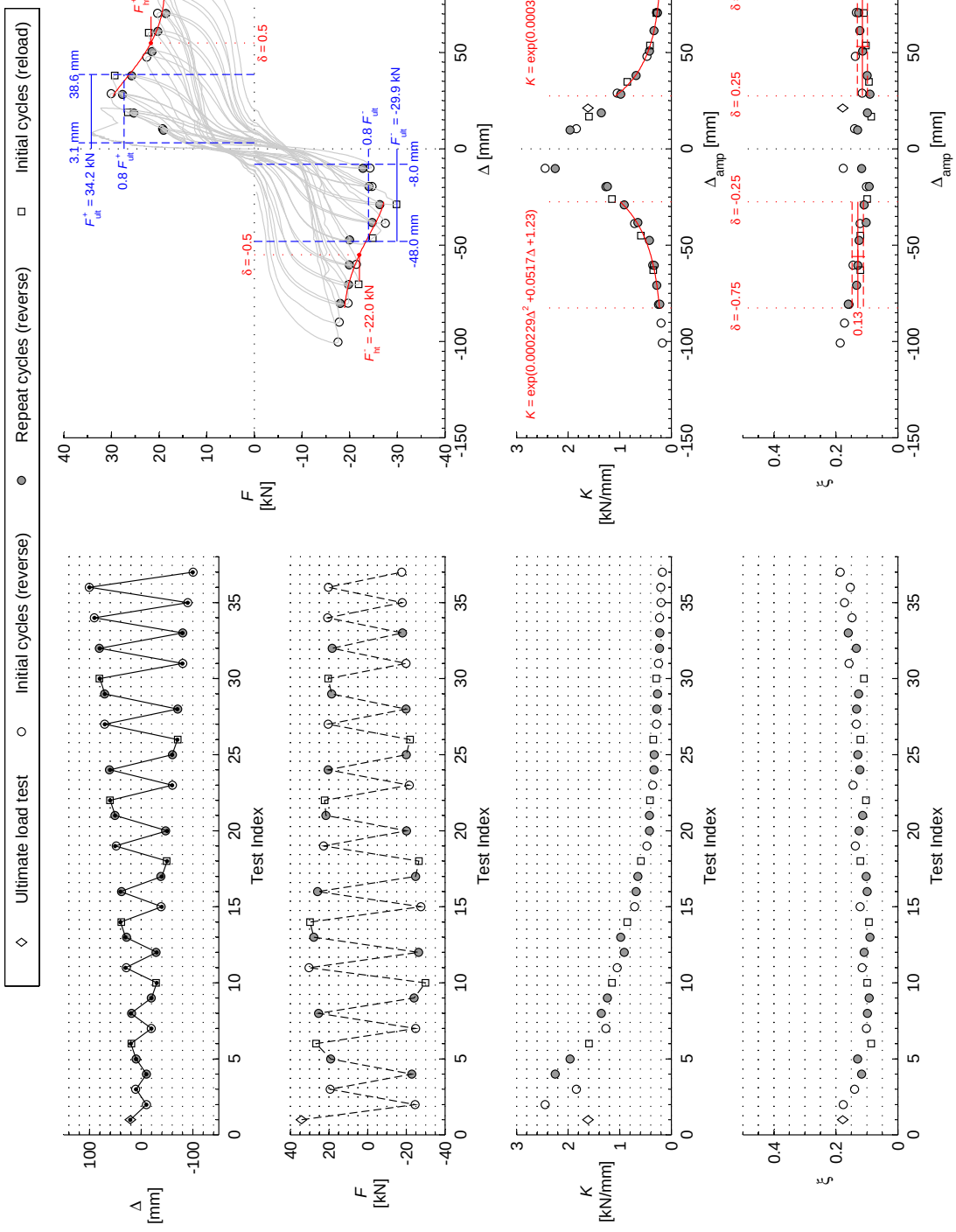

Figure B.19: Cycle analysis results for wall s4.

Table B.4: Results of individual cycles for wall s4.

Test Index	Test Type	Target Δ [mm]	Cycle Type		Measured Cycle Properties					Envelope Point	
			Rep. no	Dir.	Δ_{peak} [mm]	Δ_{amp} [mm]	F_{amp} [kN]	K [kN/mm]	ξ	Δ_{env} [mm]	F_{env} [kN]
1	ult	+21			21.2	*	34.2	1.614	0.18	19.7	31.7
2	cyc	−10	i	reverse	−10.1	*	−24.6	2.443	0.18	−9.9	−24.3
3	cyc	+10	i	reverse	10.5	*	19.3	1.840	0.14	10.5	19.2
4	cyc	−10	ii	reverse	−10.2	*	−22.9	2.250	0.12	−10.1	−22.8
5	cyc	+10	ii	reverse	9.7	*	19.1	1.960	0.13	9.7	19.0
6	cyc	+20	i	reload	19.1	16.7	26.6	1.594	0.09	19.0	26.6
7	cyc	−20	i	reverse	−19.6	*	−24.8	1.269	0.10	−19.5	−24.7
8	cyc	+20	ii	reverse	18.7	*	25.3	1.358	0.10	18.6	25.3
9	cyc	−20	ii	reverse	−19.5	*	−24.1	1.237	0.09	−19.4	−24.1
10	cyc	−30	i	reload	−28.9	−26.0	−29.9	1.149	0.10	−28.8	−29.8
11	cyc	+30	i	reverse	28.9	*	30.3	1.049	0.11	28.6	30.0
12	cyc	−30	ii	reverse	−29.0	*	−26.4	0.911	0.11	−28.9	−26.3
13	cyc	+30	ii	reverse	28.4	*	27.8	0.979	0.09	28.2	27.7
14	cyc	+40	i	reload	38.6	34.8	29.7	0.853	0.09	38.1	29.3
15	cyc	−40	i	reverse	−38.7	*	−27.6	0.713	0.12	−38.5	−27.5
16	cyc	+40	ii	reverse	38.0	*	25.8	0.679	0.10	37.9	25.8
17	cyc	−40	ii	reverse	−38.2	*	−24.8	0.649	0.10	−38.2	−24.8
18	cyc	−50	i	reload	−49.4	−45.0	−26.5	0.589	0.12	−46.3	−24.9
19	cyc	+50	i	reverse	48.1	*	22.8	0.474	0.14	47.6	22.6
20	cyc	−50	ii	reverse	−47.5	*	−20.1	0.423	0.12	−47.3	−20.0
21	cyc	+50	ii	reverse	50.8	*	21.6	0.425	0.11	50.5	21.5
22	cyc	+60	i	reload	60.6	53.7	22.3	0.415	0.10	60.3	22.1
23	cyc	−60	i	reverse	−60.4	*	−21.5	0.357	0.14	−60.0	−21.4
24	cyc	+60	ii	reverse	61.4	*	20.4	0.333	0.12	60.9	20.3
25	cyc	−60	ii	reverse	−60.4	*	−20.0	0.331	0.13	−60.2	−20.0
26	cyc	−70	i	reload	−70.5	−62.9	−22.0	0.349	0.12	−70.2	−21.9
27	cyc	+70	i	reverse	70.7	*	20.4	0.288	0.13	70.4	20.3
28	cyc	−70	ii	reverse	−70.8	*	−19.9	0.281	0.13	−70.4	−19.8
29	cyc	+70	ii	reverse	70.6	*	18.6	0.264	0.13	70.3	18.6
30	cyc	+80	i	reload	80.9	70.5	20.5	0.290	0.11	80.4	20.3
31	cyc	−80	i	reverse	−80.7	*	−19.8	0.246	0.16	−80.1	−19.7
32	cyc	+80	ii	reverse	81.2	*	18.3	0.226	0.13	80.8	18.3
33	cyc	−80	ii	reverse	−80.6	*	−18.1	0.225	0.16	−80.3	−18.0
34	cyc	+90	i	reverse	90.6	*	20.6	0.227	0.15	90.1	20.5
35	cyc	−90	i	reverse	−90.4	*	−18.0	0.199	0.17	−89.8	−17.8
36	cyc	+100	i	reverse	100.5	*	20.2	0.201	0.15	99.9	20.1
37	cyc	−100	i	reverse	−100.7	*	−17.6	0.175	0.19	−100.3	−17.6

(*) indicates that Δ_{amp} is same as Δ_{peak}, which is the case for reverse cycles.

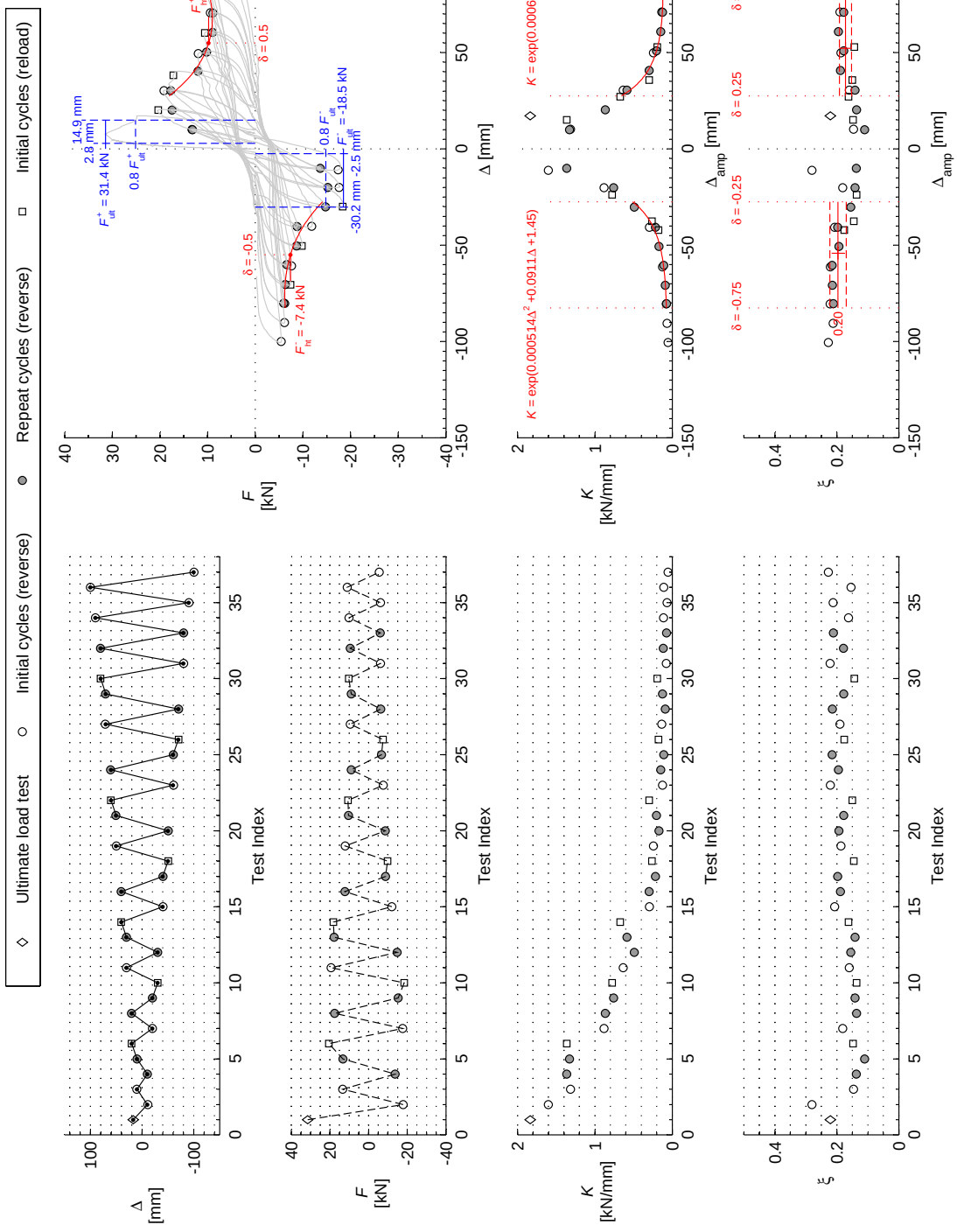

Figure B.20: Cycle analysis results for wall s5.

Table B.5: Results of individual cycles for wall s5.

Test Index	Test Type	Target Δ [mm]	Cycle Type		Measured Cycle Properties					Envelope Point	
			Rep. no	Dir.	Δ_{peak} [mm]	Δ_{amp} [mm]	F_{amp} [kN]	K [kN/mm]	ξ	Δ_{env} [mm]	F_{env} [kN]
1	ult	+17			17.1	*	31.4	1.834	0.22	14.0	25.7
2	cyc	−10	i	reverse	−11.2	*	−17.9	1.602	0.28	−10.9	−17.4
3	cyc	+10	i	reverse	10.2	*	13.4	1.314	0.15	10.1	13.3
4	cyc	−10	ii	reverse	−10.1	*	−13.7	1.363	0.14	−10.0	−13.6
5	cyc	+10	ii	reverse	10.0	*	13.2	1.328	0.11	9.9	13.2
6	cyc	+20	i	reload	20.4	15.1	20.5	1.362	0.15	20.2	20.4
7	cyc	−20	i	reverse	−20.1	*	−17.7	0.880	0.18	−20.0	−17.6
8	cyc	+20	ii	reverse	20.3	*	17.5	0.864	0.14	20.2	17.5
9	cyc	−20	ii	reverse	−20.2	*	−15.3	0.759	0.14	−20.1	−15.2
10	cyc	−30	i	reload	−30.2	−23.8	−18.5	0.777	0.14	−30.0	−18.3
11	cyc	+30	i	reverse	30.5	*	19.3	0.633	0.16	30.2	19.2
12	cyc	−30	ii	reverse	−30.3	*	−14.8	0.490	0.15	−30.1	−14.8
13	cyc	+30	ii	reverse	30.4	*	17.8	0.586	0.14	30.3	17.7
14	cyc	+40	i	reload	40.3	27.0	18.1	0.671	0.16	38.2	17.2
15	cyc	−40	i	reverse	−40.7	*	−12.0	0.295	0.21	−40.1	−11.8
16	cyc	+40	ii	reverse	40.6	*	12.1	0.298	0.19	40.3	12.0
17	cyc	−40	ii	reverse	−40.7	*	−8.8	0.217	0.20	−40.4	−8.8
18	cyc	−50	i	reload	−50.8	−37.5	−9.9	0.262	0.15	−50.3	−9.8
19	cyc	+50	i	reverse	49.9	*	12.0	0.241	0.19	49.5	12.0
20	cyc	−50	ii	reverse	−50.7	*	−8.7	0.172	0.19	−50.3	−8.7
21	cyc	+50	ii	reverse	50.9	*	10.3	0.203	0.18	50.3	10.2
22	cyc	+60	i	reload	60.7	35.7	10.6	0.298	0.15	60.2	10.6
23	cyc	−60	i	reverse	−61.2	*	−7.7	0.125	0.22	−60.7	−7.6
24	cyc	+60	ii	reverse	60.9	*	9.0	0.147	0.19	60.5	8.9
25	cyc	−60	ii	reverse	−60.4	*	−6.7	0.110	0.21	−60.1	−6.6
26	cyc	−70	i	reload	−70.8	−42.2	−7.5	0.177	0.18	−70.5	−7.4
27	cyc	+70	i	reverse	71.0	*	9.5	0.134	0.19	70.6	9.4
28	cyc	−70	ii	reverse	−70.8	*	−6.3	0.089	0.21	−70.4	−6.3
29	cyc	+70	ii	reverse	70.8	*	9.0	0.126	0.18	70.5	8.9
30	cyc	+80	i	reload	80.4	52.8	10.2	0.194	0.14	80.0	10.2
31	cyc	−80	i	reverse	−80.5	*	−6.2	0.077	0.22	−80.2	−6.2
32	cyc	+80	ii	reverse	80.3	*	9.4	0.117	0.18	80.0	9.4
33	cyc	−80	ii	reverse	−80.4	*	−6.0	0.075	0.21	−80.1	−6.0
34	cyc	+90	i	reverse	90.3	*	10.1	0.112	0.16	89.7	10.0
35	cyc	−90	i	reverse	−90.5	*	−6.2	0.068	0.21	−90.2	−6.2
36	cyc	+100	i	reverse	100.2	*	11.0	0.110	0.15	99.8	11.0
37	cyc	−100	i	reverse	−100.5	*	−5.5	0.055	0.23	−99.9	−5.5

(*) indicates that Δ_{amp} is same as Δ_{peak}, which is the case for reverse cycles.

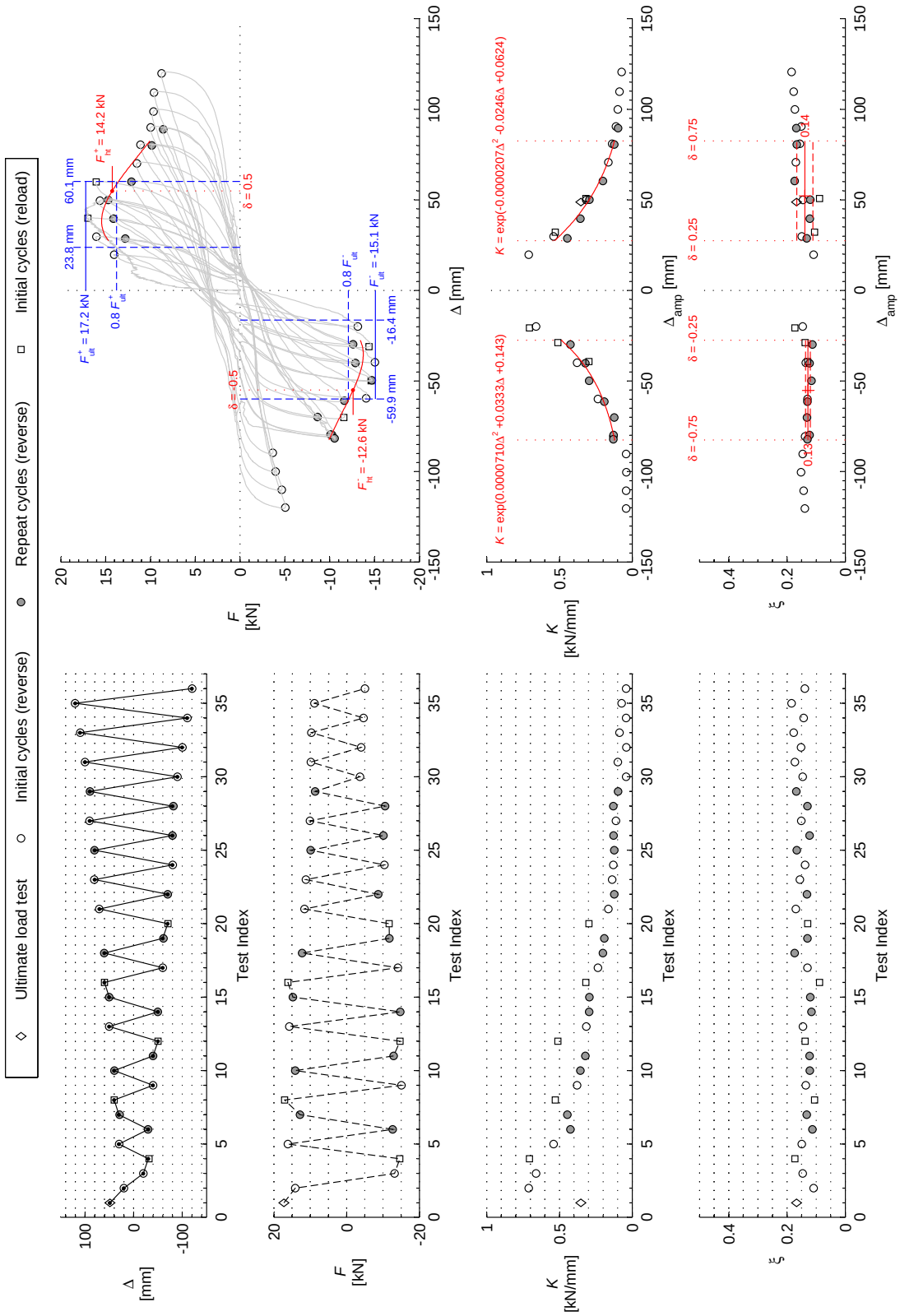

Figure B.21: Cycle analysis results for wall s6.

Table B.6: Results of individual cycles for wall s6.

Test Index	Test Type	Target Δ [mm]	Cycle Type		Measured Cycle Properties					Envelope Point	
			Rep. no	Dir.	Δ_{peak} [mm]	Δ_{amp} [mm]	F_{amp} [kN]	K [kN/mm]	ξ	Δ_{env} [mm]	F_{env} [kN]
1	ult	+49			48.9	*	17.2	0.352	0.17	46.7	16.5
2	cyc	+20	i	reverse	19.8	*	14.1	0.710	0.11	19.8	14.0
3	cyc	−20	i	reverse	−19.9	*	−13.2	0.660	0.15	−19.9	−13.1
4	cyc	−30	i	reload	−31.6	−20.7	−14.6	0.706	0.17	−31.0	−14.4
5	cyc	+30	i	reverse	29.8	*	16.1	0.540	0.15	29.7	16.0
6	cyc	−30	ii	reverse	−29.8	*	−12.7	0.424	0.11	−29.7	−12.6
7	cyc	+30	ii	reverse	28.8	*	12.8	0.446	0.13	28.7	12.8
8	cyc	+40	i	reload	40.0	32.2	17.0	0.529	0.11	39.9	17.0
9	cyc	−40	i	reverse	−39.9	*	−15.1	0.379	0.14	−39.7	−15.0
10	cyc	+40	ii	reverse	39.7	*	14.1	0.356	0.12	39.6	14.1
11	cyc	−40	ii	reverse	−40.2	*	−12.9	0.322	0.12	−40.0	−12.9
12	cyc	−50	i	reload	−50.1	−28.8	−14.7	0.510	0.14	−49.9	−14.6
13	cyc	+50	i	reverse	50.0	*	15.8	0.315	0.15	49.6	15.6
14	cyc	−50	ii	reverse	−49.8	*	−14.8	0.296	0.12	−49.6	−14.7
15	cyc	+50	ii	reverse	50.1	*	14.8	0.295	0.12	49.9	14.7
16	cyc	+60	i	reload	60.1	50.7	16.1	0.318	0.09	59.9	16.0
17	cyc	−60	i	reverse	−59.9	*	−14.1	0.236	0.13	−59.6	−14.1
18	cyc	+60	ii	reverse	60.4	*	12.2	0.202	0.17	60.0	12.1
19	cyc	−60	ii	reverse	−61.4	*	−11.8	0.191	0.13	−60.8	−11.6
20	cyc	−70	i	reload	−70.8	−39.3	−11.7	0.297	0.13	−70.1	−11.6
21	cyc	+70	i	reverse	70.8	*	11.6	0.164	0.17	70.1	11.5
22	cyc	−70	ii	reverse	−70.2	*	−8.7	0.124	0.13	−69.9	−8.6
23	cyc	+80	i	reverse	81.0	*	11.2	0.138	0.16	80.5	11.1
24	cyc	−80	i	reverse	−80.6	*	−10.4	0.129	0.14	−79.6	−10.3
25	cyc	+80	ii	reverse	80.6	*	9.9	0.123	0.17	80.1	9.8
26	cyc	−80	ii	reverse	−79.8	*	−10.1	0.127	0.12	−79.6	−10.1
27	cyc	+90	i	reverse	90.6	*	10.0	0.111	0.15	90.0	10.0
28	cyc	−80	iii	reverse	−82.2	*	−10.6	0.129	0.13	−81.7	−10.5
29	cyc	+90	ii	reverse	89.7	*	8.6	0.096	0.17	89.0	8.6
30	cyc	−90	i	reverse	−90.2	*	−3.7	0.041	0.15	−89.6	−3.7
31	cyc	+100	i	reverse	100.0	*	9.8	0.098	0.17	98.8	9.7
32	cyc	−100	i	reverse	−100.3	*	−4.0	0.040	0.15	−99.9	−4.0
33	cyc	+110	i	reverse	109.8	*	9.7	0.088	0.18	109.2	9.6
34	cyc	−110	i	reverse	−110.6	*	−4.7	0.042	0.14	−110.0	−4.7
35	cyc	+120	i	reverse	120.7	*	8.8	0.073	0.18	119.9	8.7
36	cyc	−120	i	reverse	−120.4	*	−5.1	0.042	0.14	−119.8	−5.0

(*) indicates that Δ_{amp} is same as Δ_{peak}, which is the case for reverse cycles.

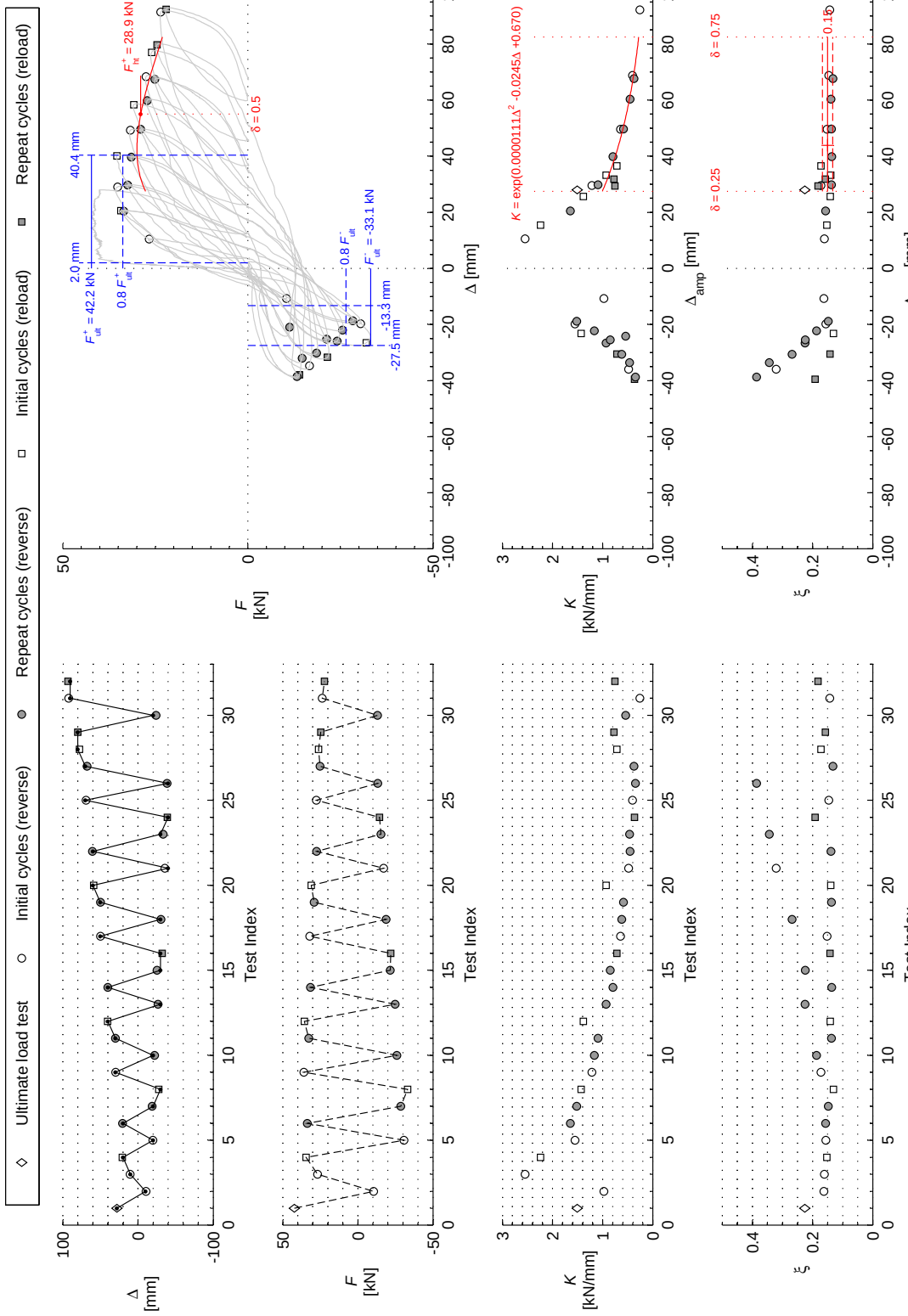

Figure B.22: Cycle analysis results for wall s7.

Table B.7: Results of individual cycles for wall s7.

Test Index	Test Type	Target Δ [mm]	Cycle Type		Measured Cycle Properties					Envelope Point	
			Rep. no	Dir.	Δ_{peak} [mm]	Δ_{amp} [mm]	F_{amp} [kN]	K [kN/mm]	ξ	Δ_{env} [mm]	F_{env} [kN]
1	ult	+28			28.0	*	42.2	1.509	0.23	26.5	40.0
2	cyc	−10	i	reverse	−10.8	*	−10.5	0.974	0.16	−10.7	−10.4
3	cyc	+10	i	reverse	10.5	*	26.9	2.550	0.16	10.4	26.6
4	cyc	+20	i	reload	20.7	15.4	34.5	2.238	0.15	20.6	34.3
5	cyc	−20	i	reverse	−19.8	*	−30.6	1.549	0.16	−19.7	−30.5
6	cyc	+20	ii	reverse	20.5	*	33.7	1.644	0.16	20.4	33.5
7	cyc	−20	ii	reverse	−18.8	*	−28.6	1.518	0.15	−18.7	−28.4
8	cyc	−30	i	reload	−27.5	−23.2	−33.1	1.428	0.13	−26.5	−32.0
9	cyc	+30	i	reverse	29.6	*	35.8	1.212	0.17	29.0	35.2
10	cyc	−20	iv	reverse	−22.3	*	−25.9	1.165	0.19	−22.0	−25.6
11	cyc	+30	ii	reverse	29.9	*	32.6	1.093	0.14	29.7	32.5
12	cyc	+40	i	reload	40.4	25.7	35.5	1.384	0.14	40.2	35.3
13	cyc	−30	ii	reverse	−26.6	*	−24.8	0.932	0.22	−25.9	−24.1
14	cyc	+40	ii	reverse	39.9	*	31.6	0.792	0.14	39.7	31.4
15	cyc	−30	iii	reverse	−25.5	*	−21.5	0.845	0.22	−25.2	−21.3
16	cyc	−30	iv	reload	−32.3	−30.6	−21.9	0.716	0.14	−31.7	−21.5
17	cyc	+50	i	reverse	49.6	*	31.9	0.644	0.15	49.3	31.7
18	cyc	−30	v	reverse	−30.6	*	−18.9	0.616	0.27	−30.2	−18.6
19	cyc	+50	ii	reverse	49.7	*	29.0	0.583	0.14	49.6	29.0
20	cyc	+60	i	reload	58.7	33.2	31.0	0.931	0.14	58.4	30.8
21	cyc	−40	i	reverse	−35.9	*	−17.2	0.480	0.32	−34.7	−16.7
22	cyc	+60	ii	reverse	60.3	*	27.4	0.454	0.14	59.9	27.2
23	cyc	−30	vii	reverse	−33.6	*	−15.4	0.459	0.34	−32.0	−14.7
24	cyc	−40	ii	reload	−39.1	−39.5	−14.4	0.363	0.19	−38.0	−13.9
25	cyc	+70	i	reverse	68.8	*	27.6	0.402	0.15	68.4	27.5
26	cyc	−40	iii	reverse	−38.7	*	−13.3	0.344	0.39	−38.6	−13.3
27	cyc	+70	ii	reverse	67.7	*	25.2	0.372	0.13	67.4	25.1
28	cyc	+80	i	reload	77.7	36.5	26.2	0.717	0.17	77.0	26.0
29	cyc	+80	ii	reload	80.1	31.8	24.7	0.774	0.16	79.7	24.5

(*) indicates that Δ_{amp} is same as Δ_{peak}, which is the case for reverse cycles.

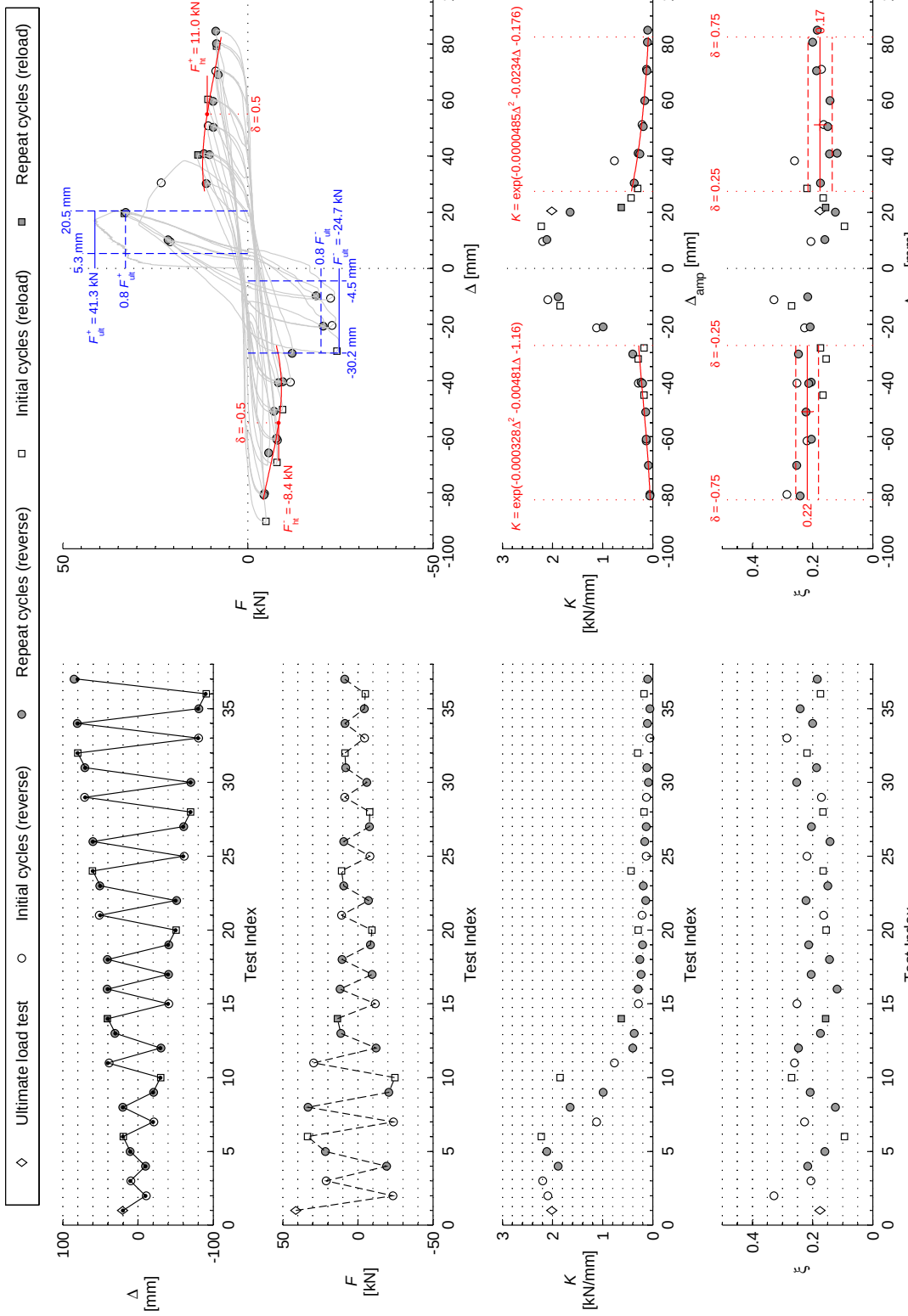

Figure B.23: Cycle analysis results for wall s8.

Table B.8: Results of individual cycles for wall s8.

Test Index	Test Type	Target Δ [mm]	Cycle Type		Measured Cycle Properties					Envelope Point	
			Rep. no	Dir.	Δ_{peak} [mm]	Δ_{amp} [mm]	F_{amp} [kN]	K [kN/mm]	ξ	Δ_{env} [mm]	F_{env} [kN]
1	ult	+20			20.5	*	41.3	2.015	0.18	19.0	38.4
2	cyc	−10	i	reverse	−11.2	*	−23.4	2.095	0.33	−10.7	−22.3
3	cyc	+10	i	reverse	9.6	*	21.0	2.196	0.21	9.5	20.9
4	cyc	−10	ii	reverse	−10.1	*	−19.1	1.890	0.22	−9.8	−18.5
5	cyc	+10	ii	reverse	10.3	*	21.7	2.112	0.16	10.2	21.6
6	cyc	+20	i	reload	19.6	15.0	33.4	2.224	0.09	19.6	33.4
7	cyc	−20	i	reverse	−21.2	*	−23.7	1.120	0.23	−20.3	−22.8
8	cyc	+20	ii	reverse	20.1	*	33.1	1.649	0.12	20.0	33.0
9	cyc	−20	ii	reverse	−20.8	*	−20.6	0.990	0.21	−20.6	−20.4
10	cyc	−30	i	reload	−30.2	−13.3	−24.7	1.851	0.27	−29.4	−24.0
11	cyc	+40	i	reverse	38.4	*	29.4	0.766	0.26	30.6	23.4
12	cyc	−30	ii	reverse	−30.5	*	−12.1	0.397	0.25	−30.2	−12.0
13	cyc	+30	ii	reverse	30.5	*	11.3	0.371	0.17	30.2	11.2
14	cyc	+40	ii	reload	40.8	21.7	13.6	0.628	0.16	40.4	13.5
15	cyc	−40	i	reverse	−40.9	*	−11.6	0.284	0.25	−40.5	−11.5
16	cyc	+40	iii	reverse	41.1	*	11.9	0.289	0.12	40.9	11.8
17	cyc	−40	ii	reverse	−40.6	*	−9.5	0.234	0.20	−40.4	−9.4
18	cyc	+40	iv	reverse	40.8	*	10.5	0.256	0.14	40.6	10.4
19	cyc	−40	iii	reverse	−41.0	*	−8.3	0.204	0.21	−40.7	−8.3
20	cyc	−50	i	reload	−50.7	−32.2	−9.4	0.292	0.15	−50.4	−9.4
21	cyc	+50	i	reverse	51.3	*	10.8	0.211	0.16	50.9	10.7
22	cyc	−50	ii	reverse	−51.2	*	−7.1	0.138	0.22	−50.9	−7.0
23	cyc	+50	ii	reverse	50.6	*	9.4	0.186	0.15	50.4	9.4
24	cyc	+60	i	reload	60.6	25.2	10.8	0.430	0.16	60.3	10.8
25	cyc	−60	i	reverse	−61.5	*	−8.1	0.131	0.22	−61.2	−8.0
26	cyc	+60	ii	reverse	59.9	*	9.4	0.157	0.14	59.6	9.4
27	cyc	−60	ii	reverse	−60.9	*	−7.8	0.128	0.20	−60.6	−7.7
28	cyc	−70	i	reload	−70.0	−45.2	−7.9	0.176	0.17	−69.2	−7.8
29	cyc	+70	i	reverse	71.0	*	8.7	0.123	0.17	70.4	8.7
30	cyc	−70	ii	reverse	−70.2	*	−6.0	0.085	0.25	−65.8	−5.6
31	cyc	+70	ii	reverse	70.5	*	8.1	0.115	0.19	69.0	8.0
32	cyc	+80	i	reload	79.9	28.5	8.5	0.299	0.22	79.3	8.5
33	cyc	−80	i	reverse	−80.6	*	−4.5	0.056	0.29	−80.2	−4.5
34	cyc	+80	ii	reverse	80.7	*	8.5	0.105	0.20	80.2	8.4
35	cyc	−80	ii	reverse	−81.1	*	−4.4	0.054	0.24	−80.7	−4.3
36	cyc	−90	i	reload	−90.6	−28.3	−4.9	0.174	0.17	−90.2	−4.9
37	cyc	+80	iii	reverse	84.9	*	8.7	0.102	0.18	84.6	8.6

(*) indicates that Δ_{amp} is same as Δ_{peak}, which is the case for reverse cycles.

B.4 WALL DEFORMATION PROFILES

Figures B.24–B.31 provide plots of each wall's deformation profile during the initial push test. The data used to generate these graphs was measured using the displacement transducer layouts shown in Figure B.4.

The graphs plot the deformations at the vertical slices A–A, B–B and C–C, located at the quarter- and mid-span positions along the wall. These deformations have been calculated as the displacement at each point along the wall relative to the supports. Each graph has two horizontal axes to denote the displacement: The top axis refers to the actual displacement, while the bottom axis shows the displacement normalised by the maximum value along the wall.[1]

For each wall, two graphs are provided: The first one shows the profile at the instance that the wall reached its maximum strength, and the second one shows the profile at the maximum imposed displacement during the initial push test. For comparison, the displacement shapes based on the idealised failure mechanisms which are assumed by the virtual work analytical method (Chapter 4) for computing the strength of the wall, are also shown. A discussion of the observed trends is provided in Section 2.6.

[1] Note that the 'normalised displacement' plotted on these graphs is distinct from the definition of the normalised displacement δ as used in other parts of this thesis and defined by Eq. (2.2).

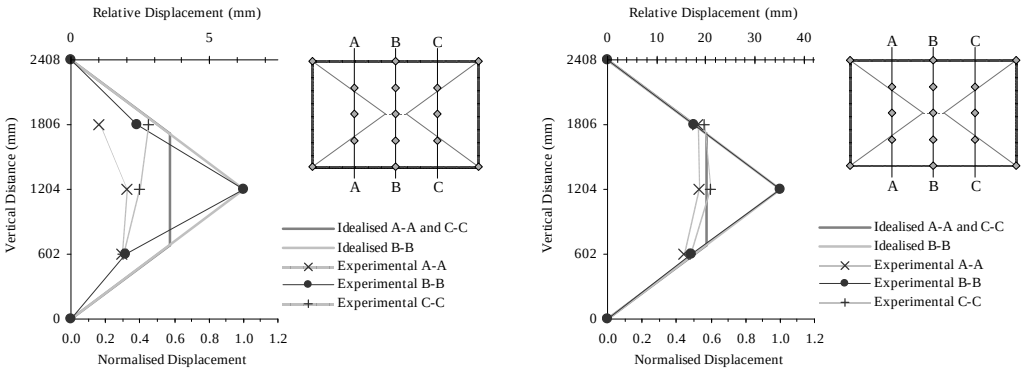

(a) During point of ultimate strength. **(b)** At maximum imposed displacement.

Figure B.24: Displacement profile for wall s1.

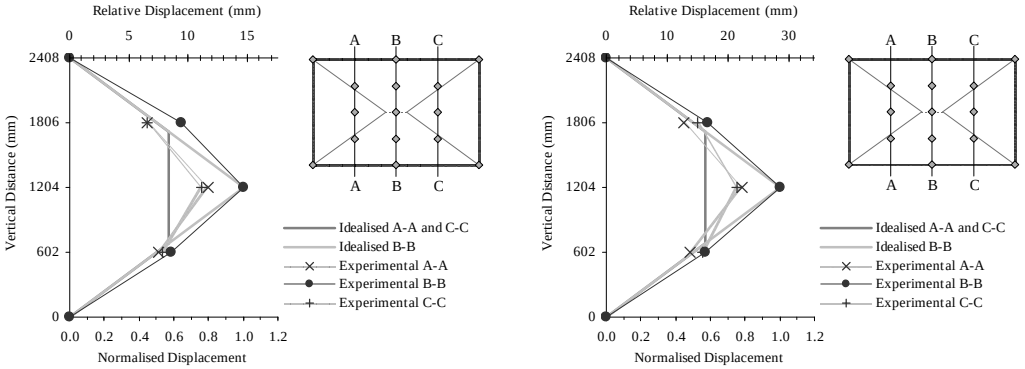

(a) During point of ultimate strength. **(b)** At maximum imposed displacement.

Figure B.25: Displacement profile for wall s2.

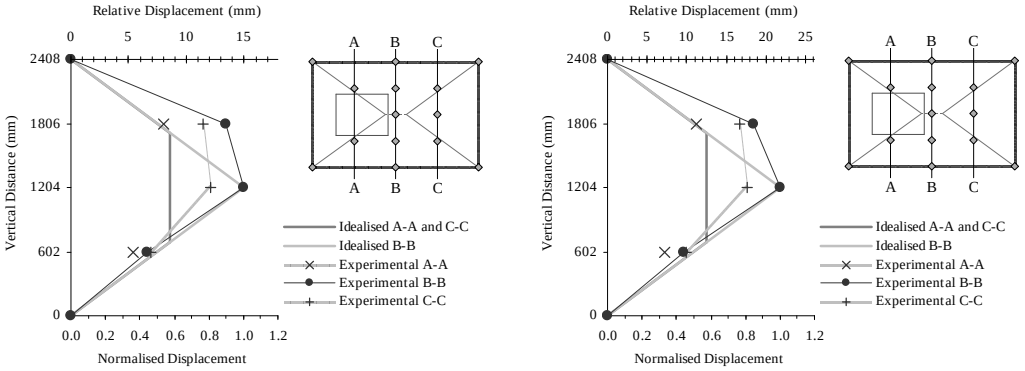

(a) During point of ultimate strength. **(b)** At maximum imposed displacement.

Figure B.26: Displacement profile for wall s3.

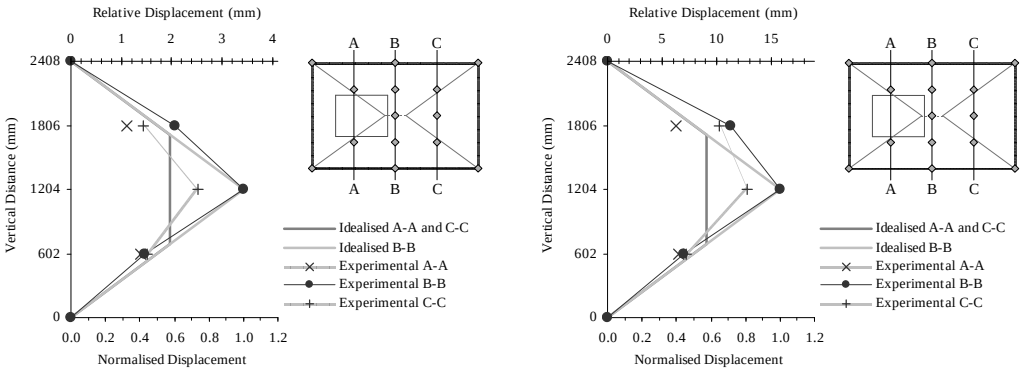

(a) During point of ultimate strength. **(b)** At maximum imposed displacement.

Figure B.27: Displacement profile for wall s4.

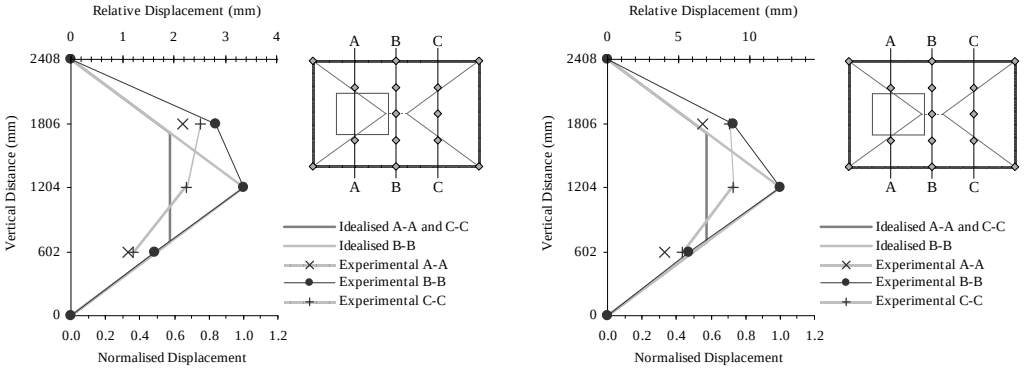

(a) During point of ultimate strength. **(b)** At maximum imposed displacement.

Figure B.28: Displacement profile for wall s5.

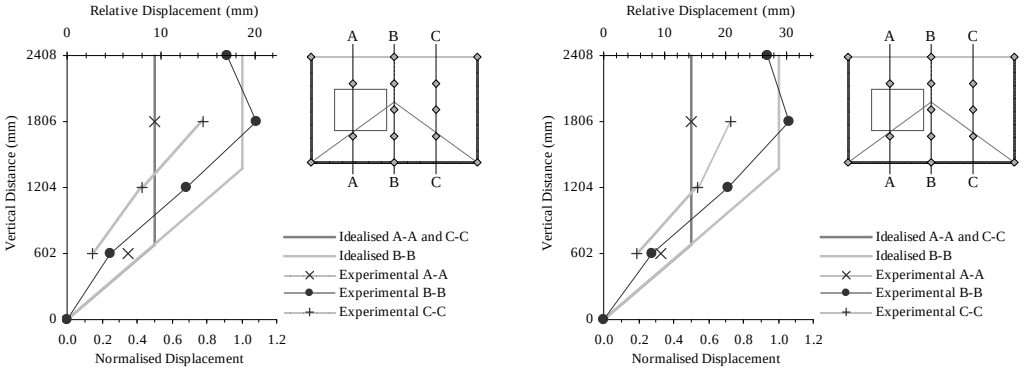

(a) During point of ultimate strength. **(b)** At maximum imposed displacement.

Figure B.29: Displacement profile for wall s6.

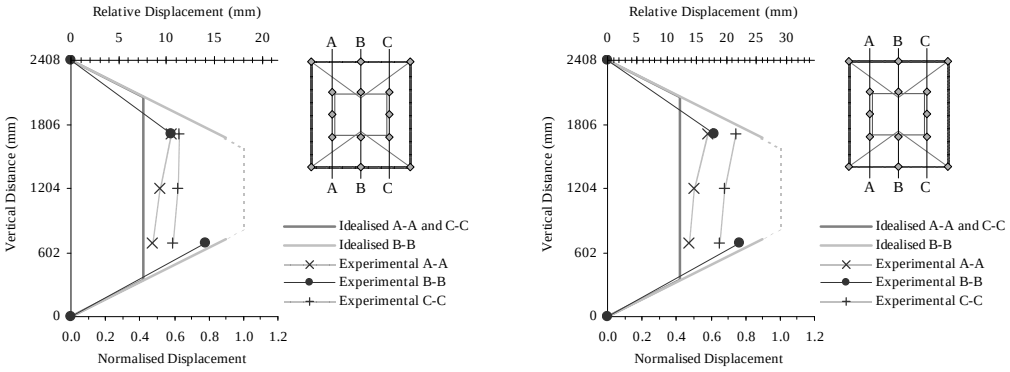

(a) During point of ultimate strength. **(b)** At maximum imposed displacement.

Figure B.30: Displacement profile for wall s7.

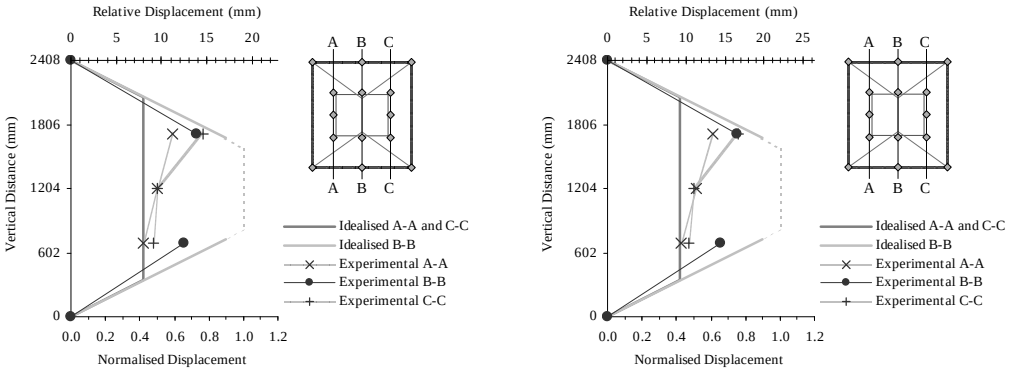

(a) During point of ultimate strength. **(b)** At maximum imposed displacement.

Figure B.31: Displacement profile for wall s8.

B.5 CRACK PATTERN PHOTOGRAPHS

Figures B.32–B.39 show photographs of the walls' crack patterns at the conclusion of the cyclic tests. Each of these depict the interior face of the respective walls. Due to spatial limitations in the laboratory, it was not possible in some cases to capture the entire wall face in a single photo, so the patterns are demonstrated by multiple photos. Illustrations of these crack patterns are also provided by Figure 2.24 based on close visual inspection of the walls.

Figure B.32: Photograph of wall s1 crack pattern at the conclusion of cyclic testing.

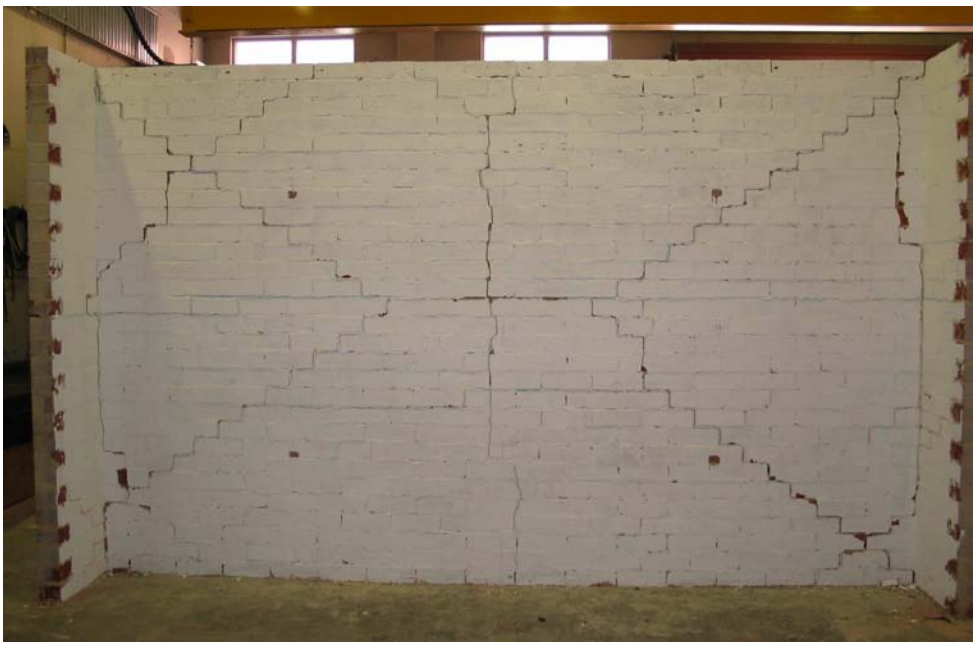

Figure B.33: Photograph of wall s2 crack pattern at the conclusion of cyclic testing.

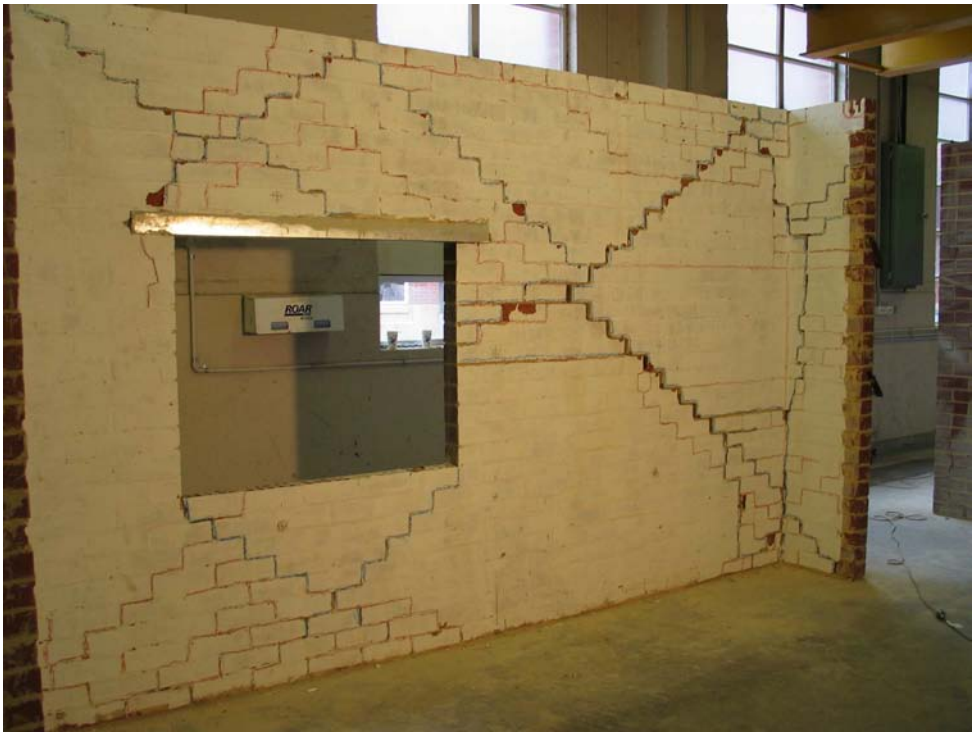

Figure B.34: Photograph of wall s3 crack pattern at the conclusion of cyclic testing.

Figure B.35: Photograph of wall s4 crack pattern at the conclusion of cyclic testing.

Figure B.36: Photograph of wall s5 crack pattern at the conclusion of cyclic testing.

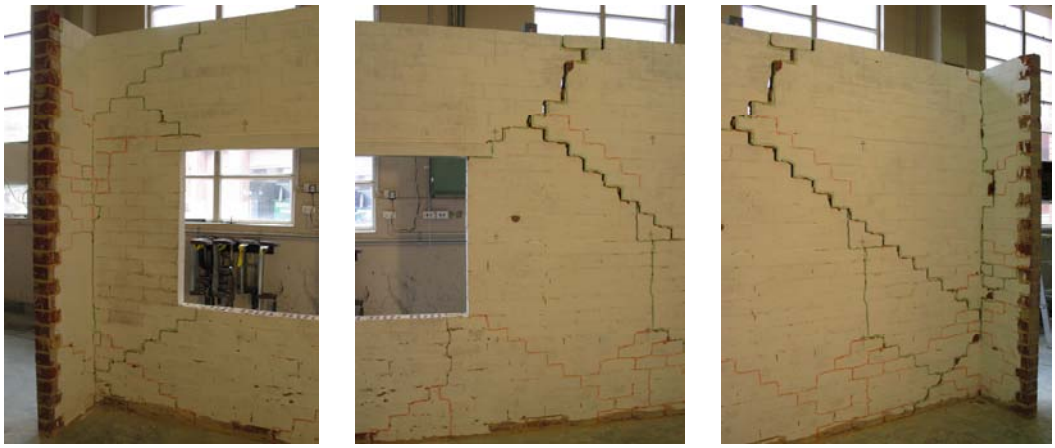

Figure B.37: Photograph of wall s6 crack pattern at the conclusion of cyclic testing.

Figure B.38: Photograph of wall s7 crack pattern at the conclusion of cyclic testing.

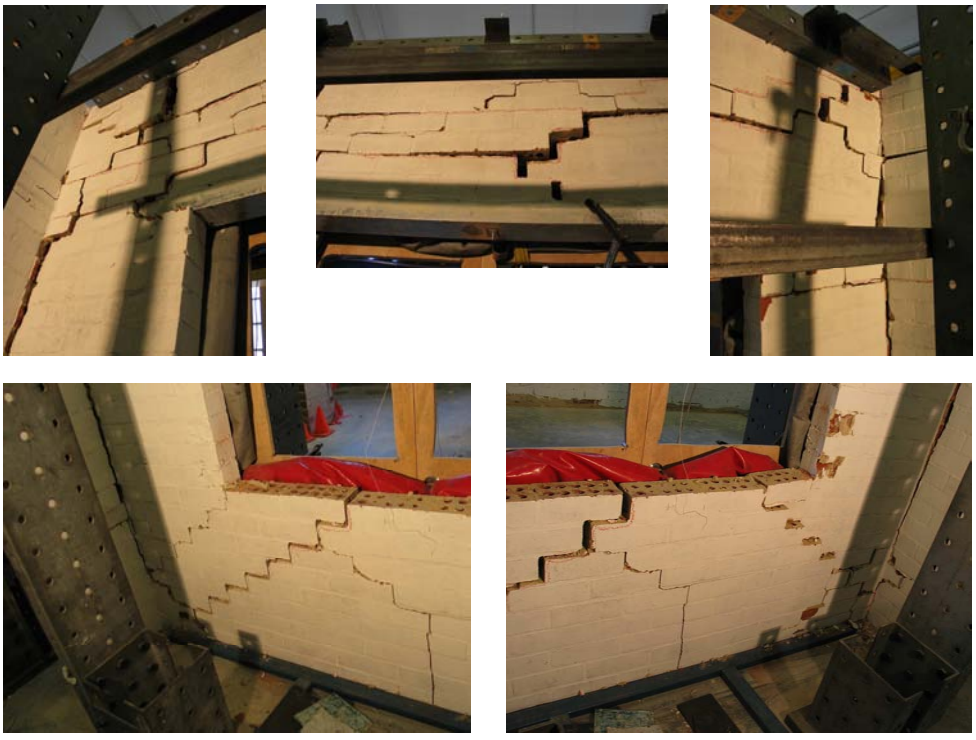

Figure B.39: Photograph of wall s8 crack pattern at the conclusion of cyclic testing.

Appendix C

SHAKETABLE TESTING

Abstract

This appendix contains additional detail related to Chapter 3.

C.1 TEST RUN NOMENCLATURE

For brevity, a standardised convention is used for naming individual test runs. It uses several arguments separated by underscores to provide a description of the tests. The first three arguments are standard[1] and provide the following information:

1. Name of the wall; for example D1, D2, D3,...
2. Index of the test run for the particular wall.
3. Type of test; whereby `R` = pulse test, `H` = harmonic test, and `EQ` = earthquake motion test.

For example, the first three arguments of test `d2_06_R_8mm_100ms` imply that it was the sixth test performed on wall D2 and used a pulse input motion. The remaining arguments contain specific information relating to the different types of tests (described in Section 3.2.5), as follows:

[1] Exceptions include test runs 1–6, 8–10 and 89–91 for wall D1, which also provide a value of the non-standard axial stress applied at the top of the wall as one of the first four arguments.

PULSE TESTS (R) In these tests, the table underwent a simple displacement step function, as shown by Figure 3.6. The first argument after `R` denotes the displacement step, and the second argument denotes the time step (defined respectively by x_o and dt in Figure 3.6). For example, in test `d2_06_R_8mm_100ms` the table was subjected to a displacement step of 8 millimetres over 100 milliseconds.

HARMONIC TESTS (H) These tests used a sinusoidal harmonic input motion, as shown by Figure 3.7. The first argument after `R` denotes the excitation frequency, and the second argument denotes the table displacement amplitude (defined respectively by f_o and x_o in Figure 3.7). For example, in test `d2_29_H_12Hz_0.3mm` the table was subjected to a harmonic motion at a frequency of 12 Hz with a targeted amplitude of 0.3 mm. It should be noted, however, that the target PGD was not always accurately reproduced by the table and hence the actual PGD was measured using instrumentation.

EARTHQUAKE MOTION TESTS (EQ) These tests used earthquake motions defined using a digitised displacement record. The first argument after `EQ` refers to the name of the earthquake motion; for example, `Taft` or one of the synthetic motions denoted by `Synth0x`. Details of these input motions are presented in Section C.2. The second argument refers to the input peak displacement (PGD) together with either '+' or '−' to denote the motion's direction (as defined in Figure C.5). For example, test `d2_39_EQ_Taft_+80mm` used the Taft earthquake motion with a PGD of 80 mm in the positive direction.

C.2 EARTHQUAKE INPUT MOTIONS

Time and frequency domain representations of the Taft earthquake motion, which served as the main input motion during these tests, are shown by Figure C.1.

In addition, eight synthetic motions were generated, referred to as Synth01–Synth08. The procedure used to generate each motion consisted of the following steps:

1. Digitised Gaussian noise was randomly generated in the time domain.
2. A lowpass filter was applied to the noise in the frequency domain, using the cutoff frequencies given in Table C.1.
3. A shape function was applied to the waveform in the time domain, consisting of three regions: linear ramp-up, constant amplitude, and linear ramp-down.

Table C.1: Synthetic earthquake motion cutoff frequencies.

Quake	Cutoff Frequency [Hz]
Syntho1	6
Syntho2	6
Syntho3	8
Syntho4	8
Syntho5	12
Syntho6	12
Syntho7	16
Syntho8	16

4. The resulting waveform was used as the synthetic motion's velocity vector.
5. The velocity was integrated to determine the displacement vector, and differentiated to determine the acceleration vector.
6. During the tests, the motion was scaled to achieve a required PGD.

Of the eight synthetic motions generated, all were used in the diagnostic tests performed on the shaketable test setup as described in Appendix D; however, only motions Syntho1, Syntho3 and Syntho5 were used during the wall tests. These are shown by Figures C.2, C.3 and C.4.

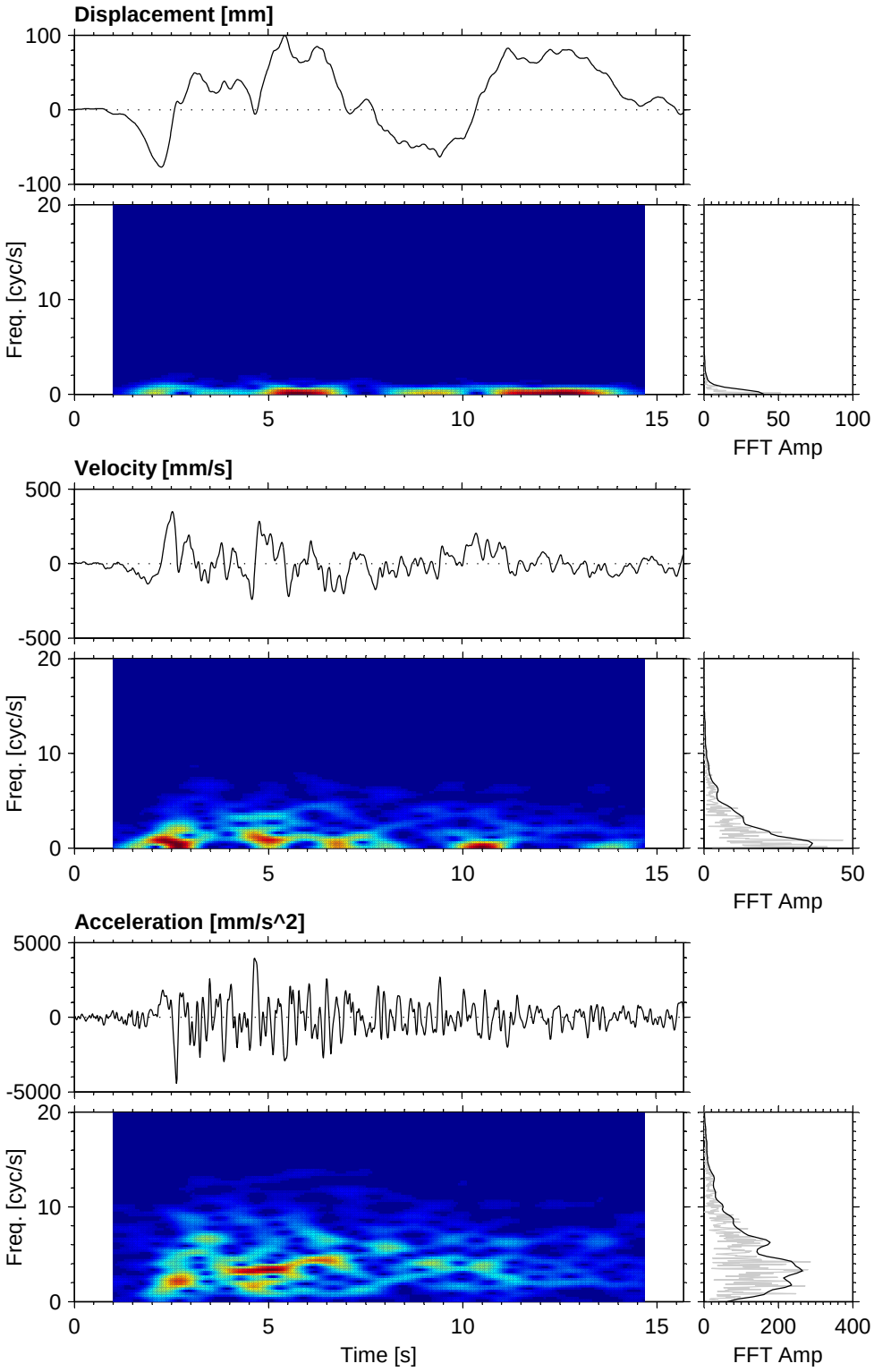

Figure C.1: Taft input motion in the time and frequency domains. (Scaled such that PGD $= +100$ mm)

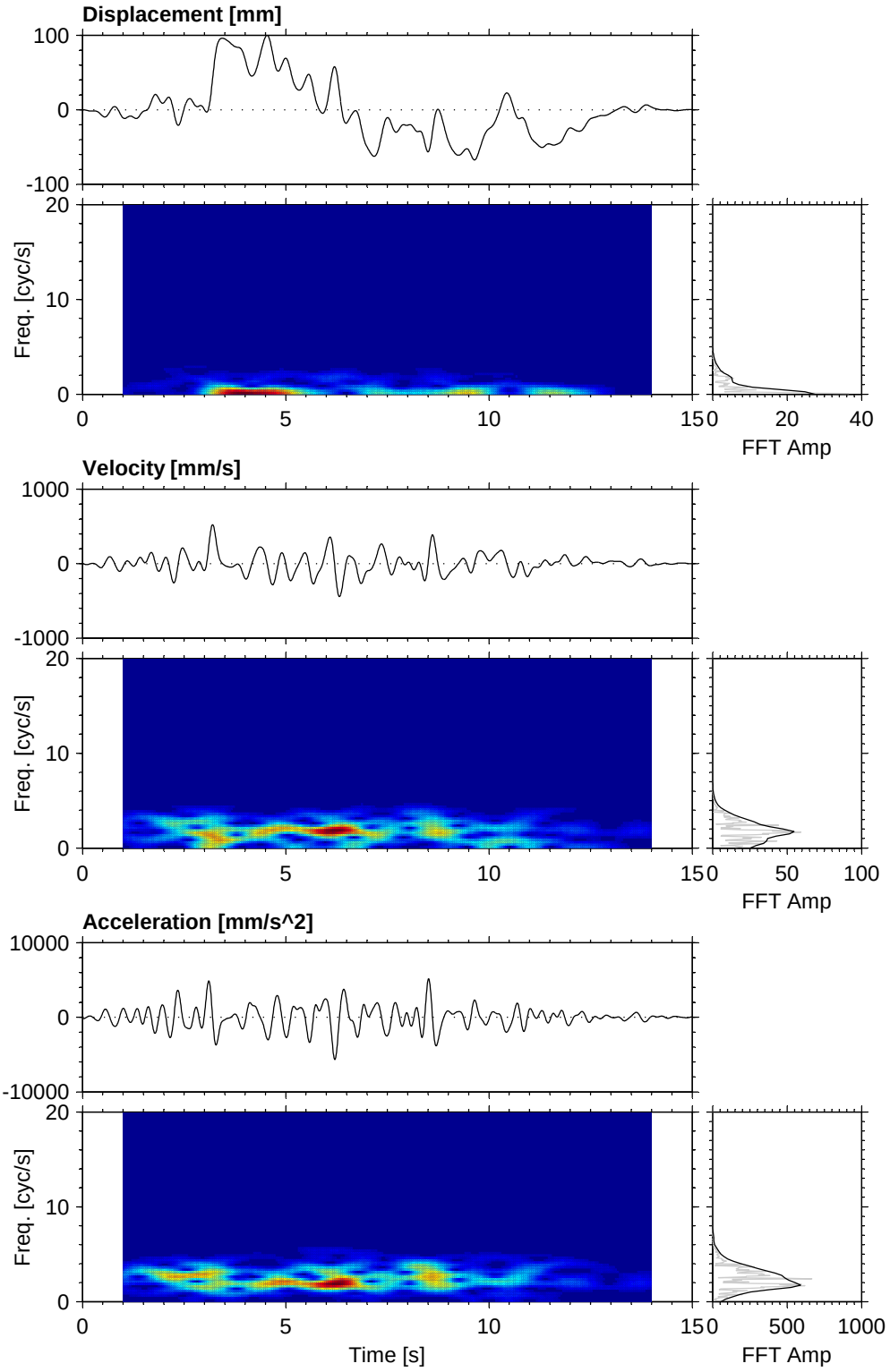

Figure C.2: Syntho1 input motion in the time and frequency domains. (Scaled such that PGD $= +100$ mm)

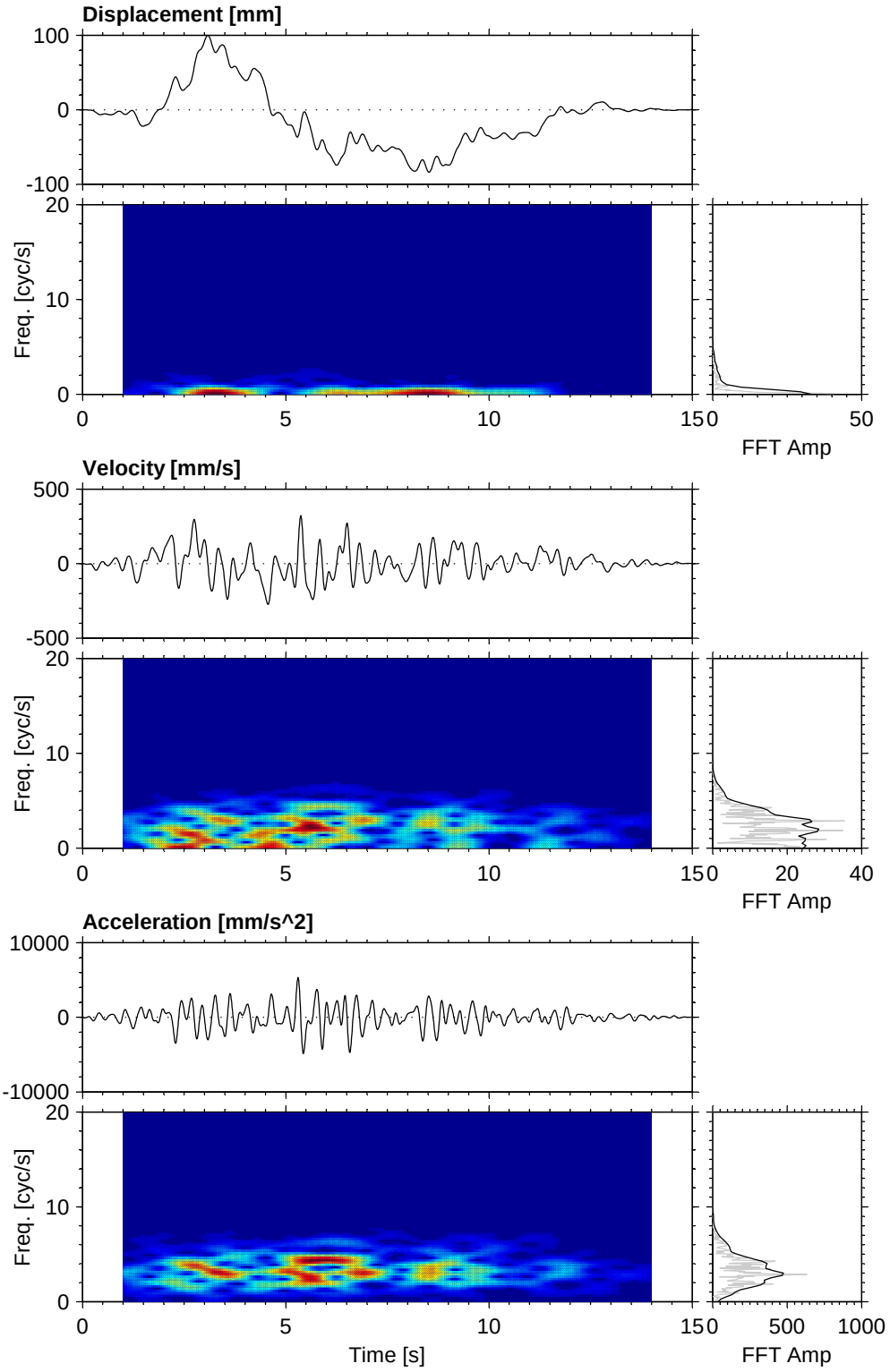

Figure C.3: Syntho3 input motion in the time and frequency domains. (Scaled such that PGD $= +100$ mm)

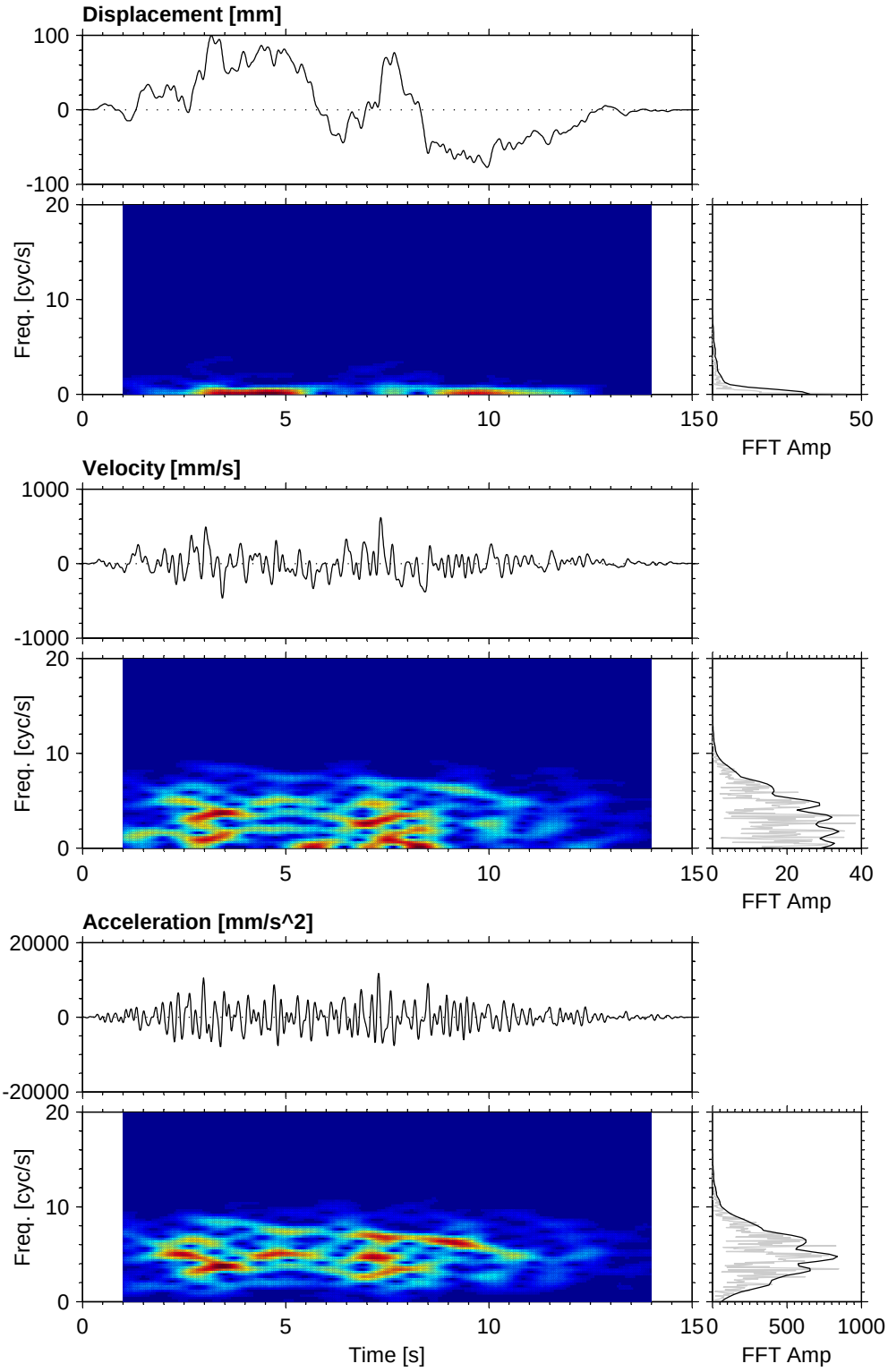

Figure C.4: Syntho5 input motion in the time and frequency domains. (Scaled such that PGD $= +100$ mm)

C.3 STANDARD DATA PROCESSING

This section details the process conducted on the raw test data to determine the time domain response of variables of interest. Section C.3.1 describes the calculations used, whilst Section C.3.2 reports peak results of selected response variables for each test run performed.

C.3.1 Calculation of Time Domain Response Vectors

The raw data acquired consisted of output from ten accelerometers and six displacement transducers, sampled at a rate of 200 Hz (Figure C.5). A computer routine was implemented to process the test data and derive time domain response vectors for variables of interest.[2] The associated calculations are discussed herein.

Positions and Displacements

Variables corresponding to positions and displacements are listed below.[3]

VECTOR	DESCRIPTION
$\boldsymbol{x}_{\text{tab}}$ and $\boldsymbol{x}_{\text{sup.bot}}$	Position of the table and position of the wall's bottom support, respectively, as measured by displacement transducer DT4 (Figure C.5). These are assumed to be effectively equal, since there was shown to be negligible slip between the table and slab.
$\boldsymbol{x}_{\text{sup.top}}$	Position of the wall's top support member, as measured by displacement transducer DT3 (Figure C.5).
$\boldsymbol{x}_{\text{sup.avg}}$	Average position of the wall's supports, taken as the average of the top and bottom supports, such that $$\boldsymbol{x}_{\text{sup.avg}} = \frac{\boldsymbol{x}_{\text{sup.bot}} + \boldsymbol{x}_{\text{sup.top}}}{2}. \quad \text{(C.1)}$$
$\boldsymbol{\Delta}_{\text{slab-tab}}$	Displacement (or slip) between the concrete slab and the table, measured using displacement transducer DT5 (Figure C.5).
$\boldsymbol{\Delta}_{\text{w.bot-slab}}$	Displacement (or slip) between the wall's bottom edge and the concrete slab, as measured by displacement transducer DT5 (Figure C.5). The displacement transducer was located on the second course of bricks from the bottom of the wall.

[2] For clarity, vector variables are denoted using bold symbols (e.g. $\boldsymbol{x}$ or $\boldsymbol{a}$), and scalar variables using italicised symbols (e.g. x or a).

[3] Note the subtle difference between these two parameters: Positions (x) are measured with respect to the *absolute* reference frame, whilst displacements (Δ) measure the relative difference between the positions of two objects.

VECTOR	DESCRIPTION
$\boldsymbol{\Delta}_{\text{sup.top-tab}}$	Relative displacement between the top and bottom supports of the wall. Calculated as $$\boldsymbol{\Delta}_{\text{sup.top-tab}} = \boldsymbol{x}_{\text{sup.top}} - \boldsymbol{x}_{\text{sup.bot}}. \quad \text{(C.2)}$$
$\boldsymbol{\Delta}_{\text{w.cent}}$	The wall's central displacement, defined as the position of the centre of the wall relative to its supports. Calculated by first determining the wall's central position $\boldsymbol{x}_{\text{w.cent}}$ as the average of the two displacement transducers DT1 and DT2 (Figure C.5). The averaging was performed in order to minimise data noise. The central displacement was then taken as $$\boldsymbol{\Delta}_{\text{w.cent}} = \boldsymbol{x}_{\text{w.cent}} - \boldsymbol{x}_{\text{sup.avg}}. \quad \text{(C.3)}$$
$\boldsymbol{\Delta}_{\text{w.cent0}}$	The wall's central displacement $\boldsymbol{\Delta}_{\text{w.cent}}$, zeroed at the start of each test run.

Accelerations

The following accelerations were determined:

VECTOR	DESCRIPTION
$\boldsymbol{a}_{\text{w.tl.corner}}$	Acceleration at the top left corner of the wall, as measured by accelerometer AC1 (Figure C.5) which was located at the top course of the return wall.
$\boldsymbol{a}_{\text{w.t.edge}}$	Acceleration at the top edge of the wall, as measured by accelerometer AC2 (Figure C.5). The accelerometer was located on the second topmost course of bricks, just below the top edge restraint member.
$\boldsymbol{a}_{\text{w.tr.corner}}$	Acceleration at the top right corner of the wall, as measured by accelerometer AC3 (Figure C.5) which was located at the top course of the return wall.
$\boldsymbol{a}_{\text{w.tl.quad}}$	Acceleration at the centre of the top left quadrant of the wall, as measured by accelerometer AC4 (Figure C.5).
$\boldsymbol{a}_{\text{w.tr.quad}}$	Acceleration at the centre of the top right quadrant of the wall, as measured by accelerometer AC5 (Figure C.5).
$\boldsymbol{a}_{\text{w.cent}}$	Acceleration at the centre of the wall, as measured by accelerometer AC6 (Figure C.5).
$\boldsymbol{a}_{\text{w.bl.quad}}$	Acceleration at the centre of the bottom left quadrant of the wall, as measured by accelerometer AC7 (Figure C.5).
$\boldsymbol{a}_{\text{w.br.quad}}$	Acceleration at the centre of the bottom right quadrant of the wall, as measured by accelerometer AC8 (Figure C.5).

VECTOR	DESCRIPTION
$\boldsymbol{a}_{\text{slab}}$	Acceleration at the centre of the slab supporting the wall, as measured by accelerometer AC9 (Figure C.5).
$\boldsymbol{a}_{\text{tab}}$	Acceleration at the centre of the table, as measured by accelerometer AC10 (Figure C.5).
$\boldsymbol{a}_{\text{sup.avg}}$	Average acceleration of the wall's supports. Calculated as a weighted average of the slab (50% contribution) and the top left and right corners of the wall (25% contribution each), such that $$\boldsymbol{a}_{\text{sup.avg}} = 0.5\,\boldsymbol{a}_{\text{slab}} + 0.25\,\boldsymbol{a}_{\text{w.tl.corner}} + 0.25\,\boldsymbol{a}_{\text{w.tr.corner}}. \quad \text{(C.4)}$$
$\boldsymbol{a}_{\text{w.avg}}$	Average acceleration of the wall, calculated as a weighted average of the contributions of the 10 accelerometers according to the summation $$\boldsymbol{a}_{\text{w.avg}} = \sum_{k=1}^{10} r_k\,\boldsymbol{a}_k, \quad \text{(C.5)}$$ where k refers to the index of each accelerometer, with $\boldsymbol{a}_k$ being its acceleration and r_k its weighting factor. The weighting factor for each accelerometer was taken as its percentage of the tributary area along the wall. The factors are given in Figure C.6. The resulting vector $\boldsymbol{a}_{\text{w.avg}}$ was used for computing the wall's resisting force and pressure.
$\boldsymbol{a}_{\text{w.cent-sup.avg}}$	Relative acceleration between the wall's centre and its top and bottom supports, calculated as $$\boldsymbol{a}_{\text{w.cent-sup.avg}} = \boldsymbol{a}_{\text{w.cent}} - \boldsymbol{a}_{\text{sup.avg}}. \quad \text{(C.6)}$$ The primary purpose of this response variable was for use in a subsequent spectral analysis for determining the wall's vibrational frequency, since it best captures the wall's fundamental mode of vibration. For comparison, this relative acceleration was also calculated by double differentiating the wall's central displacement $\Delta_{\text{w.cent}}$. The response vector resulting from this latter approach exhibited greater levels of data noise than that calculated using the above equation. However, at larger levels of shaking the resulting vectors were very similar in their peak response, waveform and spectral content.

Pressure and Force

Finally, the pressure and force resisted by the wall were calculated using the wall's average acceleration $\boldsymbol{a}_{\text{w.avg}}$. These calculations are based on the equation of motion and the assumption of negligible viscous (velocity-proportional) forces.

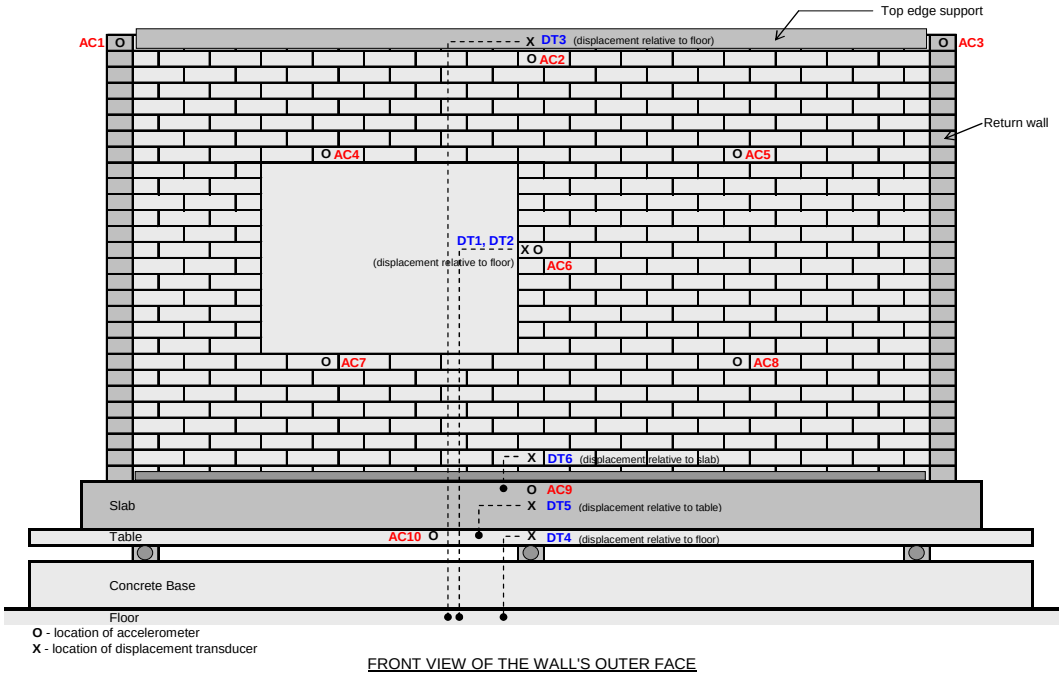

Figure C.5: Map of the instrumentation used for shaketable tests, comprising of 10 accelerometers (labelled AC1–AC10) and 6 displacement transducers (labelled DT1–DT6). Diagram is applicable to walls both with and without openings.

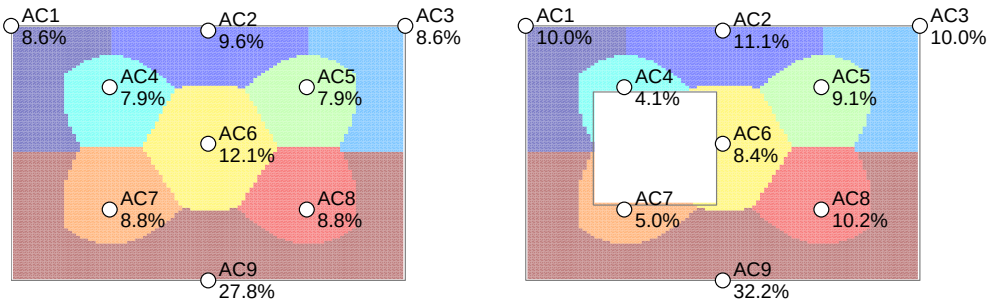

(a) Solid walls. **(b)** Walls with window.

Figure C.6: Accelerometer tributary area percentages, used as weighting factors in calculation of the wall's average acceleration.

VECTOR	DESCRIPTION
$\boldsymbol{q}_w$	Uniformly distributed face pressure resisted by the wall, calculated as $$\boldsymbol{q}_w = -\frac{\gamma\, t_u}{g}\, \boldsymbol{a}_{\text{w.avg}}, \tag{C.7}$$ where γ is the unit weight of the masonry, t_u is the thickness of the wall and g is acceleration due to gravity.
$\boldsymbol{F}_w$	Out-of-plane force resisted by the wall, calculated as $$\boldsymbol{F}_w = -M_w\, \boldsymbol{a}_{\text{w.avg}}. \tag{C.8}$$ In this expression, M_w is the mass of the wall, such that $$M_w = \frac{\gamma\, t_u\, A_w}{g}, \tag{C.9}$$ where A_w is the wall's net area.

C.3.2 Results

Table C.6 summarises the peak values for key variables in each test run performed, and also provides miscellaneous notes relating to individual test runs.

Table C.5: Legend for the notes column in Table C.6.

⊠	New cracking occurred during the test.
□	No new cracking occurred during the test. This is only shown for tests between initial and full cracking of the wall.
ϟ	Shaketable underwent unexpected impacts which generated spikes in its acceleration response (refer to Appendix D).
✇	Test was recorded using video camera.
✿	Cracking pattern was photographed after the test.

Table C.6: Peak response of key variables during individual test runs. The tests are listed in the order in which they were performed. Table C.5 provides an explanation of the symbols used in the notes column.

Test Name	Notes	Table and Supports					Wall Response					
		x_{tab} [mm]	$x_{sup.avg}$ [mm]	$\Delta_{sup.top-tab}$ [mm]	a_{tab} [g]	$a_{sup.avg}$ [g]	$\Delta_{w.cent}$ [mm]	$\Delta_{w.cent0}$ [mm]	$a_{w.cent}$ [g]	$a_{w.avg}$ [g]	q_w [kPa]	F_w [N]
d5_01_H_14Hz_0.05mm		0.1	0.2	0.4	0.08	0.08	0.3	0.3	0.19	0.10	0.10	203
d5_02_H_14Hz_0.1mm		0.2	0.4	0.5	0.21	0.23	0.5	0.5	0.57	0.29	0.30	593
d5_03_H_14Hz_0.15mm		0.6	0.8	0.6	0.50	0.54	1.3	1.3	1.51	0.72	0.76	1501
d5_04_H_14Hz_0.2mm	⊠ ✿ ☮	0.9	1.2	0.9	0.80	0.88	2.6	2.6	2.61	1.20	1.27	2498
d5_05_R_2mm_200ms	□[4]	2.2	2.2	0.2	0.08	0.09	0.5	0.3	0.36	0.10	0.11	214
d5_06_R_4mm_200ms	□	4.4	4.4	0.3	0.13	0.15	0.6	0.5	0.59	0.20	0.21	408
d5_07_R_4mm_100ms	□	4.7	4.7	0.5	0.35	0.36	1.3	1.2	1.23	0.42	0.45	875
d5_08_H_14Hz_0.2mm	□ ☮	0.3	0.5	0.6	0.31	0.31	2.4	2.3	2.11	0.68	0.72	1416
d5_09_H_14Hz_0.25mm	⊠ ✿ ☮	1.0	1.2	0.8	0.94	1.01	5.9	5.7	3.32	0.96	1.02	2003
d5_10_R_2mm_200ms	□	2.2	2.2	0.3	0.08	0.08	0.7	0.5	0.30	0.08	0.08	158
d5_11_R_4mm_200ms	□	4.5	4.5	0.5	0.14	0.16	1.1	0.9	0.55	0.16	0.17	339
d5_12_R_4mm_100ms	□	4.7	4.8	0.4	0.35	0.39	2.4	2.2	1.03	0.30	0.32	624
d5_13_H_14Hz_0.3mm	⊠[5] ☮	1.4	1.8	1.0	1.54	1.58	8.3	8.0	3.92	0.85	0.90	1762
d5_14_R_2mm_200ms		2.2	2.2	0.2	0.09	0.10	1.6	0.5	0.31	0.08	0.08	166
d5_15_R_4mm_200ms		4.4	4.4	0.4	0.14	0.16	2.1	1.1	0.49	0.13	0.14	270
d5_16_R_4mm_100ms		4.8	4.8	0.4	0.36	0.40	3.5	2.4	0.91	0.28	0.29	573
d5_17_EQ_Taft_-6mm	☮	5.5	5.5	0.4	0.04	0.05	1.2	0.2	0.12	0.04	0.04	85
d5_18_EQ_Taft_+6mm	☮	5.7	5.7	0.4	0.04	0.05	1.3	0.3	0.12	0.04	0.04	78
d5_19_EQ_Taft_+11mm	☮	11.3	11.3	0.5	0.09	0.11	1.5	0.5	0.29	0.07	0.08	148
d5_20_EQ_Taft_-11mm	☮	11.2	11.2	0.3	0.08	0.08	1.5	0.5	0.22	0.06	0.07	135
d5_21_EQ_Taft_-17mm	☮	17.0	16.9	0.5	0.11	0.11	1.7	0.6	0.34	0.09	0.10	195
d5_22_EQ_Taft_+17mm	☮	16.9	16.9	0.4	0.13	0.15	1.7	0.7	0.48	0.10	0.11	211
d5_23_EQ_Taft_+22mm	☮	22.5	22.6	0.5	0.16	0.17	1.9	0.9	0.55	0.13	0.13	260
d5_24_EQ_Taft_-22mm	☮	22.3	22.3	0.4	0.18	0.19	2.0	1.0	0.44	0.14	0.14	284
d5_25_EQ_Taft_-28mm	☮	28.1	28.1	0.4	0.20	0.20	2.2	1.1	0.49	0.16	0.17	326
d5_26_EQ_Taft_+28mm	☮	28.0	28.0	0.4	0.23	0.24	2.1	1.2	0.62	0.17	0.18	359
d5_27_EQ_Taft_+33mm	☮	33.5	33.5	0.5	0.28	0.29	2.5	1.5	0.77	0.20	0.21	418
d5_28_EQ_Taft_-33mm	☮	33.3	33.4	0.5	0.23	0.28	2.3	1.4	0.58	0.19	0.20	390
d5_29_EQ_Taft_-39mm	☮	39.0	39.0	0.5	0.30	0.37	2.5	1.6	0.63	0.23	0.25	482

continued on next page

[4]These three free vibration tests (5–7) showed the wall's frequency to be approximately 15-20 Hz. However, a preliminary free vibration test performed prior to test no. 1 by impacting the wall with a rubber mallet showed a strong signal at approximately 35 Hz. It is likely that the reduction in frequency from 35 Hz to 15-20 Hz was a result of the initial cracking of the wall.

[5]Wall became fully cracked.

Table C.6: (cont'd).

Test Name	Notes		Table and Supports					Wall Response					
			x_{tab} [mm]	$x_{sup.avg}$ [mm]	$\Delta_{sup.top-tab}$ [mm]	a_{tab} [g]	$a_{sup.avg}$ [g]	$\Delta_{w.cent}$ [mm]	$\Delta_{w.cent0}$ [mm]	$a_{w.cent}$ [g]	$a_{w.avg}$ [g]	q_w [kPa]	F_w [N]
d5_30_EQ_Taft_+39mm			39.4	39.5	0.4	0.32	0.36	2.7	1.8	0.87	0.26	0.27	537
d5_31_EQ_Taft_+45mm			44.9	44.9	0.4	0.37	0.41	2.9	2.2	0.96	0.29	0.31	605
d5_32_EQ_Taft_-45mm			45.0	45.0	0.4	0.35	0.42	2.9	2.0	0.76	0.29	0.30	593
d5_33_EQ_Taft_-50mm			50.1	50.1	0.5	0.46	0.46	4.2	3.3	1.07	0.38	0.41	798
d5_34_EQ_Taft_+50mm		✿	50.3	50.5	0.5	0.39	0.45	3.4	2.4	1.10	0.33	0.34	676
d5_35_EQ_Taft_+56mm			56.1	56.0	0.7	0.49	0.52	2.9	2.8	1.19	0.39	0.41	810
d5_36_EQ_Taft_-56mm	ϟ		56.2	56.1	0.9	1.06	1.04	6.5	6.8	2.00	0.74	0.79	1544
d5_37_EQ_Taft_-67mm	ϟ		66.7	66.6	1.4	1.96	1.76	12.0	12.1	3.52	1.29	1.37	2680
d5_38_EQ_Taft_+67mm	ϟ		67.3	67.2	0.8	1.35	1.42	8.9	9.0	3.61	1.17	1.24	2426
d5_39_R_2mm_200ms			2.4	2.2	0.6	0.08	0.10	0.8	0.5	0.29	0.07	0.08	154
d5_40_R_4mm_200ms			4.6	4.4	0.7	0.14	0.15	1.2	0.9	0.42	0.12	0.13	257
d5_41_R_4mm_100ms			5.1	4.9	0.7	0.36	0.40	2.8	2.3	0.81	0.29	0.31	610
d5_42_EQ_Taft_+73mm	ϟ		72.6	72.5	1.2	1.97	1.90	13.0	12.6	3.89	1.52	1.61	3159
d5_43_EQ_Taft_-73mm	ϟ		73.0	72.9	1.4	1.98	1.81	14.8	14.5	2.67	1.21	1.29	2523
d5_44_EQ_Taft_-78mm	ϟ		78.2	77.9	1.1	1.83	1.81	13.1	13.0	2.75	1.12	1.18	2321
d5_45_EQ_Taft_+78mm	ϟ		78.2	78.1	1.4	2.41	2.32	17.1	16.6	3.94	1.43	1.52	2976
d5_46_R_2mm_200ms			2.5	2.3	0.8	0.11	0.09	3.1	0.6	0.23	0.07	0.07	140
d5_47_R_4mm_200ms			4.6	4.5	0.6	0.13	0.17	3.9	1.3	0.36	0.13	0.13	261
d5_48_R_4mm_100ms			5.1	4.9	0.6	0.38	0.37	6.0	3.8	0.80	0.31	0.32	635
d5_49_EQ_Taft_+22mm			21.8	22.3	1.4	0.13	0.19	3.8	1.9	0.35	0.13	0.14	276
d5_50_EQ_Taft_-22mm			22.8	22.3	1.4	0.15	0.18	3.8	1.9	0.41	0.15	0.16	305
d5_51_EQ_Taft_-45mm			45.8	45.2	1.6	0.30	0.33	6.4	4.7	0.91	0.28	0.30	591
d5_52_EQ_Taft_+45mm			44.3	44.8	1.3	0.36	0.38	6.1	4.4	0.69	0.30	0.32	629
d5_53_EQ_Taft_+67mm	ϟ		66.5	67.1	1.6	1.18	1.09	8.9	10.6	2.38	0.81	0.86	1685
d5_54_EQ_Taft_-67mm	ϟ		67.4	66.6	1.8	1.95	1.64	15.6	13.9	2.48	1.13	1.20	2353
d5_55_EQ_Taft_-84mm	ϟ		84.3	83.4	2.1	1.52	1.22	10.9	10.7	1.71	0.88	0.93	1829
d5_56_EQ_Taft_+84mm	ϟ		83.7	84.2	2.1	2.55	2.64	19.0	18.5	4.91	1.50	1.59	3112
d5_57_EQ_Taft_+89mm	ϟ		88.7	89.2	2.0	2.47	2.35	17.1	17.4	4.95	1.42	1.50	2940
d5_58_EQ_Taft_-89mm	ϟ		89.9	89.0	2.1	1.27	1.16	15.9	15.4	1.59	0.67	0.71	1389
d5_59_EQ_Taft_-95mm	ϟ		95.0	94.2	2.2	1.34	1.13	18.0	18.8	1.90	0.80	0.84	1653
d5_60_EQ_Taft_+95mm	ϟ	✿	94.2	94.7	1.8	2.30	2.07	19.9	19.2	2.90	1.25	1.32	2594
d5_61_EQ_Taft_+100mm	ϟ		100.2	100.8	1.9	2.31	1.88	22.2	22.2	2.30	1.33	1.41	2771
d5_62_EQ_Taft_-100mm	ϟ[6]	✿	100.9	100.1	2.3	1.45	1.25	22.6	24.5	2.79	0.94	1.00	1963
d3_01_R_2mm_200ms			2.2	2.1	0.5	0.09	0.10	0.5	0.4	0.15	0.11	0.11	226
d3_02_R_4mm_200ms			4.1	4.2	0.3	0.17	0.17	0.3	0.3	0.25	0.19	0.20	399

continued on next page

[6]Lintel fell out due to a loss of connection with the wall at one of its ends.

Table C.6: (cont'd).

Test Name	Notes	Table and Supports					Wall Response					
		x_{tab} [mm]	$x_{sup.avg}$ [mm]	$\Delta_{sup.top-tab}$ [mm]	a_{tab} [g]	$a_{sup.avg}$ [g]	$\Delta_{w.cent}$ [mm]	$\Delta_{w.cent0}$ [mm]	$a_{w.cent}$ [g]	$a_{w.avg}$ [g]	q_w [kPa]	F_w [N]
d3_03_R_4mm_100ms		4.5	4.5	0.5	0.34	0.35	0.3	0.3	0.46	0.38	0.40	793
d3_04_R_8mm_100ms		8.9	9.1	0.7	0.74	0.79	0.7	0.6	1.37	0.92	0.97	1909
d3_05_H_13Hz_0.05mm		0.4	0.2	0.5	0.08	0.08	0.3	0.2	0.11	0.08	0.09	169
d3_06_H_13Hz_0.1mm		0.6	0.4	0.5	0.22	0.20	0.3	0.3	0.32	0.23	0.24	476
d3_07_H_13Hz_0.15mm		0.6	0.6	0.8	0.41	0.54	0.5	0.4	0.68	0.45	0.48	940
d3_08_H_13Hz_0.2mm		0.6	0.8	0.9	0.55	0.71	0.5	0.5	1.07	0.65	0.69	1358
d3_09_H_13Hz_0.25mm		0.8	1.1	1.0	0.70	1.00	0.8	0.9	1.65	0.96	1.02	1999
d3_10_H_13Hz_0.3mm	[7]	1.1	1.5	1.3	0.94	1.30	1.1	1.1	2.08	1.41	1.50	2940
d3_11_H_13Hz_0.3mm	⊠[8]	1.9	2.7	2.2	1.68	2.05	4.7	4.2	4.97	2.40	2.54	4983
d3_12_R_4mm_200ms	□	4.0	4.1	0.4	0.15	0.14	1.3	0.3	0.24	0.16	0.17	342
d3_13_R_4mm_100ms	□	4.3	4.5	0.4	0.32	0.31	1.5	0.5	0.65	0.35	0.37	723
d3_14_R_8mm_100ms	□	8.7	8.9	0.6	0.72	0.68	2.2	1.1	1.59	0.80	0.85	1670
d3_15_H_13Hz_0.35mm	⊠	1.8	2.8	2.6	1.54	2.22	5.7	4.6	5.49	2.52	2.67	5247
d3_16_H_13Hz_0.4mm	⊠	1.6	2.5	2.5	1.41	2.07	6.7	5.6	5.29	2.45	2.59	5082
d3_17_R_4mm_200ms	□	4.1	4.2	0.6	0.15	0.18	1.0	0.4	0.49	0.20	0.21	414
d3_18_R_4mm_100ms	□	4.3	4.4	0.4	0.32	0.32	1.3	0.7	0.80	0.35	0.37	733
d3_19_R_8mm_100ms	□	8.6	8.8	0.7	0.75	0.63	2.1	1.5	1.67	0.78	0.82	1616
d3_20_H_12Hz_0.4mm	⊠[9]	1.8	2.5	2.0	1.31	1.80	8.2	8.8	4.77	2.10	2.23	4374
d3_21_R_4mm_200ms		4.2	4.2	0.5	0.14	0.16	1.4	0.6	0.44	0.15	0.16	318
d3_22_R_4mm_100ms		4.6	4.6	0.4	0.33	0.34	2.4	1.6	1.06	0.32	0.34	660
d3_23_R_8mm_100ms		8.8	9.0	0.5	0.75	0.67	4.3	3.5	2.18	0.59	0.62	1222
d3_24_EQ_Taft_-5mm		5.0	5.0	0.3	0.04	0.05	1.1	0.3	0.13	0.06	0.07	128
d3_25_EQ_Taft_+5mm		5.1	5.1	0.6	0.04	0.05	1.1	0.3	0.15	0.07	0.07	136
d3_26_EQ_Taft_+10mm		10.1	10.1	0.5	0.08	0.08	1.1	0.5	0.34	0.13	0.13	262
d3_27_EQ_Taft_-10mm		9.9	9.9	0.5	0.07	0.08	1.1	0.3	0.25	0.10	0.11	214
d3_28_EQ_Taft_-20mm		20.0	20.0	0.6	0.12	0.15	1.3	0.5	0.35	0.18	0.19	370
d3_29_EQ_Taft_+20mm		19.9	19.9	0.5	0.13	0.15	1.2	0.5	0.49	0.23	0.24	476
d3_30_EQ_Taft_+30mm		30.2	29.9	0.6	0.20	0.23	1.4	0.6	0.58	0.27	0.28	555
d3_31_EQ_Taft_-30mm		30.1	30.1	0.6	0.18	0.21	1.3	0.6	0.56	0.20	0.22	425
d3_32_EQ_Taft_-40mm		39.8	39.8	0.5	0.28	0.25	1.6	0.9	0.65	0.27	0.28	558
d3_33_EQ_Taft_+40mm		40.1	40.1	0.5	0.29	0.28	1.5	0.9	0.82	0.40	0.42	822
d3_34_EQ_Taft_+50mm		49.8	49.9	0.4	0.34	0.41	1.9	1.2	0.98	0.54	0.57	1122
d3_35_EQ_Taft_-50mm		49.7	49.7	0.5	0.40	0.41	1.9	1.2	0.84	0.35	0.37	729

continued on next page

[7] Precompression springs underwent severe horizontal vibration during test 10.

[8] Precompression springs were restrained prior to conducting this test. The revised test setup was retained for all subsequent tests with precompression.

[9] Wall became fully cracked.

Table C.6: (cont'd).

Test Name	Notes	Table and Supports					Wall Response					
		x_{tab} [mm]	$x_{sup.avg}$ [mm]	$\Delta_{sup.top-tab}$ [mm]	a_{tab} [g]	$a_{sup.avg}$ [g]	$\Delta_{w.cent}$ [mm]	$\Delta_{w.cent0}$ [mm]	$a_{w.cent}$ [g]	$a_{w.avg}$ [g]	q_w [kPa]	F_w [N]
d3_36_EQ_Taft_-60mm	ϟ	60.0	60.1	1.1	1.50	1.34	5.9	5.2	3.17	1.11	1.18	2315
d3_37_EQ_Taft_+60mm	☮	59.8	60.0	0.5	0.45	0.45	2.6	2.1	1.42	0.57	0.61	1193
d3_38_EQ_Taft_+70mm	ϟ ☮	70.3	70.6	1.0	1.71	1.57	9.5	8.9	3.69	1.59	1.68	3299
d3_39_EQ_Taft_-70mm	ϟ ☮	69.9	70.0	1.5	2.16	2.04	8.5	9.3	4.89	1.39	1.47	2879
d3_40_EQ_Taft_-80mm	ϟ ☮	79.4	79.4	1.2	1.79	1.74	7.5	8.1	4.49	1.18	1.25	2451
d3_41_EQ_Taft_+80mm	ϟ ☮	80.0	80.1	1.8	2.73	2.77	15.7	15.2	4.78	1.86	1.97	3870
d3_42_R_4mm_200ms		4.2	4.3	0.4	0.16	0.16	1.8	0.8	0.52	0.22	0.24	462
d3_43_R_4mm_100ms		4.5	4.5	0.3	0.33	0.34	2.6	1.6	0.88	0.36	0.38	749
d3_44_R_8mm_100ms		8.9	9.0	0.6	0.76	0.75	5.0	3.8	2.04	0.65	0.69	1349
d3_45_EQ_Taft_+90mm	ϟ ☮	89.7	89.8	2.1	2.62	2.97	17.2	16.3	5.03	1.76	1.87	3665
d3_46_EQ_Taft_-90mm	ϟ ☮	89.6	89.7	1.0	1.37	1.33	7.8	6.6	3.52	0.98	1.04	2036
d3_47_R_4mm_200ms		4.2	4.3	0.5	0.15	0.16	1.6	0.8	0.53	0.19	0.20	385
d3_48_R_4mm_100ms		4.5	4.5	0.3	0.33	0.31	2.5	1.5	0.96	0.38	0.40	789
d3_49_R_8mm_100ms		8.9	9.0	0.6	0.75	0.77	5.2	4.2	1.99	0.63	0.66	1302
d3_50_EQ_Taft_-100mm	ϟ	99.5	99.6	0.8	1.46	1.45	6.8	6.7	3.46	1.47	1.56	3059
d3_51_EQ_Taft_+100mm	ϟ	100.2	100.4	1.7	2.47	2.33	15.5	14.7	4.31	1.50	1.59	3118
d3_52_EQ_Taft_+110mm	ϟ ✿ ☮	108.8	109.1	2.2	3.15	2.42	14.8	13.8	4.28	1.76	1.87	3665
d3_53_EQ_Taft_-110mm	ϟ ☮	108.3	108.3	1.4	2.32	1.91	11.1	9.9	4.28	1.86	1.97	3871
d3_54_EQ_Taft_-120mm	ϟ ☮	119.4	119.6	1.6	3.22	2.68	15.3	14.3	4.54	2.21	2.34	4595
d3_55_EQ_Taft_+120mm	ϟ ☮	118.4	118.7	2.4	3.55	2.80	16.3	15.2	5.18	1.81	1.91	3754
d3_56_EQ_Taft_+60mm	☮	59.7	60.0	0.6	0.50	0.57	3.7	2.5	1.06	0.48	0.51	1006
d3_57_EQ_Taft_-60mm	ϟ ☮	60.2	60.3	0.9	1.64	1.34	8.6	7.3	2.94	1.02	1.08	2125
d3_58_H_12Hz_0.1mm	☮	0.4	0.2	0.5	0.10	0.19	2.6	1.5	0.84	0.26	0.27	535
d3_59_H_12Hz_0.2mm	☮	0.5	0.4	0.4	0.16	0.32	3.4	2.4	1.32	0.35	0.37	722
d3_60_H_12Hz_0.4mm	✿ ☮	1.4	1.5	0.5	0.92	0.92	7.5	6.5	2.78	0.45	0.48	945
d4_01_R_4mm_200ms		4.2	4.3	0.4	0.18	0.18	0.3	0.2	0.27	0.21	0.22	434
d4_02_R_4mm_100ms		4.5	4.6	0.4	0.33	0.36	0.3	0.2	0.51	0.40	0.42	824
d4_03_R_8mm_100ms		9.2	9.4	1.0	0.95	0.93	0.5	0.4	1.55	1.12	1.18	2319
d4_04_H_13Hz_0.05mm		0.3	0.2	0.4	0.08	0.08	0.2	0.2	0.10	0.08	0.08	160
d4_05_H_13Hz_0.10mm	☮	0.4	0.3	0.5	0.23	0.25	0.2	0.3	0.33	0.25	0.26	515
d4_06_EQ_Taft_-40mm	[10]	40.0	39.9	0.6	0.30	0.32	0.4	0.4	0.45	0.36	0.38	740
d4_07_EQ_Taft_+40mm		40.1	40.3	0.6	0.31	0.32	0.4	0.5	0.51	0.37	0.40	778
d4_08_EQ_Taft_+80mm	⊠, ϟ	79.0	78.2	4.1	2.54	2.22	2.0	2.0	4.46	2.51	2.65	5210

continued on next page

[10] These Taft earthquake runs (6–9) were conducted early in the test sequence in order to observe the response of an uncracked wall subjected to an earthquake motion. Previously, earthquake runs were only performed once the wall was fully cracked.

Table C.6: (cont'd).

Test Name	Notes		Table and Supports					Wall Response					
			x_{tab} [mm]	$x_{sup.avg}$ [mm]	$\Delta_{sup.top-tab}$ [mm]	a_{tab} [g]	$a_{sup.avg}$ [g]	$\Delta_{w.cent}$ [mm]	$\Delta_{w.cent0}$ [mm]	$a_{w.cent}$ [g]	$a_{w.avg}$ [g]	q_w [kPa]	F_w [N]
d4_09_EQ_Taft_-80mm	⊠, ϟ		78.4	79.5	4.1	1.96	2.14	3.3	3.0	3.18	2.15	2.28	4466
d4_10_R_4mm_200ms	□		5.4	4.2	2.6	0.17	0.19	0.8	0.3	0.38	0.22	0.23	447
d4_11_R_4mm_100ms	□		5.5	4.5	2.6	0.33	0.30	1.0	0.5	0.59	0.34	0.36	711
d4_12_R_8mm_100ms	□		10.1	9.1	2.8	0.76	0.56	1.4	0.9	1.15	0.66	0.70	1365
d4_13_H_13Hz_0.15mm	□		1.7	0.6	2.6	0.35	0.34	0.9	0.6	0.69	0.43	0.45	885
d4_14_H_13Hz_0.20mm	□	☭	1.7	0.7	2.6	0.45	0.34	1.2	0.7	0.93	0.48	0.51	1005
d4_15_H_13Hz_0.25mm	□	☭	1.9	0.8	2.8	0.62	0.50	1.5	0.9	1.35	0.58	0.62	1213
d4_16_H_13Hz_0.30mm	□	☭	1.9	0.9	2.9	0.67	0.68	1.6	1.1	1.48	0.66	0.70	1376
d4_17_H_13Hz_0.35mm	□	☭	1.9	1.1	3.4	0.75	1.07	2.2	1.7	1.81	0.99	1.05	2068
d4_18_H_13Hz_0.40mm	⊠	☭	2.2	1.3	4.1	0.87	1.30	3.0	2.3	2.53	1.33	1.41	2768
d4_19_R_4mm_200ms	□		5.6	4.1	3.2	0.14	0.15	1.4	0.4	0.36	0.17	0.18	350
d4_20_R_4mm_100ms	□		5.9	4.4	3.3	0.35	0.28	1.5	0.6	0.75	0.33	0.35	689
d4_21_R_8mm_100ms	□		10.5	9.2	3.7	0.71	0.60	2.2	1.4	1.60	0.63	0.67	1307
d4_22_H_13Hz_0.45mm	⊠	☭	2.7	1.8	4.7	0.97	1.32	4.4	3.3	3.00	1.25	1.32	2595
d4_23_H_13Hz_0.50mm	⊠	☭	3.5	1.9	5.4	1.32	0.83	5.0	3.4	3.34	0.90	0.96	1880
d4_24_R_4mm_200ms	□		2.6	4.2	5.1	0.14	0.15	2.2	0.3	0.32	0.16	0.17	340
d4_25_R_4mm_100ms	□		6.9	4.5	5.1	0.34	0.28	2.7	0.7	0.65	0.29	0.30	598
d4_26_R_8mm_100ms	□		11.5	9.2	5.2	0.87	0.54	3.7	1.8	1.33	0.55	0.58	1145
d4_27_H_6Hz_0.10mm	□		2.8	0.2	5.2	0.04	0.05	2.4	0.3	0.08	0.04	0.04	80
d4_28_H_6Hz_0.20mm	□		2.7	0.3	5.1	0.06	0.08	2.5	0.4	0.18	0.09	0.09	183
d4_29_H_6Hz_0.30mm	□		2.9	0.5	5.1	0.07	0.10	2.5	0.4	0.23	0.11	0.12	232
d4_30_H_6Hz_0.40mm	□		3.1	0.6	5.2	0.09	0.12	2.4	0.4	0.30	0.13	0.13	260
d4_31_H_6Hz_0.50mm	□		3.0	0.6	5.2	0.11	0.14	2.5	0.4	0.29	0.15	0.16	305
d4_32_H_6Hz_0.75mm	□		3.3	1.0	5.2	0.15	0.17	2.4	0.4	0.30	0.17	0.18	349
d4_33_H_6Hz_1.0mm	□		3.7	1.4	5.3	0.26	0.24	2.6	0.4	0.37	0.24	0.25	489
d4_34_H_6Hz_1.5mm	□		4.8	2.3	5.3	0.43	0.45	3.4	1.8	0.82	0.48	0.51	996
d4_35_R_4mm_200ms	□		5.1	4.2	2.0	0.17	0.18	0.9	0.4	0.52	0.20	0.21	408
d4_36_R_4mm_100ms	□		5.3	4.5	2.1	0.35	0.34	1.3	0.6	0.69	0.34	0.37	717
d4_37_R_8mm_100ms	□		9.7	9.0	2.2	0.78	0.68	3.1	2.5	2.29	0.66	0.69	1362
d4_38_H_13Hz_0.10mm	□		1.2	0.3	2.0	0.15	0.14	1.1	0.3	0.26	0.15	0.16	305
d4_39_H_13Hz_0.20mm	□		1.3	0.6	2.1	0.36	0.36	1.8	1.2	1.20	0.42	0.45	883
d4_40_H_13Hz_0.30mm	□		1.4	0.7	2.1	0.53	0.48	4.2	3.5	2.33	0.78	0.82	1614
d4_41_H_13Hz_0.40mm	⊠[11]	☭	2.1	1.5	2.3	1.00	1.22	6.4	5.4	3.96	0.92	0.97	1904
d4_42_R_4mm_200ms			5.0	4.2	1.8	0.16	0.17	1.5	0.5	0.28	0.18	0.19	368
d4_43_R_4mm_100ms			5.3	4.5	2.0	0.34	0.35	2.2	1.0	0.72	0.33	0.35	688

continued on next page

[11] Wall became fully cracked.

Table C.6: (cont'd).

Test Name	Notes	Table and Supports					Wall Response					
		x_{tab} [mm]	$x_{sup.avg}$ [mm]	$\Delta_{sup.top-tab}$ [mm]	a_{tab} [g]	$a_{sup.avg}$ [g]	$\Delta_{w.cent}$ [mm]	$\Delta_{w.cent0}$ [mm]	$a_{w.cent}$ [g]	$a_{w.avg}$ [g]	q_w [kPa]	F_w [N]
d4_44_R_8mm_100ms		9.9	9.2	2.1	0.93	0.82	4.0	3.1	1.75	0.63	0.67	1310
d4_45_EQ_Taft_-10mm		9.2	10.1	2.0	0.06	0.06	1.5	0.3	0.16	0.08	0.09	171
d4_46_EQ_Taft_+10mm		10.6	9.7	1.9	0.07	0.08	1.5	0.3	0.19	0.10	0.10	204
d4_47_EQ_Taft_+20mm		21.2	20.5	2.0	0.16	0.14	1.6	0.5	0.29	0.16	0.17	328
d4_48_EQ_Taft_-20mm		18.6	19.4	1.9	0.12	0.12	1.6	0.4	0.28	0.14	0.15	295
d4_49_EQ_Taft_-30mm		30.7	31.3	1.9	0.19	0.18	1.8	0.6	0.35	0.19	0.20	393
d4_50_EQ_Taft_+30mm		29.3	28.6	2.0	0.22	0.22	1.8	0.6	0.42	0.24	0.25	492
d4_51_EQ_Taft_+40mm		41.1	40.5	2.2	0.30	0.28	2.0	0.9	0.54	0.29	0.31	603
d4_52_EQ_Taft_-40mm		39.5	40.2	2.0	0.27	0.29	1.9	0.8	0.47	0.28	0.30	582
d4_53_EQ_Taft_-50mm		49.5	50.1	2.1	0.39	0.40	2.2	1.2	0.66	0.38	0.40	792
d4_54_EQ_Taft_+50mm		51.2	50.5	2.0	0.38	0.37	2.6	1.4	0.78	0.40	0.43	838
d4_55_EQ_Taft_+60mm		60.5	59.9	2.1	0.49	0.54	2.8	1.7	1.04	0.53	0.56	1104
d4_56_EQ_Taft_-60mm	↯	59.7	60.5	2.6	1.66	1.43	6.5	5.5	2.98	1.24	1.31	2578
d4_57_R_4mm_200ms		5.3	4.3	2.0	0.12	0.13	1.4	0.3	0.22	0.13	0.14	278
d4_58_R_4mm_100ms		5.3	4.5	1.9	0.34	0.34	2.1	1.0	0.71	0.32	0.34	669
d4_59_R_8mm_100ms		9.9	9.1	2.1	0.90	0.78	4.0	3.1	1.74	0.61	0.65	1274
d4_60_EQ_Taft_+60mm	[12]	61.2	60.6	1.9	0.39	0.41	2.3	1.5	0.77	0.40	0.42	823
d4_61_EQ_Taft_-60mm	↯	59.8	60.6	2.2	1.07	1.00	4.3	3.7	1.95	0.92	0.97	1912
d4_62_EQ_Taft_-70mm	↯	69.1	69.8	2.5	1.33	1.18	6.1	4.8	2.73	1.06	1.12	2198
d4_63_EQ_Taft_+70mm	↯	71.6	70.8	2.1	0.93	0.99	4.6	3.4	2.14	0.91	0.96	1890
d4_64_EQ_Taft_+70mm	↯[13]	71.4	70.7	2.0	0.66	0.69	3.6	2.4	1.48	0.67	0.71	1388
d4_65_EQ_Taft_-70mm	↯	69.4	70.1	2.2	0.78	0.77	3.7	2.7	1.47	0.71	0.75	1471
d4_66_R_4mm_200ms	[14]	5.0	4.3	2.0	0.18	0.17	1.8	0.5	0.38	0.17	0.18	355
d4_67_R_4mm_100ms		5.3	4.5	1.9	0.37	0.35	2.3	1.1	0.76	0.32	0.34	667
d4_68_R_8mm_100ms		9.7	9.0	2.1	0.89	0.78	4.1	3.1	1.78	0.61	0.65	1267

continued on next page

[12] Tests 60–61 were repeats of tests 55–56 in that both used the same PGD; however, the PID setting of the controller was reduced from 36 dB to 30 dB in the latter tests. This was to investigate whether shaketable impacts (Appendix D) could be stopped from occurring by lowering the PID setting. However, whilst this caused the PGA generated to reduce, the impacts still occurred for the +60 mm PGD run as before. The reduced PID setting of 30 dB was also retained in tests 62–63. The influence of the PID is discussed in Appendix D.6.2.

[13] In tests 64–65, the PID was further reduced to 25 dB, but the impacts still continued to occur, even though there was a reduction in the generated PGA relative to tests 62–63 which were carried out at the same PGD.

[14] In test 66 and onwards, the PID was restored to 36 dB after it was concluded that reducing the PID setting of the controller was an unviable method of limiting the influence of the shaketable impacts.

Table C.6: (cont'd).

Test Name	Notes	Table and Supports					Wall Response					
		x_{tab} [mm]	$x_{sup.avg}$ [mm]	$\Delta_{sup.top-tab}$ [mm]	a_{tab} [g]	$a_{sup.avg}$ [g]	$\Delta_{w.cent}$ [mm]	$\Delta_{w.cent0}$ [mm]	$a_{w.cent}$ [g]	$a_{w.avg}$ [g]	q_w [kPa]	F_w [N]
d4_69_EQ_Taft_+70mm	ϟ[15]	70.9	70.2	2.0	1.46	1.47	5.8	5.3	2.75	1.25	1.33	2603
d4_70_EQ_Taft_-70mm	ϟ	69.0	69.8	2.9	2.19	1.86	9.5	8.2	4.89	1.54	1.64	3209
d4_71_EQ_Taftbf05_-70mm	ϟ	69.0	69.8	2.9	2.05	1.77	9.4	7.8	4.53	1.44	1.53	2999
d4_72_EQ_Taftbf05_+70mm	ϟ	70.5	69.9	2.0	1.43	1.37	6.3	5.3	2.86	1.23	1.30	2546
d4_73_EQ_Taftbf10_+70mm	ϟ	70.6	69.9	2.2	1.28	1.27	5.9	4.6	2.53	1.10	1.17	2293
d4_74_EQ_Taftbf10_-70mm	ϟ	69.1	69.9	2.8	1.96	1.73	9.6	8.2	4.66	1.39	1.47	2892
d4_75_EQ_Taftbf20_-70mm	ϟ	69.0	69.7	2.8	1.81	1.54	8.5	6.9	3.92	1.29	1.36	2671
d4_76_EQ_Taftbf20_+70mm	ϟ	70.5	69.9	2.0	1.25	1.22	5.6	4.4	2.39	1.08	1.14	2234
d4_77_EQ_Taftbf30_+70mm	ϟ	70.5	69.9	2.2	0.97	1.01	5.0	3.5	2.02	0.88	0.93	1826
d4_78_EQ_Taftbf30_-70mm	ϟ	69.0	69.7	2.7	1.72	1.45	8.3	6.7	3.89	1.23	1.31	2564
d4_79_EQ_Taftbf50_-70mm	ϟ	69.0	69.7	2.5	1.44	1.26	7.1	5.5	3.06	1.07	1.13	2215
d4_80_EQ_Taftbf50_+70mm	ϟ	70.5	69.8	1.9	0.82	0.78	4.3	2.8	1.63	0.73	0.77	1517
d4_81_EQ_Taftbf75_+70mm	ϟ	70.6	69.9	2.0	0.68	0.69	4.0	2.4	1.52	0.63	0.67	1309
d4_82_EQ_Taftbf75_-70mm	ϟ	68.9	69.6	2.5	1.26	1.16	6.5	4.9	2.73	0.96	1.02	2004
d4_83_EQ_Taftbf100_-70mm	ϟ	69.0	69.7	2.3	1.10	1.00	5.8	4.3	2.30	0.85	0.90	1771
d4_84_EQ_Taftbf100_+70mm	ϟ	70.4	69.7	2.0	0.62	0.63	4.4	2.9	1.77	0.60	0.63	1237
d4_85_R_4mm_200ms		5.0	4.1	1.9	0.16	0.16	2.2	0.6	0.35	0.15	0.16	314
d4_86_R_4mm_100ms		5.4	4.6	1.9	0.33	0.31	2.8	1.3	0.69	0.29	0.31	612
d4_87_R_8mm_100ms		9.7	9.0	2.1	0.85	0.73	4.5	3.2	1.80	0.59	0.62	1221
d4_88_H_13Hz_0.2mm		1.3	0.8	2.0	0.52	0.49	4.1	2.6	1.61	0.21	0.23	444
d4_89_H_13Hz_0.4mm		2.1	1.5	2.4	1.00	1.18	6.5	5.3	3.19	0.52	0.55	1079
d4_90_H_13Hz_0.6mm		2.9	2.3	2.8	1.70	1.74	8.9	7.4	4.66	0.65	0.69	1348
d4_91_R_4mm_200ms		5.0	4.2	1.9	0.13	0.15	2.5	0.6	0.36	0.13	0.14	278
d4_92_R_4mm_100ms		5.2	4.5	1.9	0.34	0.34	3.4	1.6	0.74	0.28	0.29	572
d4_93_R_8mm_100ms		9.9	9.1	2.1	0.85	0.68	5.4	3.8	1.98	0.56	0.59	1162
d4_94_EQ_Taft_+70mm	ϟ	70.9	70.3	2.3	1.69	1.64	8.7	7.7	3.49	1.37	1.45	2840
d4_95_EQ_Taft_-70mm	ϟ	69.2	70.0	2.7	2.13	1.70	12.3	10.5	5.01	1.43	1.52	2974
d4_96_EQ_Taft_-80mm	ϟ	78.8	79.6	2.7	1.74	1.59	11.8	9.8	4.66	1.26	1.34	2622
d4_97_EQ_Taft_+80mm	ϟ	80.3	79.7	2.9	2.62	2.25	12.3	11.7	4.82	1.74	1.84	3615
d4_98_EQ_Taft_+90mm	ϟ	90.2	89.5	2.9	2.48	2.49	12.2	12.5	4.56	1.72	1.82	3566

continued on next page

[15] In a further attempt to prevent the shaketable impacts, tests 69–84 trialled alternate versions of the Taft motion. Runs 69–70 used the standard Taft motion as a control reference, whilst runs 71–84 used Taft motions which had been filtered using a binomial filter in the time domain. The period of the filter (number of data points used for weighted averaging) are indicated in the test name. For example, `Taftbf05` means that the binomial filter averaged five adjacent data points in the original motion. Even though the PGA reduced as the severity of filtration was increased, the impacts still continued to occur. Hence, the original Taft motion was restored in subsequent tests.

Table C.6: (cont'd).

Test Name	Notes	Table and Supports					Wall Response					
		x_{tab} [mm]	$x_{sup.avg}$ [mm]	$\Delta_{sup.top-tab}$ [mm]	a_{tab} [g]	$a_{sup.avg}$ [g]	$\Delta_{w.cent}$ [mm]	$\Delta_{w.cent0}$ [mm]	$a_{w.cent}$ [g]	$a_{w.avg}$ [g]	q_w [kPa]	F_w [N]
d4_99_EQ_Taft_-90mm	ϟ	88.9	89.7	2.4	1.32	1.13	10.1	8.4	3.67	0.95	1.01	1975
d4_100_EQ_Taft_-100mm	ϟ	98.9	99.7	2.4	1.39	1.27	10.4	8.4	3.51	1.00	1.06	2083
d4_101_EQ_Taft_+100mm	ϟ	100.6	100.1	3.0	2.27	2.03	10.7	11.6	4.07	1.66	1.76	3445
d4_102_EQ_Taft_+110mm	ϟ	109.5	109.0	3.5	3.00	2.50	11.6	13.5	4.74	2.05	2.17	4258
d4_103_EQ_Taft_-110mm	ϟ	107.8	108.5	2.5	2.15	1.97	12.9	11.1	4.98	1.48	1.56	3069
d4_104_EQ_Taft_-120mm	ϟ	118.7	119.7	3.0	3.06	2.64	16.7	14.8	5.56	1.94	2.05	4032
d4_105_EQ_Taft_+120mm	ϟ	119.1	118.6	3.8	3.27	2.77	12.1	14.1	4.36	2.22	2.35	4611
d4_106_R_4mm_200ms		5.1	4.3	1.8	0.13	0.14	2.7	0.8	0.38	0.13	0.14	275
d4_107_R_4mm_100ms		5.3	4.6	1.8	0.34	0.33	3.5	1.8	0.77	0.28	0.29	575
d4_108_R_8mm_100ms		10.0	9.3	2.0	0.85	0.72	5.4	3.8	1.87	0.53	0.56	1093
d4_109_H_13Hz_0.1mm		1.1	0.2	1.9	0.10	0.12	2.5	0.6	0.30	0.05	0.05	95
d4_110_H_13Hz_0.2mm		1.4	0.6	1.9	0.39	0.40	3.6	2.0	1.17	0.16	0.17	337
d4_111_H_13Hz_0.3mm		2.0	1.5	2.3	0.97	0.92	6.0	4.1	2.45	0.30	0.32	623
d4_112_H_13Hz_0.4mm		2.2	1.7	2.5	1.22	1.27	7.3	5.9	3.52	0.49	0.52	1018
d4_113_H_13Hz_0.5mm		2.6	2.1	2.7	1.47	1.58	8.6	7.1	3.94	0.65	0.69	1348
d4_114_R_4mm_200ms		5.0	4.2	1.8	0.14	0.15	3.6	0.6	0.44	0.15	0.16	309
d4_115_R_4mm_100ms		5.2	4.6	1.9	0.34	0.34	4.3	1.4	0.77	0.30	0.32	622
d4_116_R_8mm_100ms	✿	9.9	9.2	2.1	0.86	0.72	6.2	3.8	1.68	0.57	0.61	1192
d2_01_R_4mm_200ms		4.4	4.4	0.3	0.12	0.15	0.2	0.2	0.18	0.16	0.17	386
d2_02_R_4mm_100ms		4.6	4.7	0.4	0.23	0.26	0.3	0.2	0.35	0.30	0.31	713
d2_03_R_8mm_100ms		9.6	9.6	0.6	0.55	0.54	0.3	0.3	0.76	0.61	0.65	1474
d2_04_R_4mm_200ms		4.1	4.1	0.3	0.16	0.19	0.2	0.2	0.24	0.21	0.22	494
d2_05_R_4mm_100ms		4.4	4.6	0.4	0.35	0.38	0.3	0.3	0.57	0.45	0.48	1080
d2_06_R_8mm_100ms	⊠[16]	9.3	9.7	1.5	1.17	1.48	0.9	0.9	1.96	1.63	1.72	3905
d2_07_H_12Hz_0.05mm	□	0.3	0.3	0.6	0.06	0.08	0.5	0.3	0.08	0.07	0.07	164
d2_08_H_12Hz_0.1mm	□	0.5	0.5	0.7	0.27	0.34	0.5	0.4	0.52	0.40	0.42	948
d2_09_H_12Hz_0.2mm	⊠	1.3	1.5	1.0	0.96	1.28	0.9	0.7	1.34	1.25	1.33	3007
d2_10_R_4mm_200ms	□	4.2	4.2	0.3	0.16	0.20	0.4	0.3	0.27	0.22	0.23	527
d2_11_R_4mm_100ms	□	4.4	4.5	0.5	0.34	0.39	0.5	0.3	0.55	0.44	0.47	1061
d2_12_R_8mm_100ms	⊠	9.1	9.5	1.0	0.93	1.21	1.1	0.9	1.27	1.12	1.19	2697
d2_13_H_12Hz_0.25mm	⊠	1.3	1.6	1.0	1.02	1.46	1.9	2.1	1.58	1.39	1.47	3339
d2_14_H_12Hz_0.25mm	⊠	0.7	0.7	0.7	0.36	0.47	1.6	1.7	0.90	0.55	0.58	1311
d2_15_Z		0.3	0.1	0.4	0.02	0.02	1.3	0.2	0.03	0.01	0.01	28
d2_16_R_4mm_200ms	□	4.1	4.2	0.7	0.17	0.18	1.3	0.3	0.31	0.22	0.23	521
d2_17_R_4mm_100ms	□	4.1	4.3	0.5	0.36	0.36	1.4	0.5	0.70	0.46	0.49	1108

continued on next page

[16] Unusually, first cracking occurred during a pulse test. All other walls tested were able to withstand the initial pulse tests without cracking.

Table C.6: (cont'd).

Test Name	Notes	Table and Supports					Wall Response					
		x_{tab} [mm]	$x_{sup.avg}$ [mm]	$\Delta_{sup.top-tab}$ [mm]	a_{tab} [g]	$a_{sup.avg}$ [g]	$\Delta_{w.cent}$ [mm]	$\Delta_{w.cent0}$ [mm]	$a_{w.cent}$ [g]	$a_{w.avg}$ [g]	q_w [kPa]	F_w [N]
d2_18_R_8mm_100ms	⊠[17]	8.9	9.3	0.8	0.84	0.68	2.5	1.5	1.92	0.95	1.01	2285
d2_19_Z		0.3	0.2	0.4	0.01	0.02	1.2	0.2	0.03	0.01	0.01	30
d2_20_H_12Hz_0.1mm	□	0.3	0.3	0.4	0.12	0.15	1.3	0.4	0.22	0.16	0.17	376
d2_21_H_12Hz_0.2mm	⊠[18]	0.7	0.8	0.6	0.52	0.51	2.2	1.9	1.30	0.84	0.88	2005
d2_22_Z		0.3	0.2	0.4	0.01	0.02	1.7	0.2	0.03	0.01	0.01	26
d2_23_H_12Hz_0.1mm	□	0.5	0.3	0.4	0.09	0.13	1.8	0.3	0.25	0.15	0.16	370
d2_24_H_12Hz_0.2mm	⊠	0.6	0.7	0.7	0.43	0.57	4.1	2.6	1.96	1.02	1.08	2439
d2_25_R_4mm_200ms	□	4.4	4.3	0.3	0.16	0.18	2.1	0.5	0.38	0.20	0.21	472
d2_26_R_4mm_100ms	□	4.4	4.4	0.4	0.33	0.36	2.7	1.2	0.82	0.40	0.42	956
d2_27_R_8mm_100ms	⊠	8.7	8.8	0.6	0.87	0.83	4.6	3.3	2.59	0.83	0.88	2003
d2_28_H_12Hz_0.25mm	⊠	0.9	1.0	0.6	0.63	0.45	5.1	3.4	1.72	0.60	0.63	1439
d2_29_H_12Hz_0.3mm	⊠[19]	1.0	1.1	0.6	0.73	0.54	4.8	3.4	1.45	0.26	0.28	632
d2_30_R_4mm_200ms		4.3	4.4	0.3	0.16	0.19	2.2	0.8	0.37	0.15	0.16	371
d2_31_R_4mm_100ms		4.3	4.5	0.4	0.35	0.39	3.1	1.9	0.74	0.30	0.31	712
d2_32_R_8mm_100ms		9.2	9.4	0.7	1.24	1.19	4.9	3.7	1.54	0.60	0.64	1445
d2_33_EQ_Taft_-20mm		20.3	20.3	0.7	0.16	0.22	2.4	0.9	0.45	0.26	0.28	632
d2_34_EQ_Taft_+20mm		19.9	20.0	0.6	0.17	0.21	2.3	0.9	0.37	0.22	0.23	517
d2_35_EQ_Taft_+40mm		40.2	40.2	0.6	0.39	0.40	3.4	2.1	0.82	0.43	0.45	1021
d2_36_EQ_Taft_-40mm		40.3	40.2	0.7	0.41	0.40	3.4	2.0	0.91	0.46	0.49	1108
d2_37_EQ_Taft_-60mm	↯	60.5	60.3	1.0	1.58	1.69	6.0	5.5	2.15	1.19	1.26	2856
d2_38_EQ_Taft_+60mm		59.5	59.4	0.7	0.60	0.65	3.9	3.1	1.04	0.58	0.62	1398
d2_39_EQ_Taft_+80mm	↯	79.5	79.6	1.8	3.08	3.06	10.2	8.8	3.83	1.85	1.96	4445
d2_40_EQ_Taft_-80mm	↯	79.7	79.3	1.6	2.34	2.85	7.2	8.0	2.96	1.58	1.67	3795
d2_41_EQ_Taft_-100mm	↯	99.3	99.1	1.6	1.85	1.85	8.9	7.5	2.08	1.14	1.21	2745
d2_42_EQ_Taft_+100mm	↯	99.4	99.6	1.9	2.71	3.72	10.5	11.4	2.98	1.73	1.83	4144
d2_43_R_4mm_200ms		4.3	4.4	0.3	0.16	0.17	2.0	1.2	0.33	0.16	0.17	381
d2_44_R_4mm_100ms		4.5	4.5	0.4	0.36	0.38	2.9	2.0	0.56	0.26	0.28	625
d2_45_R_8mm_100ms		9.3	9.6	0.8	1.31	1.21	5.1	4.5	1.46	0.84	0.89	2010
d2_46_EQ_Taft_+60mm	☭	59.5	59.6	0.6	0.68	0.72	5.6	4.5	1.04	0.57	0.60	1357
d2_47_EQ_Taft_-60mm	↯ ☭	60.4	60.2	0.8	1.55	1.57	6.3	7.4	1.72	0.98	1.03	2340

continued on next page

[17] After test 18, the vertical edges were restrained using timber members to prevent rocking of the wall away from the returns. The revised arrangement is shown in Figures 3.3 and 3.4.

[18] After test 21, the new vertical edge restraint was further stiffened using timber wedges. This setup was retained for the remainder of tests, including the current wall, D2, and the final wall tested, D1.

[19] Wall became fully cracked.

Table C.6: (cont'd).

Test Name	Notes	Table and Supports					Wall Response					
		x_{tab} [mm]	$x_{sup.avg}$ [mm]	$\Delta_{sup.top-tab}$ [mm]	a_{tab} [g]	$a_{sup.avg}$ [g]	$\Delta_{w.cent}$ [mm]	$\Delta_{w.cent0}$ [mm]	$a_{w.cent}$ [g]	$a_{w.avg}$ [g]	q_w [kPa]	F_w [N]
d2_48_EQ_Taft_-120mm	ϟ ✇	118.5	118.4	1.8	2.82	2.71	13.4	12.5	2.75	1.70	1.80	4076
d2_49_EQ_Taft_+120mm	ϟ ✇	117.4	117.5	1.8	3.36	3.28	13.8	15.2	3.34	2.15	2.28	5165
d2_50_R_4mm_200ms		4.3	4.3	0.3	0.16	0.17	2.0	1.3	0.30	0.14	0.14	325
d2_51_R_4mm_100ms		4.5	4.6	0.5	0.39	0.38	2.7	2.2	0.58	0.26	0.28	632
d2_52_R_8mm_100ms		9.4	9.7	0.9	1.46	1.40	5.8	5.3	1.28	0.93	0.99	2242
d2_53_EQ_Synth01_+20mm		19.7	19.8	0.6	0.20	0.23	2.1	1.3	0.32	0.17	0.18	406
d2_54_EQ_Synth01_-20mm		20.2	20.2	0.8	0.20	0.22	1.9	1.5	0.29	0.17	0.18	419
d2_55_EQ_Synth01_-40mm	ϟ	40.1	40.0	0.7	1.23	1.21	5.9	6.6	1.48	0.77	0.81	1839
d2_56_EQ_Synth01_+40mm		39.9	40.0	0.6	0.56	0.54	2.9	2.8	0.56	0.35	0.37	839
d2_57_EQ_Synth01_+60mm	ϟ	59.4	59.5	1.2	2.24	2.30	8.6	9.2	2.14	1.43	1.51	3430
d2_58_EQ_Synth01_-60mm	ϟ	60.1	59.9	1.4	2.21	2.17	9.7	10.9	2.13	1.40	1.48	3364
d2_59_EQ_Synth01_-80mm	ϟ, [20] ✿	79.3	79.0	2.2	3.49	3.86	14.4	15.1	3.77	2.33	2.47	5598
d2_60_R_4mm_200ms		4.3	4.3	0.3	0.16	0.18	3.1	1.4	0.33	0.12	0.13	295
d2_61_R_4mm_100ms		4.5	4.6	0.3	0.37	0.37	3.7	2.4	0.54	0.26	0.27	617
d2_62_R_8mm_100ms	✿	9.3	9.5	0.9	1.41	1.27	5.7	5.9	1.11	0.81	0.86	1955
d1_01_0MPa_R_4mm_200ms	[21]	4.2	4.3	0.5	0.18	0.17	0.2	0.2	0.29	0.21	0.22	495
d1_02_0MPa_R_4mm_100ms		4.2	4.4	0.6	0.38	0.37	0.3	0.2	0.61	0.47	0.50	1127
d1_03_0MPa_R_8mm_100ms		9.2	9.7	1.3	1.23	1.35	0.7	0.7	1.86	1.45	1.54	3482
d1_04_0.05MPa_R_4mm_200ms	[22]	4.4	4.5	0.4	0.20	0.21	0.2	0.2	0.27	0.23	0.24	540
d1_05_0.05MPa_R_4mm_100ms		4.4	4.4	0.5	0.38	0.36	0.2	0.2	0.58	0.43	0.46	1040
d1_06_0.05MPa_R_8mm_100ms		9.0	9.3	0.8	0.88	0.79	0.5	0.5	1.33	0.92	0.97	2204
d1_07_0.10MPa_Z		0.3	0.2	0.4	0.01	0.02	0.2	0.2	0.03	0.01	0.01	27
d1_08_0.10MPa_R_4mm_200ms	[23]	4.5	4.5	0.3	0.18	0.19	0.2	0.2	0.27	0.23	0.24	543
d1_09_0.10MPa_R_4mm_100ms		4.3	4.4	0.4	0.38	0.37	0.2	0.2	0.51	0.41	0.44	989
d1_10_0.10MPa_R_8mm_100ms		9.1	9.3	0.9	0.92	0.87	0.4	0.4	1.38	1.07	1.13	2561
d1_11_H_13Hz_0.25mm		1.5	1.9	1.2	1.69	1.52	0.4	0.4	1.94	1.50	1.59	3595
d1_12_H_13Hz_0.5mm		2.0	2.4	1.4	1.87	1.75	0.7	0.7	2.40	1.91	2.02	4572
d1_13_H_13Hz_0.75mm		2.4	3.0	1.6	2.18	2.12	0.9	0.9	2.97	2.27	2.40	5448

continued on next page

[20] During test 59, the sub-plates forming the mechanism underwent severe sliding along diagonal cracks. They were pushed back together prior to conducting the final free vibration tests 60–62, due to a risk of collapse.

[21] To observe the free vibration response for the same wall at different levels of axial stress, pulse tests were firstly conducted without any precompression in tests 1–3. The precompression was then increased to an intermediate value of 0.05 MPa in tests 4–6 and finally to the full value of 0.10 MPa prior to test 8.

[22] Wall was subjected to 0.05 MPa precompression.

[23] The wall was subjected to the full precompression of 0.10 MPa in test 8 and onwards.

Table C.6: (cont'd).

Test Name	Notes	Table and Supports					Wall Response					
		x_{tab} [mm]	$x_{sup.avg}$ [mm]	$\Delta_{sup.top-tab}$ [mm]	a_{tab} [g]	$a_{sup.avg}$ [g]	$\Delta_{w.cent}$ [mm]	$\Delta_{w.cent0}$ [mm]	$a_{w.cent}$ [g]	$a_{w.avg}$ [g]	q_w [kPa]	F_w [N]
d1_14_H_13Hz_1mm		2.9	3.5	2.1	2.65	2.47	1.4	1.4	3.35	2.53	2.68	6078
d1_15_EQ_Taft_-40mm		40.6	40.7	0.6	0.40	0.41	0.5	0.4	0.70	0.51	0.54	1224
d1_16_EQ_Taft_+40mm		40.3	40.4	0.6	0.42	0.39	0.4	0.4	0.68	0.47	0.50	1137
d1_17_EQ_Taft_+60mm		60.3	60.6	0.8	0.57	0.57	0.5	0.4	0.85	0.67	0.71	1599
d1_18_EQ_Taft_-60mm	ϟ	60.1	60.1	1.4	1.62	1.50	0.6	0.7	2.40	1.69	1.78	4043
d1_19_EQ_Taft_-80mm	⊠, ϟ	80.1	80.2	2.3	2.45	2.24	2.1	1.9	4.60	3.07	3.25	7368
d1_20_EQ_Taft_+80mm	⊠, ϟ	79.7	80.1	2.9	3.13	2.48	2.5	2.3	5.81	3.73	3.95	8957
d1_21_EQ_Taft_+100mm	⊠, ϟ	98.6	98.8	2.7	2.90	2.53	3.4	3.5	5.78	3.64	3.85	8736
d1_22_EQ_Taft_-100mm	⊠, ϟ	99.7	99.5	1.6	1.77	1.59	1.7	1.7	3.38	1.73	1.83	4159
d1_23_EQ_Taft_-120mm	⊠, ϟ	118.5	118.6	2.8	3.55	2.96	5.9	5.9	6.40	2.85	3.02	6839
d1_24_EQ_Taft_+120mm	⊠, ϟ ✿	119.3	119.8	2.7	3.65	3.15	7.9	7.7	6.15	2.82	2.98	6760
d1_25_R_4mm_200ms	□	4.3	4.4	0.5	0.20	0.20	0.6	0.3	0.37	0.23	0.24	540
d1_26_R_4mm_100ms	□	4.3	4.4	0.5	0.38	0.38	0.7	0.4	0.70	0.44	0.46	1044
d1_27_R_8mm_100ms	□	8.8	9.2	0.8	0.88	0.80	1.3	1.0	1.78	0.88	0.94	2123
d1_28_H_13Hz_0.1mm	□	0.5	0.2	0.5	0.04	0.05	0.5	0.3	0.06	0.04	0.05	105
d1_29_H_13Hz_0.2mm	□	0.6	0.4	0.5	0.27	0.25	0.5	0.2	0.35	0.26	0.27	619
d1_30_H_13Hz_0.4mm	⊠[24]	1.5	2.0	1.5	1.64	1.29	8.5	8.2	5.39	2.16	2.29	5188
d1_31_R_4mm_200ms		4.3	4.5	0.7	0.18	0.18	1.1	0.3	0.47	0.26	0.28	634
d1_32_R_4mm_100ms		4.3	4.4	0.5	0.38	0.39	1.3	0.5	0.82	0.43	0.46	1040
d1_33_R_8mm_100ms		8.8	9.1	0.9	0.86	0.80	2.5	1.7	1.90	0.88	0.93	2103
d1_34_EQ_Taft_+40mm		40.3	40.5	0.7	0.47	0.45	1.4	0.6	0.89	0.49	0.52	1173
d1_35_EQ_Taft_-40mm		40.3	40.3	0.7	0.44	0.45	1.3	0.6	0.91	0.44	0.47	1058
d1_36_EQ_Taft_-60mm	ϟ	60.5	60.5	1.2	1.64	1.57	4.3	3.5	3.33	1.42	1.51	3415
d1_37_EQ_Taft_+60mm		59.7	59.8	1.0	0.76	0.78	2.0	1.2	1.58	0.83	0.88	2002
d1_38_EQ_Taft_+80mm	ϟ	79.3	79.7	2.6	3.13	2.54	12.8	12.0	6.19	2.14	2.27	5146
d1_39_EQ_Taft_-80mm	ϟ	79.5	79.3	1.7	2.56	2.76	9.9	8.8	5.82	1.84	1.95	4421
d1_40_EQ_Taft_-100mm	ϟ	99.4	99.1	1.8	1.88	1.73	6.0	5.5	4.14	1.64	1.74	3935
d1_41_EQ_Taft_+100mm	ϟ	99.5	100.1	2.2	2.86	2.67	14.0	13.1	6.35	2.08	2.20	4988
d1_42_R_4mm_200ms		4.3	4.6	0.5	0.20	0.20	1.5	0.3	0.57	0.28	0.30	672
d1_43_R_4mm_100ms		4.1	4.3	0.6	0.38	0.38	1.6	0.6	0.84	0.42	0.45	1013
d1_44_R_8mm_100ms		9.0	9.0	0.9	0.92	0.83	3.0	2.0	1.86	0.84	0.89	2015
d1_45_EQ_Taft_+120mm	ϟ	117.5	117.6	2.4	3.57	2.96	11.2	10.1	5.34	2.36	2.50	5674
d1_46_EQ_Taft_-120mm	ϟ[25]	119.2	119.1	2.9	3.61	3.00	12.6	11.5	5.53	2.50	2.65	5997

continued on next page

[24] Wall became fully cracked.

[25] Severe sliding became evident along diagonal cracks between sub-plates of the mechanism after test 46. This state was left unaltered during tests 47–51, after which the wall was repaired.

Table C.6: (cont'd).

Test Name	Notes	Table and Supports					Wall Response					
		x_{tab} [mm]	$x_{sup.avg}$ [mm]	$\Delta_{sup.top-tab}$ [mm]	a_{tab} [g]	$a_{sup.avg}$ [g]	$\Delta_{w.cent}$ [mm]	$\Delta_{w.cent0}$ [mm]	$a_{w.cent}$ [g]	$a_{w.avg}$ [g]	q_w [kPa]	F_w [N]
d1_47_R_4mm_200ms		4.3	4.5	0.5	0.20	0.20	1.7	0.3	0.56	0.26	0.28	631
d1_48_R_4mm_100ms		4.1	4.3	0.5	0.38	0.38	1.9	0.6	0.87	0.42	0.44	1006
d1_49_R_8mm_100ms	✿	8.7	9.0	0.9	0.89	0.83	3.3	1.9	1.91	0.92	0.97	2200
d1_50_H_12Hz_0.1mm		0.5	0.3	0.7	0.05	0.06	1.4	0.3	0.11	0.06	0.06	144
d1_51_H_12Hz_0.2mm		1.5	1.6	1.6	1.17	1.02	7.3	6.1	3.36	1.63	1.73	3912
d1_52_R_4mm_200ms	[26]	4.3	4.4	0.8	0.21	0.23	1.4	0.2	0.48	0.25	0.26	592
d1_53_R_4mm_100ms		4.2	4.3	0.7	0.39	0.38	1.6	0.4	0.74	0.43	0.46	1034
d1_54_R_8mm_100ms		8.7	9.1	1.1	0.92	0.84	2.7	1.6	1.86	0.88	0.93	2111
d1_55_Z		0.3	0.2	0.7	0.02	0.02	1.2	0.2	0.02	0.01	0.01	26
d1_56_EQ_Synth01_+20mm		19.8	20.0	0.8	0.25	0.24	1.5	0.4	0.64	0.34	0.36	820
d1_57_EQ_Synth01_-20mm		20.4	20.3	0.8	0.21	0.23	1.4	0.4	0.41	0.29	0.30	688
d1_58_EQ_Synth01_-40mm	ϟ	40.2	40.1	1.0	1.17	1.11	3.0	2.3	2.28	1.12	1.18	2675
d1_59_EQ_Synth01_+40mm		40.0	40.0	0.9	0.50	0.51	1.6	0.6	0.95	0.55	0.58	1311
d1_60_EQ_Synth01_+60mm	ϟ	59.1	59.2	1.8	2.50	2.07	9.0	8.0	4.48	1.75	1.85	4190
d1_61_EQ_Synth01_-60mm	ϟ	60.3	60.3	1.6	2.12	1.81	7.8	7.0	3.83	1.58	1.68	3800
d1_62_EQ_Synth01_-80mm	ϟ	79.1	78.7	3.2	4.28	3.51	14.1	13.3	6.19	2.48	2.62	5945
d1_63_EQ_Synth01_+80mm	ϟ	79.6	80.1	2.9	3.92	3.55	12.1	11.3	5.60	2.35	2.49	5633
d1_64_R_4mm_200ms		4.2	4.5	0.6	0.21	0.20	1.1	0.4	0.56	0.27	0.28	639
d1_65_R_4mm_100ms		4.2	4.3	0.7	0.37	0.39	1.4	0.6	0.92	0.41	0.44	988
d1_66_R_8mm_100ms		8.6	9.1	0.9	0.91	0.84	2.8	2.0	1.92	0.88	0.94	2121
d1_67_EQ_Synth03_-20mm		20.4	20.3	0.7	0.26	0.29	1.1	0.4	0.55	0.34	0.35	805
d1_68_EQ_Synth03_+20mm		20.1	20.2	0.8	0.28	0.32	1.2	0.4	0.56	0.34	0.36	805
d1_69_EQ_Synth03_+40mm		40.2	40.3	0.9	0.45	0.51	1.4	0.7	0.98	0.60	0.64	1451
d1_70_EQ_Synth03_-40mm		40.5	40.4	1.0	0.40	0.44	1.5	0.8	1.00	0.57	0.60	1371
d1_71_EQ_Synth03_-60mm	ϟ	60.5	60.3	0.9	1.06	1.02	2.5	1.7	1.89	0.89	0.95	2142
d1_72_EQ_Synth03_+60mm		59.7	59.9	0.9	0.84	0.82	1.9	1.5	1.56	0.80	0.85	1923
d1_73_EQ_Synth03_+80mm	ϟ	79.6	79.9	2.5	2.75	2.34	9.3	8.6	4.52	1.99	2.10	4768
d1_74_EQ_Synth03_-80mm	ϟ	80.0	80.0	1.7	2.72	2.49	9.6	8.8	4.69	1.91	2.03	4593
d1_75_EQ_Synth03_-100mm	ϟ	99.9	99.5	2.4	3.47	2.90	11.2	10.5	5.51	2.15	2.28	5168
d1_76_EQ_Synth03_+100mm	ϟ	99.9	100.5	2.7	3.48	2.88	13.3	12.5	5.23	2.26	2.39	5421
d1_77_R_4mm_200ms		4.2	4.5	0.7	0.19	0.18	1.2	0.3	0.52	0.24	0.25	576
d1_78_R_4mm_100ms		4.1	4.3	0.6	0.38	0.39	1.5	0.6	0.88	0.41	0.43	977
d1_79_R_8mm_100ms		8.6	8.9	1.0	0.89	0.82	3.2	2.2	1.88	0.86	0.91	2063
d1_80_EQ_Synth05_-20mm		20.6	20.6	0.9	0.49	0.52	1.8	1.3	1.27	0.67	0.71	1601
d1_81_EQ_Synth05_+20mm		20.2	20.4	0.9	0.43	0.49	2.1	1.3	1.22	0.64	0.68	1536

continued on next page

[26] The wall was repaired by pushing the sub-plates back together prior to test 52.

Table C.6: (cont'd).

Test Name	Notes	Table and Supports					Wall Response					
		x_{tab} [mm]	$x_{sup.avg}$ [mm]	$\Delta_{sup.top-tab}$ [mm]	a_{tab} [g]	$a_{sup.avg}$ [g]	$\Delta_{w.cent}$ [mm]	$\Delta_{w.cent0}$ [mm]	$a_{w.cent}$ [g]	$a_{w.avg}$ [g]	q_w [kPa]	F_w [N]
d1_82_EQ_Synth05_+40mm	ϟ	41.0	41.4	1.3	1.18	1.17	4.0	3.2	2.46	1.18	1.25	2836
d1_83_EQ_Synth05_-40mm	ϟ	40.4	40.4	1.3	1.86	1.65	5.8	4.9	3.07	1.52	1.61	3640
d1_84_EQ_Synth05_-60mm	ϟ	60.5	61.0	2.3	3.65	3.37	12.8	12.0	5.85	2.27	2.40	5435
d1_85_EQ_Synth05_+60mm	ϟ	60.8	61.4	2.4	3.47	3.69	12.1	12.0	5.91	2.20	2.33	5281
d1_86_R_4mm_200ms		4.2	4.5	0.6	0.22	0.22	1.3	0.4	0.51	0.23	0.24	548
d1_87_R_4mm_100ms		4.1	4.3	0.7	0.36	0.36	1.6	0.7	0.86	0.38	0.40	917
d1_88_R_8mm_100ms		8.6	9.0	1.1	0.87	0.81	3.4	2.4	1.94	0.89	0.94	2134
d1_89_0MPa_R_4mm_200ms	[27]	4.1	4.3	0.8	0.17	0.17	3.8	1.9	0.42	0.19	0.21	467
d1_90_0MPa_R_4mm_100ms		4.1	4.5	0.7	0.39	0.37	5.3	3.3	0.70	0.26	0.27	615
d1_91_0MPa_R_8mm_100ms	✿	9.1	9.7	1.3	1.58	1.57	10.3	7.9	1.76	0.79	0.84	1900

[27] Vertical precompression was removed from the wall and a final pulse test was conducted in runs 89–91.

C.4 CYCLIC RESPONSE ANALYSIS

This section describes a developed data analysis procedure that was implemented on the wall's load-displacement data vectors in the time domain (obtained by methods outlined in Section C.3), to quantify key properties relating to the wall's cyclic response such as the effective stiffness and equivalent viscous damping ratio. A significant aspect of the procedure was its applicability to all types of tests performed, regardless of whether the input motion was periodic (i.e. harmonic sinusoidal motion tests) or non-periodic (e.g. pulse and earthquake motion tests).

The basis of the analysis was to firstly employ a time domain search algorithm to find and isolate individual cycles in the wall's displacement response in a particular test run. This process is described in Section C.4.1. For every valid cycle isolated, the cyclic properties of interest were then calculated using the process described in Section C.4.2. Average values of the properties were then determined by grouping cycles within a specific range of displacement (including near the maximum response, and at small displacements). Examples of the computer program output are shown in Section C.4.3. Detailed results of the analysis are presented in Section C.4.4. It is noted that prior to implementation of the data analysis procedure, the data was filtered (using the techniques described in Section C.5) in order to aid the cycle detection algorithm.

C.4.1 Cycle Isolation Algorithm

The developed cycle isolation algorithm utilised a single time domain vector, which is denoted throughout this section as $\boldsymbol{x}$. In application of the algorithm, the response vector used for this purpose was the initially zeroed central displacement of the wall, $\Delta_{\text{w.cent0}}$.

Step 1: Division of the Waveform into Segments

The first step of the procedure was to identify points in the waveform $\boldsymbol{x}$ corresponding to reversals of direction. These points are referred to as 'vertices'. The regions between vertices are referred to as 'segments'. This process is illustrated by Figure C.7, which shows that neighbouring segments always alternate between ascending and descending.

As shown by Figure C.8, a segment (denoted by the index i) is considered ascending if the values at its vertices, x_i and x_{i+1}, are such that $x_i < x_{i+1}$, or descending if $x_i > x_{i+1}$. The cycle amplitude x_{amp} of a segment is taken as half of

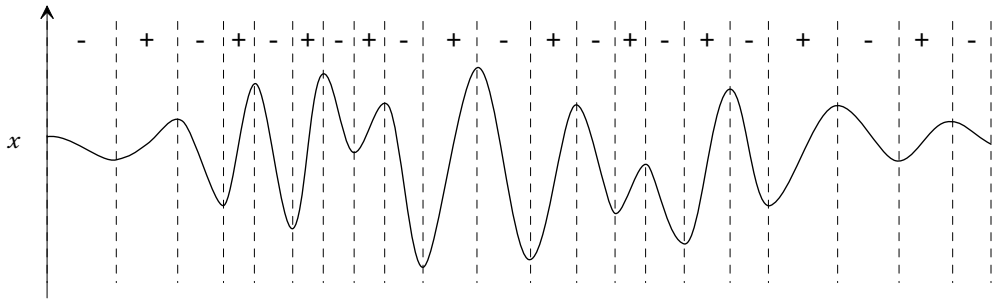

Figure C.7: Division of a generic waveform into segments for the purpose of isolating individual cycles. The segments correspond to regions of alternating positive and negative directions of movement, as indicated by the $+$ and $-$ signs.

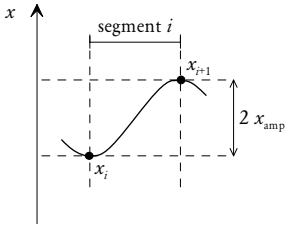

(a) Ascending segment ($x_i < x_{i+1}$).

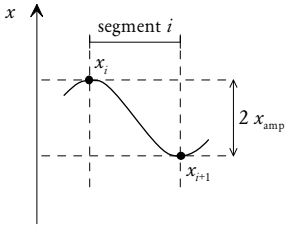

(b) Descending segment ($x_i > x_{i+1}$).

Figure C.8: Definition of segment direction and amplitude.

the absolute difference between its two vertices, such that

$$x_{\text{amp}} = 0.5\,|x_{i+1} - x_i|\,. \tag{C.10}$$

The remaining steps 2–4 were performed on every segment in the waveform, with the exception of the first and last segments.

Step 2: Classification of Cycle as Either Open or Closed

Once the waveform x has been divided into segments, it becomes possible for any segment (denoted by the index i) together with its two neighbouring segments (denoted by the indices $i-1$ and $i+1$) to be classified as either a closed or open cycle. As illustrated by Figure C.9, the type of cycle formed depends on whether there is any overlap between the outer segments $i-1$ and $i+1$. A *closed cycle* is defined as having an overlapping region, whilst an *open cycle* is defined as having no overlap (or negative overlap).

To quantify the amount of overlap, the upper and lower bounds of the overlap-

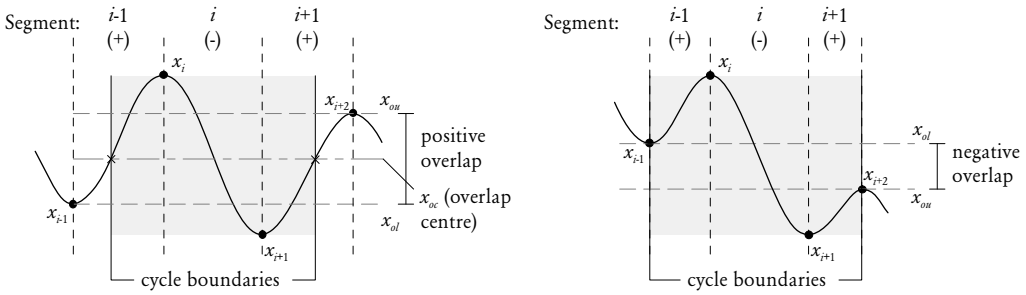

(a) Closed cycle. **(b)** Open cycle.

Figure C.9: Definition of closed and open cycles, and their boundaries. Shown for the case of a descending middle segment. Any segment i together with its two neighbouring segments $i-1$ and $i+1$ can be classified as one of these cycle types. Closed cycles have overlap across the $i-1$ and $i+1$ segments, whilst open cycles do not. For closed cycles the boundaries are taken at the central value of the overlapping region in the outside segments, whilst for open cycles the boundaries are taken at the exterior limits of the outside segments.

ping region are determined. The overlap upper bound is calculated as

$$x_{ou} = \begin{cases} \min(x_i, x_{i+2}), & \text{if segment } i \text{ is descending } (x_i > x_{i+1}); \\ \min(x_{i-1}, x_{i+1}), & \text{if segment } i \text{ is ascending } (x_i < x_{i+1}). \end{cases}$$

The overlap lower bound is calculated as

$$x_{ol} = \begin{cases} \max(x_{i-1}, x_{i+1}), & \text{if segment } i \text{ is descending } (x_i > x_{i+1}); \\ \max(x_i, x_{i+2}), & \text{if segment } i \text{ is ascending } (x_i < x_{i+1}). \end{cases}$$

The total overlap x_o is then taken as the difference, such that

$$x_o = x_{ou} - x_{ol}. \tag{C.11}$$

It is possible for the resulting value of x_o to be either positive or negative. This leads to the definition of closed and open cycles, such that if $x_o \geq 0$, then the cycle is classified as closed, and conversely if $x_o < 0$, then it is classified as open. It is worth noting that closed cycles were found to be far more common that open cycles in the test data analysed.

Step 3: Omission of Invalid Cycles

Cycles which did not meet certain criteria, in particular a minimum centrality and overlap, were omitted from subsequent calculation of hysteretic properties

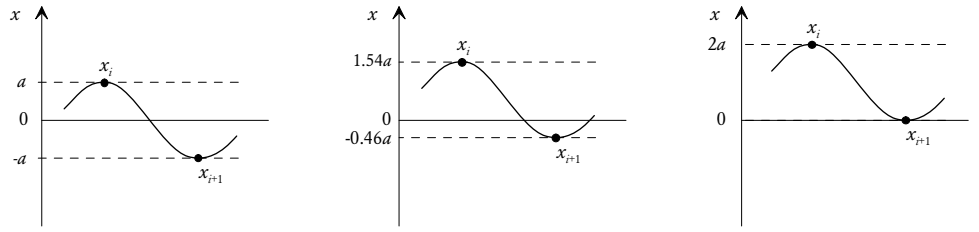

(a) $R_C = 1$. **(b)** $R_C = 0.3$. **(c)** $R_C = 0$.

Figure C.10: Demonstration of the cycle centrality parameter R_C. The cycle amplitude is denoted as a.

(described in Section C.4.2).

MINIMUM CENTRALITY CONDITION The first requirement for a cycle to be considered valid was to be sufficiently centred about $x = 0$ (i.e. zero displacement). This condition was implemented to ensure that the cycle was not biased toward a particular displacement direction. It also served to eliminate cycles which could potentially be in the 'plastic' range of the load-displacement response, as such cycles were likely to have a reduced stiffness unrepresentative of the wall's effective stiffness. Generally, it was also noticed that non-centred cycles tended to exhibit a large fluctuation in values of their equivalent viscous damping ratio, which were considered to be inaccurate of actual behaviour.

The degree of centrality for a cycle was quantified using the parameter R_C, calculated as

$$R_C = \begin{cases} -x_i / x_{i+1}, & \text{if } |x_i| \leq |x_{i+1}|; \\ -x_{i+1} / x_i, & \text{if } |x_i| > |x_{i+1}|. \end{cases} \tag{C.12}$$

Possible values of R_C can range between the limits $-1 < R_C \leq 1$. Several cases are shown by Figure C.10. A perfectly centred cycle, in which the values at the two vertices are equal and opposite, results in $R_C = 1$. A positive value of R_C corresponds to a cycle that crosses the line $x = 0$, whilst a negative value corresponds to a cycle that does not. A value of $R_C = 0$ results when one of the vertices touches the line $x = 0$. In the analysis of the wall test data, a minimum centrality condition of $R_C > 0.3$ was enforced for admissible cycles. The corresponding limiting case is illustrated by Figure C.10b.

MINIMUM OVERLAP CONDITION The second requirement for a cycle to be considered valid was to be 'sufficiently closed'. This required the cycle's outer segments (with indices $i - 1$ and $i + 1$, as shown by Figure C.9) to have sufficient overlap.

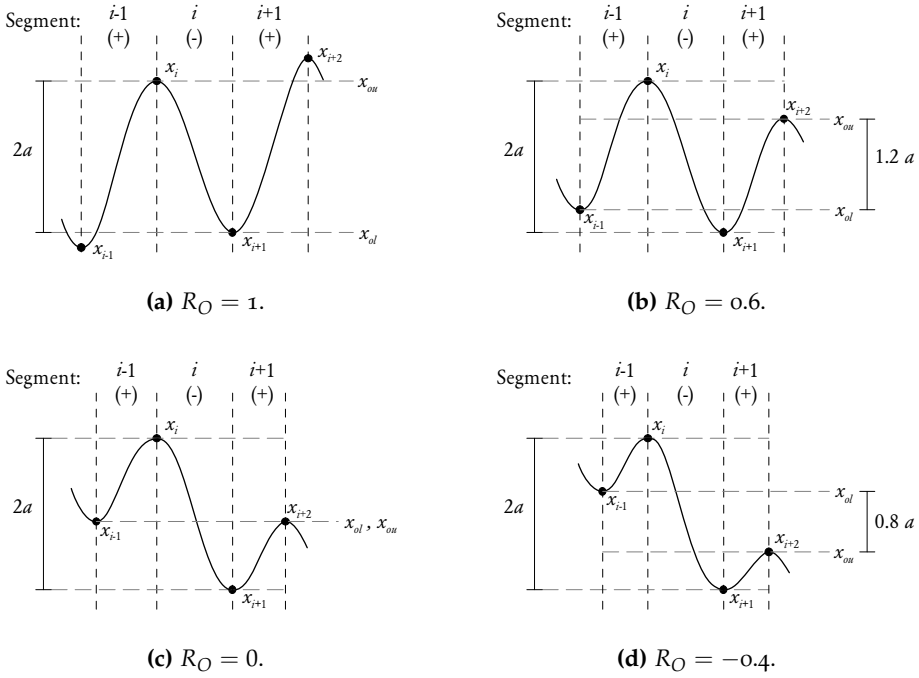

(a) $R_O = 1$. **(b)** $R_O = 0.6$.

(c) $R_O = 0$. **(d)** $R_O = -0.4$.

Figure C.11: Demonstration of the cycle overlap parameter R_O. The cycle amplitude is denoted as a.

The reason for implementing this condition was that closed cycles were deemed to be more likely to yield a representative value of the equivalent viscous damping ratio, which was calculated based on the area enclosed within the hysteresis loop.

The parameter used to quantify the degree of overlap for a cycle was the overlap ratio R_O, calculated as

$$R_O = \frac{x_o}{2\,x_{\text{amp}}}, \tag{C.13}$$

where x_o is the length of the overlap calculated using Eq. (C.11) and x_{amp} is the cycle amplitude as given by Eq. (C.10). It is possible for the value of R_O to range between the limits $-1 < R_O \leq 1$. Several cases of different overlap ratio are shown in Figure C.11. In the analysis of the wall test data, a minimum overlap condition of $R_O > -0.4$ was enforced. The limiting case is illustrated by Figure C.11d. In other words, only cycles with a negative overlap greater than $0.8\,x_{\text{amp}}$ were rejected on the basis of this condition.

Step 4: Determination of the Cycle's Boundaries and Data

Once a cycle was declared valid by satisfying the conditions outlined in step 3, the next step was to extract its load and displacement data vectors from the overall data. In order to do this, however, it was first necessary to define the cycle's boundaries

in the time domain (i.e. its first and last data points) The method implemented for defining these boundaries was dependent on whether the cycle was closed or open.

The approach used for closed cycles was to firstly calculate the central overlap value x_{oc}, as the average of the upper and lower bounds of the overlap, such that

$$x_{oc} = 0.5\,(x_{ou} + x_{ol})\,. \tag{C.14}$$

The points defining the cycle's boundaries were then taken at the intersections of the waveform with the value x_{oc} inside the outer segments, as shown by Figure C.9a. As these boundary points did not generally coincide with discrete points in the data, the corresponding values of the wall's load and displacement were determined by interpolation.

For open cycles, the cycle boundaries were simply taken at the boundaries of the outer segments, as shown by Figure C.9b.

Once the cycle's boundary points were defined, data vectors for its displacement and force (or acceleration) were extracted from the full data vectors. This included data points within the cycle boundaries and at the boundaries themselves. The vectors of interest that were used in the subsequent evaluation of cyclic properties included the zeroed central wall displacement $\Delta_{\text{w.cent0}}$, central wall acceleration $a_{\text{w.cent}}$ and average wall acceleration $a_{\text{w.avg}}$. This process is described in Section C.4.2.

It is also noted that in subsequent calculations, loops of open cycles had to be closed manually—a requirement for the calculation of the energy dissipated within the loop. This was done by replicating the first data point at the end of each of the cycle's data vectors.

Remarks

Although the developed cycle isolation algorithm was fairly versatile, in that it could be applied to the test data regardless of whether the motion was periodic (i.e. harmonic excitation tests) or non-periodic (i.e. pulse or earthquake motion tests), a certain degree of care had to be exercised during its application. For instance, in certain scenarios the algorithm failed to isolate the true cycles of interest in the wall's response. An example of such a case is shown by Figure C.12, which illustrates the wall's displacement response during a harmonic excitation test with an excitation period T_o. While the most significant periodic component of the response also occurs at the period T_o, the presence of higher frequency interference can cause additional minor peaks and troughs in the resulting waveform (as shown

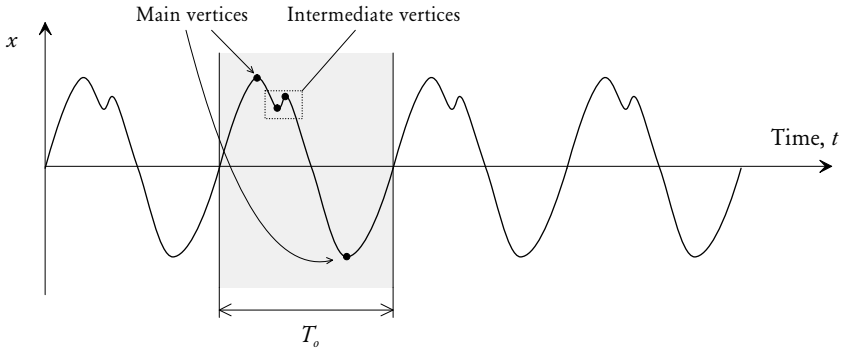

Figure C.12: Example of scenario where the cycle detection algorithm fails to detect the main response cycles in the waveform.

in this example). Even though it is obvious that the true cycles of interest must have a period equal to the excitation period, the developed algorithm would fail to detect them due to the presence of the intermediate vertices. This type of behaviour was observed in a small number of harmonic excitation tests, which contained high frequency interference believed to be due to higher vibrational modes in the wall's response. The problem was overcome by firstly filtering the wall's response vectors in the frequency domain to eliminate the contributions from the higher order harmonics, before applying the cycle detection routine. This removed the intermediate vertices from the wall's response and enabled the cycle detection algorithm to function properly. The filters used are described in Section C.5.

C.4.2 Evaluation of Key Cyclic Properties

Calculation of Properties from Each Cycle

For each valid cycle isolated using the procedure described in Section C.4.1, several key properties were calculated based on its displacement and acceleration data vectors (Figure C.13). These included: displacement and force amplitudes, effective stiffness, equivalent viscous damping, and period. The methods used to calculate these properties are as follows:

DISPLACEMENT CYCLE AMPLITUDE Since the displacement response of a cycle may not have been necessarily symmetrical about zero displacement ($\Delta = 0$), the displacement amplitude Δ_{amp} was taken as half of the difference between the maximum and minimum displacement points occurring in the cycle, such that

$$\Delta_{amp} = \frac{\Delta_{max} - \Delta_{min}}{2}, \tag{C.15}$$

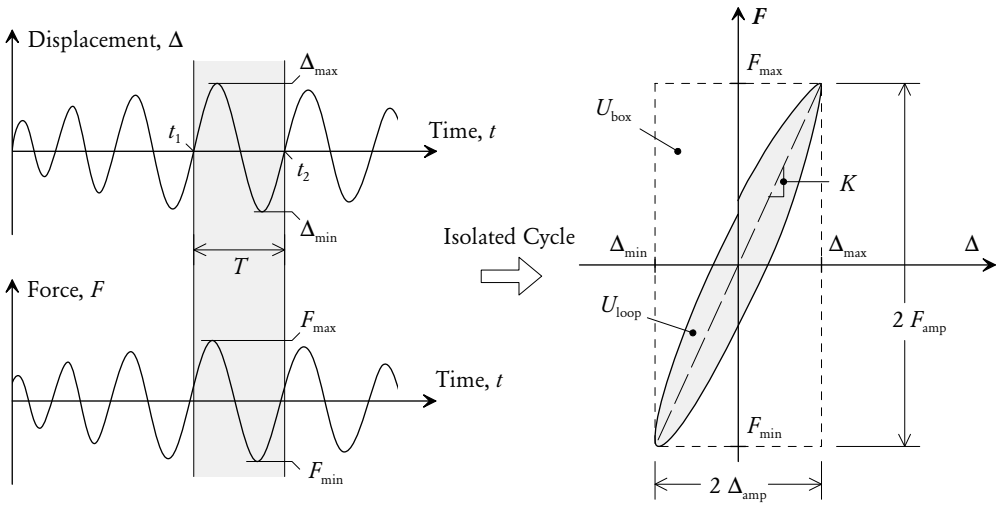

Figure C.13: Isolated hysteresis loop and the properties derived.

where Δ_{max} and Δ_{min} are the maximum and minimum displacements occurring in the loop. Alternatively, Δ_{amp} could be obtained directly as x_{amp} in the cycle isolation process, given by Eq. (C.10), since the vector $\boldsymbol{x}$ was assigned the initially zeroed central wall displacement ($\Delta_{w.cent0}$).

FORCE OR ACCELERATION CYCLE AMPLITUDE Due to the direct proportionality between the wall's restoring force F_w and its average acceleration $a_{w.avg}$ [through Eq. (C.8)], these variables are effectively interchangeable (with the relevant proportionality factors). Since the acceleration in a given cycle was not necessarily centred about zero acceleration ($a = 0$), the acceleration amplitude a_{amp} was taken as

$$a_{amp} = \frac{a_{max} - a_{min}}{2}, \tag{C.16}$$

where a_{max} and a_{min} are the maximum and minimum accelerations occurring in the loop. Similarly, for force:

$$F_{amp} = \frac{F_{max} - F_{min}}{2}. \tag{C.17}$$

EFFECTIVE STIFFNESS The cycle's effective secant stiffness K was defined as the slope of the line passing through the cycle's force-displacement curve. Two alternative methods were used to calculate its value: In the first method, the stiffness was determined by fitting a linear regression to the individual data points comprising the loop. In the second method, the stiffness was calculated as the slope of the line passing through the corner points of the loop's bounding box, as

shown by Figure C.13, or using the expression

$$K = \frac{F_{\text{amp}}}{\Delta_{\text{amp}}}. \tag{C.18}$$

It was found that both methods produced very similar values; therefore, the second approach [based on Eq. (C.18)] was adopted, since it was less computationally intensive than the first approach.

EQUIVALENT VISCOUS DAMPING The equivalent viscous damping ξ_{hyst} was calculated using the area-based method, according to the equation

$$\xi_{\text{hyst}} = \frac{2}{\pi} \frac{U_{\text{loop}}}{U_{\text{box}}}, \tag{C.19}$$

where U_{loop} is area enclosed within the hysteresis loop, and U_{box} is the area inside the loop's bounding box. From Figure C.13 it can be seen that

$$U_{\text{box}} = 4\, F_{\text{amp}}\, \Delta_{\text{amp}}. \tag{C.20}$$

The energy U_{loop} dissipated during a cycle is evaluated by the integral

$$U_{\text{loop}} = \int_{t=t_1}^{t_2} F \, \mathrm{d}\Delta, \tag{C.21}$$

in which t_1 is the time at the start of the cycle and t_2 the time at the end of the cycle. This integral was evaluated numerically using the Δ and F vectors for the cycle.

It should be noted that in the calculation of ξ_{hyst} [based on Eq. (C.19)], the energies U_{loop} and U_{box} were determined based on the wall's central acceleration ($a_{\text{w.cent}}$), as opposed to its average acceleration ($a_{\text{w.avg}}$) (upon which the wall force F_w is based). Comparison of typical hysteresis loops obtained using these two approaches is shown by Figure C.14. The reason for using $a_{\text{w.cent}}$ is that it is believed to have provided a more accurate representation of the wall's fundamental mode of vibration due to flexural response. By contrast, it is believed that $a_{\text{w.avg}}$ [calculated as a weighted average of the 10 accelerometers mounted on the wall as per Eq. (C.5)] received some interference from higher vibrational modes (possibly twisting of the specimens), resulting in an alteration of the apparent phase relationship between the force and displacement and ultimately generating fatter and more ragged hysteresis loops. The values of ξ_{hyst} calculated on the basis of $a_{\text{w.avg}}$ (generally ranging between 0.15 and 0.4) are believed to be uncharacteristically high and deemed to be unconservative. By contrast, the hysteresis loops determined using $a_{\text{w.cent}}$ tended to be significantly cleaner. The computed values of ξ_{hyst} are reported

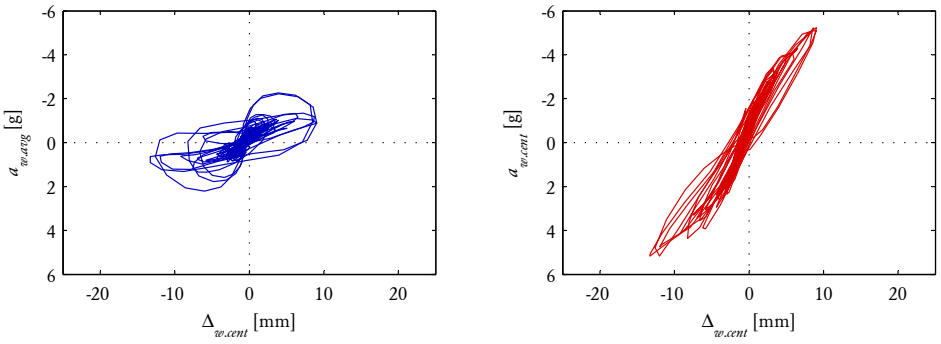

(a) Earthquake test run `d1_76_EQ_Synth03_+100mm`.

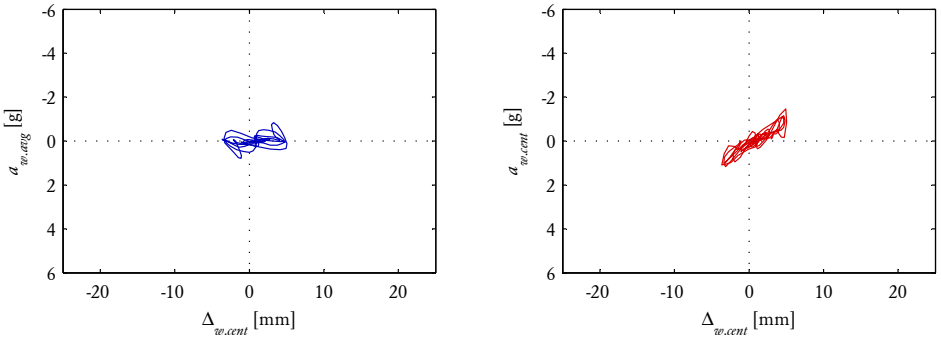

(b) Pulse test run `d2_45_R_8mm_100ms`.

Figure C.14: Typical examples demonstrating the difference between hysteresis loops based on the average wall acceleration, $a_{\text{w.avg}}$ (left) and the central wall acceleration, $a_{\text{w.cent}}$ (right).

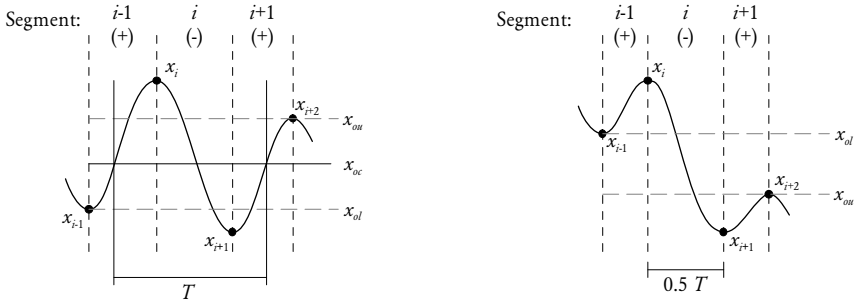

(a) Closed cycle. **(b)** Open cycle.

Figure C.15: Method used for estimating the cycle period T in closed and open cycles.

in Section C.4.4.

PERIOD AND FREQUENCY As shown by Figure C.15, the method used to evaluate the period T of the cycle depended on whether the cycle was closed or open.[28] For closed cycles, the period was taken as the duration between the start and end boundary points of the cycle (Figure C.15a). These boundary points were determined using the procedure described in Section C.4.1, as illustrated by Figure C.9a. For open cycles, the period was taken as twice the duration between the cycle's peak and trough vertices (Figure C.15b). These results are generally reported as a frequency f, where $f = 1/T$.

Calculation of Average Values in Each Test Run

Once the aforementioned properties have been calculated for all valid cycles within a test run, their average values were computed over two ranges of displacement response:

SHORT DISPLACEMENT RANGE This included cycles whose displacement amplitude was inside the range 0.5 mm $\leq \Delta_{\text{amp}} \leq$ 3 mm, which was intended to capture response along the initial loading branch of the load-displacement curve. In order to ensure a good spread of response within this range, average values were only

[28] A significant amount of effort was invested into attempting to derive values of vibrational frequency for the walls using a Fourier-based analysis of the walls' displacement and acceleration response. However, these efforts were ultimately abandoned due the finding that additional signals were present in the measured response vectors, which were evidently interfering with that of the wall's vibrational response. This interference were likely to have come from some aspect of the test arrangement such as the wall restraint frame and the shaketable rig itself. The method ultimately adopted for calculating the cyclic frequency of the walls is believed to also provide the advantage of being able to examine cycles individually.

calculated for test runs in which the maximum displacement amplitude exceeded 95% of the upper limit value of 3 mm (i.e. $\max \Delta_{amp} > 2.85$ mm). Note that for this range, 'average' values of the effective stiffness K, equivalent viscous damping ξ_{hyst} and period T, were calculated as the interquartile mean. This was done to reduce the influence of outlying values on the resulting average, as there tended to be a high level of scatter in these properties at small displacements, which could be attributed to a larger relative error in the sampling method for displacement.

PEAK RESPONSE RANGE This range included all cycles whose displacement amplitude was at least 70% of maximum value occurring in the test run, or $\Delta_{amp} \geq 0.7 \max(\Delta_{amp})$, and was intended to capture the behaviour near the maximum displacement response in the test run. Average values of properties within this range were calculated as the conventional mean.

C.4.3 Examples

Examples of the graphical output from the developed computer routine used to perform the cyclic analysis are shown by Figures C.16, C.17 and C.18 for a pulse test, harmonic test and earthquake motion test, respectively.

C.4.4 Results

Results of the cyclic analysis are presented in Table C.7 for all test runs performed in the experimental study. The hysteresis graphs corresponding to the data used within these analyses is also presented is Section C.6.

Column 1 of the table lists the test run name, as per the convention outlined in Section C.1. Column 2 gives the cutoff frequency f_c of a lowpass Butterworth filter of order $n = 10$, used to filter the results prior to performing the cyclic analysis. A value of 'default' refers to the filter for harmonic tests, corresponding to a Butterworth comb filter passing the first three harmonics of the excitation frequency with a normalised bandwidth of 0.2 (refer to Section C.5.1).

Columns 3–5 provide values of the peak cycle amplitudes for the respective properties occurring in the test run, where Δ_{amp} is the central displacement, $a_{c\,amp}$ is the central wall acceleration and $a_{a\,amp}$ is the average wall acceleration. These may not necessarily have occurred during the same cycle.

Columns 7–12 give the average results for cycles whose displacement amplitude Δ_{amp} was at least 70% of the peak displacement amplitude in the test run, where n is the number of cycles used for averaging, K is the effective stiffness, ξ_{hyst} is the

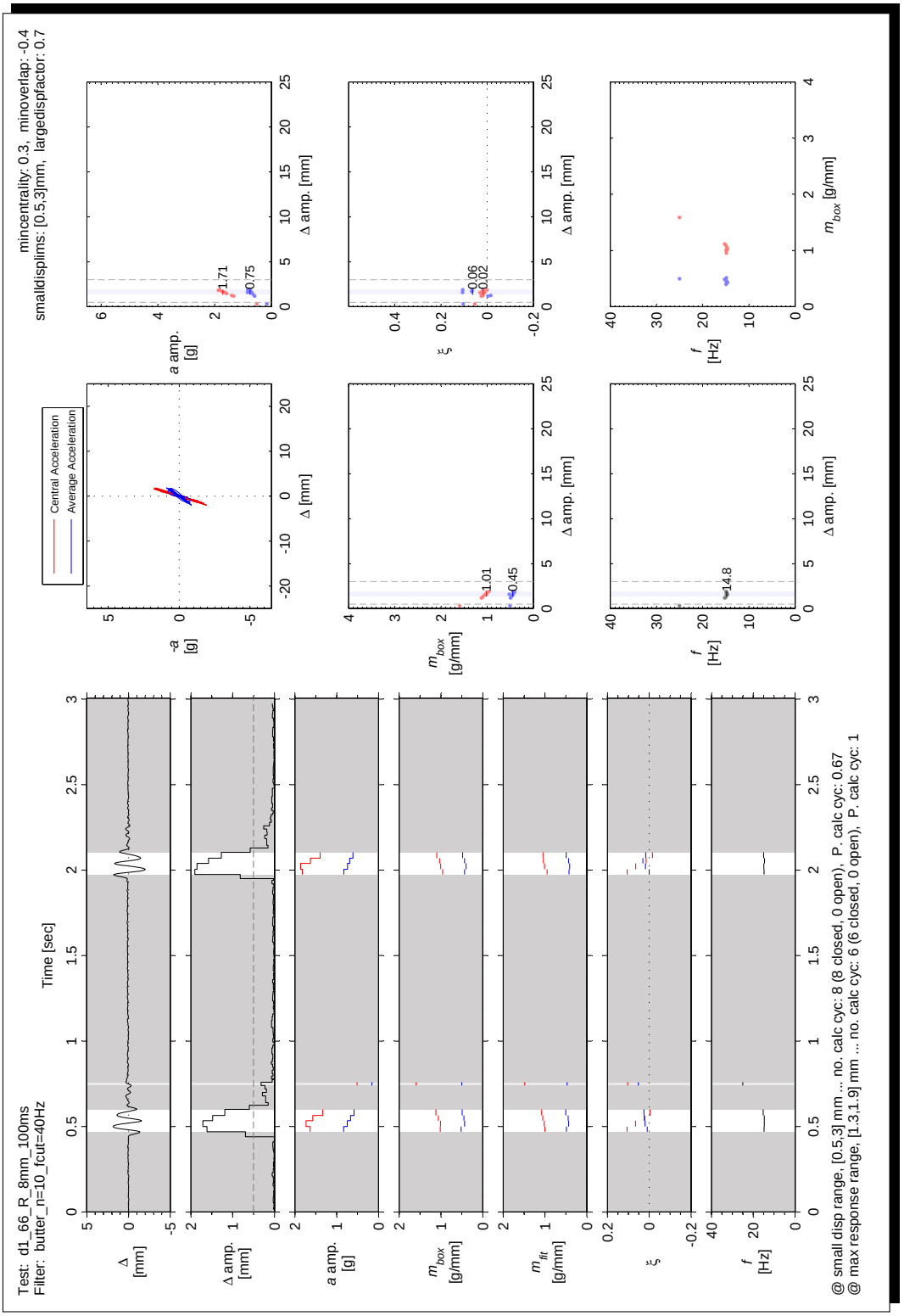

Figure C.16: Example of graphical output from the cyclic analysis of a pulse test (d1_66_R_8mm_100ms).

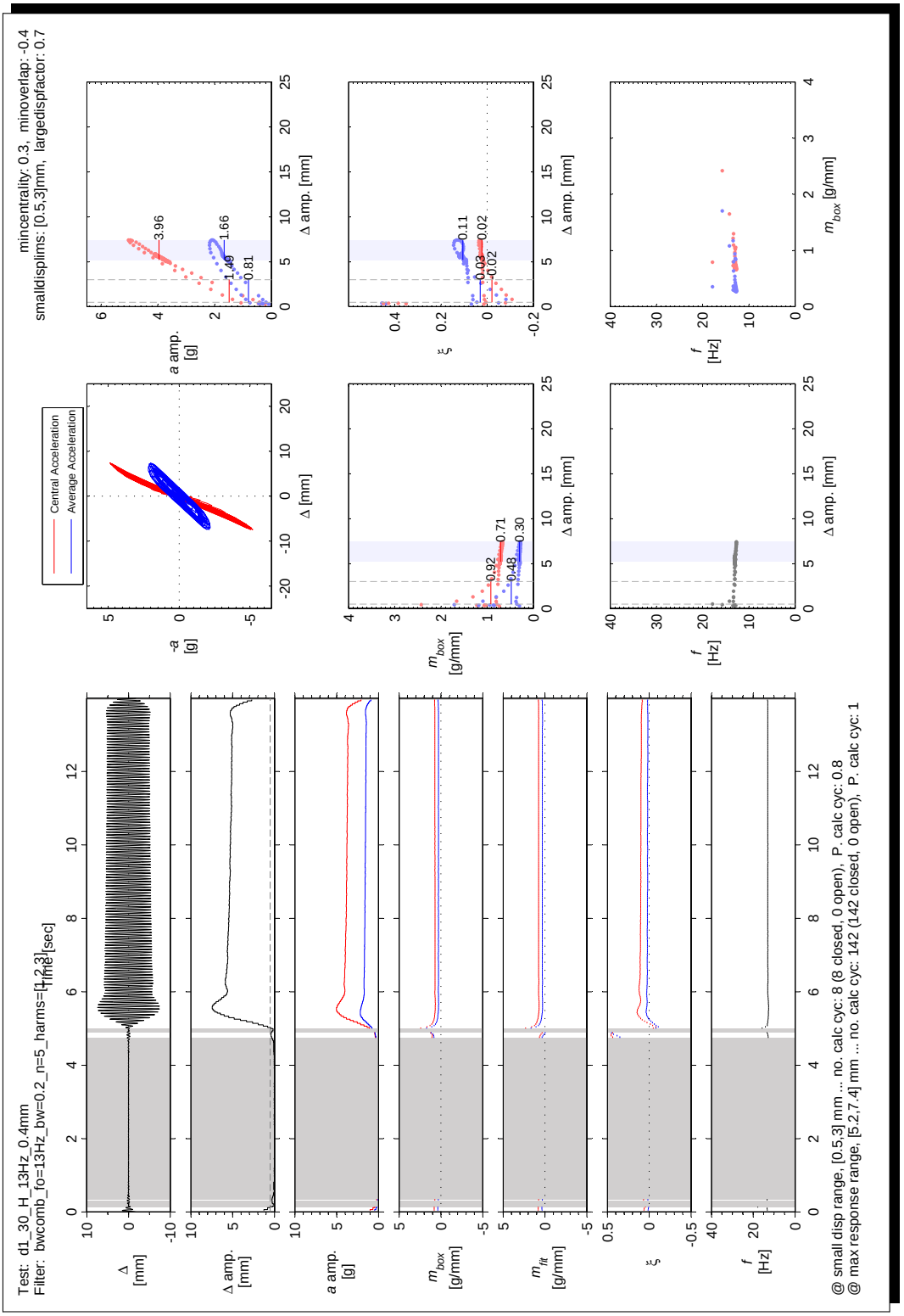

Figure C.17: Example of graphical output from the cyclic analysis of a harmonic test (d1_30_H_13Hz_0.4mm).

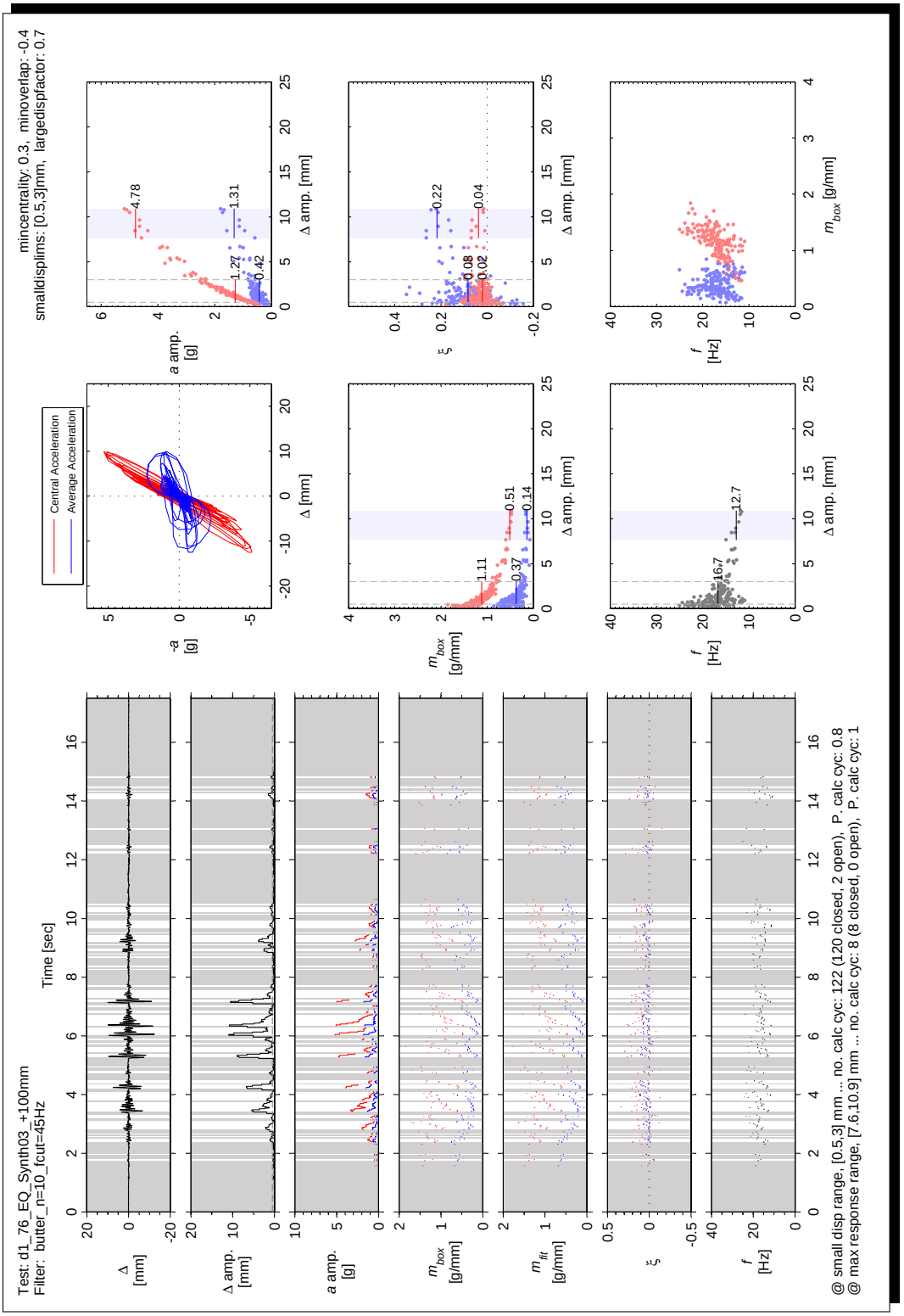

Figure C.18: Example of graphical output from the cyclic analysis of an earthquake motion test (d1_76_EQ_Synth03_+100mm).

equivalent viscous damping ratio, f is the cycle frequency, and other properties as defined previously. Note that f is not provided for harmonic test runs, since the measured cycle frequency in these tests is equal to the excitation frequency and not the vibrational frequency of the wall. Columns 13–18 give the average results for cycles whose displacement amplitude was between 0.5 mm and 3 mm.

Whilst this table does not provide the cycle amplitude of the wall's restoring force F_{amp}, this value can be calculated directly from the average wall acceleration amplitude $a_{a\,\text{amp}}$ using the relationship

$$F_{\text{amp}} = W_w \frac{a_{a\,\text{amp}}}{g}, \tag{C.22}$$

where W_w is the weight of the wall, as given in Table 3.3. The weight of the solid walls (D1 and D2) was 2400 N and the weight of the walls with a window (D3, D4 and D5) was 2079 N. For example, in run `d1_03_0MPa_R_8mm_100ms`, where the peak average wall acceleration was 1.18 g, the corresponding peak wall force was $2400\,\text{N} \times 1.18 = 2830\,\text{N}$.

Table C.7: Cyclic analysis results for individual test runs.

Test Name	Filter	Peak response cycles			Avg. results for cycles with $\Delta_{amp} \geq 0.7 \max(\Delta_{amp})$						Avg. results for cycles with $0.5\text{ mm} \leq \Delta_{amp} \leq 3\text{ mm}$					
	f_c [Hz]	Δ_{amp} [mm]	$a_{c\,amp}$ [g]	$a_{a\,amp}$ [g]	n	Δ_{amp} [mm]	$a_{a\,amp}$ [g]	K [N/mm]	ξ_{hyst}	f [Hz]	n	Δ_{amp} [mm]	$a_{a\,amp}$ [g]	K [N/mm]	ξ_{hyst}	f [Hz]
d1_01_0MPa_R_4mm_200ms	40	–	–	–	0	–	–	–	–	–	0	–	–	–	–	–
d1_02_0MPa_R_4mm_100ms	40	–	–	–	0	–	–	–	–	–	0	–	–	–	–	–
d1_03_0MPa_R_8mm_100ms	40	0.6	1.76	1.36	6	0.5	1.18	5980	0.13	16.3	2	–	–	–	–	–
d1_04_0.05MPa_R_4mm_200ms	40	–	–	–	0	–	–	–	–	–	0	–	–	–	–	–
d1_05_0.05MPa_R_4mm_100ms	40	–	–	–	0	–	–	–	–	–	0	–	–	–	–	–
d1_06_0.05MPa_R_8mm_100ms	40	–	–	–	0	–	–	–	–	–	0	–	–	–	–	–
d1_08_0.10MPa_R_4mm_200ms	40	–	–	–	0	–	–	–	–	–	0	–	–	–	–	–
d1_09_0.10MPa_R_4mm_100ms	40	–	–	–	0	–	–	–	–	–	0	–	–	–	–	–
d1_10_0.10MPa_R_8mm_100ms	40	–	–	–	0	–	–	–	–	–	0	–	–	–	–	–
d1_11_H_13Hz_0.25mm	default	–	–	–	0	–	–	–	–	–	0	–	–	–	–	–
d1_12_H_13Hz_0.5mm	default	–	–	–	93	0.4	1.40	8680	0.20	–	0	–	–	–	–	–
d1_13_H_13Hz_0.75mm	default	0.6	2.06	1.81	13	0.5	1.63	7740	0.16	–	8	–	–	–	–	–
d1_14_H_13Hz_1mm	default	1.2	3.07	2.35	39	1.0	2.05	5010	0.11	–	60	–	–	–	–	–
d1_15_EQ_Taft_-40mm	40	–	–	–	0	–	–	–	–	–	0	–	–	–	–	–
d1_16_EQ_Taft_+40mm	40	–	–	–	0	–	–	–	–	–	0	–	–	–	–	–
d1_17_EQ_Taft_+60mm	40	–	–	–	0	–	–	–	–	–	0	–	–	–	–	–
d1_18_EQ_Taft_-60mm	40	0.6	2.33	1.45	1	0.6	1.45	5570	0.08	18.4	1	–	–	–	–	–
d1_19_EQ_Taft_-80mm	45	1.6	4.07	2.70	1	1.6	2.70	4180	0.07	17.6	5	–	–	–	–	–
d1_20_EQ_Taft_+80mm	45	2.3	5.20	3.25	2	2.1	3.11	3530	0.07	17.9	6	–	–	–	–	–
d1_21_EQ_Taft_+100mm	45	3.2	5.42	3.00	4	2.9	2.50	2030	0.05	18.7	14	1.4	1.50	2980	0.06	15.2
d1_22_EQ_Taft_-100mm	45	1.6	3.17	1.56	3	1.5	1.34	2210	0.04	20.8	3	–	–	–	–	–
d1_23_EQ_Taft_-120mm	45	5.5	5.95	2.70	3	4.7	2.46	1280	0.05	15.6	30	1.1	0.91	2110	0.05	21.0
d1_24_EQ_Taft_+120mm	45	6.6	5.85	2.44	5	5.9	1.99	802	0.05	15.3	50	1.0	0.69	1810	0.04	20.1
d1_25_R_4mm_200ms	40	–	–	–	0	–	–	–	–	–	0	–	–	–	–	–
d1_26_R_4mm_100ms	40	–	–	–	1	0.3	0.37	2760	0.03	20.9	0	–	–	–	–	–
d1_27_R_8mm_100ms	40	0.9	1.66	0.86	2	0.9	0.84	2320	0.02	15.3	3	–	–	–	–	–
d1_28_H_13Hz_0.1mm	default	–	–	–	0	–	–	–	–	–	0	–	–	–	–	–
d1_29_H_13Hz_0.2mm	default	–	–	–	0	–	–	–	–	–	0	–	–	–	–	–
d1_30_H_13Hz_0.4mm	default	7.4	5.03	2.18	142	5.6	1.66	713	0.02	–	8	1.5	0.81	1150	−0.02	–
d1_31_R_4mm_200ms	40	–	–	–	0	–	–	–	–	–	0	–	–	–	–	–
d1_32_R_4mm_100ms	40	–	–	–	2	0.4	0.37	2060	−0.01	18.4	0	–	–	–	–	–
d1_33_R_8mm_100ms	40	1.5	1.76	0.84	4	1.3	0.78	1390	0.04	15.6	7	–	–	–	–	–
d1_34_EQ_Taft_+40mm	35	–	–	–	17	0.4	0.27	1750	0.03	20.8	0	–	–	–	–	–
d1_35_EQ_Taft_-40mm	35	–	–	–	16	0.4	0.28	1740	0.04	20.6	0	–	–	–	–	–
d1_36_EQ_Taft_-60mm	40	3.4	3.25	1.37	3	3.2	1.06	797	0.02	16.0	26	0.8	0.40	1480	0.04	19.0
d1_37_EQ_Taft_+60mm	40	1.2	1.58	0.63	3	1.0	0.62	1440	0.03	17.7	15	–	–	–	–	–
d1_38_EQ_Taft_+80mm	45	9.3	5.47	2.13	3	8.2	1.77	516	0.04	13.5	25	0.8	0.43	1390	0.02	19.2

continued on next page

Table C.7: (cont'd).

Test Name	Filter	Peak response cycles			Avg. results for cycles with $\Delta_{amp} \geq 0.7 \max(\Delta_{amp})$						Avg. results for cycles with $0.5\text{ mm} \leq \Delta_{amp} \leq 3\text{ mm}$					
	f_c [Hz]	Δ_{amp} [mm]	$a_{c\,amp}$ [g]	$a_{a\,amp}$ [g]	n	Δ_{amp} [mm]	$a_{a\,amp}$ [g]	K [N/mm]	ξ_{hyst}	f [Hz]	n	Δ_{amp} [mm]	$a_{a\,amp}$ [g]	K [N/mm]	ξ_{hyst}	f [Hz]
d1_39_EQ_Taft_-80mm	45	8.7	5.18	1.79	3	7.6	1.60	509	0.03	13.9	56	0.8	0.46	1390	0.02	18.1
d1_40_EQ_Taft_-100mm	45	5.3	3.92	1.42	3	4.6	1.22	641	0.02	14.9	84	1.1	0.53	1280	0.02	18.1
d1_41_EQ_Taft_+100mm	45	10.3	5.68	2.03	3	8.9	1.70	458	0.04	13.5	82	1.1	0.50	1170	0.02	17.6
d1_42_R_4mm_200ms	40	–	–	–	1	0.3	0.24	1860	0.04	20.4	0	–	–	–	–	–
d1_43_R_4mm_100ms	40	0.5	0.80	0.39	2	0.5	0.36	1750	−0.01	15.0	1	–	–	–	–	–
d1_44_R_8mm_100ms	40	1.7	1.75	0.84	4	1.6	0.79	1190	0.02	15.4	8	–	–	–	–	–
d1_45_EQ_Taft_+120mm	45	9.0	5.30	2.01	4	7.6	1.60	506	0.03	13.3	109	1.0	0.46	1180	0.02	17.7
d1_46_EQ_Taft_-120mm	45	9.8	5.33	2.05	4	9.0	1.73	463	0.05	12.1	118	1.1	0.49	1160	0.03	17.3
d1_47_R_4mm_200ms	40	–	–	–	0	–	–	–	–	–	0	–	–	–	–	–
d1_48_R_4mm_100ms	40	0.6	0.82	0.38	2	0.5	0.37	1650	−0.01	16.6	2	–	–	–	–	–
d1_49_R_8mm_100ms	40	1.7	1.77	0.84	6	1.5	0.74	1200	0.02	15.0	8	–	–	–	–	–
d1_50_H_12Hz_0.1mm	default	–	–	–	0	–	–	–	–	–	0	–	–	–	–	–
d1_51_H_12Hz_0.2mm	default	4.7	3.19	1.51	215	4.5	1.47	792	0.02	–	28	1.7	0.93	1400	0.02	–
d1_52_R_4mm_200ms	40	–	–	–	0	–	–	–	–	–	0	–	–	–	–	–
d1_53_R_4mm_100ms	40	–	–	–	1	0.4	0.38	2390	0.02	17.0	0	–	–	–	–	–
d1_54_R_8mm_100ms	40	1.4	1.74	0.87	3	1.3	0.81	1560	0.04	15.3	7	–	–	–	–	–
d1_56_EQ_Synth01_+20mm	40	–	–	–	0	–	–	–	–	–	0	–	–	–	–	–
d1_57_EQ_Synth01_-20mm	40	–	–	–	0	–	–	–	–	–	0	–	–	–	–	–
d1_58_EQ_Synth01_-40mm	40	2.1	2.28	1.11	2	2.1	1.04	1220	0.01	15.3	8	–	–	–	–	–
d1_59_EQ_Synth01_+40mm	40	–	–	–	11	0.4	0.28	1630	0.01	20.9	0	–	–	–	–	–
d1_60_EQ_Synth01_+60mm	45	7.2	4.23	1.64	6	6.3	1.39	538	0.04	13.7	36	1.1	0.45	1090	0.03	18.8
d1_61_EQ_Synth01_-60mm	45	6.0	3.73	1.43	9	5.0	1.23	598	0.02	14.0	35	1.1	0.41	1010	0.03	18.8
d1_62_EQ_Synth01_-80mm	45	11.3	5.80	1.91	6	9.7	1.38	336	0.04	13.3	82	1.1	0.44	1050	0.02	18.3
d1_63_EQ_Synth01_+80mm	45	10.5	5.55	1.90	6	9.4	1.42	362	0.04	12.8	83	1.3	0.47	941	0.02	17.1
d1_64_R_4mm_200ms	40	–	–	–	1	0.4	0.22	1550	0.06	18.4	0	–	–	–	–	–
d1_65_R_4mm_100ms	40	0.6	0.86	0.40	2	0.6	0.37	1630	0.01	17.4	1	–	–	–	–	–
d1_66_R_8mm_100ms	40	1.9	1.86	0.84	6	1.7	0.75	1070	0.02	14.8	8	–	–	–	–	–
d1_67_EQ_Synth03_-20mm	40	–	–	–	0	–	–	–	–	–	0	–	–	–	–	–
d1_68_EQ_Synth03_+20mm	40	–	–	–	0	–	–	–	–	–	0	–	–	–	–	–
d1_69_EQ_Synth03_+40mm	40	0.7	0.98	0.44	8	0.6	0.33	1440	0.06	17.7	5	–	–	–	–	–
d1_70_EQ_Synth03_-40mm	40	0.6	0.90	0.40	6	0.5	0.30	1360	0.06	18.9	2	–	–	–	–	–
d1_71_EQ_Synth03_-60mm	40	1.6	1.90	0.71	2	1.5	0.61	943	0.00	17.5	27	–	–	–	–	–
d1_72_EQ_Synth03_+60mm	40	1.3	1.48	0.62	12	1.1	0.50	1110	0.03	17.3	37	–	–	–	–	–
d1_73_EQ_Synth03_+80mm	45	8.2	4.37	1.65	2	7.8	1.41	430	0.04	12.5	74	1.0	0.45	1090	0.02	17.5
d1_74_EQ_Synth03_-80mm	45	8.5	4.43	1.64	4	7.3	1.36	454	0.02	13.0	70	0.9	0.39	1090	0.02	17.4
d1_75_EQ_Synth03_-100mm	45	10.2	5.32	1.69	6	8.9	1.36	365	0.03	12.9	101	1.2	0.46	1000	0.02	16.5
d1_76_EQ_Synth03_+100mm	45	10.9	5.17	1.78	8	9.4	1.31	329	0.04	12.7	122	1.2	0.42	886	0.02	16.7
d1_77_R_4mm_200ms	40	–	–	–	1	0.3	0.20	1550	0.04	19.7	0	–	–	–	–	–

continued on next page

Table C.7: (cont'd).

Test Name	Filter	Peak response cycles			Avg. results for cycles with $\Delta_{amp} \geq 0.7 \max(\Delta_{amp})$						Avg. results for cycles with $0.5\text{ mm} \leq \Delta_{amp} \leq 3\text{ mm}$					
	f_c [Hz]	Δ_{amp} [mm]	$a_{c\,amp}$ [g]	$a_{a\,amp}$ [g]	n	Δ_{amp} [mm]	$a_{a\,amp}$ [g]	K [N/mm]	ξ_{hyst}	f [Hz]	n	Δ_{amp} [mm]	$a_{a\,amp}$ [g]	K [N/mm]	ξ_{hyst}	f [Hz]
d1_78_R_4mm_100ms	40	0.7	0.82	0.39	2	0.6	0.38	1530	−0.02	14.6	2	–	–	–	–	–
d1_79_R_8mm_100ms	40	2.1	1.90	0.81	7	1.8	0.73	948	0.01	14.6	11	–	–	–	–	–
d1_80_EQ_Synth05_-20mm	40	1.0	1.16	0.48	3	0.9	0.41	1150	0.01	17.3	25	–	–	–	–	–
d1_81_EQ_Synth05_+20mm	40	0.8	1.03	0.44	7	0.7	0.35	1260	0.01	17.4	21	–	–	–	–	–
d1_82_EQ_Synth05_+40mm	45	3.1	2.47	0.99	2	3.0	0.91	730	0.03	13.5	125	0.8	0.36	1040	0.01	17.4
d1_83_EQ_Synth05_-40mm	45	4.8	3.05	1.23	4	4.5	1.17	636	0.04	12.5	118	0.9	0.37	1020	0.02	17.3
d1_84_EQ_Synth05_-60mm	50	11.5	5.53	1.71	6	9.2	1.30	334	0.05	12.4	173	1.1	0.42	924	0.02	16.3
d1_85_EQ_Synth05_+60mm	50	11.7	5.64	1.67	3	9.8	1.35	329	0.04	12.6	168	1.2	0.42	881	0.02	16.1
d1_86_R_4mm_200ms	40	–	–	–	1	0.4	0.21	1410	0.10	16.4	0	–	–	–	–	–
d1_87_R_4mm_100ms	40	0.7	0.81	0.38	2	0.6	0.36	1390	0.01	13.6	2	–	–	–	–	–
d1_88_R_8mm_100ms	40	2.3	1.97	0.82	8	2.1	0.73	845	0.01	14.4	12	–	–	–	–	–
d1_89_0MPa_R_4mm_200ms	40	1.7	0.40	0.17	9	1.4	0.14	230	0.05	7.7	13	–	–	–	–	–
d1_90_0MPa_R_4mm_100ms	40	2.7	0.67	0.23	4	2.4	0.22	218	0.06	6.4	9	–	–	–	–	–
d1_91_0MPa_R_8mm_100ms	40	5.8	1.60	0.66	4	5.0	0.57	274	0.02	10.6	6	1.6	0.12	190	0.09	8.1
d2_01_R_4mm_200ms	40	–	–	–	0	–	–	–	–	–	0	–	–	–	–	–
d2_02_R_4mm_100ms	40	–	–	–	0	–	–	–	–	–	0	–	–	–	–	–
d2_03_R_8mm_100ms	40	–	–	–	0	–	–	–	–	–	0	–	–	–	–	–
d2_04_R_4mm_200ms	40	–	–	–	0	–	–	–	–	–	0	–	–	–	–	–
d2_05_R_4mm_100ms	40	–	–	–	0	–	–	–	–	–	0	–	–	–	–	–
d2_06_R_8mm_100ms	40	0.8	1.72	1.47	4	0.7	1.23	4540	0.13	14.6	4	–	–	–	–	–
d2_07_H_12Hz_0.05mm	default	–	–	–	0	–	–	–	–	–	0	–	–	–	–	–
d2_08_H_12Hz_0.1mm	default	–	–	–	0	–	–	–	–	–	0	–	–	–	–	–
d2_09_H_12Hz_0.2mm	default	–	–	–	286	0.5	0.92	4790	0.16	–	0	–	–	–	–	–
d2_10_R_4mm_200ms	40	–	–	–	0	–	–	–	–	–	0	–	–	–	–	–
d2_11_R_4mm_100ms	40	–	–	–	0	–	–	–	–	–	0	–	–	–	–	–
d2_12_R_8mm_100ms	40	0.6	1.26	1.08	4	0.6	0.95	4170	0.16	13.5	3	–	–	–	–	–
d2_13_H_12Hz_0.25mm	default	1.6	1.36	1.17	444	1.3	0.41	734	0.19	–	490	–	–	–	–	–
d2_14_H_12Hz_0.25mm	default	1.4	0.76	0.34	213	1.3	0.31	571	0.20	–	230	–	–	–	–	–
d2_16_R_4mm_200ms	40	–	–	–	0	–	–	–	–	–	0	–	–	–	–	–
d2_17_R_4mm_100ms	40	–	–	–	3	0.4	0.37	2280	0.04	13.8	0	–	–	–	–	–
d2_18_R_8mm_100ms	40	1.3	1.57	0.92	7	1.1	0.79	1760	0.09	13.6	12	–	–	–	–	–
d2_20_H_12Hz_0.1mm	default	–	–	–	0	–	–	–	–	–	0	–	–	–	–	–
d2_21_H_12Hz_0.2mm	default	1.3	1.14	0.72	13	1.1	0.60	1270	0.12	–	210	–	–	–	–	–
d2_23_H_12Hz_0.1mm	default	–	–	–	0	–	–	–	–	–	0	–	–	–	–	–
d2_24_H_12Hz_0.2mm	default	2.5	1.91	1.01	20	2.2	0.88	967	0.03	–	224	–	–	–	–	–
d2_25_R_4mm_200ms	40	–	–	–	3	0.4	0.17	1080	0.08	12.3	0	–	–	–	–	–
d2_26_R_4mm_100ms	40	1.0	0.73	0.36	8	1.0	0.27	691	0.05	13.6	10	–	–	–	–	–

continued on next page

Table C.7: (cont'd).

Test Name	Filter	Peak response cycles			Avg. results for cycles with $\Delta_{amp} \geq 0.7 \max(\Delta_{amp})$						Avg. results for cycles with $0.5\text{ mm} \leq \Delta_{amp} \leq 3\text{ mm}$					
	f_c [Hz]	Δ_{amp} [mm]	$a_{c\,amp}$ [g]	$a_{a\,amp}$ [g]	n	Δ_{amp} [mm]	$a_{a\,amp}$ [g]	K [N/mm]	ξ_{hyst}	f [Hz]	n	Δ_{amp} [mm]	$a_{a\,amp}$ [g]	K [N/mm]	ξ_{hyst}	f [Hz]
d2_27_R_8mm_100ms	40	3.1	2.11	0.77	9	2.7	0.69	614	0.03	13.4	9	2.4	0.63	624	0.04	13.3
d2_28_H_12Hz_0.25mm	default	3.1	1.55	0.50	193	2.8	0.30	257	0.04	–	192	2.6	0.29	223	0.04	–
d2_29_H_12Hz_0.3mm	default	3.2	1.39	0.24	224	2.9	0.19	156	0.04	–	206	2.7	0.18	151	0.04	–
d2_30_R_4mm_200ms	40	0.7	0.35	0.15	5	0.6	0.14	542	0.11	10.1	6	–	–	–	–	–
d2_31_R_4mm_100ms	40	1.5	0.66	0.27	4	1.4	0.20	346	0.08	10.8	8	–	–	–	–	–
d2_32_R_8mm_100ms	40	3.2	1.34	0.49	8	2.6	0.27	233	0.04	12.2	17	1.7	0.18	209	0.06	12.9
d2_33_EQ_Taft_-20mm	40	0.8	0.38	0.21	8	0.7	0.16	600	0.08	9.8	11	–	–	–	–	–
d2_34_EQ_Taft_+20mm	40	0.8	0.35	0.19	5	0.6	0.16	595	0.09	9.1	12	–	–	–	–	–
d2_35_EQ_Taft_+40mm	40	1.8	0.73	0.36	13	1.5	0.31	490	0.07	8.6	75	–	–	–	–	–
d2_36_EQ_Taft_-40mm	40	2.0	0.81	0.38	7	1.6	0.30	468	0.06	9.0	75	–	–	–	–	–
d2_37_EQ_Taft_-60mm	40	5.1	1.97	0.83	1	5.1	0.83	394	0.05	9.8	120	1.2	0.21	449	0.07	9.2
d2_38_EQ_Taft_+60mm	40	2.8	0.97	0.51	16	2.2	0.38	410	0.06	8.6	130	–	–	–	–	–
d2_39_EQ_Taft_+80mm	50	8.7	3.31	1.52	1	8.7	1.52	420	0.05	12.5	148	1.4	0.21	374	0.06	9.0
d2_40_EQ_Taft_-80mm	50	7.0	2.62	1.42	3	5.8	0.87	346	0.06	8.6	121	1.4	0.18	322	0.07	8.5
d2_41_EQ_Taft_-100mm	50	6.6	1.80	1.00	12	5.3	0.66	302	0.07	6.8	134	1.6	0.19	288	0.07	8.4
d2_42_EQ_Taft_+100mm	50	7.4	2.47	1.59	13	5.9	0.69	276	0.07	6.6	108	1.7	0.19	247	0.07	7.7
d2_43_R_4mm_200ms	40	1.1	0.30	0.14	10	1.0	0.11	259	0.08	7.7	11	–	–	–	–	–
d2_44_R_4mm_100ms	40	2.0	0.53	0.22	4	1.8	0.20	257	0.08	7.3	9	–	–	–	–	–
d2_45_R_8mm_100ms	40	4.4	1.20	0.62	4	3.9	0.61	382	0.04	10.6	6	1.2	0.11	209	0.15	8.3
d2_46_EQ_Taft_+60mm	40	4.3	0.92	0.49	16	3.7	0.38	242	0.08	6.3	145	1.4	0.15	269	0.08	7.5
d2_47_EQ_Taft_-60mm	40	5.6	1.31	0.81	8	4.6	0.50	257	0.08	6.2	123	1.5	0.15	240	0.07	7.1
d2_48_EQ_Taft_-120mm	50	9.1	2.15	1.29	6	7.8	0.87	264	0.08	5.9	91	1.7	0.18	230	0.06	8.2
d2_49_EQ_Taft_+120mm	50	8.4	1.59	1.18	6	7.1	0.72	242	0.10	6.1	85	1.8	0.19	230	0.06	7.6
d2_50_R_4mm_200ms	40	1.3	0.28	0.11	10	1.1	0.09	197	0.08	7.3	12	–	–	–	–	–
d2_51_R_4mm_100ms	40	2.1	0.50	0.24	6	1.9	0.18	221	0.07	7.2	10	–	–	–	–	–
d2_52_R_8mm_100ms	40	4.3	1.05	0.71	3	3.7	0.59	389	0.06	11.2	6	1.4	0.16	269	0.12	9.4
d2_53_EQ_Synth01_+20mm	40	1.1	0.21	0.14	1	1.1	0.14	312	0.06	2.9	5	–	–	–	–	–
d2_54_EQ_Synth01_-20mm	40	1.0	0.21	0.14	1	1.0	0.14	329	0.05	3.8	4	–	–	–	–	–
d2_55_EQ_Synth01_-40mm	40	2.4	0.51	0.31	4	2.2	0.24	266	0.07	5.7	32	–	–	–	–	–
d2_56_EQ_Synth01_+40mm	40	1.6	0.49	0.14	4	1.4	0.14	233	0.03	7.8	30	–	–	–	–	–
d2_57_EQ_Synth01_+60mm	50	5.4	1.66	1.08	1	5.4	1.08	482	0.09	12.5	50	1.1	0.13	245	0.05	9.3
d2_58_EQ_Synth01_-60mm	50	3.8	1.00	0.78	2	3.2	0.58	415	0.06	7.6	58	1.3	0.18	298	0.04	9.4
d2_59_EQ_Synth01_-80mm	50	7.9	2.97	1.87	1	7.9	1.87	569	0.12	12.5	40	1.4	0.18	276	0.06	8.8
d2_60_R_4mm_200ms	40	1.4	0.28	0.11	9	1.2	0.09	180	0.05	7.2	13	–	–	–	–	–
d2_61_R_4mm_100ms	40	2.1	0.48	0.24	6	2.0	0.19	221	0.06	6.3	12	–	–	–	–	–
d2_62_R_8mm_100ms	40	3.9	0.96	0.64	3	3.4	0.54	382	0.11	10.0	3	1.5	0.22	372	0.12	8.3
d3_01_R_2mm_200ms	40	–	–	–	0	–	–	–	–	–	0	–	–	–	–	–

continued on next page

Table C.7: (cont'd).

Test Name	Filter	Peak response cycles			Avg. results for cycles with $\Delta_{amp} \geq 0.7 \max(\Delta_{amp})$						Avg. results for cycles with 0.5 mm $\leq \Delta_{amp} \leq$ 3 mm					
	f_c [Hz]	Δ_{amp} [mm]	$a_{c\,amp}$ [g]	$a_{a\,amp}$ [g]	n	Δ_{amp} [mm]	$a_{a\,amp}$ [g]	K [N/mm]	ξ_{hyst}	f [Hz]	n	Δ_{amp} [mm]	$a_{a\,amp}$ [g]	K [N/mm]	ξ_{hyst}	f [Hz]
d3_02_R_4mm_200ms	40	–	–	–	0	–	–	–	–	–	0	–	–	–	–	–
d3_03_R_4mm_100ms	40	–	–	–	0	–	–	–	–	–	0	–	–	–	–	–
d3_04_R_8mm_100ms	40	–	–	–	4	0.5	0.68	3100	0.14	17.5	0	–	–	–	–	–
d3_05_H_13Hz_0.05mm	default	–	–	–	0	–	–	–	–	–	0	–	–	–	–	–
d3_06_H_13Hz_0.1mm	default	–	–	–	0	–	–	–	–	–	0	–	–	–	–	–
d3_07_H_13Hz_0.15mm	default	–	–	–	0	–	–	–	–	–	0	–	–	–	–	–
d3_08_H_13Hz_0.2mm	default	–	–	–	204	0.3	0.49	2990	0.14	–	0	–	–	–	–	–
d3_09_H_13Hz_0.25mm	default	0.7	1.35	0.87	308	0.6	0.78	2660	0.11	–	257	–	–	–	–	–
d3_10_H_13Hz_0.3mm	default	1.0	1.87	1.25	446	0.9	1.08	2440	0.10	–	467	–	–	–	–	–
d3_11_H_13Hz_0.3mm	default	3.0	3.93	2.15	434	2.8	2.02	1540	0.03	–	474	2.6	1.94	1520	0.03	–
d3_12_R_4mm_200ms	40	–	–	–	0	–	–	–	–	–	0	–	–	–	–	–
d3_13_R_4mm_100ms	40	–	–	–	8	0.4	0.28	1460	0.12	14.4	0	–	–	–	–	–
d3_14_R_8mm_100ms	40	1.0	1.36	0.73	8	0.9	0.63	1440	0.10	14.3	9	–	–	–	–	–
d3_15_H_13Hz_0.35mm	default	3.7	4.22	2.34	455	3.4	1.91	1170	0.02	–	66	1.5	0.95	1330	0.06	–
d3_16_H_13Hz_0.4mm	default	5.0	4.41	2.34	451	4.5	1.85	863	0.03	–	59	1.4	0.76	1130	0.09	–
d3_17_R_4mm_200ms	40	–	–	–	1	0.3	0.18	1250	0.16	16.2	0	–	–	–	–	–
d3_18_R_4mm_100ms	40	0.7	0.70	0.33	7	0.6	0.29	1060	0.07	14.7	6	–	–	–	–	–
d3_19_R_8mm_100ms	40	1.5	1.59	0.68	8	1.3	0.62	998	0.09	14.4	10	–	–	–	–	–
d3_20_H_12Hz_0.4mm	default	7.4	4.35	1.99	398	5.9	1.07	370	0.04	–	48	1.7	0.51	594	0.07	–
d3_21_R_4mm_200ms	30	0.5	0.44	0.15	6	0.5	0.13	624	0.06	14.3	1	–	–	–	–	–
d3_22_R_4mm_100ms	30	1.4	0.95	0.29	8	1.2	0.22	389	0.06	13.7	12	–	–	–	–	–
d3_23_R_8mm_100ms	30	3.2	1.89	0.56	9	2.7	0.37	285	0.02	13.4	12	2.2	0.32	285	0.04	13.2
d3_24_EQ_Taft_-5mm	30	–	–	–	0	–	–	–	–	–	0	–	–	–	–	–
d3_25_EQ_Taft_+5mm	30	–	–	–	0	–	–	–	–	–	0	–	–	–	–	–
d3_26_EQ_Taft_+10mm	30	–	–	–	0	–	–	–	–	–	0	–	–	–	–	–
d3_27_EQ_Taft_-10mm	30	–	–	–	0	–	–	–	–	–	0	–	–	–	–	–
d3_28_EQ_Taft_-20mm	30	–	–	–	1	0.3	0.14	913	0.01	14.8	0	–	–	–	–	–
d3_29_EQ_Taft_+20mm	30	–	–	–	5	0.4	0.15	842	0.07	14.8	0	–	–	–	–	–
d3_30_EQ_Taft_+30mm	30	–	–	–	10	0.4	0.16	790	0.04	14.5	0	–	–	–	–	–
d3_31_EQ_Taft_-30mm	30	0.6	0.52	0.18	7	0.5	0.14	661	0.06	14.7	1	–	–	–	–	–
d3_32_EQ_Taft_-40mm	30	0.7	0.58	0.22	12	0.6	0.18	663	0.06	13.9	10	–	–	–	–	–
d3_33_EQ_Taft_+40mm	30	0.8	0.68	0.25	7	0.7	0.22	719	0.07	13.5	8	–	–	–	–	–
d3_34_EQ_Taft_+50mm	30	1.1	0.87	0.37	10	0.9	0.29	661	0.05	12.4	20	–	–	–	–	–
d3_35_EQ_Taft_-50mm	30	0.9	0.75	0.28	11	0.8	0.22	615	0.04	13.5	29	–	–	–	–	–
d3_36_EQ_Taft_-60mm	30	5.0	2.87	0.95	2	4.7	0.78	339	0.04	12.1	67	0.8	0.22	611	0.07	12.9
d3_37_EQ_Taft_+60mm	30	1.8	1.20	0.39	5	1.6	0.36	491	0.06	12.4	46	–	–	–	–	–
d3_38_EQ_Taft_+70mm	40	7.1	3.43	1.32	2	6.8	1.05	318	0.05	11.4	79	1.0	0.25	582	0.05	12.3
d3_39_EQ_Taft_-70mm	40	8.4	4.12	1.37	3	7.7	0.92	241	0.05	12.0	80	0.9	0.22	547	0.06	12.3

continued on next page

Table C.7: (cont'd).

Test Name	Filter	Peak response cycles			Avg. results for cycles with $\Delta_{amp} \geq 0.7 \max(\Delta_{amp})$						Avg. results for cycles with $0.5\text{ mm} \leq \Delta_{amp} \leq 3\text{ mm}$					
	f_c [Hz]	Δ_{amp} [mm]	$a_{c\,amp}$ [g]	$a_{a\,amp}$ [g]	n	Δ_{amp} [mm]	$a_{a\,amp}$ [g]	K [N/mm]	ξ_{hyst}	f [Hz]	n	Δ_{amp} [mm]	$a_{a\,amp}$ [g]	K [N/mm]	ξ_{hyst}	f [Hz]
d3_40_EQ_Taft_-80mm	40	7.3	3.56	1.18	3	6.6	0.79	241	0.05	12.1	115	1.0	0.24	526	0.06	12.2
d3_41_EQ_Taft_+80mm	40	11.5	4.44	1.79	1	11.5	1.79	324	0.04	10.2	60	1.3	0.30	505	0.06	11.7
d3_42_R_4mm_200ms	30	0.7	0.44	0.19	13	0.6	0.15	570	0.10	12.8	11	–	–	–	–	–
d3_43_R_4mm_100ms	30	1.3	0.84	0.31	9	1.1	0.22	403	0.05	13.5	12	–	–	–	–	–
d3_44_R_8mm_100ms	30	3.2	1.72	0.62	9	2.9	0.38	268	0.04	13.0	12	1.9	0.25	281	0.08	12.8
d3_45_EQ_Taft_+90mm	40	12.1	4.45	1.75	1	12.1	1.75	301	0.04	9.8	113	1.2	0.26	459	0.05	11.8
d3_46_EQ_Taft_-90mm	40	6.4	2.87	0.87	5	5.4	0.69	264	0.05	11.3	115	1.2	0.27	455	0.06	11.5
d3_47_R_4mm_200ms	30	0.7	0.46	0.17	8	0.6	0.15	553	0.08	12.9	8	–	–	–	–	–
d3_48_R_4mm_100ms	30	1.3	0.82	0.32	7	1.2	0.22	385	0.04	13.5	11	–	–	–	–	–
d3_49_R_8mm_100ms	30	3.3	1.64	0.61	9	2.8	0.35	247	0.03	12.9	13	1.9	0.23	249	0.07	12.7
d3_50_EQ_Taft_-100mm	40	5.8	2.73	0.96	7	5.1	0.74	306	0.05	10.5	142	1.2	0.26	455	0.06	11.9
d3_51_EQ_Taft_+100mm	40	10.3	3.78	1.48	2	8.9	1.27	295	0.04	10.0	120	1.2	0.26	476	0.06	11.2
d3_52_EQ_Taft_+110mm	40	10.0	3.94	1.34	4	8.5	1.10	268	0.04	10.3	115	1.2	0.25	455	0.06	11.3
d3_53_EQ_Taft_-110mm	40	9.7	3.57	1.27	4	8.2	0.95	239	0.07	9.7	144	1.3	0.26	407	0.06	11.4
d3_54_EQ_Taft_-120mm	40	12.6	4.18	1.55	1	12.6	1.55	256	0.03	8.5	121	1.3	0.26	422	0.05	11.4
d3_55_EQ_Taft_+120mm	40	10.8	4.20	1.40	5	8.6	1.00	241	0.05	9.3	138	1.3	0.25	412	0.06	11.2
d3_56_EQ_Taft_+60mm	40	2.0	1.03	0.32	4	1.7	0.24	303	0.06	11.9	84	–	–	–	–	–
d3_57_EQ_Taft_-60mm	40	6.4	2.78	0.82	2	5.5	0.60	218	0.07	10.8	86	0.9	0.19	424	0.05	11.5
d3_58_H_12Hz_0.1mm	default	1.3	0.78	0.23	311	1.2	0.21	364	0.05	–	332	–	–	–	–	–
d3_59_H_12Hz_0.2mm	default	2.1	1.16	0.30	319	2.0	0.28	285	0.04	–	353	–	–	–	–	–
d3_60_H_12Hz_0.4mm	default	5.6	2.63	0.43	310	5.3	0.41	160	0.03	–	50	1.7	0.23	299	0.05	–
d4_01_R_4mm_200ms	40	–	–	–	0	–	–	–	–	–	0	–	–	–	–	–
d4_02_R_4mm_100ms	40	–	–	–	0	–	–	–	–	–	0	–	–	–	–	–
d4_03_R_8mm_100ms	40	–	–	–	2	0.3	0.88	5700	0.16	16.4	0	–	–	–	–	–
d4_04_H_13Hz_0.05mm	default	–	–	–	0	–	–	–	–	–	0	–	–	–	–	–
d4_05_H_13Hz_0.10mm	default	–	–	–	0	–	–	–	–	–	0	–	–	–	–	–
d4_06_EQ_Taft_-40mm	40	–	–	–	0	–	–	–	–	–	0	–	–	–	–	–
d4_07_EQ_Taft_+40mm	40	–	–	–	0	–	–	–	–	–	0	–	–	–	–	–
d4_08_EQ_Taft_+80mm	45	1.5	4.07	2.44	3	1.4	1.57	2360	0.17	16.9	3	–	–	–	–	–
d4_09_EQ_Taft_-80mm	40	2.1	2.85	1.89	1	2.1	1.89	1860	0.14	14.0	2	–	–	–	–	–
d4_10_R_4mm_200ms	40	–	–	–	0	–	–	–	–	–	0	–	–	–	–	–
d4_11_R_4mm_100ms	40	–	–	–	1	0.3	0.33	2070	0.10	20.0	0	–	–	–	–	–
d4_12_R_8mm_100ms	40	0.8	0.99	0.55	5	0.7	0.53	1740	0.25	14.3	5	–	–	–	–	–
d4_13_H_13Hz_0.15mm	default	–	–	–	450	0.4	0.40	2370	0.16	–	0	–	–	–	–	–
d4_14_H_13Hz_0.20mm	default	0.6	0.77	0.43	449	0.5	0.40	1750	0.26	–	83	–	–	–	–	–
d4_15_H_13Hz_0.25mm	default	0.8	1.09	0.51	456	0.7	0.45	1320	0.26	–	460	–	–	–	–	–
d4_16_H_13Hz_0.30mm	default	1.0	1.31	0.58	455	0.9	0.51	1210	0.25	–	467	–	–	–	–	–

continued on next page

Table C.7: (cont'd).

Test Name	Filter	Peak response cycles			Avg. results for cycles with $\Delta_{amp} \geq 0.7 \max(\Delta_{amp})$						Avg. results for cycles with 0.5 mm $\leq \Delta_{amp} \leq$ 3 mm					
	f_c [Hz]	Δ_{amp} [mm]	$a_{c\,amp}$ [g]	$a_{a\,amp}$ [g]	n	Δ_{amp} [mm]	$a_{a\,amp}$ [g]	K [N/mm]	ξ_{hyst}	f [Hz]	n	Δ_{amp} [mm]	$a_{a\,amp}$ [g]	K [N/mm]	ξ_{hyst}	f [Hz]
d4_17_H_13Hz_0.35mm	default	1.3	1.67	0.82	457	1.3	0.72	1200	0.20	–	479	–	–	–	–	–
d4_18_H_13Hz_0.40mm	default	2.1	2.29	1.11	454	2.0	0.83	883	0.15	–	491	–	–	–	–	–
d4_19_R_4mm_200ms	40	–	–	–	0	–	–	–	–	–	0	–	–	–	–	–
d4_20_R_4mm_100ms	40	–	–	–	4	0.4	0.24	1320	0.20	13.3	0	–	–	–	–	–
d4_21_R_8mm_100ms	40	1.3	1.25	0.51	2	1.1	0.47	892	0.21	15.5	4	–	–	–	–	–
d4_22_H_13Hz_0.45mm	default	2.7	2.84	1.07	460	2.7	0.71	557	0.15	–	502	–	–	–	–	–
d4_23_H_13Hz_0.50mm	default	3.2	2.31	0.80	460	3.0	0.61	428	0.19	–	420	2.8	0.57	412	0.19	–
d4_24_R_4mm_200ms	40	–	–	–	0	–	–	–	–	–	0	–	–	–	–	–
d4_25_R_4mm_100ms	40	–	–	–	2	0.4	0.22	1070	0.27	11.1	0	–	–	–	–	–
d4_26_R_8mm_100ms	40	1.6	0.99	0.43	3	1.5	0.42	601	0.18	10.8	4	–	–	–	–	–
d4_27_H_6Hz_0.10mm	default	–	–	–	0	–	–	–	–	–	0	–	–	–	–	–
d4_28_H_6Hz_0.20mm	default	–	–	–	0	–	–	–	–	–	0	–	–	–	–	–
d4_29_H_6Hz_0.30mm	default	–	–	–	0	–	–	–	–	–	0	–	–	–	–	–
d4_30_H_6Hz_0.40mm	default	–	–	–	0	–	–	–	–	–	0	–	–	–	–	–
d4_31_H_6Hz_0.50mm	default	–	–	–	0	–	–	–	–	–	0	–	–	–	–	–
d4_32_H_6Hz_0.75mm	default	–	–	–	0	–	–	–	–	–	0	–	–	–	–	–
d4_33_H_6Hz_1.0mm	default	–	–	–	0	–	–	–	–	–	0	–	–	–	–	–
d4_34_H_6Hz_1.5mm	default	1.3	0.61	0.42	208	1.3	0.40	651	0.21	–	217	–	–	–	–	–
d4_35_R_4mm_200ms	40	–	–	–	0	–	–	–	–	–	0	–	–	–	–	–
d4_36_R_4mm_100ms	40	0.6	0.68	0.31	5	0.5	0.26	1100	0.14	14.7	2	–	–	–	–	–
d4_37_R_8mm_100ms	40	2.5	1.87	0.59	8	2.0	0.50	526	0.10	14.0	12	–	–	–	–	–
d4_38_H_13Hz_0.10mm	default	–	–	–	0	–	–	–	–	–	0	–	–	–	–	–
d4_39_H_13Hz_0.20mm	default	1.1	1.00	0.40	448	0.9	0.37	854	0.11	–	455	–	–	–	–	–
d4_40_H_13Hz_0.30mm	default	3.2	2.23	0.71	454	2.8	0.55	409	0.07	–	481	2.7	0.53	407	0.07	–
d4_41_H_13Hz_0.40mm	default	5.3	3.61	0.86	461	5.1	0.55	227	0.06	–	41	1.5	0.26	372	0.12	–
d4_42_R_4mm_200ms	30	–	–	–	3	0.4	0.12	678	0.18	13.6	0	–	–	–	–	–
d4_43_R_4mm_100ms	30	1.0	0.60	0.28	3	0.9	0.22	518	0.13	12.2	6	–	–	–	–	–
d4_44_R_8mm_100ms	30	2.6	1.43	0.56	9	2.3	0.32	281	0.08	13.1	14	–	–	–	–	–
d4_45_EQ_Taft_-10mm	30	–	–	–	0	–	–	–	–	–	0	–	–	–	–	–
d4_46_EQ_Taft_+10mm	30	–	–	–	0	–	–	–	–	–	0	–	–	–	–	–
d4_47_EQ_Taft_+20mm	30	–	–	–	1	0.3	0.11	742	0.19	10.3	0	–	–	–	–	–
d4_48_EQ_Taft_-20mm	30	–	–	–	0	–	–	–	–	–	0	–	–	–	–	–
d4_49_EQ_Taft_-30mm	30	–	–	–	2	0.4	0.13	651	0.12	12.1	0	–	–	–	–	–
d4_50_EQ_Taft_+30mm	30	0.5	0.32	0.15	6	0.4	0.12	578	0.17	12.4	1	–	–	–	–	–
d4_51_EQ_Taft_+40mm	30	0.6	0.41	0.21	6	0.5	0.17	661	0.15	11.0	3	–	–	–	–	–
d4_52_EQ_Taft_-40mm	30	0.6	0.41	0.19	4	0.5	0.14	557	0.12	11.9	2	–	–	–	–	–
d4_53_EQ_Taft_-50mm	30	0.8	0.51	0.29	10	0.7	0.21	636	0.14	11.2	14	–	–	–	–	–
d4_54_EQ_Taft_+50mm	30	1.1	0.60	0.28	8	0.9	0.20	453	0.12	11.7	16	–	–	–	–	–

continued on next page

Table C.7: (cont'd).

Test Name	Filter	Peak response cycles			Avg. results for cycles with $\Delta_{amp} \geq 0.7 \max(\Delta_{amp})$						Avg. results for cycles with 0.5 mm $\leq \Delta_{amp} \leq$ 3 mm					
	f_c [Hz]	Δ_{amp} [mm]	$a_{c\,amp}$ [g]	$a_{a\,amp}$ [g]	n	Δ_{amp} [mm]	$a_{a\,amp}$ [g]	K [N/mm]	ξ_{hyst}	f [Hz]	n	Δ_{amp} [mm]	$a_{a\,amp}$ [g]	K [N/mm]	ξ_{hyst}	f [Hz]
d4_55_EQ_Taft_+60mm	30	1.5	0.82	0.33	5	1.3	0.23	380	0.11	11.9	32	–	–	–	–	–
d4_56_EQ_Taft_-60mm	40	5.4	2.75	1.05	2	4.8	0.82	345	0.08	11.7	34	0.8	0.23	599	0.13	11.0
d4_57_R_4mm_200ms	40	–	–	–	0	–	–	–	–	–	0	–	–	–	–	–
d4_58_R_4mm_100ms	40	1.0	0.61	0.27	4	0.8	0.19	466	0.13	13.0	6	–	–	–	–	–
d4_59_R_8mm_100ms	40	2.7	1.54	0.54	9	2.3	0.32	287	0.08	13.1	14	–	–	–	–	–
d4_60_EQ_Taft_+60mm	40	1.3	0.73	0.35	3	1.2	0.33	578	0.07	10.1	11	–	–	–	–	–
d4_61_EQ_Taft_-60mm	40	3.4	1.88	0.74	1	3.4	0.74	455	0.06	10.3	11	0.9	0.22	555	0.13	11.0
d4_62_EQ_Taft_-70mm	40	4.6	2.48	0.98	2	4.0	0.78	397	0.08	11.2	27	0.9	0.22	532	0.11	10.6
d4_63_EQ_Taft_+70mm	40	3.3	1.74	0.66	2	2.9	0.50	353	0.07	10.4	37	0.8	0.22	576	0.12	10.5
d4_64_EQ_Taft_+70mm	40	2.2	1.24	0.46	1	2.2	0.46	441	0.07	10.0	5	–	–	–	–	–
d4_65_EQ_Taft_-70mm	40	2.6	1.42	0.58	1	2.6	0.58	464	0.06	10.1	10	–	–	–	–	–
d4_66_R_4mm_200ms	40	–	–	–	7	0.4	0.12	682	0.13	12.7	0	–	–	–	–	–
d4_67_R_4mm_100ms	40	1.0	0.63	0.29	8	0.9	0.16	391	0.11	13.3	10	–	–	–	–	–
d4_68_R_8mm_100ms	40	2.7	1.68	0.54	10	2.4	0.32	270	0.06	13.2	16	–	–	–	–	–
d4_69_EQ_Taft_+70mm	40	4.9	2.48	0.97	2	4.5	0.73	328	0.08	11.4	77	1.0	0.22	486	0.09	10.9
d4_70_EQ_Taft_-70mm	40	7.6	4.01	1.30	2	7.3	1.05	297	0.08	12.4	16	0.7	0.20	607	0.13	11.3
d4_71_EQ_Taftbf05_-70mm	40	7.5	3.83	1.17	2	7.1	0.91	264	0.07	12.3	29	0.8	0.23	609	0.13	11.2
d4_72_EQ_Taftbf05_+70mm	40	5.0	2.47	0.90	2	4.5	0.67	299	0.09	10.8	51	1.0	0.22	478	0.10	10.5
d4_73_EQ_Taftbf10_+70mm	40	4.5	2.19	0.80	2	4.0	0.59	293	0.08	10.9	39	0.8	0.18	472	0.10	10.8
d4_74_EQ_Taftbf10_-70mm	40	7.5	3.95	1.15	2	7.3	0.92	260	0.06	12.5	10	0.8	0.21	563	0.10	10.7
d4_75_EQ_Taftbf20_-70mm	40	6.6	3.38	1.04	2	6.2	0.79	262	0.06	11.9	31	0.7	0.16	432	0.09	11.7
d4_76_EQ_Taftbf20_+70mm	40	4.1	2.10	0.77	2	3.8	0.57	303	0.08	10.9	41	0.8	0.16	412	0.08	11.5
d4_77_EQ_Taftbf30_+70mm	40	3.5	1.63	0.61	2	3.2	0.45	287	0.08	11.0	32	0.8	0.15	391	0.08	11.2
d4_78_EQ_Taftbf30_-70mm	40	6.4	3.26	1.02	2	5.9	0.79	270	0.07	11.7	38	0.8	0.15	385	0.08	11.3
d4_79_EQ_Taftbf50_-70mm	40	5.4	2.76	0.89	2	4.9	0.69	287	0.06	11.5	26	0.9	0.15	387	0.07	11.2
d4_80_EQ_Taftbf50_+70mm	40	2.6	1.25	0.47	3	2.2	0.31	285	0.08	10.6	24	–	–	–	–	–
d4_81_EQ_Taftbf75_+70mm	40	2.4	1.16	0.41	3	2.1	0.28	270	0.07	11.1	22	–	–	–	–	–
d4_82_EQ_Taftbf75_-70mm	40	4.8	2.43	0.80	2	4.3	0.61	289	0.06	11.3	31	0.8	0.15	378	0.08	11.0
d4_83_EQ_Taftbf100_-70mm	40	4.1	2.10	0.69	2	3.7	0.53	289	0.06	11.4	22	0.9	0.14	349	0.08	11.2
d4_84_EQ_Taftbf100_+70mm	40	2.7	1.32	0.43	3	2.6	0.32	260	0.06	11.3	22	–	–	–	–	–
d4_85_R_4mm_200ms	40	–	–	–	10	0.4	0.09	484	0.13	12.3	0	–	–	–	–	–
d4_86_R_4mm_100ms	40	1.1	0.59	0.25	3	1.0	0.20	393	0.09	11.7	4	–	–	–	–	–
d4_87_R_8mm_100ms	40	2.8	1.46	0.51	4	2.5	0.35	281	0.05	12.3	14	–	–	–	–	–
d4_88_H_13Hz_0.2mm	default	2.5	1.48	0.20	316	2.1	0.16	160	0.06	–	371	–	–	–	–	–
d4_89_H_13Hz_0.4mm	default	5.0	2.74	0.44	339	4.8	0.41	175	0.05	–	43	1.5	0.13	193	0.08	–
d4_90_H_13Hz_0.6mm	default	7.2	3.88	0.60	345	6.8	0.52	158	0.04	–	28	1.5	0.12	162	0.08	–
d4_91_R_4mm_200ms	40	0.6	0.32	0.10	7	0.5	0.08	320	0.10	11.8	4	–	–	–	–	–
d4_92_R_4mm_100ms	40	1.5	0.71	0.24	2	1.3	0.23	362	0.03	10.5	4	–	–	–	–	–

continued on next page

Table C.7: (cont'd).

Test Name	Filter	Peak response cycles			Avg. results for cycles with $\Delta_{amp} \geq 0.7 \max(\Delta_{amp})$						Avg. results for cycles with $0.5\text{ mm} \leq \Delta_{amp} \leq 3\text{ mm}$					
	f_c [Hz]	Δ_{amp} [mm]	$a_{c\,amp}$ [g]	$a_{a\,amp}$ [g]	n	Δ_{amp} [mm]	$a_{a\,amp}$ [g]	K [N/mm]	ξ_{hyst}	f [Hz]	n	Δ_{amp} [mm]	$a_{a\,amp}$ [g]	K [N/mm]	ξ_{hyst}	f [Hz]
d4_93_R_8mm_100ms	40	3.4	1.62	0.47	3	3.1	0.36	233	0.05	11.5	13	1.5	0.17	260	0.08	12.2
d4_94_EQ_Taft_+70mm	40	7.4	3.03	0.99	2	6.5	0.69	214	0.09	10.0	109	1.2	0.19	339	0.06	9.8
d4_95_EQ_Taft_-70mm	40	9.5	4.10	1.10	2	8.4	0.73	173	0.06	11.1	91	1.0	0.17	355	0.05	9.8
d4_96_EQ_Taft_-80mm	40	8.4	3.65	1.01	2	7.5	0.69	181	0.05	11.5	111	1.2	0.18	328	0.06	9.7
d4_97_EQ_Taft_+80mm	40	11.0	4.37	1.47	1	11.0	1.47	279	0.05	10.2	124	1.3	0.19	326	0.06	9.9
d4_98_EQ_Taft_+90mm	40	11.4	4.40	1.55	1	11.4	1.55	283	0.05	10.3	142	1.3	0.21	353	0.06	10.0
d4_99_EQ_Taft_-90mm	40	6.8	2.90	0.75	3	6.3	0.64	212	0.05	10.2	120	1.2	0.19	333	0.06	9.7
d4_100_EQ_Taft_-100mm	40	6.8	2.98	0.77	3	6.0	0.63	218	0.05	9.6	141	1.3	0.19	310	0.05	9.6
d4_101_EQ_Taft_+100mm	40	10.0	3.75	1.22	2	9.3	1.11	247	0.04	9.4	139	1.3	0.20	314	0.06	9.5
d4_102_EQ_Taft_+110mm	40	10.8	3.93	1.29	2	9.5	1.10	241	0.05	8.9	136	1.4	0.20	299	0.06	9.3
d4_103_EQ_Taft_-110mm	40	8.8	3.61	0.94	5	7.6	0.80	222	0.06	8.6	141	1.4	0.19	285	0.06	9.3
d4_104_EQ_Taft_-120mm	40	11.6	4.27	1.27	1	11.6	1.27	229	0.05	9.1	151	1.5	0.22	295	0.06	9.2
d4_105_EQ_Taft_+120mm	40	11.1	3.79	1.45	2	9.5	1.17	252	0.05	8.3	138	1.3	0.19	297	0.06	9.3
d4_106_R_4mm_200ms	40	0.7	0.32	0.10	6	0.6	0.08	293	0.08	10.7	5	–	–	–	–	–
d4_107_R_4mm_100ms	40	1.7	0.74	0.24	2	1.5	0.22	318	0.03	9.3	3	–	–	–	–	–
d4_108_R_8mm_100ms	40	3.6	1.58	0.47	2	3.4	0.45	272	0.04	9.4	11	1.3	0.18	274	0.10	10.1
d4_109_H_13Hz_0.1mm	default	–	–	–	324	0.4	0.03	158	0.15	–	0	–	–	–	–	–
d4_110_H_13Hz_0.2mm	default	1.8	0.96	0.13	320	1.5	0.09	129	0.06	–	357	–	–	–	–	–
d4_111_H_13Hz_0.3mm	default	4.0	2.09	0.28	328	3.8	0.26	141	0.02	–	51	1.5	0.10	141	0.06	–
d4_112_H_13Hz_0.4mm	default	5.5	3.16	0.40	337	5.2	0.37	148	0.03	–	48	1.4	0.10	150	0.06	–
d4_113_H_13Hz_0.5mm	default	6.4	3.54	0.54	340	5.8	0.49	177	0.03	–	41	1.6	0.15	212	0.06	–
d4_114_R_4mm_200ms	40	–	–	–	6	0.4	0.11	501	0.12	12.9	0	–	–	–	–	–
d4_115_R_4mm_100ms	40	1.3	0.71	0.24	3	1.1	0.20	376	0.09	11.8	7	–	–	–	–	–
d4_116_R_8mm_100ms	40	3.3	1.39	0.49	3	3.0	0.41	281	0.06	10.8	6	1.8	0.24	256	0.10	12.2
d5_01_H_14Hz_0.05mm	default	–	–	–	0	–	–	–	–	–	0	–	–	–	–	–
d5_02_H_14Hz_0.1mm	default	–	–	–	423	0.3	0.26	1600	0.02	–	0	–	–	–	–	–
d5_03_H_14Hz_0.15mm	default	1.1	1.42	0.72	486	1.0	0.69	1380	−0.01	–	500	–	–	–	–	–
d5_04_H_14Hz_0.2mm	default	2.2	2.45	1.19	487	2.1	0.77	771	0.01	–	539	–	–	–	–	–
d5_05_R_2mm_200ms	40	–	–	–	0	–	–	–	–	–	0	–	–	–	–	–
d5_06_R_4mm_200ms	40	–	–	–	8	0.4	0.13	682	0.06	16.6	0	–	–	–	–	–
d5_07_R_4mm_100ms	40	1.2	1.11	0.38	7	1.0	0.32	655	0.02	15.1	12	–	–	–	–	–
d5_08_H_14Hz_0.2mm	default	2.0	1.75	0.61	493	2.0	0.58	615	0.01	–	550	–	–	–	–	–
d5_09_H_14Hz_0.25mm	default	4.8	2.81	0.89	348	4.0	0.46	245	0.02	–	78	1.7	0.38	488	0.02	–
d5_10_R_2mm_200ms	40	–	–	–	3	0.3	0.06	407	0.06	14.2	0	–	–	–	–	–
d5_11_R_4mm_200ms	40	0.8	0.49	0.13	9	0.7	0.11	322	0.02	12.9	12	–	–	–	–	–
d5_12_R_4mm_100ms	40	1.8	0.93	0.26	4	1.6	0.17	216	0.01	12.9	11	–	–	–	–	–
d5_13_H_14Hz_0.3mm	default	6.2	3.65	0.69	198	4.9	0.55	239	−0.04	–	51	1.6	0.19	245	−0.01	–

continued on next page

Table C.7: (cont'd).

Test Name	Filter	Peak response cycles			Avg. results for cycles with $\Delta_{amp} \geq 0.7 \max(\Delta_{amp})$						Avg. results for cycles with 0.5 mm $\leq \Delta_{amp} \leq$ 3 mm					
	f_c [Hz]	Δ_{amp} [mm]	$a_{c\,amp}$ [g]	$a_{a\,amp}$ [g]	n	Δ_{amp} [mm]	$a_{a\,amp}$ [g]	K [N/mm]	ξ_{hyst}	f [Hz]	n	Δ_{amp} [mm]	$a_{a\,amp}$ [g]	K [N/mm]	ξ_{hyst}	f [Hz]
d5_14_R_2mm_200ms	40	–	–	–	4	0.4	0.05	264	0.06	11.8	0	–	–	–	–	–
d5_15_R_4mm_200ms	22	0.9	0.41	0.10	4	0.8	0.08	204	0.05	11.3	5	–	–	–	–	–
d5_16_R_4mm_100ms	22	2.2	0.84	0.24	2	2.0	0.23	237	0.02	11.1	7	–	–	–	–	–
d5_17_EQ_Taft_-6mm	25	–	–	–	0	–	–	–	–	–	0	–	–	–	–	–
d5_18_EQ_Taft_+6mm	25	–	–	–	0	–	–	–	–	–	0	–	–	–	–	–
d5_19_EQ_Taft_+11mm	25	–	–	–	6	0.3	0.04	274	0.02	12.5	0	–	–	–	–	–
d5_20_EQ_Taft_-11mm	25	–	–	–	0	–	–	–	–	–	0	–	–	–	–	–
d5_21_EQ_Taft_-17mm	25	–	–	–	14	0.4	0.05	291	0.02	11.4	0	–	–	–	–	–
d5_22_EQ_Taft_+17mm	25	0.6	0.36	0.09	7	0.5	0.06	262	−0.01	12.1	2	–	–	–	–	–
d5_23_EQ_Taft_+22mm	25	0.7	0.42	0.11	15	0.6	0.07	260	0.03	11.1	16	–	–	–	–	–
d5_24_EQ_Taft_-22mm	25	0.6	0.32	0.11	12	0.5	0.08	289	0.01	10.6	9	–	–	–	–	–
d5_25_EQ_Taft_-28mm	25	0.8	0.38	0.14	17	0.7	0.09	283	0.02	10.2	26	–	–	–	–	–
d5_26_EQ_Taft_+28mm	25	0.9	0.48	0.15	9	0.8	0.09	235	0.02	10.6	26	–	–	–	–	–
d5_27_EQ_Taft_+33mm	25	1.2	0.56	0.18	8	1.0	0.12	239	0.02	10.0	54	–	–	–	–	–
d5_28_EQ_Taft_-33mm	25	1.0	0.47	0.17	16	0.8	0.11	272	0.03	9.5	54	–	–	–	–	–
d5_29_EQ_Taft_-39mm	25	1.5	0.57	0.20	6	1.2	0.16	283	0.01	8.8	64	–	–	–	–	–
d5_30_EQ_Taft_+39mm	25	1.5	0.63	0.21	10	1.2	0.13	227	0.02	9.5	68	–	–	–	–	–
d5_31_EQ_Taft_+45mm	25	1.8	0.69	0.24	10	1.5	0.15	218	0.02	9.1	76	–	–	–	–	–
d5_32_EQ_Taft_-45mm	25	1.7	0.62	0.24	15	1.4	0.16	243	0.02	8.5	71	–	–	–	–	–
d5_33_EQ_Taft_-50mm	25	2.2	0.70	0.29	6	1.9	0.23	245	0.03	7.4	85	–	–	–	–	–
d5_34_EQ_Taft_+50mm	25	2.2	0.79	0.25	12	1.8	0.18	210	0.03	8.9	94	–	–	–	–	–
d5_35_EQ_Taft_+56mm	25	2.4	0.88	0.27	18	1.9	0.21	231	0.06	8.5	86	–	–	–	–	–
d5_36_EQ_Taft_-56mm	40	2.6	1.00	0.30	7	2.2	0.26	249	0.04	7.1	91	–	–	–	–	–
d5_37_EQ_Taft_-67mm	40	9.3	3.21	0.96	1	9.3	0.96	214	0.04	9.0	115	1.2	0.13	235	0.06	9.0
d5_38_EQ_Taft_+67mm	40	8.6	3.03	0.77	1	8.6	0.77	187	0.03	10.0	81	1.5	0.15	224	0.06	8.3
d5_39_R_2mm_200ms	30	–	–	–	4	0.4	0.05	283	0.14	11.3	0	–	–	–	–	–
d5_40_R_4mm_200ms	30	0.8	0.40	0.09	4	0.7	0.07	197	0.08	10.6	4	–	–	–	–	–
d5_41_R_4mm_100ms	30	2.2	0.79	0.27	2	2.0	0.26	274	0.05	11.1	7	–	–	–	–	–
d5_42_EQ_Taft_+73mm	40	11.9	3.51	1.09	1	11.9	1.09	191	0.04	10.0	82	1.3	0.12	191	0.07	8.0
d5_43_EQ_Taft_-73mm	40	6.0	1.44	0.45	9	4.9	0.32	137	0.07	5.6	90	1.3	0.11	179	0.07	7.8
d5_44_EQ_Taft_-78mm	40	8.6	2.23	0.89	4	7.1	0.53	150	0.04	7.4	58	1.3	0.12	187	0.07	7.9
d5_45_EQ_Taft_+78mm	40	16.3	2.76	1.24	1	16.3	1.24	158	0.01	4.8	19	1.0	0.08	191	0.08	8.8
d5_46_R_2mm_200ms	30	0.6	0.18	0.05	6	0.5	0.04	193	0.10	7.6	2	–	–	–	–	–
d5_47_R_4mm_200ms	30	1.0	0.28	0.09	6	0.9	0.07	158	0.08	7.2	10	–	–	–	–	–
d5_48_R_4mm_100ms	30	3.3	0.63	0.24	4	3.0	0.21	141	0.06	5.7	7	1.5	0.09	116	0.16	6.3
d5_49_EQ_Taft_+22mm	30	1.6	0.31	0.11	12	1.4	0.09	135	0.08	6.3	51	–	–	–	–	–
d5_50_EQ_Taft_-22mm	30	1.8	0.37	0.11	11	1.5	0.09	125	0.08	6.3	58	–	–	–	–	–
d5_51_EQ_Taft_-45mm	30	4.6	0.72	0.27	8	3.8	0.19	102	0.07	5.5	104	1.2	0.08	135	0.07	6.7

continued on next page

Table C.7: (cont'd).

Test Name	Filter	Peak response cycles			Avg. results for cycles with $\Delta_{amp} \geq 0.7 \max(\Delta_{amp})$						Avg. results for cycles with $0.5\text{ mm} \leq \Delta_{amp} \leq 3\text{ mm}$					
	f_c [Hz]	Δ_{amp} [mm]	$a_{c\,amp}$ [g]	$a_{a\,amp}$ [g]	n	Δ_{amp} [mm]	$a_{a\,amp}$ [g]	K [N/mm]	ξ_{hyst}	f [Hz]	n	Δ_{amp} [mm]	$a_{a\,amp}$ [g]	K [N/mm]	ξ_{hyst}	f [Hz]
d5_52_EQ_Taft_+45mm	30	4.1	0.61	0.23	11	3.4	0.16	98	0.08	5.8	108	1.3	0.08	139	0.07	6.6
d5_53_EQ_Taft_+67mm	30	8.6	1.56	0.54	4	7.0	0.34	98	0.08	5.1	94	1.4	0.08	121	0.06	6.7
d5_54_EQ_Taft_-67mm	40	11.5	1.72	0.84	1	11.5	0.84	152	0.02	4.3	31	1.6	0.10	127	0.05	6.9
d5_55_EQ_Taft_-84mm	45	9.5	1.40	0.69	10	7.8	0.38	100	0.07	4.8	64	1.6	0.09	118	0.05	7.0
d5_56_EQ_Taft_+84mm	45	17.5	3.29	1.32	1	17.5	1.32	156	−0.01	4.5	23	1.6	0.11	133	0.04	7.3
d5_57_EQ_Taft_+89mm	45	15.6	2.71	1.24	4	12.9	0.67	104	0.03	4.2	17	1.7	0.08	81	0.04	6.6
d5_58_EQ_Taft_-89mm	45	12.4	1.16	0.57	14	10.0	0.33	69	0.09	3.9	26	1.8	0.08	89	0.07	5.3
d5_59_EQ_Taft_-95mm	45	13.4	1.24	0.55	12	11.5	0.35	62	0.09	3.8	34	1.9	0.09	85	0.06	5.4
d5_60_EQ_Taft_+95mm	45	14.7	1.98	1.10	9	11.7	0.45	77	0.07	3.5	36	2.0	0.08	77	0.05	5.7
d5_61_EQ_Taft_+100mm	45	17.1	1.84	1.03	6	13.8	0.47	71	0.09	3.5	11	2.0	0.10	83	0.04	6.0
d5_62_EQ_Taft_-100mm	45	21.6	1.42	0.56	2	19.1	0.45	50	0.09	2.9	16	2.0	0.07	71	0.05	5.6

C.5 DATA FILTERING

Despite an analogue frequency domain filter being incorporated into the data acquisition system throughout the tests,[29] the data obtained inherently exhibited some degree of high frequency noise. Consequently, frequency domain filtering was performed on the digitised data in order to remove high frequency noise content, thereby smoothing the appearance of the hysteresis loops for the subsequent use of the data in the cyclic response analysis (presented in Section C.4). The type of filter applied depended on the type of test run under consideration: in particular, whether the loading and wall response was periodic (i.e. harmonic tests) or non-periodic (i.e. pulse and earthquake tests).

C.5.1 Periodic Tests

Because of the periodic nature of excitation in the harmonic tests, the Fourier spectra of the associated data vectors (displacement or acceleration) inherently contained peaks at integer multiples of the fundamental excitation frequency f_o. This is demonstrated by Figure C.19 which shows a typical example of unfiltered wall response during a harmonic test. Whilst it can be seen that most of the spectral content is in the first harmonic, the number of peaks included in the overall response after filtering affected the amount of detail retained in the shape of the hysteresis loops. For example, inclusion of only the fundamental frequency resulted in hysteresis loops that were elliptical in shape, whilst the inclusion of the higher order harmonics was necessary for the generation of details such as loop pinching. Because of these considerations, several different types of frequency filters were trialled to assess their suitability. The filters considered included the following, as illustrated by Figure C.20:

1. A bandpass filter retaining only spectral content at f_o. The filter tested was a Butterworth filter of order $n = 5$ with a cutoff frequency bandwidth of ± 1 Hz centred around f_o. For example, if the fundamental frequency was $f_o = 12$ Hz, then the filter had a cutoff band of $[11, 13]$ Hz.

2. A bandpass filter retaining spectral content across the first and second harmonics of f_o. The trialled filter was a Butterworth filter of order $n = 7$, with a cutoff frequency bandwidth between $0.5f_o$ and $2.5f_o$. For example, if the fundamental frequency was $f_o = 12$ Hz, then the filter used a cutoff band of $[6, 30]$ Hz.

[29] Lowpass Butterworth filter with a cutoff frequency of 50 Hz.

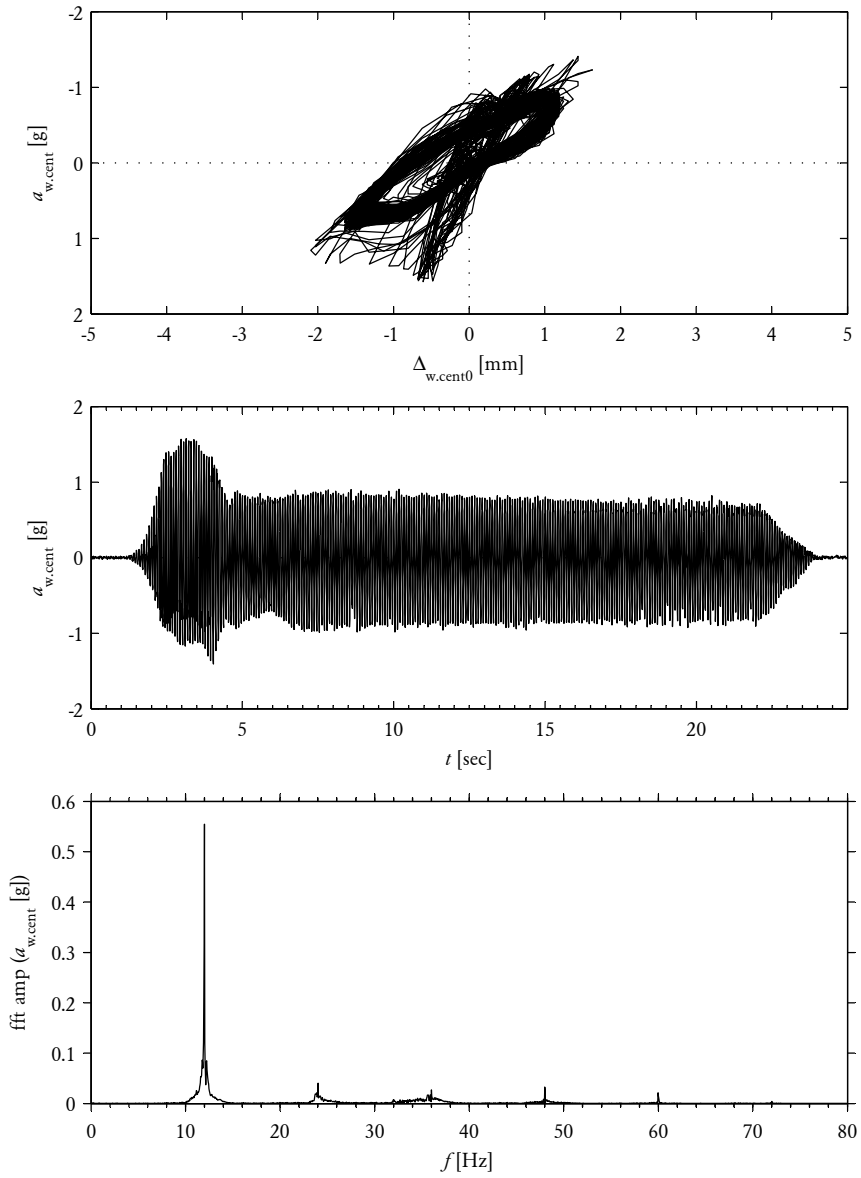

Figure C.19: Example of unfiltered response from harmonic test, including hysteresis plot (top), time domain response (middle) and frequency domain response (bottom). Shown for test run `d2_13_H_12Hz_0.25mm`.

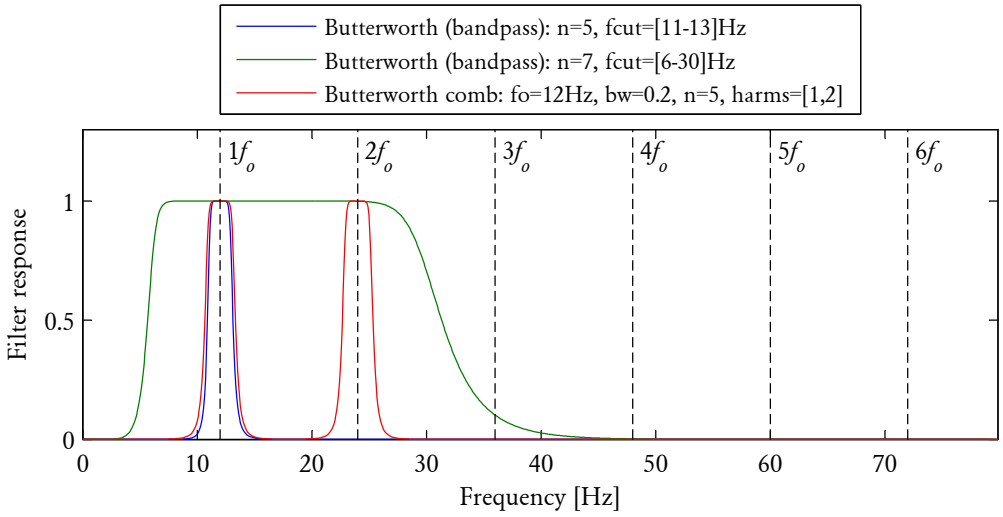

Figure C.20: Types of filters trialled for harmonic test data. For the filters shown, the fundamental frequency is taken as $f_o = 12$ Hz.

3. A comb filter passing only spectral content at the first and second harmonics of f_o (i.e. f_o and $2f_o$). The filter used was an original filter design based on the Butterworth filter equations. The cutoff frequency bandwidth for each peak was 20% of f_o centred around the harmonic frequency, with a filter order of $n = 5$. For example, if the fundamental frequency was $f_o = 12$ Hz, then the first harmonic at 12 Hz had a cutoff band of $[10.8, 13.2]$ Hz and the second harmonic at 24 Hz had a cutoff band of $[22.8, 25.2]$ Hz.

An example of the hysteresis loop shapes produced by the different filters is shown by Figure C.21. As shown by Figure C.21b, the bandpass filter retaining content only across f_o (filter option 1) had the inherent effect of producing hysteresis loops which were elliptical in shape. Whilst such loops become cleaner in appearance in comparison to those for unfiltered data, they lose certain shape characteristics such as pinching, due to the removal of the spectral content at the higher harmonics ($2f_o$, $3f_o \ldots$). This is a natural result of including only a single harmonic frequency in the response spectrum, thus causing the signal to become approximately sinusoidal in shape. By contrast, filter options 2 and 3 were chosen so as to retain the spectral content at the second harmonic ($2f_o$) and in doing so, preserve some of the shape detail.

To provide a quantitative measure of the filter performance, a series of analyses were performed in which the parameters Δ_{amp}, a_{amp}, K and ζ_{hyst} were calculated during a 2 second time window in the middle of the test run.[30] This analysis

[30]Note that the calculation of these parameters used the wall's average acceleration $a_{\text{w.avg}}$, whereas in the final results reported (in Section C.4) the wall's central acceleration $a_{\text{w.cent}}$ was used to calculate

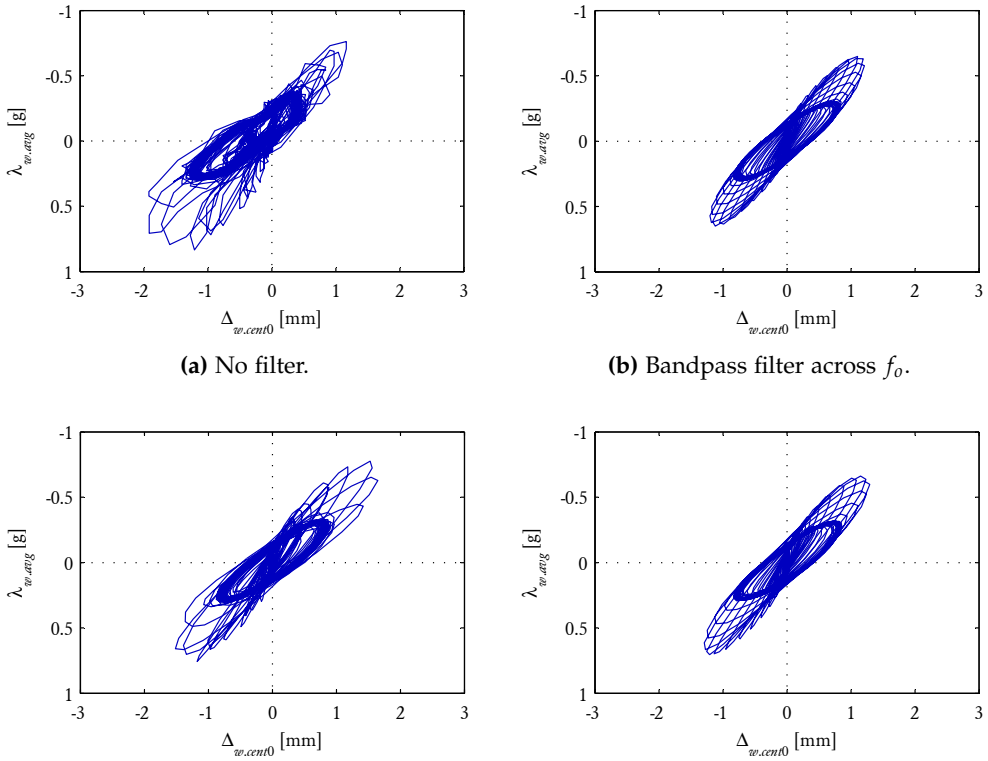

(a) No filter.

(b) Bandpass filter across f_o.

(c) Bandpass filter across f_o and $2f_o$.

(d) Comb filter across f_o and $2f_o$.

Figure C.21: Example comparing the hysteresis loop shape for data filtered using different types of filter. Shown for test run `d2_21_H_12Hz_0.2mm`.

was conducted for all harmonic test runs, using data filtered using the three aforementioned filters as well as for unfiltered data. The criteria used to evaluate the suitability of the candidate filters were as follows:

- To ensure that the mean parameter values calculated from filtered data were not significantly altered from those based on unfiltered data. This criterion was intended to ensure that the strength of the signal was not excessively diminished due to over-filtering.

- To reduce the amount of noise in the data, thereby generating cleaner hysteresis loops. This condition was assessed quantitatively by comparing the variability of the parameter values determined during the 2 second time window.

Of the three filters considered (Figure C.20), the comb filter retaining spectral content at f_o and $2f_o$ had the best performance with respect to the above evaluation

the hysteretic damping ratio ξ_{hyst}.

criteria. In general, the resulting mean values of parameters obtained using this filter were very comparable to those obtained from the unfiltered data, whilst the variability had been considerably reduced. This can be seen from Figure C.22 which graphs the filtered versus unfiltered results for each of the five parameters.

By comparison, the bandpass filter retaining only the content at f_o produced loops that were inherently elliptical in shape (as shown by the example in Figure C.21b). This filter was quite successful in minimising scatter in the results; however, due to the elliptical shape of the loops, it had a tendency to produce higher apparent values of equivalent damping ζ_{hyst} and effective stiffness K relative to the unfiltered data. As a result, this filter was deemed to be unconservative for derivation of these values.

The mean values of parameters derived from the data filtered using the bandpass filter retaining the content between $0.5f_o$ and $2.5f_o$ had better accuracy than the bandpass filter retaining only the content at f_o. The scatter in the results, however, tended to be higher and similar in magnitude to the results from unfiltered data. An example of the resulting hysteresis loops is shown by Figure C.21c.

On the basis of this study, the comb filter was deemed to be the most appropriate for application to the harmonic test data and was adopted in subsequent analyses whose results are reported in Section C.4.4. The final choice of filter used for harmonic tests was a comb filter passing the spectral content at the first three harmonics, with a normalised bandwidth of 0.2 (20% of the fundamental frequency). Figure C.23 shows an example of response obtained using this filter, which can be compared to the original unfiltered response in Figure C.19.

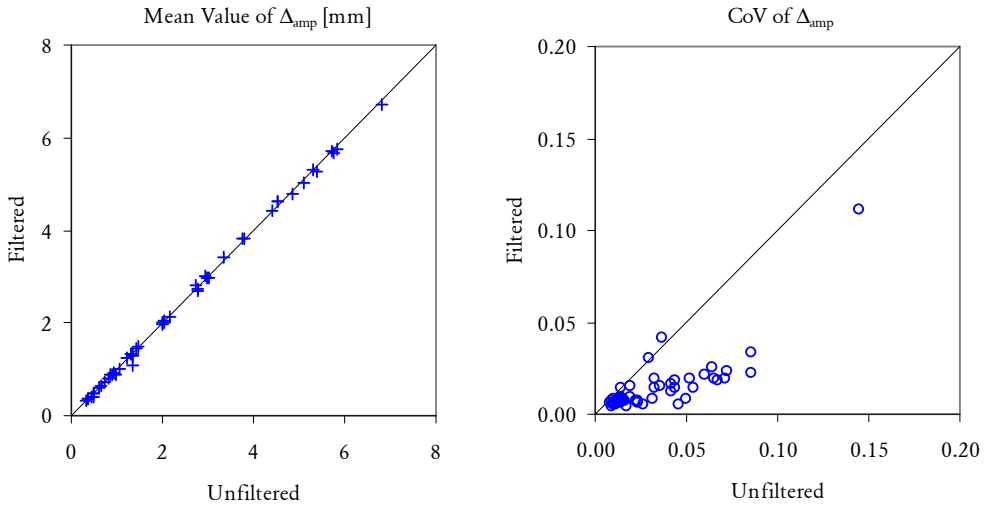

(a) Displacement cycle amplitude Δ_{amp}.

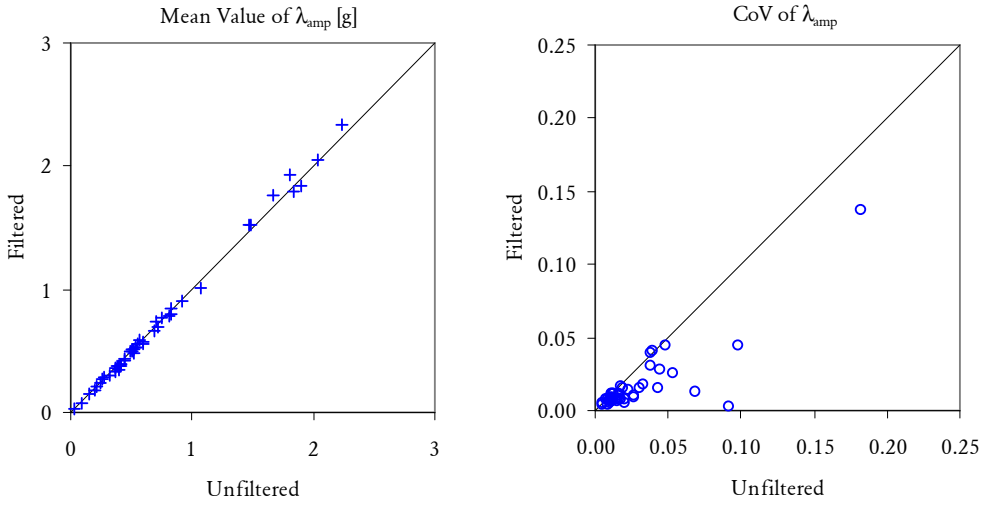

(b) Acceleration cycle amplitude a_{amp}.

Figure C.22: Comparison of key parameters derived from filtered and unfiltered harmonic test data. In the case of filtered data, a comb filter was applied capturing the response at the first and second harmonics of the excitation frequency. Each parameter was calculated over a time window of 2 seconds in the middle of the test run, with the mean value and level of variability (as CoV or StD) over this duration being plotted in these graphs. Results are plotted for all harmonic test runs performed, except for runs where the mean displacement amplitude was small (< 0.3 mm), which are omitted.

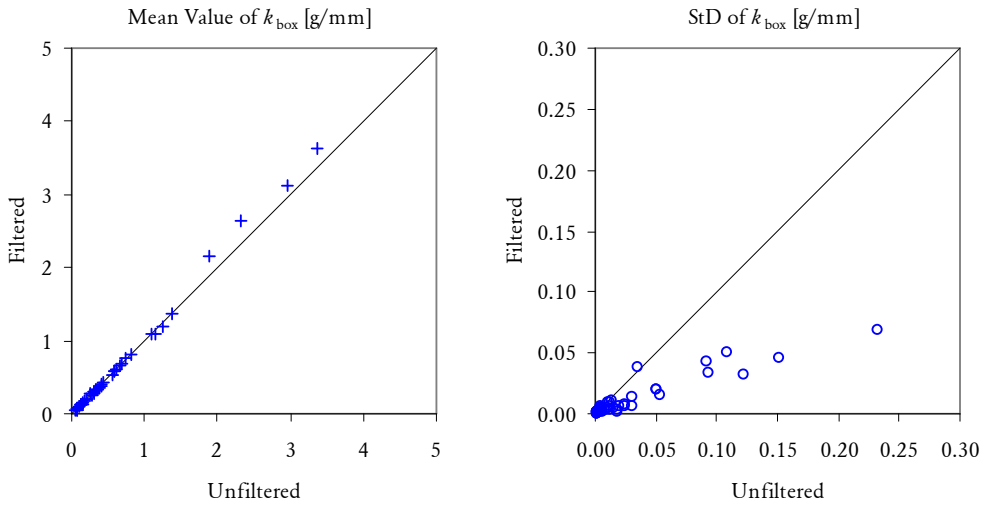

(c) Effective secant stiffness K (as a/Δ).

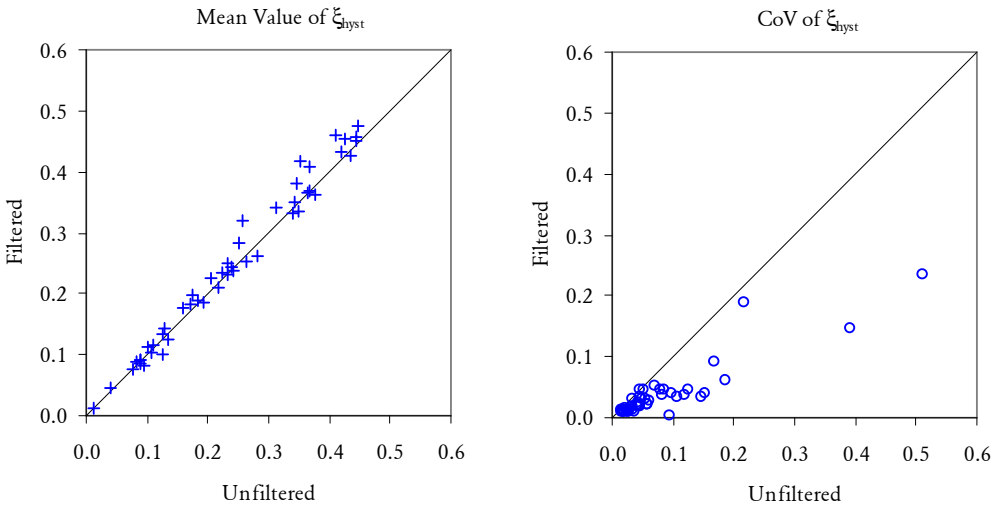

(d) Hysteretic damping ratio ξ_{hyst}.

Figure C.22: (cont'd).

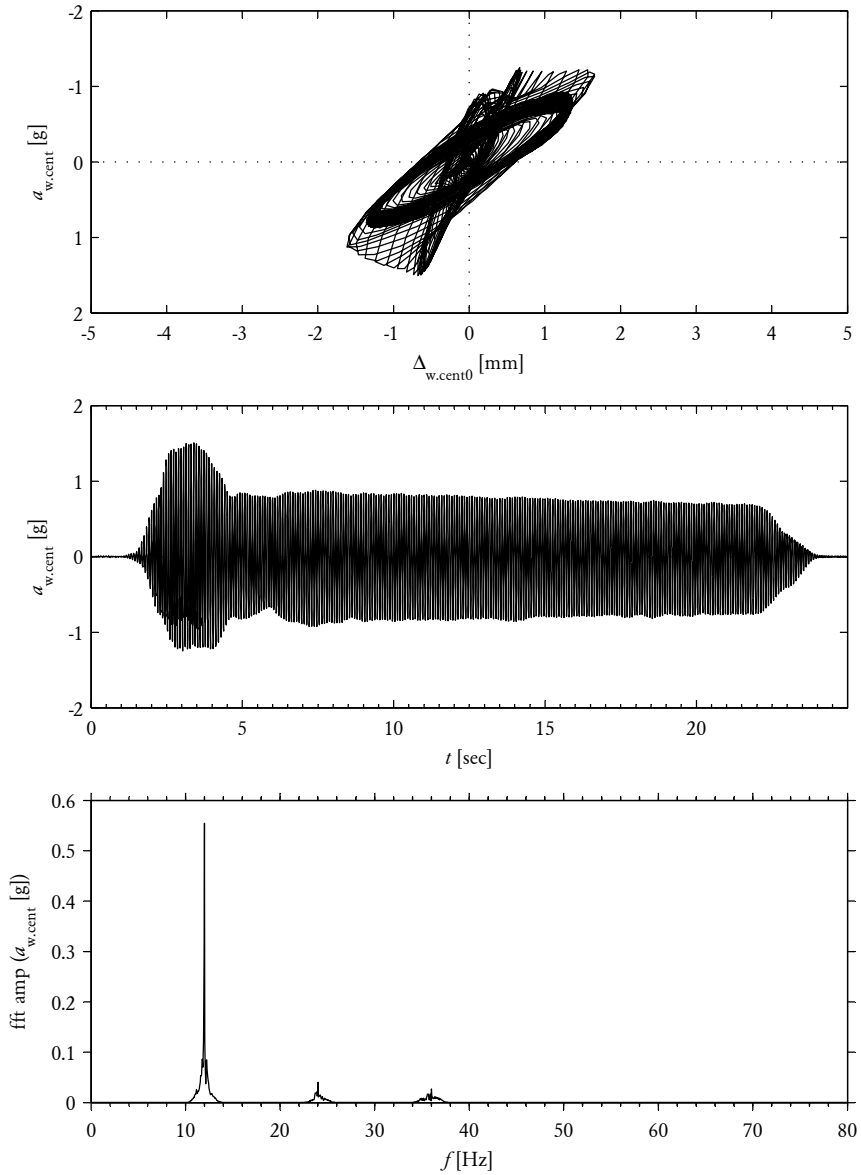

Figure C.23: Example of filtered response from harmonic test, including hysteresis plot (top), time domain response (middle) and frequency domain response (bottom). Shown for test run `d2_13_H_12Hz_0.25mm` combined with comb filter passing the spectral content at the first three harmonics (i.e. f_0, $2f_0$ and $3f_0$).

C.5.2 Non-Periodic Tests

Due to the non-periodic nature of the pulse and earthquake tests performed in this study, the Fourier spectra of the associated data vectors were markedly different to those from the periodic harmonic tests and therefore required a different filtering approach. Typical examples of unfiltered response from earthquake and pulse tests are shown by Figures C.24 and C.26, respectively, where it is seen that the associated Fourier spectra possessed a broad frequency content, as opposed to the harmonic tests where the peaks were concentrated at integer multiples of the fundamental frequency (Figure C.19). This made it possible to utilise a lowpass filter in order to eliminate the high frequency noise content from the data. Examples of the filtered response for earthquake and pulse test runs are shown by Figures C.25 and C.27, which can be compared to the unfiltered versions of the response shown by Figures C.24 and C.26.

Prior to conducting the cyclic response analysis reported in Section C.4, data from all earthquake and pulse test runs was filtered using a lowpass Butterworth filter with order $n = 10$. The cutoff frequency f_c of the filter was manually chosen on a case-by-case basis for each individual test run. The criteria used to select an appropriate value of f_c was to make f_c as low as possible without significantly reducing the maximum response of key variables, including the wall's central displacement $\Delta_{\text{w.cent}}$, central acceleration $a_{\text{w.cent}}$, table acceleration a_{tab}, support acceleration $a_{\text{sup.avg}}$, and relative acceleration between the centre of the wall and the supports, $a_{\text{w.cent-sup.avg}}$. The cutoff frequency used for each test run is summarised in the main results table for the cyclic response analysis, Table C.7.

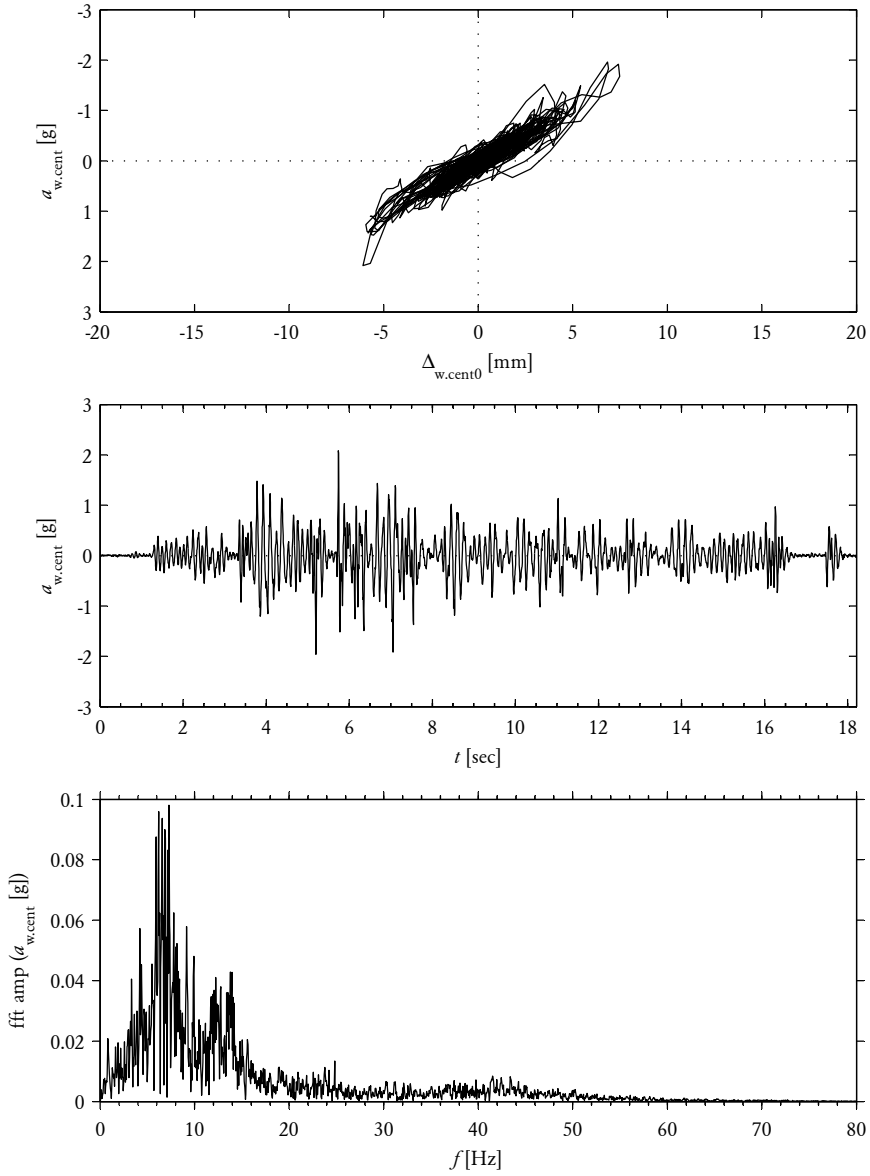

Figure C.24: Example of unfiltered response from earthquake test, including hysteresis plot (top), time domain response (middle) and frequency domain response (bottom). Shown for test run `d2_41_EQ_Taft_-100mm`.

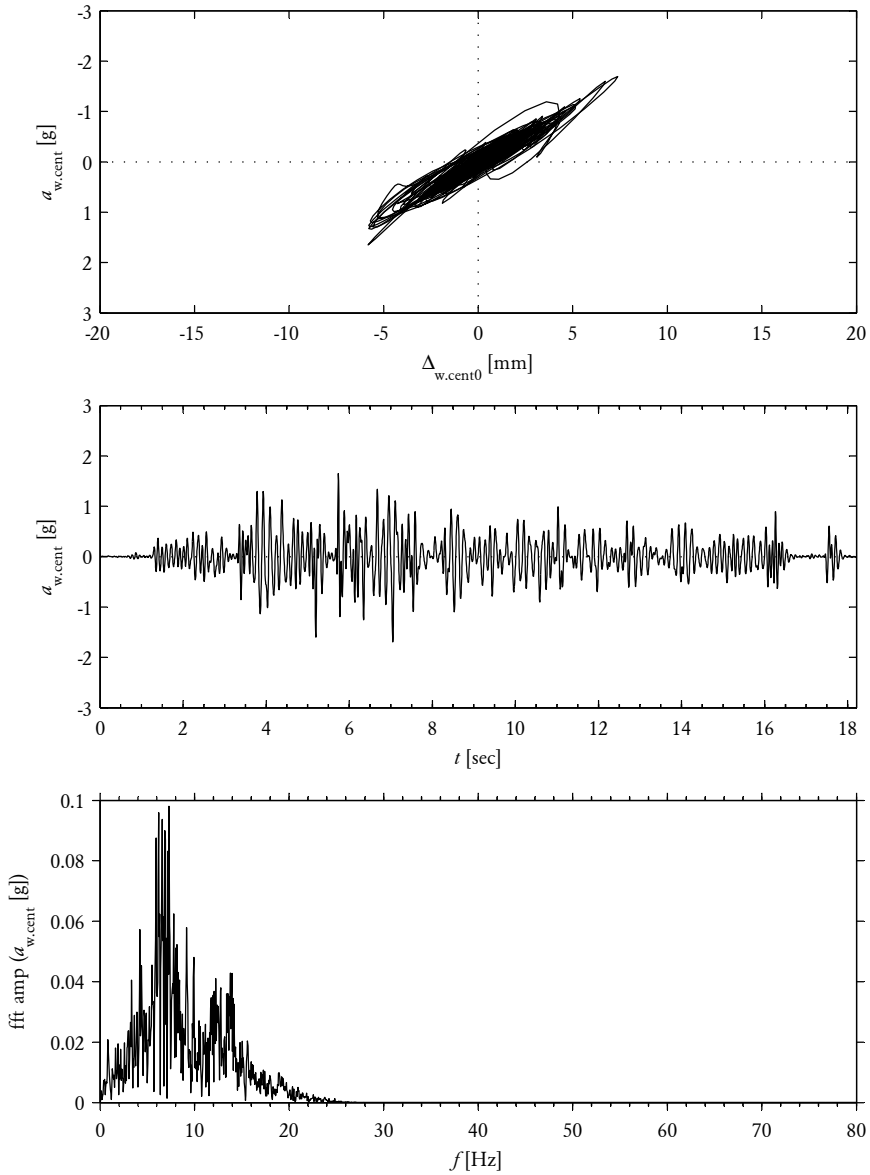

Figure C.25: Example of filtered response from earthquake test, including hysteresis plot (top), time domain response (middle) and frequency domain response (bottom). Shown for test run `d2_41_EQ_Taft_-100mm` combined with lowpass Butterworth filter with order $n = 10$ and cutoff frequency $f_c = 20$ Hz.

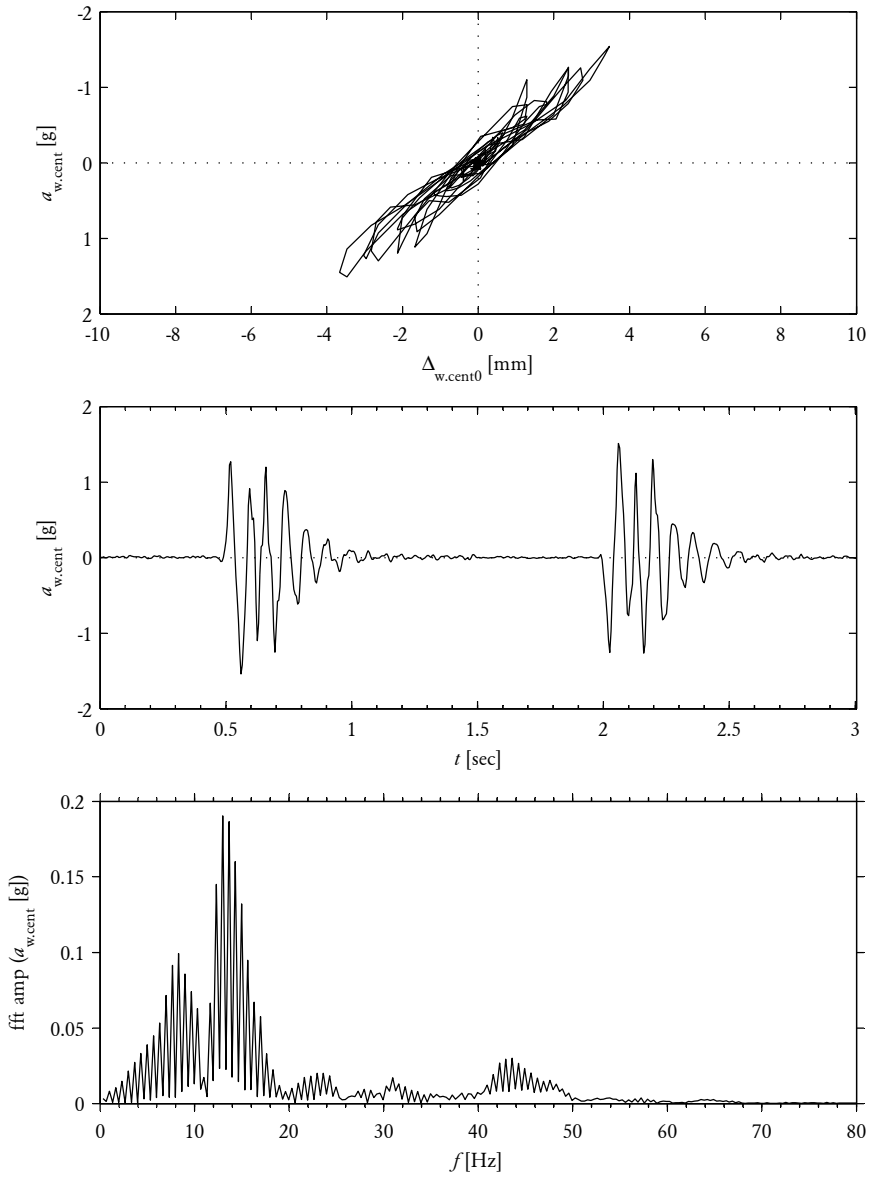

Figure C.26: Example of unfiltered response from pulse test, including hysteresis plot (top), time domain response (middle) and frequency domain response (bottom). Shown for test run `d2_32_R_8mm_100ms`.

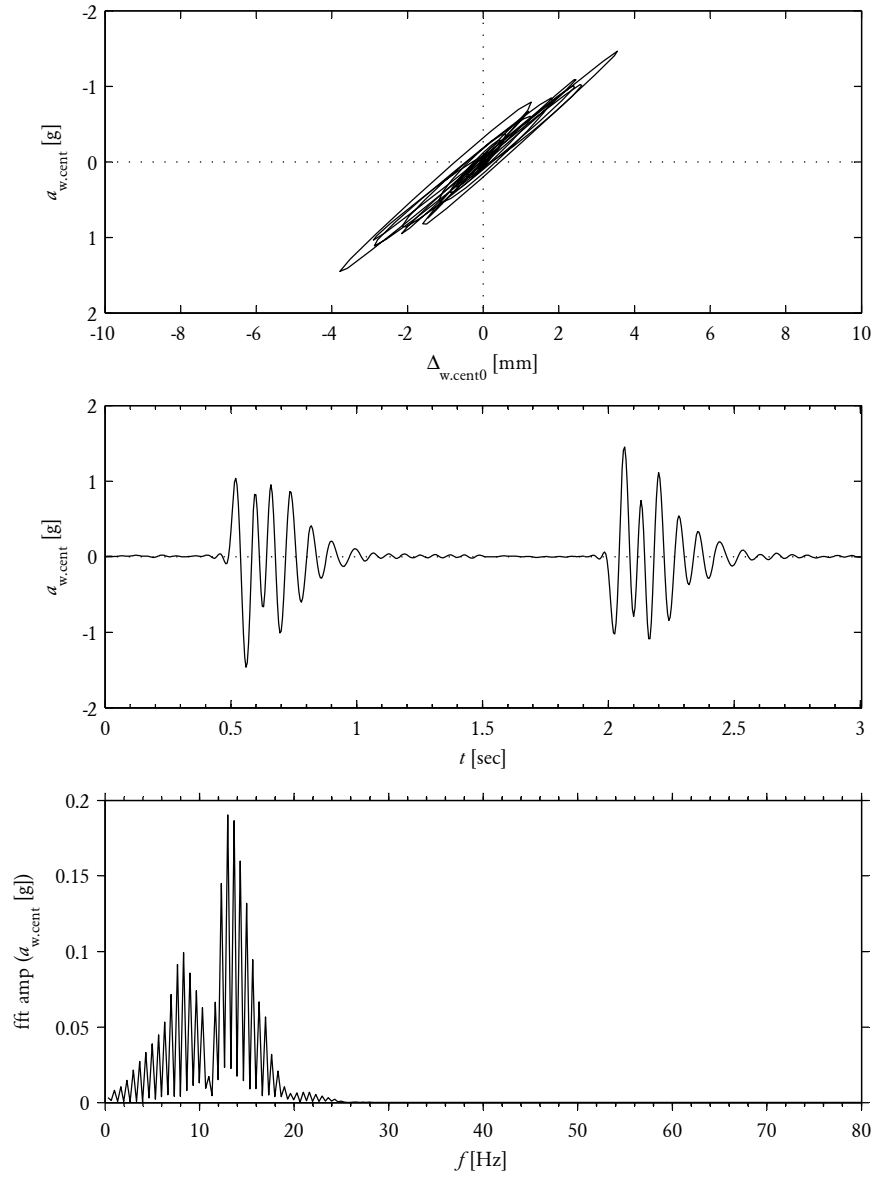

Figure C.27: Example of filtered response from pulse test, including hysteresis plot (top), time domain response (middle) and frequency domain response (bottom). Shown for test run `d2_32_R_8mm_100ms` combined with lowpass Butterworth filter with order $n = 10$ and cutoff frequency $f_c = 20$ Hz.

C.6 LOAD-DISPLACEMENT GRAPHS

This section provides load-displacement response plots from all individual test runs performed. The data plotted was filtered using the techniques described in Section C.5 and corresponds to the same data used for the cyclic response analysis (Section C.4). Two sets of axes are provided for each test run: The left axes plot the wall's central acceleration $a_{\text{w.cent}}$ versus the normalised central displacement $\delta_{\text{w.cent}}$ (i.e. $\Delta_{\text{w.cent}}$ divided by the wall thickness of 50 mm). The right axes plot the wall's average acceleration $a_{\text{w.avg}}$ versus $\delta_{\text{w.cent}}$. The largest displacement cycle occurring in each test run is also highlighted, but only for cycles whose displacement amplitude exceeded 0.3 mm.

C.6.1 Wall D1

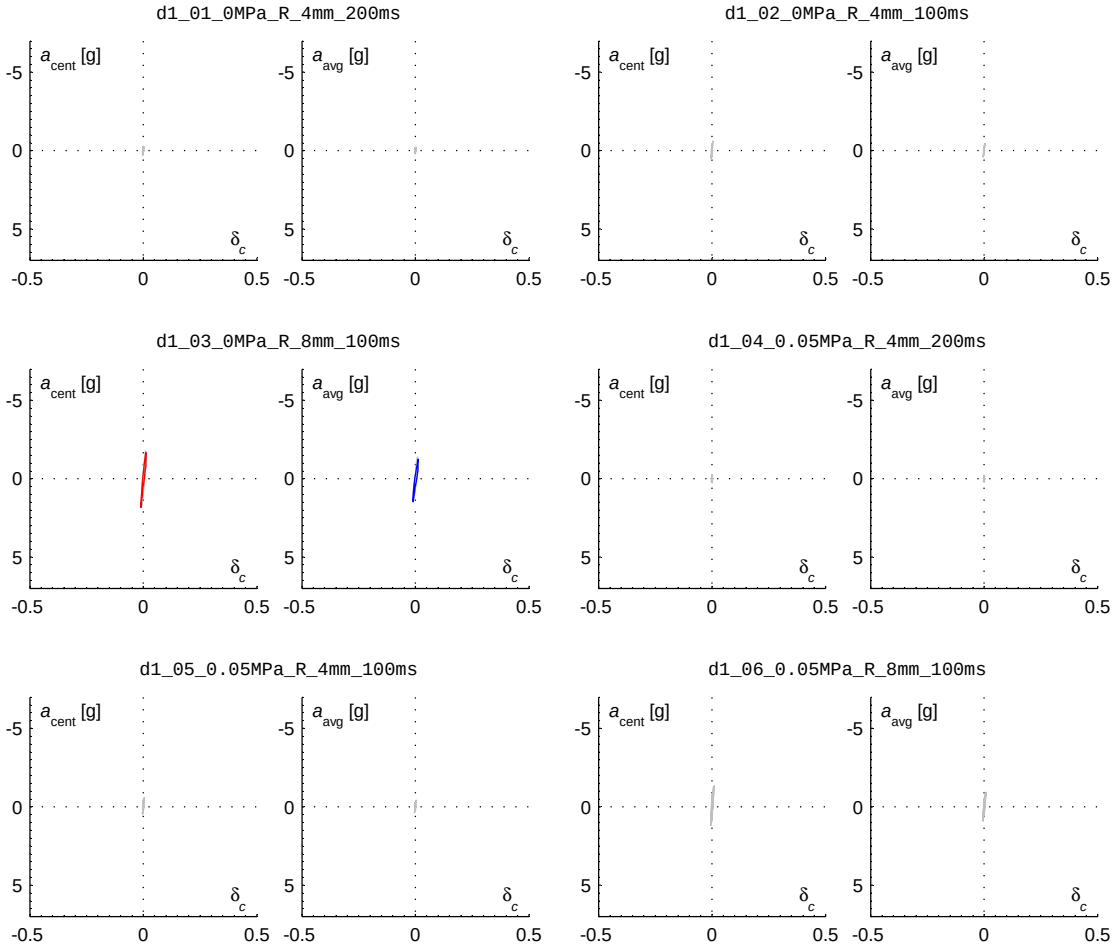

d1_08_0.10MPa_R_4mm_200ms

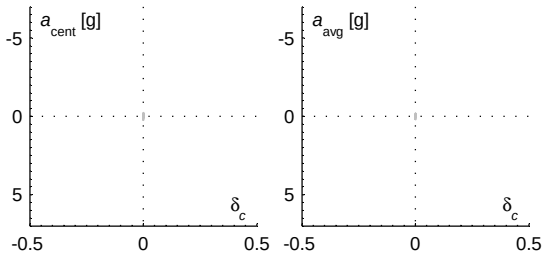

d1_09_0.10MPa_R_4mm_100ms

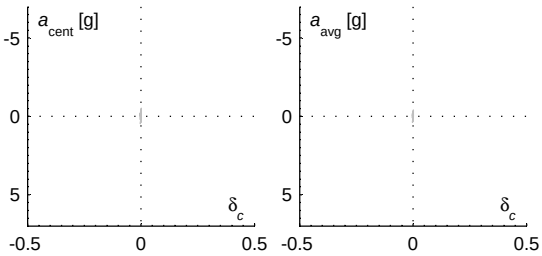

d1_10_0.10MPa_R_8mm_100ms

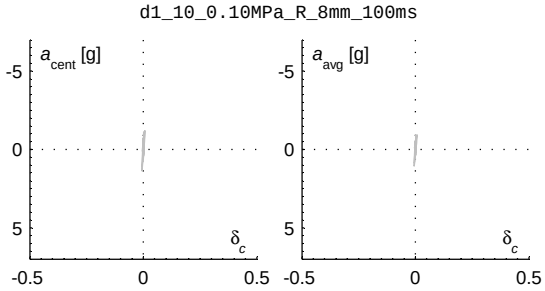

d1_11_H_13Hz_0.25mm

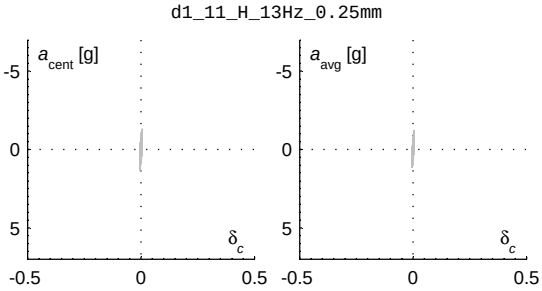

d1_12_H_13Hz_0.5mm

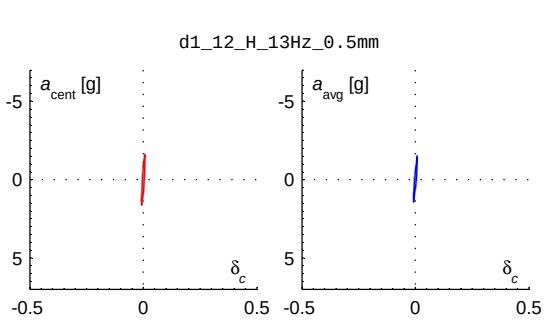

d1_13_H_13Hz_0.75mm

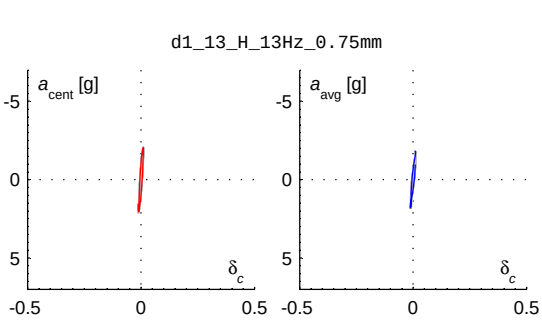

d1_14_H_13Hz_1mm

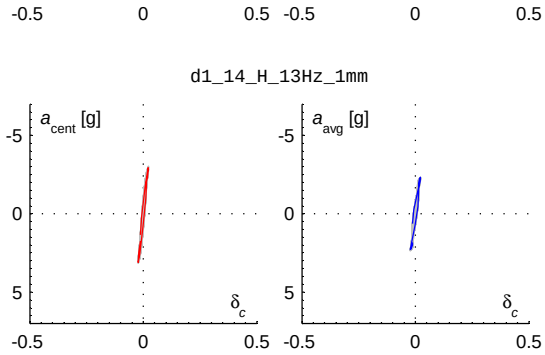

d1_15_EQ_Taft_-40mm

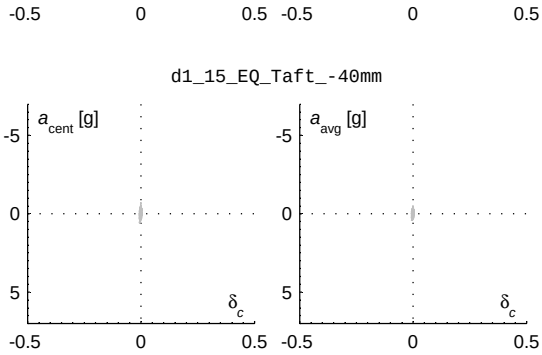

d1_16_EQ_Taft_+40mm

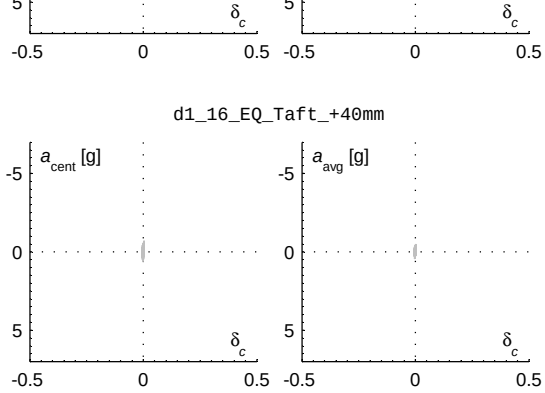

d1_17_EQ_Taft_+60mm

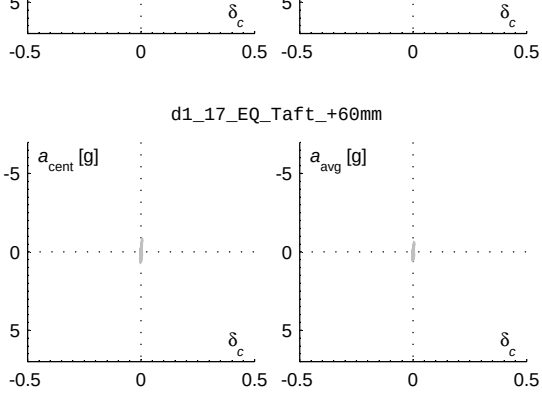

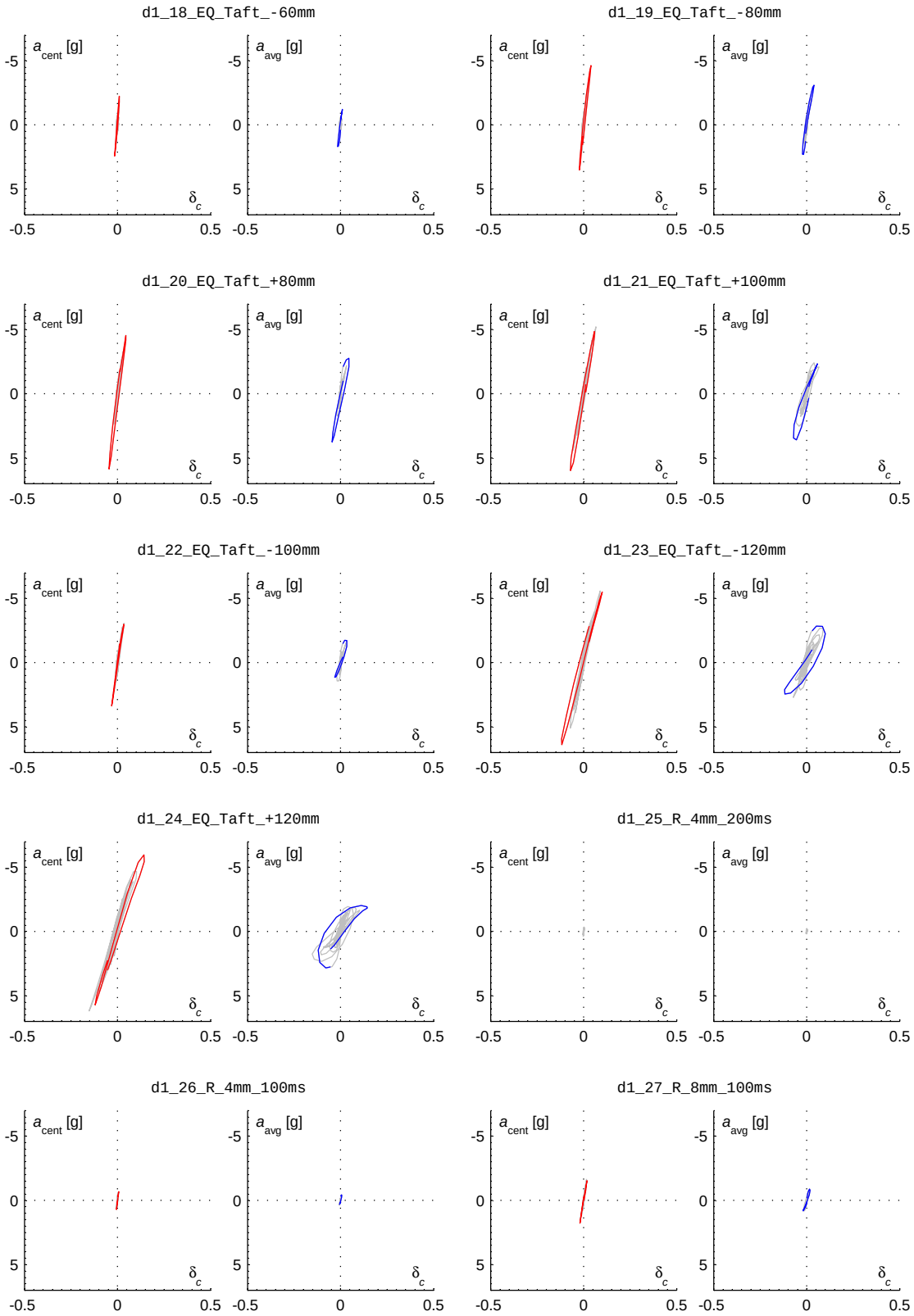
d1_18_EQ_Taft_-60mm
d1_19_EQ_Taft_-80mm
d1_20_EQ_Taft_+80mm
d1_21_EQ_Taft_+100mm
d1_22_EQ_Taft_-100mm
d1_23_EQ_Taft_-120mm
d1_24_EQ_Taft_+120mm
d1_25_R_4mm_200ms
d1_26_R_4mm_100ms
d1_27_R_8mm_100ms
a cent [g]
a avg [g]
δc
-5
0
5
-0.5
0
0.5

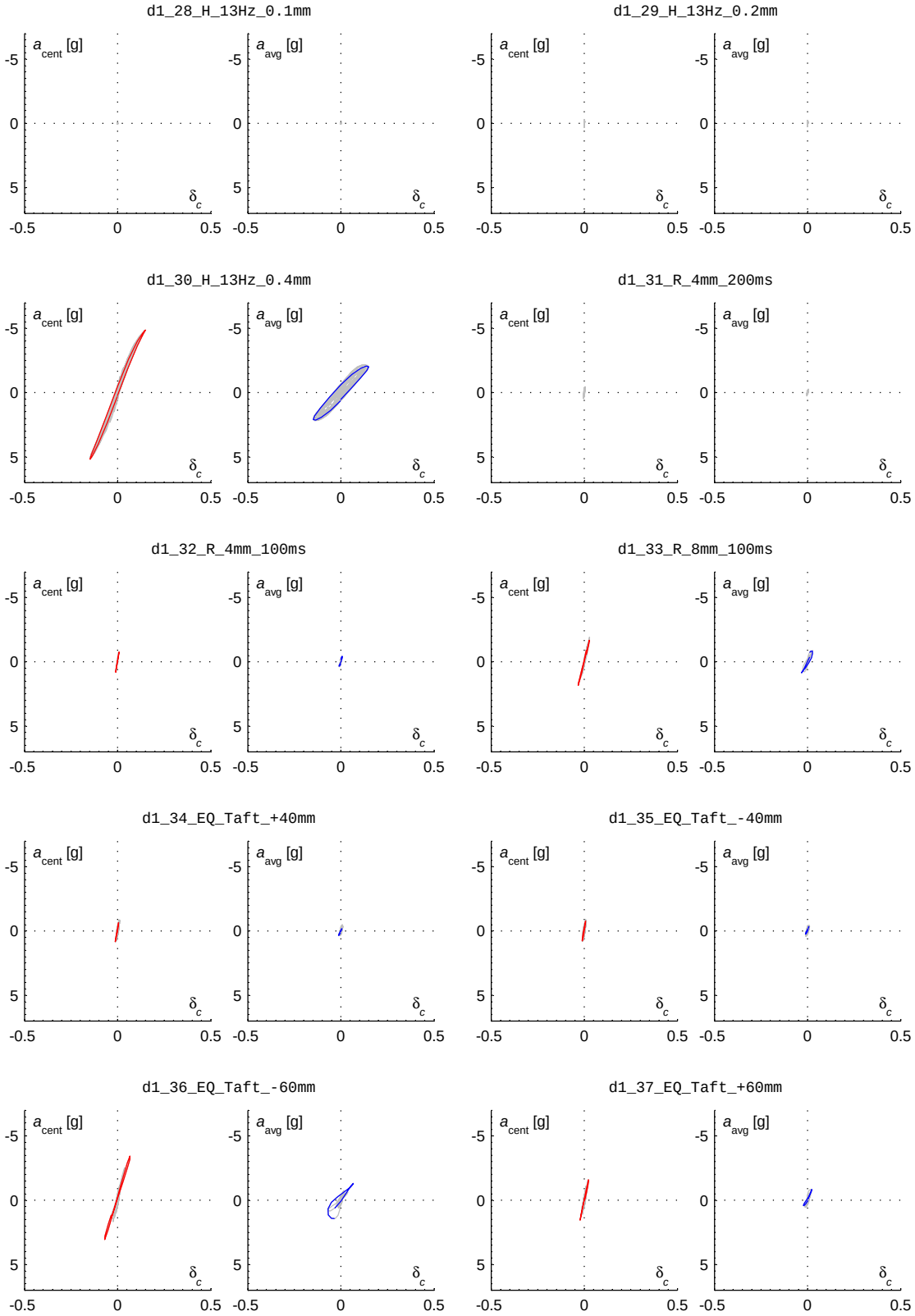
d1_28_H_13Hz_0.1mm
d1_29_H_13Hz_0.2mm
d1_30_H_13Hz_0.4mm
d1_31_R_4mm_200ms
d1_32_R_4mm_100ms
d1_33_R_8mm_100ms
d1_34_EQ_Taft_+40mm
d1_35_EQ_Taft_-40mm
d1_36_EQ_Taft_-60mm
d1_37_EQ_Taft_+60mm
a cent [g]
a avg [g]
δ c
-5
0
5
-0.5
0
0.5

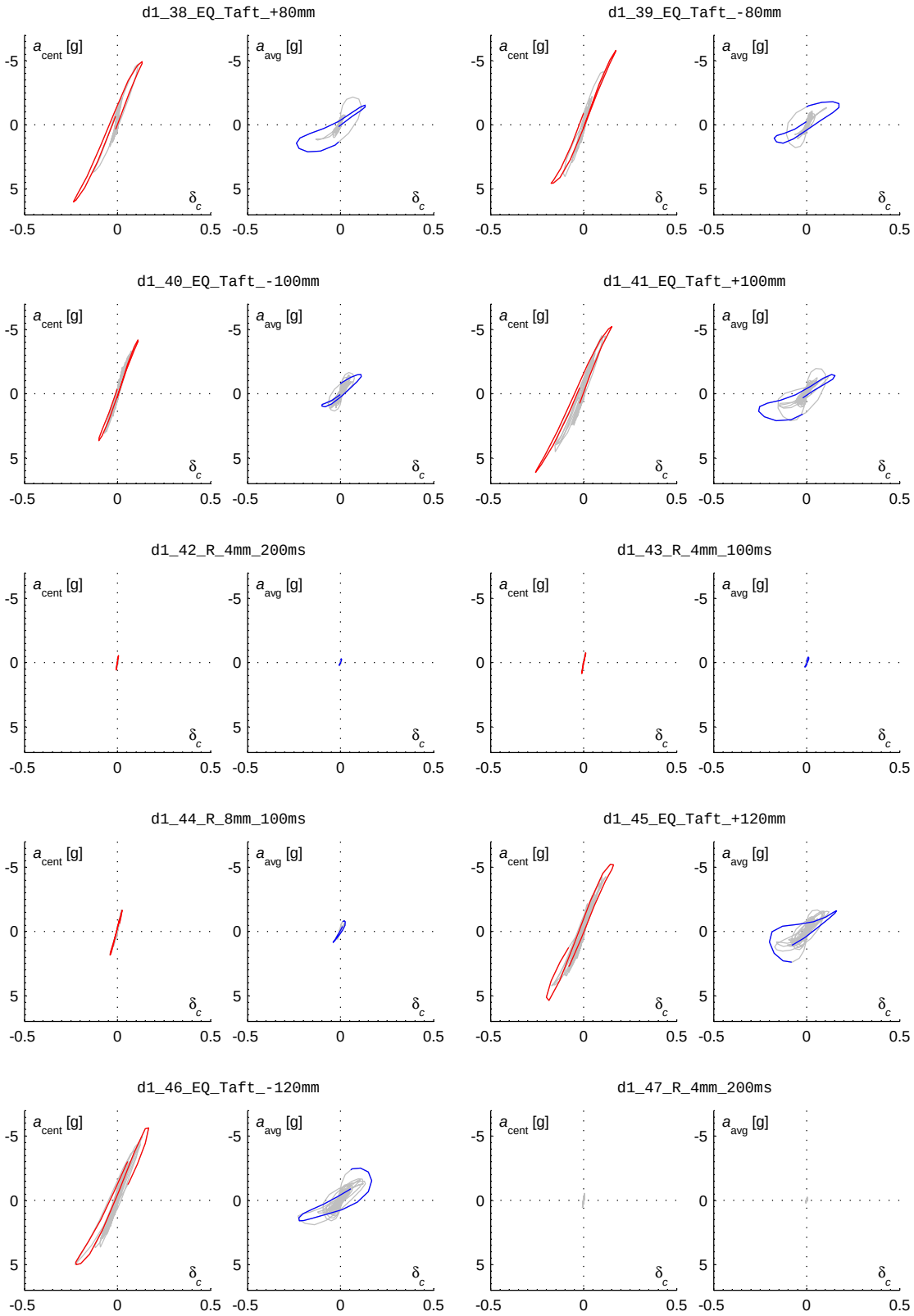
d1_38_EQ_Taft_+80mm
d1_39_EQ_Taft_-80mm
d1_40_EQ_Taft_-100mm
d1_41_EQ_Taft_+100mm
d1_42_R_4mm_200ms
d1_43_R_4mm_100ms
d1_44_R_8mm_100ms
d1_45_EQ_Taft_+120mm
d1_46_EQ_Taft_-120mm
d1_47_R_4mm_200ms
a cent [g]
a avg [g]
δc
-5
0
5
-0.5
0
0.5

d1_48_R_4mm_100ms

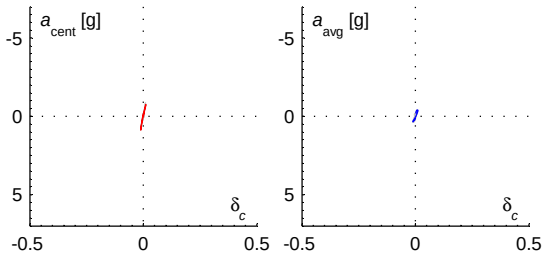

d1_49_R_8mm_100ms

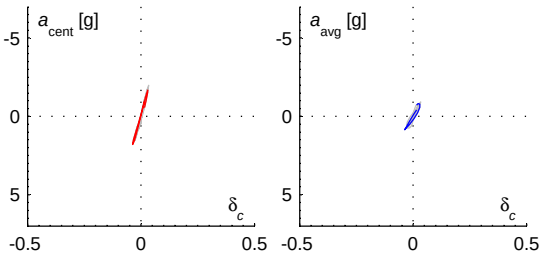

d1_50_H_12Hz_0.1mm

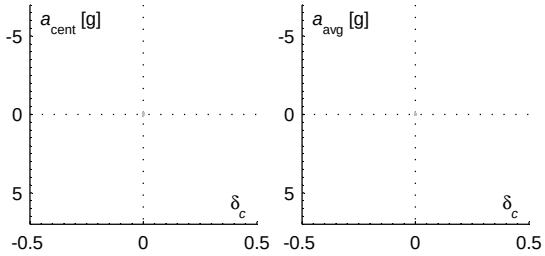

d1_51_H_12Hz_0.2mm

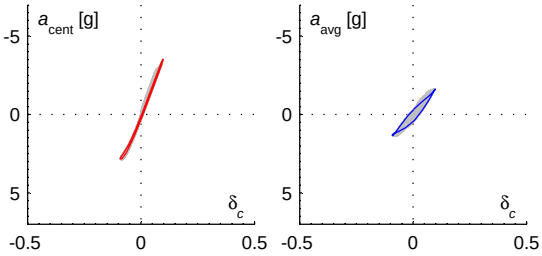

d1_52_R_4mm_200ms

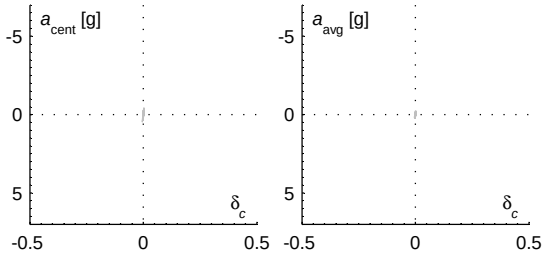

d1_53_R_4mm_100ms

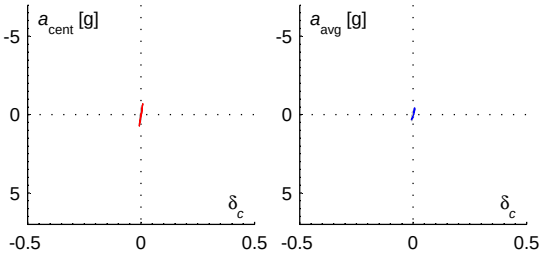

d1_54_R_8mm_100ms

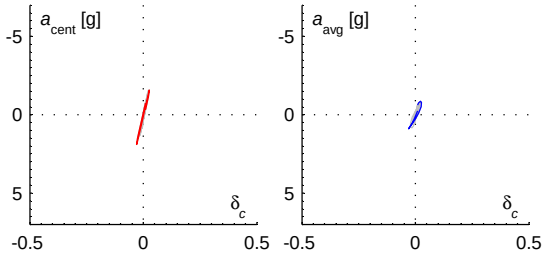

d1_56_EQ_Synth01_+20mm

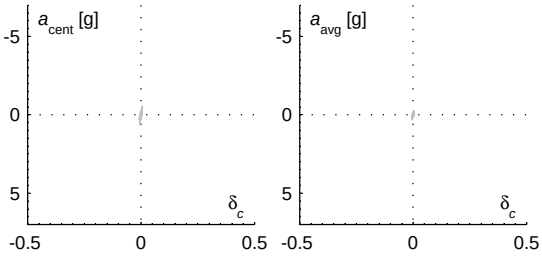

d1_57_EQ_Synth01_-20mm

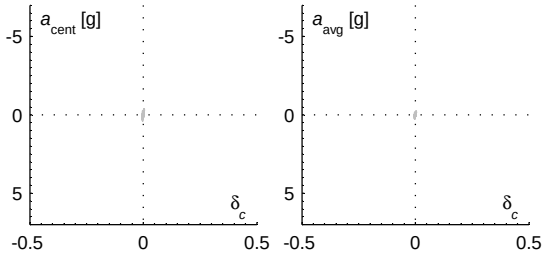

d1_58_EQ_Synth01_-40mm

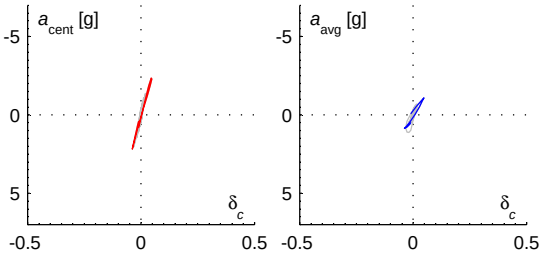

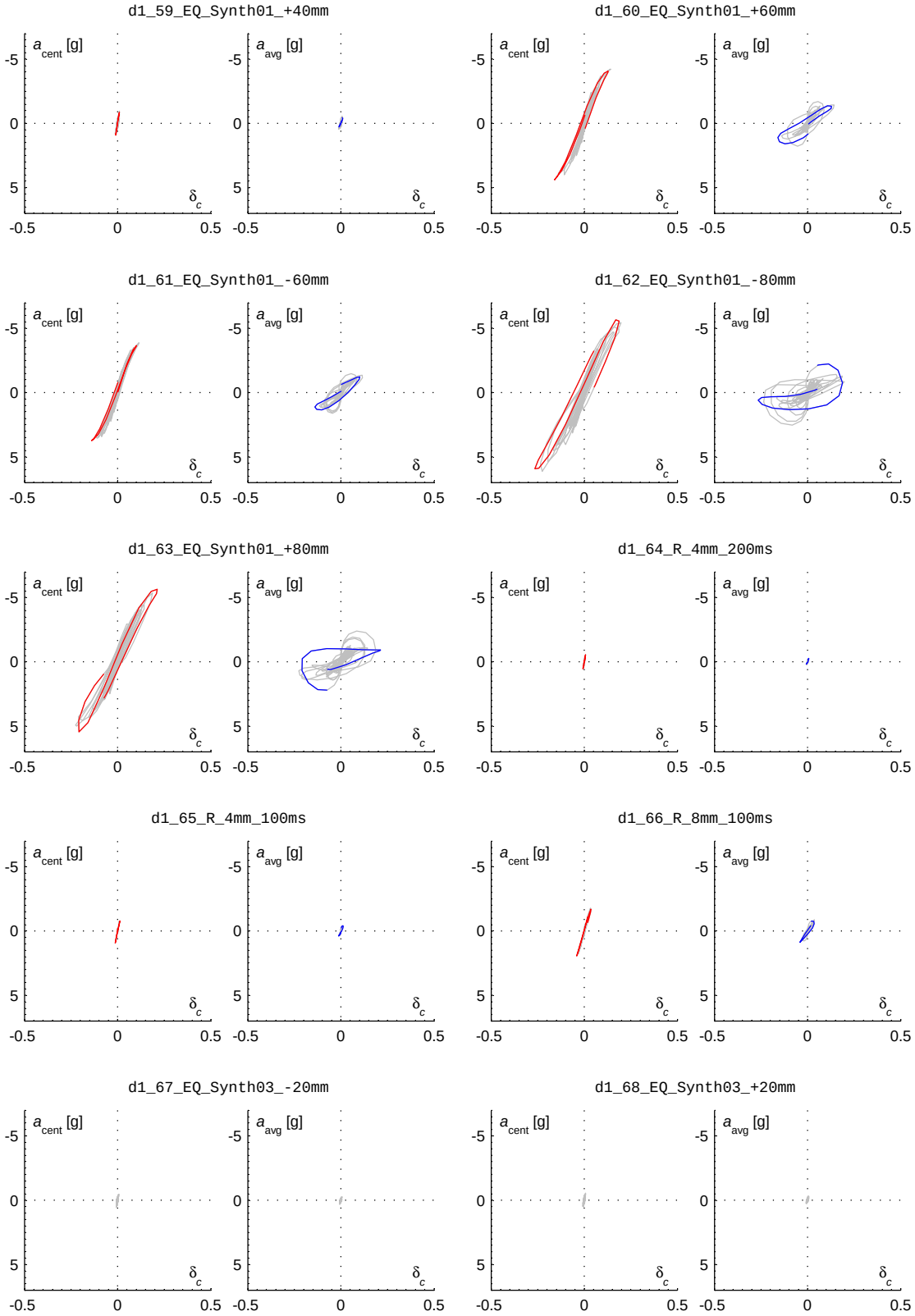
d1_59_EQ_Synth01_+40mm
d1_60_EQ_Synth01_+60mm
d1_61_EQ_Synth01_-60mm
d1_62_EQ_Synth01_-80mm
d1_63_EQ_Synth01_+80mm
d1_64_R_4mm_200ms
d1_65_R_4mm_100ms
d1_66_R_8mm_100ms
d1_67_EQ_Synth03_-20mm
d1_68_EQ_Synth03_+20mm
a cent [g]
a avg [g]
δc
-5
0
5
-0.5
0
0.5

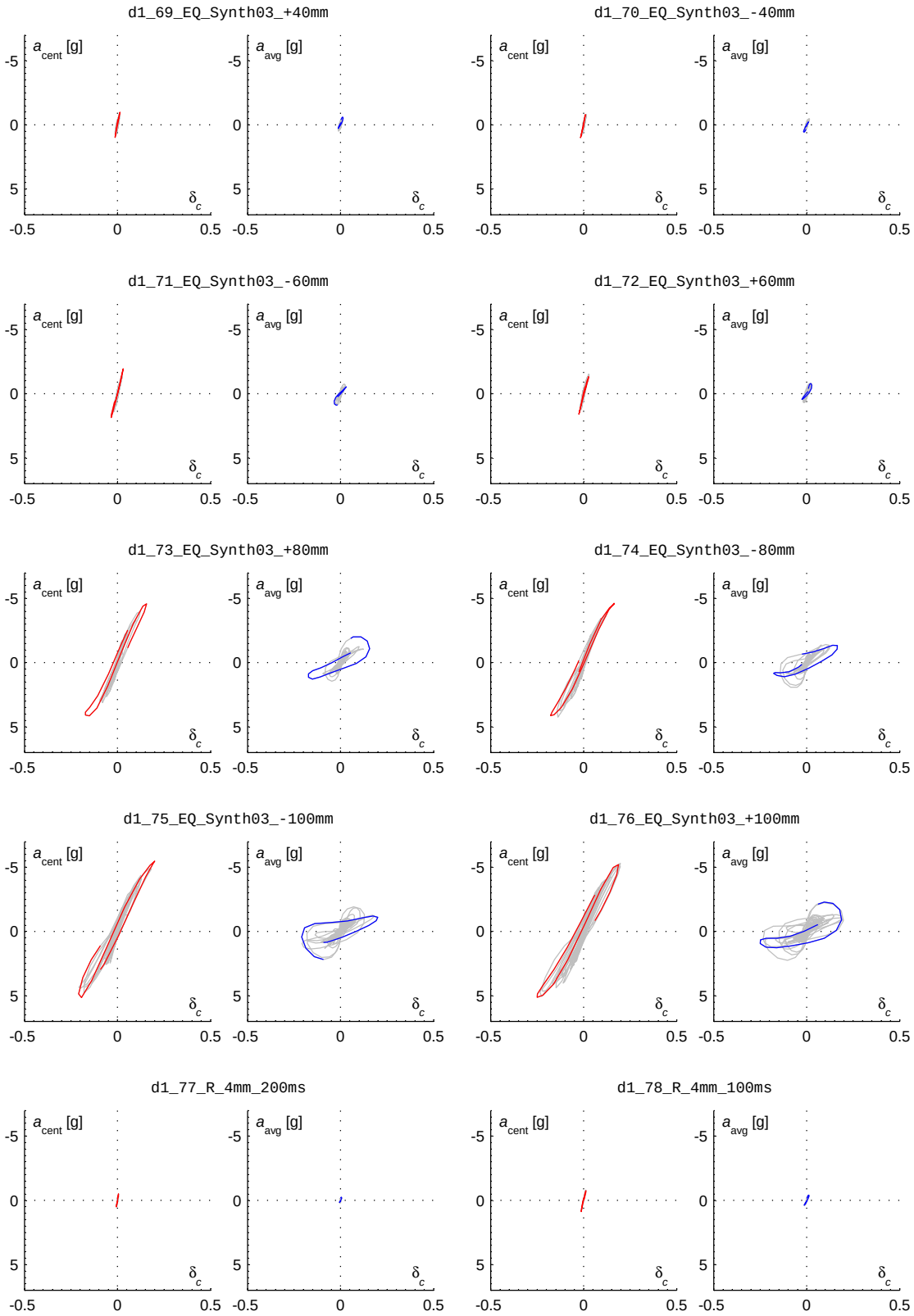
d1_69_EQ_Synth03_+40mm
d1_70_EQ_Synth03_-40mm
d1_71_EQ_Synth03_-60mm
d1_72_EQ_Synth03_+60mm
d1_73_EQ_Synth03_+80mm
d1_74_EQ_Synth03_-80mm
d1_75_EQ_Synth03_-100mm
d1_76_EQ_Synth03_+100mm
d1_77_R_4mm_200ms
d1_78_R_4mm_100ms
a cent [g]
a avg [g]
δc
-5
0
5
-0.5
0
0.5

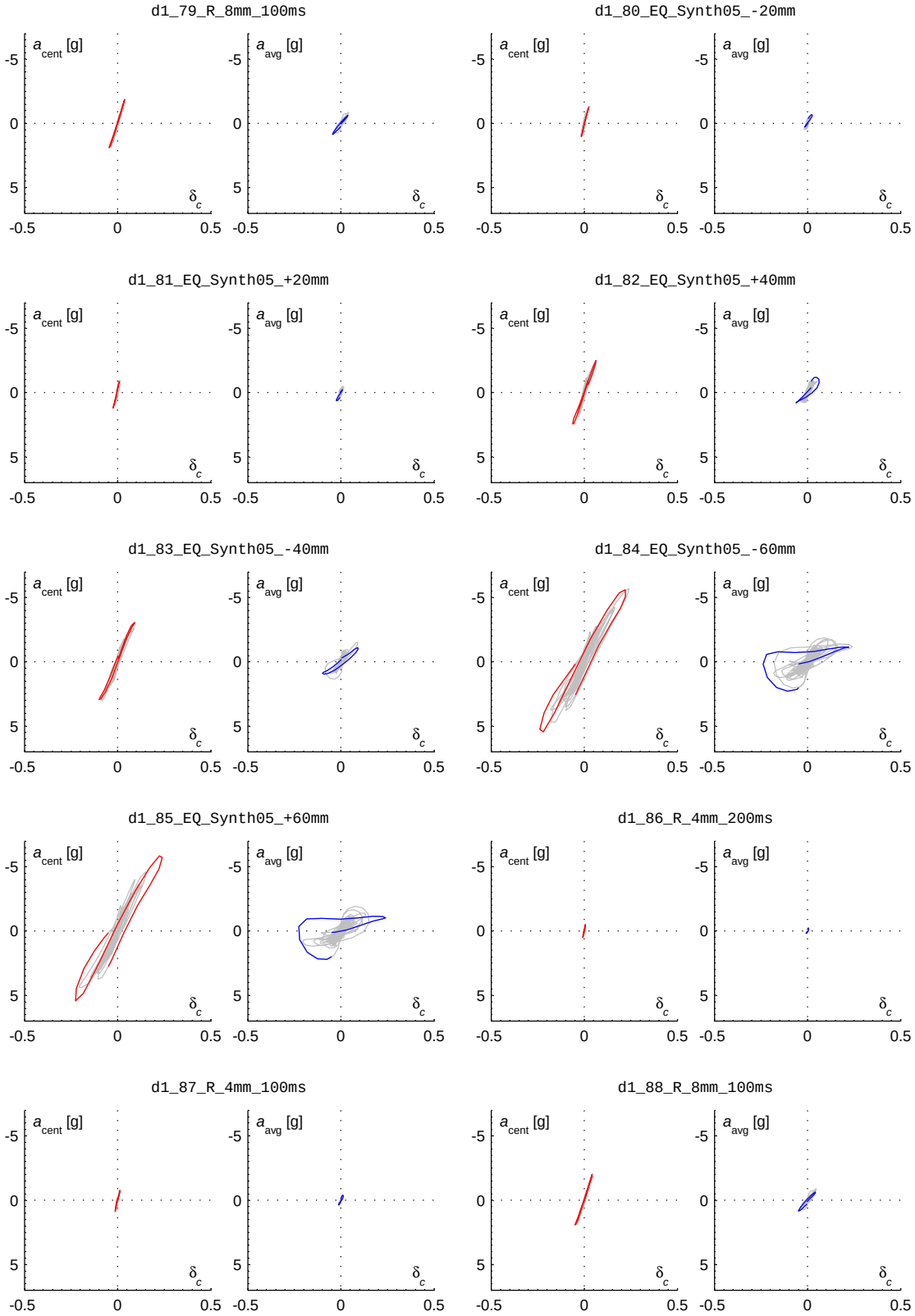
d1_79_R_8mm_100ms
d1_80_EQ_Synth05_-20mm
d1_81_EQ_Synth05_+20mm
d1_82_EQ_Synth05_+40mm
d1_83_EQ_Synth05_-40mm
d1_84_EQ_Synth05_-60mm
d1_85_EQ_Synth05_+60mm
d1_86_R_4mm_200ms
d1_87_R_4mm_100ms
d1_88_R_8mm_100ms
a cent [g]
a avg [g]
δc
-5
0
5
-0.5
0
0.5

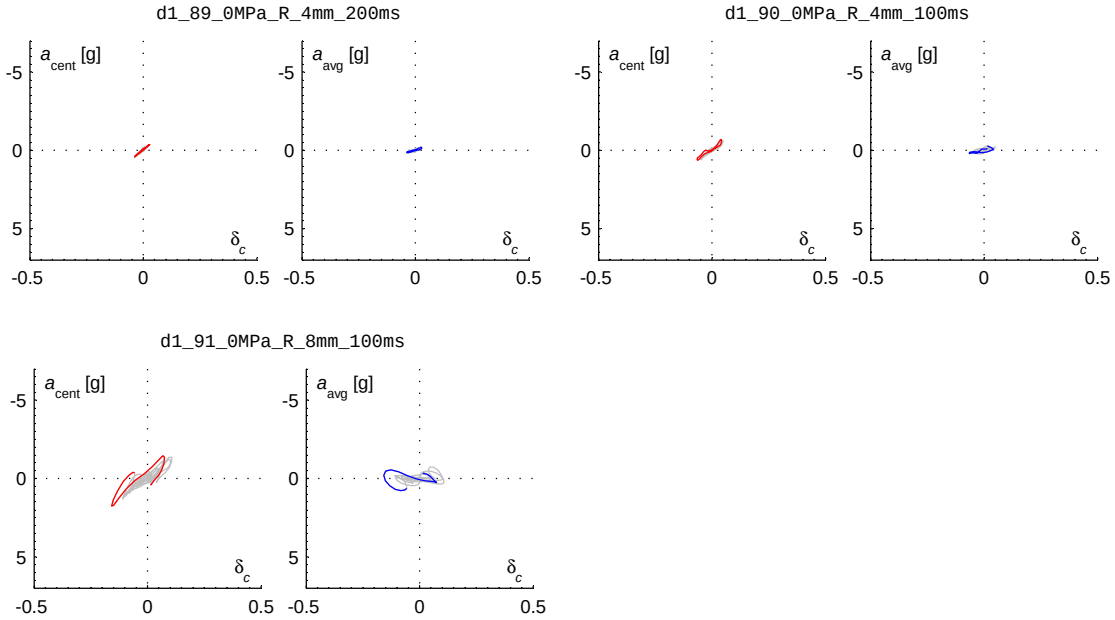
d1_89_0MPa_R_4mm_200ms
d1_90_0MPa_R_4mm_100ms
d1_91_0MPa_R_8mm_100ms
a cent [g]
a avg [g]
δc
-5
0
5
-0.5
0
0.5

C.6.2 Wall D2

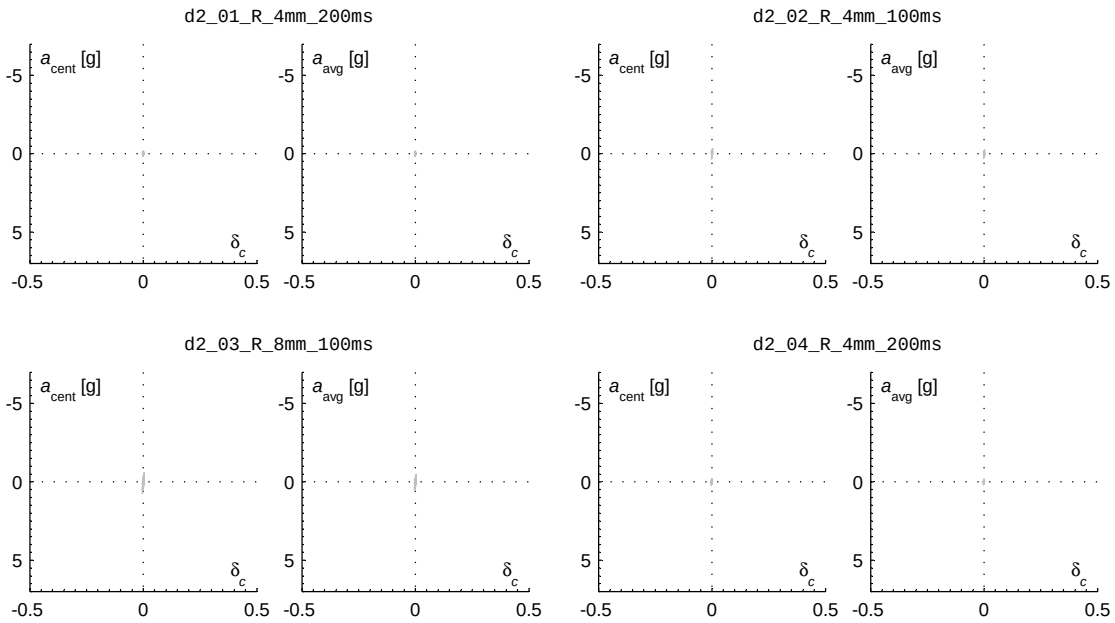
d2_01_R_4mm_200ms
d2_02_R_4mm_100ms
d2_03_R_8mm_100ms
d2_04_R_4mm_200ms
a cent [g]
a avg [g]
δc
-5
0
5
-0.5
0
0.5

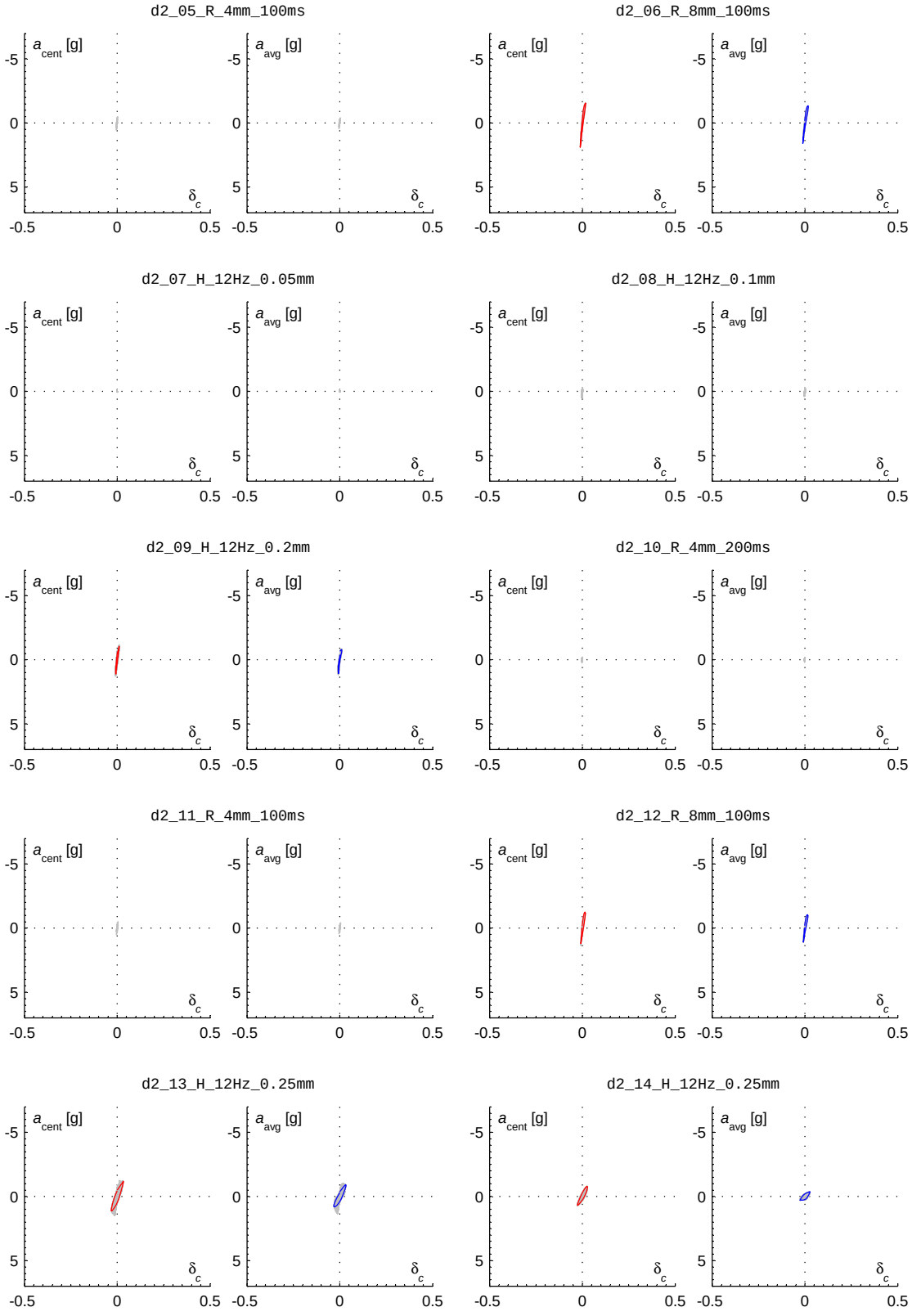
d2_05_R_4mm_100ms
d2_06_R_8mm_100ms
d2_07_H_12Hz_0.05mm
d2_08_H_12Hz_0.1mm
d2_09_H_12Hz_0.2mm
d2_10_R_4mm_200ms
d2_11_R_4mm_100ms
d2_12_R_8mm_100ms
d2_13_H_12Hz_0.25mm
d2_14_H_12Hz_0.25mm
a cent [g]
a avg [g]
δc
-5
0
5
-0.5
0
0.5

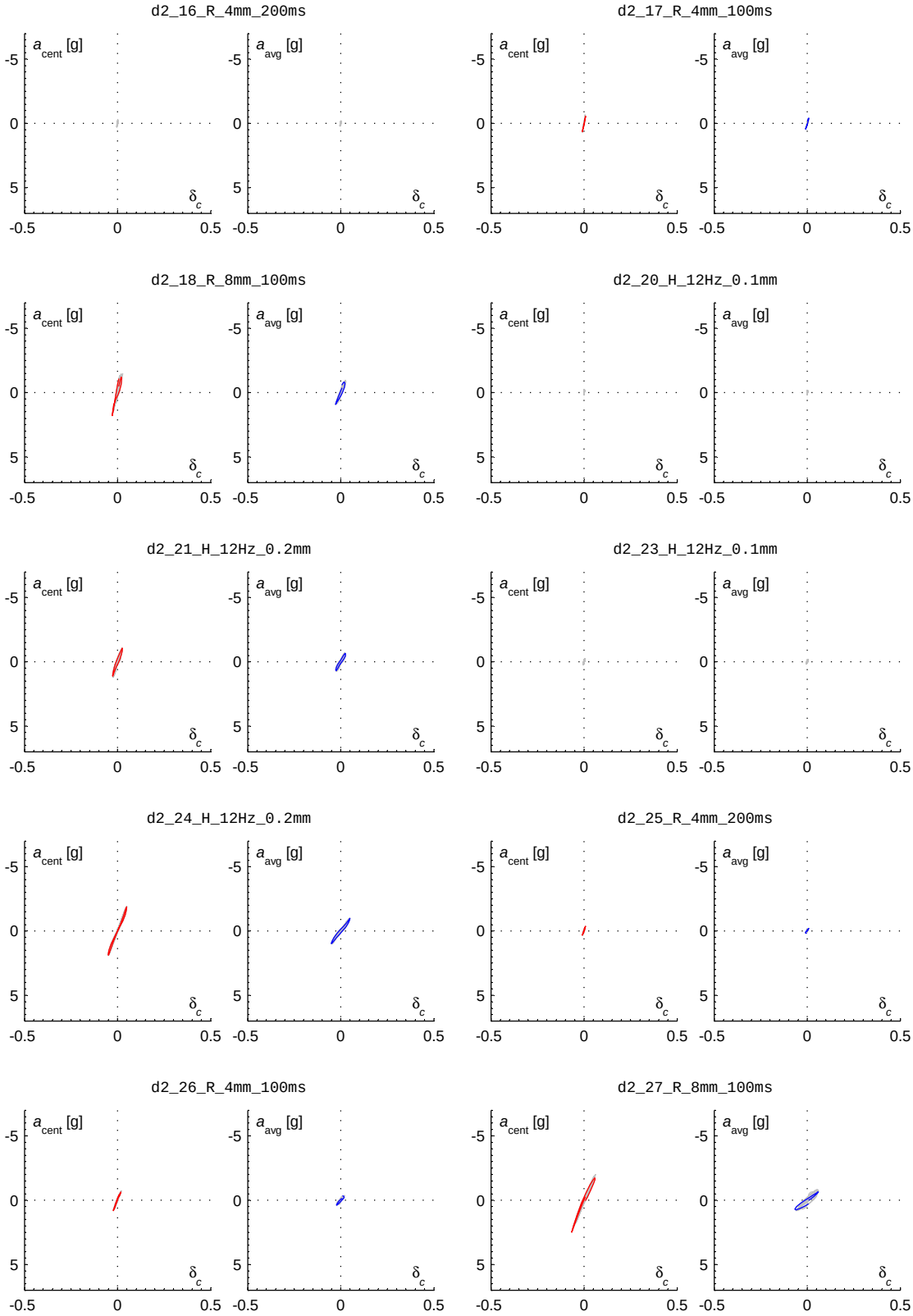
d2_16_R_4mm_200ms
d2_17_R_4mm_100ms
d2_18_R_8mm_100ms
d2_20_H_12Hz_0.1mm
d2_21_H_12Hz_0.2mm
d2_23_H_12Hz_0.1mm
d2_24_H_12Hz_0.2mm
d2_25_R_4mm_200ms
d2_26_R_4mm_100ms
d2_27_R_8mm_100ms
a cent [g]
a avg [g]
δc
-5
0
5
-0.5
0
0.5

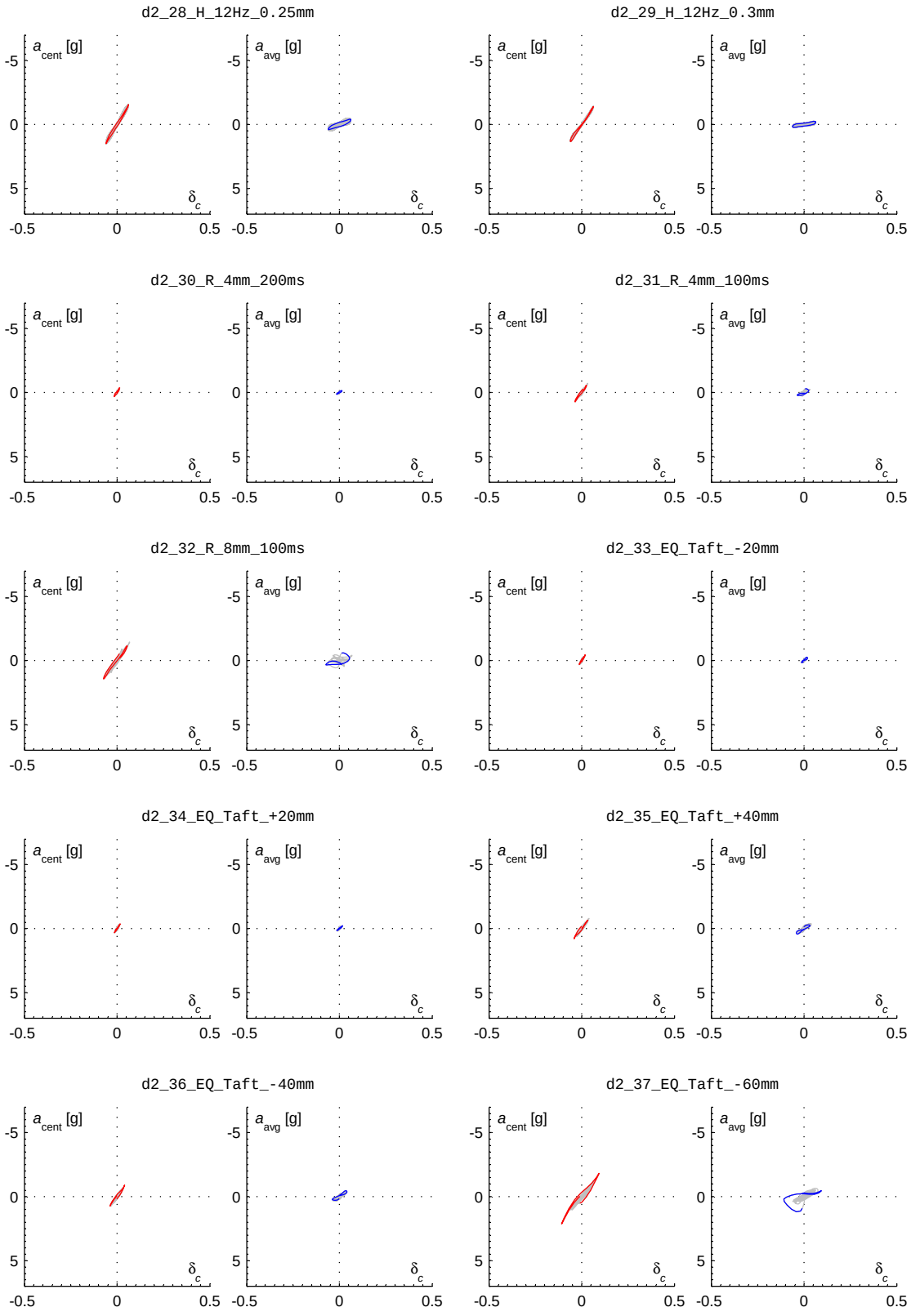
d2_28_H_12Hz_0.25mm
d2_29_H_12Hz_0.3mm
d2_30_R_4mm_200ms
d2_31_R_4mm_100ms
d2_32_R_8mm_100ms
d2_33_EQ_Taft_-20mm
d2_34_EQ_Taft_+20mm
d2_35_EQ_Taft_+40mm
d2_36_EQ_Taft_-40mm
d2_37_EQ_Taft_-60mm
a cent [g]
a avg [g]
δc
-5
0
5
-0.5
0
0.5

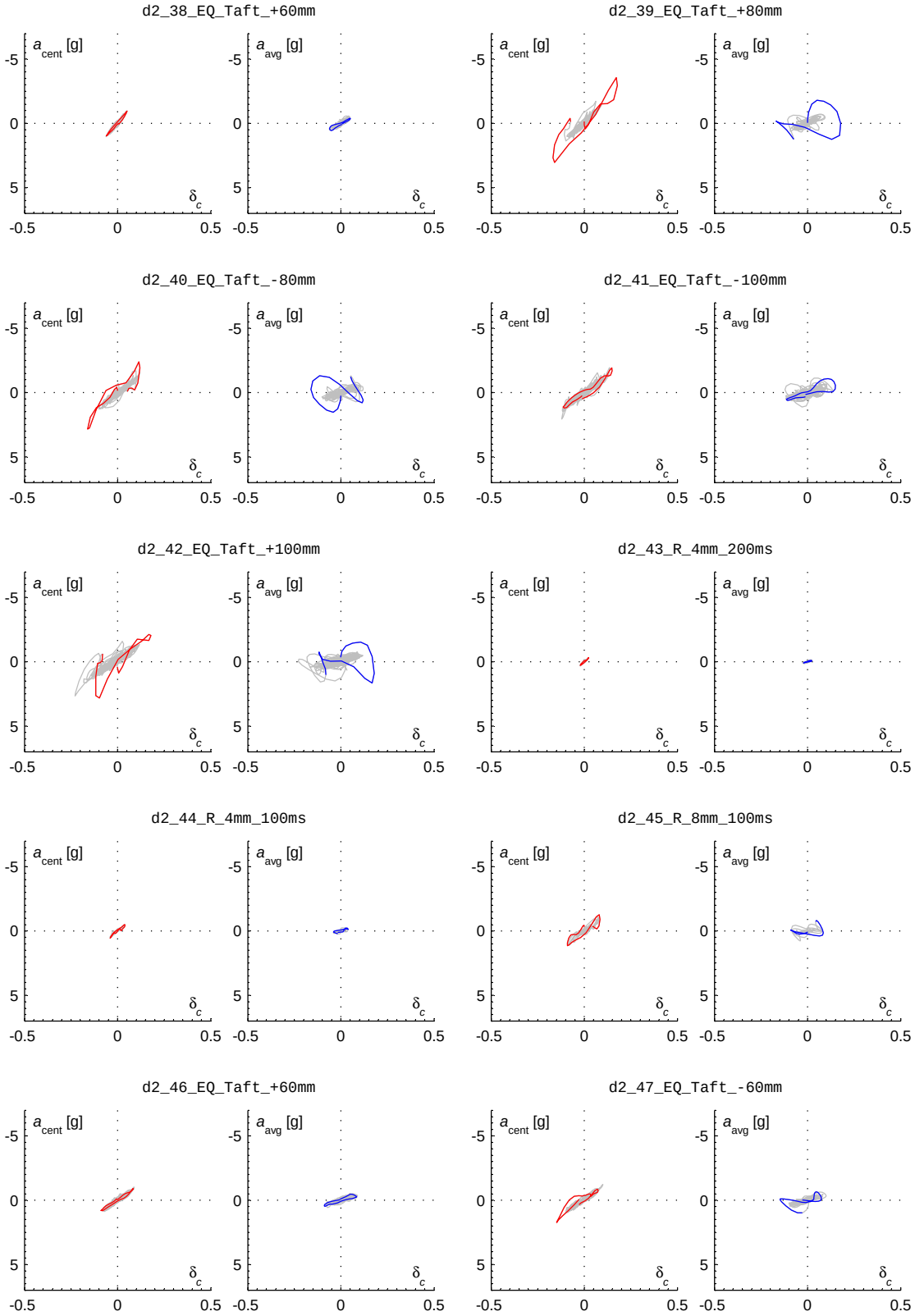
d2_38_EQ_Taft_+60mm
d2_39_EQ_Taft_+80mm
d2_40_EQ_Taft_-80mm
d2_41_EQ_Taft_-100mm
d2_42_EQ_Taft_+100mm
d2_43_R_4mm_200ms
d2_44_R_4mm_100ms
d2_45_R_8mm_100ms
d2_46_EQ_Taft_+60mm
d2_47_EQ_Taft_-60mm
a cent [g]
a avg [g]
δ c
-5
0
5
-0.5
0
0.5

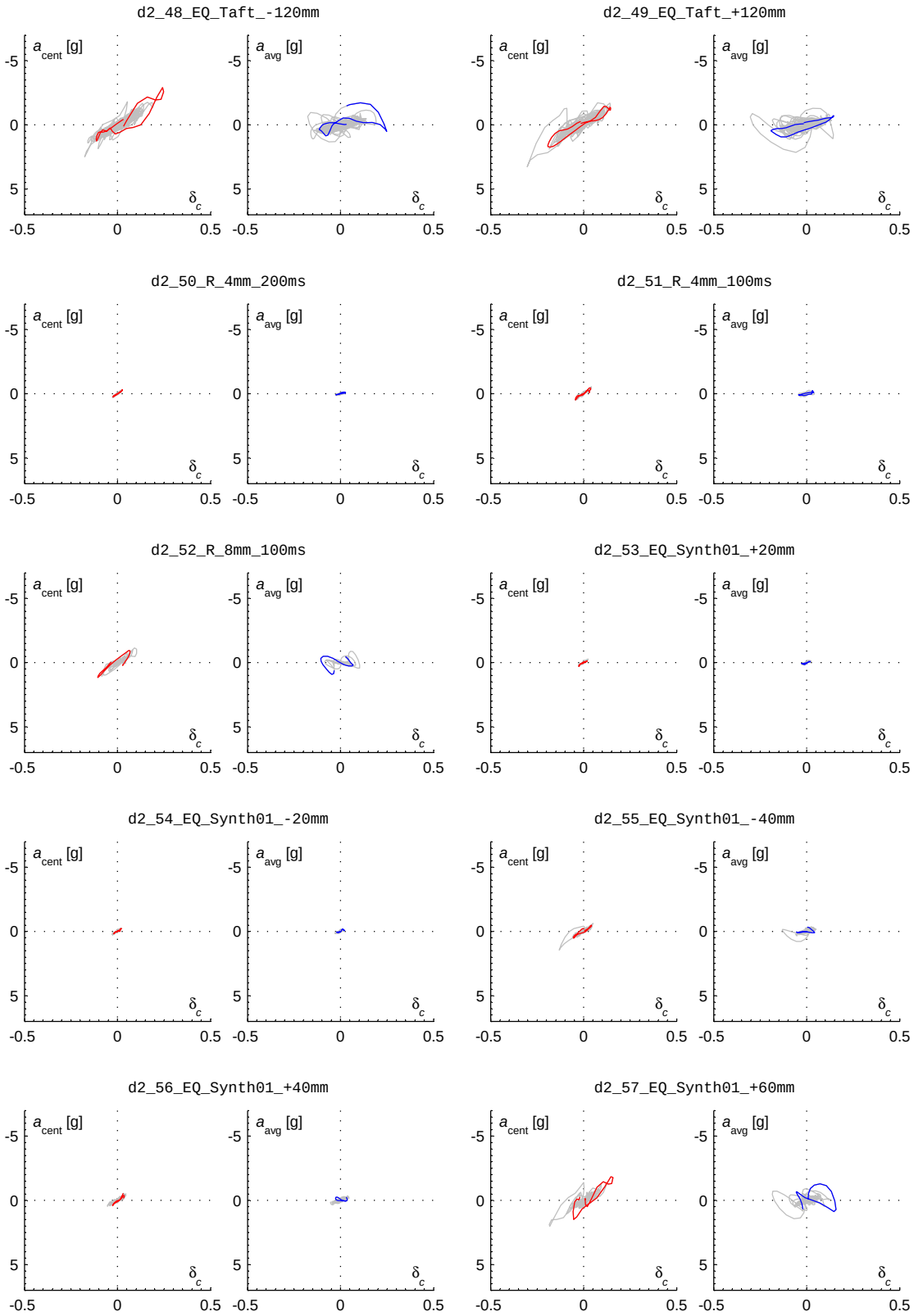
d2_48_EQ_Taft_-120mm
d2_49_EQ_Taft_+120mm
d2_50_R_4mm_200ms
d2_51_R_4mm_100ms
d2_52_R_8mm_100ms
d2_53_EQ_Synth01_+20mm
d2_54_EQ_Synth01_-20mm
d2_55_EQ_Synth01_-40mm
d2_56_EQ_Synth01_+40mm
d2_57_EQ_Synth01_+60mm
a cent [g]
a avg [g]
δc
-5
0
5
-0.5
0
0.5

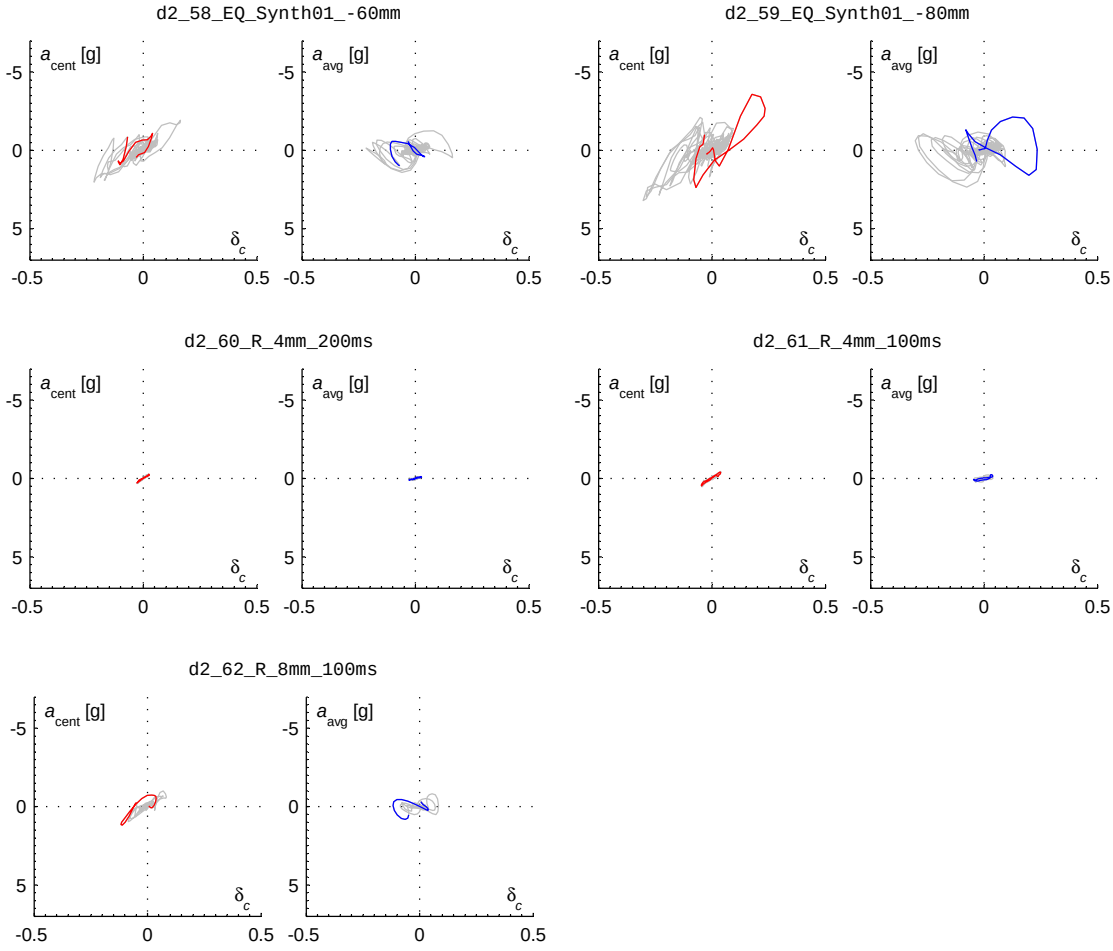
d2_58_EQ_Synth01_-60mm
d2_59_EQ_Synth01_-80mm
d2_60_R_4mm_200ms
d2_61_R_4mm_100ms
d2_62_R_8mm_100ms
a cent [g]
a avg [g]
δc
-5
0
5
-0.5
0
0.5

C.6.3 Wall D3

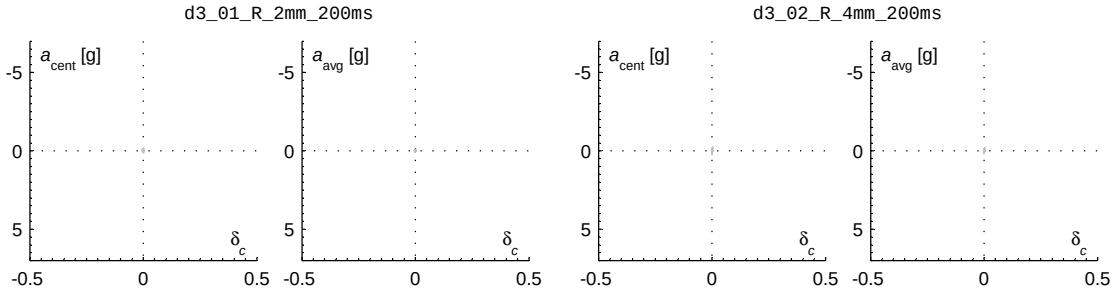
d3_01_R_2mm_200ms
d3_02_R_4mm_200ms
a cent [g]
a avg [g]
δc
-5
0
5
-0.5
0
0.5

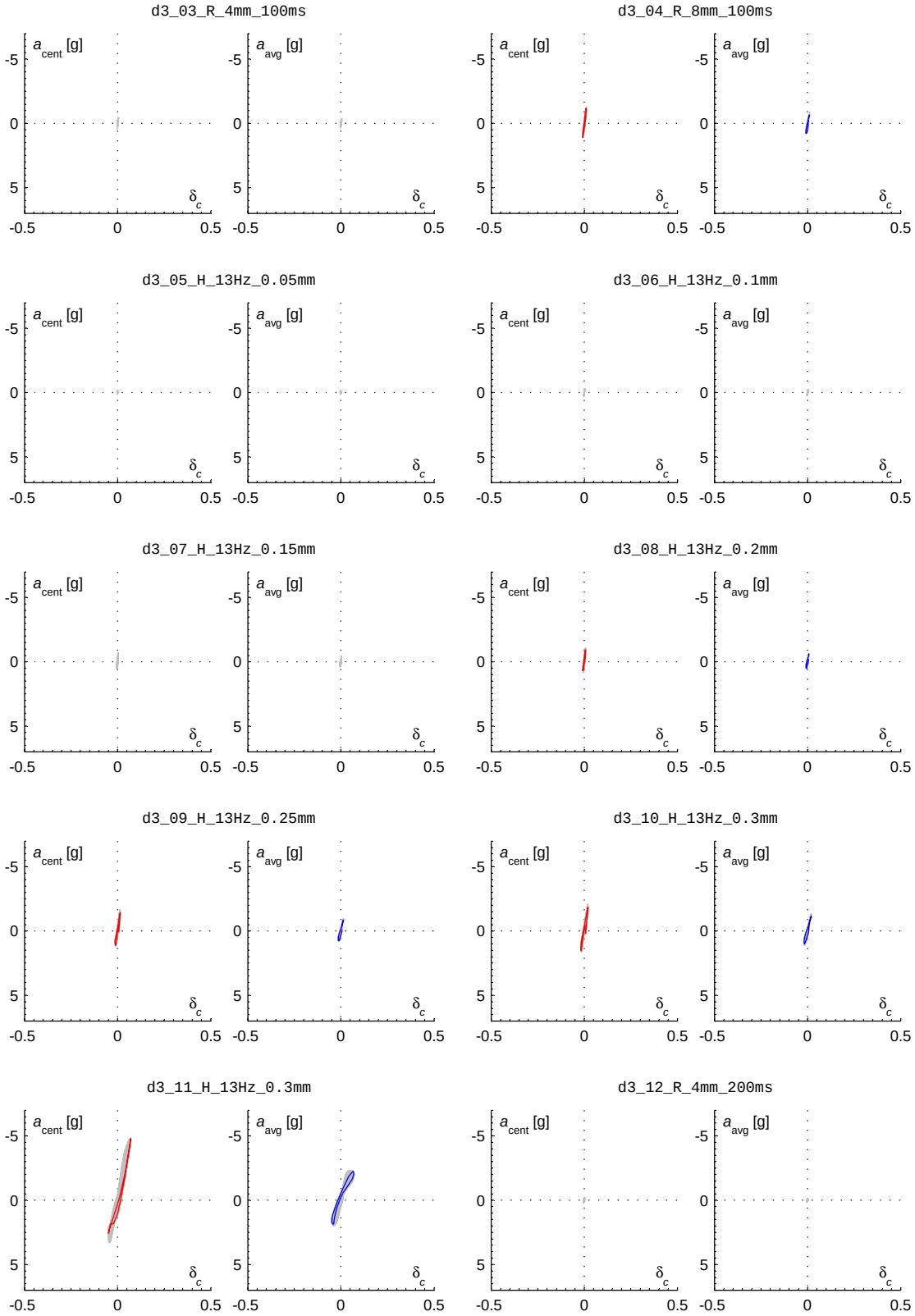
d3_03_R_4mm_100ms
d3_04_R_8mm_100ms
d3_05_H_13Hz_0.05mm
d3_06_H_13Hz_0.1mm
d3_07_H_13Hz_0.15mm
d3_08_H_13Hz_0.2mm
d3_09_H_13Hz_0.25mm
d3_10_H_13Hz_0.3mm
d3_11_H_13Hz_0.3mm
d3_12_R_4mm_200ms
a cent [g]
a avg [g]
δc
-5
0
5
-0.5
0
0.5

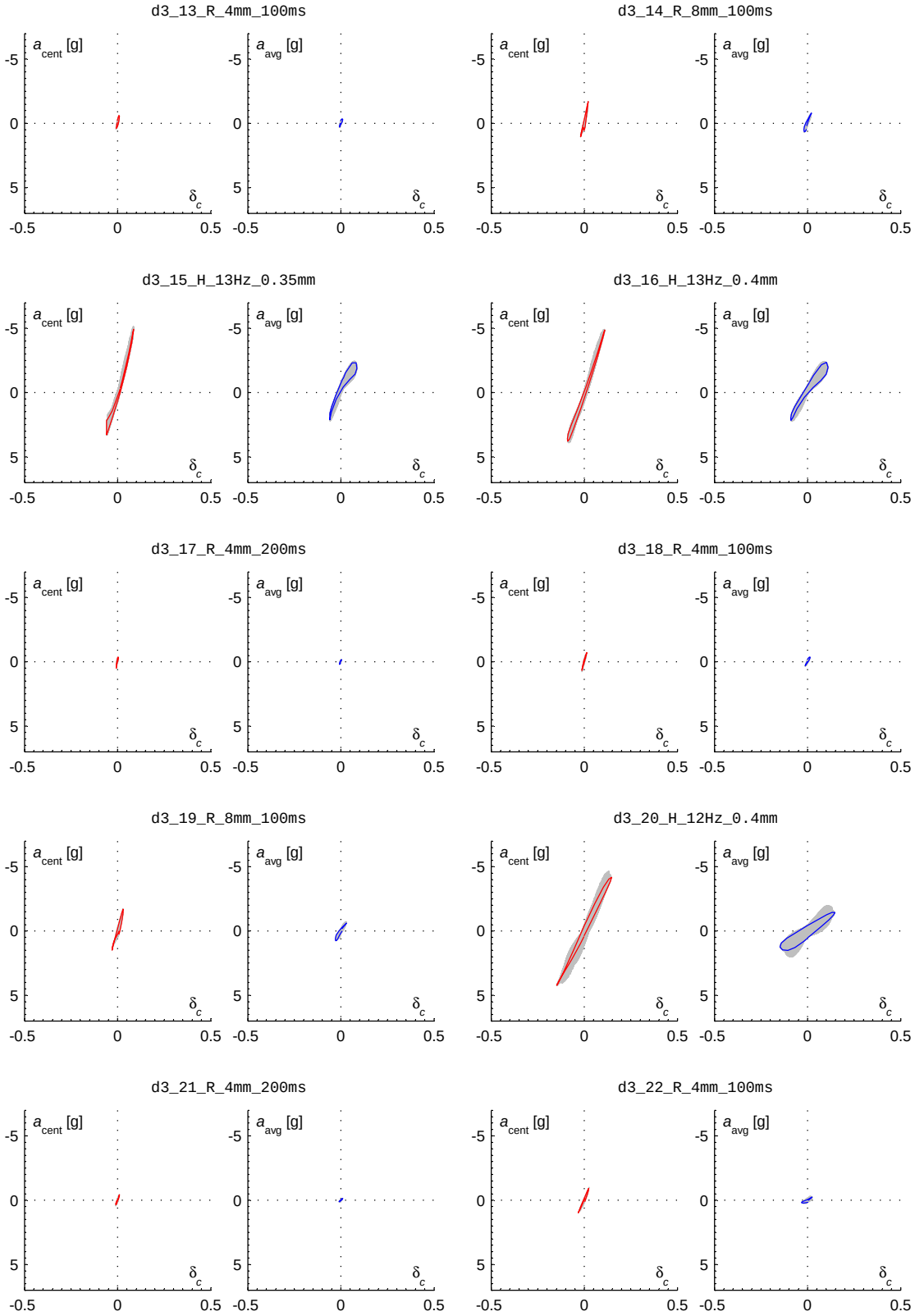
d3_13_R_4mm_100ms
d3_14_R_8mm_100ms
d3_15_H_13Hz_0.35mm
d3_16_H_13Hz_0.4mm
d3_17_R_4mm_200ms
d3_18_R_4mm_100ms
d3_19_R_8mm_100ms
d3_20_H_12Hz_0.4mm
d3_21_R_4mm_200ms
d3_22_R_4mm_100ms
a cent [g]
a avg [g]
δc
-5
0
5
-0.5
0
0.5

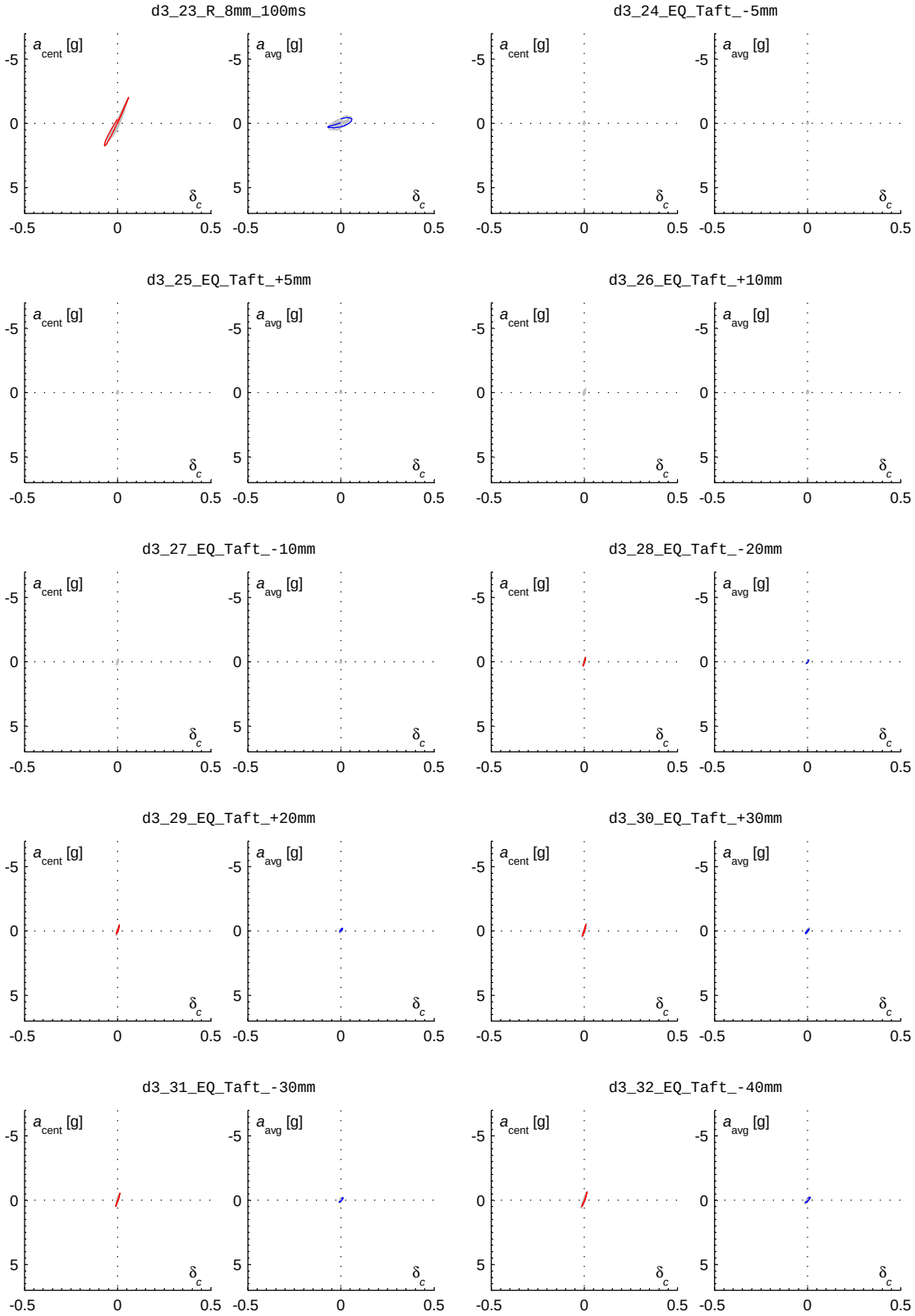
d3_23_R_8mm_100ms
d3_24_EQ_Taft_-5mm
d3_25_EQ_Taft_+5mm
d3_26_EQ_Taft_+10mm
d3_27_EQ_Taft_-10mm
d3_28_EQ_Taft_-20mm
d3_29_EQ_Taft_+20mm
d3_30_EQ_Taft_+30mm
d3_31_EQ_Taft_-30mm
d3_32_EQ_Taft_-40mm
a cent [g]
a avg [g]
δ c
-5
0
5
-0.5
0
0.5

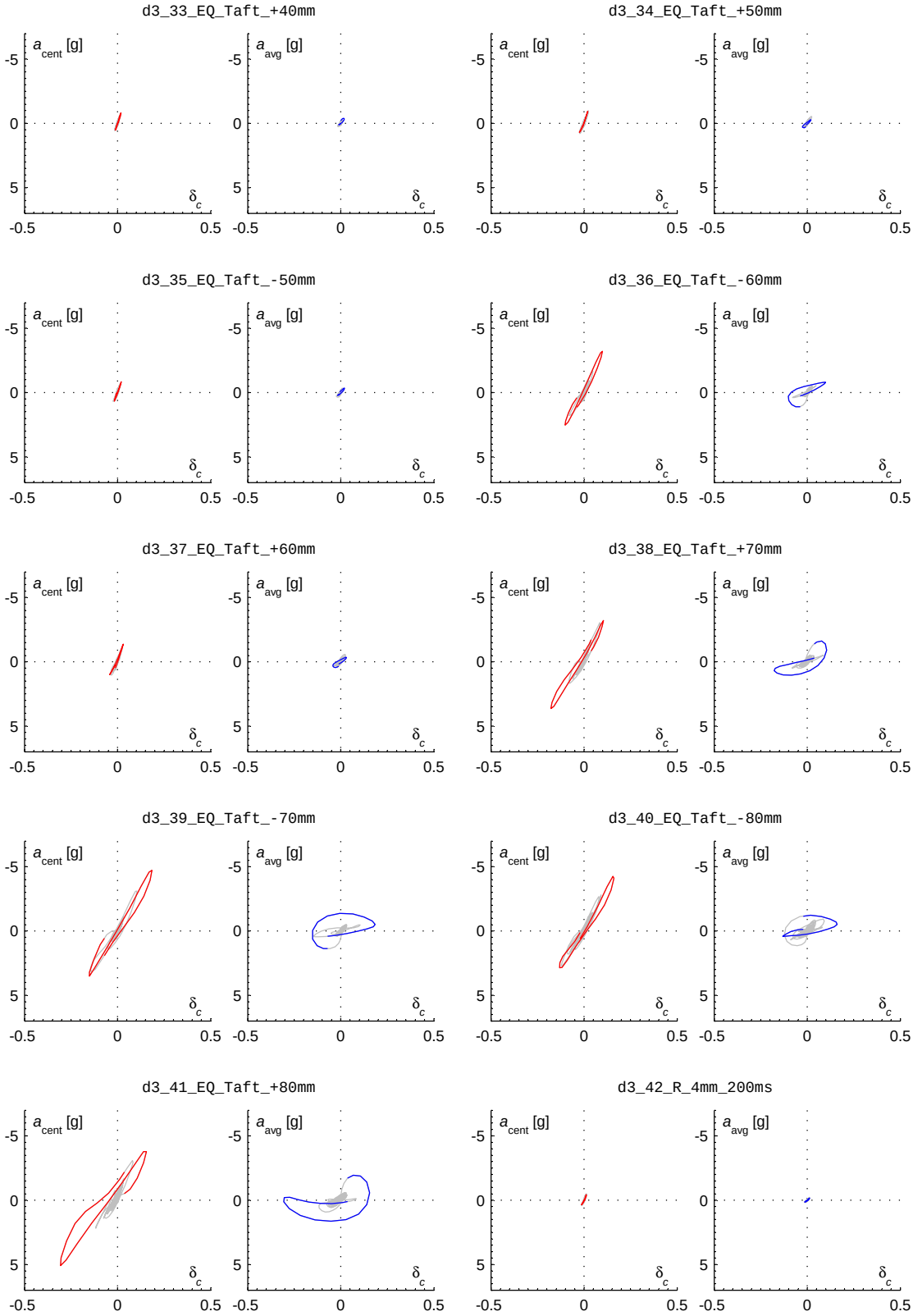
d3_33_EQ_Taft_+40mm
d3_34_EQ_Taft_+50mm
d3_35_EQ_Taft_-50mm
d3_36_EQ_Taft_-60mm
d3_37_EQ_Taft_+60mm
d3_38_EQ_Taft_+70mm
d3_39_EQ_Taft_-70mm
d3_40_EQ_Taft_-80mm
d3_41_EQ_Taft_+80mm
d3_42_R_4mm_200ms
a cent [g]
a avg [g]
δc
-5
0
5
-0.5
0
0.5

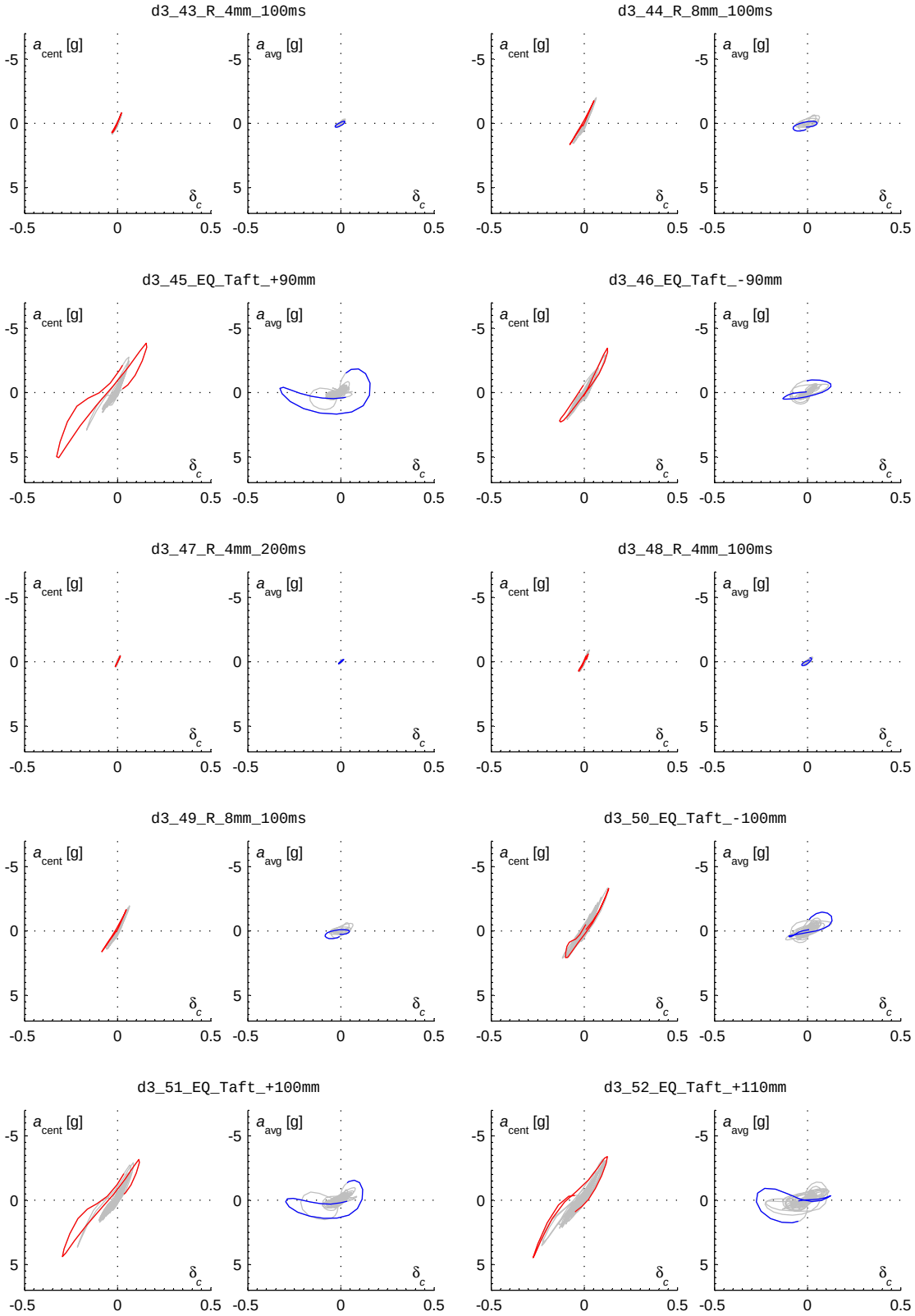
d3_43_R_4mm_100ms
d3_44_R_8mm_100ms
d3_45_EQ_Taft_+90mm
d3_46_EQ_Taft_-90mm
d3_47_R_4mm_200ms
d3_48_R_4mm_100ms
d3_49_R_8mm_100ms
d3_50_EQ_Taft_-100mm
d3_51_EQ_Taft_+100mm
d3_52_EQ_Taft_+110mm
a cent [g]
a avg [g]
δ c
-5
0
5
-0.5
0
0.5

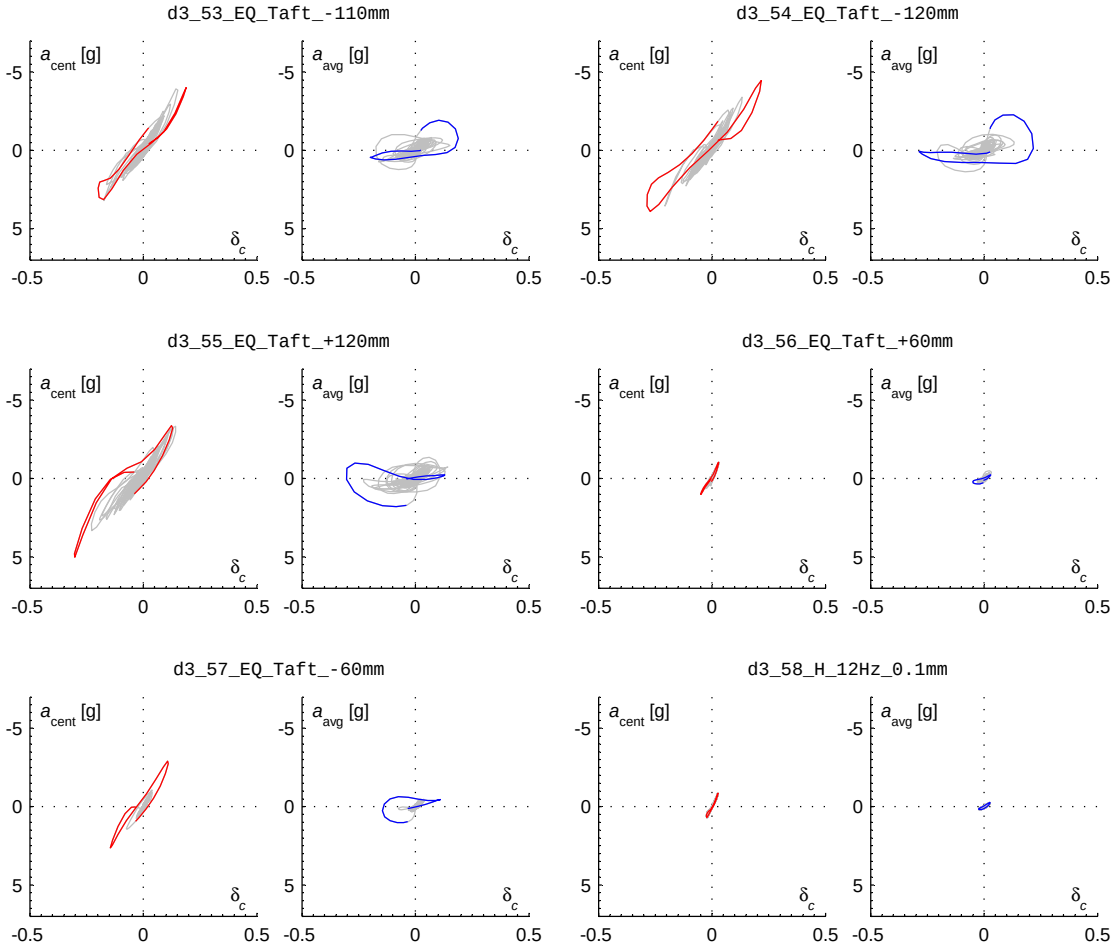
d3_53_EQ_Taft_-110mm
d3_54_EQ_Taft_-120mm
d3_55_EQ_Taft_+120mm
d3_56_EQ_Taft_+60mm
d3_57_EQ_Taft_-60mm
d3_58_H_12Hz_0.1mm
a cent [g]
a avg [g]
δc
-5
0
5
-0.5
0
0.5

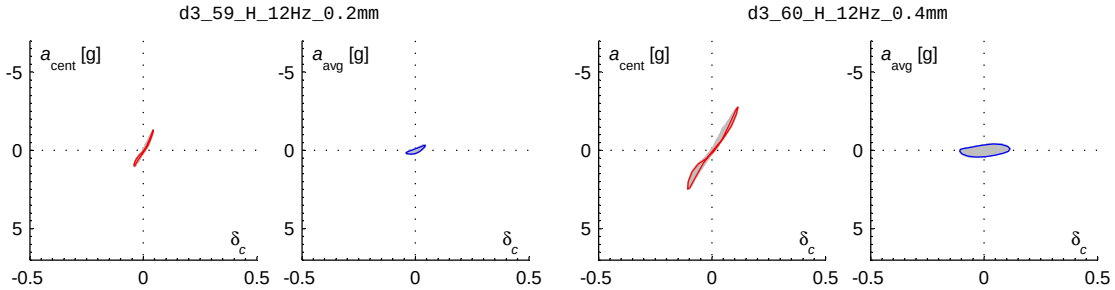
d3_59_H_12Hz_0.2mm
d3_60_H_12Hz_0.4mm
a cent [g]
a avg [g]
δc
-5
0
5
-0.5
0
0.5

C.6.4 Wall D4

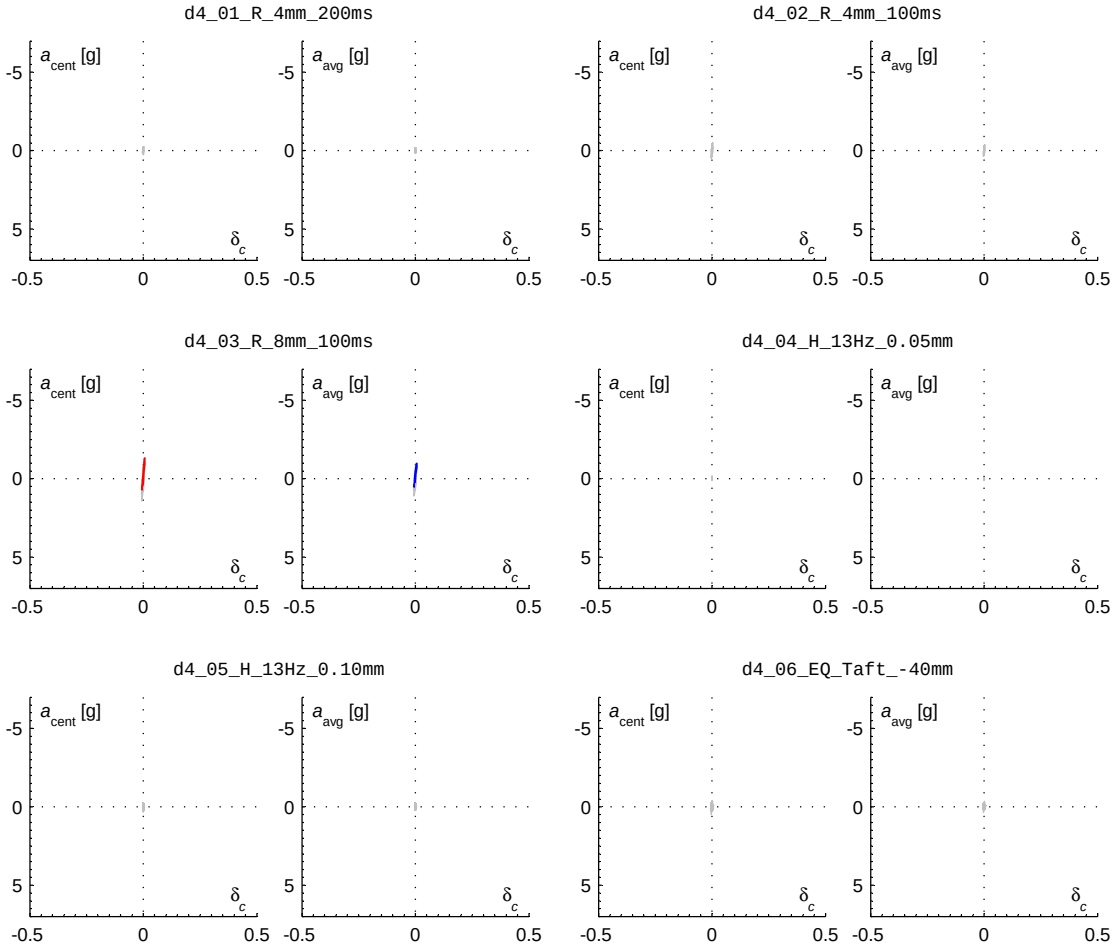
d4_01_R_4mm_200ms
d4_02_R_4mm_100ms
d4_03_R_8mm_100ms
d4_04_H_13Hz_0.05mm
d4_05_H_13Hz_0.10mm
d4_06_EQ_Taft_-40mm
a cent [g]
a avg [g]
δc
-5
0
5
-0.5
0
0.5

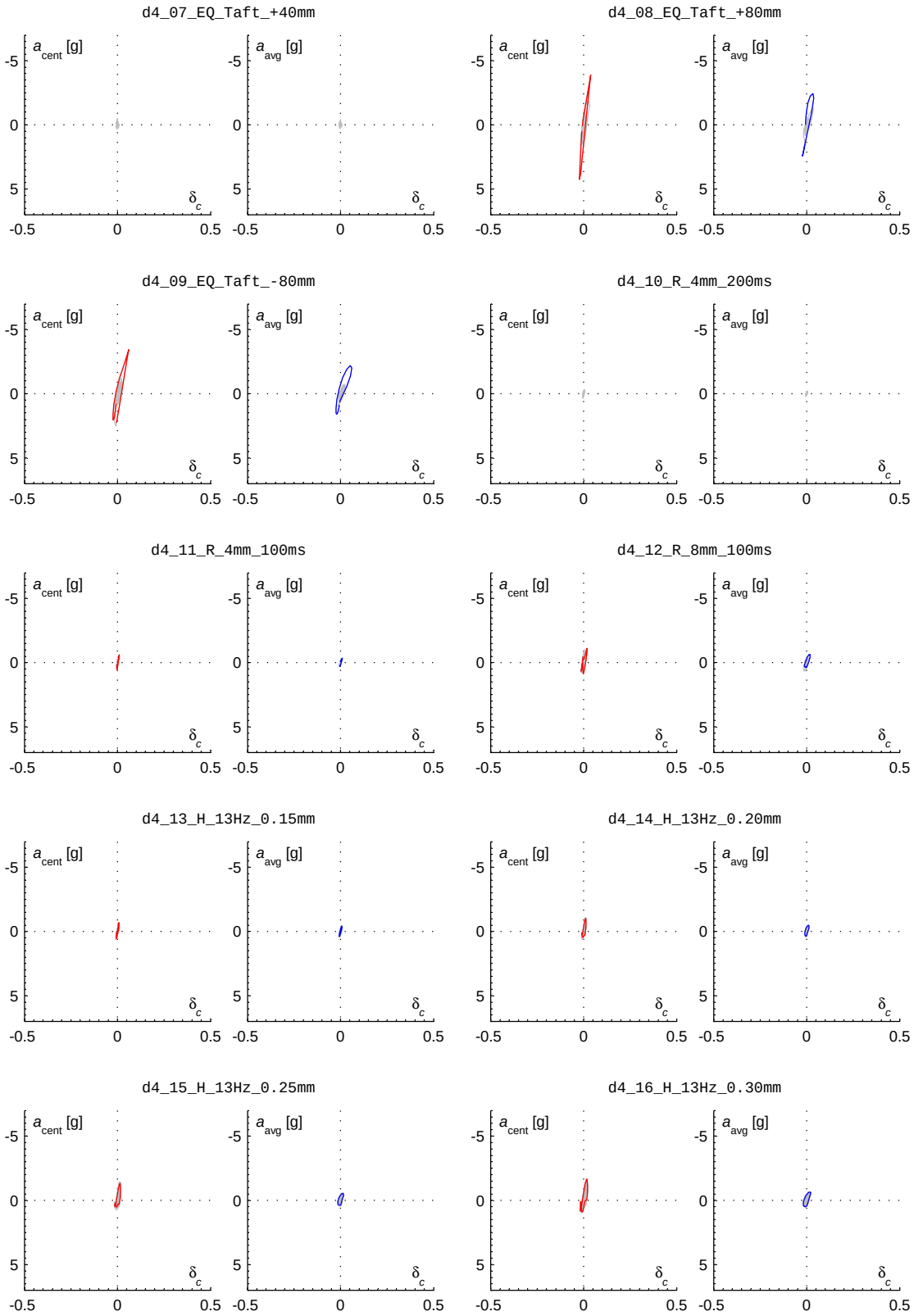
d4_07_EQ_Taft_+40mm
d4_08_EQ_Taft_+80mm
d4_09_EQ_Taft_-80mm
d4_10_R_4mm_200ms
d4_11_R_4mm_100ms
d4_12_R_8mm_100ms
d4_13_H_13Hz_0.15mm
d4_14_H_13Hz_0.20mm
d4_15_H_13Hz_0.25mm
d4_16_H_13Hz_0.30mm
a cent [g]
a avg [g]
δc
-5
0
5
-0.5
0
0.5

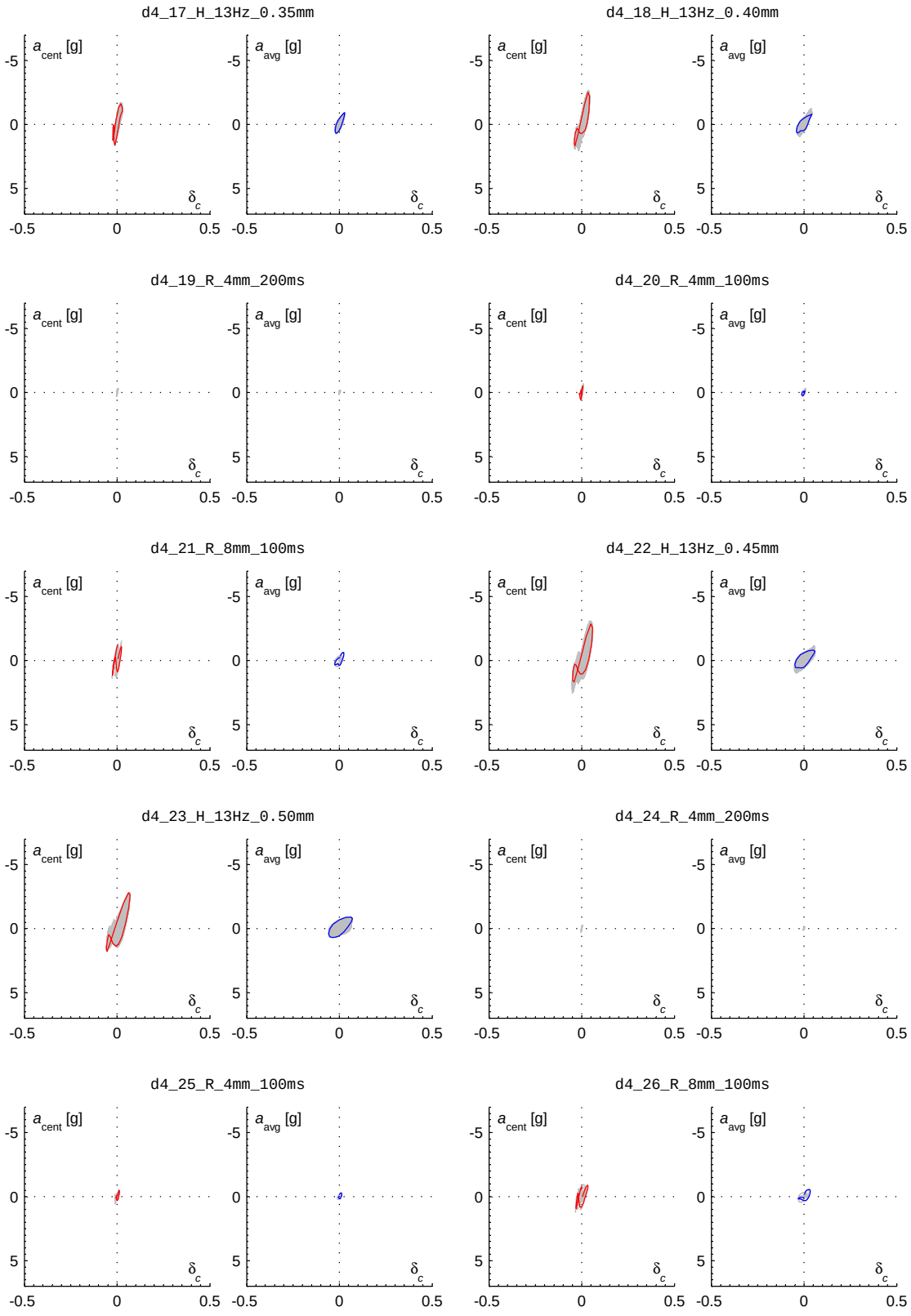
d4_17_H_13Hz_0.35mm
d4_18_H_13Hz_0.40mm
d4_19_R_4mm_200ms
d4_20_R_4mm_100ms
d4_21_R_8mm_100ms
d4_22_H_13Hz_0.45mm
d4_23_H_13Hz_0.50mm
d4_24_R_4mm_200ms
d4_25_R_4mm_100ms
d4_26_R_8mm_100ms
a cent [g]
a avg [g]
δc
-5
0
5
-0.5
0
0.5

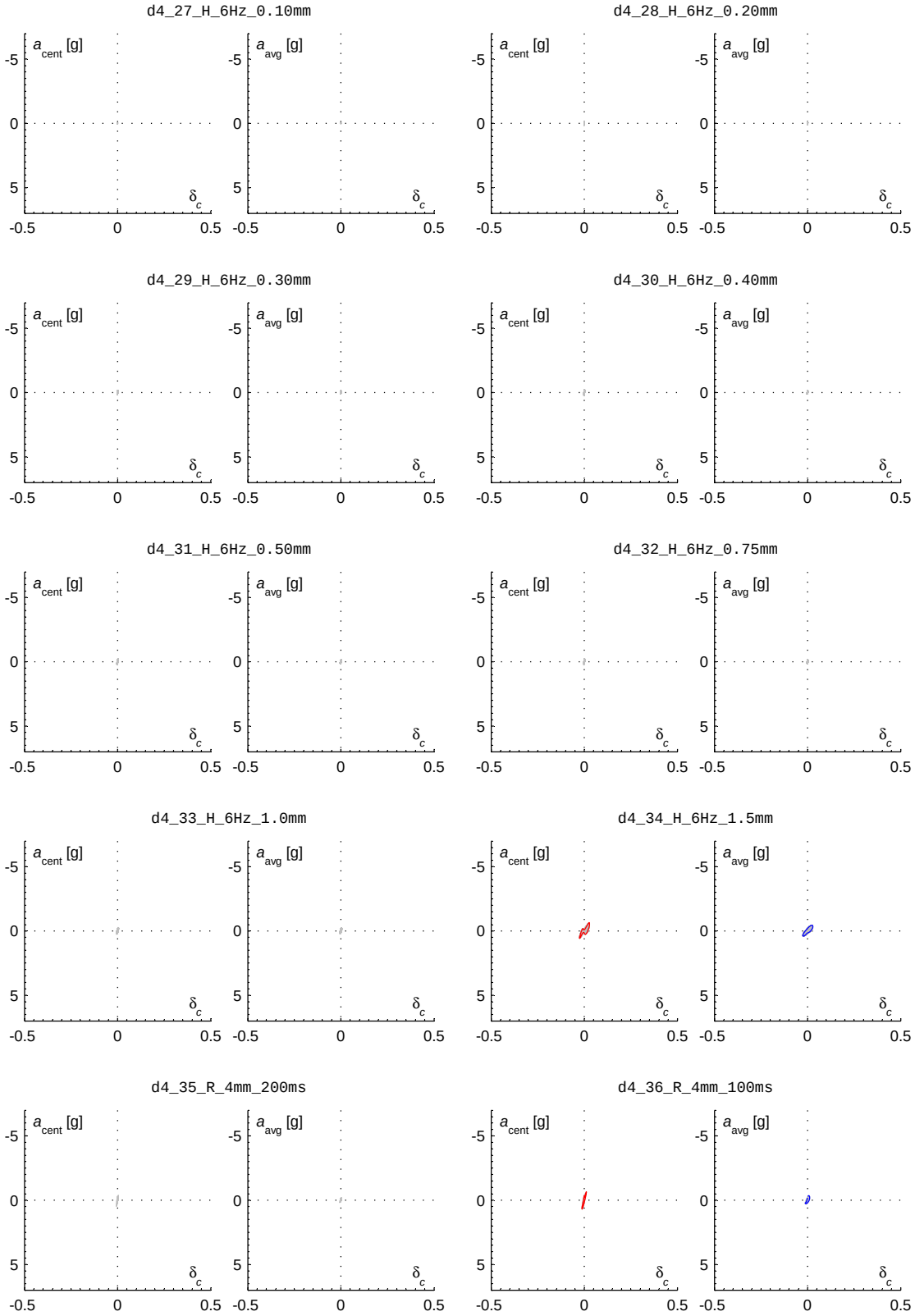
d4_27_H_6Hz_0.10mm
d4_28_H_6Hz_0.20mm
d4_29_H_6Hz_0.30mm
d4_30_H_6Hz_0.40mm
d4_31_H_6Hz_0.50mm
d4_32_H_6Hz_0.75mm
d4_33_H_6Hz_1.0mm
d4_34_H_6Hz_1.5mm
d4_35_R_4mm_200ms
d4_36_R_4mm_100ms
a cent [g]
a avg [g]
δ c
-5
0
5
-0.5
0
0.5

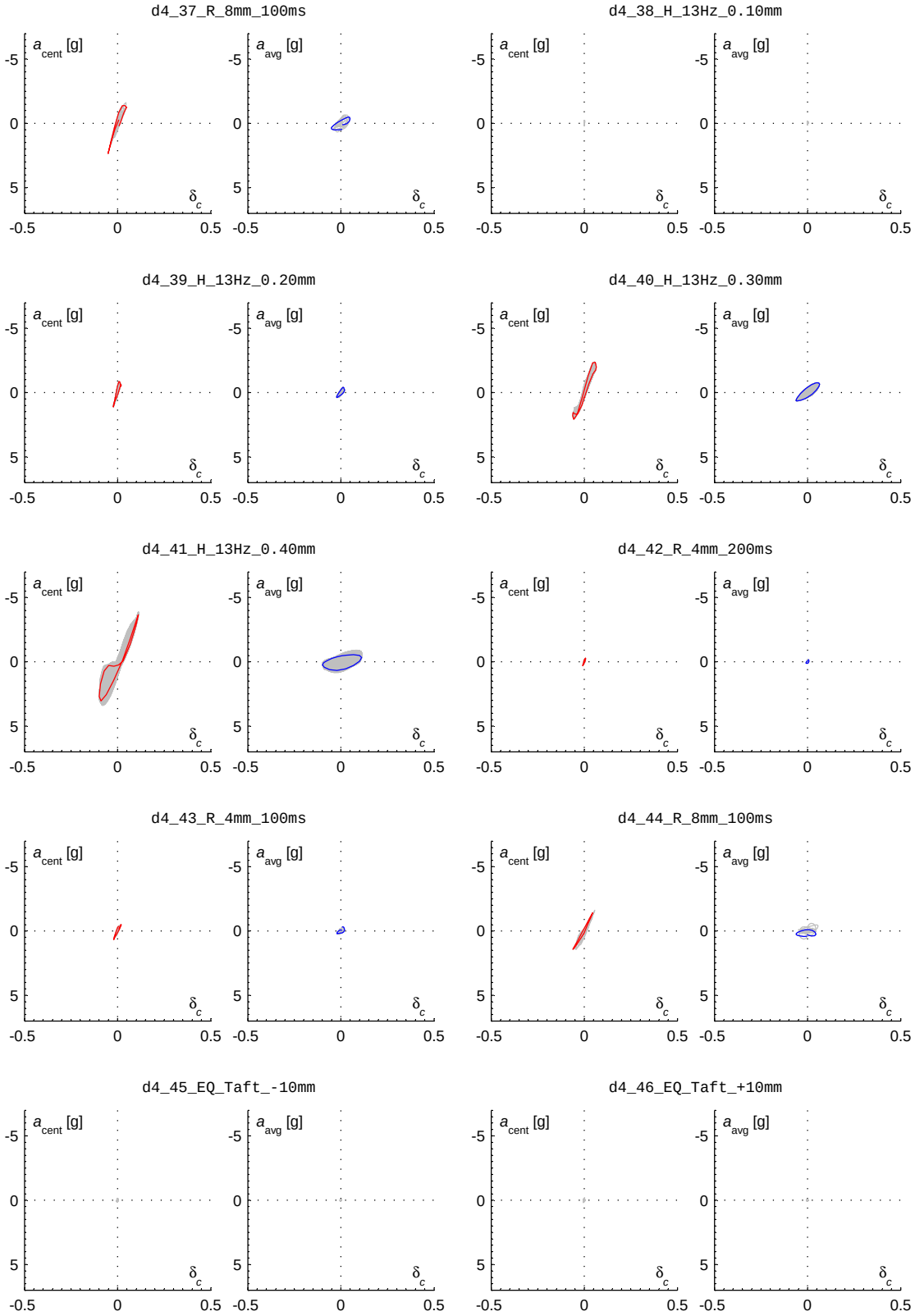
d4_37_R_8mm_100ms
d4_38_H_13Hz_0.10mm
d4_39_H_13Hz_0.20mm
d4_40_H_13Hz_0.30mm
d4_41_H_13Hz_0.40mm
d4_42_R_4mm_200ms
d4_43_R_4mm_100ms
d4_44_R_8mm_100ms
d4_45_EQ_Taft_-10mm
d4_46_EQ_Taft_+10mm
a cent [g]
a avg [g]
δc
-5
0
5
-0.5
0
0.5

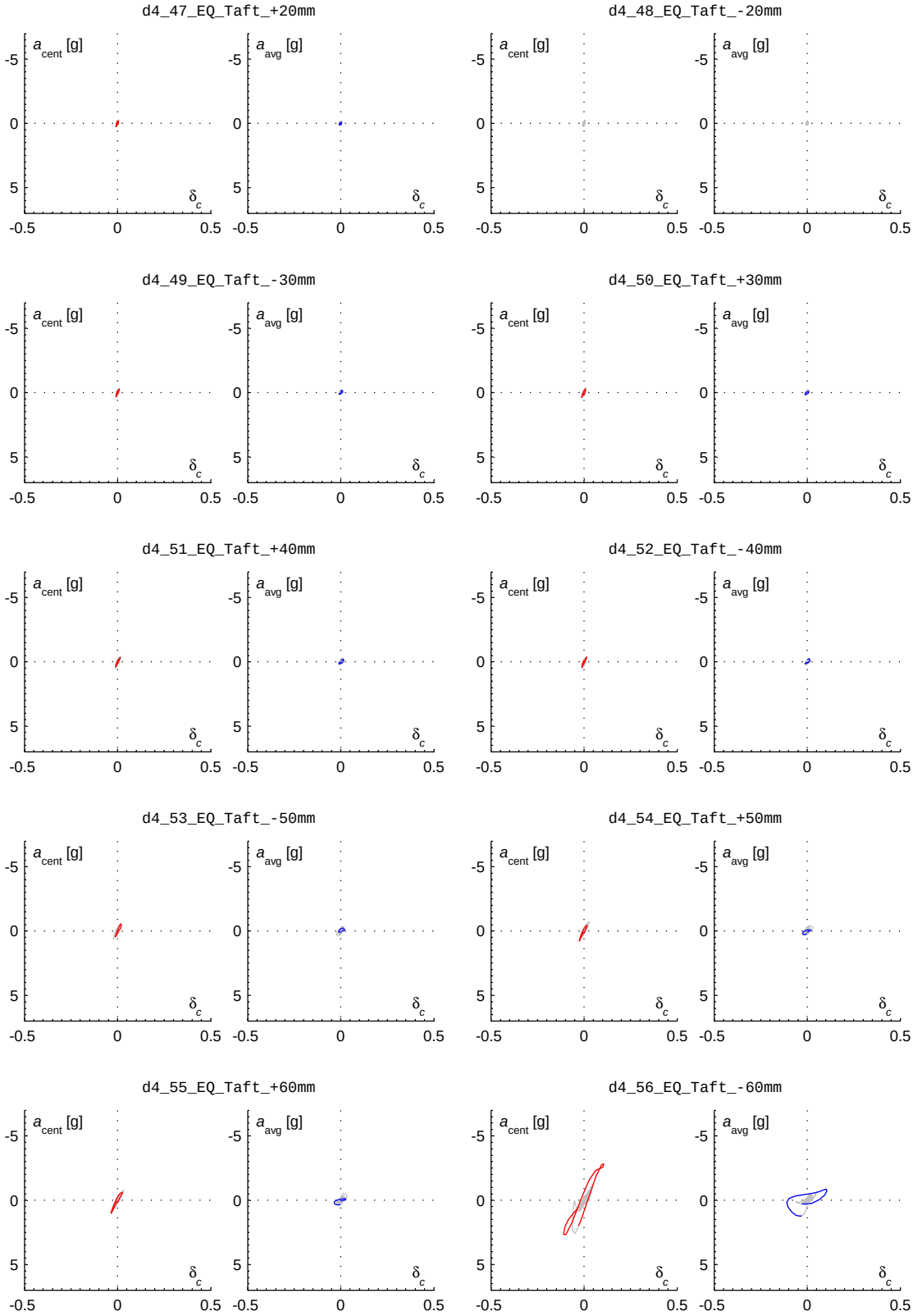
d4_47_EQ_Taft_+20mm
d4_48_EQ_Taft_-20mm
d4_49_EQ_Taft_-30mm
d4_50_EQ_Taft_+30mm
d4_51_EQ_Taft_+40mm
d4_52_EQ_Taft_-40mm
d4_53_EQ_Taft_-50mm
d4_54_EQ_Taft_+50mm
d4_55_EQ_Taft_+60mm
d4_56_EQ_Taft_-60mm
a cent [g]
a avg [g]
δ c
-5
0
5
-0.5
0
0.5

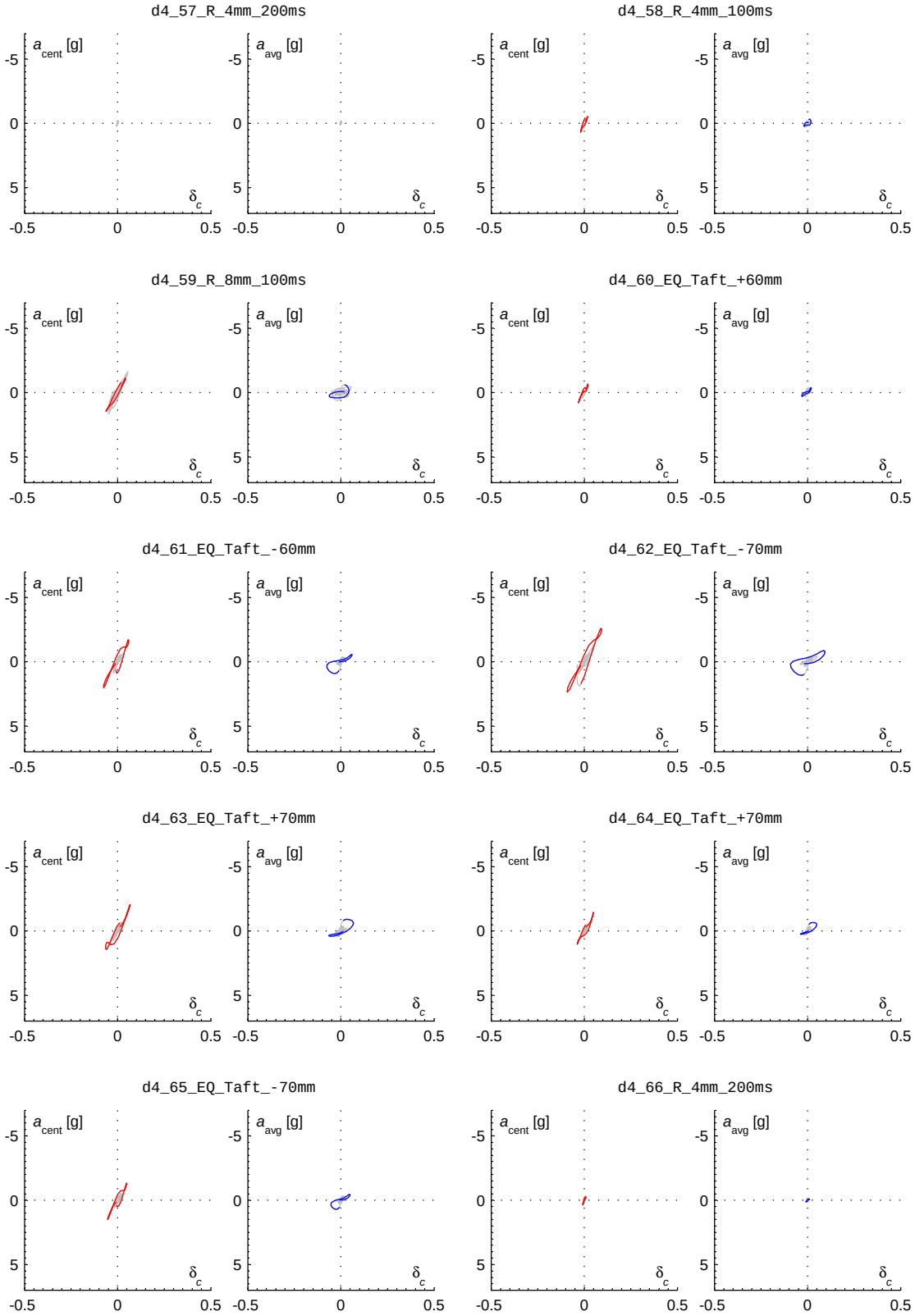
d4_57_R_4mm_200ms
d4_58_R_4mm_100ms
d4_59_R_8mm_100ms
d4_60_EQ_Taft_+60mm
d4_61_EQ_Taft_-60mm
d4_62_EQ_Taft_-70mm
d4_63_EQ_Taft_+70mm
d4_64_EQ_Taft_+70mm
d4_65_EQ_Taft_-70mm
d4_66_R_4mm_200ms
a cent [g]
a avg [g]
δc
-5
0
5
-0.5
0
0.5

d4_67_R_4mm_100ms

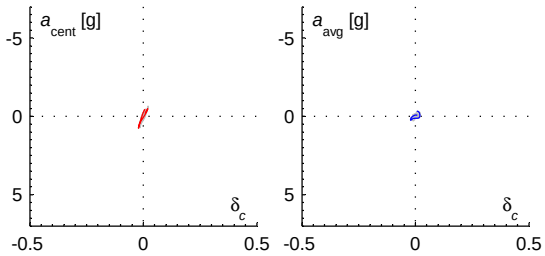

d4_68_R_8mm_100ms

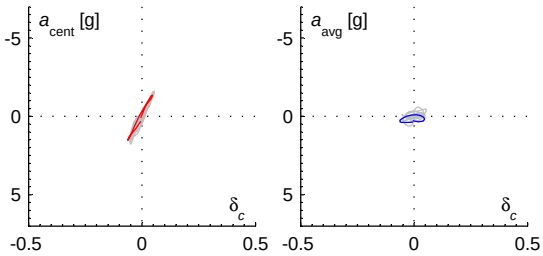

d4_69_EQ_Taft_+70mm

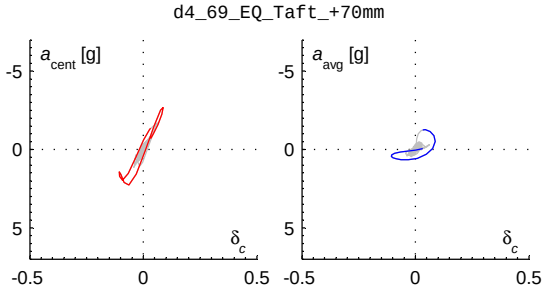

d4_70_EQ_Taft_-70mm

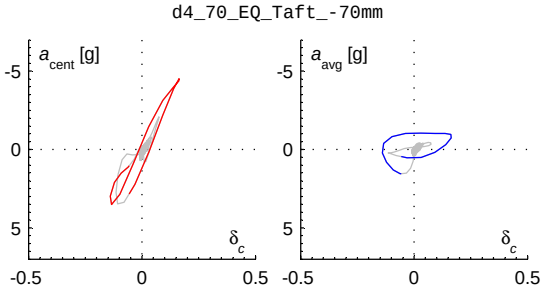

d4_71_EQ_Taftbf05_-70mm

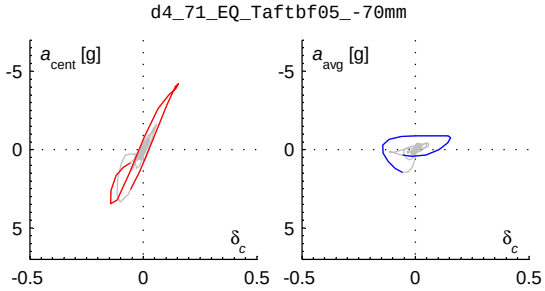

d4_72_EQ_Taftbf05_+70mm

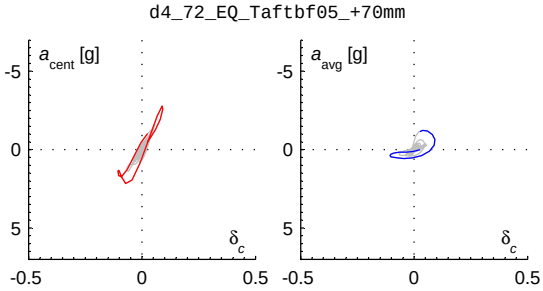

d4_73_EQ_Taftbf10_+70mm

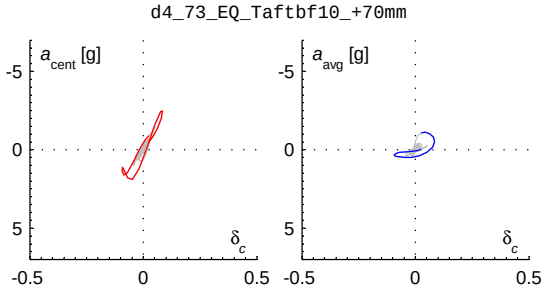

d4_74_EQ_Taftbf10_-70mm

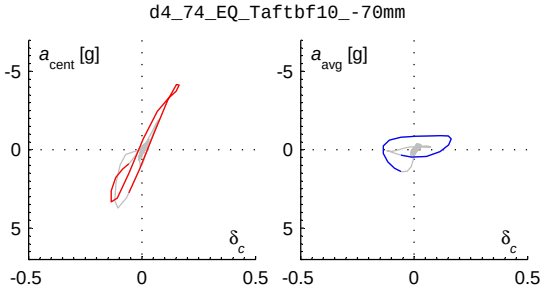

d4_75_EQ_Taftbf20_-70mm

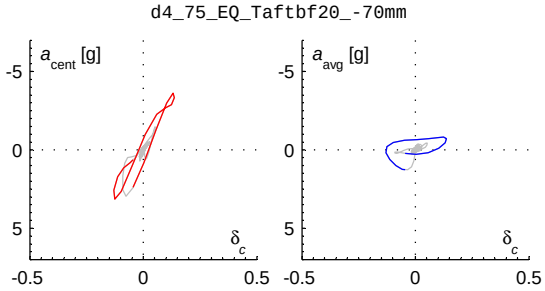

d4_76_EQ_Taftbf20_+70mm

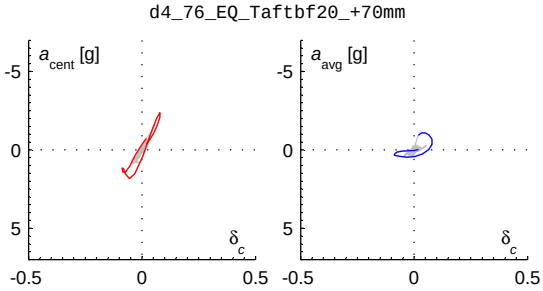

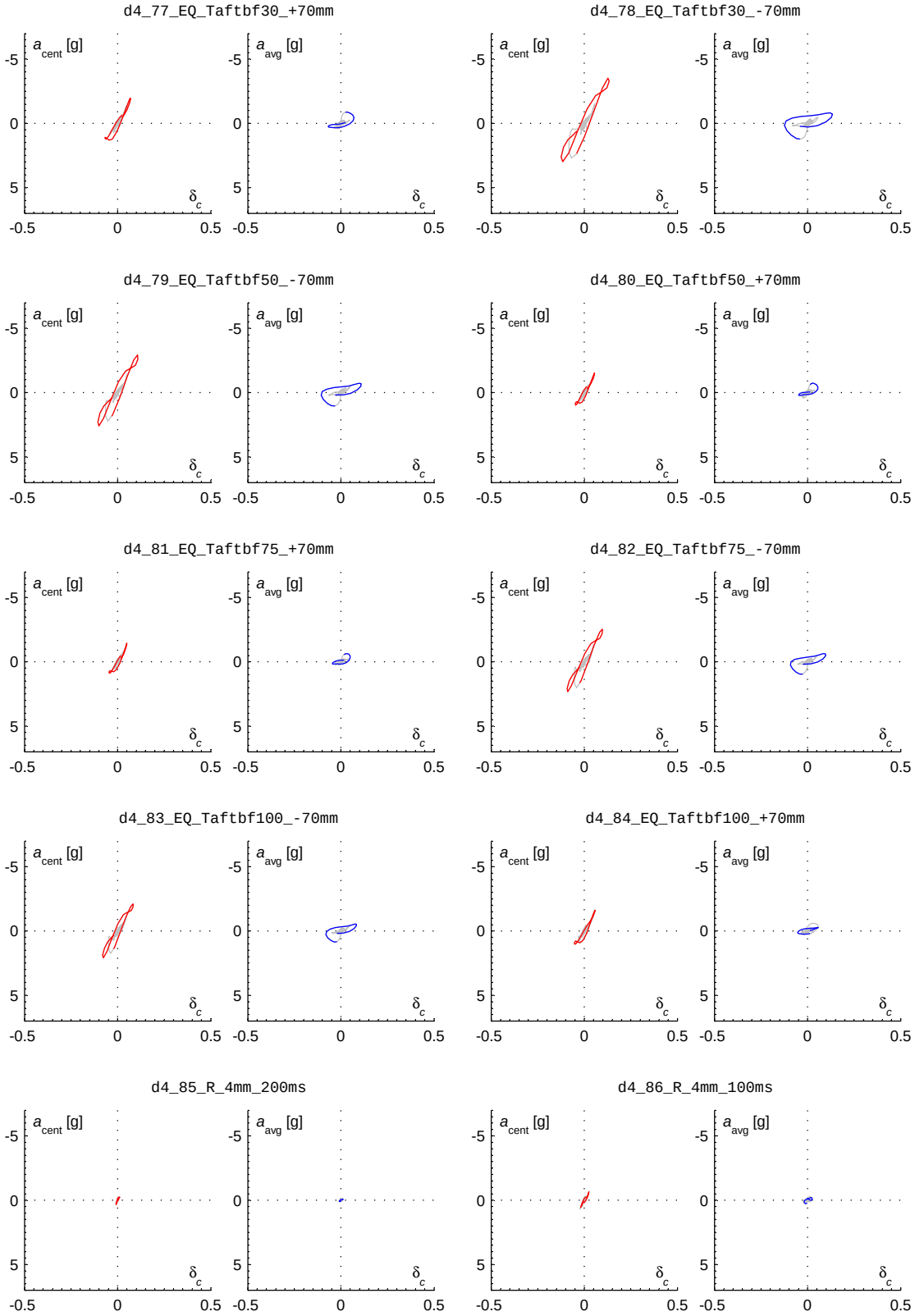
d4_77_EQ_Taftbf30_+70mm
d4_78_EQ_Taftbf30_-70mm
d4_79_EQ_Taftbf50_-70mm
d4_80_EQ_Taftbf50_+70mm
d4_81_EQ_Taftbf75_+70mm
d4_82_EQ_Taftbf75_-70mm
d4_83_EQ_Taftbf100_-70mm
d4_84_EQ_Taftbf100_+70mm
d4_85_R_4mm_200ms
d4_86_R_4mm_100ms
a cent [g]
a avg [g]
δc
-5
0
5
-0.5
0
0.5

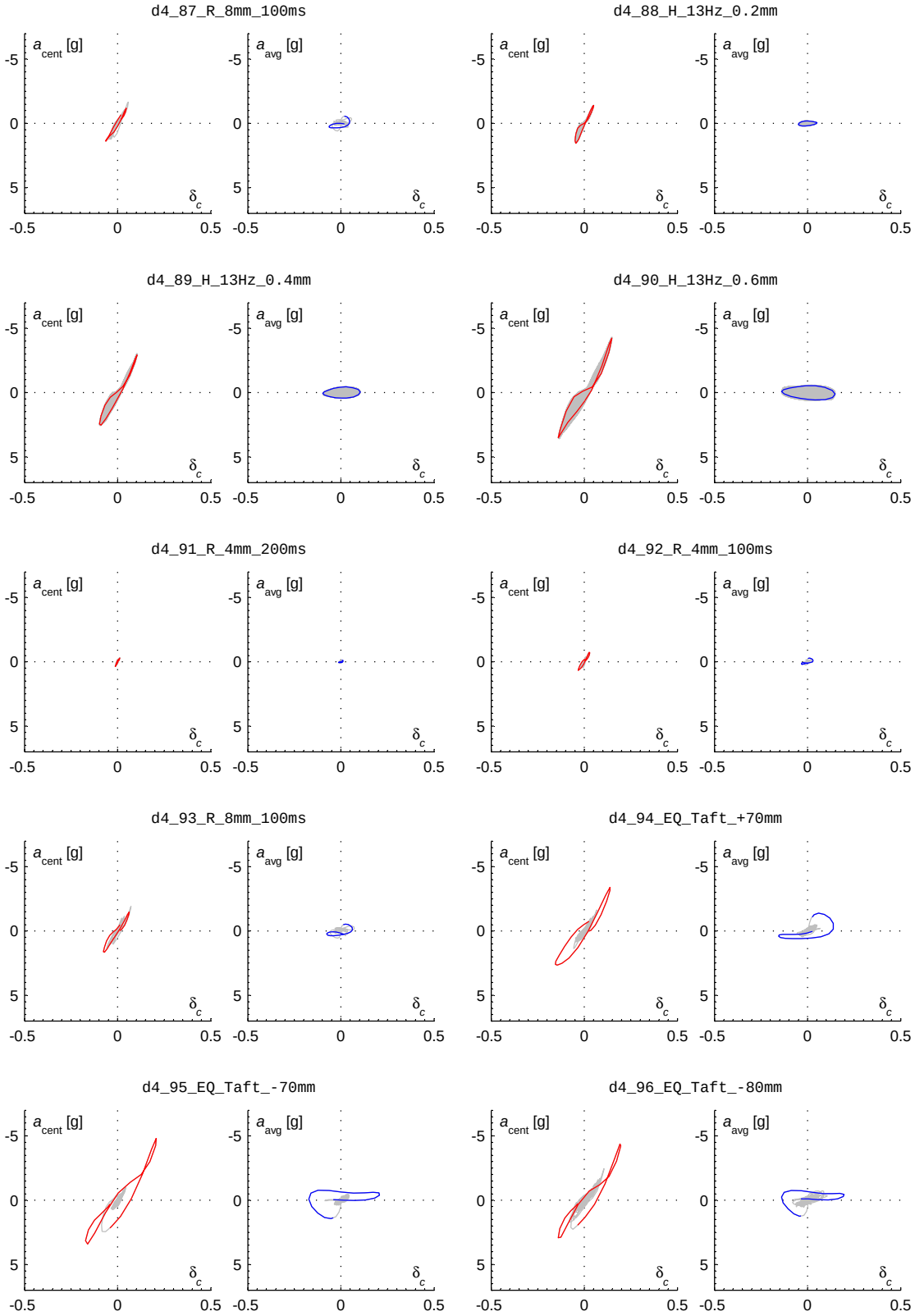
d4_87_R_8mm_100ms
d4_88_H_13Hz_0.2mm
d4_89_H_13Hz_0.4mm
d4_90_H_13Hz_0.6mm
d4_91_R_4mm_200ms
d4_92_R_4mm_100ms
d4_93_R_8mm_100ms
d4_94_EQ_Taft_+70mm
d4_95_EQ_Taft_-70mm
d4_96_EQ_Taft_-80mm
a cent [g]
a avg [g]
δ c
-5
0
5
-0.5
0
0.5

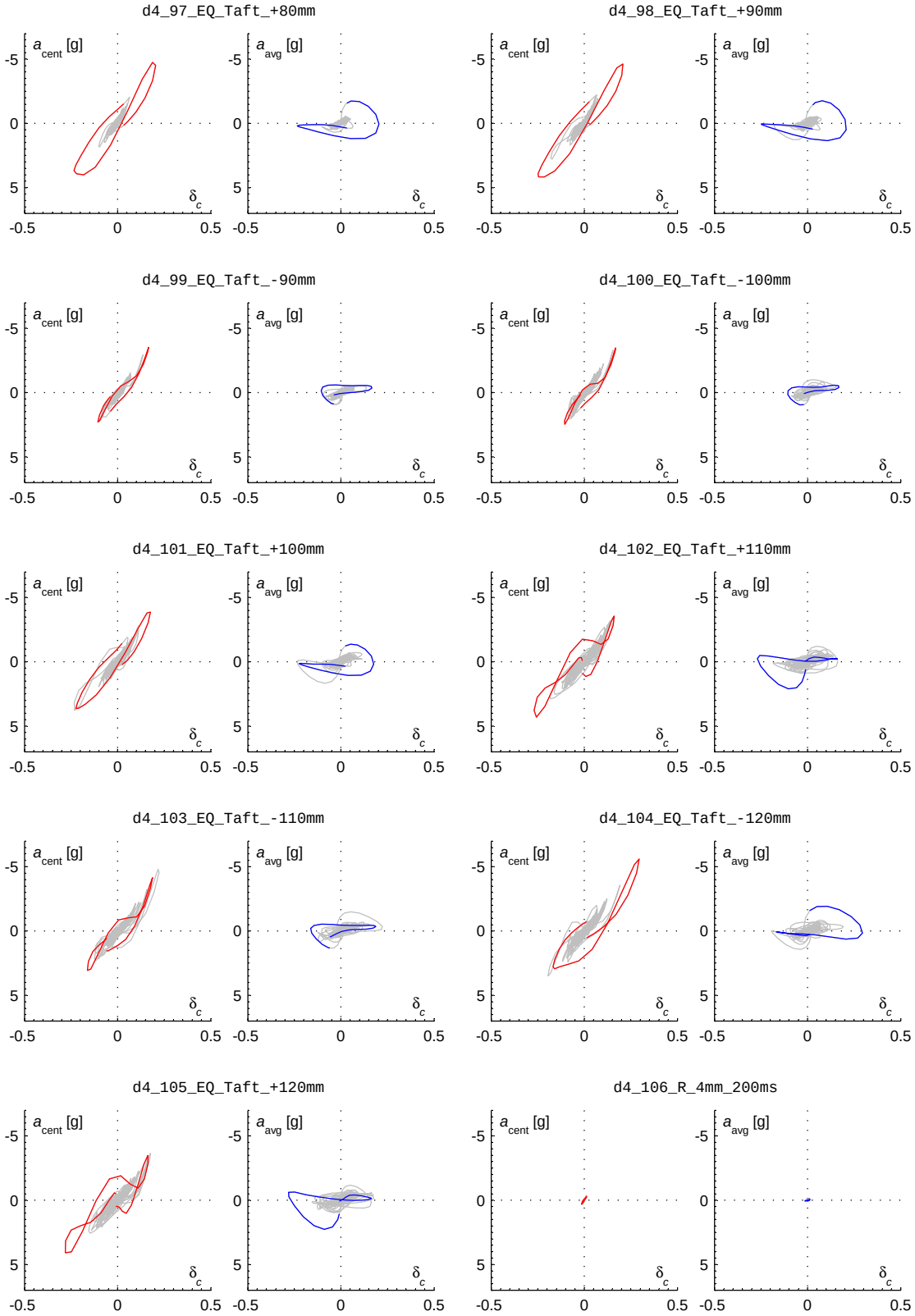
d4_97_EQ_Taft_+80mm
d4_98_EQ_Taft_+90mm
d4_99_EQ_Taft_-90mm
d4_100_EQ_Taft_-100mm
d4_101_EQ_Taft_+100mm
d4_102_EQ_Taft_+110mm
d4_103_EQ_Taft_-110mm
d4_104_EQ_Taft_-120mm
d4_105_EQ_Taft_+120mm
d4_106_R_4mm_200ms
a cent [g]
a avg [g]
δc
-5
0
5
-0.5
0
0.5

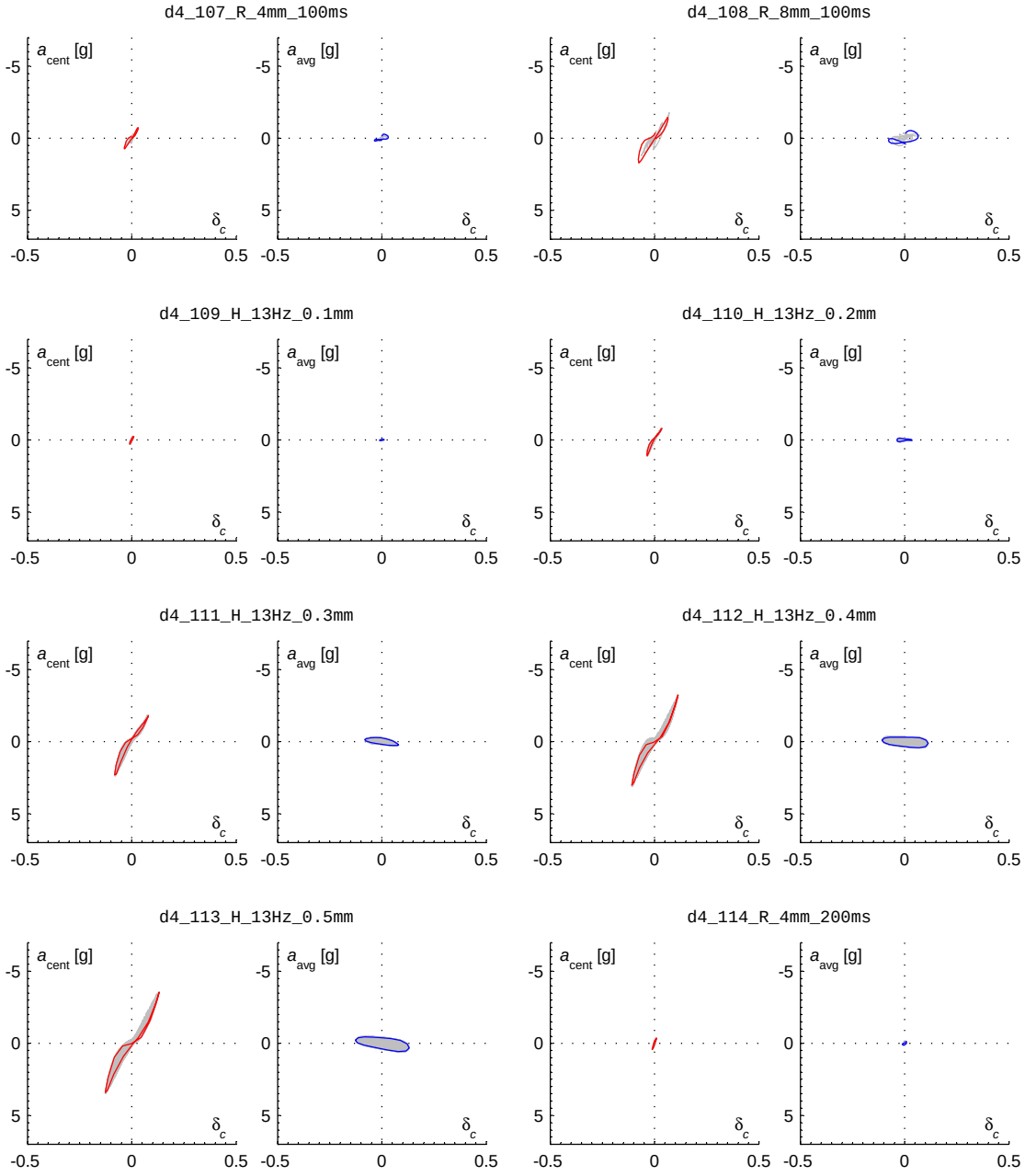
d4_107_R_4mm_100ms
d4_108_R_8mm_100ms
d4_109_H_13Hz_0.1mm
d4_110_H_13Hz_0.2mm
d4_111_H_13Hz_0.3mm
d4_112_H_13Hz_0.4mm
d4_113_H_13Hz_0.5mm
d4_114_R_4mm_200ms
a cent [g]
a avg [g]
δ c
-5
0
5
-0.5
0
0.5

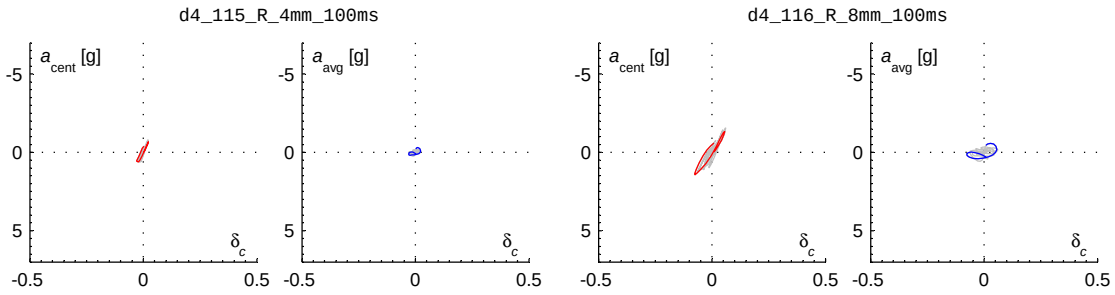
d4_115_R_4mm_100ms
d4_116_R_8mm_100ms
a cent [g]
a avg [g]
δc
-5
0
5
-0.5
0
0.5

C.6.5 Wall D5

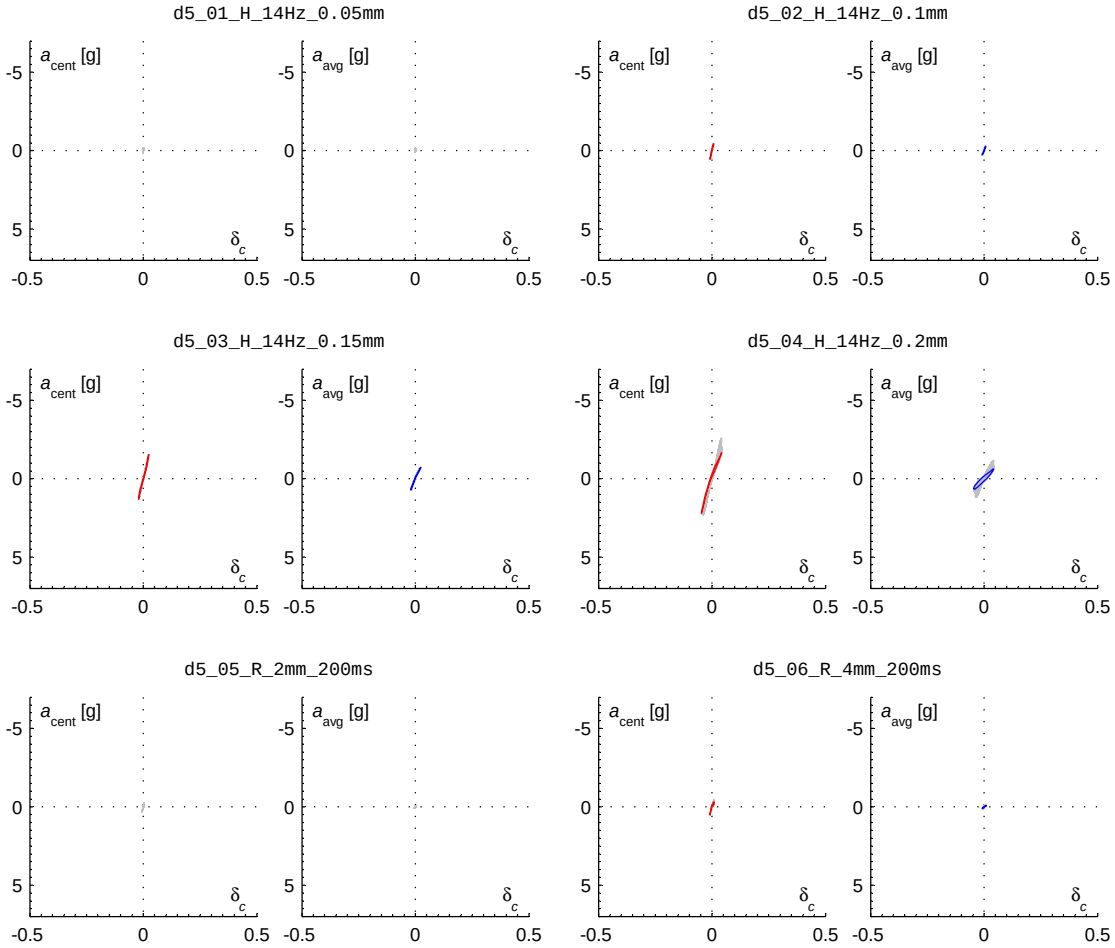
d5_01_H_14Hz_0.05mm
d5_02_H_14Hz_0.1mm
d5_03_H_14Hz_0.15mm
d5_04_H_14Hz_0.2mm
d5_05_R_2mm_200ms
d5_06_R_4mm_200ms
a cent [g]
a avg [g]
δc
-5
0
5
-0.5
0
0.5

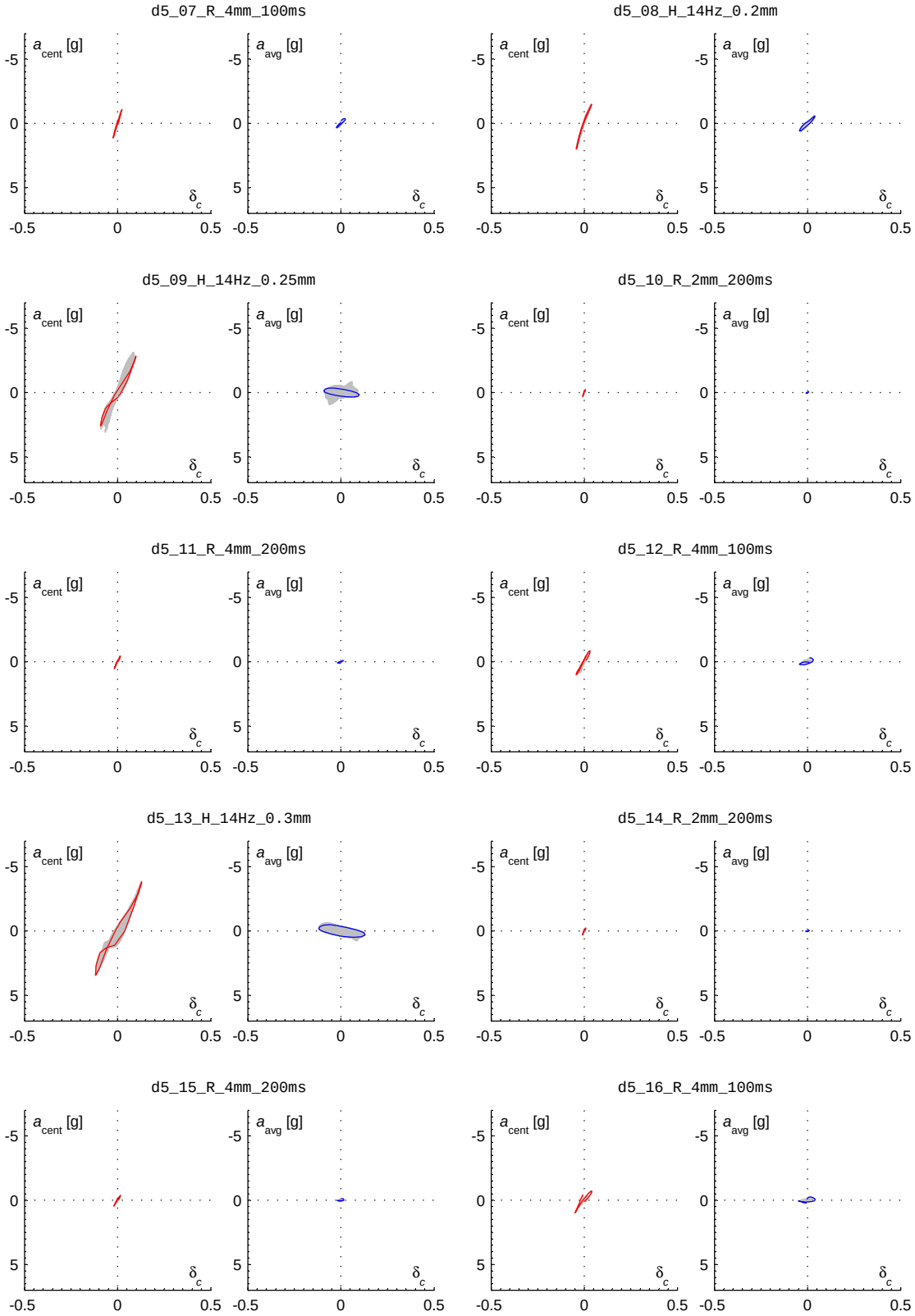
d5_07_R_4mm_100ms
d5_08_H_14Hz_0.2mm
d5_09_H_14Hz_0.25mm
d5_10_R_2mm_200ms
d5_11_R_4mm_200ms
d5_12_R_4mm_100ms
d5_13_H_14Hz_0.3mm
d5_14_R_2mm_200ms
d5_15_R_4mm_200ms
d5_16_R_4mm_100ms
a cent [g]
a avg [g]
δc
-5
0
5
-0.5
0
0.5

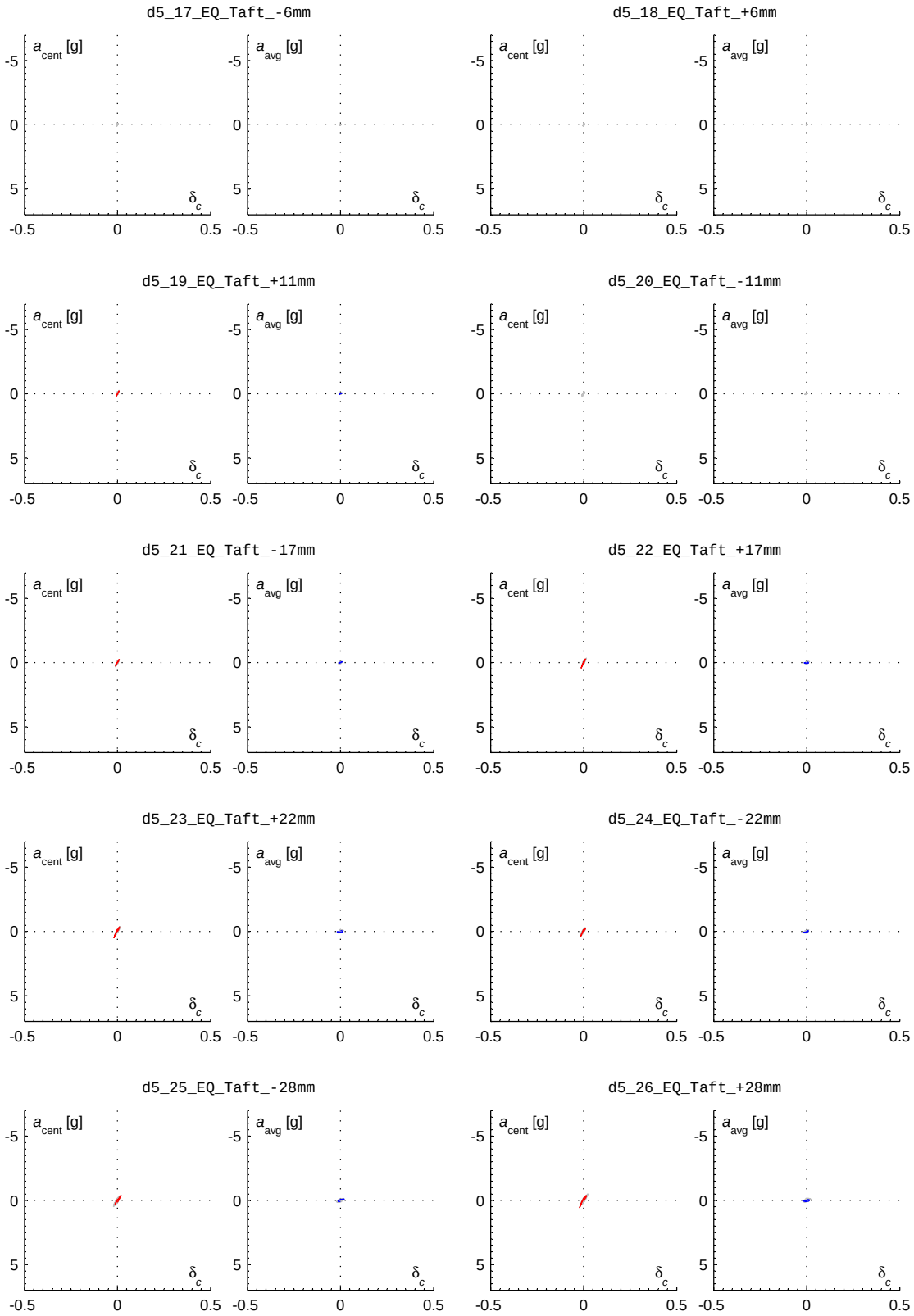
d5_17_EQ_Taft_-6mm
d5_18_EQ_Taft_+6mm
d5_19_EQ_Taft_+11mm
d5_20_EQ_Taft_-11mm
d5_21_EQ_Taft_-17mm
d5_22_EQ_Taft_+17mm
d5_23_EQ_Taft_+22mm
d5_24_EQ_Taft_-22mm
d5_25_EQ_Taft_-28mm
d5_26_EQ_Taft_+28mm
a cent [g]
a avg [g]
δc
-5
0
5
-0.5
0
0.5

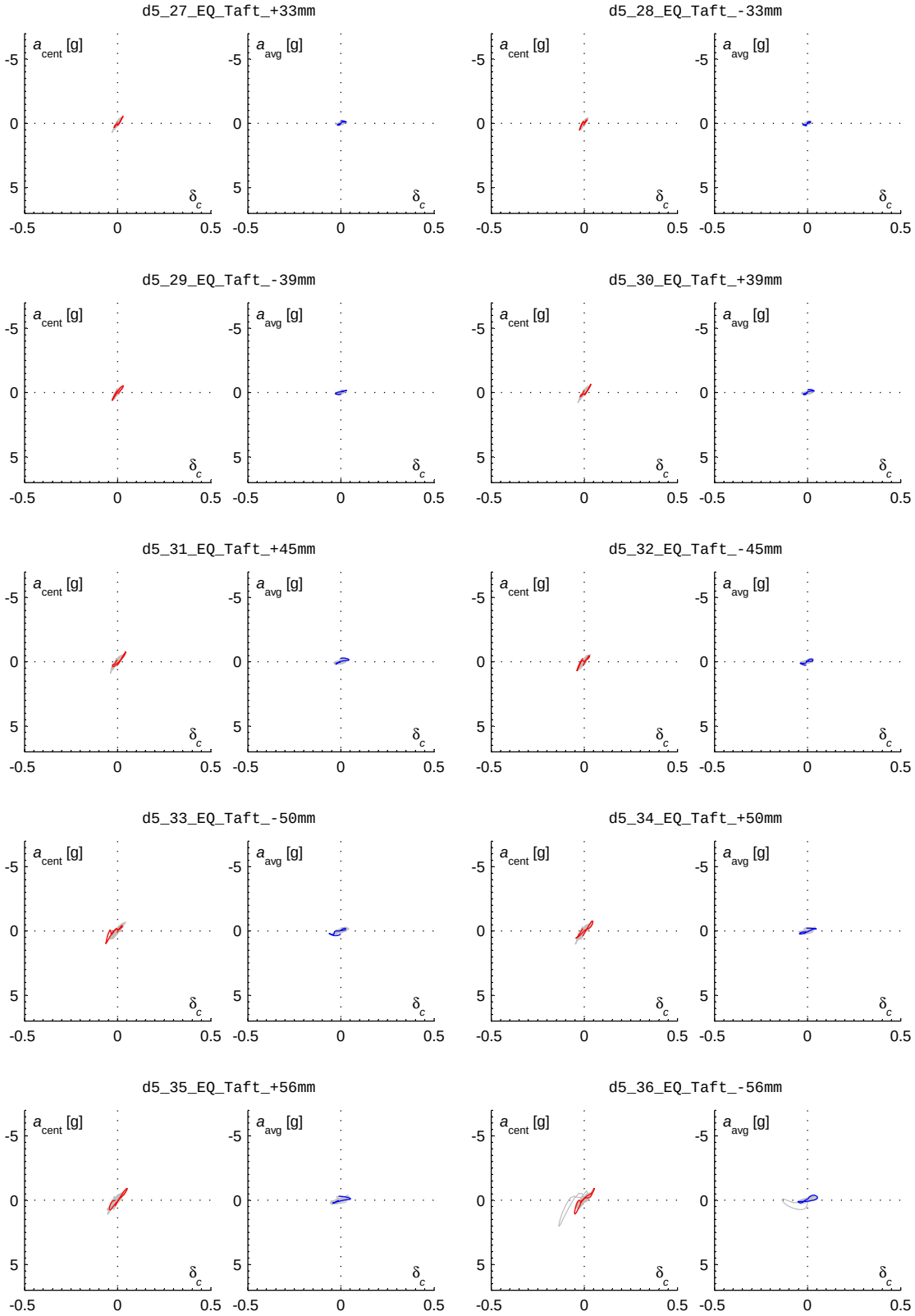
d5_27_EQ_Taft_+33mm
d5_28_EQ_Taft_-33mm
d5_29_EQ_Taft_-39mm
d5_30_EQ_Taft_+39mm
d5_31_EQ_Taft_+45mm
d5_32_EQ_Taft_-45mm
d5_33_EQ_Taft_-50mm
d5_34_EQ_Taft_+50mm
d5_35_EQ_Taft_+56mm
d5_36_EQ_Taft_-56mm
a cent [g]
a avg [g]
δc
-5
0
5
-0.5
0
0.5

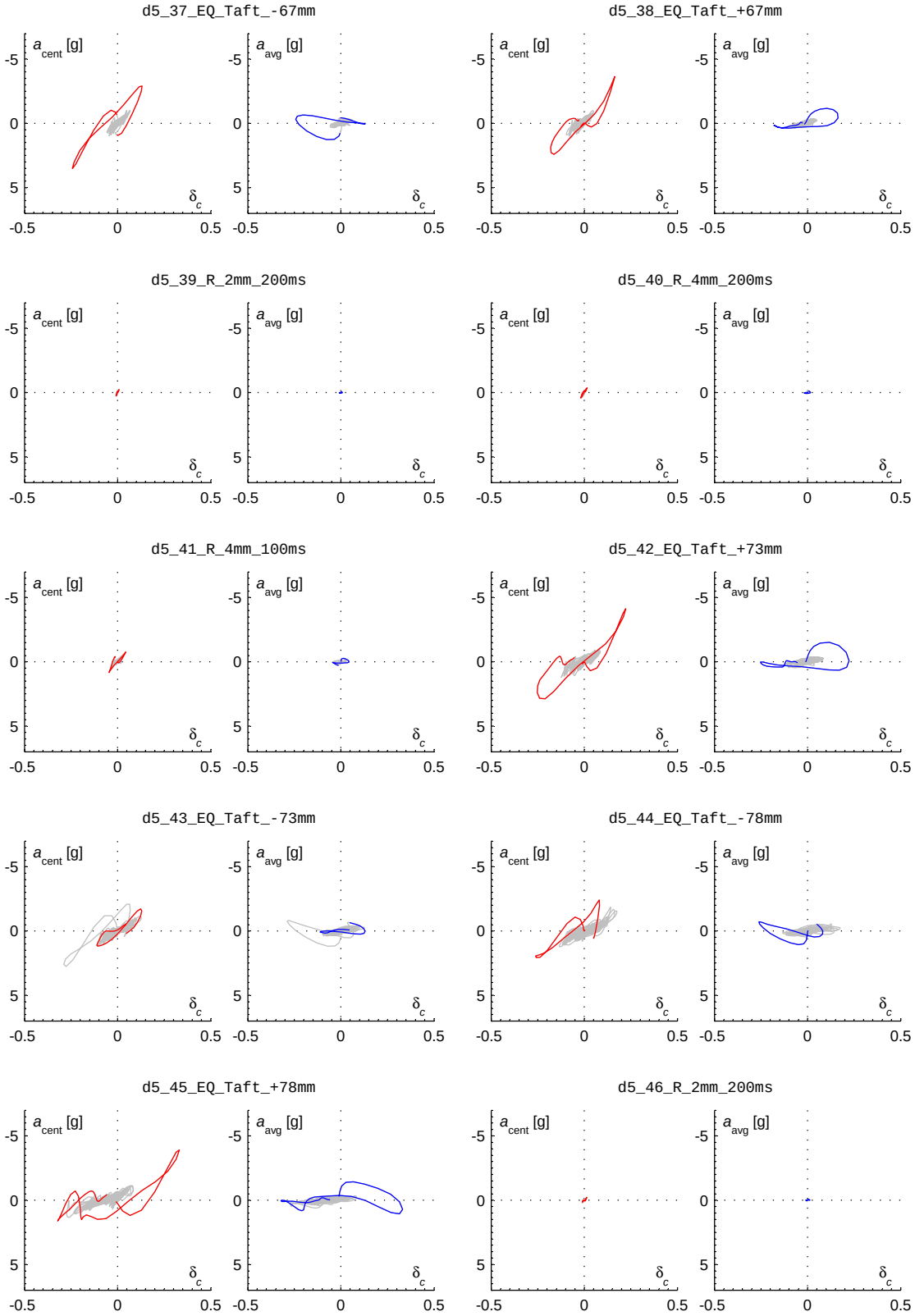
d5_37_EQ_Taft_-67mm
d5_38_EQ_Taft_+67mm
d5_39_R_2mm_200ms
d5_40_R_4mm_200ms
d5_41_R_4mm_100ms
d5_42_EQ_Taft_+73mm
d5_43_EQ_Taft_-73mm
d5_44_EQ_Taft_-78mm
d5_45_EQ_Taft_+78mm
d5_46_R_2mm_200ms
a cent [g]
a avg [g]
δc
-5
0
5
-0.5
0
0.5

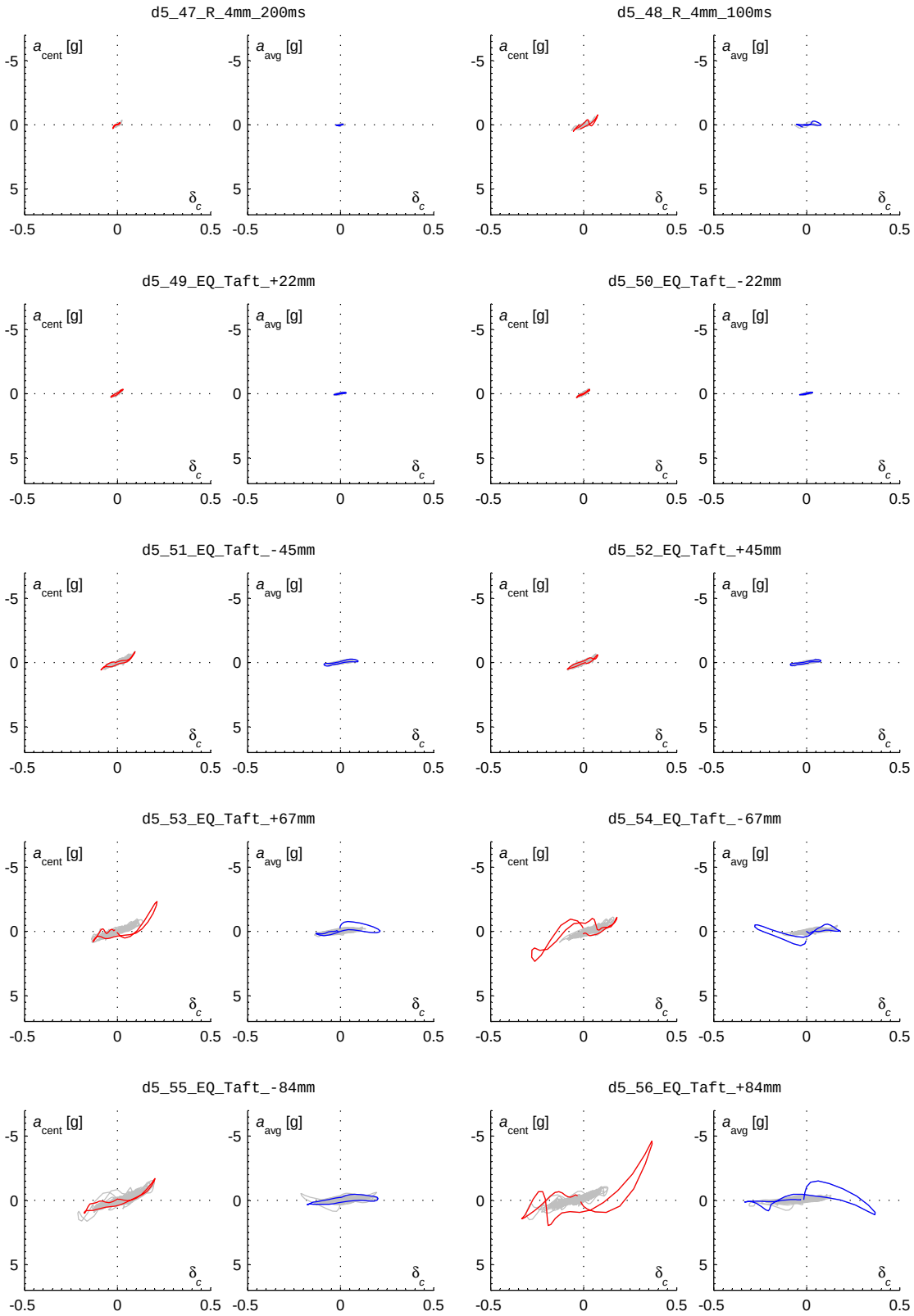
d5_47_R_4mm_200ms
d5_48_R_4mm_100ms
d5_49_EQ_Taft_+22mm
d5_50_EQ_Taft_-22mm
d5_51_EQ_Taft_-45mm
d5_52_EQ_Taft_+45mm
d5_53_EQ_Taft_+67mm
d5_54_EQ_Taft_-67mm
d5_55_EQ_Taft_-84mm
d5_56_EQ_Taft_+84mm
a cent [g]
a avg [g]
δc
-5
0
5
-0.5
0
0.5

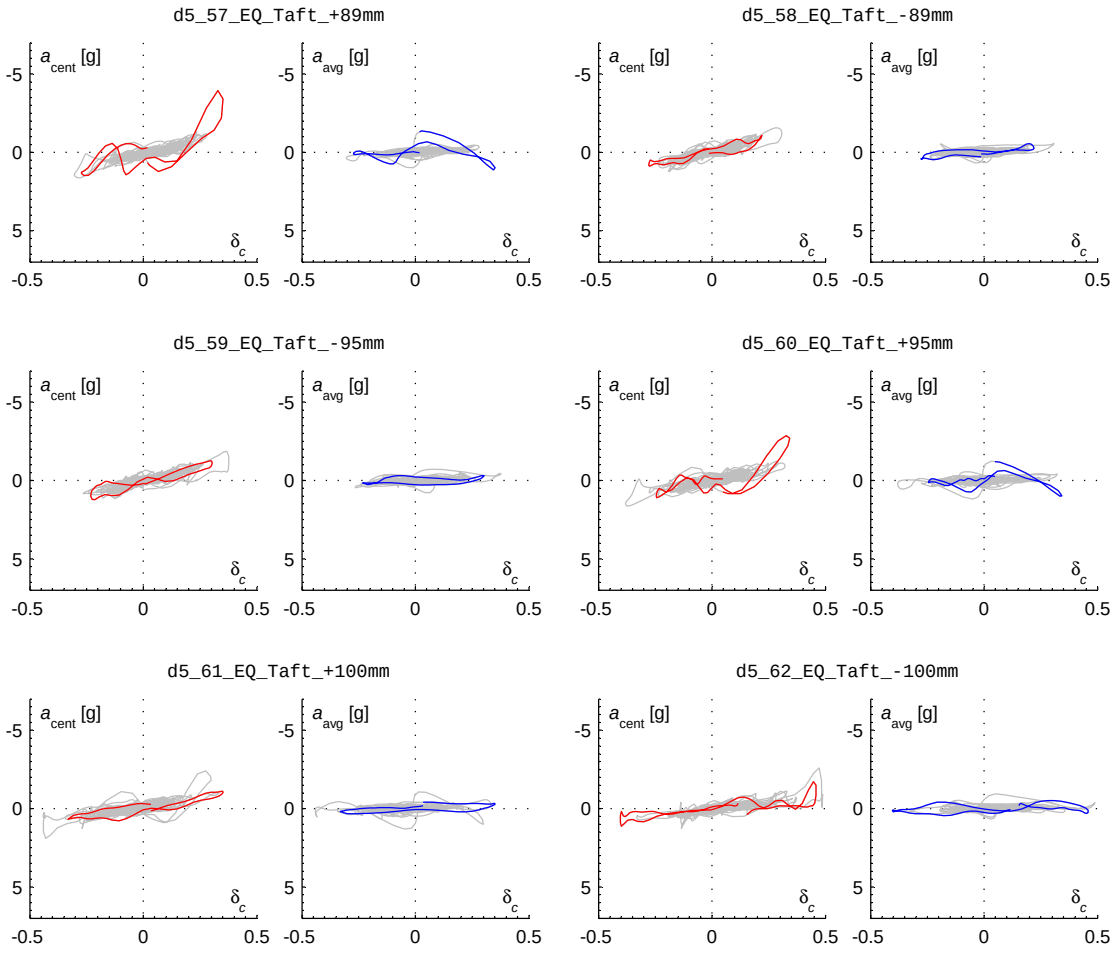
d5_57_EQ_Taft_+89mm
d5_58_EQ_Taft_-89mm
d5_59_EQ_Taft_-95mm
d5_60_EQ_Taft_+95mm
d5_61_EQ_Taft_+100mm
d5_62_EQ_Taft_-100mm
a cent [g]
a avg [g]
δc
-5
0
5
-0.5
0
0.5

Appendix D

DIAGNOSIS OF SHAKETABLE IMPACTS

Abstract

This appendix contains a diagnostic study performed to identify the causes of 'impacts' underwent by the shaketable when run at higher levels of motion intensity, as part of the work reported in Chapter 3. These impacts causes a marked difference to the walls' F-Δ loops, as demonstrated by examples. The study discovered that the impacts were generated by a velocity limitation of the hydraulic ram used to move the shaketable. In the opinion of the author, the impacts could not be avoided with the shaketable hardware available. However, it is proposed that the influence of the impacts may be alleviated using frequency domain filtering, as part of post-processing of the data.

D.1 INTRODUCTION

Throughout the course of the dynamic test study reported in Chapter 3, the shaketable underwent unexpected 'impacts' during tests in which earthquake motions were run at stronger levels of intensity. These impacts were characterised by disproportionally large acceleration spikes in the table's response, as well as a distinctive 'banging' noise enabling them to be easily recognised during testing. The resulting effects can be seen by comparing the input motion for the Taft earthquake (Figure D.1) to typical motion generated by the table at progressively increasing levels of intensity, as shown by Figures D.2, D.3 and D.4. In these examples, the impacts begin to take place at a peak displacement (PGD)[1] of −60

[1]Throughout this appendix, the abbreviations PGA, PGV and PGD refer to the peak acceleration, velocity and displacement, respectively, of the shaketable or the hydraulic ram itself.

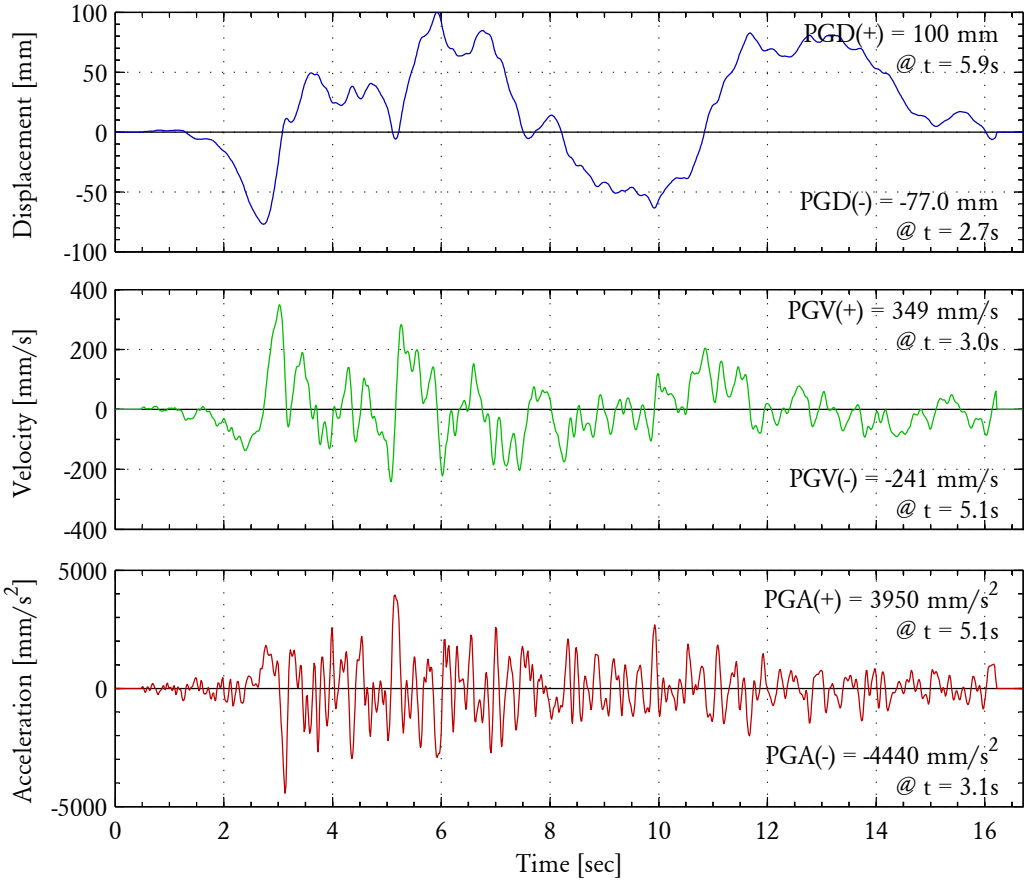

Figure D.1: Taft earthquake input motion. Scaled such that PGD $= +100$ mm.

mm in the negative direction and $+80$ mm in the positive direction and then persist at all higher intensities.[2]

The impacts were deemed to be an undesirable with respect to wall testing, for the following reasons.

- The waveform generated (Figures D.2, D.3 and D.4) in the presence of the impacts deviated from the original input motion (Figure D.1). Furthermore, the peak acceleration (PGA) generated during such test runs greatly exceeded the intended value.

- The wall load-displacement hysteresis loops produced during the impacts (Figure D.5) had a distinctively different shape in comparison to loops generated in the absence of the impacts and also when compared to typical loops

[2]The $(+$ or $-)$ sign convention in reference to the PGD refers to the direction in which the earthquake was run. As defined in Figure C.5, movement in the positive direction corresponds to the hydraulic actuator retracting inwards. For example, a $+100$mm PGD means that the maximum table displacement corresponded to the actuator being retracted 100 mm inward from its resting position.

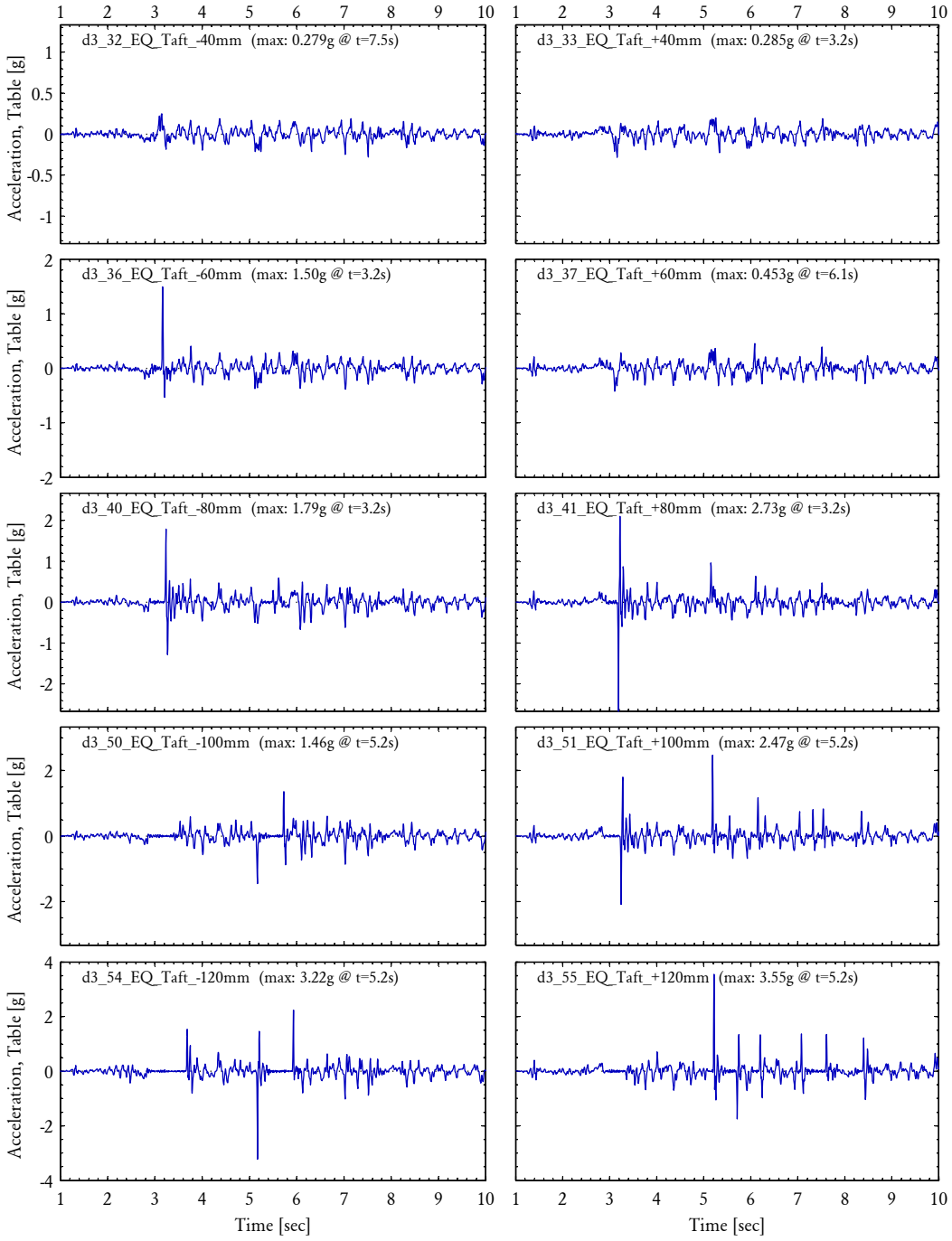

Figure D.2: Table acceleration response for Taft earthquake runs on wall D3. The vertical axis for each graph has been scaled by the shaking intensity based on the input PGD.

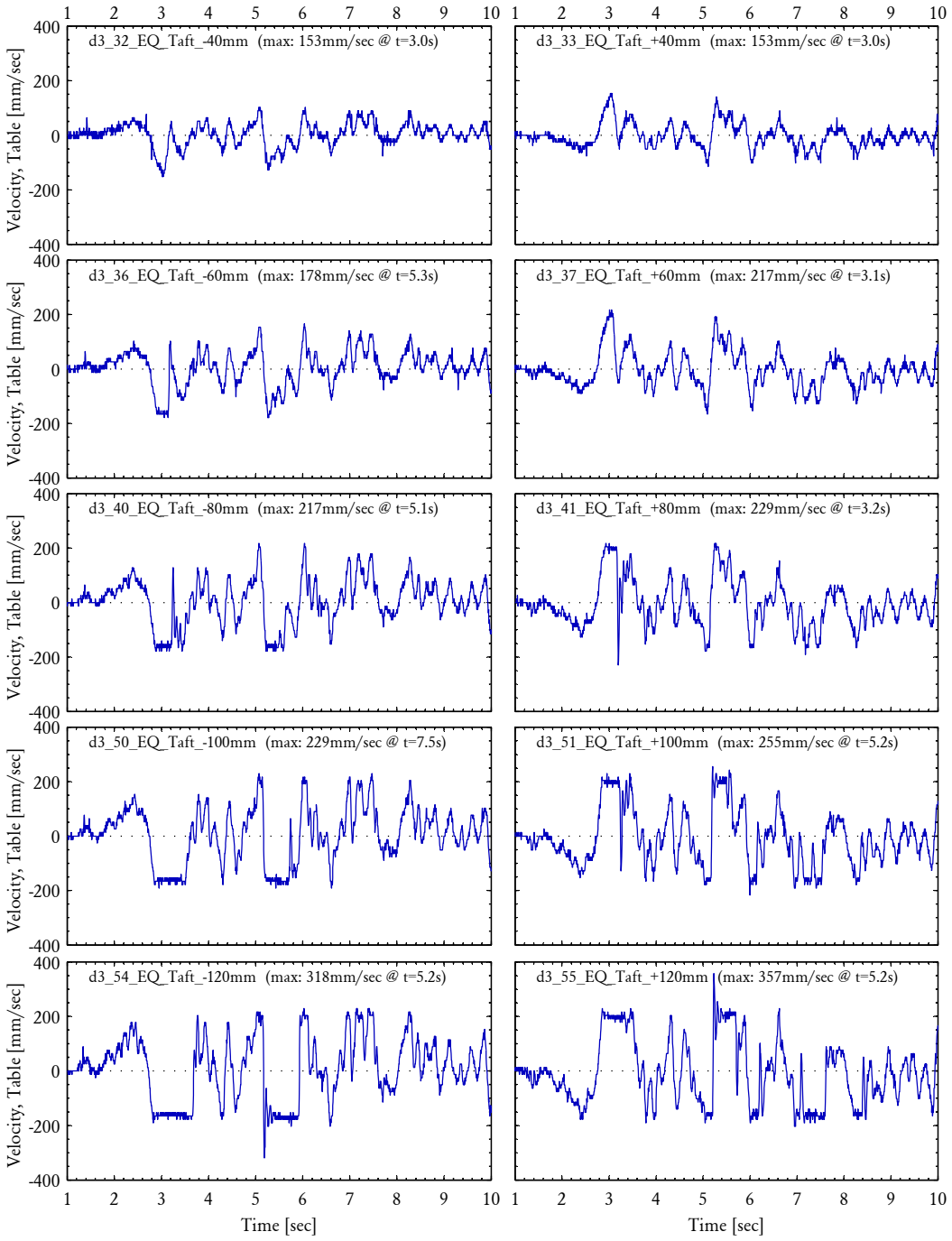

Figure D.3: Table velocity response for Taft earthquake runs on wall D3.

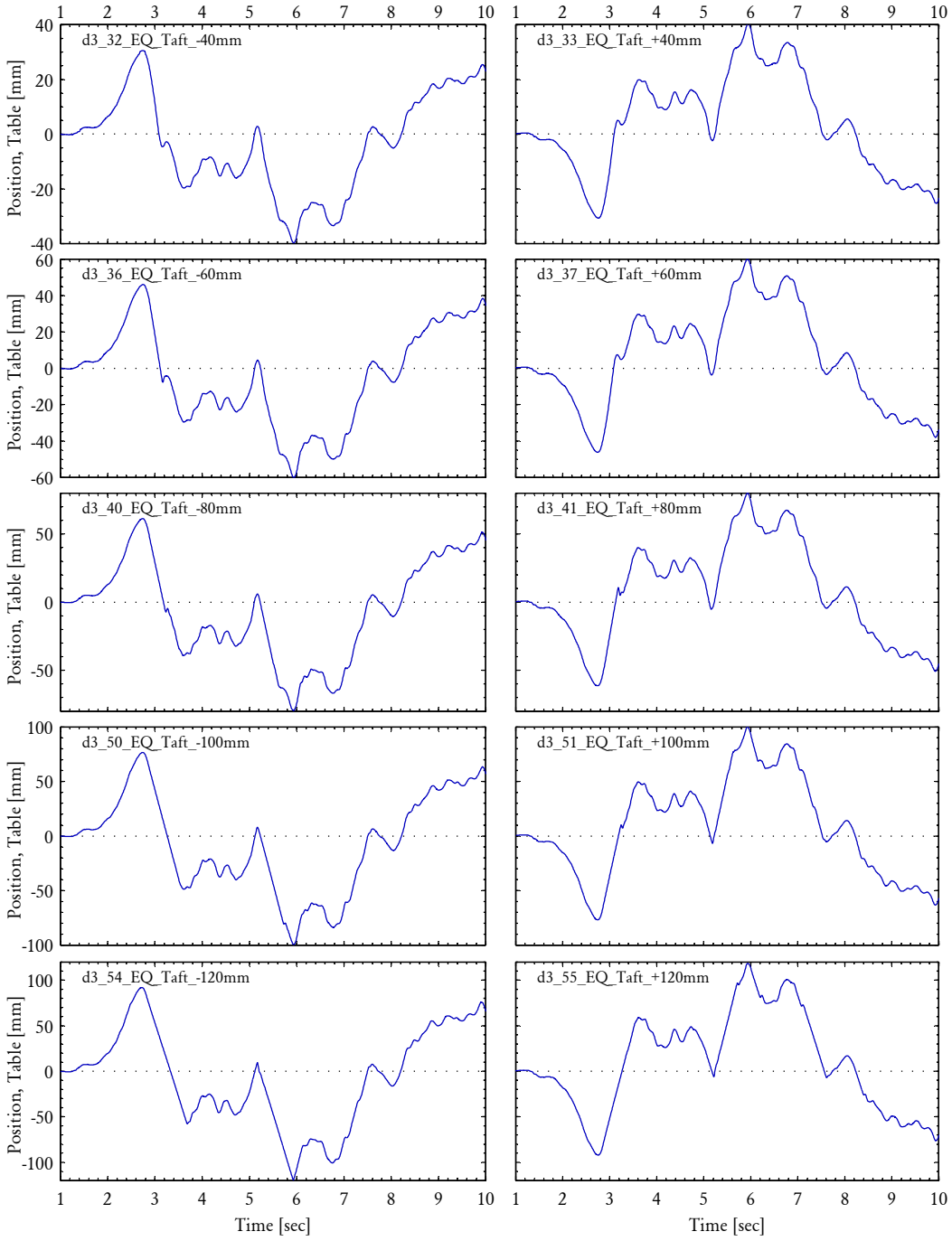

Figure D.4: Table position for Taft earthquake runs on wall D3. The vertical axis for each graph has been scaled by the shaking intensity based on the input PGD.

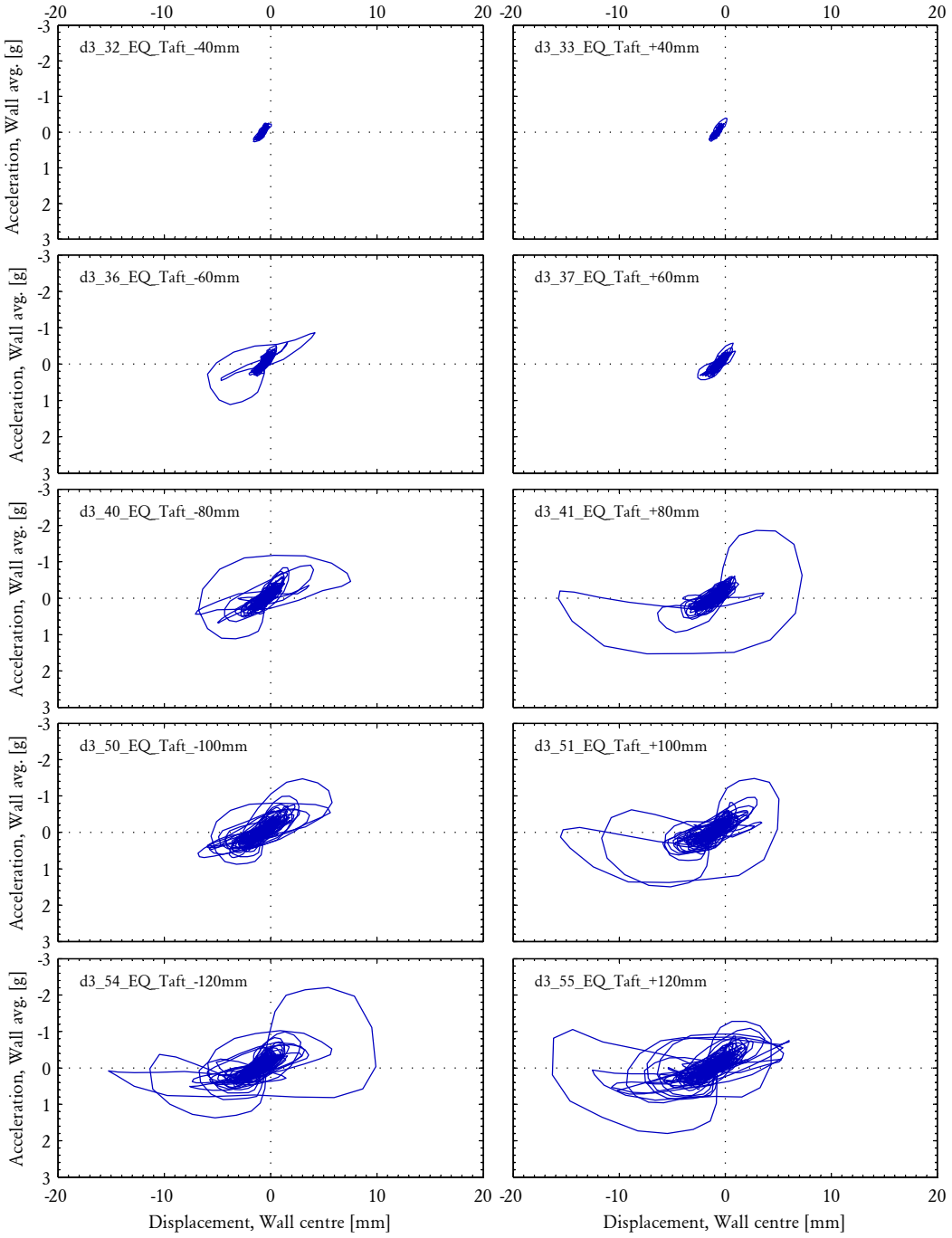

Figure D.5: Hysteresis plots of the average wall acceleration versus the wall displacement for Taft earthquake runs on wall D3.

observed during quasistatic testing (refer to Figures 2.14–2.21).

Table C.6 specifies whether or not the impacts occurred during individual test runs conducted in the main wall test programme. In testing the first two walls, D5 and D3, the impacts were observed for Taft runs at strong intensity; however, they were ignored. During testing of wall D4, efforts were made to stop the impacts from occurring, including runs 60–66 which experimented with different PID settings for the controller (refer to Section D.6.2); and runs 69–84 which trialled filtered versions of the Taft input motion. However, neither of these attempts were successful in preventing the impacts.

After testing wall D4, the main test programme was temporarily suspended and a series of diagnostic tests were performed to investigate the cause of the impacts and assess whether the test setup or procedure could be modified to prevent them from occurring. These included:

- Testing of various aspects of the experimental arrangement such as the wall restraint frame and the table itself,
- Modifying the settings of the hydraulic actuator controller,
- Testing of a second hydraulic actuator (identical to the shaketable actuator), and
- Trial runs using alternative earthquake input motions.

This appendix presents the findings of investigations relating to the shaketable impacts. The diagnosed causes of the impacts are presented in Section D.2. The trends in the experimental behaviour are discussed in Section D.3. A developed numerical simulation for predicting the time history of the shaketable's motion is presented in Section D.4 and a simplified procedure for predicting the input motion intensities at which the first onset of the impacts is expected to take place is presented in Section D.5. The aforementioned diagnostic experimental tests are reported in Section D.6, and finally, conclusions of the investigations and recommendations for future use of the shaketable are given in Section D.7.

D.2 DIAGNOSED CAUSE OF THE IMPACTS

The diagnoses made herein are based on the judgement of the author with support of various evidence presented throughout this appendix, including experimental data from the main test programme, special diagnostic tests on the apparatus and a numerical simulation developed to simulate the ram's motion.

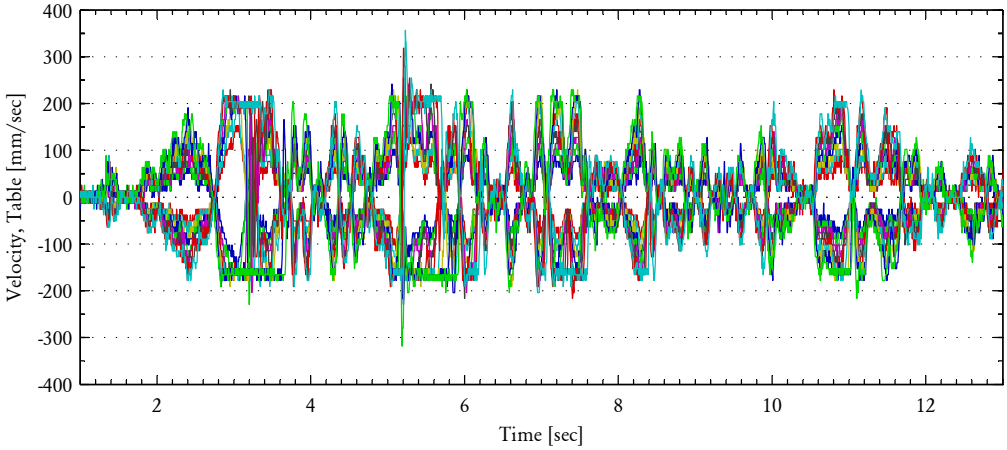

Figure D.6: Superimposed plots of the table velocity response for Taft earthquake runs on wall D3, with PGD ranging between ±40 and ±120 mm. The graph demonstrates the existence of a maximum velocity at which the ram can travel, equal to approximately +200 mm/s and −165 mm/s in the positive and negative directions, respectively.

The underlying cause of the impacts is an upper limit of the velocity at which the shaketable actuator (hydraulic ram) can travel in both the positive and negative directions. Existence of these limits is evident from plots of the table's velocity, including for tests from the main programme shown by Figure D.3, which are superimposed together in Figure D.6, and also for tests where the hydraulic ram was disconnected from the table (refer to Figure D.13). Diagnosing the mechanical causes responsible for these limits is beyond the scope of this study; however, they are likely to be due to a maximum rate at which hydraulic fluid can flow in and out of the actuator, which in turn is likely to be governed by the capacity of the pump driving the hydraulics. The values of the velocity limits are obtained graphically. Based on the figures, the limit is approximately $\dot{u}^{+}_{\text{lim}} = +200\,\text{mm/s}$ in the positive direction (ram retracting inwards), and $\dot{u}^{-}_{\text{lim}} = -165\,\text{mm/s}$ in the negative direction (ram extending outwards).

The existence of the velocity limits alone, however, is insufficient to explain the acceleration spikes generated. The secondary cause of the spikes is that once the velocity limit is reached, a lag develops between the displacement of the actuator and the input (target) displacement which the actuator attempts to track. As long as the displacement lag is in the same direction as the ram's travel, the ram will continue moving smoothly toward the target displacement at the limiting velocity. However, once the target displacement switches to the opposite direction relative to the ram's travel, the ram must undergo an abrupt change in direction in order to follow the target displacement. This sudden reversal in direction is believed to generate the apparent impact and cause a spike in the acceleration response.

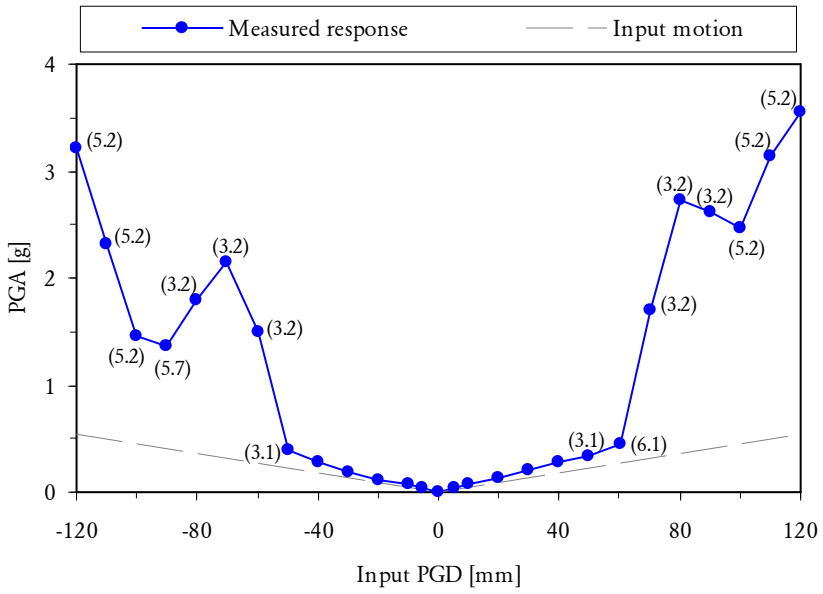

Figure D.7: Measured PGA response plot for Taft earthquake runs performed on wall D3. The bracketed values show the time (in seconds) at which the PGA occurred during the shaking.

D.3 EXPERIMENTAL BEHAVIOUR

The Taft earthquake runs performed on wall D3 are used as the main experimental data set referred to throughout these discussions. These series of tests have been chosen as the associated results are representative of all the tests performed in this experimental study, whilst incorporating the most extensive range of shaking intensities considered. Several figures are provided based on these test runs. Response plots of the table's acceleration (Figure D.2), velocity (Figure D.3) and displacement (Figure D.4) are shown for selected runs at PGDs of ±40, ±60, ±80, ±100 and ±120 mm. Figure D.7 graphs the associated PGA response for the different PGD intensities used.

It should be noted that for all results presented in this appendix, the acceleration and displacement data was obtained through direct measurement, using accelerometers and displacement transducers, respectively. By contrast, velocity data was derived by numerically differentiating the measured displacement data.

D.3.1 PGA Response

The trend in the measured PGA for different intensities of the input motion is illustrated by Figure D.7. The figure plots the measured PGA of the table against

the input PGD for the full range of input PGDs for which tests were carried out, ranging between ±5 and ±120 mm. For comparison, the relationship between the PGA and PGD in the input motion itself, which would be produced if the shaketable perfectly tracked the input motion, is also plotted. It is seen that at low shaking intensities when the magnitude of the PGD is 50 mm or less, the measured PGA is approximately linear with respect to the PGD and in good agreement with the idealised input motion. The data points inside this linear range correlate directly to the test runs where the impacts do not occur. However, as the shaking intensity is increased to a PGD magnitude beyond approximately 60 mm, the impacts begin to occur, which causes the PGA to become highly nonlinear with respect to the PGD and up to 3 to 7 times higher than the theoretical value.

D.3.2 Time History Waveforms

Close inspection of the acceleration, velocity and displacement waveforms, provided as Figures D.2, D.3 and D.4 supports the hypothesised reasons for the impacts provided in Section D.3. For example, consider the initial spike in the Taft motion at approximately $t = 3.2$ sec (Figure D.2). This spike first occurs at -60 mm and $+70$ mm PGD in the negative and positive directions respectively, but interestingly, becomes attenuated at higher input motion intensities (Figure D.7). This trend can be explained by the hypothesis as follows.

In the original input motion shown in Figure D.1 there is a 'kink' in the displacement trace at approximately $t = 3.2$ sec, which requires a slight reversal in the movement direction. Incidentally, this point also coincides with the PGA of the input motion. The kink at $t = 3.2$ sec is well captured by the ram at low shaking intensities where the velocity threshold is not reached, as can be seen for the -40 mm, $+40$ mm, $+60$ mm PGD runs in Figures D.2, D.3 and D.4. Consequently impacts do not occur at these low input intensities.

At intermediate intensities, corresponding to PGD $= -60$ mm, -80 mm $+40$ mm and $+60$ mm, the velocity begins to reach its limit at approximately $t = 2.9$ sec (Figure D.3). These shaking intensities also correlate well with the intensity at which the impacts begin to occur in the $t = 3.2$ sec region, as can be seen through comparison of Figures D.3 and D.2. The impacts occur at these intermediate intensities because the attainment of the threshold velocity at $t = 2.9$ sec causes a lag to develop between the ram's actual displacement and its target displacement. Consequently, by the time the ram arrives in the kink region at $t = 3.2$ sec it needs to suddenly reverse its direction in order to track the target displacement, which causes the associated acceleration spike.

That the acceleration spikes in this region disappear for high shaking intensities, including PGD $= -100$ mm, -120 mm and $+120$ mm in the runs is also consistent with the hypothesis. It can be seen from Figure D.3, that for these test runs the ram simply travels at its threshold velocity in this region and does not reproduce the kink at $t = 3.2$ sec. The reason for this is that when the motion is run at these high intensities, the lag between the ram's actual displacement and its target displacement becomes so large that by the time the actuator arrives at the kink region, the target displacement is already further ahead in the input motion. This causes the ram to simply continue travelling toward the target at its threshold velocity, thus causing the kink to be ignored in the reproduced motion. As a result, the PGA occurs at a later point, at approximately $t = 5.2$ sec.

D.4 NUMERICAL SIMULATION OF THE RAM'S MOTION

In order to test the hypothesised reasons for the impacts discussed in Section D.2, a numerical simulation of the ram's motion was developed. The basis of the simulation is to step forward in the time domain and calculate the position of the ram at each time point by enforcing limits on the maximum velocity at which the ram can travel. The velocity limits used in the simulation were those determined graphically from the wall's response (Figure D.6).

D.4.1 Algorithm

The basic steps in the simulation algorithm are as follows.

1. Start with a digitised input displacement record $\boldsymbol{u}_{\text{targ}}$. This represents the target motion which is used as input for defining the motion to the shaketable controller.

2. Numerically differentiate the displacement record to obtain the target velocity record $\dot{\boldsymbol{u}}_{\text{targ}}$, and differentiate for a second time to obtain the target acceleration record $\ddot{\boldsymbol{u}}_{\text{targ}}$.

The remaining steps are used to calculate the predicted motion of the ram, including its displacement $\boldsymbol{u}_{\text{ram}}$, velocity $\dot{\boldsymbol{u}}_{\text{ram}}$ and acceleration $\ddot{\boldsymbol{u}}_{\text{ram}}$.

3. At the first time point, assign the ram displacement, velocity and acceleration using the first entry of the target motion, such that

$$u_{\text{ram}}^{i=1} = u_{\text{targ}}^{i=1}, \quad \dot{u}_{\text{ram}}^{i=1} = \dot{u}_{\text{targ}}^{i=1}, \quad \ddot{u}_{\text{ram}}^{i=1} = \ddot{u}_{\text{targ}}^{i=1}.$$

In the motions considered in these tests, the above initial quantities were all equal to zero.

At every subsequent point, the ram displacement is calculated using a step-by-step process by repeating steps 4 and 5 until the end of the record.

4. At the current (i^{th}) point, calculate the ram velocity needed at the step between the previous and current time points in order to reach the target displacement at the current time point. The required velocity is

$$\dot{u}_{\text{req}} = \left(u^{i}_{\text{targ}} - u^{i-1}_{\text{ram}} \right) / \Delta t,$$

where Δt is the time step.

5. If the required ram velocity $\dot{u}_{\text{req}}$ lies within the velocity threshold bounds $\dot{u}^{-}_{\text{lim}}$ and $\dot{u}^{+}_{\text{lim}}$, then the ram is able to track the target motion properly at the i^{th} point and the ram displacement at that point is assigned as the target displacement, $u^{i}_{\text{ram}} = u^{i}_{\text{targ}}$.

   Otherwise, if the required ram velocity exceeds one of the threshold bounds, then the ram's velocity assumes the value of the threshold that is exceeded. Consequently the ram loses track of the target motion, causing a displacement lag to develop. The corresponding displacement at the i^{th} point becomes

$$u^{i}_{\text{ram}} = u^{i-1}_{\text{ram}} + \dot{u}_{\text{lim}} \, \Delta t,$$

   where $\dot{u}_{\text{lim}}$ is the critical velocity threshold that was exceeded (either $\dot{u}^{-}_{\text{lim}}$ or $\dot{u}^{+}_{\text{lim}}$).

Steps 4 and 5 are repeated until the ram displacement $\boldsymbol{u}_{\text{ram}}$ is calculated for the entire duration of the motion. Finally the following step is performed.

6. Numerically differentiate the calculated ram displacement record $\boldsymbol{u}_{\text{ram}}$ to obtain the ram velocity $\dot{\boldsymbol{u}}_{\text{ram}}$, and differentiate for a second time to obtain the ram acceleration $\ddot{\boldsymbol{u}}_{\text{ram}}$.

At the end of the process described by steps 1 to 6, the user will end up with histories for the displacement, velocity and acceleration of the target motion ($\boldsymbol{u}_{\text{targ}}$, $\dot{\boldsymbol{u}}_{\text{targ}}$, $\ddot{\boldsymbol{u}}_{\text{targ}}$) and the predicted motion of the ram ($\boldsymbol{u}_{\text{ram}}$, $\dot{\boldsymbol{u}}_{\text{ram}}$, $\ddot{\boldsymbol{u}}_{\text{ram}}$).

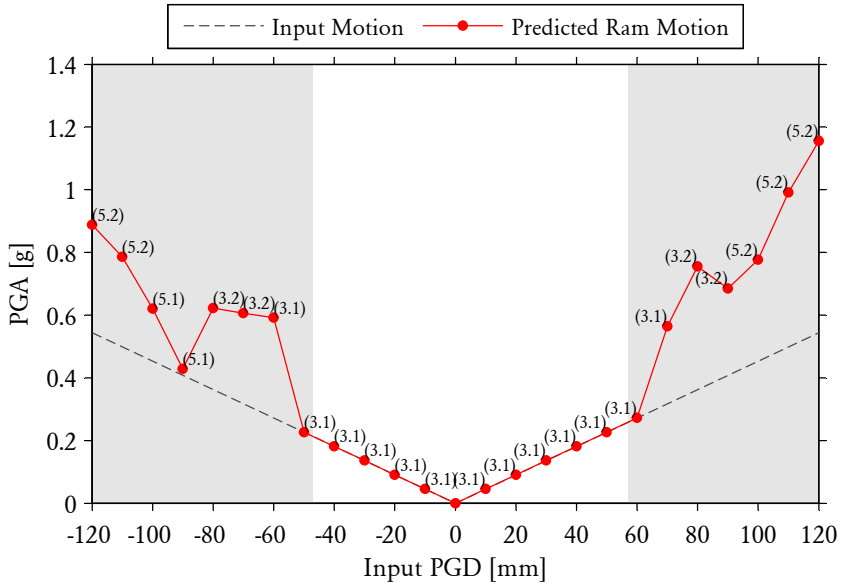

Figure D.8: Predicted PGA response plot for the Taft earthquake based on numerical simulation. The predicted motion was obtained by implementing velocity threshold limits of -165 and $+200$ mm/s. Bracketed values show the time (in seconds) at which the PGA occurs during the motion. Grey shaded regions show PGDs at which synchronisation is lost between the ram and target displacement.

D.4.2 Results

The proposed numerical analysis was conducted using the Taft motion at different PGD intensities, using the velocity threshold limits $\dot{u}^{+}_{\text{lim}} = +200$ mm/s and $\dot{u}^{-}_{\text{lim}} = -165$ mm/s. A full PGA response plot for the Taft earthquake predicted by the simulation is shown by Figure D.8. Examples of the ram's motion for the associated simulated runs are also provided by Figure D.9, which plots the ram's predicted displacement, velocity and acceleration time histories for PGDs of -60 mm, -80 mm, -100 mm and -120 mm.

D.4.3 Comparison of Predicted PGA Response with Experiment

Comparison of the PGA response plot obtained computationally (Figure D.8) and experimentally (Figure D.7) shows favourable correlation between several characteristics.

Both curves show that the impacts do not occur for PGDs equal to or less severe than -50 mm in the negative direction and $+60$ mm in the positive direction. Conversely, the numerical analysis predicts the impacts to occur for all intensities greater than -60 mm in the negative direction and $+70$ mm in the positive direction,

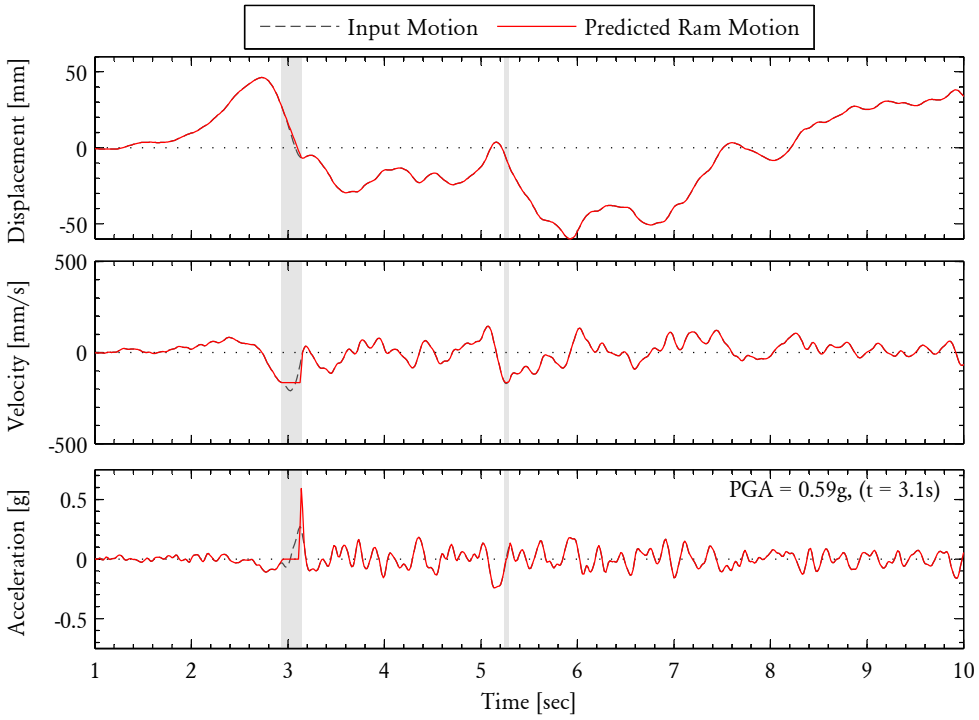

(a) PGD $= -60$ mm.

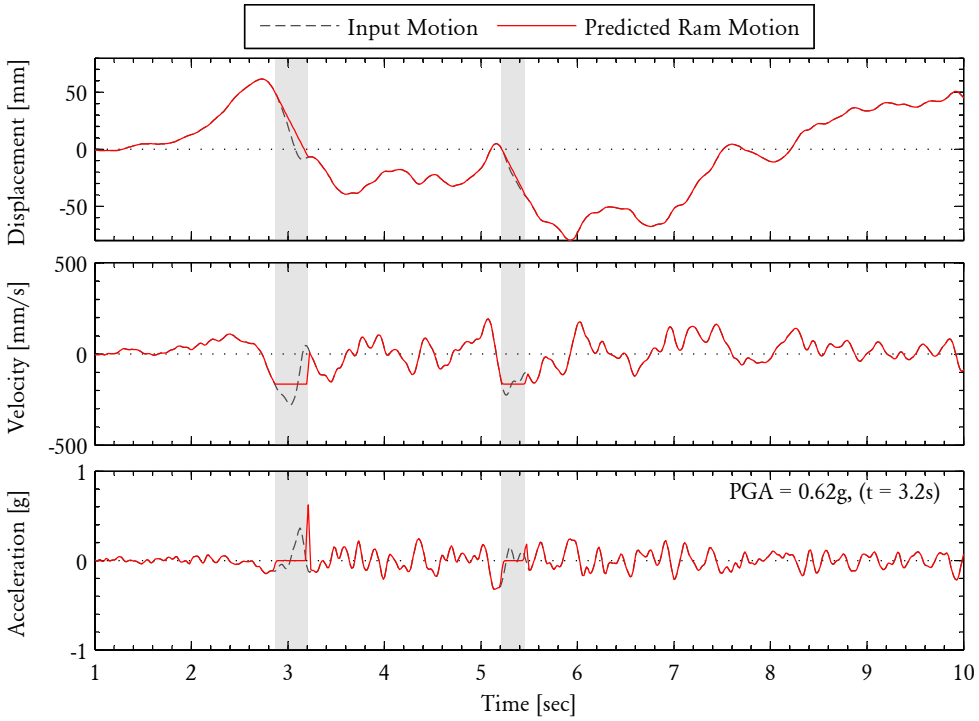

(b) PGD $= -80$ mm.

Figure D.9: Examples of simulated ram motion for the Taft earthquake. The motion was calculated by implementing velocity threshold limits of -165 and $+200$ mm/s. Grey shaded regions show lost synchronisation between the ram and target displacement.

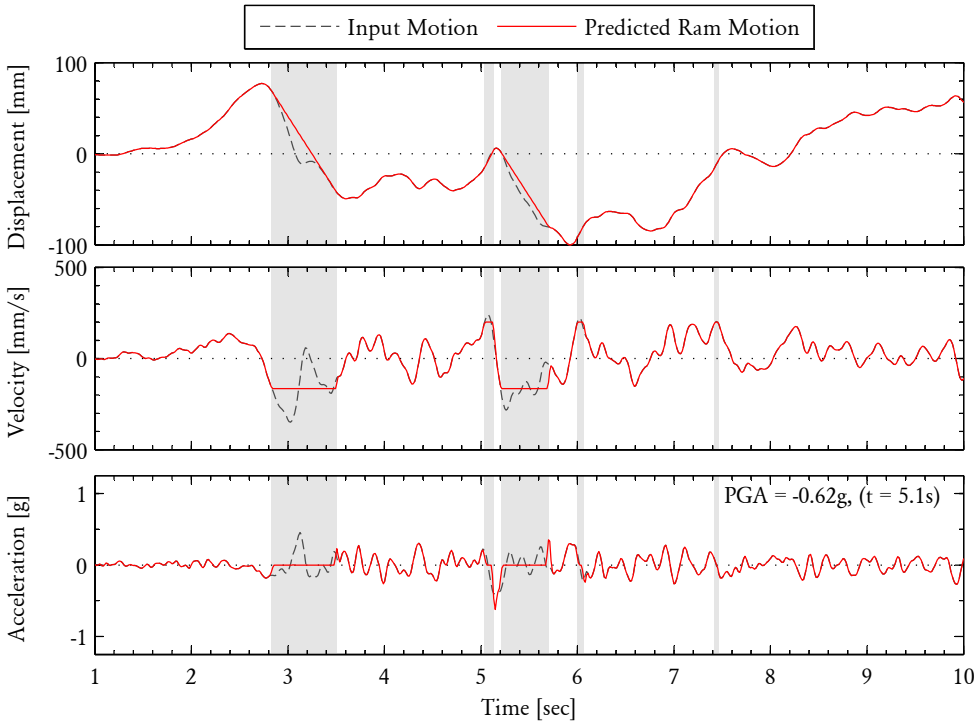

(c) PGD $= -100$ mm.

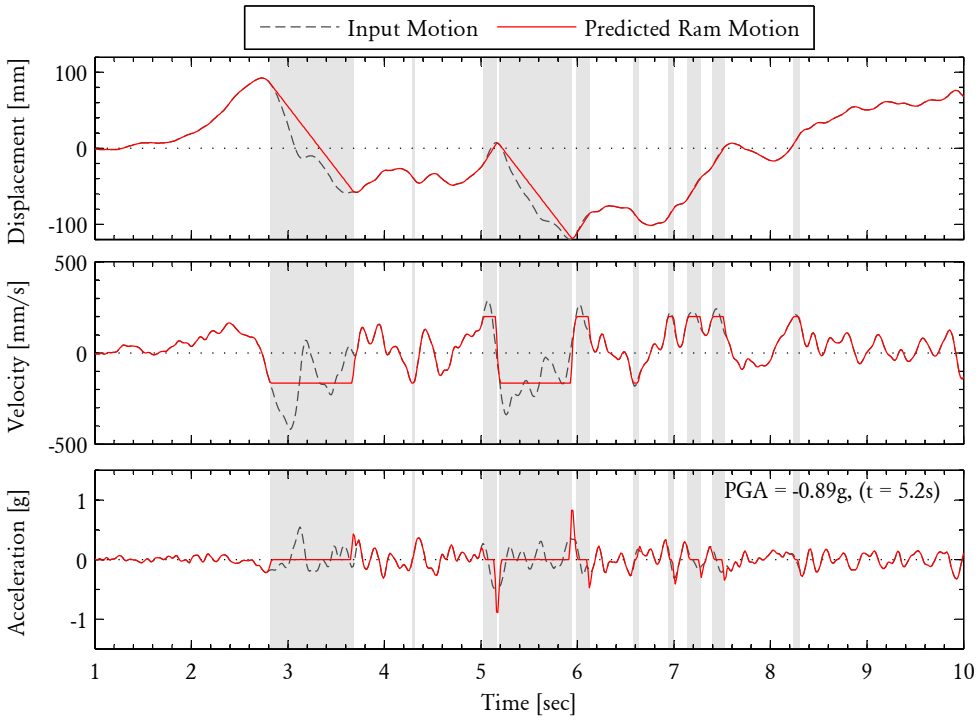

(d) PGD $= -120$ mm.

Figure D.9: (cont'd).

which is validated by the experimental results.

Furthermore, the analysis predicts with good accuracy the time at which the PGA is expected to occur. At low levels of intensity and in the absence of impacts, both the analysis and experiment demonstrate the PGA to occur at $t = 3.1$ sec.[3] At intermediate levels of shaking intensity, corresponding to PGD between $+70$ mm and $+90$ mm on the positive side and between -60 mm and -80 mm on the negative side, both the analysis and experiment exhibit impacts which result in the PGA at approximately $t = 3.2$ sec. At high intensity shaking, corresponding to PGD between $+100$ mm and $+120$ mm on the positive side and between -90 mm and -120 mm on the negative side, the critical impacts causing the PGA are shown by both the analysis and experiment to occur at approximately $t = 5.2$ sec. The resulting shift in the time at which the PGA occurs to a later point in the motion is due to the 'smoothing' of the displacement trace at the $t = 3.2$ sec region, as discussed previously in Section D.3.2, which is also captured in the simulation (Figure D.9).

There is also good correlation between the overall shapes of the PGA response curves obtained experimentally (Figure D.7) and computationally (Figure D.8). For example, on the positive displacement side, the PGA increases as the PGD is increased from $+60$ mm to $+80$ mm, but then begins to reduce slightly at $+90$ mm. The PGA then increases again once the critical impacts begin to occur at $t = 5.2$ sec, as the PGD is increased from $+100$ mm to $+120$ mm. Similarly, on the negative displacement side, the PGA increases as the PGD is increased from -50 mm to -70 mm. The PGA then reduces slightly at approximately a PGD of -90 mm and then continues to increase further as the critical impacts move to $t = 5.2$ sec, as the PGD is increased from -100 mm to -120 mm. These trend is reflected by both the experimental and computational results. In addition, both sets of curves show that the PGA generated is slightly greater in the positive PGD direction as opposed to the negative PGD direction.

D.4.4 Comparison of Predicted Waveforms with Experiment

Another aspect where the simulation correlates favourably with experimental data is by comparing the time history waveforms themselves. Comparisons can be made between the selected analytical runs for PGDs of -60 mm, -80 mm, -100 mm and -120 mm, as shown by Figure D.9, with the respective experimental runs given in Figures D.2, D.3 and D.4.

[3] With the exception of PGD $= +60$ mm, whereby the largest measured acceleration was at $t = 6.1$ sec, which was marginally larger than the second largest acceleration which occurred at the predicted time of $t = 3.1$ sec

For the run at PGD $= -60$ mm, as shown by Figure D.9a, the simulation predicts that synchronisation between the ram and the target motion is lost on two occasions, firstly at around $t = 3.0$ sec and secondly at $t = 5.2$ sec. However, the acceleration trace shows that only the first instance causes an impact, at approximately $t = 3.2$ sec. Indeed, the corresponding plot of the experimental response in Figure D.2 confirms this, exhibiting a single spike at the same location.

For the run at PGD $= -80$ mm, as shown by Figure D.9b, again two losses of synchronisation are predicted at the same points in the response as for the run at PGD $= -60$ mm. Similarly, only a single acceleration spike is predicted at $t = 3.2$ sec, which is once again confirmed by the corresponding experimental plot in Figure D.2.

For the run at PGD $= -100$ mm, as shown by Figure D.9c, the behaviour becomes slightly different. Loss of synchronisation is predicted at numerous points in the response; however, two of these zones these appear to be most significant. The first zone is between 2.8 sec and 3.6 sec, even though it is not predicted to generate any acceleration spikes. The second zone is between 5.2 sec and 6.0 sec, which generates two spikes, one at each of the zone's boundaries. Again the corresponding experimental plot in Figure D.2 compares favourably, showing clear spikes at the same locations in the second zone, as well as an absence of spikes in the first zone.

The final run at PGD $= -120$ mm, as shown by Figure D.9d, is somewhat similar to the run at PGD $= -100$ mm, however, loss of synchronisation is predicted at numerous additional zones. Similarly though, the first zone between 2.8 sec and 3.6 sec, and the second zone between 5.2 sec and 6.0 sec are again the most significant. There is no impact at the start of the first zone; however, a moderate spike is predicted to occur at the end of the zone at 3.6 sec. The second zone again corresponds to the most significant spikes in the response with the largest one occurring at 5.2 sec and the other at 6.0 sec. In addition, four additional moderate spikes are predicted to occur at 6.1 sec, 7.0 sec, 7.3 sec and 7.5 sec. Remarkably, these spikes are all exhibited by the experimental response as shown by the corresponding plot in Figure D.2.

D.4.5 Limitations

Despite being able to predict certain characteristics of the ram's motion with reasonable accuracy, the simulation is unable to accurately predict the actual value of the PGA. It generally underpredicts the value of the PGA quite significantly when compared to the experimental results (Figure D.7).

This error could be due to numerous sources. For example, the actual physical system experiences inertial loading due to the presence of actual mass, which is not accounted for in the simulation. Such effects are demonstrated in Section D.6.1 where it is demonstrated that when the ram is disconnected from the rest of the shaketable test arrangement, the resulting PGAs become significantly lower. Further inaccuracies could also result from numerical error in the simulation. For example, given that the numerical differentiation of the ram's motion relies on division by the time step Δt to obtain the acceleration record, a small change in Δt can have a significant influence on the computed PGA. By contrast, the value of Δt used in the analysis is based solely on the digitised input motion used and hence cannot be adjusted.

D.4.6 Summary

The simulation has been shown to predict numerous characteristics of the response with good accuracy, including

- The shaking intensity, as a PGD, at which the impacts are expected to begin to occur,
- The general shape of the PGA response curve as a function of the PGD,
- The time at which the PGA is expected to occur, and
- Detailed aspects of the time history waveform such as the occurrence of secondary impacts.

Consequently the simulation is believed to provide a good model for predicting the motion of the ram, as well as strong support for the hypothesised causes of the impacts as discussed in Section D.2.

D.5 PREDICTING THE ONSET OF THE IMPACTS

A computational model was presented in Section D.4 for simulating the motion of the ram when subjected to maximum velocity limits, which exhibited good correlation with various aspects of the experimentally observed motion. A significant outcome of the model was that it was able to predict, with good accuracy, the PGD intensity at which the impacts are expected to occur, by generating a response curve for the predicted PGA for different levels of input intensity, such as that shown by Figure D.8 for the Taft motion. That the numerical model performed

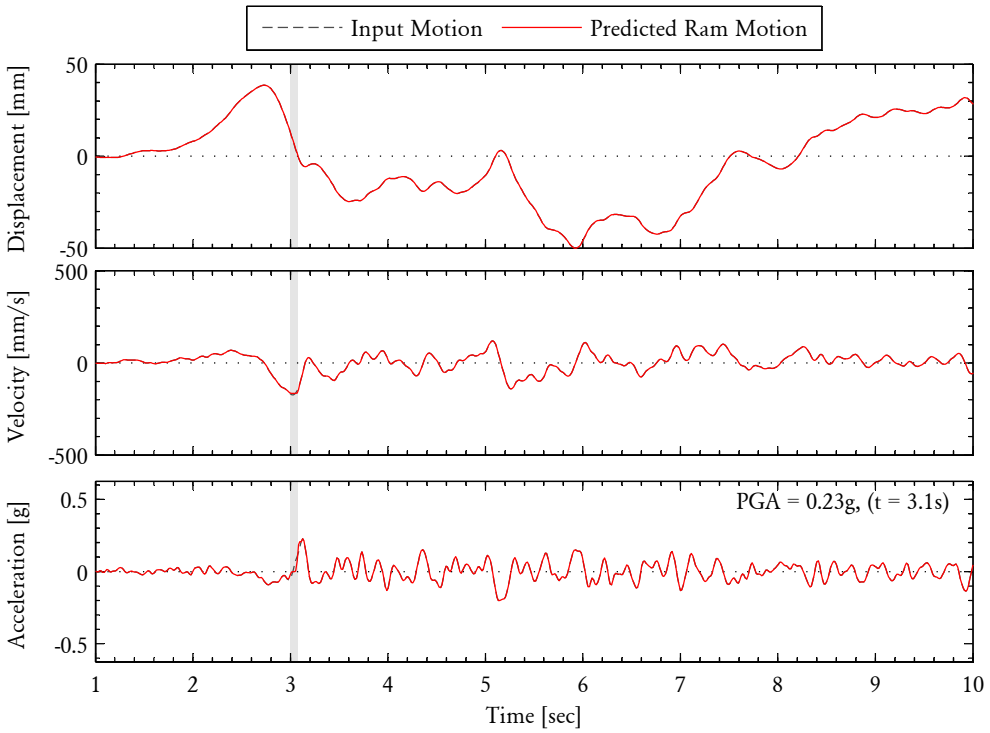

Figure D.10: Simulated ram motion for the Taft earthquake at PGD $= -50$ mm, calculated by implementing the velocity threshold limits of -165 and $+200$ mm/s. Grey shaded regions show lost synchronisation between the ram and target displacement.

with such good accuracy provided strong evidence for the hypothesised reason of the impacts, which is that the impacts are caused by a loss of synchronisation between the ram displacement and the target displacement that occurs when the peak velocity (PGV) of the input motion exceeds the ram's threshold velocity.

The numerical model can also be used to demonstrate, however, that loss of synchronisation between the ram and the target displacement is a necessary, but not sufficient, condition for the generation of the acceleration spikes. An example of this is shown by Figure D.10, which shows the predicted motion of the ram for the Taft earthquake at PGD $= -50$ mm. It is seen that although the ram loses track of the target displacement at approximately $t = 3.0$ sec, the loss of synchronisation does not generate an acceleration spike in this instance. The likely reason for this behaviour is that when the ram catches up with the target displacement after the loss of synchronisation, the target displacement is still travelling in the same direction and therefore the ram does not need to undergo a direction reversal.

Consequently, a simple yet conservative estimate of the intensity at which the impacts first begin to occur for a particular input motion can be provided by calculating the lowest PGD at which the threshold velocity of the ram is first exceeded. In order to calculate these PGD limits, it is necessary to know the PGV

Table D.1: The PGD, PGV and PGA of the various shaketable input motions, in both the positive and negative directions. The motions have been scaled such that the PGD occurs in the positive direction and is equal to +100 mm.

Quake	PGD [mm]		PGV [mm/s]		PGA [g]		
	(+)	(−)	(+)	(−)	(+)	(−)	(*abs*)
Taft	+100	−77.0	+349	−241	+0.40	−0.45	0.45
Syntho1	+100	−67.4	+522	−444	+0.53	−0.58	0.58
Syntho2	+100	−93.9	+492	−314	+0.55	−0.46	0.55
Syntho3	+100	−83.9	+322	−274	+0.55	−0.50	0.55
Syntho4	+100	−91.0	+416	−372	+0.76	−0.62	0.76
Syntho5	+100	−77.4	+619	−463	+1.20	−0.80	1.20
Syntho6	+100	−92.4	+568	−673	+1.06	−1.30	1.30
Syntho7	+100	−97.4	+586	−534	+2.27	−1.51	2.27
Syntho8	+100	−88.1	+483	−438	+1.46	−1.05	1.46

Table D.2: Calculated PGDs in the negative and positive directions at which the ram loses synchronisation with the target motion. The calculations are based on the input motion velocity exceeding one of the velocity limits of the ram, either +200 mm/s or −165 mm/s. In most cases the −165 mm/s limit is critical, except where indicated by an asterisk (*)

Quake	PGD [mm]	
	(−)	(+)
Taft	−47.2	+57.3*
Syntho1	−31.6	+37.2
Syntho2	−33.6	+40.7*
Syntho3	−51.2	+60.3
Syntho4	−39.7	+44.4
Syntho5	−26.7	+32.3*
Syntho6	−29.1	+24.5
Syntho7	−28.2	+30.9
Syntho8	−34.1	+37.7

of the input motion in both the positive and negative displacement directions. These values can be derived from a digitised velocity record for the particular input motion, which may be obtained by numerically differentiating its digitised displacement record. The resulting information is given in Table D.1 for the different seismic motions used in this experimental study.

Table D.2 provides the calculated PGD limits in the positive and negative directions at which the threshold velocity of the ram is first exceeded. The associated calculations assumed the ram velocity threshold limits to be $\dot{u}^{+}_{\text{lim}} = +200\,\text{mm/s}$ and $\dot{u}^{-}_{\text{lim}} = -165\,\text{mm/s}$. Comparison of the calculated limits for the Taft motion with Figure D.7 show that as expected, they provide an accurate, yet slightly conservative prediction of the shaking intensities at which the impacts begin to occur. In Section D.6.3 it is shown that the predictions are also accurate for the synthetically generated motions Syntho1–Syntho8. Furthermore, the predictions show good correlation with results from the main test programme (Table C.6).

D.6 DIAGNOSTIC EXPERIMENTAL TESTS

During the process of attempting to diagnose the cause of the shaketable impacts, a series of experimental tests were conducted focusing on various aspects of the test setup and method. The general approach used in these tests was to run the earthquake motions on the shaketable at varying levels of intensity and measure the resulting displacement and acceleration response. Although the actual cause of the impacts (discussed in Section D.2) was found to be none of those that were directly investigated in these diagnostic tests, the results of the tests are nonetheless reported as they also support the final conclusions reached.

D.6.1 Tests on the Shaketable and Wall Restraint System

The first phase of diagnostic tests aimed to determine if the impacts were caused by the presence of a particular part of the overall test arrangement such as the wall, restraint frame, or the shaketable itself. Starting with the original test setup used for wall tests (refer to Figure 3.4), these diagnostic tests involved gradual removal of these components from the test arrangement and conducting trial runs of the Taft earthquake motion. The various configurations that were considered included:

- The hydraulic ram connected to the shaketable, together with the restraint frame mounted on the table, but without a wall,
- Hydraulic ram connected to only the bare shaketable, and
- The hydraulic ram by itself.

In addition to the above tests, data had already been acquired for the full test arrangement during the original wall tests. In all of these trial runs, the actuator controller proportional-integral-derivative (PID) was set to 36 dB (the influence of this parameter is discussed in greater detail Section D.6.2).

Results

Table D.3 provides the measured PGA data at varied input PGD intensity. Qualitative assessment of whether the impacts were deemed to have occurred based on the recorded acceleration time history, is also provided. The table also indicates the shaking intensities at which the ram is expected to lose synchronisation with the target motion and the impacts are predicted to occur (based on Table D.2).

The results demonstrate that the test arrangement had no bearing on whether or not the impacts occurred. Significantly, the impacts occurred even when the

Table D.3: Results from tests on various test arrangements. The Taft earthquake motion was used in all tests and the controller PID was set to 36 dB. Gray shading indicates the PGDs at which synchronisation is expected to be lost, based on Table D.2.

Config:	Table + Frame + Wall (D3)		Table + Frame		Table (no Frame)		Ram only	
PGD [mm]	PGA [g]	Note	PGA [g]	Note	PGA [g]	Note	PGA [g]	Note
+120	3.55	↯	4.45	↯	–	–	–	–
+110	2.32	↯	–	–	–	–	–	–
+100	2.47	↯	3.14	↯	3.58	↯	1.68	↯
+90	1.37	↯	–	–	–	–	–	–
+80	2.73	↯	3.61	↯	4.27	↯	1.81	↯
+70	2.16	↯	2.72	↯	–	–	–	–
+60	0.45	○	0.93	↯	1.03	↯	0.40	○
+50	0.40	○	0.87	○	–	–	–	–
+40	0.29	○	0.48	○	0.71	○	0.22	○
+30	0.18	○	–	–	–	–	–	–
+20	0.13	○	0.20	○	–	–	–	–
+10	0.07	○	–	–	–	–	–	–
+5	0.04	○	–	–	–	–	–	–
−5	0.04	○	–	–	–	–	–	–
−10	0.08	○	–	–	–	–	–	–
−20	0.12	○	0.22	○	–	–	–	–
−30	0.20	○	–	–	–	–	–	–
−40	0.28	○	0.45	○	0.55	○	0.23	○
−50	0.34	○	0.65	○	–	–	–	–
−60	1.50	↯	1.89	↯	2.14	↯	1.06	↯
−70	1.71	↯	3.03	↯	–	–	–	–
−80	1.79	↯	2.63	↯	3.49	↯	1.47	↯
−90	2.62	↯	–	–	–	–	–	–
−100	1.46	↯	2.63	↯	3.15	↯	1.21	↯
−110	3.15	↯	–	–	–	–	–	–
−120	3.22	↯	4.47	↯	–	–	–	–

Notes: ↯ = Impacts occurred during run; ○ = Run was clean from impacts.

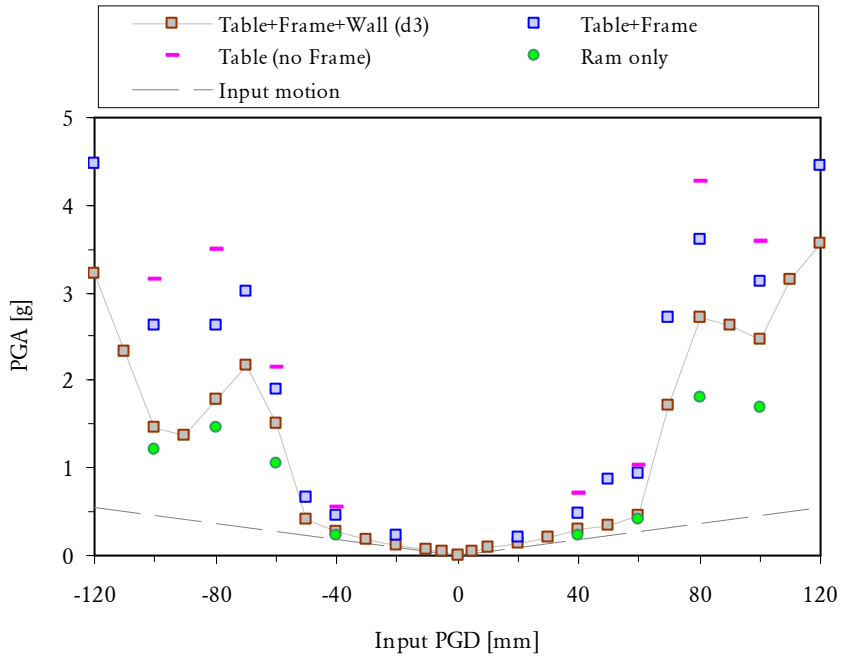

Figure D.11: Peak acceleration measured during tests on various test arrangements.

hydraulic ram was detached from any additional mass, meaning that the impacts were not due to the shaketable, the wall restraint frame, or the wall. Generally, the impacts began to occur for PGD greater than or equal to +60 mm on the positive side and −60 mm on the negative side. The results exhibit good correlation between the shaking intensity at which the impacts occurred and the intensity at which they are expected to occur based on the predictions in Table D.2.

The PGA response for the different test arrangements is also shown graphically on Figure D.11. The graph indicates that regardless of the test arrangement used, the PGA was slightly greater in the positive PGD direction as opposed to the negative direction. This trend is consistent with the results for tests on wall D3, and also with the predicted response based on the computational simulation performed (refer to Table D.8).

Whilst the PGD intensity at which the impacts occurred was independent of the test arrangement, the value of the measured PGA for the different arrangements varied depending on the configuration, as seen from Figure D.11. For runs at which the impacts took place, the measured PGA was consistently highest for the configuration involving only the bare shaketable, second highest for the configuration involving the table and frame, and lowest for the configuration involving the table, frame and wall. In other words, the measured PGA reduced as the mass of the system was increased. The apparent inverse relationship between the mass

and resulting acceleration suggests that the force limit of the ram may have been reached in these scenarios. Curiously though, this trend is not consistent with the tests using only the hydraulic ram, whereby the generated accelerations are consistently lower compared to the other three configurations having additional mass. A possible explanation for this is that the force limit of the ram may not have been reached when it was detached from the table, due to the absence of the additional mass.

Conclusions

The observation that the impacts occurred regardless of the test arrangement used, and most significantly, even in the case when no additional mass was connected to the hydraulic ram, had shown that the cause of the impacts was not due to the presence of any of these components of the test arrangement. Instead, these results indicate that the impacts must be due to an inability of the actual hydraulic ram to track the motion at higher levels of shaking intensity. This finding indeed agrees with the underlying cause diagnosed, as discussed in Section D.2.

D.6.2 Tests Using an Alternate Hydraulic Ram and Different PID Settings

Having previously established that the impacts were not caused by any particular part of the overall shaketable test arrangement (Section D.6.1), the second phase of diagnostic tests studied the motion of the hydraulic ram itself when disconnected from the rest of the shaketable test setup.

The aims of the second phase of experimental diagnostic tests were twofold:

The first aim was to determine whether the impacts may have been caused by a particular defect of the ram which had been used to drive the shaketable. This was achieved by testing an alternate 'reserve' ram using the same Taft input motion at the levels of intensity used previously. The reserve ram had identical specifications to the shaketable ram and was operated using the same controller computer and software.

The second aim was to investigate the influence of the proportional-integral-derivative (PID) setting[4] of the controller computer on the generation of the impacts

[4]The PID setting of the controller computer which drives the hydraulic ram indirectly determines the impetus with which the ram is forced toward its target displacement under displacement-controlled loading. At any instance in time during the tracking process, there is some, albeit small, difference between the physical position of the ram and the target position at which it is 'meant to' be. The PID setting relates to the energy with which the controller tries to correct this difference at any point in time—a higher PID value means that the actuator is driven with greater impetus to correct the error, with the converse being true for a smaller PID value.

Table D.4: Results from tests on the shaketable ram and reserve ram at different PID settings. All tests used the Taft earthquake motion. Gray shading indicates the PGDs at which synchronisation is expected to be lost, based on Table D.2.

Ram:	Shaketable 36 dB		Reserve 36 dB		Shaketable 26 dB		Reserve 26 dB	
PID:								
PGD [mm]	PGA [g]	Note	PGA [g]	Note	PGA [g]	Note	PGA [g]	Note
+120	–	–	–	–	0.79	○	–	–
+100	1.68	ϟ	1.28	ϟ	0.56	○	0.46	○
+80	1.81	ϟ	1.41	ϟ	0.59	○	0.54	○
+60	0.40	○	0.35	○	0.27	○	0.24	○
+40	0.22	○	–	–	0.19	○	0.18	○
+20	–	–	–	–	–	–	–	–
−20	–	–	–	–	–	–	–	–
−40	0.23	○	–	–	0.18	○	0.20	○
−60	1.06	ϟ	0.93	ϟ	0.39	○	0.37	○
−80	1.47	ϟ	1.23	ϟ	0.58	○	0.44	○
−100	1.21	ϟ	0.95	ϟ	0.46	○	0.40	○
−120	–	–	–	–	0.65	○	–	–

Notes: ϟ = Impacts occurred during run; ○ = Run was clean from impacts.

and to determine whether the setting could be altered in order to prevent the impacts from occurring. A PID setting of 36 dB had been previously used in all tests conducted prior to those reported in this section, including the first three walls tested (D5, D3 and D4) and diagnostic tests investigating the influence of the test arrangement (Section D.6.1). In these tests, the original PID setting of 36 dB is compared to a reduced setting of 26 dB, for both the shaketable ram and reserve ram. All runs performed used the original Taft earthquake input motion.

Results

Table D.4 shows the measured PGA for the different scenarios considered, including a qualitative assessment of whether the impacts were deemed to occur based on the recorded acceleration time history. The table also highlights the PGD intensities at which the impacts were expected to occur based on the loss of synchronisation between the ram and the target motion (as per Table D.2). The measured PGA response is also shown graphically on Figure D.13.

When run at 36 dB PID, both hydraulic rams generated acceleration spikes which are characteristic of the impacts, although the PGAs were slightly larger for

Whilst the value of the PID setting needs to be sufficiently high in order for the input motion record to be reproduced with an acceptable accuracy, if it is too high, the system can potentially become unstable through feedback effects due to continual overcorrection of the displacement error. At the time that these tests were being conducted, it was hypothesised that the impacts generated could be a result of such effects.

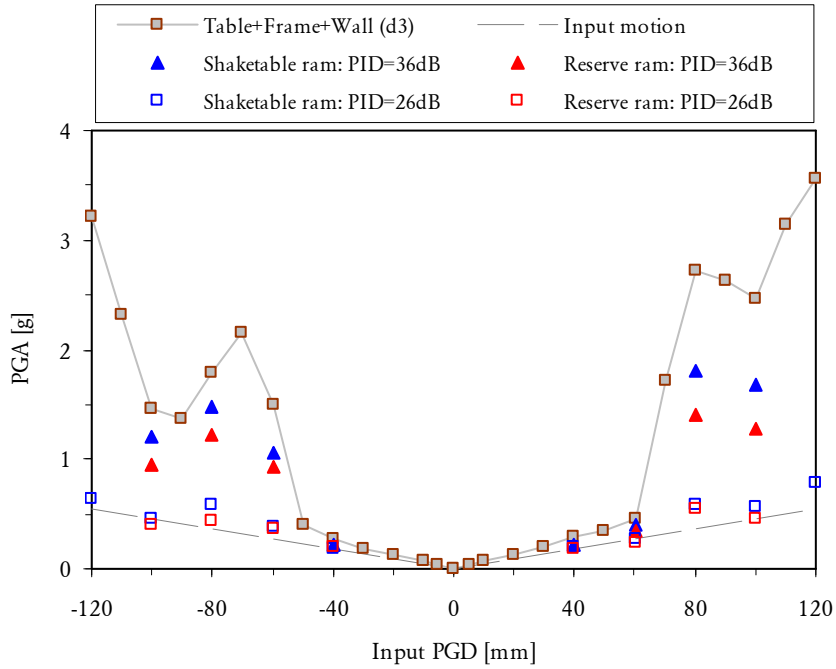

Figure D.12: Peak acceleration measured during tests on the shaketable ram and reserve ram at different PID settings. In these tests the ram was not connected to the shaketable.

the shaketable ram than for the reserve ram (Figure D.12). The impacts for both rams occurred at the same levels of shaking intensity. For the intensities considered in these tests, impacts first occurred at -60 mm PGD in the negative direction and $+80$ mm PGD in the positive direction and persisted at stronger levels of shaking. These results are consistent with the PGD predicted to result in impacts due to a loss of synchronisation between the ram and target motion.

Figure D.13 demonstrates that both rams possess peak velocity limits, which were reached at stronger PGD intensities. These velocity limits appear to be equal for both rams, approximately -165 mm/s in the negative direction and $+200$ mm/s in the positive direction. It is therefore concluded that neither of these rams has any particular malfunction which generates the impacts, but rather that tracking the Taft motion at higher levels of intensity is beyond the capability of both rams.

Comparing the response for the two PID levels considered in these tests reveals that the magnitude of the acceleration generated during the impacts can be alleviated by reducing the PID to the lower value of 26 dB. As shown by Figure D.12, the PGA generated for a 26 dB PID is much more comparable to the PGA expected based on the input motion, as opposed to a 36 dB PID. This is the case for both rams.

Close inspection of the 26 dB PID response of the two rams (Figure D.12), however, shows a trend which is consistent with tests where the impacts were

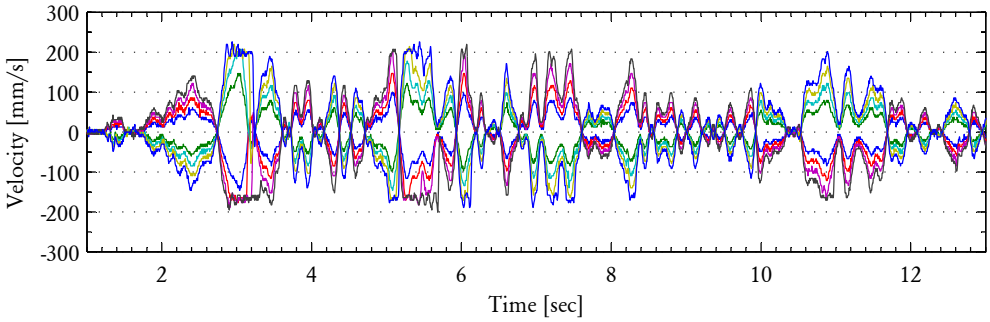

(a) Shaketable ram, PID = 36 dB (PGD = ±40, ±60, ±80, ±100 mm)

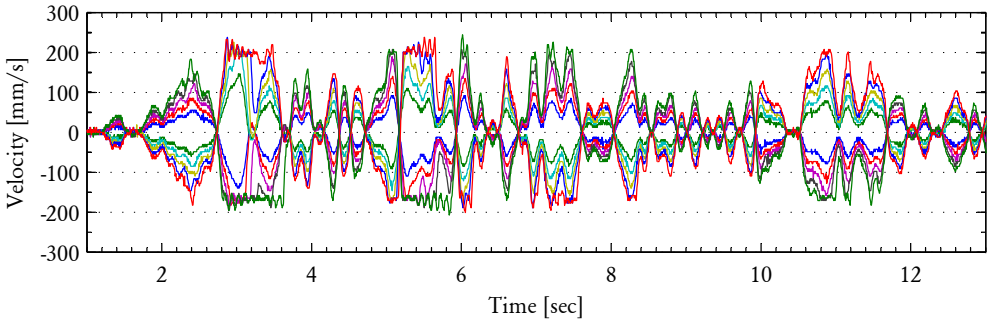

(b) Shaketable ram, PID = 26 dB (PGD = ±40, ±60, ±80, ±100, ±120 mm)

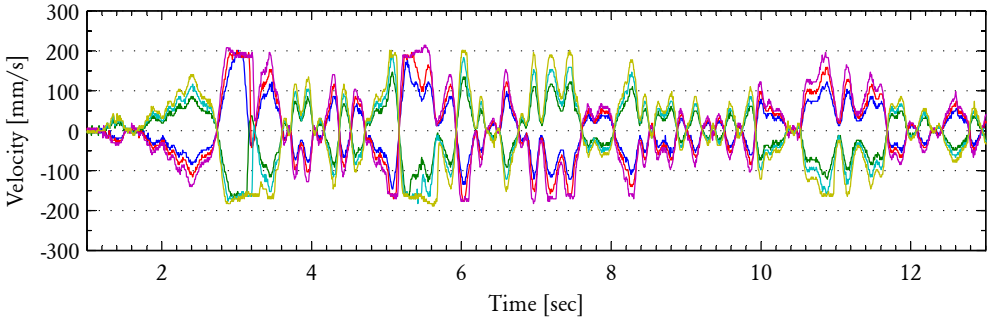

(c) Reserve ram, PID = 36 dB (PGD = ±60, ±80, ±100 mm)

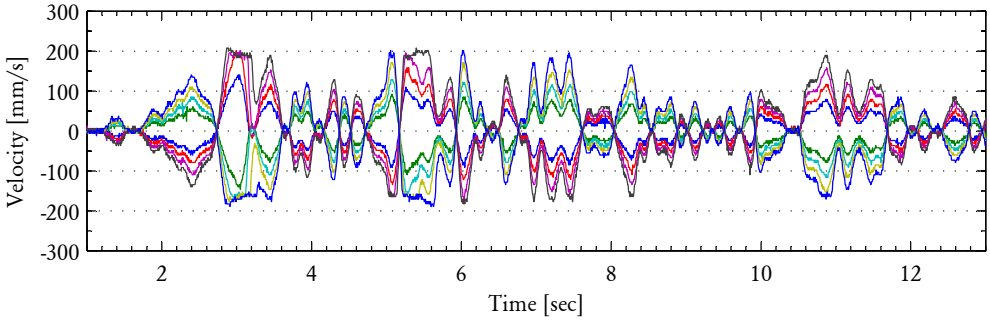

(d) Reserve ram, PID = 26 dB (PGD = ±40, ±60, ±80, ±100 mm)

Figure D.13: Velocity response of the shaketable ram and reserve ram for varied PID settings during the Taft earthquake motion. Several runs with different PGD intensities are plotted on each graph as indicated.

observed to occur. In particular, there is an increase in the PGA from ±60 mm PGD to ±80 mm PGD, a slight reduction at ±100 mm PGD, followed by another rise at ±120 mm PGD. Whilst the magnitude of the measured PGA for the 26 dB PID response is significantly lower, this general trend is consistent with that observed previously in tests where the impacts caused significant acceleration spikes. This includes, for example, tests on wall D3 (shown in Figure D.12 for comparison) and also the predicted PGA response based on the simulation of the ram's motion as a result of the impacts (Figure D.8). Furthermore, the velocity threshold is shown to be reached irrespective of the PID setting (Figure D.13), despite the acceleration spikes being far more prominent at a PID setting of 36 dB as opposed to 26 dB. These results suggest that reducing the PID does not completely prevent the impacts for occurring, but rather that it reduces the PGA which is generated.

Conclusions

Since both hydraulic rams possessed equal peak velocity limits and exhibited impacts at the same levels of input motion intensity, it was concluded that the reserve ram would provide no benefit over the original ram.

Reducing the controller PID from 36 dB to 26 dB was found to attenuate the accelerations generated for runs where the ram was disconnected from the shaketable. However, this was found not to be the case in runs where the full test arrangement was present, as indicated by test runs 60–66 on wall D4, where the impacts were demonstrated to occur even for a reduced PID setting (Table C.6).

D.6.3 Trial Runs Using Different Seismic Input Motions

The third phase of diagnostic tests involved trial runs using different seismic motions on the shaketable. The eight seismic motions trialled in this phase of testing were synthetically generated motions Syntho1–Syntho8, which are described in Appendix C.2. The associated peak responses of the motions in both the positive and negative directions including the PGD, PGV and PGA are given in Table D.1.

The test arrangement during these tests consisted of the ram being connected to the shaketable and the wall restraint frame, but without the presence of a wall. These conditions were intended to recreate as close as possible the conditions used during actual wall tests, by including as much weight as possible.

Table D.5: Results of tests on various synthetic earthquake motions. The test arrangement included the table and the restraint frame and the controller PID was set to 36 dB. Gray shading indicates the PGDs at which synchronisation is expected to be lost, based on Table D.2.

Quake:	Syntho1		Syntho2		Syntho3		Syntho4		Syntho5		Syntho6		Syntho7		Syntho8	
PGD [mm]	PGA [g]	Note	PGA [g]	Note	PGA [g]	Note	PGA [g]	Note	PGA [g]	Note	PGA [g]	Note	PGA [g]	Note	PGA [g]	Note
+120	–	–	–	–	–	–	–	–	–	–	–	–	–	–	–	–
+110	–	–	–	–	–	–	–	–	–	–	–	–	–	–	–	–
+100	5.11	↯	5.30	↯	4.14	↯	5.05	↯	5.46	↯	6.19	↯	–	–	5.20	↯
+90	–	–	–	–	–	–	–	–	–	–	–	–	–	–	–	–
+80	4.69	↯	3.25	↯	2.50	↯	4.38	↯	5.13	↯	5.50	↯	–	–	4.52	↯
+70	–	–	–	–	–	–	–	–	–	–	–	–	–	–	–	–
+60	2.51	↯	1.92	↯	0.68	○	2.19	↯	3.49	↯	4.71	↯	4.62	↯	2.14	↯
+50	–	–	–	–	–	–	–	–	–	–	–	–	–	–	–	–
+40	0.57	○	0.43	○	0.44	○	0.60	○	1.39	↯	1.86	↯	1.87	↯	0.93	↯
+30	–	–	–	–	–	–	–	–	–	–	–	–	–	–	–	–
+20	–	–	–	–	–	–	–	–	–	–	–	–	0.62	○	0.54	○
+10	–	–	–	–	–	–	–	–	–	–	–	–	–	–	–	–
−10	–	–	–	–	–	–	–	–	–	–	–	–	–	–	–	–
−20	–	–	–	–	–	–	–	–	–	–	–	–	0.85	○	0.54	○
−30	–	–	–	–	–	–	–	–	–	–	–	–	–	–	–	–
−40	1.21	↯	1.32	↯	0.36	○	0.57	○	1.64	↯	3.08	↯	2.30	↯	1.21	↯
−50	–	–	–	–	–	–	–	–	–	–	–	–	–	–	–	–
−60	2.41	↯	1.45	↯	1.16	↯	2.52	↯	2.95	↯	5.75	↯	4.74	↯	2.97	↯
−70	–	–	–	–	–	–	–	–	–	–	–	–	–	–	–	–
−80	4.85	↯	3.31	↯	2.91	↯	5.35	↯	4.33	↯	4.70	↯	–	–	3.85	↯
−90	–	–	–	–	–	–	–	–	–	–	–	–	–	–	–	–
−100	4.74	↯	5.43	↯	3.77	↯	4.65	↯	4.98	↯	6.44	↯	–	–	4.78	↯
−110	–	–	–	–	–	–	–	–	–	–	–	–	–	–	–	–
−120	–	–	–	–	–	–	–	–	–	–	–	–	–	–	–	–

Notes: ↯ = Impacts occurred during run; ○ = Run was clean from impacts.

Results

Table D.5 provides the PGA data at varied input PGD intensity, including an assessment of whether the impacts were deemed to have occurred. The table also indicates the shaking intensities for each seismic motion at which the impacts are expected to occur, based on loss of synchronisation between the ram and input motion, as per Table D.2.

For each of the seismic motions considered, the impacts began to occur once the PGD intensity was sufficiently high. Comparison of the experimental results and analytical predictions shows that the impacts only occurred in cases where they were predicted to occur based on the simplified procedure, as described in Section D.5. Although the PGD was increased at the fairly large increments of 20 mm and in certain cases only a small number of tests were carried out[5], the results indicate that for the different shaking motions the simplified procedure (Table D.2) provides conservative estimates of the PGD intensities at which the impacts first begin to occur.

The results are also displayed graphically on Figure D.14, which compares the measured PGA response to the predicted response for each of the seismic motions considered. The predicted response curve is based on simulating the ram's motion using the procedure presented in Section D.4. Whilst the amount of experimental data obtained is not sufficient to compare the shape of these curves in great detail, the graphs indicate that when the impacts are predicted not to occur (the unshaded area of the graphs), the measured and expected PGAs are relatively close. By contrast, when the impacts are predicted to occur (shaded area), the measured accelerations become much larger than those expected in the absence of the impacts, which would occur if the input motion was tracked correctly. Furthermore, when the impacts did occur, the PGA generated is also significantly larger than that predicted by the numerical simulation. Possible reasons for this discrepancy were discussed in Section D.4.5.

Conclusions

For each of the shaking motions considered, the impacts occurred when the shaking intensity was sufficiently high. This intensity can be predicted using the simplified procedure presented in Section D.5 as a PGD.

The finding that the impacts are caused by the velocity threshold of the hydraulic ram could be used for selecting or generating new shaking motions for future use

[5]This is because at the time these tests were conducted, the aim was to simply determine whether the impacts would take place and not to provide detailed data.

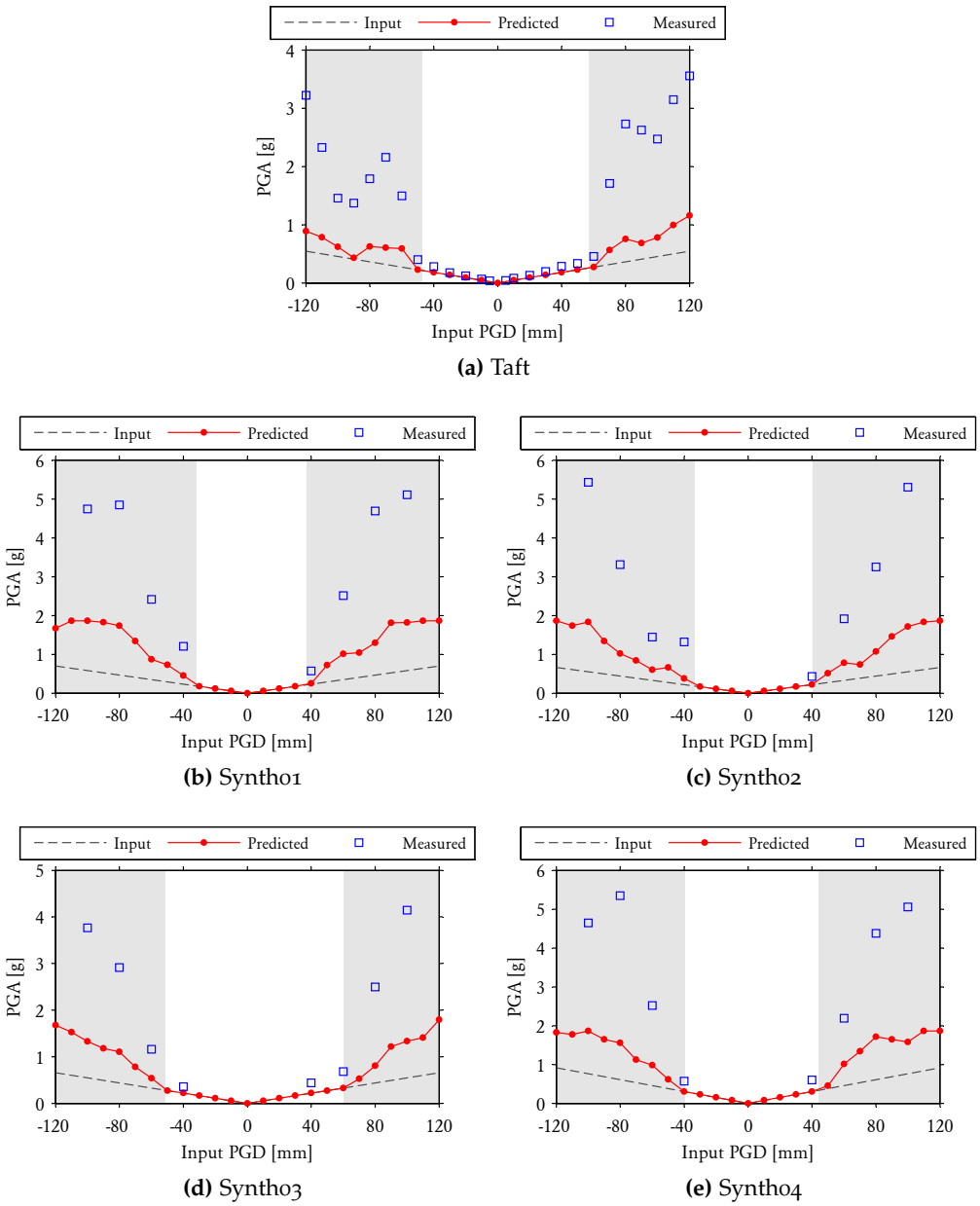

(a) Taft

(b) Syntho1

(c) Syntho2

(d) Syntho3

(e) Syntho4

Figure D.14: Comparison of predicted and experimentally measured PGA response for the different seismic motions. The predicted ram motion was calculated by implementing velocity threshold limits of -165 and $+200$ mm/s. Grey regions show PGDs at which synchronisation is lost between the ram and target displacement.

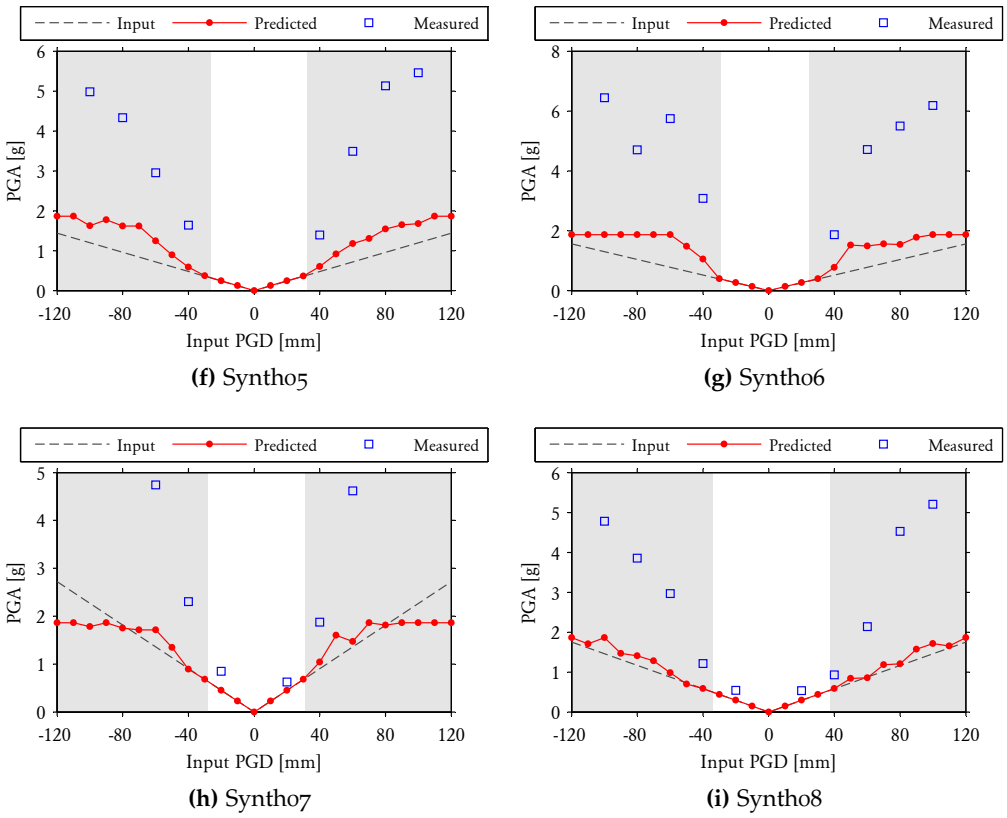

(f) Syntho5 **(g)** Syntho6

(h) Syntho7 **(i)** Syntho8

Figure D.14: (cont'd).

of the shaketable. However, because of the innate relationship between a signal's frequency and amplitudes of acceleration, velocity and displacement, seismic motions designed to satisfy the prevention of the impacts will typically need to have a low frequency content.

D.7 CONCLUSIONS AND RECOMMENDATIONS

The underlying cause of the shaketable impacts was identified as a velocity limiting condition of the hydraulic ram used to drive the table. These velocity limits have been experimentally measured to be -165 mm/s in the negative direction (ram extending outwards) and $+200$ mm/s in the positive direction (ram retracting inwards). The impacts occur in test runs where the peak velocity of the input motion exceeds the maximum capacity of the hydraulic ram, which causes a loss of synchronisation between the ram and the target displacement. The actual instance at which an impact occurs is when the hydraulic ram travels at its threshold velocity and abruptly experiences a change in the direction of travel

A numerical simulation of the ram's motion has been developed based on implementing the maximum velocity condition. The simulation strongly supports the aforementioned reasons for the impacts, by not only predicting with good accuracy the motion intensity at which the impacts are expected to occur, but also the specific points in the motion at which they occur. The predicted response also exhibits good correlation with experimental results in terms of the trend in the generated PGA for different shaking intensities.

A simplified procedure was also proposed for predicting the motion intensity at which the impacts are expected to occur. The premise of the method is to calculate the PGD at which the PGV in the input motion begins to exceed the velocity limits of the ram. This approach gives good correlation with the motion intensities at which the impacts were observed experimentally.

In the opinion of the author, the only way in which the impacts can be prevented whilst preserving the spectral content of the input motion would be through an upgrade of the shaketable hardware, in particular, replacing the hydraulic ram with one capable of reaching higher velocities. Nonetheless, the findings made in this study may be of benefit during future use of the shaketable; for example, as an aid in the selection of suitable input earthquake motions.

Appendix E

MOMENT CAPACITIES

Abstract

This appendix contains additional detail related to moment capacity expressions, as dealt with in Chapter 4.

E.1 AS 3700 EXPRESSIONS FOR ULTIMATE MOMENT CAPACITIES

This section reproduces expressions for the ultimate moment capacities in vertical, horizontal and diagonal bending provided in the Australian masonry code AS 3700 [*Standards Australia*, 2001] for ultimate strength design.[1]

E.1.1 Vertical Bending

AS 3700 prescribes the vertical moment capacity as

$$\bar{M}_v = \left(\phi\, k_{mt}\, f'_{mt} + f_d\right) \bar{Z}_d, \tag{E.1}$$

where ϕ is the capacity reduction factor (stipulated as 0.6), k_{mt} is a bending moment capacity factor dependent on the type of masonry material (1.0 for standard clay brick masonry), f'_{mt} is the characteristic flexural tensile strength of masonry, $\bar{Z}_d$ is the elastic section modulus of the bedded area per unit length, and f_d is the minimum design vertical compressive stress. Equation (E.1) is based on simple linear elastic response, with the moment being taken as the product of the necessary

[1] Since these expressions are used for design, they contain capacity reduction factors and characteristic values of material properties.

flexural stress to cause cracking ($f_{mt} + f_d$) and the elastic section modulus ($\bar{Z}_d$). The code also provides a second equation that limits the usable axial stress to

$$f_d \leq 2.0\,\phi\,k_{mt}\,f'_{mt}.$$

E.1.2 Horizontal Bending

AS 3700 specifies the horizontal moment capacity as

$$\bar{M}_h = \text{lesser of} \begin{cases} 2.0\phi\,k_p\sqrt{f'_{mt}}\left(1+\dfrac{f_d}{f'_{mt}}\right)\bar{Z}_d & \text{for stepped failure,} \quad \text{(E.2a)} \\ \phi\left(0.44\,f'_{ut}\,\bar{Z}_u + 0.56\,f'_{mt}\,\bar{Z}_p\right) & \text{for line failure,} \quad \text{(E.2b)} \end{cases}$$

where ϕ is the capacity reduction factor; k_p is a perpend spacing factor taken as the lesser of s_p/t_u and s_p/h_u, but no greater than 1.0; s_p is the minimum overlap of masonry units in successive courses; t_u is width of the masonry unit; h_u is the height of the masonry unit; f'_{mt} is the characteristic flexural tensile strength of the masonry in MPa; f'_{ut} is the characteristic lateral modulus of rupture of the masonry units; f_d is the minimum design vertical compressive stress; $\bar{Z}_d$ is the elastic section modulus of the bedded area; $\bar{Z}_u$ is the lateral section modulus of the masonry units; and $\bar{Z}_p$ is the lateral section modulus of the mortar contact area of perpend joints. The section moduli per unit length of the crack may all be calculated from elastic beam theory as

$$\bar{Z}_d, \bar{Z}_u, \bar{Z}_p = t_u^2/6, \tag{E.3}$$

where t_u is the width of the brick unit.

Equation (E.2a) is an empirical expression representing the moment capacity against stepped failure (refer to Figure 4.4a), similar to a relationship derived by *Lawrence* [1975] using a regression analysis on brickwork panel flexural strength test data. The code also provides an additional expression, which enforces an upper limit on the maximum usable compressive stress f_d within equation (E.2a), so that

$$f_d \leq f'_{mt}.$$

This limitation implies that in the absence of bond strength ($f'_{mt} = 0$), the masonry will possess zero moment capacity. Such a treatment is likely to be overly conservative for walls with low axial stress, since unreinforced masonry (URM) attains some moment resistance from friction along the bed joints. A further problem of equation (E.2a) is that it is dimensionally incorrect due to the presence of the $\sqrt{f'_{mt}}$ term, which can introduce unit inconsistency (thus requiring f'_{mt} to be in MPa).

The resistance to line failure (refer to Figure 4.4b), represented by equation (E.2b), is based on elastic sectional capacity of the vertical crack. The equation includes strength contributions from rupture of the brick units in addition to flexural capacity of the perpend joints, whilst making the approximation that 44% of the failure plane cuts through brick units and 56% through a combination of perpend and bed mortar joints.[2]

E.1.3 Diagonal Bending

AS 3700 specifies the diagonal bending capacity per unit length according to the equation

$$\bar{M}_d = \phi \, f'_t \, \bar{Z}_t, \tag{E.4}$$

where ϕ is the capacity reduction factor, f'_t is an equivalent characteristic torsional strength and $\bar{Z}_t$ is the equivalent torsional section modulus per unit length along the axis of the diagonal crack line.

This approach to calculating the diagonal moment capacity was developed by *Lawrence and Marshall* [1996] based on the assumption that the diagonal crack behaves as a rectangular shaft subjected to pure torsion. The effective rectangular section is assumed to have the dimensions $B \times t_u$, where t_u is the width of the masonry unit and the length B is given by

$$B = \frac{h_u + t_j}{\sqrt{1 + {G_n}^2}}, \tag{E.5}$$

where h_u is the height of the masonry unit, t_j is the thickness of mortar joint, l_u is the length of the masonry unit, and G_n is the natural slope of the diagonal crack line [calculated using equation (4.13)].

The provided expressions for $\bar{Z}_t$ are based on elastic theory [e.g. *Timoshenko and Goodier*, 1934] and cater for two possibilities regarding the location of the maximum shear stress along the section, depending on the relative size of B and t_u. For solid

[2] These are values representative of standard Australian brickwork, corresponding to 76 mm brick unit height and 10 mm mortar joint thickness.

rectangular sections, the torsional modulus is given as

$$\bar{Z}_t = \begin{cases} \dfrac{\dfrac{2\,B^2\,t_u^2}{3\,B + 1.8\,t_u}}{(l_u + t_j)\,\sqrt{1 + G_n{}^2}} & \text{for} \quad B \geq t_u, \\ \\ \dfrac{\dfrac{2\,B^2\,t_u^2}{1.8\,B + 3\,t_u}}{(l_u + t_j)\,\sqrt{1 + G_n{}^2}} & \text{for} \quad B \leq t_u. \end{cases} \tag{E.6}$$

The equivalent torsional stress term f'_t within expression (E.4) was calibrated by *Lawrence and Marshall* [1996] using experimental data for 49 test walls, to achieve good fit between the wall ultimate load capacities measured experimentally and predictions made using the virtual work method. This resulted in the empirically derived expression

$$f'_t = 2.25\sqrt{f'_{mt}}. \tag{E.7}$$

Lawrence and Marshall reasoned that any deviations in behaviour from the theoretical idealisation should be compensated for by the empirical nature of this term.

The primary shortcoming of this model is that it contains dimensional inconsistency due to the $\sqrt{f'_{mt}}$ term within equation (E.7) [similarly to (E.2a) for horizontal bending stepped failure]. Furthermore, the equations do not account for the strengthening influence due to vertical compressive stress and imply that in the absence of mortar bond cohesion a wall will have zero moment capacity in diagonal bending. This is contrary to the generally accepted view that the masonry undergoes some degree of rocking behaviour along diagonal crack lines and must therefore possess some moment resistance even after cracking. Consequently, neglecting this contribution is likely to be overly conservative, particularly for masonry with low bond strength or moderate vertical compressive stress.

E.2 TORSIONAL CAPACITY OF A MORTAR-BONDED SECTION

This section presents an analytical expression for calculating the ultimate torsional capacity in horizontal bending with respect to the stepped failure mode (refer to Figure 4.4a), which makes a slight alteration to an expression developed by Willis.

E.2.1 Original Equation by Willis

In his doctoral thesis, *Willis* [2004] (also published in *Willis et al.*, 2004) proposed that the ultimate moment capacity of an individual bed joint subjected to torsion

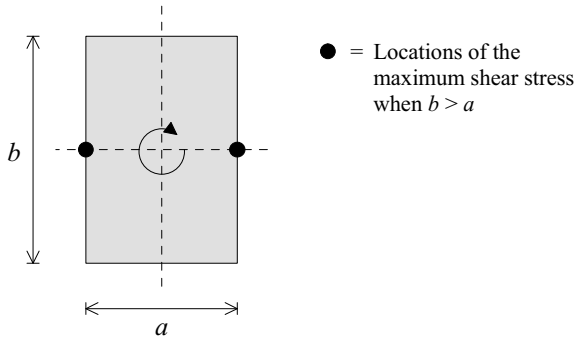

Figure E.1: Rectangular section subjected to elastic torsion about the centre.

can be calculated using the equation

$$m_h = k_{b2}\,\tau_{um}\,\frac{\left(l_u + t_j\right)\,t_u^2}{2}, \tag{E.8}$$

where m_h is the ultimate moment in horizontal bending over a single element (refer to Figure 4.2), l_u is the length of brick unit, t_j is the mortar joint thickness, t_u is the brick unit width, τ_{um} is the ultimate shear stress capacity of the masonry [calculated using Eq. (4.24)], and k_{b2} is a dimensionless factor based purely on the geometry of the bed joint. The expression was derived from elastic theory and assumes that failure occurs when the maximum torsional shear stress developed along the section reaches the ultimate shear stress capacity. The factor k_{b2} may be calculated using the *Timoshenko and Goodier* [1934] formula

$$k_{b2} = \frac{\frac{1}{3}\left[1 - \frac{192}{\pi^5 r}\sum_{n=1,3,5,\ldots}^{\infty}\frac{1}{n^5}\tanh\left(\frac{n\pi r}{2}\right)\right]}{1 - \frac{8}{\pi^2}\sum_{n=1,3,5,\ldots}^{\infty}\frac{1}{n^2\cosh\left(\frac{n\pi r}{2}\right)}}, \tag{E.9}$$

where r is the ratio of longer side to the shorter side lengths of the section (or b/a as shown in Figure E.1), which accounts for the fact that the maximum shear stress occurs at the midpoint of the longer edge. Since Willis' equation does not make any distinction between which is the longer and shorter side, it has the minor shortcoming that it is only applicable when the bed joint has good overlap, or $s_b \geq t_u$ (refer to Figure 4.2). Willis does state however, that k_{b2} can be conservatively assumed to be 0.208, which is the value corresponding to a square bed joint.

E.2.2 Revised Equation

As an alternative expression to that of Willis [equation (E.8)], the author proposes the slightly modified equation

$$m_h = k_{be}\,\tau_{um}\,t_u^3, \tag{E.10}$$

which becomes applicable to any value of bed joint overlap, due to the method used to calculate the coefficient k_{be}. From the definition of the bed joint overlap ratio as $r_o = s_b/t_u$ [equation (4.26)], the value r that must be used in the calculation of k_{b2} using equation (E.9) is

$$r = \max\left(r_o, \frac{1}{r_o}\right), \tag{E.11}$$

which accounts for the location of the maximum elastic shear stress along the rectangular section (Figure E.1). From this, the coefficient k_{be} becomes

$$k_{be} = \begin{cases} k_{b2}\,r_o^2, & \text{for } r_o < 1; \\ k_{b2}\,r_o, & \text{for } r_o \geq 1. \end{cases} \tag{E.12}$$

Figure 4.6 plots the resulting coefficient for varying overlap ratio r_o.

E.3 TORSIONAL FRICTION CAPACITY OF A DRY MASONRY SECTION

This section provides a developed analytical expression for calculating the residual moment capacity in horizontal bending due to frictional torsion along the bed joint. Previous models for calculating the frictional torsion capacity are presented in Section E.3.1. The author believes the new approach to be more robust than the previous ones for reasons outlined therein. Derivation of the model is presented in Section E.3.2.

E.3.1 Previous Models

Willis [2004] (also published in *Willis et al.*, 2004) proposed that the post-cracked frictional torque capacity over a single bed joint can be calculated using the expression

$$m_h = \xi_f\,\sigma_v\,\frac{(l_u + t_j)\,t_u}{2}, \tag{E.13}$$

in which ξ_f is an empirical index of frictional torque resistance and other symbols as defined previously (refer to Figure 4.2). The equation is based on the following

assumed relationship between the torque resistance T and applied axial force P:

$$T = \xi_f \, P. \tag{E.14}$$

The coefficient ξ_f, which has dimensions of length, was empirically calibrated by Willis through torsional tests on bed joints and found to be approximately 40 mm for the standard Australian brickwork on which these tests were conducted ($230 \times 110 \times 76$ mm units with 10 mm mortar joints). The inherent shortcoming of this expression is that it is only applicable to masonry units having the same dimensions as those to which the value of ξ_f was calibrated—for each new type of masonry it would be necessary to empirically derive a new value of ξ_f. This is evident from equation (E.14), which implies that for a fixed axial load P and coefficient ξ_f the resulting frictional torque capacity T will be constant, irrespective of scale effects. This clearly cannot hold, since the scale of the masonry units influences the size of the internal lever arm and therefore the torque capacity. The applicability of Willis' equation is further limited by not being expressed in terms of the friction coefficient, and can therefore only be applied to the particular type of masonry used in the calibration data set, both in terms of scale and frictional characteristics.

As an alternative approach for calculating the frictional torque capacity along a bed joint that does take into account geometric scale effects and the friction coefficient along the interface, the author proposed the following equation in previous research [*Vaculik et al.*, 2003]:

$$m_h = \frac{\mu \, \sigma_v \, t_u^3}{2.614}, \tag{E.15}$$

where μ is the friction coefficient, σ_v is the axial stress acting on the bed joint, and t_u is the width of the bed joint. This expression is based on the assumptions of a uniform stress distribution along the section, with rotation occurring about the centre of the bed joint (same assumptions and principles used to develop the new model in Section E.3.2).

Since equation (E.15) is formulated in terms of the friction coefficient and directly accounts for scale effects, the author considers it to be more versatile than equation (E.13). By setting equal the moment capacities predicted by equations (E.13) and (E.15), it can be shown that masonry used by Willis to obtain the value $\xi_f = 40$ mm has an equivalent friction coefficient of $\mu = 1.04$. Nonetheless, equation (E.15) is limited in that it is only applicable to a square bed joint. To overcome this, a more general form of the equation applicable to a generic rectangular section is derived in the following section.

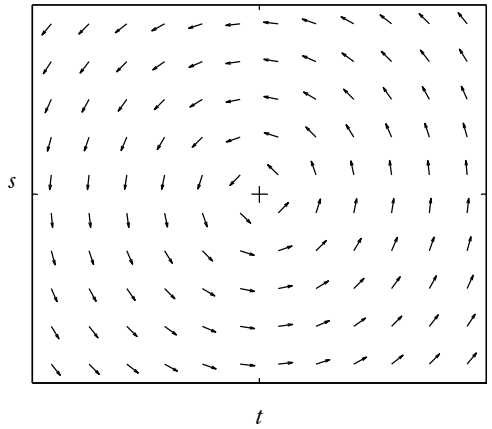

Figure E.2: Uniform shear stress field generated from torsion about the centre of the section.

E.3.2 New Model

Derivation of an analytical expression for calculating the moment capacity of a rectangular bed joint subjected to rotation friction will now be presented. For a list of the assumptions made in the development of the model, the reader is referred to Section 4.3.3 (p. 133).

It is worth noting that the model described here is very similar to a torsional friction model developed by *Orduña and Lourenço* [2005a], which also has the ability to deal with different (non centred) positions of the rotation point along the rectangular section.[3] The identical equations developed in both cases can be considered a verification for the derivation process used.

General

Consider a rectangular cross section having the dimensions t and s (representing the width t_u and overlap s_b of the bed joint respectively), subjected to torsion about its centre as shown in Figure E.2. The strategy of the derivation is to divide the rectangle into two types of triangles: $\triangle$A and $\triangle$B, as shown by Figure E.3. An expression is first derived for the torque about the acute vertex of a right triangle. The contributions of the constituent triangles are subsequently combined to obtain the torque acting about the overall rectangle (as per Figure E.3).

[3] This work was belatedly discovered by the author during the course of this research.

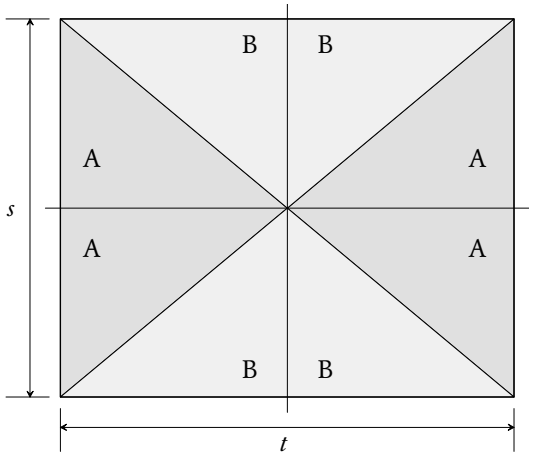

Figure E.3: Rectangular section divided into two types of right triangles.

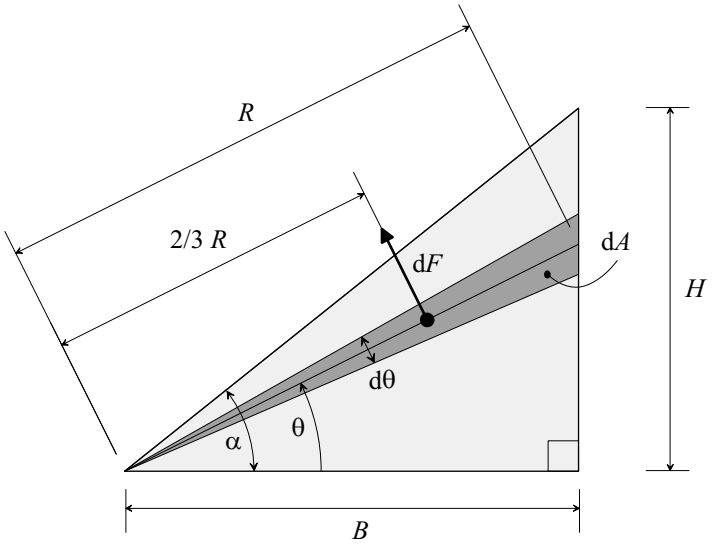

Figure E.4: A right triangle section subjected to plastic torsion about one of its acute vertices (bottom left corner in diagram shown).

Torsion About the Acute Vertex of a Right Triangle

The torsion along a generic right triangle cross section having the base B and height H as shown by Figure E.4 will now be derived. The total torque along the triangle may be obtained by integrating the torque contributions of the radial elements from which it is comprised. Consider a single radial element with length R and angle $\mathrm{d}\theta$ (Figure E.4). At the limit $\mathrm{d}\theta \to 0$, the element becomes triangular and therefore its area becomes

$$\mathrm{d}A = \frac{1}{2} R^2 \, \mathrm{d}\theta. \tag{E.16}$$

The shear force developed along the element by resisting the uniform shear stress τ is

$$\mathrm{d}F = \tau \, \mathrm{d}A = \frac{1}{2}\tau R^2 \, \mathrm{d}\theta. \tag{E.17}$$

As the element is triangular, its centroid is located at a distance $\frac{2}{3}R$ from the pivot of rotation. Hence, the torsion generated by the element is

$$\mathrm{d}T = \frac{2}{3}R \, \mathrm{d}F = \frac{1}{3}\tau R^3 \, \mathrm{d}\theta. \tag{E.18}$$

The radius R of the element is related to the angle θ by the expression

$$R = B \sec\theta. \tag{E.19}$$

The torsion $T_\triangle$ along the overall right triangle (Figure E.4) is obtained by integrating $\mathrm{d}T$ between the angles $\theta = 0$ and $\theta = \alpha$, such that

$$T_\triangle = \int_{\theta=0}^{\alpha} \frac{1}{3}\tau B^3 \left(\sec\theta\right)^3 \, \mathrm{d}\theta. \tag{E.20}$$

Or alternatively,

$$T_\triangle = k_\triangle \tau B^3, \tag{E.21}$$

where $k_\triangle$ evaluates to

$$\begin{aligned} k_\triangle &= \int_{\theta=0}^{\alpha} \frac{1}{3} \left(\sec\theta\right)^3 \, \mathrm{d}\theta \\ &= \frac{1}{6} \left[\sec\alpha \cdot \tan\alpha + \ln\left|\sec\alpha + \tan\alpha\right|\right]. \end{aligned} \tag{E.22}$$

This can be further simplified using the associated trigonometric identities [see for example *Abramowitz and Stegun*, 1964]

$$\tan\alpha = m \qquad \text{and} \qquad \sec\alpha = \sqrt{1+m^2},$$

to give

$$k_\triangle = \frac{1}{6}\left[m\sqrt{1+m^2} + \ln\left(m + \sqrt{1+m^2}\right)\right], \tag{E.23}$$

where m represents the triangle's height to base ratio,

$$m = H/B. \tag{E.24}$$

Torsion About the Centre of a Rectangle

The previously derived equation (E.23) is applicable a right triangle cross section[4] with rotation about the acute vertex at its base (Figure E.4). To derive a similar expression for rotation about the centre of a rectangular cross section[5], we divide the rectangle into two types of right triangles: $\triangle$A and $\triangle$B (Figure E.3), and use the previous result. Since, in the generic case where $s \neq t$, these triangles have non-identical dimensions when considered with respect to the point of rotation, they will generate different amounts of torsion and hence their contributions need to be considered separately.

Define r as the aspect ratio of the rectangular section [analogous to the overlap ratio as per equation (4.26)], such that

$$r = s/t. \tag{E.25}$$

Triangle A has the base $B = \frac{1}{2}t$ and aspect ratio $m = r$, whilst triangle B has the base $B = \frac{1}{2}s = \frac{1}{2}rt$ and aspect ratio $m = r^{-1}$. By substituting these into equations (E.21) and (E.23), the respective torques of triangles A and B become

$$T_{\triangle \mathrm{A}} = \frac{1}{48}\tau t^3 \left[r\sqrt{1+r^2} + \ln\left(r + \sqrt{1+r^2}\right)\right] \tag{E.26}$$

and

$$T_{\triangle \mathrm{B}} = \frac{1}{48}\tau r^3 t^3 \left[r^{-1}\sqrt{1+r^{-2}} + \ln\left(r^{-1} + \sqrt{1+r^{-2}}\right)\right]. \tag{E.27}$$

In the overall rectangular section, there are four instances of each type of triangle A and B. Therefore, the total torsion about the centre of the rectangle is obtained as

$$T_{\boxdot} = 4\left(T_{\triangle \mathrm{A}} + T_{\triangle \mathrm{B}}\right). \tag{E.28}$$

Substituting $T_{\triangle \mathrm{A}}$ and $T_{\triangle \mathrm{B}}$ into the above equation gives the generalised expression

$$T_{\boxdot} = k_{\boxdot}\tau t^3, \tag{E.29}$$

where

$$k_{\boxdot} = \frac{1}{12}\left[2r\sqrt{1+r^2} + \ln\left(r + \sqrt{1+r^2}\right) + r^3 \ln\left(r^{-1} + \sqrt{1+r^{-2}}\right)\right]. \tag{E.30}$$

[4] Associated variables denoted using the subscript $\triangle$.
[5] Associated variables denoted using the subscript $\boxdot$.

Capacity of a Masonry Bed Joint

The residual horizontal bending moment capacity of a single masonry bed joint due to frictional torsion is obtained by substituting the relevant variables into equations (E.29) and (E.30). The frictional shear stress parallel to the bed joint's surface is $\tau = \mu\sigma_v$, where μ is the coefficient of friction and σ_v is the vertical axial stress acting normal to the joint. Hence, for a masonry bed joint whose dimensions are t_u by s_b, where t_u is the brick width and s_b is the joint overlap, the horizontal bending moment capacity m_h for a single joint becomes

$$m_h = k_{bp}\,\mu\,\sigma_v\,t_u^3. \tag{E.31}$$

The parameter k_{bp}, referred to as the plastic torsion coefficient, is calculated using equation (E.30) by taking r as the bed joint's overlap ratio r_o [refer to equation (4.26)]. Figure 4.6 plots the coefficient for varying values of the overlap ratio.

E.4 BIAXIAL FAILURE CRITERION MODEL FOR ULTIMATE MOMENT CAPACITY

This section provides the derivation of an expression for the ultimate moment capacity in diagonal bending, based on a biaxial failure criterion model.

E.4.1 Biaxial Failure Envelope

Suppose that a masonry wall subjected to flexural actions develops a combination of the vertical and horizontal moments $\bar{M}_v$ and $\bar{M}_h$ at some arbitrary location. Let us define the corresponding slope κ and angle θ_κ of the applied moment, such that

$$\kappa = \tan\theta_\kappa = \frac{\bar{M}_h}{\bar{M}_v}, \tag{E.32}$$

which represents the loading line at the particular point in the wall, as shown by Figure E.5.

Now, let us denote the uniaxial moment capacities with respect to vertical and horizontal bending by $\bar{M}_{vc}$ and $\bar{M}_{hc}$, which may be calculated using the analytical expressions presented in Sections 4.3.2 and 4.3.3. From this, the orthogonal strength ratio is defined as

$$\eta = \frac{\bar{M}_{hc}}{\bar{M}_{vc}}. \tag{E.33}$$

The proposed model developed in this section is based on the assumption

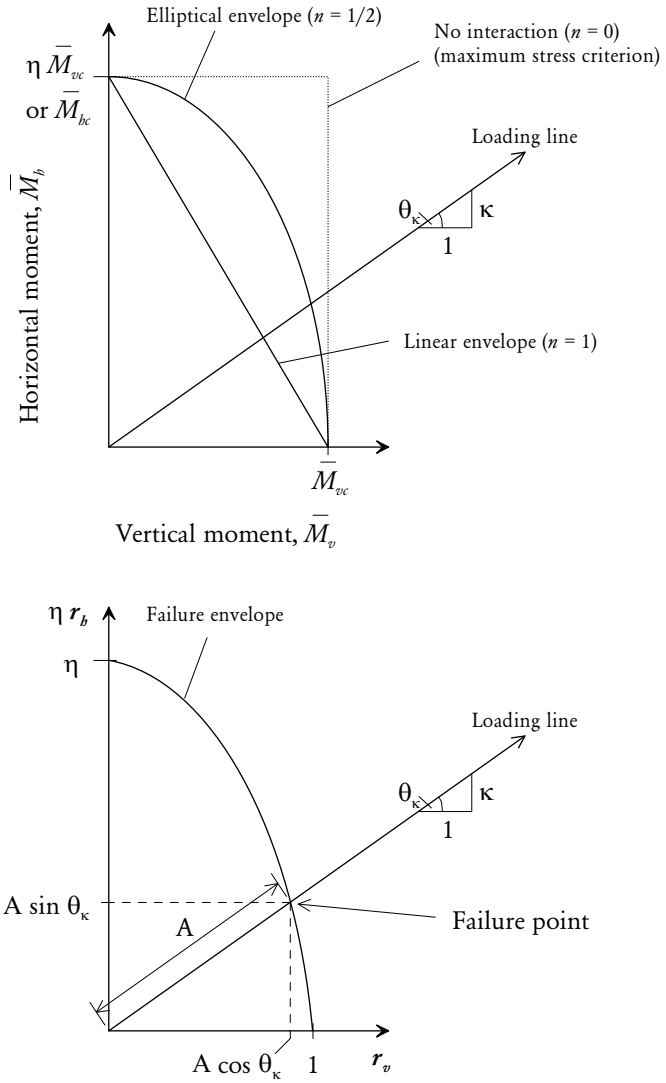

Figure E.5: Biaxial bending failure criterion, in the $\bar{M}_h$ vs. $\bar{M}_v$ format (top), and ηr_h vs. r_v format (bottom).

that failure occurs when the loading line intersects the biaxial failure envelope, as shown by Figure E.5. The overall role of the envelope is to provide a transition between the orthogonal moment capacities, as well as to account for interaction (a strengthening or weakening effect) between the flexure and torsion along the failure surface. The typical approach used to define a failure envelope [e.g. *Baker*,

1979; *Sinha et al.*, 1997] is through an empirical relationship between the parameters

$$r_v = \frac{\bar{M}_v}{\bar{M}_{vc}} \tag{E.34}$$

and

$$r_h = \frac{\bar{M}_h}{\bar{M}_{hc}}, \tag{E.35}$$

which represent the respective ratios of the applied moments at failure and their uniaxial moment capacities. By combining equations (E.32), (E.33), (E.34) and (E.35), it becomes evident that the loading line (in Figure E.5) can be represented as

$$\frac{r_h}{r_v} = \frac{\kappa}{\eta}. \tag{E.36}$$

At the present state of research, there is still uncertainty regarding the appropriate form of a failure envelope to describe the failure criterion of unreinforced masonry subjected to the biaxial bending, largely due to a lack of available experimental data. For example, *Baker* [1979] proposed the elliptical relationship

$$r_v{}^2 + r_h{}^2 = 1,$$

which implies a mutually weakening influence between the orthogonal moment capacities at the point of failure. Similarly, the work by *Willis* [2004] on diagonal bending also suggested a mutually weakening influence. By contrast, *Sinha et al.* [1997] proposed the relationship

$$r_v{}^2 - 0.75\, r_h\, r_v{}^2 - 0.25\, r_h\, r_v + r_h{}^2 = 1,$$

which instead implies a strengthening effect between the two failure modes.

Since all of these failure envelope relationships are empirical in nature, there is no reason why the exponents of r_v and r_h need to necessarily adhere to integer values. As such, in the proposed approach we will assume the generalised symmetric failure envelope

$$r_v{}^{1/n} + r_h{}^{1/n} = 1, \tag{E.37}$$

where n may assume any value greater than zero. As shown by Figure E.5, setting $n = 1$ represents a linear envelope and $n = 1/2$ gives an elliptical envelope. In general, as n becomes smaller, the weakening effect between the two orthogonal failure modes also becomes less significant. Therefore, the limit $n \to 0$ represents the boundary case of no interaction between the failure modes, where failure occurs once either moment $\bar{M}_v$ or $\bar{M}_h$ reaches its respective unfactored capacity.

E.4.2 Ultimate Moment Capacity Along an Inclined Axis

The basic formula to resolve a combined vertical and horizontal moment along an inclined axis can be written in the moment per length ($\bar{M}$) form as

$$\bar{M}_d = \bar{M}_v \cos^2 \varphi + \bar{M}_h \sin^2 \varphi, \tag{E.38}$$

where $\bar{M}_v$, $\bar{M}_h$ and $\bar{M}_d$ are the vertical, horizontal and diagonal (inclined) moments per length, and φ is the angle of the inclined axis with respect to the horizontal. By substituting equations (E.34) and (E.35) into (E.38), we obtain the moment capacity $\bar{M}_{dc}$ along the inclined axis, as

$$\begin{aligned} \bar{M}_{dc} &= \bar{M}_{vc}\, r_v \cos^2 \varphi + \bar{M}_{hc}\, r_h \sin^2 \varphi, \\ &= \bar{M}_{vc} \left[r_v \cos^2 \varphi + \eta\, r_h \sin^2 \varphi \right]. \end{aligned} \tag{E.39}$$

A generic formulation of the coefficients r_v and r_h can be obtained by treating the envelope diagram using polar coordinates. From Figure E.5 it is seen that at the failure point, we have

$$r_v = A \cos \theta_\kappa \tag{E.40}$$

and

$$r_h = A \eta^{-1} \sin \theta_\kappa, \tag{E.41}$$

with A as defined in the diagram.

If we assume the symmetrical failure envelope defined by equation (E.37) and substitute in equations (E.40) and (E.41), we get

$$A = \left[(\cos \theta_\kappa)^{1/n} + \left(\eta^{-1} \sin \theta_\kappa \right)^{1/n} \right]^{-n}. \tag{E.42}$$

Substituting these back into equation (E.39) yields the general inclined moment capacity formula

$$\bar{M}_{dc} = \bar{M}_{vc} \frac{\cos \theta_\kappa \, (\cos \varphi)^2 + \sin \theta_\kappa \, (\sin \varphi)^2}{\left[(\cos \theta_\kappa)^{1/n} + (\eta^{-1} \sin \theta_\kappa)^{1/n} \right]^n}. \tag{E.43}$$

In order to utilise this equation for calculating the moment resistance along an inclined crack line as part of a virtual work analysis, it seems reasonable to assume that the angle of moment inclination is approximately equal to the angle of the crack:

$$\theta_\kappa \approx \varphi. \tag{E.44}$$

Implementing this approximation reduces equation (E.43) to

$$\bar{M}_{dc} = \bar{M}_{vc} \frac{(\cos\varphi)^3 + (\sin\varphi)^3}{\left[(\cos\varphi)^{1/n} + (\eta^{-1}\sin\varphi)^{1/n}\right]^n}, \tag{E.45}$$

where the diagonal moment capacity $\bar{M}_{dc}$ becomes a function of only the crack angle φ (since $\bar{M}_{vc}$, η and n are constants).

E.4.3 Model Calibration Using Equation by Willis

In the development of his diagonal moment capacity model, *Willis* [2004] used the results of four experimental tests on wallette specimens to calibrate his analytical expression [equation (4.32)]. The brickwork used comprised standard clay brick masonry ($230 \times 110 \times 76$ mm units with 10 mm mortar joints) with no applied axial load ($\sigma_v = 0$) and were subjected to bending along the natural diagonal slope (hence $\kappa = G_n$). These conditions can therefore be used to calibrate the interaction exponent n in the developed model, so that both models produce identical moment predictions for the given set of parameters.

The diagonal moment capacity by Willis [equation (4.32)] can be written in the $\bar{M}$ form as

$$\bar{M}_{dc} = \bar{M}_{vc}\left[\cos^4\varphi + \eta\sin^4\varphi\right]. \tag{E.46}$$

Combining equations (E.46) and (E.39) shows that at the calibration state, the required coefficients r_v and r_h in the proposed model become

$$r_v = \frac{\cos^4\varphi + \eta\sin^4\varphi}{\cos^2\varphi + G_n\sin^2\varphi} \qquad \text{and} \qquad r_h = r_v\frac{G_n}{\eta}.$$

Evaluating the strength orthotropy for the aforementioned set of parameters from the wallette tests using equation (4.34) gives $\eta = 2.86$. Similarly, the diagonal crack angle and slope evaluated using equation (4.13) are $G_n = 0.717$ and $\varphi = \varphi_n = 0.622$ rad. Entering these values into the above equations gives the required coefficients as $r_v = 0.847$ and $r_h = 0.212$, which when substituted into the symmetrical interaction envelope equation, (E.37), produces equality between the two models at $n = 0.88$. This corresponds to a failure envelope that lies between elliptical and linear interaction (Figure E.5).

Implementing this result into equation (E.45) yields the calibrated moment

capacity expression

$$\bar{M}_{dc} = \bar{M}_{vc} \frac{(\cos\varphi)^3 + (\sin\varphi)^3}{\left[(\cos\varphi)^{1.14} + (\eta^{-1}\sin\varphi)^{1.14}\right]^{0.88}}. \tag{E.47}$$

Alternatively, a slightly conservative and simplified version of the moment capacity equation can be obtained by assuming a linear failure envelope ($n = 1$), which gives

$$\bar{M}_{dc} = \bar{M}_{vc} \frac{(\cos\varphi)^3 + (\sin\varphi)^3}{\cos\varphi + \eta^{-1}\sin\varphi}. \tag{E.48}$$

For the particular set of calibration parameters, equation (E.48) predicts a moment capacity which is only 6% smaller than the calibrated equation, (E.47). By contrast, assuming an elliptical interaction ($n = 1/2$) would result in a moment capacity only 14% larger than that given by the calibrated equation. The apparent low sensitivity of the predicted moment capacity on the type of interaction relationship chosen is because at the given strength orthotropy and crack inclination parameters used for calibration, failure is governed primarily by the vertical moment capacity $\bar{M}_{vc}$, and therefore interaction does not have a significant effect. This, however, also highlights the need for additional experimental data to enable calibration of the model at different diagonal crack inclinations.

Appendix F

PROBABILISTIC METHODOLOGY FOR HORIZONTAL BENDING

Abstract

This appendix contains additional detail related to Chapter 5.

F.1 DISTRIBUTION FITTING TO MATERIAL PROPERTIES

Figures F.1–F.8 demonstrate fits of the normal, lognormal and Weibull distributions to the experimental flexural tensile strength (f_{mt}) data for test walls S1–S8 (based on material tests reported in Appendix A). Similar graphs are provided for the pooled f_{mt} data for walls S1–S8 in Figure 5.2; pooled f_{mt} data for walls D1–D5 in Figure 5.3; and f_{ut} data for walls S1–S8 in Figure 5.4.

F.2 COMPARISON OF ANALYTICAL RESULTS TO TEST DATA

Table F.1 provides a summary of experimental results on small scale wallettes conducted by *Willis* [2004], as well as detailed results of the stochastic methodology in Chapter 5 applied to these specimens.

Table F.2 presents detailed experimental and analytical results for walls S1–S8 (Chapter 2) relating to the observed and predicted likelihood of stepped failure.

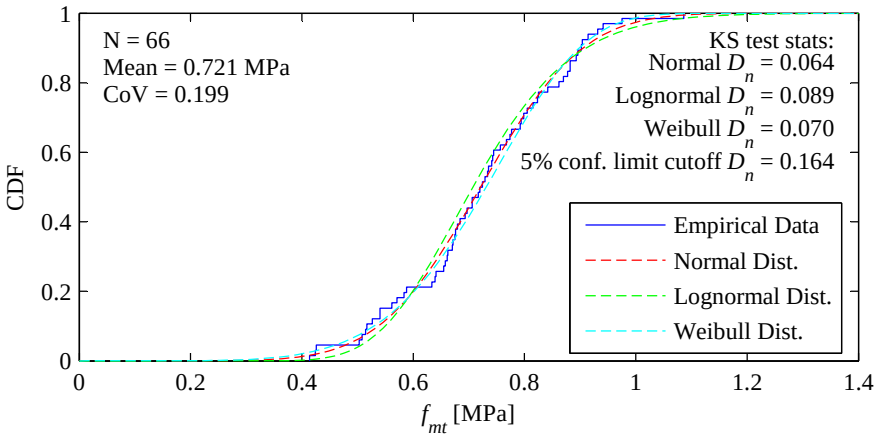

Figure F.1: Distribution of f_{mt} for panel s1.

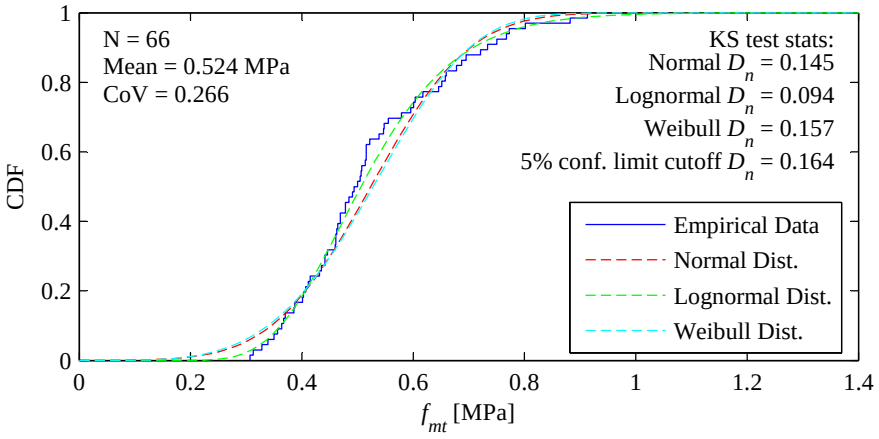

Figure F.2: Distribution of f_{mt} for panel s2.

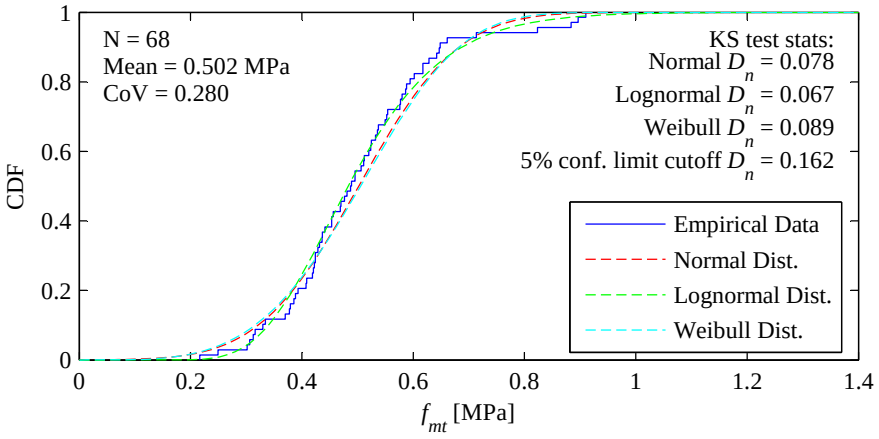

Figure F.3: Distribution of f_{mt} for panel s3.

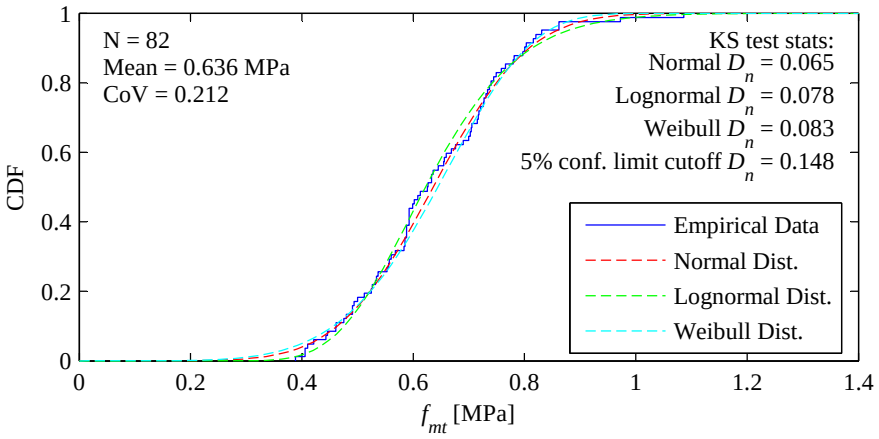

Figure F.4: Distribution of f_{mt} for panel s4.

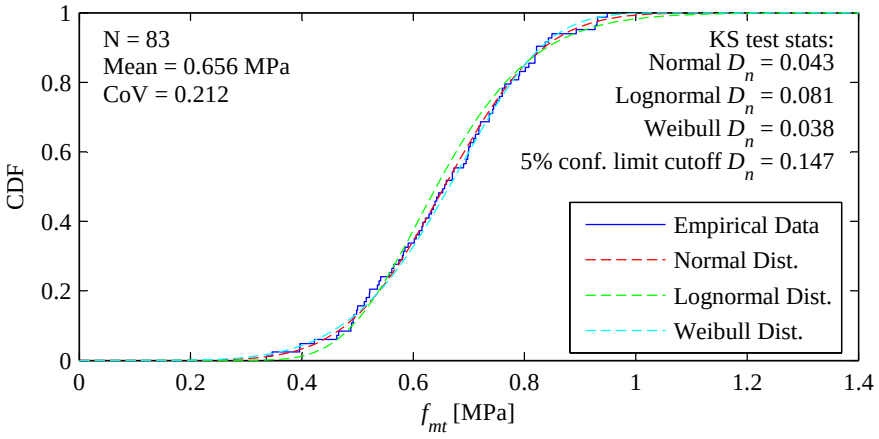

Figure F.5: Distribution of f_{mt} for panel s5.

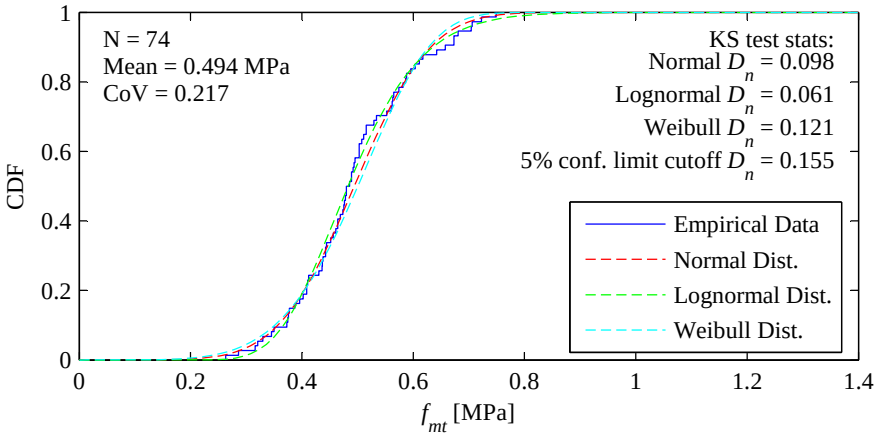

Figure F.6: Distribution of f_{mt} for panel s6.

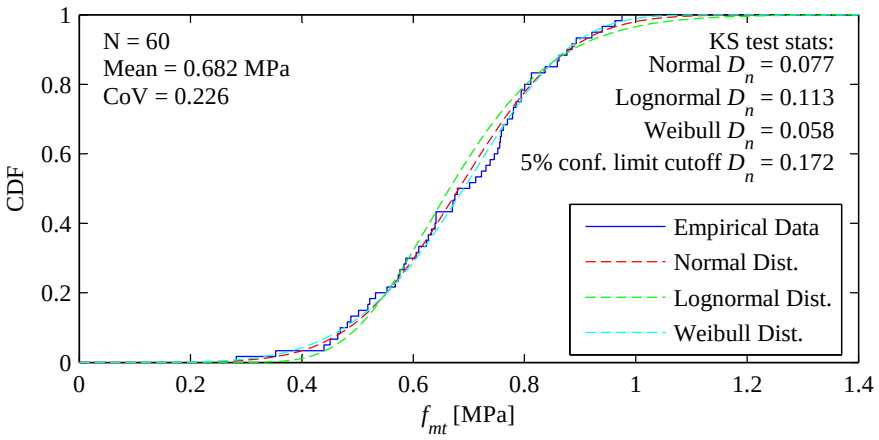

Figure F.7: Distribution of f_{mt} for panel s7.

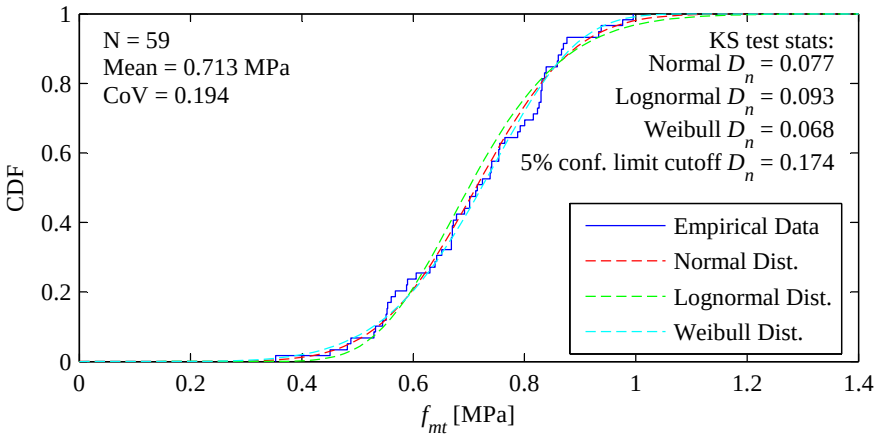

Figure F.8: Distribution of f_{mt} for panel s8.

Table F.1: Analytical and experimental results for wallettes tested by *Willis* [2004].

Test Id.			Analysis input parameters				Analysis results						Experimental		Comparison		
σ_v [MPa]	Pos. *	Rep.	$\widehat{f}_{mt}$ [MPa]	$\mathbb{C}\langle f_{mt}\rangle$	F_{ut}	Σ_v	η_{step}	η_{line}	η_{min} †	η_{mix}	ϕ_{mean} ‡	P_{step} §	η	P_{step}	$\frac{\eta_{\text{min}}}{\eta_{\text{test}}}$	$\frac{\eta_{\text{mix}}}{\eta_{\text{test}}}$	$(P_{\text{step}})_{\text{calc}} - (P_{\text{step}})_{\text{test}}$
0	H	1	0.78	0.14	6.41	0	3.25	2.78	2.78	2.62	0.94	0.29	2.88	0.6	0.96	0.91	−0.31
		2	0.78	0.14	6.41	0	3.25	2.78	2.78	2.62	0.94	0.29	2.47	0.6	1.13	1.06	−0.31
		3	0.74	0.23	6.76	0	3.25	2.93	2.93	2.65	0.90	0.38	3.31	0.6	0.89	0.80	−0.22
		4	0.74	0.23	6.76	0	3.25	2.93	2.93	2.65	0.90	0.38	3.16	0.2	0.93	0.84	+0.18
		5	0.58	0.31	8.62	0	3.25	3.74	3.25	2.91	0.90	0.64	4.87	0.6	0.67	0.60	+0.04
0	V	1	0.67	0.24	7.46	0	3.25	3.23	3.23	2.79	0.86	0.50	2.99	1.0	1.08	0.93	−0.50
		2	0.67	0.24	7.46	0	3.25	3.23	3.23	2.79	0.86	0.50	3.36	1.0	0.96	0.83	−0.50
		3	0.67	0.24	7.46	0	3.25	3.23	3.23	2.79	0.86	0.50	3.32	1.0	0.98	0.84	−0.50
		4	0.67	0.24	7.46	0	3.25	3.23	3.23	2.79	0.86	0.50	3.88	1.0	0.83	0.72	−0.50
		5	0.56	0.10	8.93	0	3.25	3.87	3.25	3.09	0.95	0.72	3.39	1.0	0.96	0.91	−0.28
0.075	V	1	0.78	0.14	6.41	0.10	3.42	2.77	2.77	2.65	0.96	0.22	3.90	0.2	0.71	0.68	+0.02
		2	0.78	0.14	6.41	0.10	3.42	2.77	2.77	2.65	0.96	0.22	3.62	0.6	0.76	0.73	−0.38
		3	0.56	0.10	8.93	0.13	3.49	3.86	3.49	3.25	0.93	0.64	4.22	1.0	0.83	0.77	−0.36
		4	0.58	0.31	8.62	0.13	3.48	3.73	3.48	3.05	0.88	0.57	4.58	1.0	0.76	0.67	−0.43
		5	0.58	0.31	8.62	0.13	3.48	3.73	3.48	3.05	0.88	0.57	3.96	1.0	0.88	0.77	−0.43
0.15	V	1	0.68	0.26	7.35	0.22	3.65	3.17	3.17	2.91	0.92	0.34	3.51	0.6	0.90	0.83	−0.26
		2	0.68	0.26	7.35	0.22	3.65	3.17	3.17	2.91	0.92	0.34	3.39	0.4	0.93	0.86	−0.06
		3	0.68	0.26	7.35	0.22	3.65	3.17	3.17	2.91	0.92	0.34	3.17	0.6	1.00	0.92	−0.26
		4	0.56	0.10	8.93	0.27	3.74	3.85	3.74	3.38	0.90	0.54	4.51	0.6	0.83	0.75	−0.06
		5	0.68	0.26	7.35	0.22	3.65	3.17	3.17	2.91	0.92	0.34	3.89	1.0	0.81	0.75	−0.66
0.25	V	1	0.59	0.20	8.48	0.42	4.02	3.64	3.64	3.34	0.92	0.37	5.19	0.6	0.70	0.64	−0.23
		2	0.59	0.20	8.48	0.42	4.02	3.64	3.64	3.34	0.92	0.37	5.13	0.4	0.71	0.65	−0.03
		3	0.59	0.20	8.48	0.42	4.02	3.64	3.64	3.34	0.92	0.37	4.83	0.2	0.75	0.69	+0.17
		4	0.59	0.20	8.48	0.42	4.02	3.64	3.64	3.34	0.92	0.37	3.99	0.6	0.91	0.84	−0.23
		5	0.56	0.10	8.93	0.45	4.06	3.83	3.83	3.51	0.92	0.41	3.37	0.6	1.14	1.04	−0.19
														Mean:	0.88	0.80	−0.25
														StD:	0.13	0.12	0.22
														CoV:	0.15	0.15	

NOTES:
· Brick units comprised extruded clay brick pavers with nominal dimensions of 230 × 114 × 65 mm and 10 mm mortar joints.
· Modulus of rupture had a mean value of $\widehat{f}_{ut} = 5.00$ MPa, and CoV of $\mathbb{C}\langle f_{ut}\rangle = 0.26$.
· The self-weight of the specimens was considered negligible relative to the applied axial stress.

*Denotes the position of the specimen during test. Specimens marked 'H' were tested horizontally and specimens marked 'V' were tested vertically.
†Represents the direct minimum of the predicted values for stepped and line failure, i.e. $\eta_{\text{min}} = \min(\eta_{\text{step}}, \eta_{\text{line}})$.
‡Strength reduction factor for mean capacity, taken as $\phi_{\text{mean}} = \eta_{\text{mix}}/\eta_{\text{min}}$.
§Observed P_{step} taken as $n_b/5$, where n_b is the number of failed bed joints and 5 is the total number of bed joints that could fail.

Table F.2: Predicted and observed proportion of stepped failure along the vertical edge cracks of quasistatic test panels .

Wall	Analysis parameters and results						Experimental test results								Error in P_{step} (calc − test)	
							Left edge				Right edge					
	$\widehat{f}_{mt}$ [MPa]	$\mathbb{C}\langle f_{mt}\rangle$	σ_v [MPa]	F_{ut}	Σ_v	P_{step}	n_b	n_u	uncr	P_{step}	n_b	n_u	uncr	P_{step}	L edge	R edge
S1	0.721	0.199	0.124	4.92	0.172	0.12	10	9	0	0.36	4	12	0	0.14	−0.24	−0.03
S2	0.520	0.266	0.024	6.83	0.046	0.53	12	8	0	0.43	15	6	1	0.56	+0.10	−0.03
S3	0.499	0.280	0.135	7.11	0.270	0.44	5	11.5	0	0.18	–	–	–	–	+0.26	–
S4	0.639	0.212	0.079	5.56	0.124	0.25	8	10	0	0.29	–	–	–	–	−0.04	–
S5	0.655	0.212	0.024	5.42	0.037	0.28	12	8	0	0.43	–	–	–	–	−0.15	–
S6	0.496	0.217	0.024	7.16	0.048	0.58	14	7	0	0.50	10	9	0	0.36	+0.08	+0.23
S7	0.682	0.226	0.145	5.21	0.212	0.15	2	13	0	0.07	4	12	0	0.14	+0.08	+0.01
S8	0.714	0.194	0.025	4.97	0.034	0.19	6	11	0	0.21	8	10	0	0.29	−0.03	−0.10
														Mean:	+0.01	
														StD:	0.14	

NOTES:
· Modulus of rupture had a mean value of $\widehat{f}_{ut} = 3.55$ MPa, and CoV of $\mathbb{C}\langle f_{ut}\rangle = 0.267$.
· Vertical compressive stress σ_v used to calculate Σ_v was taken as the average value along the two vertical edges of the panel.
· Vertical edges referred to as *left* or *right* when viewed from the exterior face of each wall, as shown by diagrams on right-hand side of Figure 2.24.
· n_u = number of units undergoing line failure; n_b = number of bed joints undergoing stepped failure.
· 'uncr' indicates number of courses remaining uncracked (undergoing neither stepped nor line failure).
· As each panel consisted of 29 courses, by ignoring the base joint the observed proportion of stepped failure was taken as $P_{\text{step}} = n_b/(29-1)$.

Appendix G

COLLAPSE LOAD PREDICTION IN DRY MASONRY WALLS

Abstract

This appendix contains additional detail related to Chapter 6.

G.1 INTERNAL WORK FOR AN IN-PLANE SHEAR PANEL

This section presents the derivation of a model for calculating the internal work of a dry-stack masonry (DSM) in-plane panel subjected to shear deformation, as shown in Figure 6.11. The need for such a model arises due to in-plane deformation present in the hybrid mechanisms J and B (refer to Figure 6.14). The total resistance of the in-plane panel when connected to an adjacent out-of-plane panel consists of three sources:

1. Frictional resistance to the internal shear deformation within the mobilised panel itself,
2. Frictional resistance to shear sliding along the diagonal crack, and
3. Vertical bending at the interface between the sliding in-plane panel and the adjacent out-of-plane panel.

The expression derived in this section accounts for the resistance due to the sum of the first two components above, which are based on translational friction.

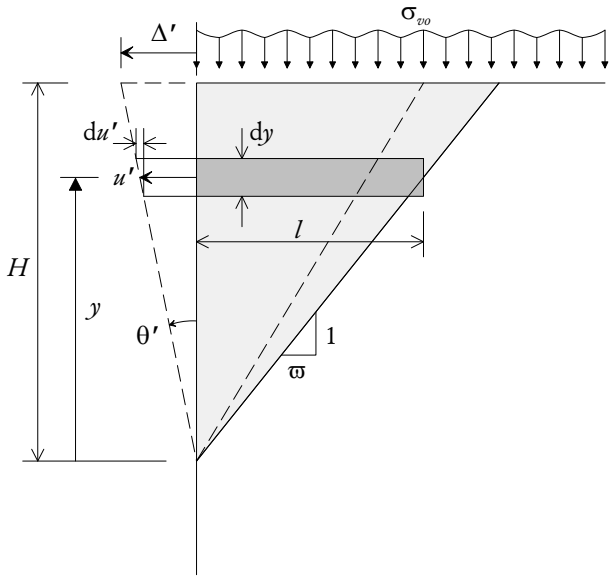

Figure G.1: Triangular panel undergoing in-plane shear deformation. The solid outline indicates its original position and the dashed outline its deformed position.

G.1.1 Assumptions

The following assumptions are made:

1. The mobilised panel is assumed to have a triangular shape.
2. Shear deformation within the in-plane panel has a linear profile. This condition is necessary in order to provide displacement compatibility between the in-plane and out-of-plane panels in mechanisms J and B (refer to Figure 6.14). As a result
$$\frac{du'}{dy} = \text{constant},$$
where y is the vertical position along the panel and u is the displacement.
3. Displacements are assumed to be sufficiently small, such that any reduction in the bedded area along the diagonal crack can be neglected.

G.1.2 General

Consider the triangular panel subjected to linear in-plane shear deformation along its height as shown in Figure G.1. The panel has the height H, thickness t, and the slope of the shear crack measured with respect to the vertical is ϖ. The reference virtual displacement at the top of the panel is Δ' and the corresponding virtual

rotation is equal to

$$\theta' = \frac{\Delta'}{H}.$$

The panel is also subjected to vertical precompression σ_{vo} along its top edge.

Vertical position is measured from the bottom of the panel and is denoted by y. Variables that are a function of y, include the vertical compressive stress:

$$\sigma_v = \sigma_{vo} + \gamma\,(H - y)\,,$$

the horizontal span:

$$l = \varpi y,$$

and the virtual displacement:

$$u' = \theta' y.$$

G.1.3 Internal Shear Deformation Within the Panel

At a given vertical position y, the axial force within the triangular panel is

$$N = \sigma_v t\, l = [\sigma_{vo} + \gamma\,(H - y)]\, t\varpi y.$$

The resulting frictional force resisting the shear deformation is

$$V = \mu_m N,$$

where μ_m is the coefficient of friction along the masonry's bed joints. For a horizontal strip with the width $\mathrm{d}y$ as shown by Figure G.1, the increment of virtual work due to internal shear deformation within the triangular panel is equal to

$$\begin{aligned} \mathrm{d}U'_{s\,\text{panel}} &= \mathrm{d}u'\, V \\ &= \mathrm{d}y\, \frac{\Delta'}{H} \mu_m\, [\sigma_{vo} + \gamma\,(H - y)]\, t\varpi y. \end{aligned} \tag{G.1}$$

G.1.4 Shear Sliding Across the Crack

Regardless of whether certain portions of the crack are 'stepped' or 'toothed', as long as the slope ϖ of the inclined shear crack is within the limits

$$0 \le \varpi \le \frac{1}{G_n},$$

then the overlapping bedded area along the crack per unit height, $\bar{A}$, will stay independent from the crack slope and equal to

$$\bar{A} = t\,\frac{\frac{1}{2}\left(l_u + t_j\right)}{h_u + t_j} = \frac{t}{G_n},$$

where l_u is the brick length, h_u is the brick height, t_j is the mortar joint thickness, and G_n is the natural slope of the masonry [refer to equation (4.13)]. Therefore, the bedded area across the rectangular strip with the width $\mathrm{d}y$, as shown by Figure G.1, is

$$\mathrm{d}A = \bar{A}\,\mathrm{d}y.$$

The corresponding increment of axial force acting across the bedded area $\mathrm{d}A$ is

$$\mathrm{d}N = \sigma_v\,\mathrm{d}A,$$

and the resulting increment of shear force resisting sliding across the crack is

$$\mathrm{d}V = \mu_m\,\mathrm{d}N.$$

The increment of virtual work across the rectangular strip due to sliding along the crack becomes

$$\begin{aligned}\mathrm{d}U'_{s\,\mathrm{crack}} &= u'\,\mathrm{d}V \\ &= \frac{\Delta'}{H} y \mu_m \left[\sigma_{vo} + \gamma\left(H - y\right)\right] t\,\frac{1}{G_n}\,\mathrm{d}y. \end{aligned} \tag{G.2}$$

G.1.5 Total Internal Work

The total increment of virtual work is the combined work from internal deformation within the panel and sliding across the crack. For a horizontal strip with width $\mathrm{d}y$ (Figure G.1), this is obtained by summing equations (G.1) and (G.2):

$$\begin{aligned}\mathrm{d}U'_{s\,\mathrm{tot}} &= \mathrm{d}U'_{s\,\mathrm{panel}} + \mathrm{d}U'_{s\,\mathrm{crack}} \\ &= \frac{\Delta'}{H}\mu_m t y \left[\sigma_{vo} + \gamma\left(H - y\right)\right]\left(\frac{1}{G_n} + \varpi\right)\mathrm{d}y. \end{aligned} \tag{G.3}$$

To obtain an expression for the virtual work for the entire panel, $U'_{s\,\mathrm{tot}}$, the above expression must be integrated between $y = 0$ and $y = H$. This becomes

$$U'_{s\,\mathrm{tot}} = \int_{y=0}^{H} \mathrm{d}U'_{s\,\mathrm{tot}}$$

$$= \frac{\Delta'}{H}\mu_m t\left(\frac{1}{G_n}+\varpi\right)\int_{y=0}^{H} y\left[\sigma_{vo}+\gamma\left(H-y\right)\right]\mathrm{d}y$$
$$= \Delta'\mu_m t\left(\frac{1}{G_n}+\varpi\right)\left[\frac{1}{2}\sigma_{vo}H+\frac{1}{6}\gamma H^2\right]. \tag{G.4}$$

An alternative form of this equation, expressed in terms of the stress capacity function $f\langle\cdots\rangle$ for dry-stack masonry [equation (6.22)], is

$$U'_{s\,\mathrm{tot}} = \tfrac{1}{2}\Delta'\mu_m t H\left(\frac{1}{G_n}+\varpi\right) f\langle\tfrac{1}{3}H\rangle. \tag{G.5}$$

It should be noted that the reference virtual displacement Δ' in these expressions is taken at the top edge of the panel, as shown in Figure G.1. When applying these expressions as part of a virtual work analysis for an overall collapse mechanism, it is important to account for the ratio between this displacement and the mechanism's reference displacement.

G.2 FORMULATIONS FOR TYPE G, J, B, K1 AND K2 MECHANISMS

This appendix contains derivations of analytical expressions for calculating the collapse load multiplier λ_o for mechanisms $\mathrm{G_x}$, $\mathrm{G_y}$, J, B, $\mathrm{K1_x}$, $\mathrm{K1_y}$, $\mathrm{K2_x}$ and $\mathrm{K2_y}$ (refer to Figure 6.3). Sections G.2.1–G.2.8 provide expressions for the total internal virtual work U'_{tot}, and the total external virtual work premultiplied by the reciprocal of the lateral load multiplier, $\lambda^{-1}E'_{\mathrm{tot}}$, for each of the mechanisms. From this, the collapse multiplier λ_o is evaluated as

$$\lambda_o = \frac{U'_{\mathrm{tot}}}{\lambda^{-1}E'_{\mathrm{tot}}}. \tag{G.6}$$

Section G.2.9 gives the derivation of the additional internal or external work generated in type-1 mechanisms as a result of a restrained/unrestrained overburden load (OBL). Finally, Section G.2.10 provides the derivation of the top edge rotational restraint factor R_{ts}, to account for the rotational restraint provided by an OBL.

G.2.1 Mechanism J

Mechanism J, whose basic deflected shape is shown in Figure 6.14a, is a proposed hybrid mechanism that incorporates deformations in orthogonal out-of-plane panels with in-plane shear deformation in adjacent return walls. An important feature of the mechanism is its ability to span across multiple out-of-plane and in-plane panels, depending on the configuration of the masonry specimen. In this section, we derive equations of work for individual out-of-plane and in-plane modules. We then consider a simple form of the mechanism in which

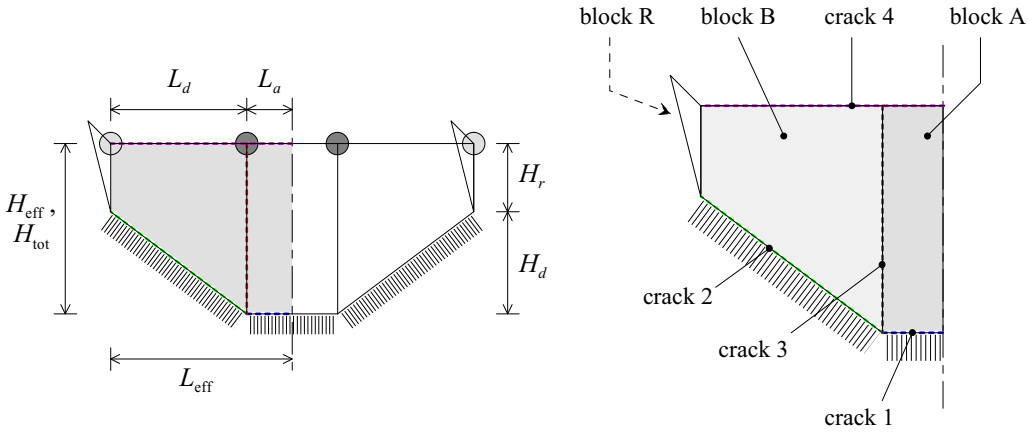

Figure G.2: Individual out-of-plane module involved in mechanism J.

all participating out-of-plane and in-plane modules are assumed to be identical, and formulate the equations of work for a mechanism comprising of a generic number of each type of module. The resulting simplified approach is applicable to simple masonry configurations, including the basic variants shown by Figure 6.3, where the aforementioned assumption will hold due to symmetry. For such configurations, the simplified approach is guaranteed to find optimal solutions. For configurations in which the participating out-of-plane and in-plane modules are not guaranteed to be identical, such as the complex variants shown in Figure 6.3, the simplified approach becomes either inapplicable, or is not guaranteed to find optimal solutions. A refined analysis capable of dealing with the complex variants is described in Appendix G.3.

Independent Geometric Variables

Figure G.2 shows the dimensions of a single out-of-plane module involved in the mechanism. Let the independent variables defining the geometry include: the total mechanism height H_t, shape parameter a, and the slope of the in-plane shear crack, ω (as shown in Figure 6.14a).[1]

As shown by the deflected shape (Figure 6.14a), the reference displacement increment $d\Delta$ is taken as the largest displacement along the out-of-plane module.

[1] As a result, shape parameter r becomes a dependent variable; however, the choice of which parameter is taken as independent (a or r) is arbitrary.

Dependent Geometric Variables

The out-of-plane component of the mechanism must span the full available length of the wall, and the length of an out-of-plane module is therefore predetermined. In the simplified treatment, we take the effective length L_e as

$$L_e = L_w / n_{vs},$$

where L_w is the length of the out-of-plane wall, and n_{vs} is its number of vertical supports. Other dependent geometric variables (refer to Figure G.2) include: the effective mechanism height H_e, which [from equation (6.39) with $n_{hs} = 1$] is equal to the total height H_t,

$$H_e = H_t;$$

the horizontal span of block A, defined as

$$L_a = aL_e;$$

the horizontal span of block B and the diagonal crack,

$$L_d = (1 - a)\, L_e;$$

the corresponding vertical span of the diagonal crack,

$$H_d = G_n L_d = (1 - r)\, H_t;$$

and the vertical span of the in-plane block,

$$H_r = rH_t.$$

Additional dependent variables include β, calculated using equation (6.43); and α, calculated using equation (6.44). The dependent shape parameter r can be calculated from a, using

$$r = 1 - \alpha(1 - a)\,.$$

As can be seen from Figure 6.14a, the relationship between the displacement $\mathrm{d}\Delta_r$ occurring at the top of the in-plane panel and the maximum displacement $\mathrm{d}\Delta$ of an adjacent out-of-plane module is

$$\mathrm{d}\Delta_r = r\,\mathrm{d}\Delta, \qquad \text{or} \qquad \Delta_r' = r. \tag{G.7}$$

Geometric Constraints

The independent variables defined previously may assume any values, as long as the following constraints are adhered to. The total mechanism height must not exceed the available height of the wall, so that

$$0 < H_t \leq H_w.$$

The shape parameters a and r must be within the limits

$$0 \leq a \leq 1, \qquad 0 \leq r \leq 1.$$

And as discussed in Section 6.4.3, the slope of the in-plane shear crack must be inside the range

$$0 \leq \varpi \leq 1/G_n.$$

Internal Work for a Single Out-of-Plane Module

As shown by Figure G.2, an out-of-plane module receives internal work contributions from four flexural cracks, including the bottom horizontal crack (1), diagonal crack (2), internal vertical crack (3), and the top edge pseudo-crack (4). In addition, it may receive the additional work contribution U'_{Om} from the presence of a restrained OBL. Hence, its internal virtual work is obtained from the formula

$$U'_m = U'_{(1)} + U'_{(2)} + \zeta_{hi} U'_{(3)} + U'_{(4)} + U'_{Om}, \tag{G.8}$$

where $U'_{(1)}$–$U'_{(4)}$ are the contributions from the respective cracks.

The factor ζ_{hi} in equation (G.8) is used to account for the activeness of the internal vertical crack (crack 3 in Figure G.2), effectively acting as a rotation reduction factor as illustrated by Figure G.3. When considering a wall supported along both vertical edges (Figure G.3a), the crack must undergo its full required rotation due to the zero slope condition at the midspan of the overall mechanism. Therefore, in this scenario the crack will develop its full rotation, and consequently ζ_{hi} is taken as 1. However, when the wall is supported at only one vertical edge (Figure G.3b), the free edge will tend to exhibit some nonzero slope, which will act to reduce the rotation of the internal vertical crack. It is evident that the activeness of crack must be related to the mechanism's normalised aspect ratio α [equation (6.44)]: For a mechanism with small α, the crack's close proximity to the unsupported vertical edge with which it is parallel will cause it not to develop its full internal work capacity, since the free edge will tend to exhibit a slope about

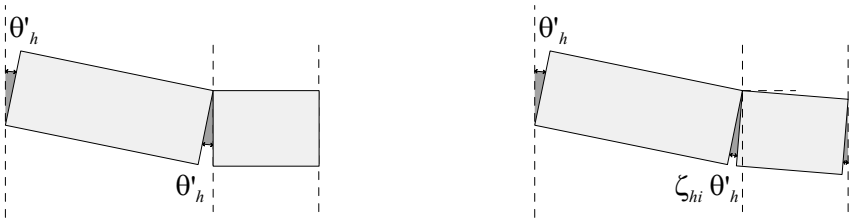

(a) Rotations as implied by the basic mechanism shape, with zero slope at the free vertical edge and full rotation along the internal vertical crack. This scenario is only applicable only when the wall has both vertical edges supported.

(b) Implemented crack rotation factor for the internal vertical crack, for the case when the wall has only one of its vertical edges supported, thus allowing for a nonzero slope at the free vertical edge.

Figure G.3: Crack rotation factor for the internal vertical crack undergoing horizontal bending, in mechanisms J and G_x (plan view).

the vertical axis, and therefore, the crack will rotate to a lesser extent. However, for a wall with a higher α, the crack will be more distant from the unsupported edge and will therefore undergo a larger rotation, thus causing it realise more of its capacity. In the most extreme case where the wall's length tends toward infinity, the vertical crack will need to undergo its full rotation since the free edge will exhibit zero slope, and so the crack will reach its full capacity. Therefore, it follows that when a is equal to 0, ζ_{hi} must also equal 0; and when a is 1, ζ_{hi} must also equal 1. Because the actual relationship between these two extreme cases is not known, a semi-rational approach is adopted, whereby ζ_{hi} is assumed to vary linearly and be equal to the parameter a. Therefore, in the overall implemented approach, ζ_{hi} is taken as

$$\zeta_{hi} = \begin{cases} a, & \text{if one vertical edge is supported, i.e. } n_{vs} = 1; \\ 1, & \text{if two vertical edges are supported, i.e. } n_{vs} = 2. \end{cases} \tag{G.9}$$

As discussed further in Section G.2.4, mechanism G_x is a special case of mechanism J in which the parameter r is taken as zero. It is therefore noteworthy that the factor ζ_{hi} acts to ensure continuity in the calculated value of λ_o when transitioning between the complimentary pair of mechanisms G_x and G_y. It does so by making the contribution of the internal vertical crack gradual, rather than sudden, when the aspect ratio α becomes greater than 1.

BOTTOM HORIZONTAL CRACK (1), VERTICAL BENDING: The crack spans the length L_a and its centroid is located at a distance H_t below the top of the wall.

From equation (6.24) the moment capacity is

$$M_v = \boldsymbol{f}\langle H_t \rangle \, L_a \bar{Z}_v,$$

together with the virtual rotation

$$\theta'_v = \frac{1}{H_t},$$

which gives the internal virtual work contribution

$$\begin{aligned} U'_{(1)} = \theta'_v M_v &= \frac{L_a}{H_t} \bar{Z}_v \boldsymbol{f}\langle H_t \rangle \\ &= \beta a \bar{Z}_v \boldsymbol{f}\langle H_t \rangle \,. \end{aligned} \tag{G.10}$$

DIAGONAL CRACK (2): The crack spans the horizontal projection L_d and its centroid is located at a distance $H_t - \frac{1}{2}H_d$ below the top of the wall. Hence, from equation (6.29), the moment capacity is

$$M_d = \boldsymbol{f}\langle H_t - \tfrac{1}{2}H_d \rangle \, L_d \bar{Z}_v \cos\varphi,$$

which, together with the virtual rotation

$$\theta'_d = \frac{1}{H_t \cos\varphi},$$

gives the internal virtual work contribution

$$\begin{aligned} U'_{(2)} = \theta'_d M_d &= \frac{L_d}{H_t} \bar{Z}_v \boldsymbol{f}\langle H_t - \tfrac{1}{2}H_d \rangle \\ &= \beta \, (1-a) \, \bar{Z}_v \boldsymbol{f}\langle \left(\tfrac{1+r}{2}\right) H_t \rangle \,. \end{aligned} \tag{G.11}$$

INTERNAL VERTICAL CRACK (3), HORIZONTAL BENDING: The crack's height is H_t and its centroid is located at a distance $\frac{1}{2}H_t$ from the top of the wall. Therefore, from equation (6.30), the moment capacity is

$$M_h = \boldsymbol{f}\langle \tfrac{1}{2}H_t \rangle \, H_t \bar{Z}_h,$$

which, together with the virtual rotation

$$\theta'_h = \frac{1}{H_t / G_n},$$

gives the internal virtual work contribution

$$U'_{(3)} = \theta'_h M_h = G_n \bar{Z}_h \boldsymbol{f} \left\langle \tfrac{1}{2} H_t \right\rangle . \tag{G.12}$$

TOP EDGE PSEUDO-CRACK (4), VERTICAL BENDING: This hinge spans the length L_e, so its moment capacity according to equation (6.28) is

$$M_{vo} = R_{ts} \boldsymbol{f} \langle 0 \rangle \, L_e \bar{Z}_v .$$

It has the virtual rotation

$$\theta'_v = \frac{1}{H_t};$$

therefore, its contribution to the internal virtual work is

$$U'_{(4)} = \theta'_v M_{vo} = R_{ts} \beta \bar{Z}_v \boldsymbol{f} \langle 0 \rangle . \tag{G.13}$$

FRICTION AGAINST RESTRAINED OBL: This contribution is calculated according to equation (G.126) as

$$U'_{Om} = (1 - \Phi_m) \, \mu_o e'_m , \tag{G.14}$$

where [from equations (G.117) and (G.124)] e'_m is given by

$$e'_m = \tfrac{1}{2}(1 + a + r - ar) \, L_e \, t_u \sigma_{vom} . \tag{G.15}$$

TOTAL: The total internal work for a single out-of-plane module is obtained by substituting equations (G.10)–(G.15) into (G.8). This yields the expression

$$\begin{aligned} U'_m = \bar{Z}_v \beta \left(\boldsymbol{f} \left\langle \tfrac{1}{2}(1 + a + r - ar) H_t \right\rangle + R_{ts} \boldsymbol{f} \langle 0 \rangle \right) \\ + \zeta_{hi} \bar{Z}_h G_n \boldsymbol{f} \left\langle \tfrac{1}{2} H_t \right\rangle + (1 - \Phi_m) \, \mu_o e'_m . \end{aligned} \tag{G.16}$$

External Work for a Single Out-of-Plane Module

The external work of an individual out-of-plane module includes the self-weight contributions of blocks (A) and (B) (Figure G.2), in addition to a possible contribution E'_{Om} from an unrestrained OBL. This gives

$$E'_m = E'_{W(A)} + E'_{W(B)} + E'_{Om} , \tag{G.17}$$

where $E'_{W(A)}$ and $E'_{W(B)}$ are contributions from the respective blocks.

SELF-WEIGHT OF BLOCK (A): From Table 6.1, the virtual volume of the wedge block is

$$V'_{(A)} = \tfrac{1}{2} L_a H_t,$$

which gives the external virtual work

$$\begin{aligned} E'_{W(A)} &= \lambda \gamma t_u \left(\tfrac{1}{2} L_a H_t\right) \\ &= \lambda \gamma t_u H_t^2 \left(\tfrac{1}{2} a\beta\right). \end{aligned} \tag{G.18}$$

SELF-WEIGHT OF BLOCK (B): From Table 6.1, the virtual volume of the truncated triangular pyramid block is

$$V'_{(B)} = \frac{1}{6} \frac{H_t^2}{G_n} \left(1 - r^3\right),$$

resulting in the external virtual work

$$E'_{W(B)} = \lambda \gamma t_u H_t^2 \left(\frac{1}{6} \frac{\left(1 - r^3\right)}{G_n} \right). \tag{G.19}$$

WEIGHT OF UNRESTRAINED OBL: This contribution is calculated according to equation (G.125) as

$$E'_{Om} = \Phi_m \lambda \eta_m e'_m, \tag{G.20}$$

where e'_m is given by equation (G.15).

TOTAL: The total external work for an out-of-plane module is obtained by substituting equations (G.18)–(G.20) into (G.17). Dividing by λ yields the expression

$$\lambda^{-1} E'_m = \gamma t_u H_t^2 \left(\tfrac{1}{2} a\beta + \tfrac{1}{6} \tfrac{1 - r^3}{G_n} \right) + \Phi_m \eta_m e'_m. \tag{G.21}$$

Internal Work for a Single In-Plane Module

The internal work U'_r of an in-plane module receives contributions from: internal deformation due to shear and bending, given by the function $\boldsymbol{U'_r}\langle \Delta'_r, H_r, \varpi \rangle$ [from equation (6.36)]; and any additional contribution U'_{Or} from a restrained OBL [according to equation (G.126)]. Hence, the general expression for the internal work of a single in-plane module becomes

$$U'_r = \boldsymbol{U'_r}\langle \Delta'_r, H_r, \varpi \rangle + \left(1 - \Phi_r\right) \mu_o e'_r, \tag{G.22}$$

where [from equations (G.124) and (G.121)] e'_r is given by

$$e'_r = \Delta'_r \varpi H_r t_u \sigma_{vor}. \tag{G.23}$$

External Work for a Single In-Plane Module

The external work E'_r for single in-plane module consists of

$$E'_r = E'_{W(R)} + E'_{Or}, \tag{G.24}$$

where $E'_{W(R)}$ is the work due to self-weight, and E'_{Or} is any additional contribution from a restrained OBL.

SELF-WEIGHT OF BLOCK (R): From Table 6.1, the virtual displaced volume of the block is

$$V'_{(R)} = \Delta'_r \left[\tfrac{1}{3} H_r^2 \varpi\right].$$

This results in the external virtual work

$$E'_{W(R)} = \Delta'_r \left[\lambda \gamma t_u \left(\tfrac{1}{3} H_r^2 \varpi\right)\right]. \tag{G.25}$$

WEIGHT OF UNRESTRAINED OBL: This contribution is calculated according to equation (G.125) as

$$E'_{Or} = \Phi_r \lambda \eta_r e'_r, \tag{G.26}$$

where e'_r is given by equation (G.23).

TOTAL: The total external work for a single in-plane module is obtained by substituting equations (G.25) and (G.26) into (G.24). Dividing by λ yields the expression

$$\lambda^{-1} E'_r = \Delta'_r \left[\gamma t_u \left(\tfrac{1}{3} H_r^2 \varpi\right)\right] + \Phi_r \eta_r e'_r. \tag{G.27}$$

Total Internal and External Work in the Simplified Approach

In the simplified treatment, it is assumed that the overall mechanism consists of N_m identical out-of-plane modules and N_r identical in-plane modules. Hence, the total internal virtual work is obtained from the formula

$$U'_{\text{tot}} = N_m U'_m + N_r U'_r. \tag{G.28}$$

Substituting in equations (G.16) and (G.22), whilst also making the replacements $H_r = rH_t$ and $\Delta'_r = r$, yields the expression

$$\begin{aligned} U'_{\text{tot}} = N_m \big[\bar{Z}_v \beta \left(\boldsymbol{f} \left\langle \tfrac{1}{2}(1 + a + r - ar) H_t \right\rangle + R_{ts} \boldsymbol{f} \langle 0 \rangle \right) \\ + \zeta_{hi} \bar{Z}_h G_n \boldsymbol{f} \left\langle \tfrac{1}{2} H_t \right\rangle + (1 - \Phi_m) \mu_o e'_m \big] \\ + N_r \left[\boldsymbol{U}'_{\boldsymbol{r}} \langle r, rH_t, \varpi \rangle + (1 - \Phi_r) \mu_o e'_r \right]. \end{aligned} \tag{G.29}$$

Similarly, the total external virtual work is obtained using the formula

$$E'_{\text{tot}} = N_m E'_m + N_r E'_r. \tag{G.30}$$

Substituting in equations (G.21) and (G.27), and making the replacements $H_r = rH_t$ and $\Delta'_r = r$, yields the expression

$$\begin{aligned} \lambda^{-1} E'_{\text{tot}} = N_m \left[\gamma t_u H_t^2 \left(\tfrac{1}{2} a \beta + \tfrac{1}{6} \tfrac{1 - r^3}{G_n} \right) + \Phi_m \eta_m e'_m \right] \\ + N_r \left[\gamma t_u H_t^2 \left(\tfrac{1}{3} r^3 \varpi \right) + \Phi_r \eta_r e'_r \right]. \end{aligned} \tag{G.31}$$

G.2.2 Mechanism B

Figure 6.14b shows the mechanism's deflected shape, and Figure G.4 shows the dimensions of a single out-of-plane module. The independent variables defining the mechanism's geometry include: the total height H_t; and the in-plane shear crack slope ϖ. The mechanism must span the full available length of the wall, and therefore, the length L_e is predetermined as

$$L_e = L_w / n_{vs},$$

where L_w is the length of the out-of-plane wall, and n_{vs} is its number of vertical supports.

As was done for mechanism J in Section G.2.1, a general case of the mechanism is considered here, in which the overall mechanism comprises of N_m out-of-plane modules and N_r in-plane modules.

Dependent Geometric Variables

The dependent geometric variables include the effective mechanism height H_e, which [from equation (6.39) with $n_{hs} = 1$] is equal to the total height H_t,

$$H_e = H_t;$$

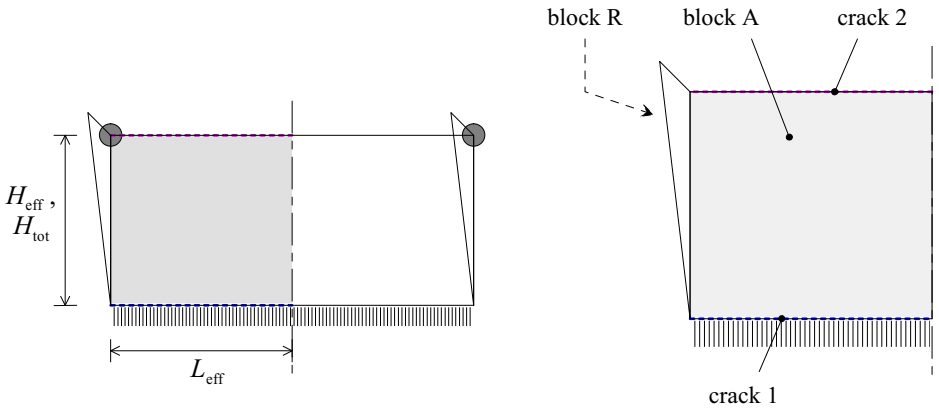

Figure G.4: Individual out-of-plane module involved in mechanism B.

and β, calculated using equation (6.43).

Geometric Constraints

The total mechanism height must not exceed the available height of the wall, so that

$$0 < H_t \leq H_w;$$

and the slope of the in-plane shear crack must be inside the range

$$0 \leq \omega \leq 1/G_n,$$

as discussed in Section 6.4.3.

Internal Work for a Single Out-of-Plane Module

As shown by Figure G.4, two cracks contribute to the internal work for a single out-of-plane module: the bottom horizontal crack (1) and the pseudo-crack along the top edge (2). In addition, it may receive the additional work contribution U'_{Om} from the presence of a restrained OBL. Therefore, the contribution for a single out-of-plane module is

$$U'_m = U'_{(1)} + U'_{(2)} + U'_{Om}, \tag{G.32}$$

where $U'_{(1)}$ and $U'_{(2)}$ are the contributions from the respective cracks.

BOTTOM HORIZONTAL CRACK (1), VERTICAL BENDING: The crack spans the length L_e, with its centroid located at a distance H_t below the top of the wall. From

equation (6.24), its moment capacity is

$$M_v = \boldsymbol{f}\langle H_t\rangle\, L_e \bar{Z}_v,$$

which, together with the virtual rotation

$$\theta'_v = \frac{1}{H_t},$$

provides the internal virtual work contribution

$$\begin{aligned} U'_{(1)} = \theta'_v M_v &= \frac{L_e}{H_t}\bar{Z}_v \boldsymbol{f}\langle H_t\rangle \\ &= \beta \bar{Z}_v \boldsymbol{f}\langle H_t\rangle\,. \end{aligned} \tag{G.33}$$

TOP EDGE PSEUDO-CRACK (2), VERTICAL BENDING: This hinge spans the length L_e; hence, its moment capacity according to equation (6.28) is

$$M_{vo} = R_{ts}\boldsymbol{f}\langle 0\rangle\, L_e \bar{Z}_v.$$

It has the virtual rotation

$$\theta'_v = \frac{1}{H_t},$$

giving the internal virtual work contribution

$$U'_{(2)} = \theta'_v M_{vo} = R_{ts}\beta \bar{Z}_v \boldsymbol{f}\langle 0\rangle\,. \tag{G.34}$$

FRICTION AGAINST RESTRAINED OBL: This contribution is calculated according to equation (G.126) as

$$U'_{Om} = (1-\Phi_m)\,\mu_o e'_m, \tag{G.35}$$

where [from equations (G.118) and (G.124)] e'_m is given by

$$e'_m = L_e\, t_u \sigma_{vom}. \tag{G.36}$$

TOTAL: The total internal work of the out-of-plane module is obtained by substituting equations (G.33)–(G.35) into (G.32). This yields the expression

$$U'_m = \bar{Z}_v \beta\,(\boldsymbol{f}\langle H_t\rangle + R_{ts}\boldsymbol{f}\langle 0\rangle) + (1-\Phi_m)\,\mu_o e'_m. \tag{G.37}$$

External Work for a Single Out-of-Plane Module

The external work of an individual out-of-plane module includes the self-weight contributions of block (A), $E'_{W(A)}$ (Figure G.4), in addition to a possible contribution E'_{Om} from an unrestrained OBL. This gives

$$E'_m = E'_{W(A)} + E'_{Om}. \tag{G.38}$$

WEDGE BLOCK (A): The virtual volume of the wedge block is (based on Table 6.1)

$$V'_{(A)} = \tfrac{1}{2} L_e H_t,$$

which gives the external virtual work

$$\begin{aligned} E'_{W(A)} &= \lambda \gamma t_u \left(\tfrac{1}{2} L_e H_t\right) \\ &= \lambda \gamma t_u H_t^2 \left(\tfrac{1}{2}\beta\right). \end{aligned} \tag{G.39}$$

WEIGHT OF UNRESTRAINED OBL: This contribution is calculated according to equation (G.125) as

$$E'_{Om} = \Phi_m \lambda \eta_m e'_m, \tag{G.40}$$

where e'_m is given by equation (G.36).

TOTAL: The total external work for an out-of-plane module is obtained by substituting equations (G.39) and (G.40) into (G.38). Dividing by λ yields the expression

$$\lambda^{-1} E'_m = \gamma t_u H_t^2 \left(\tfrac{1}{2}\beta\right) + \Phi_m \eta_m e'_m. \tag{G.41}$$

Internal and External Work for a Single In-Plane Module

Expressions for the total internal and external work for a single in-plane module in mechanism B are obtained by setting $\Delta'_r = \Delta'$ (defined as 1) and $H_r = H_t$ to the respective equations for mechanism J. From equation (G.27), the internal work becomes

$$U'_r = \boldsymbol{U'_r} \langle 1, H_t, \varpi \rangle + (1 - \Phi_r)\, \mu_o e'_r, \tag{G.42}$$

whilst from equation (G.22), the external work is

$$\lambda^{-1} E'_r = \gamma t_u H_t^2 \left(\tfrac{1}{3}\varpi\right) + \Phi_r \eta_r e'_r, \tag{G.43}$$

where e'_r is determined as

$$e'_r = \varpi H_t t_u \sigma_{vor}. \tag{G.44}$$

Total Internal and External Work in the Simplified Approach

The total internal virtual work for a total of N_m out-of-plane modules and N_r in-plane modules is obtained from the formula

$$U'_{\text{tot}} = N_m U'_m + N_r U'_r. \tag{G.45}$$

Substituting in equations (G.37) and (G.42) yields

$$\begin{aligned} U'_{\text{tot}} = N_m \left[\bar{Z}_v \beta \left(\boldsymbol{f}\langle H_t\rangle + R_{ts}\boldsymbol{f}\langle 0\rangle\right) + \left(1-\Phi_m\right)\mu_o e'_m\right] \\ + N_r \left[\boldsymbol{U'_r}\langle 1, H_t, \varpi\rangle + \left(1-\Phi_r\right)\mu_o e'_r\right]. \end{aligned} \tag{G.46}$$

Similarly, the total external virtual work is obtained using the formula

$$E'_{\text{tot}} = N_m E'_m + N_r E'_r. \tag{G.47}$$

Substituting in equations (G.41) and (G.43), yields

$$\begin{aligned} \lambda^{-1} E'_{\text{tot}} = N_m \left[\gamma t_u H_t^2 \left(\tfrac{1}{2}\beta\right) + \Phi_m \eta_m e'_m\right] \\ + N_r \left[\gamma t_u H_t^2 \left(\tfrac{1}{3}\varpi\right) + \Phi_r \eta_r e'_r\right]. \end{aligned} \tag{G.48}$$

G.2.3 Mechanism G_x

Figure 6.15a shows the mechanism's deflected shape, and Figure G.5 shows the dimensions of a single out-of-plane module. Let us treat the effective length L_e and total height H_t as the independent variables defining the mechanism's geometry. In order to obtain expressions for the total internal and external work for mechanism G_x, we can take advantage of the fact that the mechanism represents a specific case of mechanism J (Section G.2.1) where the shape parameter r is set to zero.

Dependent Geometric Variables

The dependent geometric variables (refer to Figure G.5) include: the effective mechanism height H_e, which [from equation (6.39) with $n_{hs} = 1$] is equal to the total height H_t,

$$H_e = H_t;$$

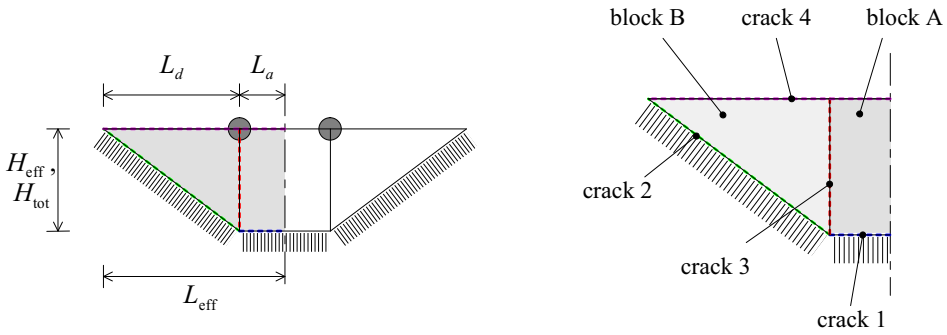

Figure G.5: Individual out-of-plane module involved in mechanism G_x.

as well as β from equation (6.43); and α from equation (6.44). From this, the shape parameter a is obtained as

$$a = 1 - \frac{1}{\alpha}.$$

Geometric Constraints

The independent variables L_e and H_t may assume any values, as long as the following constraints are adhered to. The total mechanism height must not exceed the available height of the wall, or

$$0 < H_t \leq H_w.$$

The effective mechanism length cannot exceed the available length of the wall, and must stay within the limits

$$0 < L_e \leq L_w / n_{vs},$$

where n_{vs} is the number of vertical supports for the out-of-plane wall. Finally, the normalised aspect ratio α must satisfy the condition

$$\alpha \geq 1.$$

Internal Work

Setting $r = 0$ to equation (G.29) for mechanism J, the total internal work for a single out-of-plane module ($N_m = 1$) in mechanism G_x becomes

$$\begin{aligned} U'_{\text{tot}} = \bar{Z}_v \beta \left[\boldsymbol{f} \left\langle \tfrac{1}{2}(1+a) H_t \right\rangle + R_{ts} \boldsymbol{f} \langle 0 \rangle \right] \\ + \zeta_{hi} \bar{Z}_h G_n \boldsymbol{f} \left\langle \tfrac{1}{2} H_t \right\rangle + (1 - \Phi_m) \mu_o e'_m. \end{aligned} \tag{G.49}$$

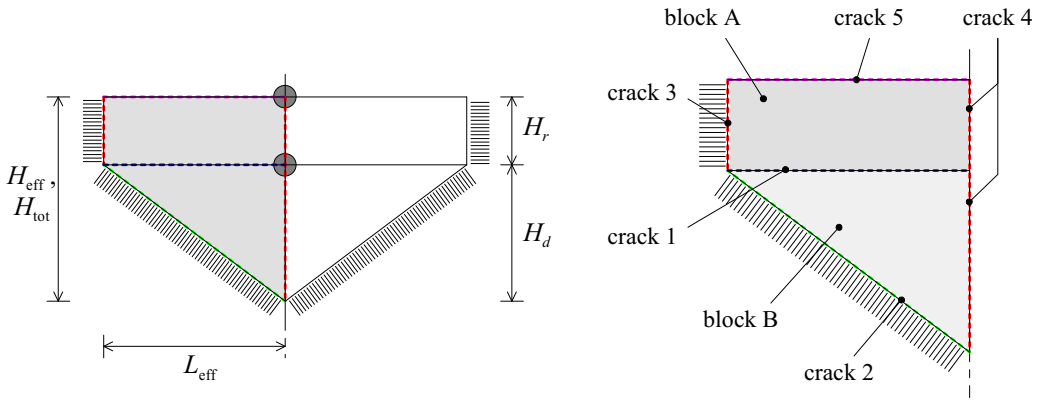

Figure G.6: Individual out-of-plane module involved in mechanism $\mathsf{G_y}$.

Here, ζ_{hi} is the work contribution factor for the vertical crack labelled as (3) in Figure G.5 and is obtained from equation (G.9). The virtual energy quantity e'_m is obtained by setting $r = 0$ to equation (G.15), which gives

$$e'_m = \tfrac{1}{2}(1+a)\, L_e\, t_u \sigma_{vom}. \tag{G.50}$$

External Work

Setting $r = 0$ to equation (G.31) for mechanism J, the total external work for a single out-of-plane module ($N_m = 1$) in mechanism $\mathsf{G_x}$ becomes

$$\lambda^{-1} E'_{\text{tot}} = \gamma t_u L_e H_t \left(\tfrac{1}{6} + \tfrac{1}{3}a\right) + \Phi_m \eta_m e'_m, \tag{G.51}$$

where e'_m is obtained from equation (G.50).

G.2.4 Mechanism $\mathsf{G_y}$

Figure 6.15b shows the mechanism's deflected shape, and Figure G.6 shows the dimensions of a single out-of-plane module. Let us treat the effective length L_e and total height H_t as the independent variables defining the mechanism's geometry.

Dependent Geometric Variables

The dependent geometric variables (refer to Figure G.6) include: the effective mechanism height H_e, which [from equation (6.39) with $n_{hs} = 1$] is equal to the total height H_t,

$$H_e = H_t;$$

the vertical span of block A, defined as

$$H_r = rH_t;$$

and the height of the diagonal crack,

$$H_d = (1 - r)\, H_t.$$

In addition, we need to calculate β using equation (6.43) and α using equation (6.44). From this, the shape parameter r is calculated as

$$r = 1 - \alpha.$$

Geometric Constraints

The independent variables L_e and H_t may assume any values, as long as the following constraints are adhered to. The total mechanism height must not exceed the available height of the wall, and the effective mechanism length cannot exceed the available length of the wall. They must therefore be within the limits

$$0 < H_t \leq H_w \qquad \text{and} \qquad 0 < L_e \leq L_w / n_{vs}.$$

In addition, the normalised aspect ratio α must satisfy the condition

$$\alpha \leq 1.$$

Internal Work

As shown by Figure G.6, there are four flexural cracks contributing to the internal work of a single out-of-plane module, including the internal horizontal crack (1), diagonal crack (2), vertical edge crack (3), if both vertical edges are supported then the central vertical crack (4), and the top edge pseudo-crack (5). In addition, it may receive the additional work contribution U'_{Om} from the presence of a restrained OBL. The total internal work for a single out-of-plane module is therefore obtained using the formula

$$U'_{\text{tot}} = \zeta_{vi} U'_{(1)} + U'_{(2)} + U'_{(3)} + \zeta_{hi} U'_{(4)} + \zeta_{vo} U'_{(5)} + U'_{Om}, \tag{G.52}$$

where $U'_{(1)}$–$U'_{(5)}$ are the contributions from the respective cracks.

Factor ζ_{vi} in equation (G.52) represents the activeness of the internal horizontal crack (crack 1 as shown in Figure G.6). Effectively it accounts for a reduction in the

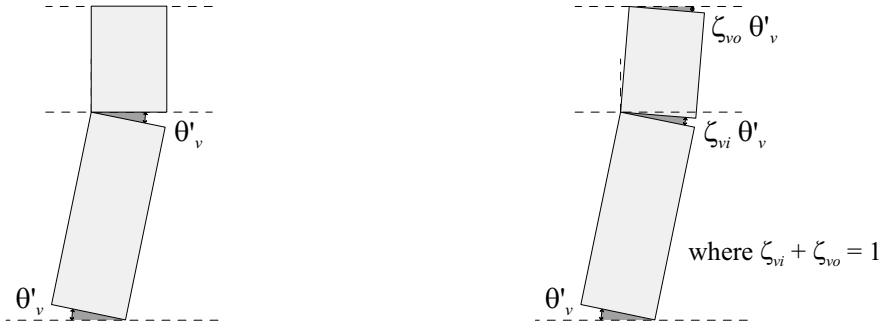

(a) Rotations as implied by the basic mechanism shape.

(b) Implemented crack rotation factors allowing for slope at the top edge.

Figure G.7: Crack rotation factors in mechanism $\mathsf{G_y}$.

crack's rotation since the crack is parallel with the unsupported top edge, which, due to its translational as well as rotational degrees of freedom, will tend to exhibit some slope and not have zero slope as implied by the basic mechanism shape. This is illustrated by Figure G.7. Using the same rationalisation as for the factor ζ_{hi} in mechanism J [refer to equation (G.9) and the accompanying discussion in Section G.2.1], the factor ζ_{vi} is taken as

$$\zeta_{vi} = r. \tag{G.53}$$

This means that when the height H_r (refer to Figure G.6) is small compared to the overall height, the contribution from the crack will also be small, and as H_r gets longer, the crack's contribution factor ζ_{vi} will approach 1.

Since the rotation reduction factor ζ_{vi} is applied to the internal horizontal crack (1), a rotation enhancement factor ζ_{vo} also needs to be applied to the top edge. As a result of the top edge exhibiting some rotation, we need to account for the moment developed in the case of an overburden load providing rotational restraint to the edge. From basic geometry as shown by Figure G.7b, it follows that the sum of these two factors must equal 1, and hence ζ_{vo} is taken as

$$\zeta_{vo} = 1 - \zeta_{vi}. \tag{G.54}$$

It is important to note that the implemented factors ζ_{vo} and ζ_{vi} also act to ensure continuity in the calculated λ_o value when transitioning between the pair of complimentary mechanisms $\mathsf{G_x}$ and $\mathsf{G_y}$. They do this by making the internal work contributions of the horizontal cracks gradual, rather than sudden, across the limiting condition $\alpha = 1$.

Factor ζ_{hi} in equation (G.52) accounts for the activeness of the central vertical

crack (4), since the crack only becomes active when both of the wall's vertical edges are supported, and therefore

$$\zeta_{hi} = \begin{cases} 0, & \text{if one vertical edge is supported, i.e. } n_{vs} = 1; \\ 1, & \text{if two vertical edges are supported, i.e. } n_{vs} = 2. \end{cases}$$

INTERNAL HORIZONTAL CRACK (1), VERTICAL BENDING: The crack spans the length L_e, with its centroid located at a depth H_r below the top edge of the wall; hence, the moment capacity [from equation (6.24)] is

$$M_v = \boldsymbol{f}\langle H_r \rangle \, L_e \bar{Z}_v.$$

It has the virtual rotation

$$\theta'_v = \frac{1}{H_d},$$

thus giving the internal virtual work contribution

$$\begin{aligned} U'_{(1)} = \theta'_v M_v &= \boldsymbol{f}\langle H_r \rangle \, \frac{L_e}{H_d} \bar{Z}_v \\ &= \frac{\bar{Z}_v}{G_n} \boldsymbol{f}\langle r H_t \rangle \, . \end{aligned} \tag{G.55}$$

DIAGONAL CRACK (2): The crack's horizontal projection is L_e, with its centroid located at a distance of $H_t - \frac{1}{2}H_d$ below the top of the wall. From equation (6.29), this gives the moment capacity

$$M_d = \boldsymbol{f}\langle H_t - \tfrac{1}{2}H_d \rangle \, L_e \bar{Z}_v \cos\varphi,$$

which, combined with the virtual rotation

$$\theta'_d = \frac{1}{L_e \sin\varphi},$$

gives the internal virtual work

$$\begin{aligned} U'_{(2)} = \theta'_d M_d &= \boldsymbol{f}\langle H_t - \tfrac{1}{2}H_d \rangle \, \frac{L_e \cos\varphi}{L_e \sin\varphi} \bar{Z}_v \\ &= \frac{\bar{Z}_v}{G_n} \boldsymbol{f}\langle \tfrac{1}{2}(1+r) H_t \rangle \, . \end{aligned} \tag{G.56}$$

EDGE VERTICAL CRACK (3), HORIZONTAL BENDING: The vertical span of the crack is H_r, with its centroid located at a depth of $\frac{1}{2}H_r$ below the top edge. Its moment capacity is obtained by multiplying equation (6.30) by the vertical edge

restraint factor R_{vs} [determined using equation (6.8)], which gives

$$M_h = R_{vs} \boldsymbol{f}\left\langle \tfrac{1}{2} H_r \right\rangle H_r \bar{Z}_h.$$

Combined with the virtual rotation

$$\theta'_h = \frac{1}{L_e},$$

this gives the internal virtual work contribution

$$\begin{aligned} U'_{(3)} = \theta'_h M_h &= R_{vs} \boldsymbol{f}\left\langle \tfrac{1}{2} H_r \right\rangle \frac{H_r}{L_e} \bar{Z}_h \\ &= R_{vs} \frac{\bar{Z}_h r}{\beta} \boldsymbol{f}\left\langle \tfrac{1}{2} r H_t \right\rangle . \end{aligned} \tag{G.57}$$

INTERNAL VERTICAL CRACK (4), HORIZONTAL BENDING: The crack's height span is H_t and its centroid is located $\frac{1}{2}H_t$ below the top edge of the wall. Its moment capacity from equation (6.30) is therefore

$$M_h = \boldsymbol{f}\left\langle \tfrac{1}{2} H_t \right\rangle H_t \bar{Z}_h,$$

whilst its virtual rotation is the same as for crack (3). This gives the internal virtual work contribution

$$\begin{aligned} U'_{(4)} = \theta'_h M_h &= \boldsymbol{f}\left\langle \tfrac{1}{2} H_t \right\rangle \frac{H_t}{L_e} \bar{Z}_h \\ &= \frac{\bar{Z}_h}{\beta} \boldsymbol{f}\left\langle \tfrac{1}{2} H_t \right\rangle . \end{aligned} \tag{G.58}$$

TOP EDGE PSEUDO-CRACK (5), VERTICAL BENDING: This hinge spans the length L_e, so its moment capacity according to equation (6.28) is

$$M_{vo} = R_{ts} \boldsymbol{f}\langle 0 \rangle L_e \bar{Z}_v,$$

which, together with the virtual rotation

$$\theta'_v = \frac{1}{H_d},$$

gives the internal virtual work contribution

$$U'_{(5)} = \theta'_v M_{vo} = R_{ts} \boldsymbol{f}\langle 0 \rangle \frac{L_e}{H_d} \bar{Z}_v$$

$$= R_{ts}\frac{\bar{Z}_v}{G_n}\boldsymbol{f}\langle 0\rangle\,. \tag{G.59}$$

FRICTION AGAINST RESTRAINED OBL: This contribution is calculated according to equation (G.126) as

$$U'_{Om} = (1-\Phi_m)\,\mu_o e'_m, \tag{G.60}$$

where [from equations (G.120) and (G.124)] e'_m is given by

$$e'_m = \tfrac{1}{2}L_e\,t_u\sigma_{vom}. \tag{G.61}$$

TOTAL: The total internal work is obtained by substituting equations (G.55)–(G.60) into (G.52). This yields the expression

$$\begin{aligned} U'_{\text{tot}} = {} & \frac{\bar{Z}_v}{G_n}\left[\zeta_{vi}\boldsymbol{f}\langle rH_t\rangle + \boldsymbol{f}\left\langle\tfrac{1}{2}(1+r)H_t\right\rangle + R_{ts}\zeta_{vo}\boldsymbol{f}\langle 0\rangle\right] \\ & + \frac{\bar{Z}_h}{\beta}\left[\zeta_{hi}\boldsymbol{f}\left\langle\tfrac{1}{2}H_t\right\rangle + R_{vs}r\boldsymbol{f}\left\langle\tfrac{1}{2}rH_t\right\rangle\right] + (1-\Phi_m)\mu_o e'_m. \end{aligned} \tag{G.62}$$

External Work

The external work of an individual out-of-plane module includes the self-weight contributions of blocks (A) and (B) (Figure G.6), in addition to a possible contribution E'_{Om} from an unrestrained OBL. This gives

$$E'_{\text{tot}} = E'_{W(A)} + E'_{W(B)} + E'_{Om}, \tag{G.63}$$

where $E'_{W(A)}$ and $E'_{W(B)}$ are contributions from the respective blocks.

SELF-WEIGHT OF BLOCK (A): From Table 6.1, the virtual volume of the wedge block is

$$V'_{(A)} = \tfrac{1}{2}L_e H_r,$$

which gives the external virtual work

$$\begin{aligned} E'_{W(A)} &= \lambda\gamma t_u\left(\tfrac{1}{2}H_r L_e\right) \\ &= \lambda\gamma t_u L_e H_t\left(\tfrac{1}{2}r\right). \end{aligned} \tag{G.64}$$

SELF-WEIGHT OF BLOCK (B): From Table 6.1, the virtual volume of the triangular pyramid block is

$$V'_{(B)} = \tfrac{1}{6}L_e H_d,$$

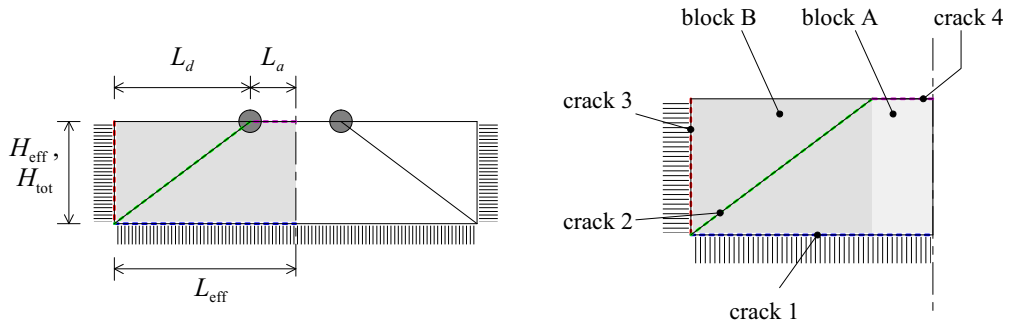

Figure G.8: Individual out-of-plane module involved in mechanism $\mathsf{K1}_{\mathsf{x}}$.

which gives the external virtual work

$$\begin{aligned} E'_{W(B)} &= \lambda\gamma t_u \left(\tfrac{1}{6} L_e H_d\right) \\ &= \lambda\gamma t_u L_e H_t \left(\tfrac{1}{6}\left(1-r\right)\right). \end{aligned} \tag{G.65}$$

WEIGHT OF UNRESTRAINED OBL: This contribution is calculated according to equation (G.125) as

$$E'_{Om} = \Phi_m \lambda \eta_m e'_m, \tag{G.66}$$

where e'_m is given by equation (G.61).

TOTAL: The total external work for a single out-of-plane module is obtained by substituting contributions from equations (G.64)–(G.66) into (G.63). Dividing by λ yields the expression

$$\lambda^{-1} E'_{\text{tot}} = \gamma t_u L_e H_t \left(\tfrac{1}{6} + \tfrac{1}{3} r\right) + \Phi_m \eta_m e'_m. \tag{G.67}$$

G.2.5 Mechanism $\mathsf{K1}_{\mathsf{x}}$

Figure 6.16a shows the mechanism's deflected shape, and Figure G.8 shows the dimensions of a single out-of-plane module. Let us take the effective length L_e and total height H_t as independent variables that define the mechanism's geometry.

Dependent Geometric Variables

The dependent geometric variables (refer to Figure G.8) include: the effective mechanism height H_e, which [from equation (6.39) with $n_{hs} = 1$] is equal to the

total height H_t,

$$H_e = H_t;$$

the horizontal span of block A,

$$L_a = aL_e;$$

and the horizontal projection of the diagonal crack,

$$L_d = (1 - a)\, L_e.$$

In addition, we need to calculate β using equation (6.43) and α using equation (6.44). From this, the shape parameter a becomes

$$a = 1 - \frac{1}{\alpha}.$$

Geometric Constraints

The independent variables L_e and H_t may assume any values, as long as the following constraints are satisfied. The total mechanism height must not exceed the available height of the wall, and must stay within the limits

$$0 < H_t \leq H_w.$$

The effective mechanism length cannot exceed the available length of the wall, and must be within

$$0 < L_e \leq L_w / n_{vs},$$

where n_{vs} is the number of vertical supports for the out-of-plane wall. Finally, the normalised aspect ratio α must satisfy the condition

$$\alpha \geq 1.$$

Internal Work

As shown by Figure G.8, there are four flexural cracks contributing to the internal work of an out-of-plane module, including the bottom horizontal crack (1), diagonal crack (2), vertical edge crack (3), and the top edge pseudo-crack (4). In addition, it may receive the additional work contribution U'_{Om} from the presence of a restrained OBL. The total internal work for a single out-of-plane module is therefore determined from the formula

$$U'_{\text{tot}} = U'_{(1)} + U'_{(2)} + U'_{(3)} + U'_{(4)} + U'_{Om}, \tag{G.68}$$

where $U'_{(1)}$–$U'_{(4)}$ are the contributions from the respective cracks.

BOTTOM HORIZONTAL CRACK (1), VERTICAL BENDING: The crack spans the length L_e, with its centroid located at a depth of H_t below the top edge of the wall. Hence, its moment capacity [from equation (6.24)] is

$$M_v = \boldsymbol{f}\langle H_t \rangle \, L_e \bar{Z}_v,$$

which, together with the virtual rotation

$$\theta'_v = \frac{1}{H_t},$$

provides the internal virtual work

$$\begin{aligned} U'_{(1)} = \theta'_v M_v &= \boldsymbol{f}\langle H_t \rangle \, \frac{L_e}{H_t} \bar{Z}_v \\ &= \bar{Z}_v \beta \boldsymbol{f}\langle H_t \rangle \, . \end{aligned} \tag{G.69}$$

DIAGONAL CRACK (2): The crack's horizontal projection is L_d, with its centroid located at a distance of $\frac{1}{2}H_t$ below the top of the wall. From equation (6.29), the crack has the moment capacity

$$M_d = \boldsymbol{f}\langle \tfrac{1}{2}H_t \rangle \, L_d \bar{Z}_v \cos\varphi.$$

Combined with the virtual rotation

$$\theta'_d = \frac{1}{H_t \cos\varphi},$$

the internal virtual work becomes

$$\begin{aligned} U'_{(2)} = \theta'_d M_d &= \boldsymbol{f}\langle \tfrac{1}{2}H_t \rangle \, \frac{L_d}{H_t \cos\varphi} \bar{Z}_v \cos\varphi \\ &= \frac{\bar{Z}_v}{G_n} \boldsymbol{f}\langle \tfrac{1}{2}H_t \rangle \, . \end{aligned} \tag{G.70}$$

EDGE VERTICAL CRACK (3), HORIZONTAL BENDING: The crack's vertical span is H_t, with its centroid located at a depth of $\frac{1}{2}H_t$ below the top edge. The moment capacity is obtained by multiplying equation (6.30) by the vertical edge restraint factor R_{vs} [determined using equation (6.8)], giving

$$M_h = R_{vs} \boldsymbol{f}\langle \tfrac{1}{2}H_t \rangle \, H_t \bar{Z}_h.$$

Combined with the virtual rotation

$$\theta'_h = \frac{1}{L_d},$$

the internal virtual work contribution becomes

$$\begin{aligned} U'_{(3)} = \theta'_h M_h &= R_{vs} \boldsymbol{f} \left\langle \tfrac{1}{2} H_t \right\rangle \frac{H_t}{L_d} \bar{Z}_h \\ &= R_{vs} \bar{Z}_h G_n \boldsymbol{f} \left\langle \tfrac{1}{2} H_t \right\rangle . \end{aligned} \tag{G.71}$$

TOP EDGE PSEUDO-CRACK (4), VERTICAL BENDING: The hinge has the length span L_a, so its moment capacity according to equation (6.28) is

$$M_{vo} = R_{ts} \boldsymbol{f} \langle 0 \rangle \, L_a \bar{Z}_v.$$

Together with the virtual rotation

$$\theta'_v = \frac{1}{H_t},$$

its internal virtual work is

$$\begin{aligned} U'_{(4)} = \theta'_v M_{vo} &= R_{ts} \boldsymbol{f} \langle 0 \rangle \frac{L_a}{H_t} \bar{Z}_v \\ &= R_{ts} \bar{Z}_v a \beta \boldsymbol{f} \langle 0 \rangle . \end{aligned} \tag{G.72}$$

FRICTION AGAINST RESTRAINED OBL: This contribution is calculated according to equation (G.126) as

$$U'_{Om} = (1 - \Phi_m) \, \mu_o e'_m, \tag{G.73}$$

where [from equations (G.119) and (G.124)] e'_m is given by

$$e'_m = \tfrac{1}{2}(1 + a) \, L_e \, t_u \sigma_{vom}. \tag{G.74}$$

TOTAL: The total internal work is obtained by substituting equations (G.69)–(G.73) into (G.68). This yields the expression

$$\begin{aligned} U'_{\text{tot}} = \bar{Z}_v \beta \left[\boldsymbol{f} \langle H_t \rangle + R_{ts} \, a \boldsymbol{f} \langle 0 \rangle + (1 - a) \, \boldsymbol{f} \left\langle \tfrac{1}{2} H_t \right\rangle \right] \\ + R_{vs} \bar{Z}_h G_n \boldsymbol{f} \left\langle \tfrac{1}{2} H_t \right\rangle + (1 - \Phi_m) \mu_o e'_m. \end{aligned} \tag{G.75}$$

External Work

The external work of an individual out-of-plane module includes the self-weight contributions of blocks (A) and (B) (Figure G.8), in addition to a possible contribution E'_{Om} from an unrestrained OBL. This gives

$$E'_{\text{tot}} = E'_{W(A)} + E'_{W(B)} + E'_{Om}, \tag{G.76}$$

where $E'_{W(A)}$ and $E'_{W(B)}$ are contributions from the respective blocks.

SELF-WEIGHT OF BLOCK (A): From Table 6.1, the virtual volume of the wedge block is

$$V'_{(A)} = \tfrac{1}{2} L_a H_t,$$

giving the external virtual work

$$\begin{aligned} E'_{W(A)} &= \lambda \gamma t_u \left(\tfrac{1}{2} L_a H_t\right) \\ &= \lambda \gamma t_u L_e H_t \left(\tfrac{1}{2} a\right). \end{aligned} \tag{G.77}$$

SELF-WEIGHT OF BLOCK (B): From Table 6.1, the virtual volume of the rectangular pyramid block is

$$V'_{(B)} = \tfrac{1}{3} L_d H_t,$$

which gives the external virtual work

$$\begin{aligned} E'_{W(B)} &= \lambda \gamma t_u \left(\tfrac{1}{3} L_d H_t\right) \\ &= \lambda \gamma t_u L_e H_t \left(\tfrac{1}{3} (1 - a)\right). \end{aligned} \tag{G.78}$$

WEIGHT OF UNRESTRAINED OBL: This contribution is calculated according to equation (G.125) as

$$E'_{Om} = \Phi_m \lambda \eta_m e'_m, \tag{G.79}$$

where e'_m is given by equation (G.74).

TOTAL: The total external work for a single out-of-plane module is obtained by substituting contributions from equations (G.77)–(G.79) into (G.76). Dividing by λ yields the expression

$$\lambda^{-1} E'_{\text{tot}} = \gamma t_u L_e H_t \left(\tfrac{1}{3} + \tfrac{1}{6} a\right) + \Phi_m \eta_m e'_m. \tag{G.80}$$

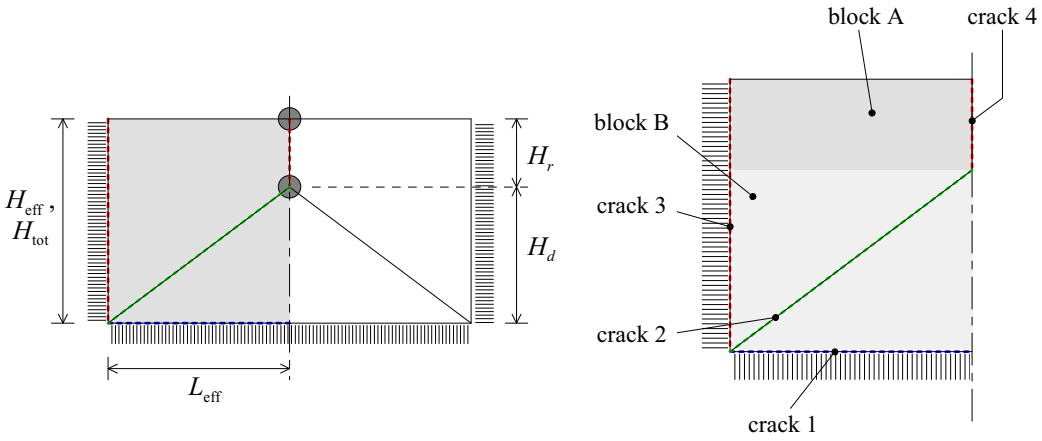

Figure G.9: Individual out-of-plane module involved in mechanism K1_y.

G.2.6 Mechanism K1_y

Figure 6.16b shows the mechanism's deflected shape, and Figure G.9 shows the dimensions of a single out-of-plane module. Let us treat the effective length L_e and total height H_t as the independent variables defining the mechanism's geometry.

Dependent Geometric Variables

The dependent geometric variables (refer to Figure G.9) include: the effective mechanism height H_e, which [from equation (6.39) with $n_{hs} = 1$] is equal to the total height H_t,

$$H_e = H_t;$$

the vertical span of block A, defined as

$$H_r = rH_t;$$

and the height of the diagonal crack,

$$H_d = (1 - r)\, H_t.$$

In addition, we need to calculate β using equation (6.43) and α using equation (6.44). From this, the shape parameter r is calculated as

$$r = 1 - \alpha.$$

Geometric Constraints

The independent variables L_e and H_t may assume any values, as long as the following constraints are adhered to. The total mechanism height must not exceed the available height of the wall and the effective mechanism length cannot exceed the available length of the wall. They must therefore be within the limits

$$0 < H_t \leq H_w \qquad \text{and} \qquad 0 < L_e \leq L_w / n_{vs}.$$

In addition, the normalised aspect ratio α must satisfy the condition

$$\alpha \leq 1.$$

Internal Work

As shown by Figure G.9, there are four flexural cracks contributing to the internal work of an out-of-plane module, including the bottom horizontal crack (1), diagonal crack (2), vertical edge crack (3), and if both vertical edges are supported, then the central vertical crack (4). In addition, it may receive the additional work contribution U'_{Om} from the presence of a restrained OBL. The total internal work for a single out-of-plane module is therefore determined using the formula

$$U'_{\text{tot}} = U'_{(1)} + U'_{(2)} + U'_{(3)} + \zeta_{hi} U'_{(4)} + U'_{Om}, \tag{G.81}$$

where $U'_{(1)}$–$U'_{(4)}$ are the contributions from the respective cracks.

Factor ζ_{hi} in equation (G.81) accounts for the activeness of the central vertical crack (4), since the crack is only active when both of the wall's vertical edges are supported, and therefore

$$\zeta_{hi} = \begin{cases} 0, & \text{if one vertical edge is supported, i.e. } n_{vs} = 1; \\ 1, & \text{if two vertical edges are supported, i.e. } n_{vs} = 2. \end{cases}$$

BOTTOM HORIZONTAL CRACK (1), VERTICAL BENDING: The crack spans the length L_e, with its centroid located at a depth H_t below the top edge of the wall; hence, its moment capacity [from equation (6.24)] is

$$M_v = \boldsymbol{f}\langle H_t \rangle \, L_e \bar{Z}_v.$$

Combined with the virtual rotation

$$\theta'_v = \frac{1}{H_d},$$

it provides the internal work contribution

$$\begin{aligned} U'_{(1)} = \theta'_v M_v &= \boldsymbol{f}\langle H_t \rangle \frac{L_e}{H_d} \bar{Z}_v \\ &= \frac{\bar{Z}_v}{G_n} \boldsymbol{f}\langle H_t \rangle . \end{aligned} \tag{G.82}$$

DIAGONAL CRACK (2): The internal work contribution of this crack is the same as that of crack (2) in mechanism G_y (Figure G.6). Hence, from equation (G.56) we get

$$U'_{(2)} = \frac{\bar{Z}_v}{G_n} \boldsymbol{f}\left\langle \tfrac{1}{2}(1+r) H_t \right\rangle . \tag{G.83}$$

EDGE VERTICAL CRACK (3), HORIZONTAL BENDING: Crack spans the height H_t, with its centroid located at a depth of $\frac{1}{2}H_t$ below the top edge. Its moment capacity is obtained by multiplying equation (6.30) by the vertical edge restraint factor R_{vs} [determined using equation (6.8)], giving

$$M_h = R_{vs} \boldsymbol{f}\left\langle \tfrac{1}{2} H_t \right\rangle H_t \bar{Z}_h,$$

which, together with the virtual rotation

$$\theta'_h = \frac{1}{L_e},$$

provides the internal work contribution

$$\begin{aligned} U'_{(3)} = \theta'_h M_h &= R_{vs} \boldsymbol{f}\left\langle \tfrac{1}{2} H_t \right\rangle \frac{H_t}{L_e} \bar{Z}_h \\ &= R_{vs} \frac{\bar{Z}_h}{\beta} \boldsymbol{f}\left\langle \tfrac{1}{2} H_t \right\rangle . \end{aligned} \tag{G.84}$$

INTERNAL VERTICAL CRACK (4), HORIZONTAL BENDING: The crack spans the height H_r, with its centroid being located $\frac{1}{2}H_r$ below the top edge of the wall. Its moment capacity from equation (6.30) is therefore

$$M_h = \boldsymbol{f}\left\langle \tfrac{1}{2} H_r \right\rangle H_r \bar{Z}_h,$$

whilst its virtual rotation is the same as for crack (3). It hence provides the internal virtual contribution

$$U'_{(4)} = \theta'_h M_h = f\langle \tfrac{1}{2} H_r \rangle \frac{H_r}{L_e} \bar{Z}_h = \frac{\bar{Z}_h r}{\beta} f\langle \tfrac{1}{2} r H_t \rangle . \tag{G.85}$$

FRICTION AGAINST RESTRAINED OBL: This contribution is calculated according to equation (G.126) as

$$U'_{Om} = (1 - \Phi_m)\, \mu_o e'_m, \tag{G.86}$$

where [from equations (G.120) and (G.124)] e'_m is given by

$$e'_m = \tfrac{1}{2} L_e\, t_u \sigma_{vom}. \tag{G.87}$$

TOTAL: The total internal work is obtained by substituting equations (G.82)–(G.86) into (G.81). This yields the expression

$$\begin{aligned} U'_{\text{tot}} = {} & 2\frac{\bar{Z}_v}{G_n} f\langle (\tfrac{3}{4} + \tfrac{1}{4} r) H_t \rangle \\ & + \frac{\bar{Z}_h}{\beta} \left[R_{vs} f\langle \tfrac{1}{2} H_t \rangle + \zeta_{hi} r f\langle \tfrac{1}{2} r H_t \rangle \right] + (1 - \Phi_m) \mu_o e'_m. \end{aligned} \tag{G.88}$$

External Work

The external work of an individual out-of-plane module includes the self-weight contributions of blocks (A) and (B) (Figure G.9), in addition to a possible contribution E'_{Om} from an unrestrained OBL. This gives

$$E'_{\text{tot}} = E'_{W(A)} + E'_{W(B)} + E'_{Om}, \tag{G.89}$$

where $E'_{W(A)}$ and $E'_{W(B)}$ are contributions from the respective blocks.

SELF-WEIGHT OF BLOCK (A): The external work of this wedge block is equivalent to that of block (A) in mechanism G_y (Section G.2.4). Hence, from equation (G.64),

$$E'_{W(A)} = \lambda \gamma t_u L_e H_t \left(\tfrac{1}{2} r \right). \tag{G.90}$$

SELF-WEIGHT OF BLOCK (B): From Table 6.1, the virtual volume of the rectangular pyramid block is

$$V'_{(B)} = \tfrac{1}{3} L_e H_d,$$

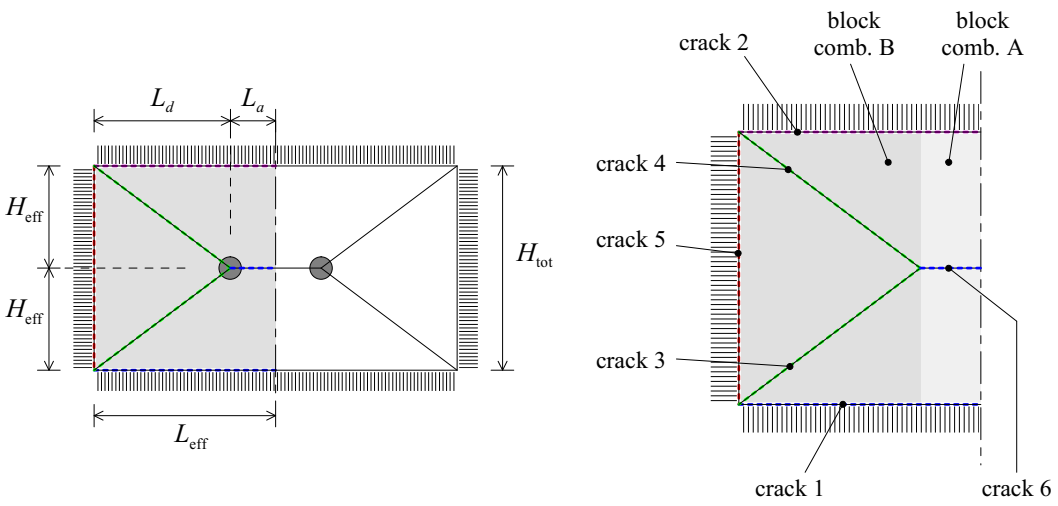

Figure G.10: Individual out-of-plane module involved in mechanism $\mathsf{K2}_{\mathsf{x}}$.

which gives the external virtual work

$$\begin{aligned} E'_{W(B)} &= \lambda\gamma t_u \left(\tfrac{1}{3} L_e H_d\right) \\ &= \lambda\gamma t_u L_e H_t \left(\tfrac{1}{3}\left(1-r\right)\right). \end{aligned} \tag{G.91}$$

WEIGHT OF UNRESTRAINED OBL: This contribution is calculated according to equation (G.125) as

$$E'_{Om} = \Phi_m \lambda \eta_m e'_m, \tag{G.92}$$

where e'_m is given by equation (G.87).

TOTAL: The total external work for a single out-of-plane module is obtained by substituting contributions from equations (G.90) and (G.91) into (G.89). Dividing by λ yields the expression

$$\lambda^{-1} E'_{\text{tot}} = \gamma t_u L_e H_t \left(\tfrac{1}{3} + \tfrac{1}{6} r\right) + \Phi_m \eta_m e'_m. \tag{G.93}$$

G.2.7 Mechanism $\mathsf{K2}_{\mathsf{x}}$

Figure 6.17a shows the mechanism's deflected shape, and Figure G.10 shows the dimensions of a single out-of-plane module. Let us take the effective length L_e and total height H_t as independent variables that define the mechanism's geometry.

Dependent Geometric Variables

The dependent geometric variables (refer to Figure G.10) include: the effective mechanism height H_e, which [from equation (6.39) with $n_{hs} = 2$] is equal to half of the total height $\frac{1}{2}H_t$,

$$H_e = \tfrac{1}{2}H_t;$$

the horizontal span of block combination A,

$$L_a = aL_e;$$

and the horizontal projection of the diagonal cracks,

$$L_d = (1 - a)\, L_e.$$

In addition, we need to calculate β and α according to equations (6.43) and (6.44). From this, the shape parameter a becomes

$$a = 1 - \frac{1}{\alpha}.$$

Geometric Constraints

The independent variables L_e and H_t may assume any values, as long as the following constraints are satisfied. The total mechanism height must not exceed the available height of the wall, and must stay within the limits

$$0 < H_t \leq H_w.$$

The effective mechanism length cannot exceed the available length of the wall, and must be within

$$0 < L_e \leq L_w / n_{vs},$$

where n_{vs} is the number of vertical supports for the out-of-plane wall. Finally, the normalised aspect ratio α must satisfy the condition

$$\alpha \geq 1.$$

Internal Work

As shown by Figure G.10, there are six flexural cracks contributing to the overall strength, including the bottom horizontal crack (1), top edge pseudo-crack (2), diagonal cracks (3) and (4), vertical edge crack (5), and the internal horizontal

crack (6). The total internal work for a single out-of-plane module is therefore determined from the formula

$$U'_{\text{tot}} = U'_{(1)} + U'_{(2)} + U'_{(3)} + U'_{(4)} + U'_{(5)} + U'_{(6)}, \tag{G.94}$$

where $U'_{(1)}$–$U'_{(6)}$ are the contributions from the respective cracks.

BOTTOM HORIZONTAL CRACK (1), VERTICAL BENDING: The crack spans the length L_e, with its centroid being located at a depth of $2H_e$ below the top edge of the wall. Hence, from equation (6.24), it has the moment capacity

$$M_v = \boldsymbol{f}\langle 2H_e\rangle \, L_e \bar{Z}_v,$$

which, combined with the virtual rotation

$$\theta'_v = \frac{1}{H_e},$$

provides the internal virtual work

$$\begin{aligned} U'_{(1)} = \theta'_v M_v &= \boldsymbol{f}\langle 2H_e\rangle \, \frac{L_e}{H_e} \bar{Z}_v \\ &= \bar{Z}_v \beta \boldsymbol{f}\langle 2H_e\rangle \, . \end{aligned} \tag{G.95}$$

TOP EDGE PSEUDO-CRACK (2), VERTICAL BENDING: The horizontal span of the hinge is L_e; thus, from equation (6.28) it has the moment capacity

$$M_{vo} = R_{ts} \boldsymbol{f}\langle 0\rangle \, L_e \bar{Z}_v.$$

Since the hinge has the same rotation as crack (1), its internal virtual work contribution becomes

$$\begin{aligned} U'_{(2)} = \theta'_v M_{vo} &= R_{ts} \boldsymbol{f}\langle 0\rangle \, \frac{L_e}{H_e} \bar{Z}_v \\ &= R_{ts} \bar{Z}_v \beta \boldsymbol{f}\langle 0\rangle \, . \end{aligned} \tag{G.96}$$

DIAGONAL CRACKS (3) AND (4): The combined resistance of the two cracks is equivalent to a single diagonal crack with vertical projection $2H_e$ and whose centroid is located at the midheight of the mechanism or H_e below the top edge of the wall. Hence, from equation (6.29), the equivalent crack has the moment capacity

$$M_d = \boldsymbol{f}\langle H_e\rangle \, \frac{2H_e}{G_n} \bar{Z}_v \cos\varphi.$$

The cracks undergo the virtual rotation

$$\theta'_d = \frac{1}{H_e \cos\varphi},$$

so their combined internal virtual work becomes

$$U'_{(3)} + U'_{(4)} = \theta'_d M_d = \frac{2\bar{Z}_v}{G_n} \boldsymbol{f}\langle H_e \rangle \,. \tag{G.97}$$

EDGE VERTICAL CRACK (5), HORIZONTAL BENDING: Crack spans the height $2H_e$ and its centroid is located at a depth of H_e below the top edge. Its moment capacity is obtained by multiplying equation (6.30) by the vertical edge restraint factor R_{vs} [determined using equation (6.8)], which gives

$$M_h = R_{vs} \boldsymbol{f}\langle H_e \rangle \, 2H_e \bar{Z}_h.$$

Combined with the virtual rotation

$$\theta'_h = \frac{1}{L_d},$$

this gives the internal virtual work contribution

$$U'_{(3)} = \theta'_h M_h = 2R_{vs} \bar{Z}_h G_n \boldsymbol{f}\langle H_e \rangle \,. \tag{G.98}$$

MIDHEIGHT HORIZONTAL CRACK (6), VERTICAL BENDING: The crack spans the length L_a, with its centroid located at a depth of H_e below the top edge of the wall, so it has the moment capacity [from equation (6.24)]

$$M_v = \boldsymbol{f}\langle H_e \rangle \, L_a \bar{Z}_v.$$

Combining with the virtual rotation

$$\theta'_v = \frac{2}{H_e},$$

gives the internal virtual work

$$\begin{aligned} U'_{(6)} = \theta'_v M_v &= \boldsymbol{f}\langle H_e \rangle \, \frac{2L_a}{H_e} \bar{Z}_v \\ &= 2\bar{Z}_v a\beta \boldsymbol{f}\langle H_e \rangle \,. \end{aligned} \tag{G.99}$$

TOTAL: The total internal work is obtained by substituting equations (G.95)–(G.99) into (G.94). By also replacing H_e with $\frac{1}{2}H_t$, this yields the expression

$$\begin{aligned} U'_{\text{tot}} = \bar{Z}_v \beta \left[\boldsymbol{f}\langle H_t \rangle + R_{ts} \boldsymbol{f}\langle 0 \rangle + 2\boldsymbol{f}\left\langle \tfrac{1}{2} H_t \right\rangle \right] \\ + 2R_{vs} \bar{Z}_h G_n \boldsymbol{f}\left\langle \tfrac{1}{2} H_t \right\rangle . \end{aligned} \tag{G.100}$$

External Work

As shown by Figure G.10, the external work for an individual out-of-plane module is the sum of contributions from block combinations (A) and (B), calculated according to the formula

$$E'_{\text{tot}} = E'_{W(A)} + E'_{W(B)}. \tag{G.101}$$

SELF-WEIGHT OF BLOCK COMBINATION (A): From Table 6.1, the virtual volume of the combined wedge blocks is

$$V'_{(A)} = \tfrac{1}{2} L_a H_t,$$

giving the external virtual work

$$\begin{aligned} E'_{W(A)} &= \lambda \gamma t_u \left(\tfrac{1}{2} L_a H_t \right) \\ &= \lambda \gamma t_u L_e H_t \left(\tfrac{1}{2} a \right) . \end{aligned} \tag{G.102}$$

SELF-WEIGHT OF BLOCK COMBINATION (B): From Table 6.1, the virtual volume of the combined rectangular pyramid blocks is

$$V'_{(B)} = \tfrac{1}{3} L_d H_t,$$

which gives the external virtual work

$$\begin{aligned} E'_{W(B)} &= \lambda \gamma t_u \left(\tfrac{1}{3} L_d H_t \right) \\ &= \lambda \gamma t_u L_e H_t \left(\tfrac{1}{3} \left(1 - a \right) \right) . \end{aligned} \tag{G.103}$$

TOTAL: The total external work for a single out-of-plane module is obtained by substituting contributions from equations (G.102) and (G.103) into (G.101). Dividing by λ yields the expression

$$\lambda^{-1} E'_{\text{tot}} = \gamma t_u L_e H_t \left(\tfrac{1}{3} + \tfrac{1}{6} a \right) . \tag{G.104}$$

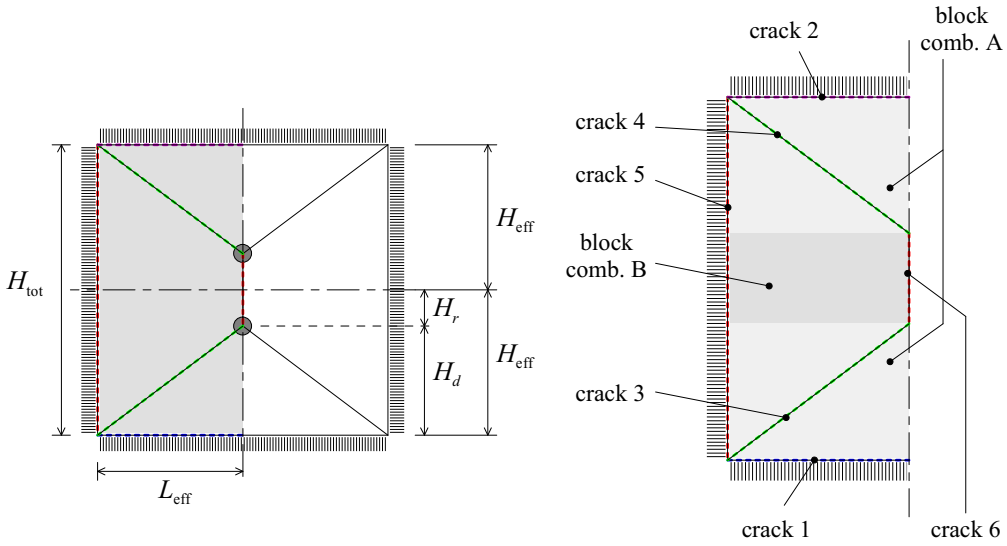

Figure G.11: Individual out-of-plane module involved in mechanism $\mathsf{K2_y}$.

G.2.8 Mechanism $\mathsf{K2_y}$

Figure 6.17b shows the mechanism's deflected shape, and Figure G.11 shows the dimensions of a single out-of-plane module. Let us treat the effective length L_e and total height H_t as the independent variables defining the mechanism's geometry.

Dependent Geometric Variables

The dependent geometric variables (refer to Figure G.11) include: the effective mechanism height H_e, which [from equation (6.39) with $n_{hs} = 2$] is equal to half of the total height $\frac{1}{2}H_t$,

$$H_e = \tfrac{1}{2}H_t;$$

the vertical span

$$H_r = rH_e;$$

and the height of the diagonal crack,

$$H_d = (1 - r)\, H_e.$$

In addition, we need to calculate β using equation (6.43) and α using equation (6.44). From this, the shape parameter r is calculated as

$$r = 1 - \alpha.$$

Geometric Constraints

The independent variables L_e and H_t may assume any values, as long as the following constraints are adhered to. The total mechanism height must not exceed the available height of the wall, and the effective mechanism length cannot exceed the available length of the wall. They must therefore be within the limits

$$0 < H_t \leq H_w \qquad \text{and} \qquad 0 < L_e \leq L_w / n_{vs}.$$

In addition, the normalised aspect ratio α must satisfy the condition

$$\alpha \leq 1.$$

Internal Work

As shown by Figure G.11, there are six flexural cracks contributing to the overall strength, including the bottom horizontal crack (1), top edge pseudo-crack (2), diagonal cracks (3) and (4), vertical edge crack (5), and the internal vertical crack (6). The total internal work for a single out-of-plane module is therefore determined from the formula

$$U'_{\text{tot}} = U'_{(1)} + U'_{(2)} + U'_{(3)} + U'_{(4)} + U'_{(5)} + \zeta_{hi} U'_{(6)}. \tag{G.105}$$

where $U'_{(1)}$–$U'_{(6)}$ are the contributions from the respective cracks. Factor ζ_{hi} accounts for the activeness of the internal vertical crack (6), since the crack is only active when both of the wall's vertical edges are supported, and therefore

$$\zeta_{hi} = \begin{cases} 0, & \text{if one vertical edge is supported, i.e. } n_{vs} = 1; \\ 1, & \text{if two vertical edges are supported, i.e. } n_{vs} = 2. \end{cases}$$

BOTTOM HORIZONTAL CRACK (1), VERTICAL BENDING: The crack spans the length L_e and its centroid is located at a depth $2H_e$ below the top edge of the wall. Hence, it has the moment capacity [from equation (6.24)]

$$M_v = f\langle 2H_e \rangle \, L_e \bar{Z}_v,$$

combined with the virtual rotation

$$\theta'_v = \frac{1}{H_d},$$

which gives the internal virtual work

$$U'_{(1)} = \theta'_v M_v = f\langle 2H_e\rangle \frac{L_e}{H_d}\bar{Z}_v = \frac{\bar{Z}_v}{G_n} f\langle 2H_e\rangle . \tag{G.106}$$

TOP EDGE PSEUDO-CRACK (2), VERTICAL BENDING: The horizontal span of the hinge is L_e, so it has the moment capacity [according to equation (6.28)]

$$M_{vo} = R_{ts} f\langle 0\rangle \, L_e \bar{Z}_v.$$

Since the hinge has the same rotation as crack (1), it provides the internal virtual work contribution

$$U'_{(2)} = \theta'_v M_{vo} = R_{ts} f\langle 0\rangle \frac{L_e}{H_d}\bar{Z}_v = R_{ts}\frac{\bar{Z}_v}{G_n} f\langle 0\rangle . \tag{G.107}$$

DIAGONAL CRACKS (3) AND (4): The combined resistance of the two cracks is equivalent to a single diagonal crack with vertical projection $2H_d$ and whose centroid is located at the midheight of the mechanism or H_e below the top edge of the wall. Hence, from equation (6.29) the equivalent crack has the moment capacity

$$M_d = f\langle H_e\rangle \frac{2H_d}{G_n}\bar{Z}_v \cos\varphi.$$

Both cracks undergo the virtual rotation

$$\theta'_d = \frac{1}{H_d \cos\varphi},$$

so their combined internal virtual work becomes

$$U'_{(3)} + U'_{(4)} = \theta'_d M_d = \frac{2\bar{Z}_v}{G_n} f\langle H_e\rangle . \tag{G.108}$$

EDGE VERTICAL CRACK (5), HORIZONTAL BENDING: The crack has the vertical span $2H_e$, with its centroid being located at a depth of H_e below the top edge. Its moment capacity is obtained by multiplying equation (6.30) by the vertical edge restraint factor R_{vs} [determined using equation (6.8)], which gives

$$M_h = R_{vs} f\langle H_e\rangle \, 2H_e \bar{Z}_h.$$

Together with the virtual rotation

$$\theta'_h = \frac{1}{L_e},$$

the internal virtual work becomes

$$U'_{(5)} = \theta'_h M_h = 2R_{vs}\frac{\bar{Z}_h}{\beta} f\langle H_e\rangle\,. \tag{G.109}$$

INTERNAL VERTICAL CRACK (6), HORIZONTAL BENDING: The crack vertical span is $2H_r$ and its centroid is H_e below the top edge of the wall. Its moment capacity from equation (6.30) is therefore

$$M_h = f\langle H_e\rangle\, 2H_r\bar{Z}_h,$$

whilst its virtual rotation is the same as for crack (5). This gives the internal virtual work contribution

$$\begin{aligned} U'_{(6)} = \theta'_h M_h &= f\langle H_e\rangle\,\frac{2H_r}{L_e}\bar{Z}_h \\ &= \frac{2r\bar{Z}_h}{\beta} f\langle H_e\rangle\,. \end{aligned} \tag{G.110}$$

TOTAL: The total internal work is obtained by substituting equations (G.106)–(G.110) into (G.105). By also replacing H_e with $\frac{1}{2}H_t$, this yields the expression

$$\begin{aligned} U'_{\text{tot}} = \frac{\bar{Z}_v}{G_n}&\left[f\langle H_t\rangle + R_{ts} f\langle 0\rangle + 2f\left\langle \tfrac{1}{2}H_t\right\rangle\right] \\ &+ 2\frac{\bar{Z}_h}{\beta}\left(R_{vs} + \zeta_{hi} r\right) f\left\langle \tfrac{1}{2}H_t\right\rangle. \end{aligned} \tag{G.111}$$

External Work

As shown by Figure G.11, the external work for an individual out-of-plane module is the sum of contributions from block combinations (A) and (B), calculated according to the formula

$$E'_{\text{tot}} = E'_{W(A)} + E'_{W(B)}. \tag{G.112}$$

SELF-WEIGHT OF BLOCK COMBINATION (A): From Table 6.1, the virtual volume of the combined rectangular pyramid blocks is

$$V'_{(A)} = \tfrac{1}{3}L_e\,(2H_d)\,,$$

which gives the external virtual work

$$E'_{W(A)} = \lambda \gamma t_u L_e H_t \left(\tfrac{1}{3}\left(1 - r\right)\right). \tag{G.113}$$

SELF-WEIGHT OF BLOCK COMBINATION (B): From Table 6.1, the virtual volume of the combined wedge blocks is

$$V'_{(B)} = \tfrac{1}{2} L_e \left(2 H_r\right),$$

giving the external virtual work

$$E'_{W(B)} = \lambda \gamma t_u L_e H_t \left(\tfrac{1}{2} r\right). \tag{G.114}$$

TOTAL: The total external work for a single out-of-plane module is obtained by substituting contributions from equations (G.113) and (G.114) into (G.112). Dividing by λ yields the expression

$$\lambda^{-1} E'_{\text{tot}} = \gamma t_u L_e H_t \left(\tfrac{1}{3} + \tfrac{1}{6} r\right). \tag{G.115}$$

G.2.9 Effects of OBL Restraint in Type-1 Mechanisms

As discussed in Section 6.3, the presence of an OBL at the top of the wall has the following influences on the internal and external work terms when considering type-1 mechanisms in which the top edge is considered laterally unrestrained:

1. Additional internal work is done by translational friction between the wall and the OBL. This comes into effect only when the OBL is restrained against lateral movement.

2. Additional external work is done on the wall by the horizontal component of the OBL, if the OBL is not restrained against lateral movement.

3. An increase occurs in the internal crack energies due to a higher internal vertical stress throughout the wall. This is already accounted for by the precompression stress σ_{vo} in the stress capacity function $f\langle \cdots \rangle$ [equation (6.22)] used within the moment capacity expressions for the various types of bending.

Therefore, we need expressions for calculating the additional energies resulting from points 1 and 2 above.

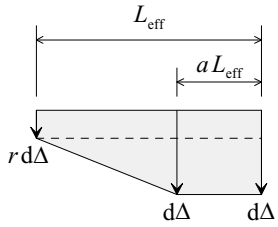

(a) Mechanism J out-of-plane module.

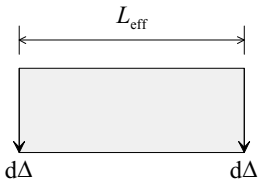

(b) Mechanism B out-of-plane module.

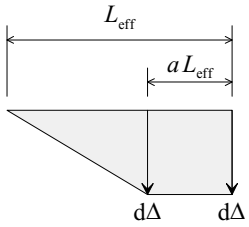

(c) Mechanism G_x and $\mathsf{K1}_\mathsf{x}$ out-of-plane module.

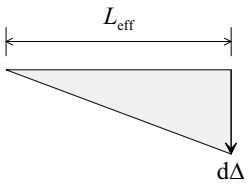

(d) Mechanism G_y and $\mathsf{K1}_\mathsf{y}$ out-of-plane module.

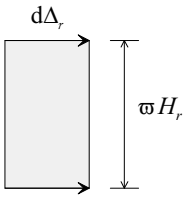

(e) Mechanism J and B in-plane module.

Figure G.12: Increments of displaced area at the top of the wall for the various mechanisms.

Virtual Displaced Areas

We start by deriving expressions for the increment of displaced area at the top edge of each mechanism. We can denote the displaced area in either the incremental notation as $\mathrm{d}A$, or as A' in Lagrange notation [refer to equation (6.9)], where

$$A' = \frac{\mathrm{d}A}{\mathrm{d}\Delta}.$$

We define the virtual displaced area as the virtual displacement $u'\langle x\rangle$ at the top of the wall, integrated over the length of the wall L as

$$A' = \int_{x=0}^{L} u'\langle x\rangle \,\mathrm{d}x, \tag{G.116}$$

in which x is the horizontal position.

MECHANISM J: For a single out-of-plane module in mechanism J (Figure G.12a), we have

$$\mathrm{d}A = \mathrm{d}\Delta\, a\, L_e + \tfrac{1}{2}\left(r\,\mathrm{d}\Delta + \mathrm{d}\Delta\right)\left(L_e - aL_e\right),$$

which gives

$$A' = \tfrac{1}{2}\left(1 + a + r - ar\right) L_e. \tag{G.117}$$

MECHANISM B: For a single out-of-plane module in mechanism B (Figure G.12b), we have

$$\mathrm{d}A = \mathrm{d}\Delta\, L_e,$$

which gives

$$A' = L_e. \tag{G.118}$$

MECHANISMS G_x AND $\mathsf{K1}_\mathsf{x}$: For a single module in mechanisms G_x and $\mathsf{K1}_\mathsf{x}$ (Figure G.12c), we have

$$\mathrm{d}A = \mathrm{d}\Delta\, a\, L_e + \tfrac{1}{2}\mathrm{d}\Delta\,(L_e - aL_e)\,,$$

which gives

$$A' = \tfrac{1}{2}\,(1+a)\,L_e. \tag{G.119}$$

MECHANISMS G_y AND $\mathsf{K1}_\mathsf{y}$: For a single module in mechanisms G_y and $\mathsf{K1}_\mathsf{y}$ (Figure G.12d), we have

$$\mathrm{d}A = \tfrac{1}{2}\mathrm{d}\Delta\, L_e,$$

which gives

$$A' = \tfrac{1}{2}L_e. \tag{G.120}$$

IN-PLANE MODULES IN HYBRID MECHANISMS J AND B: For a single in-plane module (Figure G.12e), the increment of displaced area is

$$\mathrm{d}A = \mathrm{d}\Delta_r \varpi H_r,$$

which gives

$$A' = \Delta'_r \varpi H_r. \tag{G.121}$$

External Work from an Unrestrained OBL

The external virtual work performed on the wall by an unrestrained OBL is obtained by integrating the product of the virtual displacement $u'\langle x\rangle$ and the acting lateral force F_h from the OBL over the length of the wall, according to the formula

$$E' = \int_{x=0}^{L} \left(u'\langle x\rangle \, \frac{\mathrm{d}F_h}{\mathrm{d}x} \right) \mathrm{d}x.$$

When the axial load is uniformly distributed along the wall, the lateral force per unit length is constant such that

$$\frac{\mathrm{d}F_h}{\mathrm{d}x} = \Phi\lambda\eta\sigma_{vo}t,$$

where: Φ is the degree-of-freedom (DOF) factor for the OBL, taken as 1 when the OBL is unrestrained and 0 when it is restrained; λ is the lateral load multiplier; η is the ratio of the component of the overburden weight free to act laterally and that which acts vertically, defined according to equation (6.4); σ_{vo} is the vertical stress acting at the top of the wall due to the OBL; and t is the thickness of the wall. Therefore, we get

$$E' = \Phi\lambda\eta\sigma_{vo}t\int_{x=0}^{L} u'\langle x\rangle\,\mathrm{d}x,$$

where the integral term is equivalent to the virtual displaced area A' for the mechanism, as per equation (G.116). This results in the expression

$$E' = \Phi\lambda\eta\sigma_{vo}tA'. \tag{G.122}$$

The external work contribution is easily calculated using the above formula, by substituting in A' from equations (G.117)–(G.121) for the mechanism under consideration.

Internal Work from a Restrained OBL

The internal virtual work performed due to friction between the wall and a restrained OBL is obtained as the product of the virtual displacement $u'\langle x\rangle$ and the acting frictional force F_f, integrated over the length of the wall according to the formula

$$U' = \int_{x=0}^{L}\left(u'\langle x\rangle\frac{\mathrm{d}F_f}{\mathrm{d}x}\right)\mathrm{d}x.$$

For an axial load which is uniformly distributed along the wall, the frictional force per unit length is constant and equal to

$$\frac{\mathrm{d}F_f}{\mathrm{d}x} = (1-\Phi)\,\mu_o\sigma_{vo}t,$$

where μ_o is the coefficient of friction along the interface between the wall and the OBL. The factor $(1-\Phi)$ makes the term only active when the OBL is restrained and therefore $\Phi = 0$. From this we get

$$U' = (1-\Phi)\,\mu_o\sigma_{vo}t\int_{x=0}^{L} u'\langle x\rangle\,\mathrm{d}x,$$

where the integral term is equivalent to the virtual displaced area A' [as per equation (G.116)], and therefore, we can simplify this to get the expression

$$U' = (1 - \Phi)\, \mu_o \sigma_{vo} t A'. \tag{G.123}$$

The internal work contribution for the predefined mechanisms is readily calculated using the above formula, by substituting in A' from equations (G.117)–(G.121) for the mechanism under consideration.

A Minor Simplification

By recognising that the external and internal work contributions [equations (G.122) and (G.123)] both contain the terms $\sigma_{vo} t A'$, we can define this as the reference virtual energy e', such that

$$e' = \sigma_{vo} t A'. \tag{G.124}$$

The external work contribution then becomes

$$E' = \Phi \lambda \eta e', \tag{G.125}$$

whilst the internal work contribution becomes

$$U' = (1 - \Phi)\, \mu_o e'. \tag{G.126}$$

This formulation is used for the equations presented in Section 6.5.

G.2.10 Top Edge Rotational Restraint Factor R_{ts}

Here we derive the equivalent rotational restraint factor R_{ts} used for calculating the moment capacity about the top edge of the wall in the presence of an overburden load. The factor is subsequently used in the developed virtual work (VW) approach for calculating the load capacity of the various mechanisms and is applicable to any part of the top edge belonging to a sub-plate undergoing rotation about the horizontal axis. This includes: type-2 mechanisms, where the top edge also has translational restraint; as well as certain type-1 mechanisms in which the top edge is free to move laterally, but satisfies the aforementioned condition. Of the mechanisms considered here, this moment capacity becomes applicable to type-1 mechanisms G_x, J, B and $\mathsf{K1}_x$; and type-2 mechanisms $\mathsf{K2}_x$ and $\mathsf{K2}_y$. It is also applied to mechanism G_y, for reasons discussed in Section G.2.4. Hence, only $\mathsf{K1}_y$ is unaffected by the OBL eccentricity.

As can be seen from Figure 6.6, the moment M_{vo} acting about the centroid of the cross section is

$$M_{vo} = W_{vo} l_a,$$

where W_{vo} is the precompression force and l_a is the lever arm, which is equal to

$$l_a = \left(\tfrac{1}{2} - \epsilon\right) t_u,$$

with t_u being the thickness of the wall. For a hinge with length L, the acting force W_{vo} is related to the acting vertical stress σ_{vo} according to

$$W_{vo} = \sigma_{vo} L t_u.$$

This gives the acting moment M_{vo} as

$$M_{vo} = \sigma_{vo} L t_u^2 \left(\tfrac{1}{2} - \epsilon\right). \tag{G.127}$$

We define the rotational restraint factor R_{ts} as

$$M_{vo} = R_{ts} M_v, \tag{G.128}$$

where M_v is the moment capacity of a crack in vertical bending calculated from equation (6.24). By substituting in M_{vo} from equation (G.127) and M_v from equations (6.24) and (6.25), we get the expression

$$R_{ts} = 1 - 2\epsilon. \tag{G.129}$$

Hence, the rotational restraint factor is dependent only on the load eccentricity ϵ. When the load acts upon the upward-deflecting point along the section ($\epsilon = 0$), as is the case for a slab connection, the restraint factor achieves its maximum value of 1. When the load acts at the centre of the wall's thickness ($\epsilon = 1/2$), the restraint factor becomes zero and the hinge provides zero net moment. If the load was to act at the downward-deflecting edge ($\epsilon = 1$) then the restraint factor would be -1, since the hinge would provide a negative moment contribution, or in other words, it would exert an overturning moment onto the wall.

G.3 GENERAL FORMULATION FOR MECHANISM J

A significant feature of the hybrid mechanism J is its ability to span over multiple consecutive out-of-plane walls separated by in-plane return walls. As discussed in Section 6.5.2, since the simple treatment of the mechanism derived in Section

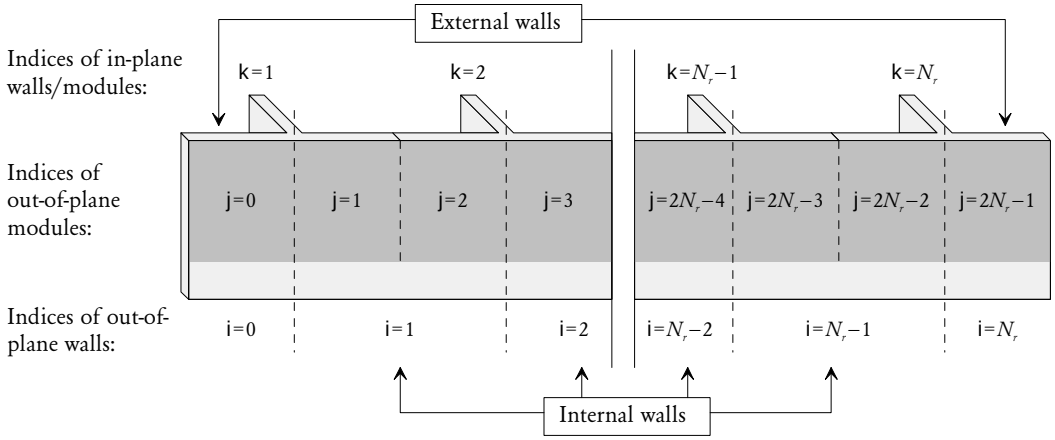

Figure G.13: Generic configuration of out-of-plane walls connected in series.

G.2.1 makes the inherent assumption that all out-of-plane and in-plane modules present in the overall mechanism are equivalent, it can only be applied to simple specimen configurations in which all out-of-plane walls have the same length, such as those shown in Figure 6.12. Furthermore, from the configurations shown in Figure 6.12, the simple approach is only guaranteed to find optimal solutions for (a), (b) and (c), but not (d). This is because at the optimal state, all non-equivalent modules will tend to adopt different geometries, which the simple treatment is unable to deal with due a insufficient number of shape variables that are treated as independent. A more versatile approach is developed here, which overcomes these limitations and may be applied to any generic configuration consisting of a chain of out-of-plane walls separated by in-plane walls, as shown in Figure G.13. The approach is best suited to implementation using computer software such as EXCEL or MATLAB.

G.3.1 Assumptions

In addition to assumptions made previously by the simplified approach, the main assumption made by the presented approach is that all participating in-plane and out-of-plane walls undergo an equal unit rotation about the horizontal axis. This assumption is valid as long as torsional deformation of the out-of-plane panels about the horizontal axis remains negligible. We denote the reference increment of rotation as $d\theta_v$, which may be assigned any arbitrary value.

G.3.2 Definition of Specimen Configuration

As shown by Figure G.13, a generic specimen may consist of a series of internal out-of-plane walls, and two external out-of-plane walls, one on each end. The configuration of the specimen is specified by the user at the start of the analysis using the following information:

- The number of in-plane walls/modules present, denoted by N_r. This value must be greater than or equal to 1.
- Whether or not a left-most external wall is present. We denote this by the Boolean variable `firstExtWall` (= either true or false).
- Whether or not a right-most external wall is present. We denote this by the Boolean variable `lastExtWall` (= either true or false).

G.3.3 Indexing

Figure G.13 demonstrates the indexing convention used for in-plane walls, out-of-plane walls and out-of-plane modules.

In-Plane Walls/Modules

In-plane walls are referred to using the index k, which ranges from $\mathsf{k} = 1$ to N_r.

Out-of-Plane Walls

Out-of-plane walls are referred to using the index i.

The number of internal out-of-plane walls in the specimen, N_{iw}, is directly calculated from the number of return walls, as

$$N_{iw} = N_r - 1. \tag{G.130}$$

Hence, the indices of internal out-of-plane walls range from $\mathsf{i} = 1$ to N_{iw}.

As shown by Figure G.13, if a left-most external wall is present, then it is assigned the index $\mathsf{i} = 0$. If a right-most external wall is present, then its index is $\mathsf{i} = N_r$.

Therefore, the index of the first out-of-plane wall in any configuration is

$$\mathsf{i}_{\mathsf{start}} = \begin{cases} 0, & \text{if } \texttt{firstExtWall} = \mathsf{true}, \\ 1, & \text{if } \texttt{firstExtWall} = \mathsf{false}. \end{cases} \tag{G.131}$$

Similarly, the index of the last out-of-plane wall is

$$i_{\text{end}} = \begin{cases} N_r - 1, & \text{if } \texttt{lastExtWall} = \text{false}, \\ N_r, & \text{if } \texttt{lastExtWall} = \text{true}. \end{cases} \tag{G.132}$$

Out-of-Plane Modules

Out-of-plane modules are referred to using the index j. As shown by Figure G.14, these modules can be either *left* or *right*. Left modules are defined as those that are coupled to a return wall on their left, and have odd indices $j = 1, 3, 5, \ldots$. Right modules are coupled to a return wall on their right, and have even indices $j = 0, 2, 4, \ldots$.

Indices of left modules within internal out-of-plane walls range from $j = 1$ to $2N_{iw} - 1$, whilst indices of right modules within internal out-of-plane walls range from $j = 2$ to $2N_{iw}$.

The module that corresponds to the left-most external out-of-plane wall has the index $j = 0$. Similarly, the module corresponding to the right-most external out-of-plane wall has the index $j = 2N_{iw} + 1$.

Therefore, the index of the first out-of-plane module in any configuration is

$$j_{\text{start}} = i_{\text{start}}, \tag{G.133}$$

and the index of the last out-of-plane module is

$$j_{\text{end}} = \begin{cases} 2N_{iw}, & \text{if } \texttt{lastExtWall} = \text{false}, \\ 2N_{iw} + 1, & \text{if } \texttt{lastExtWall} = \text{true}. \end{cases} \tag{G.134}$$

G.3.4 Summary of Properties

The geometric properties described here are also illustrated by Figure G.14.

In-Plane Walls/Modules

Properties belonging to individual in-plane walls are denoted using the index k, ranging from $k = 1$ to N_r. The following properties are constants based on the specimen geometry, that need to be defined at the start of the analysis:

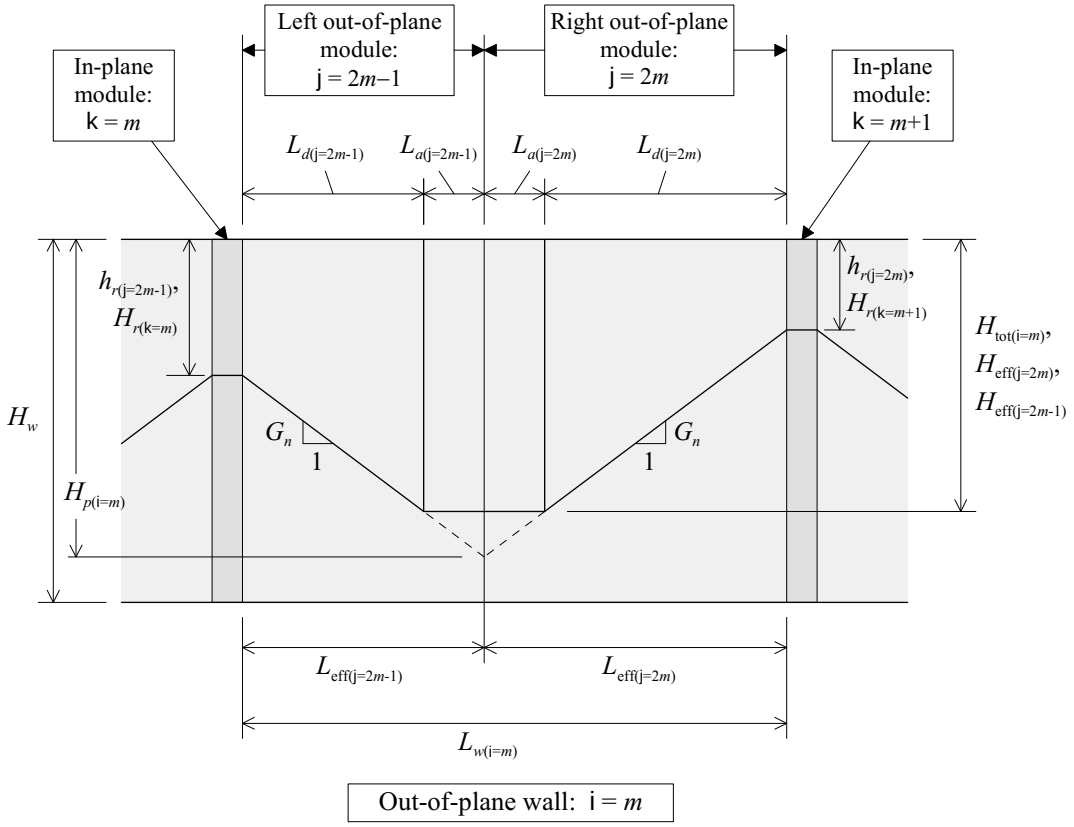

Figure G.14: Geometry of an internal out-of-plane wall and its associated modules.

CONSTANTS	
$\sigma_{vor(\mathsf{k})}$	Precompression stress acting on the k^{th} in-plane wall.
$\Phi_{r(\mathsf{k})}$	OBL degree-of-freedom factor for the k^{th} in-plane wall.
$\eta_{r(\mathsf{k})}$	OBL orthogonal factor for the k^{th} in-plane wall.

The following variables are treated as independent:

INDEPENDENT VARIABLES	
$H_{r(\mathsf{k})}$	Height of the mobilised in-plane panel in the k^{th} in-plane module.
$\varpi_{(\mathsf{k})}$	Slope of the in-plane shear crack in the k^{th} in-plane module.

Dependent properties that get assigned during the analysis include:

DEPENDENT VARIABLES	
$\mathrm{d}\Delta_{r(\mathsf{k})}$	Increment of displacement at the top of the k^{th} in-plane module.
$\mathrm{d}U_{r(\mathsf{k})}$	Internal work increment for the k^{th} in-plane module.
$\lambda^{-1}\mathrm{d}E_{r(\mathsf{k})}$	External work increment for the k^{th} in-plane module, premultiplied by λ^{-1}.
$\mathbb{C}_1$–$\mathbb{C}_4$	Optimisation constraints for the k^{th} in-plane module.

Out-of-Plane Walls

Properties belonging to individual out-of-plane walls are denoted using the index i, ranging from $\mathsf{i} = \mathsf{i}_{\mathsf{start}}$ to $\mathsf{i}_{\mathsf{end}}$. The following are constants based on the specimen geometry, that are defined at the start of the analysis:

CONSTANTS	
$L_{w(\mathsf{i})}$	Length of the i^{th} out-of-plane wall.
$\sigma_{vow(\mathsf{i})}$	Precompression stress acting on the i^{th} out-of-plane wall.
$\Phi_{w(\mathsf{i})}$	OBL degree-of-freedom factor for the i^{th} out-of-plane wall.
$\eta_{w(\mathsf{i})}$	OBL orthogonal factor for the i^{th} out-of-plane wall.
$R_{tsw(\mathsf{i})}$	Top edge rotational restraint factor for the i^{th} out-of-plane wall.

The following variables are treated as independent:

INDEPENDENT VARIABLES	
$L_{t(\mathsf{i})}$	Length of mechanism covering the i^{th} out-of-plane wall.
$H_{t(\mathsf{i})}$	Height of the mechanism covering the i^{th} out-of-plane wall.

Dependent properties that become assigned during the analysis include:

DEPENDENT VARIABLES	
$\mathrm{d}\Delta_{w(\mathrm{i})}$	Increment of displacement at the top of the i^{th} out-of-plane wall.
$H_{p(\mathrm{i})}$	Projected maximum height of the mechanism along the i^{th} out-of-plane wall.
$\mathrm{d}U_{w(\mathrm{i})}$	Internal work increment for the i^{th} out-of-plane wall.
$\mathbb{C}_5$–$\mathbb{C}_8$	Optimisation constraints for the i^{th} out-of-plane wall.

Note that in the simple treatment of mechanism J presented in Section G.2.1, the mechanism length L_t was not treated as independent, and was assumed to span the full available length of the wall. In the treatment presented here, we allow for the possibility that the overall mechanism does not span the full available length of the overall specimen, as it is possible for the optimal solution (at which the collapse multiplier is minimised) to correspond to such scenarios.

Out-of-Plane Modules

Properties which belong to individual out-of-plane mechanism modules are denoted using the index j, ranging from $\mathrm{j} = \mathrm{j}_{\mathrm{start}}$ to $\mathrm{j}_{\mathrm{end}}$. All of these properties are dependent variables that become assigned during the analysis, and include:

DEPENDENT VARIABLES	
$L_{e(\mathrm{j})}$	Length of the j^{th} out-of-plane module.
$H_{e(\mathrm{j})}$	Height of the j^{th} out-of-plane module.
$L_{a(\mathrm{j})}$	Length of horizontal crack in the j^{th} out-of-plane module.
$L_{d(\mathrm{j})}$	Horizontal projection of diagonal crack in the j^{th} out-of-plane module.
$H_{d(\mathrm{j})}$	Vertical projection of diagonal crack in the j^{th} out-of-plane module.
$h_{r(\mathrm{j})}$	Height of the adjacent in-plane module for the j^{th} out-of-plane module.
$\zeta_{hi(\mathrm{j})}$	Work contribution factor for the vertical crack in the j^{th} out-of-plane module.
$\sigma_{vom(\mathrm{j})}$	Precompression stress acting on the j^{th} out-of-plane module.
$\Phi_{m(\mathrm{j})}$	OBL degree-of-freedom factor for the j^{th} out-of-plane module.
$\eta_{m(\mathrm{j})}$	OBL orthogonal factor for the j^{th} out-of-plane module.
$R_{tsm(\mathrm{j})}$	Top edge rotational restraint factor for the j^{th} out-of-plane module.
$\mathrm{d}U_{m(\mathrm{j})}$	Internal work increment for the j^{th} out-of-plane module.
$\lambda^{-1}\mathrm{d}E_{m(\mathrm{j})}$	External work increment for the j^{th} out-of-plane module, premultiplied by λ^{-1}.
$\mathbb{C}_9$–$\mathbb{C}_{11}$	Optimisation constraints for the j^{th} out-of-plane module.

G.3.5 Calculations

In-Plane Walls/Modules

The calculations presented here are performed for each in-plane wall present, for indices ranging from $\mathsf{k} = 1$ to N_r.

First, calculate the increment of displacement at the top of the mobilised in-plane panel as

$$\mathrm{d}\Delta_{r(\mathsf{k})} = \mathrm{d}\theta_v H_{r(\mathsf{k})}, \tag{G.135}$$

where $\mathrm{d}\theta_v$ is the reference increment of rotation for the overall mechanism. We define the stress capacity function for the particular in-plane wall under consideration as

$$\boldsymbol{f_{r(\mathsf{k})}}\langle d \rangle = \sigma_{vor(\mathsf{k})} + \gamma d. \tag{G.136}$$

By expanding equation (G.22) using equations (6.36) and (G.23), the increment of internal work for the in-plane wall becomes

$$\begin{aligned} \mathrm{d}U_{r(\mathsf{k})} = \mathrm{d}\Delta_{r(\mathsf{k})} \Bigg[& \tfrac{1}{2}\,\mu_m\, t_u H_{r(\mathsf{k})} \left(\frac{1}{G_n} + \varpi_{(\mathsf{k})} \right) \boldsymbol{f_{r(\mathsf{k})}} \left\langle \tfrac{1}{3} H_{r(\mathsf{k})} \right\rangle \\ & + \frac{\bar{Z}_v}{G_n} \boldsymbol{f_{r(\mathsf{k})}} \left\langle \tfrac{1}{2} H_{r(\mathsf{k})} \right\rangle \\ & + \left(1 - \Phi_{r(\mathsf{k})}\right) \mu_o \varpi_{(\mathsf{k})} H_{r(\mathsf{k})} t_u \sigma_{vor(\mathsf{k})} \Bigg]. \end{aligned} \tag{G.137}$$

Similarly, from equation (G.27), the increment of external work premultiplied by λ^{-1} is calculated as

$$\lambda^{-1}\mathrm{d}E_{r(\mathsf{k})} = \mathrm{d}\Delta_{r(\mathsf{k})} \left[\gamma t_u \left(\tfrac{1}{3} H_{r(\mathsf{k})}^2 \varpi_{(\mathsf{k})} \right) + \Phi_{r(\mathsf{k})} \eta_{r(\mathsf{k})} \varpi_{(\mathsf{k})} H_{r(\mathsf{k})} t_u \sigma_{vor(\mathsf{k})} \right]. \tag{G.138}$$

Out-of-Plane Walls

For all out-of-plane walls ($\mathsf{i} = \mathsf{i}_{\mathsf{start}}$ to $\mathsf{i}_{\mathsf{end}}$), calculate the increment of displacement at the top of the wall as

$$\mathrm{d}\Delta_{w(\mathsf{i})} = \mathrm{d}\theta_v H_{t(\mathsf{i})}. \tag{G.139}$$

For internal out-of-plane walls only ($\mathsf{i} = 1$ to N_{iw}), we need to define the boundary between its pair of out-of-plane modules. As shown by Figure G.14, the boundary is taken at the intersection of the diagonal projections made from the bottom of the adjacent in-plane modules. The projected height at the intersection is calculated as

$$H_{p(\mathsf{i})} = \tfrac{1}{2} \left(H_{r(\mathsf{k}=\mathsf{i})} + H_{r(\mathsf{k}=\mathsf{i}+1)} + G_n L_{t(\mathsf{i})} \right), \tag{G.140}$$

where $k = i$ is the adjacent in-plane wall to the left, and $k = i + 1$ is the adjacent in-plane wall to the right of the out-of-plane wall under consideration.

Out-of-Plane Modules

The calculations presented here are performed for each out-of-plane module present, for indices ranging from $j = j_{start}$ to j_{end}.

One of the main considerations in formulating the VW equations is ensuring that the formulation is numerically stable and that any potential divisions by zero are avoided for all admissible values of the independent variables. A problem with directly using the equations derived in Section G.2.1 for a single out-of-plane module [equations (G.16) and (G.21)], is the dependence on the parameter β [calculated using equation (6.43)], which contains H_e in the denominator and will therefore cause numerical problems when $H_e \to 0$. This is because for certain wall configurations, the optimal state corresponds to particular walls becoming effectively inactive, which will cause their H_e to approach 0 during the optimisation process. The equations presented here are slight reformulations of the equations presented in Section G.2.1, which will avoid the associated numerical problems.

Certain dependent properties of the out-of-plane module take on values directly from its parent out-of-plane wall or adjacent in-plane wall.

The index of the parent out-of-plane wall is

$$i_p = \begin{cases} (j+1)/2, & \text{for left out-of-plane modules } (j = 1, 3, 5, \ldots), \\ j/2, & \text{for right out-of-plane modules } (j = 0, 2, 4, \ldots). \end{cases} \tag{G.141}$$

The associated properties include: axial stress at the top of the wall,

$$\sigma_{vom(j)} = \sigma_{vow(i=i_p)}; \tag{G.142}$$

OBL degree-of-freedom factor,

$$\Phi_{m(j)} = \Phi_{w(i=i_p)}; \tag{G.143}$$

OBL orthogonal factor,

$$\eta_{m(j)} = \eta_{w(i=i_p)}; \tag{G.144}$$

the top edge rotational restraint factor,

$$R_{tsm(j)} = R_{tsw(i=i_p)}; \tag{G.145}$$

the displacement increment,

$$\mathrm{d}\Delta_{m(\mathsf{j})} = \mathrm{d}\Delta_{w(\mathsf{i}=\mathsf{i_p})}; \tag{G.146}$$

and the effective module height,

$$H_{e(\mathsf{j})} = H_{t(\mathsf{i}=\mathsf{i_p})}. \tag{G.147}$$

The index of the adjacent in-plane wall is

$$\mathsf{k_a} = \begin{cases} (\mathsf{j}+1)/2, & \text{for left out-of-plane modules } (\mathsf{j} = 1,3,5,\ldots), \\ (\mathsf{j}+2)/2, & \text{for right out-of-plane modules } (\mathsf{j} = 0,2,4,\ldots), \end{cases} \tag{G.148}$$

which relates to the height of the adjacent in-plane module,

$$h_{r(\mathsf{j})} = H_{r(\mathsf{k}=\mathsf{k_a})}. \tag{G.149}$$

The length of the out-of-plane module is

$$L_{e(\mathsf{j})} = \begin{cases} L_{t(\mathsf{i}=\mathsf{i_p})}, & \text{if } \mathsf{j} = 0 \quad \text{or} \quad \mathsf{j} = 2N_{iw}+1, \\ \left(H_{p(\mathsf{i}=\mathsf{i_p})} - h_{r(\mathsf{j})}\right)/G_n, & \text{otherwise.} \end{cases} \tag{G.150}$$

The first case above corresponds to the out-of-plane module belonging to an external out-of-plane wall, in which case the length is taken as the full length of mechanism covering the wall. The second case corresponds to the out-of-plane module belonging to an internal out-of-plane wall, whereby L_e is taken as the span to the intersection point of the diagonal projections, as illustrated in Figure G.14.

The remaining properties are all dependent only on properties of the out-of-plane module itself. They include: the vertical projection of the diagonal crack,

$$H_{d(\mathsf{j})} = H_{e(\mathsf{j})} - h_{r(\mathsf{j})}; \tag{G.151}$$

horizontal projection of the diagonal crack,

$$L_{d(\mathsf{j})} = H_{d(\mathsf{j})}/G_n; \tag{G.152}$$

and the length of the horizontal crack,

$$L_{a(\mathsf{j})} = L_{e(\mathsf{j})} - L_{d(\mathsf{j})}. \tag{G.153}$$

The work contribution factor for the vertical crack [refer to equation (G.9)] is taken

as

$$\zeta_{hi(\mathrm{j})} = \begin{cases} L_{a(\mathrm{j})}/L_{e(\mathrm{j})}, & \text{if } \mathrm{j}=0 \quad \text{or} \quad \mathrm{j}=2N_{iw}+1, \\ 1, & \text{otherwise.} \end{cases} \tag{G.154}$$

We define the stress capacity function for the particular out-of-plane module under consideration as

$$\boldsymbol{f_{m(\mathrm{j})}}\langle d\rangle = \sigma_{vom(\mathrm{j})} + \gamma d. \tag{G.155}$$

By expanding the internal work for an out-of-plane module from equation (G.8) using equations (G.10)–(G.14), expressing it in terms of the various crack spans previously calculated, and premultiplying it by the increment of displacement at the top of the module $\mathrm{d}\Delta_{m(\mathrm{j})}$, we obtain the following expression for the increment of internal work:

$$\begin{aligned} \mathrm{d}U_{m(\mathrm{j})} = \mathrm{d}\theta_v \Big\{ & \bar{Z}_v L_{a(\mathrm{j})} \boldsymbol{f_{m(\mathrm{j})}} \left\langle H_{e(\mathrm{j})} \right\rangle \\ & + \bar{Z}_v L_{d(\mathrm{j})} \boldsymbol{f_{m(\mathrm{j})}} \left\langle H_{e(\mathrm{j})} - \tfrac{1}{2} H_{d(\mathrm{j})} \right\rangle \\ & + \zeta_{hi(\mathrm{j})} \bar{Z}_h G_n H_{e(\mathrm{j})} \boldsymbol{f_{m(\mathrm{j})}} \left\langle \tfrac{1}{2} H_{e(\mathrm{j})} \right\rangle \\ & + R_{tsm(\mathrm{j})} \bar{Z}_v L_{e(\mathrm{j})} \boldsymbol{f_{m(\mathrm{j})}} \langle 0 \rangle \\ & + \left(1 - \Phi_{m(\mathrm{j})}\right) \mu_o \sigma_{vom(\mathrm{j})} t_u \left[L_{a(\mathrm{j})} H_{e(\mathrm{j})} + \tfrac{1}{2} L_{d(\mathrm{j})} \left(h_{r(\mathrm{j})} + H_{e(\mathrm{j})} \right) \right] \Big\}. \end{aligned} \tag{G.156}$$

Similarly, from equation (G.17) with equations (G.18)–(G.20), we get the following expression for the increment of external work premultiplied by λ^{-1}:

$$\begin{aligned} \lambda^{-1} \mathrm{d}E_{m(\mathrm{j})} = \mathrm{d}\theta_v \Big\{ & \gamma t_u \left[\tfrac{1}{2} H_{e(\mathrm{j})}^2 L_{a(\mathrm{j})} + \tfrac{1}{6} \left(H_{e(\mathrm{j})}^3 - h_{r(\mathrm{j})}^3 \right) / G_n \right] \\ & + \Phi_{m(\mathrm{j})} \eta_{m(\mathrm{j})} \sigma_{vom(\mathrm{j})} t_u \left[L_{a(\mathrm{j})} H_{e(\mathrm{j})} + \tfrac{1}{2} L_{d(\mathrm{j})} \left(h_{r(\mathrm{j})} + H_{e(\mathrm{j})} \right) \right] \Big\}. \end{aligned} \tag{G.157}$$

Total Internal and External Work, and Collapse Multiplier

The total increments of internal and external work for the overall mechanism are calculated by summing the contributions from all participating out-of-plane and in-plane modules. Hence, the total internal work increment is calculated as

$$\mathrm{d}U_{\mathrm{tot}} = \sum_{\mathrm{j}=\mathrm{j}_{\mathrm{start}}}^{\mathrm{j}_{\mathrm{end}}} \mathrm{d}U_{m(\mathrm{j})} + \sum_{\mathrm{k}=1}^{N_r} \mathrm{d}U_{r(\mathrm{k})}, \tag{G.158}$$

and the total external work increment premultiplied by λ^{-1} is calculated as

$$\lambda^{-1}\mathrm{d}E_{\mathrm{tot}} = \sum_{\mathsf{j}=\mathsf{j}_{\mathsf{start}}}^{\mathsf{j}_{\mathsf{end}}} \lambda^{-1}\mathrm{d}E_{m(\mathsf{j})} + \sum_{\mathsf{k}=1}^{N_r} \lambda^{-1}\mathrm{d}E_{r(\mathsf{k})}. \tag{G.159}$$

From this, the collapse multiplier becomes

$$\lambda_o = \frac{\mathrm{d}U_{\mathrm{tot}}}{\lambda^{-1}\mathrm{d}E_{\mathrm{tot}}}. \tag{G.160}$$

G.3.6 Optimisation and Constraints

The constraints enforced during the optimisation process used to solve for the critical value of λ_o depend on the type of analysis being conducted. Two types of analysis should be considered for any wall specimen, which include:

1. *Unrestricted wall participation*, whereby all walls/modules are allowed to participate in the overall mechanism;

2. and *restricted wall participation*, whereby certain walls are selectively denied from participating in the overall mechanism. This analysis is further subdivided into each of the various permutations of active and inactive walls that are possible for a given wall configuration.

Analysis Permutations

By recognising that an admissible mechanism must have a horizontal span that is continuous over the wall specimen, we can restrict wall participation by declaring in-plane walls that will act as boundaries to the mechanism. These in-plane boundary walls not only prohibit any outside walls/modules from participating, but also become inactive themselves ($H_{r(\mathsf{k})} = 0$). The additional important effect of this is that the out-of-plane wall that is immediately adjacent to a boundary in-plane wall will have relaxed constraints on the length of mechanism ($L_{t(\mathsf{i})}$) that it can accommodate. Two boundary in-plane walls may be declared: a left one and a right one. We denote their respective indices (equivalent to k) as B_{left} and B_{right}. For the left boundary, B_{left} may assume integer values in the range

$$0 \leq B_{\mathrm{left}} \leq N_r, \tag{G.161}$$

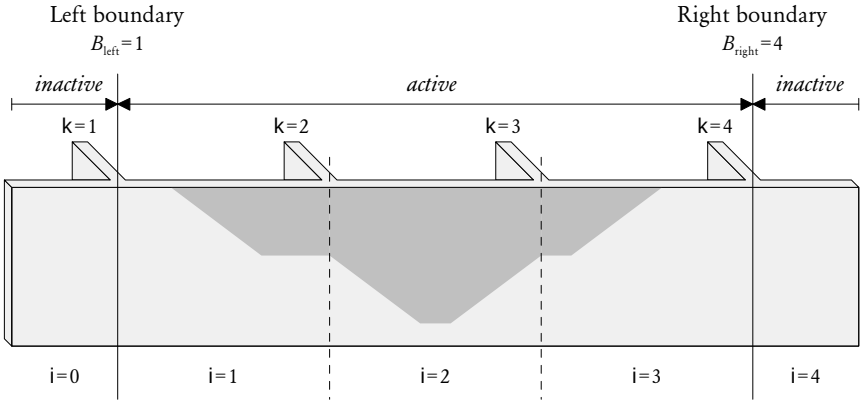

Figure G.15: Example of an analysis with enforced limited wall participation.

whereby $B_{\text{left}} = 0$ corresponds to the left boundary being effectively unrestricted. For the right boundary, B_{right} may assume integer values in the range

$$1 \leq B_{\text{right}} \leq N_r + 1, \tag{G.162}$$

such that the case $B_{\text{right}} = N_r + 1$ corresponds to the right boundary being effectively unrestricted. Furthermore, any selected values of B_{left} and B_{right} must satisfy

$$B_{\text{left}} < B_{\text{right}}. \tag{G.163}$$

Figure G.15 shows an example of enforced limited wall participation for a wall specimen with $N_r = 4$ and both external out-of-plane walls. The left boundary in-plane wall is placed at $B_{\text{left}} = 1$ and the right wall at $B_{\text{right}} = 4$. Doing this precludes the external walls from participating in the mechanism, and allows only the internal out-of-plane walls to participate. Furthermore, since the boundary in-plane walls are, by definition, non-participating, this allows the mechanism along internal walls which are immediately inside of the boundaries ($i = 1$ and $i = 3$) to not be restricted to the full length of the wall. By contrast, any walls that are not adjacent to the boundary in-plane walls, such as wall $i = 2$ in this example, must accommodate a mechanism along its full length.

The number of analysis permutations that need to be considered depend on the configuration of the specimen. Figure G.16a illustrates the three permutations which exist for a specimen with $N_r = 1$, whilst Figure G.16a shows the six possible permutations for a specimen with $N_r = 2$. In general, the number of permutations, P, that need to be considered is

$$P = \tfrac{1}{2}\left(N_r + 1\right)\left(N_r + 2\right). \tag{G.164}$$

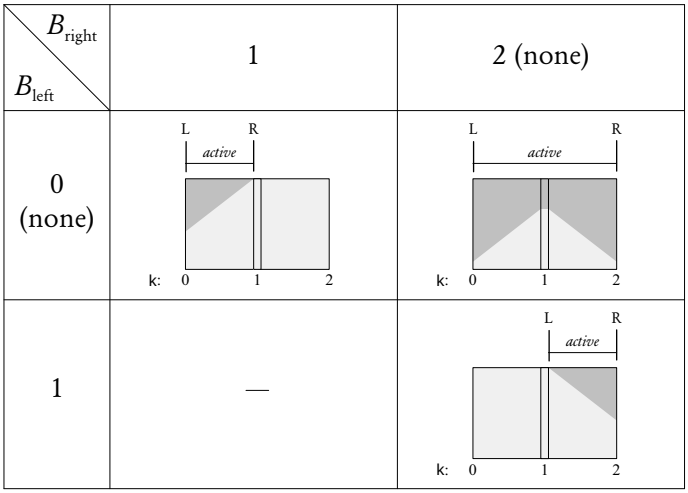

(a) Specimen with a single in-plane wall, $N_r = 1$.

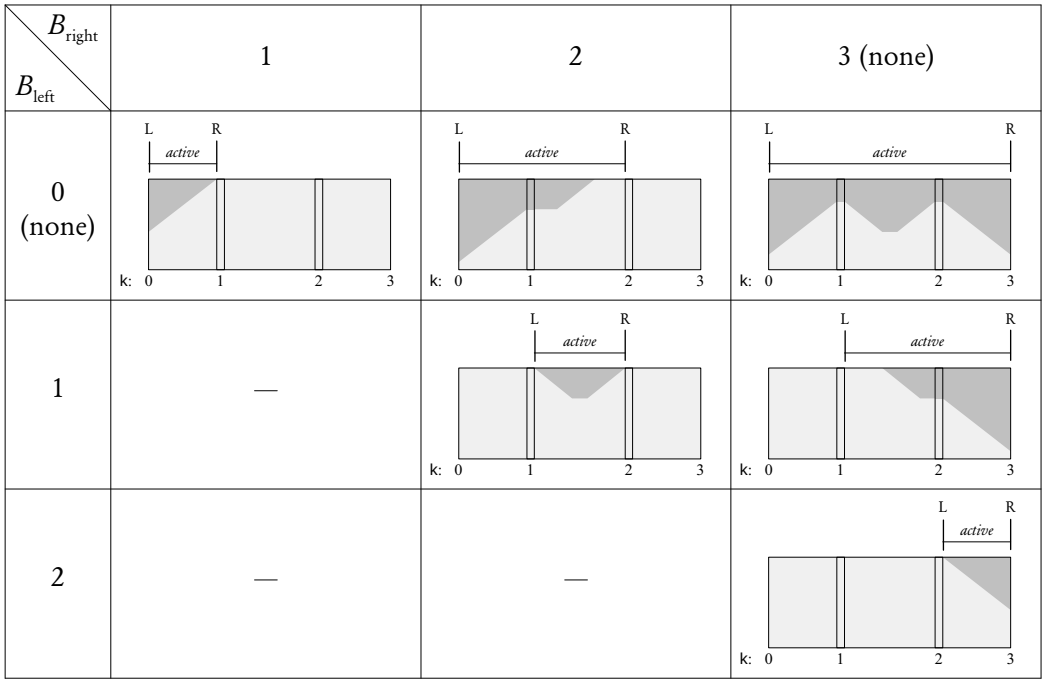

(b) Specimen with two in-plane walls, $N_r = 2$.

Figure G.16: Possible analysis permutations for specimens with $N_r = 1$ and $N_r = 2$.

Furthermore, it is seen from Figures G.16a and G.16b that the unrestricted wall participation scenario mentioned earlier effectively corresponds to the particular case of the restricted participation analysis, with $B_{\text{left}} = 0$ and $B_{\text{right}} = N_r + 1$. Therefore, it becomes sufficient to consider all of the permutations in the restricted participation analysis. In implementing the method using a programming approach, the optimisation process may be placed two nested loops as follows:

```
for Bleft = 1 to NR
  for Bright = Bleft+1 to NR+1
    ... perform optimisation ...
  end
end
```

Constraints

In total, there are 11 different types of constraint that need to be satisfied in the optimisation process. We denote these as

$$\mathbb{C}_1, \mathbb{C}_2, \mathbb{C}_3, \ldots, \mathbb{C}_{11},$$

and formulate them so that each must satisfy

$$\mathbb{C}_1 \geq 0, \quad \mathbb{C}_2 \geq 0, \quad \mathbb{C}_3 \geq 0, \quad \ldots, \quad \mathbb{C}_{11} \geq 0.$$

IN-PLANE WALLS For every in-plane wall with the index k, there are four constraints, $\mathbb{C}_{1(k)}$–$\mathbb{C}_{4(k)}$. These must satisfy

$$\left\{\mathbb{C}_{1(k)}, \mathbb{C}_{2(k)}, \mathbb{C}_{3(k)}, \mathbb{C}_{1(k)}\right\} \geq 0, \qquad \text{for } k = 1 \text{ to } N_r. \tag{G.165}$$

The first constraint is

$$\mathbb{C}_{1(k)} = H_{r(k)}, \tag{G.166}$$

which ensures that $H_{r(k)}$ always stays positive.

The second constraint enforces an upper limit on $H_{r(k)}$, and is formulated as

$$\mathbb{C}_{2(k)} = H_{r\max} - H_{r(k)}, \tag{G.167}$$

where $H_{r\max}$ is the maximum allowed height, such that

$$H_{r\max} = \begin{cases} H_w, & \text{if } B_{\text{left}} < \mathsf{k} < B_{\text{right}}, \\ 0, & \text{otherwise.} \end{cases} \tag{G.168}$$

The two cases above correspond to in-plane walls that are participating and non-participating, respectively.

The third and fourth constraints

$$\mathbb{C}_{3(\mathsf{k})} = \varpi_{(\mathsf{k})} \qquad \text{and} \qquad \mathbb{C}_{4(\mathsf{k})} = 1/G_n - \varpi_{(\mathsf{k})} \tag{G.169}$$

act to ensure that the in-plane crack slope stays inside the limits prescribed by equation (6.33).

OUT-OF-PLANE WALLS For every out-of-plane wall with the index i, there are four constraints: $\mathbb{C}_{5(\mathsf{i})}$–$\mathbb{C}_{8(\mathsf{i})}$, which must satisfy

$$\left\{\mathbb{C}_{5(\mathsf{i})}, \mathbb{C}_{6(\mathsf{i})}, \mathbb{C}_{7(\mathsf{i})}, \mathbb{C}_{8(\mathsf{i})}\right\} \geq 0, \qquad \text{for } \mathsf{i} = \mathsf{i}_{\text{start}} \text{ to } \mathsf{i}_{\text{end}}. \tag{G.170}$$

The first constraint

$$\mathbb{C}_{5(\mathsf{i})} = H_{t(\mathsf{i})} \tag{G.171}$$

is used to ensure that $H_{t(\mathsf{i})}$ stays positive.

The second constraint places an upper limit on $H_{t(\mathsf{i})}$, and is formulated as

$$\mathbb{C}_{6(\mathsf{i})} = H_{t\,\max} - H_{t(\mathsf{i})}, \tag{G.172}$$

where $H_{t\,\max}$ is the maximum allowed height, and is taken as

$$H_{t\,\max} = \begin{cases} H_w, & \text{if } B_{\text{left}} \leq \mathsf{i} \leq B_{\text{right}} - 1, \\ 0, & \text{otherwise.} \end{cases} \tag{G.173}$$

The two cases above correspond to out-of-plane walls that are participating and non-participating, respectively.

The third constraint places a lower bound value on the length $L_{t(\mathsf{i})}$, and is formulated as

$$\mathbb{C}_{7(\mathsf{i})} = L_{t\,\max} - L_{t(\mathsf{i})}, \tag{G.174}$$

where $L_{t\,\max}$ is the minimum allowed value, taken as

$$L_{t\,\max} = \begin{cases} 0, & \text{if } \mathsf{i} = B_{\text{left}} \quad \text{and} \quad \mathsf{i} \neq 0, \\ 0, & \text{if } \mathsf{i} = B_{\text{right}} - 1 \quad \text{and} \quad \mathsf{i} \neq N_r, \\ L_w, & \text{otherwise.} \end{cases} \tag{G.175}$$

The first two cases above correspond to scenarios where the out-of-plane wall under consideration is a participating internal wall adjacent to one of the boundary in-plane walls. This constraint effectively acts to relax the length restriction for such walls. The third case corresponds to any other wall.

The fourth constraint ensures that $L_{t(\mathsf{i})}$ does not exceed the length of the wall, and is taken as

$$\mathbb{C}_{8(\mathsf{i})} = L_w - L_{t(\mathsf{i})}. \tag{G.176}$$

OUT-OF-PLANE MODULES For every out-of-plane module having the index j, there are three constraints: $\mathbb{C}_{9(\mathsf{j})}$–$\mathbb{C}_{11(\mathsf{j})}$, which must satisfy

$$\left\{\mathbb{C}_{9(\mathsf{j})}, \mathbb{C}_{10(\mathsf{j})}, \mathbb{C}_{11(\mathsf{j})}\right\} \geq 0, \qquad \text{for } \mathsf{j} = \mathsf{j}_{\text{start}} \text{ to } \mathsf{j}_{\text{end}}. \tag{G.177}$$

These constraints are

$$\mathbb{C}_{9(\mathsf{j})} = L_{a(\mathsf{j})}, \qquad \mathbb{C}_{10(\mathsf{j})} = L_{d(\mathsf{j})}, \qquad \mathbb{C}_{11(\mathsf{j})} = H_{d(\mathsf{j})}, \tag{G.178}$$

which act to ensure that the spans $L_{a(\mathsf{j})}$, $L_{d(\mathsf{j})}$ and $H_{d(\mathsf{j})}$ all stay positive.

G.4 WORKED EXAMPLES

This section contains several examples demonstrating calculation of the collapse load multiplier λ_o using the DSM mechanisms presented in Section 6.5.

G.4.1 Example 1: A Non-Loadbearing Wall

Problem

Using mechanism J*, calculate the collapse load multiplier (λ_o) for the non-loadbearing wall shown in Figure G.17. The wall spans 10 bricks in length and 21 courses in height. Both of its vertical edges are supported whilst the top edge is free. Use the brick dimensions and material properties from Restrepo Vélez's tests given in Table 6.2. Whereas normally the independent variables parameters a, ω and H_t would be optimised to minimise λ_o, in*

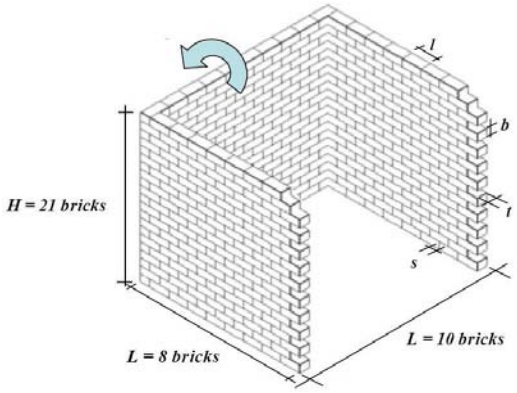

Figure G.17: Non-loadbearing wall used in Example 1. Illustration from *Restrepo Vélez and Magenes* [2009]. (Graphic used with permission from IUSS Press.)

this example assume that $a = 0.15$, $\varpi = 0$ (i.e. that the in-plane shear crack is oriented vertically) and that the height of the mechanism spans vertically across 12 courses of bricks.

Solution

Start by calculating the geometric constants for this type of masonry, which include the moment moduli for vertical and horizontal bending, $\bar{Z}_v$ and $\bar{Z}_h$ respectively and the diagonal crack slope G_n. These parameters should be calculated first because they are independent of the type of mechanism and its dimensions.

The modulus for vertical bending is calculated using equation (6.24) as

$$\bar{Z}_v = t_u^2/2 = (39.7\,\text{mm})^2/2 = 788.0\,\text{mm}^3 \text{ per mm.}$$

For horizontal bending, firstly calculate the bed joint overlap which for DSM is half of the brick length $s_b = l_u/2 = (79.8\,\text{mm})/2 = 39.9\,\text{mm}$, from which the bed joint overlap ratio is obtained as $r_o = s_b/t_u = 39.9/39.7 = 1.005$. Substituting r_o into equation (4.31) gives $k_{bp} = 0.3855$. The resulting moment modulus is evaluated using equation (6.31) as

$$\begin{aligned}\bar{Z}_h = \mu_m\, k_{bp}\, t_u^3/(h_u + t_j) &= 0.71 \times 0.3855 \times (39.7\,\text{mm})^3/28.2\,\text{mm} \\ &= 607.3\,\text{mm}^3 \text{ per mm.}\end{aligned}$$

The diagonal crack slope [from equation (4.13)] is

$$G_n = 2 \times \frac{28.2\,\text{mm}}{79.8\,\text{mm}} = 0.7068.$$

Next, determine the number out-of-plane and in-plane modules involved in the

mechanism. The scenario considered in this example can be visualised through Figure 6.14a, which depicts a single out-of-plane wall ($N_w = 1$) with both of its vertical edges supported ($n_{vs} = 2$). The resulting number out-of-plane modules, as per equation (6.45), is $N_m = 1 \times 2 = 2$, which correspond to the two identical halves of the out-of-plane panel mirrored by the vertical line of symmetry as shown in Figure 6.14a. The number of in-plane modules simply equals to the total number of return walls in the specimen; therefore $N_r = 2$.

Now determine the dimensions of each of the out-of-plane modules. The length of the wall is specified to be 10 bricks across, which equates to $L_w = 10 \times 79.8\,\text{mm} = 798\,\text{mm}$. For mechanism J, the length of the out-of-plane module is always predetermined, such that the mechanism spans the maximum available length across the wall. Therefore, [from equation (6.42)] the length of a single out-of-plane module is $L_e = 798\,\text{mm}/2 = 399\,\text{mm}$. The height of the mechanism is not predetermined; however, in this example it has been assumed to span over 12 courses of bricks. This corresponds to a height of $H_t = 12 \times 28.2\,\text{mm} = 338\,\text{mm}$. The resulting out-of-plane module aspect ratio [from equation (6.43)] is $\beta = 399\,\text{mm}/338\,\text{mm} = 1.18$.

Now determine values of the auxiliary variables, including r, ζ_{hi}, e'_m and e'_r, using the specific equations for mechanism J, provided in Section 6.5.2. Using the assumed value $a = 0.15$, from equation (6.46) we get

$$r = 1 - \beta G_n(1-a) = 1 - 1.18 \times 0.7068 \times (1 - 0.15) = 0.292.$$

Since both vertical edges are supported, the central vertical cracks are able to develop their full internal work and the factor ζ_{hi} is taken as 1 [as per equation (6.47)]. As the wall is non-loadbearing, $\sigma_{vom} = \sigma_{vor} = 0$ and hence $e'_m = e'_r = 0$, which causes the associated internal and external work contributions to drop out.

Furthermore, for a non-loadbearing wall the total internal and external work terms can be simplified by recognising that the stress capacity function [equation (6.22)] reduces to $\boldsymbol{f}\langle d\rangle = \gamma d$. By substituting equation (6.36) into (6.50), the total internal work becomes

$$\begin{aligned} U'_{\text{tot}} = {} & \gamma H_t N_m \left[\tfrac{1}{2}\bar{Z}_v \beta\,(1 + a + r - ar) + \tfrac{1}{2}\zeta_{hi}\bar{Z}_h G_n\right] \\ & + r^2 \gamma H_t N_r \left[\tfrac{1}{6}\mu_m t_u r H_t \left(\tfrac{1}{G_n} + \varpi\right) + \tfrac{1}{2}\tfrac{\bar{Z}_v}{G_n}\right], \end{aligned}$$

whilst the external work term, from equation (6.51) becomes

$$\lambda^{-1} E'_{\text{tot}} = \gamma H_t^2 t_u \left[N_m \left(\tfrac{1}{2}a\beta + \tfrac{1}{6}\tfrac{1-r^3}{G_n}\right) + N_r \left(\tfrac{1}{3}r^3\varpi\right)\right].$$

That both of these terms are directly proportional to the unit weight γ means that λ_o becomes independent of the density of the material and solely dependent on unit geometry and frictional properties. In fact, this is the case for all non-loadbearing DSM walls, regardless of the mechanism used for the analysis.

Dividing the above expressions for internal and external work by γH_t and evaluating, gives

$$\begin{aligned}(\gamma H_t)^{-1} U'_{\text{tot}} &= 2 \times \Big[\tfrac{1}{2} \times 788.0\,\text{mm}^2 \times 1.18 \times (1 + 0.15 + 0.292 - 0.15 \times 0.292) \\ &\quad + 1/2 \times 1 \times 607.3\,\text{mm}^2 \times 0.7068\Big] \\ &\quad + (0.292)^2 \times 2 \times \Big[\tfrac{1}{6} \times 0.71 \times 39.7\,\text{mm} \times 0.292 \times 338\,\text{mm} \\ &\quad \times (1/0.7068 + 0) \\ &\quad + \tfrac{1}{2} \times 788.0\,\text{mm}^2/0.7068\Big] \\ &= 1,935\,\text{mm}^2,\end{aligned}$$

and

$$\begin{aligned}(\gamma H_t)^{-1} \lambda^{-1} E'_{\text{tot}} &= 338\,\text{mm} \times 39.7\,\text{mm} \times \Big[2 \times \Big(\tfrac{1}{2} \times 0.15 \times 0.292 \\ &\quad + \tfrac{1}{6}\left(1 - (0.292)^3\right)/0.7068\Big) + 0\Big] \\ &= 8,555\,\text{mm}^2.\end{aligned}$$

From this, the collapse multiplier is evaluated as

$$\lambda_o = \frac{1,935\,\text{mm}^2}{8,555\,\text{mm}^2} = 0.226.$$

In this example, λ_o has been calculated using arbitrarily chosen values of the independent variables a, ϖ and H_t. By using the optimisation tool SOLVER in EXCEL, the critical solution is shown to be $\lambda_o = 0.224$, occurring for $a = 0.160$, $\varpi = 0$ and $H_t = 365\,\text{mm}$. Although the height H_t corresponds to a non-integer value for the number of brick courses ($365\,\text{mm}/28.2\,\text{mm} = 12.9$), accepting such a solution is conservative, in that any deviation from the optimal values of independent variables will result in a higher value of λ_o.

G.4.2 Example 2: Loadbearing Walls

Figure G.18 shows examples of different types of overburden load conditions and the resulting implications toward the parameters used in the analysis. In Figures

G.18a and G.18b, the wall is subjected to an overburden load using joists supported by the façade panel and return walls, respectively. In both of these cases, the joists are unrestrained from lateral movement and therefore they are able to perform additional external work on the wall. In Figure G.18c, the joists are supported by on the façade panel; however, they are restrained from lateral movement. This example considers the two cases where the joists are supported by the façade panel.

Problem

Recalculate λ_o for the same wall as used in Example 1 (Section G.4.1), if it is subjected to each of the loadbearing conditions described below. In each scenario, the overburden load is applied onto the façade through eight equally spaced joists as shown in Figures G.18a and G.18c, with each joist exerting a vertical reaction of 16.46 N. Assume that the joists place the load at the midpoint of the wall's cross section. There is no loading on the return walls.

Consider the following situations:

A. *The joists are restrained from horizontal motion (Figure G.18c) and the surface between the joists and wall is smooth enough that any friction should be ignored ($\mu_o = 0$).*

B. *As in Part A, the joists are restrained (Figure G.18c), but the surface between the joists and wall provides some frictional resistance. Assume a friction coefficient of $\mu_o = 0.4$.*

C. *The joists are not restrained against lateral movement (Figure G.18a) and the ratio of the total overburden weight to the resulting vertical reaction is $\eta_m = 1.3$.*

Apply mechanism J *and use the same values for a, ω and H_t as were used in Example 1.*

Solution Steps Common to All Three Parts

Values of certain parameters can be directly retained from Example 1, including: $\bar{Z}_v$, $\bar{Z}_h$ and G_n, since the type of masonry remains unchanged; n_{vs}, N_m, N_r and L_w, since the wall geometry is unchanged and; β and r, since we are assuming the same values for a, ω and H_t. The main differences between the analysis of a loadbearing wall as opposed to a non-loadbearing wall are that in the case of a loadbearing wall, the full stress capacity function must be used including the σ_{vo} term [equation (6.22)], and furthermore, that the additional terms in the internal and external work due to e'_m and e'_r can potentially become active depending on the nature of the overburden load's restraint.

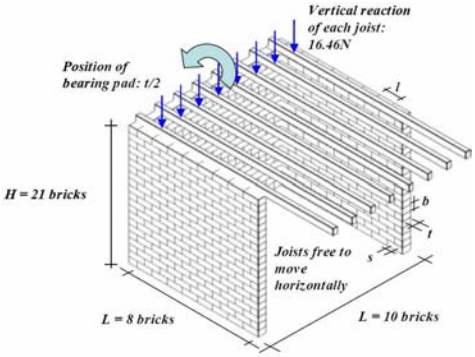

(a) Wall R35. Joists present on main wall and free to move horizontally; hence $\Phi_m = 1$. Due to the position of the weights along the joists, $\eta_m = 1.3$ (from the lever arm ratio).

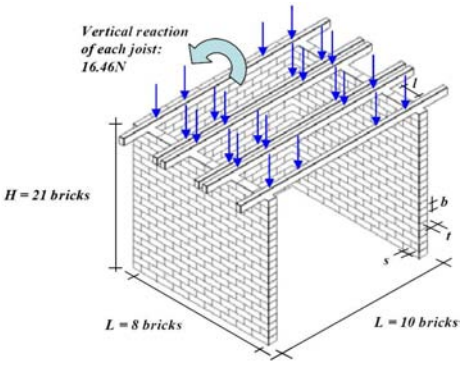

(b) Wall R36. Joists present on return wall and free to move horizontally; hence $\Phi_r = 1$. Weights are evenly distributed between the left and right return walls; therefore, $\eta_r = 1.0$.

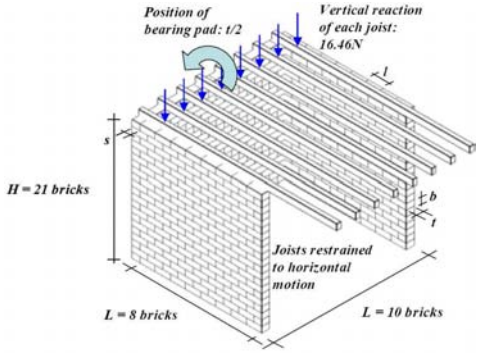

(c) Wall R41. Joists present on main wall and restrained from moving horizontally; hence $\Phi_m = 0$. Since the overburden load cannot perform work on the wall, the η_m factor becomes irrelevant.

Figure G.18: Examples of various types of overburden load conditions and the resulting influence on parameters used in the analysis. The shown walls correspond to test walls R35, R36 and R41 tested by *Restrepo Vélez and Magenes* [2009] (Graphics used with permission from IUSS Press.).

By making the assumption that the joists are spaced closely enough so that a uniformly distributed load develops at the top of the wall, the acting stress can be calculated the total load spread over the out-of-plane wall's total bedded area, as

$$\sigma_{vom} = 8 \times 16.46\,\mathrm{N} / \left(10 \times 79.8\,\mathrm{mm} \times 39.7\,\mathrm{mm}\right) = 4.156 \times 10^{-3}\,\mathrm{N/mm^2}.$$

From equation (6.48), the e'_m term is

$$\begin{aligned} e'_m &= \tfrac{1}{2} \times (1 + 0.15 + 0.292 - 0.15 \times 0.292) \times 399\,\mathrm{mm} \times 39.7\,\mathrm{mm} \\ &\quad \times 4.156 \times 10^{-3}\,\mathrm{N/mm^2} \\ &= 46.05\,\mathrm{N}. \end{aligned}$$

There is no overburden load being supported by the return walls ($\sigma_{vor} = 0$); therefore $e'_r = 0$.

Since the joists apply the vertical load at the centre of the wall's cross section, the eccentricity parameter ϵ is taken as $1/2$. Hence, the rotational restraint factor along the vertical edge [from equation (6.27)] becomes $R_{ts} = 0$. As a result, the term $R_{ts}\boldsymbol{f}\langle 0 \rangle$ in equation (6.50) does not provide an internal work contribution.

Next, the stress capacity function $\boldsymbol{f}\langle d \rangle$ needs to be evaluated using equation (6.22) for the various arguments of d occurring in the internal work term, given by equation (6.50). A question then arises, whether σ_{vom} or σ_{vor} should be assigned as σ_{vo} in equation (6.22) for the internal work contribution along the vertical edges themselves. Whilst the flow of the applied stress through the masonry panel is complex and could be calculated to a better accuracy using more refined methods, the approach used here and recommended by the author is a simplified one, where the stress applied to the main wall σ_{vom} is used for all cracks along the main wall (the $\boldsymbol{f}\langle \cdots \rangle$ terms in the internal work expression which are multiplied by N_m) and the stress applied to the return wall σ_{vor} is used for all cracks along the return wall ($\boldsymbol{f}\langle \cdots \rangle$ terms which are multiplied by N_r). The user may otherwise choose to implement a more refined approach if required.

The two $\boldsymbol{f}\langle \cdots \rangle$ terms for the out-of-plane wall evaluate to

$$\begin{aligned} \boldsymbol{f}\left\langle \tfrac{1}{2}(1 + a + r - ar)H_t \right\rangle &= 4.156 \times 10^{-3}\,\mathrm{N/mm^2} \\ &\quad + \tfrac{1}{2} \times (1 + 0.15 + 0.292 - 0.15 \times 0.292) \\ &\quad \times 338\,\mathrm{mm} \times 26.8 \times 10^{-6}\,\mathrm{N/mm^3} \\ &= 10.50 \times 10^{-3}\,\mathrm{N/mm^2}, \end{aligned}$$

$$\begin{aligned} f\langle \tfrac{1}{2}H_t\rangle &= 4.156\times10^{-3}\,\mathrm{N/mm^2} \\ &\quad + \tfrac{1}{2}\times 338\,\mathrm{mm}\times 26.8\times10^{-6}\,\mathrm{N/mm^3} \\ &= 8.694\times10^{-3}\,\mathrm{N/mm^2}. \end{aligned}$$

Noting that

$$H_r = rH_t = 0.292\times 338\,\mathrm{mm} = 98.7\,\mathrm{mm},$$

and that no vertical precompression is acting on the return walls, the two $f\langle\cdots\rangle$ terms for the in-plane component of the mechanism [introduced through equation (6.36)] are evaluated as follows:

$$\begin{aligned} f\langle \tfrac{1}{2}H_r\rangle &= 0 + \tfrac{1}{2}\times 98.7\,\mathrm{mm}\times 26.8\times10^{-6}\,\mathrm{N/mm^3} = 1.323\times10^{-3}\,\mathrm{N/mm^2}, \\ f\langle \tfrac{1}{3}H_r\rangle &= 0 + \tfrac{1}{3}\times 98.7\,\mathrm{mm}\times 26.8\times10^{-6}\,\mathrm{N/mm^3} = 0.8818\times10^{-3}\,\mathrm{N/mm^2}. \end{aligned}$$

Solution for Part A—Restrained OBL with Frictionless Connection

Since the overburden load is restrained ($\Phi_m = 0$), there is no external work contribution from e'_m. As the boundary surface has been assumed to be smooth ($\mu_o = 0$), the frictional internal work term due to e'_m is also zero. Hence, the only influence of the overburden load is the strengthening effect due to an increase in the crack capacities and the associated $f\langle\cdots\rangle$ terms.

The total internal work from equation (6.50) incorporating equation (6.36) evaluates to

$$\begin{aligned} U'_{\mathrm{tot}} &= 2\times\big[788.0\,\mathrm{mm^2}\times 1.18\times 10.50\times10^{-3}\,\mathrm{N/mm^2} \\ &\qquad + 1\times 607.3\,\mathrm{mm^2}\times 0.7068\times 8.694\times10^{-3}\,\mathrm{N/mm^2} \\ &\qquad + 0\big] \\ &\quad + 2\times\Big[0.292\times\big[\tfrac{1}{2}\times 0.71\times 39.7\,\mathrm{mm}\times 98.7\,\mathrm{mm}\times\big(\tfrac{1}{0.7068}+0\big) \\ &\qquad \times 0.8818\times10^{-3}\,\mathrm{N/mm^2} \\ &\qquad + \tfrac{788.0\,\mathrm{mm^2}}{0.7068}\times 1.323\times10^{-3}\,\mathrm{N/mm^2}\big] \\ &\qquad + 0\Big] \\ &= 28.85\,\mathrm{N}. \end{aligned}$$

The external work in this case is the same as in Example 1, which by using the earlier result[2], gives

$$\lambda^{-1}E'_{\mathrm{tot}} = 8,555\,\mathrm{mm^2}\times 26.8\times10^{-6}\,\mathrm{N/mm^3}\times 338\,\mathrm{mm} = 77.59\,\mathrm{N}.$$

[2]Where the external work term had been divided by λH_t.

Therefore, the collapse multiplier becomes

$$\lambda_o = \frac{28.85\,\text{N}}{77.59\,\text{N}} = 0.372.$$

Using EXCEL'S SOLVER, the critical collapse multiplier is found to be $\lambda_o = 0.316$ (for $a = 0.132$, $\varpi = 0$ and $H_t = 465\,\text{mm}$) which corresponds to a 41% increase in strength compared to the non-loadbearing wall from Example 1. This increase in strength is solely caused by the increased crack capacities due to the additional axial load.

Solution for Part B—Restrained OBL with Frictional Connection ($\mu_o = 0.4$)

In this scenario, there is a further strengthening effect relative to Part A, due to the friction developed between the top of the wall and the joists. This increase in strength is accounted for by the additional internal work term

$$\begin{aligned} N_m \left[(1 - \Phi_m)\,\mu_o e'_m\right] &= 2 \times [(1-0) \times 0.4 \times 46.05\,\text{N}] \\ &= 36.84\,\text{N}. \end{aligned}$$

Adding this to the internal work computed in Part A and dividing by the external work, results in

$$\lambda_o = \frac{28.85\,\text{N} + 36.84\,\text{N}}{77.59\,\text{N}} = 0.847.$$

This value is more than double of that previously calculated in Part A where the boundary friction was neglected and the same values of a, ϖ and H_t were used. Using EXCEL'S SOLVER, the critical solution is found to be $\lambda_o = 0.521$, occurring at the values $a = 0.266$, $\varpi = 1.41$ and $H_t = 592\,\text{mm}$. In this case, conducting the minimisation process alleviates λ_o quite significantly; however, the overall increase in strength relative to Part A is still considerable. At the optimal state, the mechanism spans the wall's full height of 21 courses and the angle of the in-plane shear crack follows the natural diagonal slope of the masonry ($\varpi = 1/G_n$). This result indicates that frictional restraint along the top edge of the out-of-plane wall makes it energetically feasible for the mechanism to adopt a form tending more toward shear failure of the in-plane walls as opposed to flexural failure of the out-of-plane panel.

Solution for Part C—Unrestrained OBL with Orthogonal Factor of $\eta_m = 1.3$

In this scenario, the wall undergoes a weakening effect since it must resist a horizontal component of the OBL. When conducting an analysis using the equations

presented in Section 6.5, it is assumed that the strength of the connection between the joists and wall is sufficient to generate full transfer of horizontal load (i.e. that slip between wall and OBL will not occur). As the load is unrestrained, Φ_m is taken as 1. The corresponding additional external work term becomes

$$N_m \left(\Phi_m \eta_m e'_m\right) = 2 \times (1 \times 1.3 \times 146.05\,\text{N}) = 119.74\,\text{N}.$$

Noting that the internal work remains unchanged from Part A and adding the above contribution to the external work already calculated in Part A, gives

$$\lambda_o = \frac{28.85\,\text{N}}{77.59\,\text{N} + 119.74\,\text{N}} = 0.146.$$

Using EXCEL'S SOLVER, the critical solution is found to be $\lambda_o = 0.143$, occurring at $a = 0.232$, $\varpi = 0$ and $H_t = 355$ mm. This corresponds to a 55% strength reduction compared to the scenario in Part A in which the load was assumed to be restrained.

G.5 ADDITIONAL PARAMETRIC STUDY RESULTS

Figures G.19 and G.20 provide results for additional parametric studies to compliment the discussions in Section 6.7. The results are for the same type of wall configuration as the analyses used to generate Figures 6.21 and 6.22 (i.e. based on walls R7–R10 tested by Restrepo Vélez); however, with different fixed length and height dimensions of the mechanism. For varied H_t (Figures G.19a and G.20a), L_e was kept fixed such that $L_e/l_u = 3$ and $L_e/t_u = 6.0$. For varied L_e (Figures G.19b and G.20b), H_t was kept fixed such that $H_t/h_u = 21$ and $H_t/t_u = 14.9$.

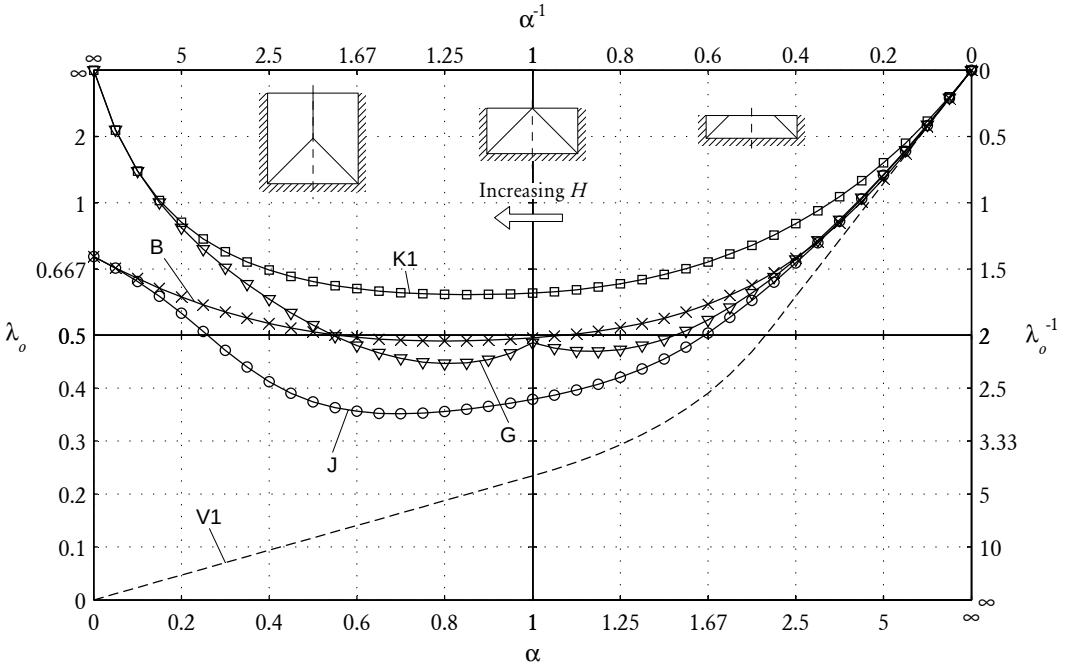

(a) Varied H_t (for fixed $L_e/l_u = 3$ bricks, $L_e/t_u = 6.0$).

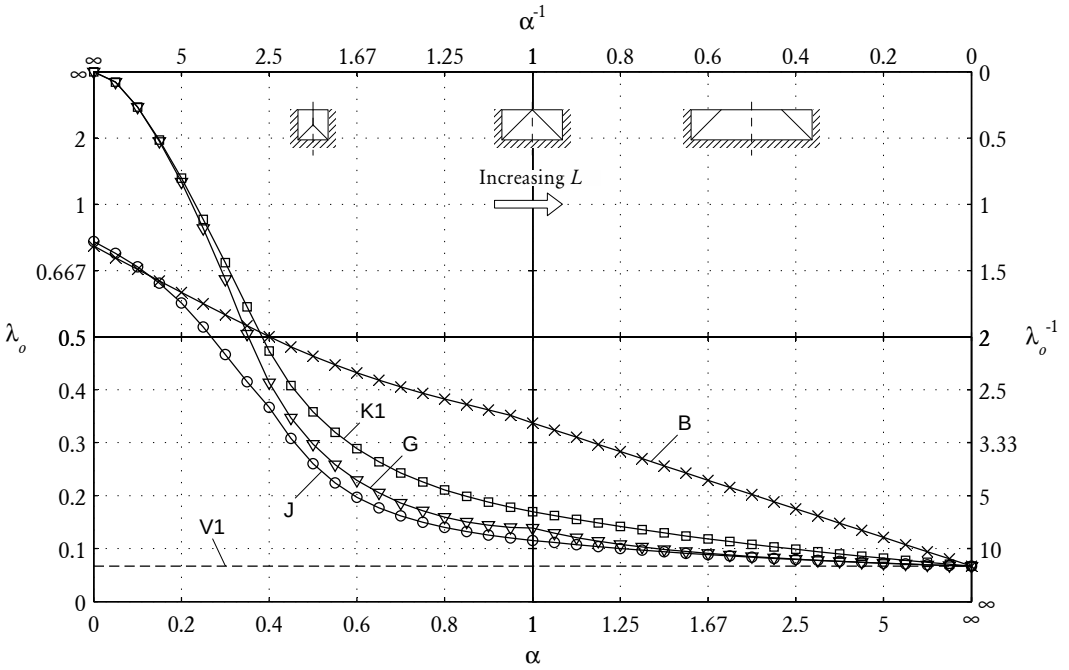

(b) Varied L_e (for fixed $H_t/h_u = 21$ courses, $H_t/t_u = 14.9$).

Figure G.19: Parametric study implementing a weight-proportional stress capacity function. This is representative of non-loadbearing DSM or mortar-bonded URM with very weak bond cohesion.

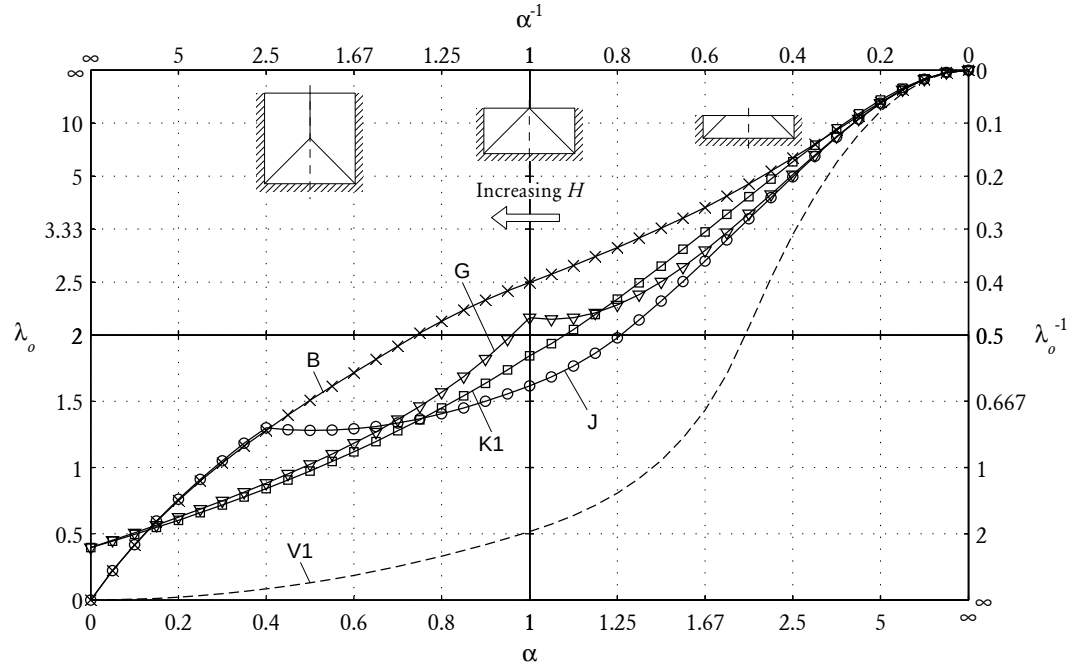

(a) Varied H_t (for fixed $L_e/l_u = 3$ bricks, $L_e/t_u = 6.0$).

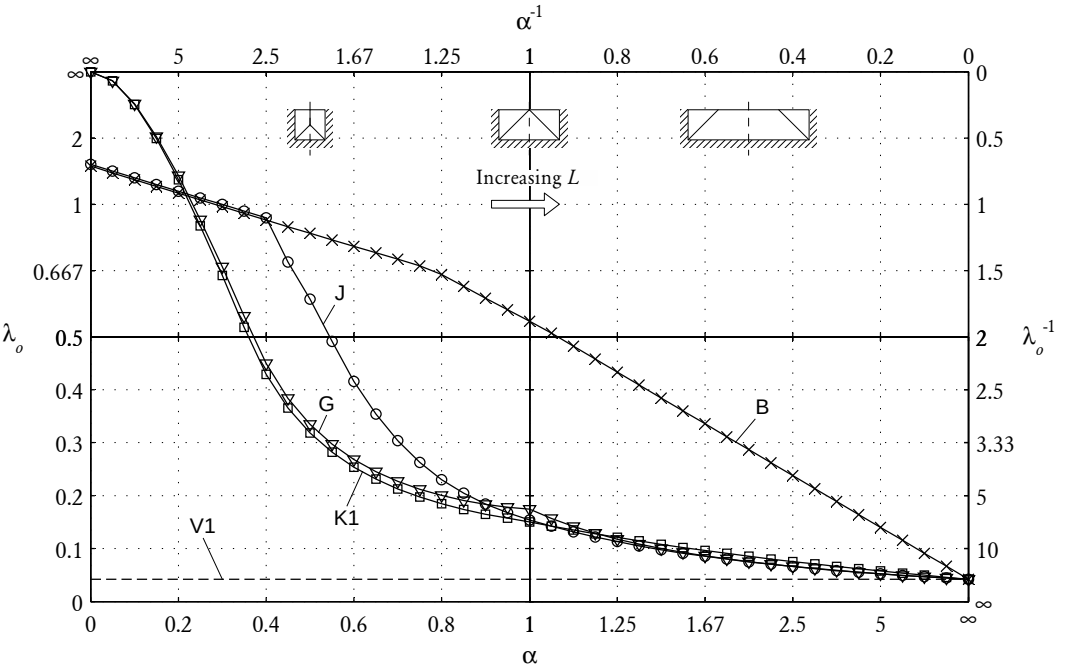

(b) Varied L_e (for fixed $H_t/h_u = 21$ courses, $H_t/t_u = 14.9$).

Figure G.20: Parametric study implementing a constant stress capacity function. This is analogous to mortar-bonded URM with strong bond cohesion.

Appendix H

LOAD-DISPLACEMENT MODELLING

Abstract

This appendix contains additional detail related to Chapter 7.

H.1 LOAD-DISPLACEMENT CAPACITY BASED ON ROCKING

This appendix contains derivations of the load-displacement relationships for the rocking component of a wall's response presented in Table 7.1. The relationships are derived for the full family of type K mechanisms (discussed in Section 6.2.3 and illustrated by Figure 6.3), which are subdivided into: type K1 where, the top edge of the wall is unrestrained; and type K2, where the top edge is laterally restrained. Each of these types are further subcategorised into their x and y forms, $\mathsf{K1}_\mathsf{x}/\mathsf{K1}_\mathsf{y}$ and $\mathsf{K2}_\mathsf{x}/\mathsf{K2}_\mathsf{y}$, with x occurring for a high L/H aspect ratio ($\alpha \geq 1$) and y occurring for a low aspect ratio ($\alpha \leq 1$).

H.1.1 General

Sources of Resistance

The derived relationships are based on the rocking response of blocks comprising each mechanism. As a lateral load and displacement are applied to the wall, the blocks rotate about some fixed set of pivot points. The resulting uplift of the blocks provides a restoration moment and therefore resistance to the applied load. This corresponds to the r-component (Section 7.2.1) of the wall's overall load-displacement capacity model presented in Section 7.2.

Allowance is also made for the presence of an overburden load (OBL) at the top of the wall with respect to the considerations outlined in Section 6.3.2. These include:

- Enhancement of the wall's general strength due to increased restoration moment;
- Ability of the OBL to act as an additional unrestrained mass along the top edge of the wall (possible for type K1 mechanisms only); and
- Control over the vertical line of action of the OBL by the eccentricity parameter ϵ (refer to Figure 6.6).

Note that throughout the derivations for the type K1 mechanisms (Section H.1.3), allowance is also made for the presence of a restoring frictional force exerted onto the wall by a restrained OBL, which effectively corresponds to the s-component described in Section 7.2.3. Because of its frictional nature, this load becomes always oriented opposite to the wall's motion and therefore has inelastic hysteresis. As such, it is not a part of the wall's *elastic* resistance due to rocking. Nonetheless, this frictional force is still included during the derivation process, as it is easily separated from the elastic rocking component at the end of the derivation.

Frictional resistance from horizontal bending is ignored in the presented derivations; however, its contribution is included in the overall load-displacement capacity model as an additional inelastic component whose capacity may be calculated using the virtual work method (the h-component described in Section 7.2.2).

Symbolic Notation

The load-displacement relationships are derived in the λ-δ format, with λ as defined by equation (2.3) and δ defined by equation (2.2).

For definition of properties related to overburden loads, including overburden weight ratio ψ, degree-of-freedom (DOF) factor Φ, orthogonal factor η, and eccentricity factor ϵ, the reader is referred to Section 6.3.2.

Properties specifically related to the type K mechanisms, including L_e, H_e, H_t, a, r and α, are defined in Section 6.5.

Derivation Strategy

The first step of the derivation process is to formulate equations of force equilibrium for a generic cross section of the mechanism when subjected to a known reference

displacement δ and an unknown lateral load multiplier λ. The geometry of a cross section is expressed in terms of a dimensionless shape parameter ρ, which varies along the horizontal position x according to a known relationship. By considering a vertical strip with thickness $\mathrm{d}x$, a moment equilibrium equation is derived in the differential form $\mathrm{d}M/\mathrm{d}x$ in terms of only δ, λ and ρ and other known constants. The differential moment equation is then integrated along x, so that the zero net moment condition is satisfied for the overall mechanism, which leads to an equation relating λ to δ.

Assumptions

The following general assumptions are made:

1. The wall is subjected to a uniformly distributed lateral load according to its mass, to reflect the inertial nature of seismic loading.[1]
2. Wall deformations are assumed to be limited to rotations about crack lines, and the sub-plates forming the mechanism are assumed to act as rigid blocks.
3. Horizontal and diagonal cracks are assumed to undergo rotations with stresses being concentrated along the extreme compressive fibre of the section.
4. Moment contributions from vertical cracks where horizontal bending may be present are ignored, and furthermore, supported vertical edges are assumed to provide only simple support without any moment restraint.
5. As described previously, in the derivation process the wall is discretised into a series of vertical strips. It is assumed that both the lateral and vertical inertia-based external forces applied onto each strip are transmitted to the supported horizontal (top or bottom) edges of the wall within the strip itself. In other words, there is no net flow of these forces between adjacent strips.

H.1.2 Type K2 Mechanisms ($\mathrm{K2_x}$ and $\mathrm{K2_y}$)

Equilibrium Equations for a Vertical Strip

Consider mechanisms $\mathrm{K2_x}$ and $\mathrm{K2_y}$ when subjected to the maximum surface displacement Δ_c (Figure H.1). The cross section of a generic vertical strip with thickness $\mathrm{d}x$, taken along either of the mechanisms, is shown by Figure H.2. The shape of the

[1] In the type K1 mechanisms, where the top edge is free, allowance is made for the possibility that an unrestrained OBL could apply additional horizontal loading to the wall.

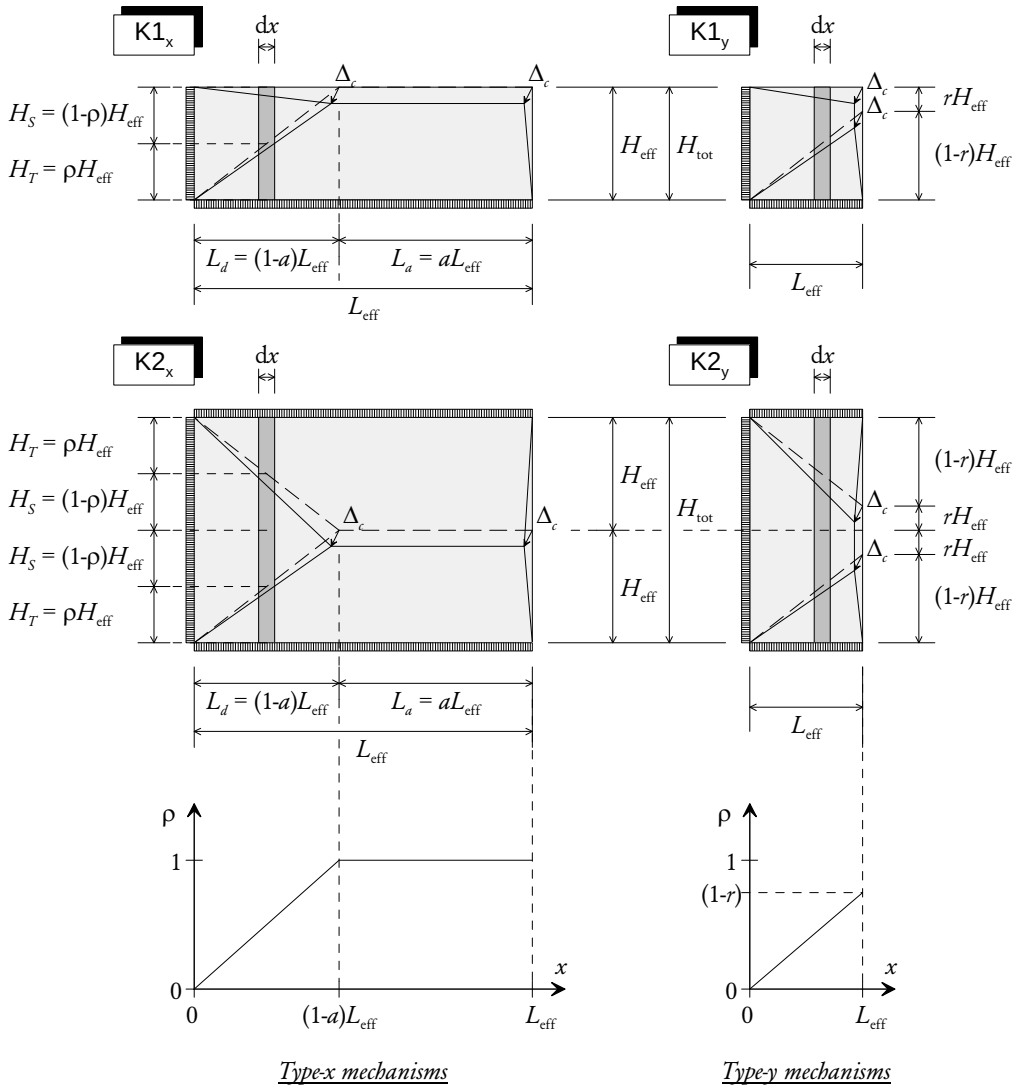

Figure H.1: Class K mechanisms ($K1_x$, $K1_y$, $K2_x$ and $K2_y$) subjected to the maximum surface displacement Δ_c. The shape of a generic vertical cross section is dependent on ρ, which varies along x as shown.

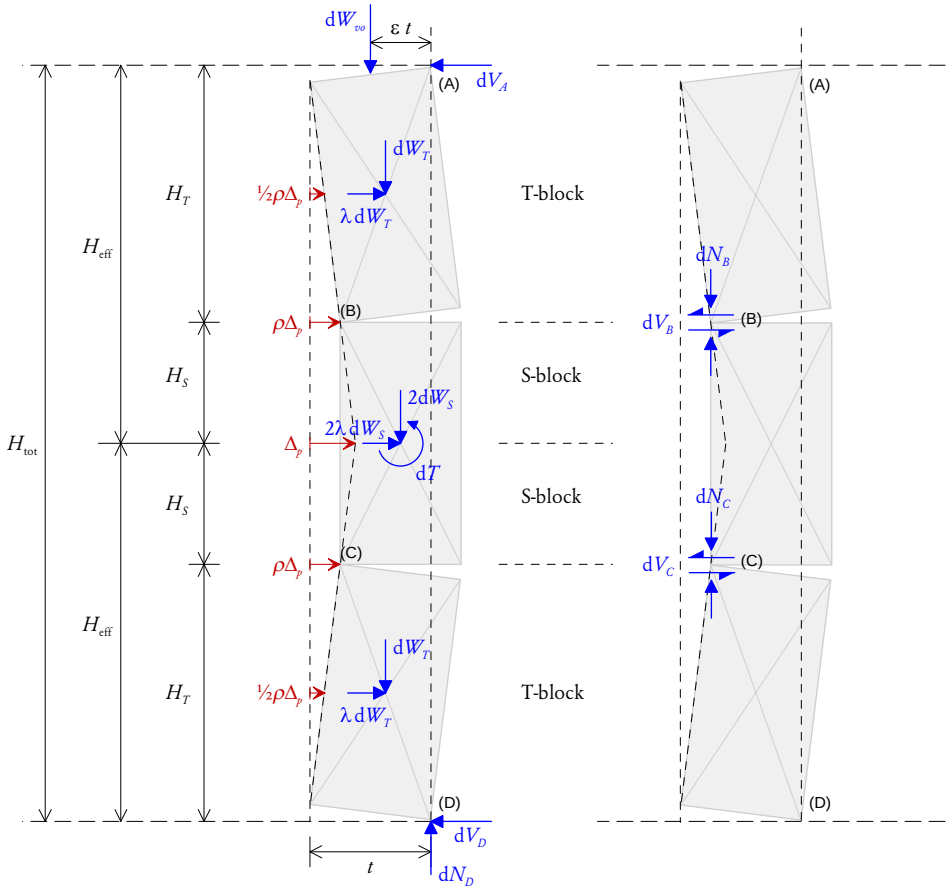

Figure H.2: Generic cross section for mechanisms $\mathsf{K2}_\mathsf{x}$ and $\mathsf{K2}_\mathsf{y}$.

cross section relates to the parameter ρ, which varies along the horizontal position x and can assume values in the range $0 \leq \rho \leq 1$. When the section cuts across the diagonal cracks ($\rho < 1$) the cross section effectively consists of three rigid blocks: two individual T-blocks and a pair of combined S-blocks forming a single rigid block.

Since mechanisms $\mathsf{K2}_\mathsf{x}$ and $\mathsf{K2}_\mathsf{y}$ have both of their top and bottom horizontal edges supported, the deflected shape becomes mirrored by the horizontal line along the mid-height. Therefore, as per equation (6.39), the effective height H_e is equal to

$$H_e = \frac{1}{2} H_t \quad \text{(for type K2 mechanisms).} \tag{H.1}$$

The various block heights and incremental weights may subsequently be defined in terms of H_e.

BLOCK HEIGHTS Referring to Figures H.1 and H.2, the height of a T-block is

$$H_T = \rho H_e, \tag{H.2}$$

and the height a single S-block is

$$H_S = (1 - \rho)\, H_e. \tag{H.3}$$

BLOCK WEIGHTS For a strip of thickness $\mathrm{d}x$, the effective weight $\mathrm{d}W_{\text{eff}}$ (which is used as the reference weight in the derivations) is defined as weight over the effective height H_e, such that

$$\mathrm{d}W_{\text{eff}} = \mathrm{d}x\, t\, H_e\, \gamma, \tag{H.4}$$

where t is the thickness of the wall, and γ is the weight density of the masonry material. From this, the height of a T-block is

$$\mathrm{d}W_T = \rho\, \mathrm{d}W_{\text{eff}}, \tag{H.5}$$

and the height of a single S-block is

$$\mathrm{d}W_S = (1 - \rho)\, \mathrm{d}W_{\text{eff}}. \tag{H.6}$$

The total weight over the full height H_t is therefore

$$\mathrm{d}W_{\text{tot}} = 2\, \mathrm{d}W_{\text{eff}} \quad \text{(for type K2 mechanisms)}. \tag{H.7}$$

Noting equation (6.1), the weight of the overburden load, $\mathrm{d}W_{vo}$, is related to the OBL weight ratio ψ through the expression

$$\psi = \frac{\mathrm{d}W_{vo}}{\mathrm{d}W_{\text{tot}}}, \tag{H.8}$$

which gives

$$\mathrm{d}W_{vo} = 2\psi\, \mathrm{d}W_{\text{eff}} \quad \text{(for type K2 mechanisms)}. \tag{H.9}$$

DISPLACEMENTS Throughout the derivations, it is convenient to measure the displacement profile along the height of a generic cross section with respect a projected reference displacement Δ_p, as defined in the respective Figures H.2 and H.3. This reference displacement is related to the maximum surface displacement

along the overall mechanism, Δ_c, according to

$$\Delta_c = \begin{cases} \Delta_p, & \text{for the x-form mechanisms } \mathsf{K1_x} \text{ and } \mathsf{K2_x}, \\ (1-r)\,\Delta_p, & \text{for the y-form mechanisms } \mathsf{K1_y} \text{ and } \mathsf{K2_y}. \end{cases} \tag{H.10}$$

As stated previously, the first aim of the derivation is to obtain an expression for $\mathrm{d}M/\mathrm{d}x$, where $\mathrm{d}M$ is the moment taken about a fixed axis. For this, the axis passing through point A will be used (Figure H.2), as its global position remains fixed regardless of ρ. The unknown variables include the following external reactions:

- horizontal force reactions at the top and bottom edges, $\mathrm{d}V_A$ and $\mathrm{d}V_D$;
- vertical force reaction at the base, $\mathrm{d}N_D$; and
- moment $\mathrm{d}T$ which keeps the combined S-blocks in rotational equilibrium and is transferred to the adjacent vertical edge support;

As well as the unknown internal forces:

- shear forces $\mathrm{d}V_B$ and $\mathrm{d}V_C$; and
- axial forces $\mathrm{d}N_B$ and $\mathrm{d}N_C$.

The last unknown is the lateral load multiplier, λ. This gives a total of nine unknowns, which can be solved for using the nine available equations of equilibrium (three equilibrium equations for each of the three rigid blocks).

STEP 1 Take moment equilibrium for the combined S-blocks about point C, to obtain a relationship between $\mathrm{d}T$ and $\mathrm{d}V_B$ in terms of λ:

$$\begin{aligned} 0 &= \sum M_\mathrm{C} \\ 0 &= \mathrm{d}T - 2\,\mathrm{d}W_S \times \tfrac{1}{2}t - 2\lambda\,\mathrm{d}W_S \times (1-\rho)\,H_e \\ &\quad + \mathrm{d}V_B \times 2\,(1-\rho)\,H_e. \end{aligned} \tag{H.11}$$

STEP 2 Take vertical force equilibrium for top T-block:

$$\begin{aligned} 0 &= \sum F_y \\ 0 &= \mathrm{d}N_B - \mathrm{d}W_{vo} - \mathrm{d}W_T, \end{aligned} \tag{H.12}$$

which enables direct solution for $\mathrm{d}N_B$, such that

$$\mathrm{d}N_B = (2\psi + \rho)\,\mathrm{d}W_\mathrm{eff}. \tag{H.13}$$

STEP 3 Take moment equilibrium for the free body consisting of the combined S-blocks and the bottom T-block about point D in order to obtain a second relationship between $\mathrm{d}T$ and $\mathrm{d}V_B$ in terms of λ:

$$\begin{aligned} 0 &= \sum M_{\mathrm{D}} \\ 0 &= \mathrm{d}T + \mathrm{d}V_B \times (2-\rho)\, H_e - 2\lambda\, \mathrm{d}W_S \times H_e \\ &\quad - \mathrm{d}W_T \lambda \times \tfrac{1}{2}\rho H_e + \mathrm{d}N_B \times \left(t - \rho\Delta_p\right) \\ &\quad + 2\,\mathrm{d}W_S \times \left(\tfrac{1}{2}t - \rho\Delta_p\right) + \mathrm{d}W_T \times \left(\tfrac{1}{2}t - \tfrac{1}{2}\rho\Delta_p\right). \end{aligned} \tag{H.14}$$

The two equations (H.11) and (H.14) contain only two unknowns, $\mathrm{d}T$ and $\mathrm{d}V_B$; hence, they can be solved simultaneously. Substituting $\mathrm{d}N_B$ from equation (H.13) into (H.14) and solving for $\mathrm{d}V_B$ gives

$$\mathrm{d}V_B = \frac{1}{2}\frac{\mathrm{d}W_{\mathrm{eff}}}{\rho H_e}\left(-4t + \rho t + 4\lambda H_e \rho - 3\rho^2 \lambda H_e - 4\psi t + 4\psi\rho\Delta_p - \rho^2\Delta_p + 4\rho\Delta_p\right). \tag{H.15}$$

STEP 4 Take moment equilibrium for the top T-block about point A, in order to obtain an expression for the moment increment $\mathrm{d}M$:

$$\begin{aligned} \mathrm{d}M &= \sum M_{\mathrm{A}} \\ \mathrm{d}M &= \mathrm{d}W_{vo} \times \epsilon\, t + \mathrm{d}W_T \times \left(\tfrac{1}{2}t - \tfrac{1}{2}\rho\Delta_p\right) + \lambda\, \mathrm{d}W_T \times \tfrac{1}{2}\rho H_e \\ &\quad + \mathrm{d}V_B \times \rho H_e - \mathrm{d}N_B \times \left(t - \rho\Delta_p\right). \end{aligned} \tag{H.16}$$

The axis along point A remains fixed regardless of ρ; therefore, it will be possible to subsequently integrate $\mathrm{d}M$ to obtain the total moment for the top sub-plate in the respective mechanisms $\mathsf{K2}_{\mathsf{x}}$ and $\mathsf{K2}_{\mathsf{y}}$. Into the above equation, substitute $\mathrm{d}N_B$ [from equation (H.13)], $\mathrm{d}V_B$ [from equation (H.15)], $\mathrm{d}W_{\mathrm{eff}}$ [from equation (H.4)] and replace $\Delta_p = \delta_p t$. After rearranging, we get

$$\begin{aligned} \frac{1}{\gamma t^2 H_e} \cdot \frac{\mathrm{d}M}{\mathrm{d}x} &= [2\psi\epsilon - 2\psi - 2] \\ &\quad + \rho\left[4\psi\delta_p + 2\delta_p + 2\lambda\frac{H_e}{t}\right] \\ &\quad + \rho^2\left[-\lambda\frac{H_e}{t}\right], \end{aligned} \tag{H.17}$$

This is the fundamental equation relating λ to δ for the generic mechanism K2 cross section (Figure H.2). All parameters in this equation are physical constants, except for the independent variable δ; dependent variable λ; and shape parameter ρ, which is related to x according to the relationships shown in Figure H.1. Equation

(H.17) is a second order polynomial with respect to ρ; hence, it is convenient to express it in terms of its coefficients as

$$\frac{\mathrm{d}M}{\mathrm{d}x} = \gamma t^2 H_e \left(C_0 + C_1\rho + C_2\rho^2\right) \equiv \mathcal{R}_{\mathsf{K2}}\langle\rho\rangle, \tag{H.18}$$

where

$$C_0 = \left[2\psi\epsilon - 2\psi - 2\right], \quad C_1 = \left[4\psi\delta_p + 2\delta_p + 2\lambda\frac{H_e}{t}\right], \quad C_2 = \left[-\lambda\frac{H_e}{t}\right]. \tag{H.19}$$

For simplicity, equation (H.18) together with its coefficients (H.19) will be referred to using the notation $\mathcal{R}_{\mathsf{K2}}\langle\rho\rangle$. This equation will now be integrated for the $\mathsf{K2}_\mathsf{x}$ and $\mathsf{K2}_\mathsf{y}$ mechanisms to obtain their respective λ-δ relationships.

Mechanism $\mathsf{K2}_\mathsf{x}$

The total moment of a free body corresponding to the top sub-plate taken about point A (Figure H.2) is obtained by summing the integrals of $\mathcal{R}_{\mathsf{K2}}\langle\rho\rangle$ [equation (H.18)] over the diagonal crack region and the central horizontal crack region (refer to Figure H.1). To satisfy moment equilibrium this sum must equal zero; therefore

$$0 = \underbrace{\int_0^{L_d} \mathcal{R}_{\mathsf{K2}}\left\langle \tfrac{1}{L_d}x \right\rangle \mathrm{d}x}_{=\mathcal{I}_1} + \underbrace{\int_0^{L_a} \mathcal{R}_{\mathsf{K2}}\langle 1\rangle \,\mathrm{d}x}_{=\mathcal{I}_2}. \tag{H.20}$$

The first integral, $\mathcal{I}_1$, corresponds to diagonal crack region where the shape parameter ρ is dependent on the horizontal position such that $\rho = x/L_d$, with L_d being the horizontal projection of the diagonal crack (refer to Figure H.1). The second integral, $\mathcal{I}_2$, corresponds to the central horizontal crack region along which $\rho = 1$ and where L_a is the length of the central horizontal crack.

Evaluating $\mathcal{I}_1$ gives

$$\begin{aligned}
\mathcal{I}_1 &= \int_0^{L_d} \mathcal{R}_{\mathsf{K2}}\left\langle \tfrac{1}{L_d}x \right\rangle \mathrm{d}x \\
&= \gamma t^2 H_e \int_0^{L_d} \left(C_0 + C_1\frac{1}{L_d}x + C_2\frac{1}{L_d^2}x^2\right) \mathrm{d}x \\
&= \gamma t^2 H_e\, L_d \left[C_0 + \tfrac{1}{2}C_1 + \tfrac{1}{3}C_2\right],
\end{aligned} \tag{H.21}$$

and evaluating $\mathcal{I}_2$ gives

$$\mathcal{I}_2 = \int_0^{L_a} \mathcal{R}_{\mathsf{K2}}\langle 1\rangle \,\mathrm{d}x$$

$$= \gamma t^2 H_e \int_0^{L_a} (C_0 + C_1 + C_2)\, \mathrm{d}x$$
$$= \gamma t^2 H_e\, L_a \left[C_0 + C_1 + C_2\right]. \tag{H.22}$$

Adding $\mathcal{I}_1$ and $\mathcal{I}_2$, as per equation (H.20), and substituting $L_a = aL_e$ and $L_d = (1-a)\, L_e$ results in

$$0 = C_0 + C_1 \left(\tfrac{1}{2} + \tfrac{1}{2}a\right) + C_2 \left(\tfrac{1}{3} + \tfrac{2}{3}a\right). \tag{H.23}$$

This equation ensures that moment equilibrium is satisfied for mechanism $\mathsf{K2}_\mathsf{x}$. By substituting coefficients C_0, C_1 and C_2, given by equations (H.19), into equation (H.23), we get

$$\begin{aligned} 0 = {} & [2\psi\epsilon - 2\psi - 2] \\ & + \left[4\psi\delta_p + 2\delta_p + 2\lambda\frac{H_e}{t}\right]\left(\tfrac{1}{2} + \tfrac{1}{2}a\right) \\ & + \left[-\lambda\frac{H_e}{t}\right]\left(\tfrac{1}{3} + \tfrac{2}{3}a\right). \end{aligned}$$

Rearranging in terms of λ and making the substitutions $\delta_p = \delta_c$ [from equation (H.10)] and $H_e = \frac{1}{2}H_t$ [from equation (H.1)], gives

$$\lambda = \lambda_\mathsf{r} = \frac{t}{H_t} \cdot \frac{4\left[1 + \psi\left(2 - \epsilon\right)\right] - \delta_c \left[2\left(1 + a\right)\left(1 + 2\psi\right)\right]}{\frac{2}{3} + \frac{1}{3}a}. \tag{H.24}$$

This defines the fundamental elastic rocking λ-δ relationship in the positive displacement range ($\delta > 0$). The ultimate load resistance from rocking, λ_{ro}, occurs at the limit

$$\lambda_{ro} = \lim_{\delta \to 0^+} \lambda_\mathsf{r},$$

which, due to the continuous nature of the equation with respect to δ, is obtained simply by assigning $\delta = 0$. This yields

$$\lambda_{ro} = \frac{t}{H_t} \cdot \frac{4\left[1 + \psi\left(2 - \epsilon\right)\right]}{\frac{2}{3} + \frac{1}{3}a}. \tag{H.25}$$

The rocking instability displacement δ_{ru}, defined as the displacement at which $\lambda_\mathsf{r} = 0$, is equal to

$$\delta_{ru} = \frac{2\left[1 + \psi\left(2 - \epsilon\right)\right]}{\left(1 + a\right)\left(1 + 2\psi\right)}. \tag{H.26}$$

Mechanism $\mathsf{K2_y}$

The total moment of the top sub-plate taken about point A (Figure H.2) is obtained by integrating $\mathcal{R}_{\mathsf{K2}}\langle\rho\rangle$ [equation (H.18)] over the diagonal crack region (refer to Figure H.1). In the y-form mechanisms $\mathsf{K2_y}$ and $\mathsf{K1_y}$, the cross sectional shape parameter ρ varies along the horizontal position x according to

$$\rho = \left(\frac{1-r}{L_e}\right) x = \left(\frac{\alpha}{L_e}\right) x,$$

where r is the shape parameter for the y-form mechanisms as illustrated in Figure H.1, and α is the normalised mechanism aspect ratio defined by equation (6.44). Therefore, in order to satisfy moment equilibrium, the equation

$$0 = \int_0^{L_e} \mathcal{R}_{\mathsf{K2}} \left\langle \frac{\alpha}{L_e} x \right\rangle \mathrm{d}x \tag{H.27}$$

must hold. Evaluating, yields

$$\begin{aligned} 0 &= \int_0^{L_e} \left(C_0 + C_1 \frac{\alpha}{L_e} x + C_2 \frac{\alpha^2}{L_e^2} x^2 \right) \mathrm{d}x \\ &= \gamma t^2 H_e L_e \left[C_0 + \tfrac{1}{2}\alpha C_1 + \tfrac{1}{3}\alpha^2 C_2 \right], \end{aligned}$$

from which we get the moment equilibrium equation

$$0 = C_0 + \tfrac{1}{2}\alpha C_1 + \tfrac{1}{3}\alpha^2 C_2, \tag{H.28}$$

which is applicable to both mechanisms $\mathsf{K2_y}$ and $\mathsf{K1_y}$ when used with their respective C coefficients. For mechanism $\mathsf{K2_y}$, coefficients C_0, C_1 and C_2 as given by equations (H.19) are substituted into (H.28), yielding

$$\begin{aligned} 0 = {} & [2\psi\epsilon - 2\psi - 2] \\ & + \tfrac{1}{2}\alpha \left[4\psi\delta_p + 2\delta_p + 2\lambda \frac{H_e}{t} \right] \\ & + \tfrac{1}{3}\alpha^2 \left[-\lambda \frac{H_e}{t} \right]. \end{aligned}$$

Rearranging in terms of λ and making the substitutions $\delta_c = \alpha\delta_p$ [from equation (H.10)], $H_e = \frac{1}{2}H_t$ [from equation (H.1)], and $\alpha = 1 - r$ [from equation (6.59)], gives

$$\lambda = \lambda_{\mathsf{r}} = \frac{t}{H_t} \cdot \frac{4\left[1 + \psi\left(2 - \epsilon\right)\right] - \delta_c \left[2\left(1 + 2\psi\right)\right]}{\alpha\left(\frac{2}{3} + \frac{1}{3}r\right)}. \tag{H.29}$$

This is the elastic rocking λ-δ relationship in the positive displacement range ($\delta > 0$). The corresponding ultimate load resistance λ_{ro} is determined by assigning $\delta = 0$, which yields

$$\lambda_{ro} = \frac{t}{H_t} \cdot \frac{4\left[1 + \psi\left(2 - \epsilon\right)\right]}{\alpha\left(\frac{2}{3} + \frac{1}{3}r\right)}. \tag{H.30}$$

The rocking instability displacement δ_{ru} is obtained by assigning $\lambda = 0$, as

$$\delta_{ru} = \frac{2\left[1 + \psi\left(2 - \epsilon\right)\right]}{1 + 2\psi}. \tag{H.31}$$

H.1.3 Type K1 Mechanisms ($K1_x$ and $K1_y$)

Equilibrium Equations for a Vertical Strip

Consider mechanisms $K1_x$ and $K1_y$, when subjected to a maximum surface displacement Δ_c, as shown in Figure H.1. The generic cross sectional shape, shown by Figure H.3, relates to the parameter ρ, which varies along the horizontal position in the mechanism and may assume values within the range $0 \leq \rho \leq 1$. Two cross sections need to be considered: (i) $\rho < 1$, where the vertical component of the overburden load dW_{vo} acts upon the S-block (Figure H.3a); and (ii) $\rho = 1$ (occurring only in mechanism $K1_x$), where dW_{vo} acts directly on the T-block (Figure H.3b). The reason that these sections need to be considered separately is that dW_{vo} produces a different amount of moment about the rotating T-block in each case.

Since mechanisms $K1_x$ and $K1_y$ have only one of their horizontal edges supported, the effective height becomes equal to the full height [as per equation (6.39)]. Therefore, we have

$$H_e = H_t \quad \text{(for type K1 mechanisms)}. \tag{H.32}$$

Similarly, the weight of a strip of thickness dx is

$$dW_{\text{eff}} = dW_{\text{tot}} \quad \text{(for type K1 mechanisms)}. \tag{H.33}$$

Combining equation (H.8) with (H.33) gives

$$dW_{vo} = \psi\, dW_{\text{eff}} \quad \text{(for type K1 mechanisms)}. \tag{H.34}$$

Several equations presented previously for type K2 mechanisms are also applicable to type K1 mechanisms, including heights of the T and S blocks (H_T and H_S) [equations (H.2) and (H.3)], effective weight dW_{eff} [equation (H.4)], and weights of the T and S blocks (dW_T and dW_S) [equations (H.5) and (H.6)]. For convenience,

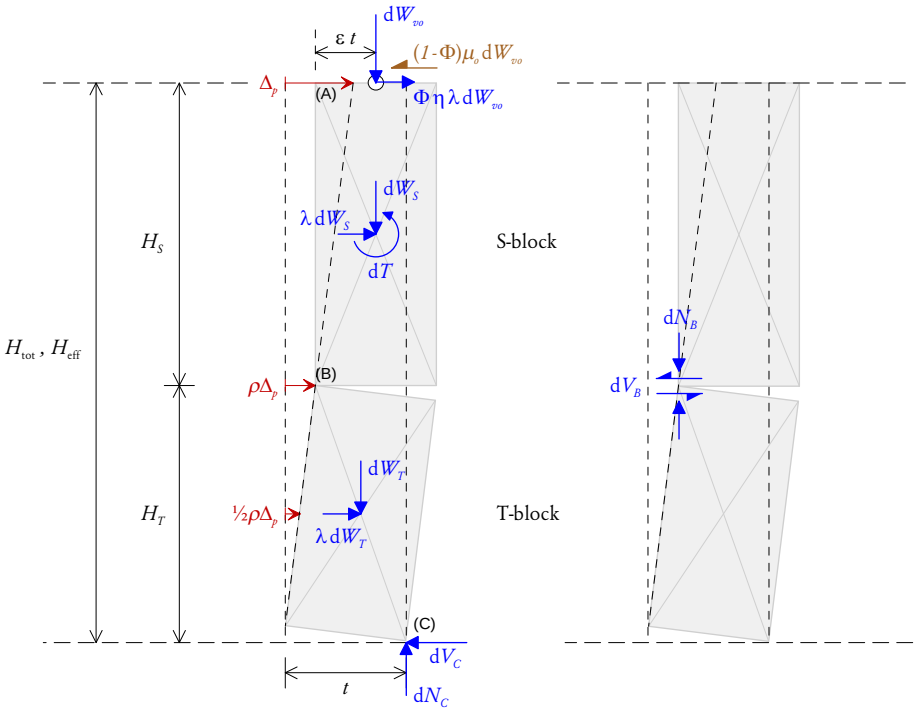

(a) Case for $\rho < 1$ (Overburden load dW_{vo} acting upon the S-block).

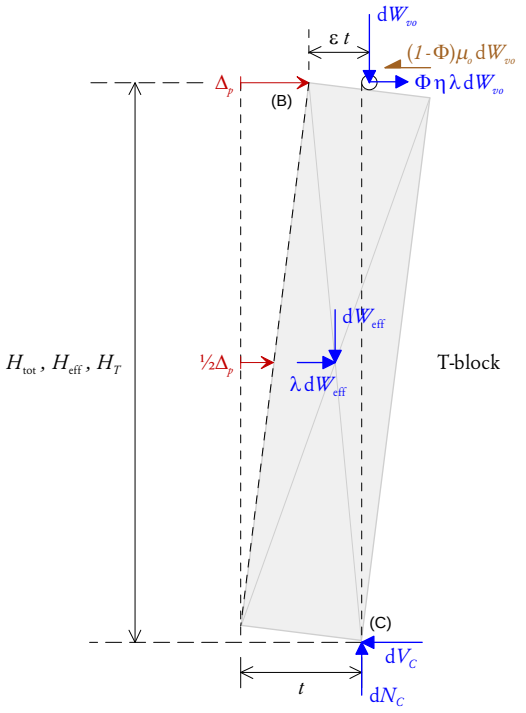

(b) Case for $\rho = 1$ (Overburden load dW_{vo} acting upon the T-block).

Figure H.3: Generic cross section for mechanisms $K1_x$ and $K1_y$. Orientation of the inelastic frictional force between the wall and OBL assumes that wall movement is in the same direction as its displacement.

the projected displacement at the top edge Δ_p is used as the reference displacement along the cross section (Figure H.3). This displacement is related to the maximum surface displacement Δ_c through equation (H.10).

To derive an expression for $\mathrm{d}M/\mathrm{d}x$ for a generic cross section, the axis along point C (Figure H.3) will be used, since its global position remains fixed regardless of ρ. The two cases shown by Figures H.3a and H.3b need to be considered individually. Steps 1–3 lead to the derivation of the $\mathrm{d}M/\mathrm{d}x$ expression for the first case ($\rho < 1$), whilst step 4 considers the second case ($\rho = 1$).

In the case where $\rho < 1$, the unknown variables include the external reactions $\mathrm{d}N_C$, $\mathrm{d}V_C$ and $\mathrm{d}T$; internal forces $\mathrm{d}V_B$ and $\mathrm{d}N_B$; and λ. These six unknowns can be solved for using the six available equations of equilibrium (three equations for each of the two blocks).

STEP 1 In the case where $\rho < 1$, take vertical force equilibrium of the S-block:

$$\begin{aligned} 0 &= \sum F_y \\ 0 &= \mathrm{d}N_B - \mathrm{d}W_S - \mathrm{d}W_{vo}, \end{aligned} \tag{H.35}$$

which allows for direct solution for $\mathrm{d}N_B$, such that

$$\mathrm{d}N_B = (1 - \rho + \psi)\,\mathrm{d}W_{\text{eff}}. \tag{H.36}$$

STEP 2 Take horizontal force equilibrium of the S-block (for $\rho < 1$):

$$\begin{aligned} 0 &= \sum F_x \\ 0 &= \Phi\eta\lambda\,\mathrm{d}W_{vo} - (1 - \Phi)\,\mu_o\,\mathrm{d}W_{vo} + \lambda\,\mathrm{d}W_S - \mathrm{d}V_B. \end{aligned} \tag{H.37}$$

This provides $\mathrm{d}V_B$ in terms of λ, such that

$$\mathrm{d}V_B = [\Phi\eta\lambda\psi - (1 - \Phi)\,\mu_o\psi + \lambda\,(1 - \rho)]\,\mathrm{d}W_{\text{eff}}. \tag{H.38}$$

STEP 3 Take moment equilibrium of the T-block about point C, in order to determine an expression for the increment of moment $\mathrm{d}M$ for this particular case (i.e. $\rho < 1$):

$$\begin{aligned} \mathrm{d}M &= \sum M_{\mathrm{C}} \\ \mathrm{d}M &= \mathrm{d}N_B \times \left(t - \rho\Delta_p\right) - \mathrm{d}V_B \times \rho H_e \\ &\qquad + \mathrm{d}W_T \times \left(\tfrac{1}{2}t - \tfrac{1}{2}\rho\Delta_p\right) - \lambda\,\mathrm{d}W_T \times \tfrac{1}{2}\rho H_e. \end{aligned} \tag{H.39}$$

The axis along point C remains fixed regardless of ρ; therefore, it will be possible to subsequently integrate $\mathrm{d}M$ to obtain the total moment for the bottom sub-plate in the respective mechanisms $\mathsf{K1}_\mathsf{x}$ and $\mathsf{K1}_\mathsf{y}$. Substitute in $\mathrm{d}N_B$ [from equation (H.36)], $\mathrm{d}V_B$ [from equation (H.38)], $\mathrm{d}W_{\text{eff}}$ [from equation (H.4)] and replace $\Delta_p = \delta_p t$. After rearranging, we get

$$\begin{aligned}\frac{1}{\gamma t^2 H_e}\cdot\frac{\mathrm{d}M}{\mathrm{d}x} = {}& [1+\psi] \\ & + \rho\left[-\tfrac{1}{2} - \delta_p - \psi\delta_p - \lambda\frac{H_e}{t}\left(1+\Phi\eta\psi\right) + \frac{H_e}{t}\left(1-\Phi\right)\mu_o\psi\right] \\ & + \rho^2\left[\tfrac{1}{2}\delta_p + \tfrac{1}{2}\lambda\frac{H_e}{t}\right].\end{aligned} \tag{H.40}$$

This is the fundamental equation relating λ to δ for the K1 cross section when $\rho < 1$ (Figure H.3a). The equation is a second order polynomial with respect to ρ; hence, it is convenient to express it in terms of its coefficients, such that

$$\frac{\mathrm{d}M}{\mathrm{d}x} = \gamma t^2 H_e\left(C_0 + C_1\rho + C_2\rho^2\right) \equiv \mathcal{R}_{\mathsf{K1},\rho<1}\langle\rho\rangle, \tag{H.41}$$

where

$$\begin{aligned}C_0 &= [1+\psi], \\ C_1 &= \left[-\tfrac{1}{2} - \delta_p - \psi\delta_p - \lambda\frac{H_e}{t}\left(1+\Phi\eta\psi\right) + \frac{H_e}{t}\left(1-\Phi\right)\mu_o\psi\right], \\ C_2 &= \left[\tfrac{1}{2}\delta_p + \tfrac{1}{2}\lambda\frac{H_e}{t}\right].\end{aligned} \tag{H.42}$$

For simplicity, equation (H.41) together with its coefficients (H.42) will be referred to using the notation $\mathcal{R}_{\mathsf{K1},\rho<1}\langle\rho\rangle$.

STEP 4 In order to determine an expression for the increment of moment $\mathrm{d}M$ for the case where $\rho = 1$ (Figure H.3b), take moment equilibrium of the T-block about point C:

$$\begin{aligned}\mathrm{d}M &= \sum M_\mathrm{C} \\ \mathrm{d}M &= \mathrm{d}W_{vo}\times\left(t\left(1-\epsilon\right)\Delta_p\right) - \Phi\eta\lambda\,\mathrm{d}W_{vo}\times H_e + \left(1-\Phi\right)\mu_o\,\mathrm{d}W_{vo}\times H_e \\ &\quad + \mathrm{d}W_{\text{eff}}\times\left(\tfrac{1}{2}t - \tfrac{1}{2}\Delta_p\right) - \lambda\,\mathrm{d}W_{\text{eff}}\times\tfrac{1}{2}H_e.\end{aligned} \tag{H.43}$$

Note that the only difference between this case and $\rho < 1$ (Figure H.3a) is the length of the lever arm at which the overburden load $\mathrm{d}W_{vo}$ acts on the rotating

T-block. When $\rho < 1$, the force $\mathrm{d}W_{vo}$ is always transferred to the T-block at the hinge point B (Figure H.3), regardless of the value of ϵ. However, when $\rho = 1$, $\mathrm{d}W_{vo}$ is transferred to the T-block at the specific point as defined by ϵ.

Next, substitute $\mathrm{d}W_{\text{eff}}$ from equation (H.4) into equation (H.43) and replace $\Delta_p = \delta_p t$. This gives

$$\begin{aligned}\frac{1}{\gamma t^2 H_e} \cdot \frac{\mathrm{d}M}{\mathrm{d}x} &= \tfrac{1}{2} - \tfrac{1}{2}\delta_p + \psi - \psi\epsilon - \psi\delta_p - \lambda\frac{H_e}{t}\left(\tfrac{1}{2} + \Phi\eta\psi\right) + \frac{H_e}{t}\left(1 - \Phi\right)\mu_o\psi \\ &\equiv K_0,\end{aligned} \tag{H.44}$$

where the right-hand side of the equation will be abbreviated as K_0. Alternatively, the above can be written as

$$\frac{\mathrm{d}M}{\mathrm{d}x} = \gamma t^2 H_e K_0 \equiv \mathcal{R}_{\mathsf{K1},\rho=1}, \tag{H.45}$$

which we shall denote using the notation $\mathcal{R}_{\mathsf{K1},\rho=1}$. Since ρ is constant in this case ($\rho = 1$) with respect to x, the moment derivative equation $\mathcal{R}_{\mathsf{K1},\rho=1}$ is also constant.

Mechanism $\mathsf{K1_x}$

Moment equilibrium for the bottom sub-plate in mechanism $\mathsf{K1_x}$ is satisfied when the following holds:

$$0 = \underbrace{\int_0^{L_d} \mathcal{R}_{\mathsf{K1},\rho<1}\left\langle \tfrac{1}{L_d}x \right\rangle \mathrm{d}x}_{=\mathcal{I}_1} + \underbrace{\int_0^{L_a} \mathcal{R}_{\mathsf{K1},\rho=1}\,\mathrm{d}x}_{=\mathcal{I}_2}. \tag{H.46}$$

The first integral, $\mathcal{I}_1$, corresponds to the diagonal crack region where $\rho = x/L_d$, with L_d being the horizontal projection of the diagonal crack (refer to Figure H.1). The second integral, $\mathcal{I}_2$, corresponds to portion of the mechanism along the length L_a (Figure H.1). Integral $\mathcal{I}_1$ has already been evaluated previously, resulting in equation (H.21). Noting that $\mathcal{R}_{\mathsf{K1},\rho=1}$ is independent of x, integral $\mathcal{I}_2$ evaluates to

$$\mathcal{I}_2 = \gamma t^2 H_e\, L_a K_0. \tag{H.47}$$

Adding $\mathcal{I}_1$ and $\mathcal{I}_2$, and substituting $L_a = aL_e$ and $L_d = (1-a)\,L_e$ gives

$$0 = (1-a)\left[C_0 + \tfrac{1}{2}C_1 + \tfrac{1}{3}C_2\right] + aK_0. \tag{H.48}$$

This equation ensures that moment equilibrium is satisfied for mechanism $\mathsf{K1_x}$. Substituting coefficients C_0, C_1 and C_2, as per equations (H.42) and K_0 from equation

(H.44), results in

$$\begin{aligned}0 = {} & (1-a)\left[1+\psi\right] \\ & + (1-a)\left[-\tfrac{1}{2} - \delta_p - \psi\delta_p - \lambda\frac{H_e}{t}\left(1+\Phi\eta\psi\right) + \frac{H_e}{t}\left(1-\Phi\right)\mu_o\psi\right] \\ & + (1-a)\left[\tfrac{1}{2}\delta_p + \tfrac{1}{2}\lambda\frac{H_e}{t}\right] \\ & + a\left[\tfrac{1}{2} - \tfrac{1}{2}\delta_p + \psi - \psi\epsilon - \psi\delta_p - \lambda\frac{H_e}{t}\left(\tfrac{1}{2}+\Phi\eta\psi\right) + \frac{H_e}{t}\left(1-\Phi\right)\mu_o\psi\right].\end{aligned}$$

Rearranging in terms of λ and making the substitutions $\delta_p = \delta_c$ [from equation (H.10)] and $H_e = H_t$ [from equation (H.32)], gives

$$\lambda = \frac{t}{H_t}\cdot\frac{\left[\frac{3}{2} - \frac{1}{2}a + 2\psi\left(1-a\epsilon\right)\right] - \delta_c\left[\frac{2}{3} + \frac{1}{3}a + \psi\left(1+a\right)\right] + \frac{H_t}{t}\left(1-\Phi\right)\mu_o\psi\left(1+a\right)}{\frac{2}{3} + \frac{1}{3}a + \Phi\eta\psi\left(1+a\right)}. \tag{H.49}$$

We can split this relationship into the separate components

$$\lambda = \lambda_{\mathrm{r}} + \lambda_{so}, \tag{H.50}$$

where λ_{r} is the fundamental elastic rocking λ-δ relationship in the positive displacement range ($\delta > 0$), given by

$$\lambda_{\mathrm{r}} = \frac{t}{H_t}\cdot\frac{\left[\frac{3}{2} - \frac{1}{2}a + 2\psi\left(1-a\epsilon\right)\right] - \delta_c\left[\frac{2}{3} + \frac{1}{3}a + \psi\left(1+a\right)\right]}{\frac{2}{3} + \frac{1}{3}a + \Phi\eta\psi\left(1+a\right)}, \tag{H.51}$$

and λ_{so} is the capacity from the friction between the wall and OBL (active only when $\Phi = 0$), which is taken as

$$\lambda_{so} = \left(1-\Phi\right)\frac{\mu_o\psi\left(1+a\right)}{\frac{2}{3} + \frac{1}{3}a}. \tag{H.52}$$

The ultimate load resistance from rocking, λ_{ro}, is obtained by assigning $\delta = 0$ to equation (H.51), yielding

$$\lambda_{ro} = \frac{t}{H_t}\cdot\frac{\frac{3}{2} - \frac{1}{2}a + 2\psi\left(1-a\epsilon\right)}{\frac{2}{3} + \frac{1}{3}a + \Phi\eta\psi\left(1+a\right)}, \tag{H.53}$$

whilst the rocking instability displacement δ_{ru} is obtained by assigning $\lambda_{\mathrm{r}} = 0$ to equation (H.51), which gives

$$\delta_{ru} = \frac{\frac{3}{2} - \frac{1}{2}a + 2\psi\left(1-a\epsilon\right)}{\frac{2}{3} + \frac{1}{3}a + \psi\left(1+a\right)}. \tag{H.54}$$

Mechanism $\mathsf{K1_y}$

Moment equilibrium for mechanism $\mathsf{K1_y}$ is satisfied through equation (H.28) (previously used for mechanism $\mathsf{K2_y}$) by incorporating the coefficients for the K1 cross section, as per equations (H.42). Substituting these into equation (H.28) gives

$$\begin{aligned} 0 = {} & [1+\psi] \\ & + \tfrac{1}{2}\alpha \left[-\tfrac{1}{2} - \delta_p - \psi\delta_p - \lambda \frac{H_e}{t}\left(1 + \Phi\eta\psi\right) + \frac{H_e}{t}\left(1-\Phi\right)\mu_o\psi \right] \\ & + \tfrac{1}{3}\alpha^2 \left[\tfrac{1}{2}\delta_p + \tfrac{1}{2}\lambda\frac{H_e}{t} \right]. \end{aligned}$$

Rearranging in terms of λ and making the substitutions $\delta_c = \alpha\delta_p$ [from equation (H.10)], $H_e = H_t$ [from equation (H.32)], and $\alpha = 1 - r$ [from equation (6.59)], produces the expression

$$\lambda = \frac{t}{H_t} \cdot \frac{\left[\frac{3}{2} + \frac{1}{2}r + 2\psi\right] - \delta_c\left[\frac{2}{3} + \frac{1}{3}r + \psi\right] + \frac{H_t}{t}\left(1-\Phi\right)\mu_o\psi\alpha}{\alpha\left(\frac{2}{3} + \frac{1}{3}r + \Phi\eta\psi\right)}. \tag{H.55}$$

This may be split into λ_{r} and λ_{so}, as per equation (H.50), where

$$\lambda_{\mathsf{r}} = \frac{t}{H_t} \cdot \frac{\left[\frac{3}{2} + \frac{1}{2}r + 2\psi\right] - \delta_c\left[\frac{2}{3} + \frac{1}{3}r + \psi\right]}{\alpha\left(\frac{2}{3} + \frac{1}{3}r + \Phi\eta\psi\right)} \tag{H.56}$$

is the fundamental λ-δ relationship due to elastic rocking in the positive displacement range ($\delta > 0$), and

$$\lambda_{so} = \left(1-\Phi\right)\frac{\mu_o\psi}{\frac{2}{3} + \frac{1}{3}r} \tag{H.57}$$

is the capacity of the friction between the wall and OBL (active only when $\Phi = 0$). The ultimate strength λ_{ro} due to rocking is obtained by assigning $\delta = 0$ to equation (H.56), which yields

$$\lambda_{ro} = \frac{t}{H_t} \cdot \frac{\frac{3}{2} + \frac{1}{2}r + 2\psi}{\alpha\left(\frac{2}{3} + \frac{1}{3}r + \Phi\eta\psi\right)}. \tag{H.58}$$

The rocking instability displacement δ_{ru} is obtained by assigning $\lambda_{\mathsf{r}} = 0$ in equation (H.56), resulting in

$$\delta_{ru} = \frac{\frac{3}{2} + \frac{1}{2}r + 2\psi}{\frac{2}{3} + \frac{1}{3}r + \psi}. \tag{H.59}$$

H.2 INFLUENCE OF THE LOAD SHAPE FUNCTION ON THE LOAD CAPACITY

The modal response analysis procedure, which forms the basis for displacement-based (DB) seismic analysis, requires that the structure (i.e. the wall) is subjected to a loading pattern spatially distributed according to the acting inertial force. Under dynamic loading, the spatial distribution of the inertial force is in turn dependent on not only the mass distribution but also the mode shape, since regions of higher displacement will undergo proportionally higher accelerations.[2] However, the various load capacity prediction methods presented throughout this thesis have been based on the assumption that the acting load is spatially distributed directly according to the wall's mass (i.e. a uniform acceleration profile). These include the virtual work (VW) method, which was applied to prediction of the load capacity of mortar-bonded walls in Chapter 4 and dry masonry walls in Chapter 6; as well as the rocking load-displacement relationships derived in Appendix H.1.

A factor will now be derived, which for a given mode shape relates a force capacity based on a mass-proportional load distribution, to a force capacity based on a modal inertia-proportional load distribution. This derivation is made possible by the assumption that the mode shape, and therefore the internal work of the structure (wall), is independent of the loading function. It will be demonstrated that the resulting factor is in fact equivalent to the ratio of the effective mass and actual mass (M^*/M) used in the substitute structure approach [equation (7.41)]. A practical implication of this result is that the value of λ calculated using the λ-δ capacity relationships presented in Section 7.2, which are based on mass-proportional loading, can be used directly in the capacity spectrum (CS) method without the need for scaling of the capacity curve along the acceleration axis of the a-Δ diagram. This is demonstrated in Section 7.4.2. A similar simplification also results in the case of DB assessment using the secant stiffness approach, as demonstrated therein.

Consider a generic MDOF structure in a single spatial dimension, x, as shown in Figure H.4. Let the spatial distribution of the structure's mass M be defined according to the mass density function

$$\rho\langle x\rangle = \frac{\mathrm{d}M}{\mathrm{d}x}. \tag{H.60}$$

The deformation profile of the structure is defined by the displacement function $\Delta\langle x\rangle$ in accordance with the mode shape function $\Phi\langle x\rangle$, which are in turn related

[2] This is based on the assumption that the structure undergoes purely harmonic response, which is used in transformation of the actual multi-degree-of-freedom (MDOF) system to an equivalent single-degree-of-freedom (SDOF) system.

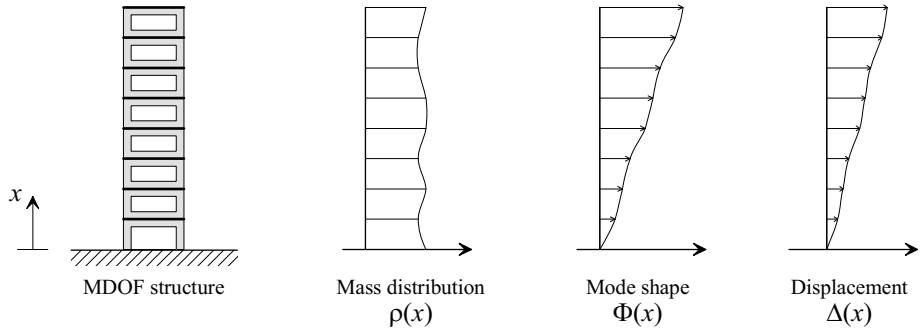

Figure H.4: MDOF structure and its spatially distributed properties.

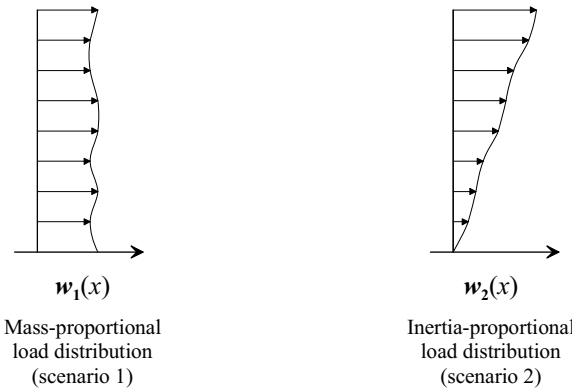

Figure H.5: The two alternative types of loading patterns.

by

$$\Phi\langle x\rangle = \frac{\Delta\langle x\rangle}{\Delta_{\text{ref}}}, \tag{H.61}$$

where Δ_{ref} is some reference displacement.

Let us denote the spatial distribution of the force F acting on the structure by the function

$$w\langle x\rangle = \frac{\mathrm{d}F}{\mathrm{d}x}, \tag{H.62}$$

and consider the following pair of loading scenarios shown by Figure H.5:

SCENARIO 1 The structure is subjected to a load function directly proportional to its mass distribution, such that

$$w_1\langle x\rangle = \rho\langle x\rangle\, a_1, \tag{H.63}$$

where a_1 is an acceleration scalar. This is analogous to the structure experiencing a uniform acceleration along x. In terms of seismic loading, this scenario assumes modal acceleration to be negligible compared to ground acceleration.

SCENARIO 2 The structure is subjected to a load function proportional to the modal inertia force (product of the mass and mode shape functions), such that

$$w_2\langle x\rangle = \rho\langle x\rangle\, \Phi\langle x\rangle\, a_2, \tag{H.64}$$

where a_2 is an acceleration scalar. In relation to seismic loading, this condition treats the ground acceleration as being negligible in comparison to the structure's modal acceleration, and corresponds to the loading scenario typically assumed in the modal response analysis.

In the general case, the external work done on the structure by the applied load is given by the integral

$$E = \int_X \mathrm{d}E, \tag{H.65}$$

where the external work increment $\mathrm{d}E$ is the product of the displacement and force increment, such that

$$\mathrm{d}E = \Delta\langle x\rangle\, \mathrm{d}F. \tag{H.66}$$

Combining equations (H.61), (H.65) and (H.66), the total external work becomes

$$E = \Delta_{\mathrm{ref}} \int_X \Phi\langle x\rangle\, w\langle x\rangle\, \mathrm{d}x. \tag{H.67}$$

Let us now consider the specific loading scenarios discussed previously, as shown in Figure H.5. The total external work for the first scenario is obtained by substituting equation (H.63) into (H.67), giving

$$E_1 = \Delta_{\mathrm{ref}}\, a_1 \int_X \Phi\langle x\rangle\, \rho\langle x\rangle\, \mathrm{d}x. \tag{H.68}$$

For the second scenario, substituting equation (H.64) into (H.67) gives

$$E_2 = \Delta_{\mathrm{ref}}\, a_2 \int_X (\Phi\langle x\rangle)^2\, \rho\langle x\rangle\, \mathrm{d}x. \tag{H.69}$$

However, since the structure is subjected to the same deformation function $\Delta\langle x\rangle$ in both of these scenarios, in each case it must undergo the same internal work U. From conservation of energy it therefore follows that

$$U = E_1 = E_2. \tag{H.70}$$

By equating equations (H.68) and (H.69), the ratio of the scalar accelerations a_1 and a_2 must be

$$\frac{a_2}{a_1} = \frac{\int_X \Phi\langle x\rangle \, \rho\langle x\rangle \, \mathrm{d}x}{\int_X \left(\Phi\langle x\rangle\right)^2 \rho\langle x\rangle \, \mathrm{d}x}. \tag{H.71}$$

In other words, the ratio a_2/a_1 must satisfy the above equation in order for both loading functions $w_1\langle x\rangle$ and $w_2\langle x\rangle$ to generate the same amount of external work.

Now consider the total force F (or base shear) resisted by the structure in the two scenarios. In the general case, the total force is obtained by the integral

$$F = \int_X \mathrm{d}F, \tag{H.72}$$

which, by noting equation (H.62), can also be expressed as

$$F = \int_X w\langle x\rangle \, \mathrm{d}x. \tag{H.73}$$

In the first scenario, the force resisted is obtained by substituting equation (H.63) into (H.73), which gives

$$F_1 = a_1 \int_X \rho\langle x\rangle \, \mathrm{d}x. \tag{H.74}$$

In the second scenario, substituting equation (H.64) into (H.73) gives

$$F_2 = a_2 \int_X \rho\langle x\rangle \, \Phi\langle x\rangle \, \mathrm{d}x. \tag{H.75}$$

Therefore, the ratio of the two force capacities becomes

$$\frac{F_2}{F_1} = \frac{a_2}{a_1} \cdot \frac{\int_X \rho\langle x\rangle \, \Phi\langle x\rangle \, \mathrm{d}x}{\int_X \rho\langle x\rangle \, \mathrm{d}x}. \tag{H.76}$$

Finally, substituting in a_2/a_1 from equation (H.71) and using F_o to denote the force capacity under uniform acceleration loading and F_o^* for the force capacity under modal acceleration loading, yields the formula

$$\frac{F_o^*}{F_o} = \frac{\left(\int_X \rho\langle x\rangle \, \Phi\langle x\rangle \, \mathrm{d}x\right)^2}{\left(\int_X \rho\langle x\rangle \, \mathrm{d}x\right)\left(\int_X \rho\langle x\rangle \, \left(\Phi\langle x\rangle\right)^2 \mathrm{d}x\right)}. \tag{H.77}$$

It can be seen that this ratio is equivalent to the ratio of the effective and actual mass used in transformation of the system from MDOF to SDOF in the substitute

structure approach [as per equation (7.41)]. That is,

$$\frac{F_o^*}{F_o} = \frac{M^*}{M}. \tag{H.78}$$

The implication of this result toward the DB assessment approach (either by the CS method or secant stiffness method) was discussed earlier.